# Unsteady multi-component simulations dedicated to the impact of the combustion chamber on the turbine of aeronautical gas turbines

Charlie Koupper


# THÈSE

**En vue de l'obtention du**

# DOCTORAT DE L'UNIVERSITÉ DE TOULOUSE

**Délivré par :**

Institut National Polytechnique de Toulouse (INP Toulouse)

**Discipline ou spécialité :**

Dynamique des fluides

---

## Présentée et soutenue par :

M. CHARLIE KOUPPER

le lundi 11 mai 2015

## Titre :

UNSTEADY MULTI-COMPONENT SIMULATIONS DEDICATED TO THE IMPACT OF THE COMBUSTION CHAMBER ON THE TURBINE OF AERONAUTICAL GAS TURBINES

---

**Ecole doctorale :**

Mécanique, Energétique, Génie civil, Procédés (MEGeP)

**Unité de recherche :**

CERFACS

**Directeur(s) de Thèse :**

M. LAURENT GICQUEL

**Rapporteurs :**

M. PASCAL BRUEL, UNIVERSITE DE PAU ET DES PAYS DE L ADOUR

M. TOM VERSTRAETE, VON KARMAN INSTITUTE RHODE SAINT GENESE

**Membre(s) du jury :**

M. LAURENT JOLY, ISAE TOULOUSE, Président

M. BRUNO FACCHINI, UNIVERSITA DEGLI STUDI DI FIRENZE, Membre

M. LAURENT GICQUEL, CERFACS, Membre

M. LI HE, UNIVERSITY OF OXFORD, Membre

# Remerciements

Cette thèse CIFRE a pu voir le jour grâce à une collaboration étroite entre Turbomeca (groupe SAFRAN), le CERFACS (Centre Européen de Recherche et de Formation Avancée en Calcul Scientifique) et l'Université de Florence, et je tiens à remercier chacun de ses membres qui y ont contribué.

Mes premiers remerciements vont aux membres du jury pour avoir accepté de juger et discuter de mes travaux de thèse lors de la soutenance à Toulouse, ouvrant des perspectives intéressantes pour la suite des recherches. Je remercie particulièrement les rapporteurs Pascal Bruel et Tom Verstraete pour leur travail de relecture et les suggestions proposées.

Je tiens à remercier chaleureusement Laurent Gicquel et Florent Duchaine pour leur encadrement académique rigoureux, dynamique et enrichissant. Ce fût un réél plaisir de travailler ensemble au cours de ces trois années. Merci également à Thierry Poinsot pour son aide et ses conseils sur l'étude NSCBC/équilibre radial. Je remercie sincèrement Guillaume Bonneau et Lorenzo Pons à Turbomeca pour m'avoir accordé leur pleine confiance, une grande autonomie et avoir systématiquement soutenu mes efforts, notamment pour le montage du banc d'essai FACTOR avec l'Université de Florence. J'adresse mes plus vifs remerciements à Jean-Louis Champion pour sa collaboration sur les aspects expérimentaux.

Vorrei ringraziare particolarmente Bruno Facchini e Lorenzo Tarchi per il mio soggiorno a Firenze dove ho scoperto la fisica sperimentale con specialisti. Ho anche incontrato ragazzi molto simpatici e veramente calorosi. Grazie mille Gianlu e Valentina per tutto. Vorrei anche dire grazie a Alessio, Riccardo, Tommaso, il cinese, e schifo guy ! Non sarà possibile dimenticare i miei tre mesi a Firenze, una città straordinaria con tanti simpatici amici. Spero tornare presto...

Il va sans dire que je tiens à saluer mes camarades de thèse du CERFACS, et particulièrement Thomas qui est devenu mon jovial acolyte de doctorat et également mon démystificateur de traitement du signal.

S'il est trivial de dire que sans eux rien n'aurait été possible, il n'en est pas moins important pour moi de remercier mes parents, mon frère Tom, mon pedescaou Julie, qui ont su m'épauler et m'accompagner particulièrement à la fin de ma thèse.

Mes pensées vont également à mes grands-parents avec qui j'aurais été fier de partager l'aboutissement de ces années d'études.

Charlie Koupper
Buros, le 23 mai 2015

# Preamble

This PhD work was performed within the framework of the FACTOR project (`www.factor-fp7.eu`) that has received funding from the European Union Seventh Framework Programme (FP7/ 2007-2013) under grant agreement number 265985.

This work was granted access to the HPC resources of IDRIS (`www.idris.fr`) under the allocation 2013-x20132b5031 made by GENCI (Grand Equipement National de Calcul Intensif).

# Contents

**Nomenclature** **ix**

**General introduction** **1**

**Part I An introduction to combustor turbine interactions** **9**

**Chapter 1 Literature review** **11**
1.1 The combustor and turbine modules . . . . . 12
1.1.1 Technological layout and flow characteristics . . . . . 12
1.1.2 Characterisation of the temperature field distortions . . . . . 15
1.2 Influence of the combustor on the turbine . . . . . 18
1.2.1 Research facilities dedicated to hot streak transport . . . . . 18
1.2.2 Main results of the past studies . . . . . 25
1.3 Influence of the vanes on the combustor . . . . . 34
1.3.1 Potential effect . . . . . 34
1.3.2 Acoustics . . . . . 37
1.4 Concluding remarks . . . . . 39

**Part II Development of an engine representative combustor simulator dedicated to hot streak generation** **43**

**Chapter 2 Design of the combustor simulator and preliminary assessment by LES** **45**
2.1 Design process of the combustor simulator for FACTOR . . . . . 46
2.1.1 Requirements and target . . . . . 47
2.1.2 Final design and operating conditions . . . . . 48
2.2 Numerical insight on the flow topologies with and without confinement 50
2.2.1 Set up of the LES . . . . . 50
2.2.2 Flow inside the chamber . . . . . 52
2.2.3 Duct effect on the swirler flow . . . . . 55
2.2.4 Hydrodynamic instability: the PVC . . . . . 58
2.3 Intermediate conclusions on the initial design phase . . . . . 62

**Chapter 3 Trisector test rig experimental validation and investigation** **63**

3.1 UNIFI trisector rig . . . 64
3.1.1 Presentation of the test facility . . . 64
3.1.2 Instrumentation . . . 65
3.2 Isothermal operating point . . . 70
3.2.1 Algebraic representation of the test rig . . . 70
3.2.2 Selection of the isothermal operating point . . . 75
3.2.3 Validation by LES . . . 77
3.3 Summary of the available experimental investigations . . . 84

**Chapter 4 Experimental flow characterization and validation of the computational approach 85**
4.1 Isothermal PIV inside the chamber . . . 86
4.2 Time-averaged aerothermal field in plane 40 . . . 90
4.2.1 Flow velocity . . . 91
4.2.2 Temperature field . . . 97
4.3 Conclusions . . . 99

**Part III Advanced diagnostics for the exploitation of the combustor simulator setup 101**

**Chapter 5 Sensitivity of the LES to the numerical parameters 103**
5.1 Numerical parameters under study . . . 104
5.1.1 Mesh . . . 104
5.1.2 Sub-grid scale model . . . 104
5.1.3 List of the cases . . . 106
5.2 LES quality criteria . . . 106
5.3 Prediction of the mean flow and turbulence . . . 109
5.3.1 Flow field inside the swirler . . . 110
5.3.2 Flow field in the chamber . . . 114
5.4 Comparison with experimental results . . . 117
5.4.1 PIV results in the central plane . . . 117
5.4.2 Swirl and temperature distortion in plane 40 . . . 119
5.5 Conclusions . . . 121

**Chapter 6 Advanced diagnostics for the numerical and experimental turbulence characterization 123**
6.1 Configurations under study and available data . . . 124
6.2 Turbulence intensity in plane 40 . . . 125
6.2.1 Assessment of the convergence . . . 125
6.2.2 Comparison between experiments and LES . . . 126
6.3 Evaluation of an integral scale of turbulence . . . 129
6.3.1 Methodology . . . 129
6.3.2 Sensitivity to the measurement parameters . . . 132
6.3.3 Comparison between experiments and LES . . . 136
6.4 Conclusions . . . 139

**Chapter 7 Advanced statistical representation of temperature 141**
7.1 Statistical framework . . . 142
7.2 Advanced characterization of the combustor temperature field . . . 146
7.2.1 Validation of the sampling . . . 147
7.2.2 Results and discussion . . . 147
7.2.3 Statistical representation of the radial profile of temperature 152
7.3 Conclusion . . . 154

**Part IV Integrated approach of the combustor-turbine interaction in LES 155**

**Chapter 8 Impact of the presence of vanes at the exit of the combustor simulator 157**
8.1 Geometry and mesh . . . 158
8.2 Influence of the clocking position . . . 161
8.2.1 Migration of the hot streak . . . 161
8.2.2 Vane surface temperature . . . 164
8.3 Potential effect induced by the vanes . . . 165
8.3.1 Mass flow distribution . . . 166
8.3.2 Temperature . . . 168
8.3.3 Turbulence level . . . 171
8.4 Conclusions . . . 175

**General conclusion and perspectives 177**

**Appendix A Characterization of the effusion cooling system 183**

**Appendix B Full experimental and numerical results in plane 40 189**

**Appendix C Large Eddy Simulations with the AVBP solver 195**

**Appendix D Publications 203**

**Bibliography 287**

# Nomenclature

**Acronyms**

| | |
|---|---|
| $5HP$ | 5 Holes pressure Probe |
| $ACL$ | Axial Chord Length |
| $CFD$ | Computational Fluid Dynamics |
| $CFL$ | Courant Friedrich Levy |
| $CPU$ | Central processing unit |
| $CRZ$ | Corner RZ |
| $CS$ | Combustor Simulator |
| $CTRZ$ | Central Toroidal RZ |
| $DMD$ | Direct Mode Decomposition |
| $DNS$ | Direct Numerical Simulation |
| $DP$ | Design Point |
| $FFT$ | Fast Fourier Transform |
| $HP$ | High Pressure |
| $HPC$ | High Performance Computing |
| $HPR$ | High Pressure Rotor |
| $HS$ | Hot Streak |
| $HWA$ | Hot Wire Anemometry |
| $IOP$ | Isothermal Operating Point |
| $LE$ | Leading Edge |
| $LES$ | Large Eddy Simulation |
| $LOTDF$ | Local OTDF |
| $LPV$ | Low Pressure Vane |
| $LRTDF$ | Local RTDF |
| $NGV$ | Nozzle Guide Vane |
| $NS$ | Navier-Stokes equations |
| $OF$ | Orifice Flowmeter |
| $OPR$ | Overall Pressure Ratio |
| $OTDF$ | Overall TDF |
| $PA$ | Passage between two vanes |
| $PIV$ | Particle Image Velocimetry |
| $PS$ | Pressure Side |
| $PSD$ | Power Spectral Density |
| $PVC$ | Precessing Vortex Core |
| $RANS$ | Reynolds-Averaged Navier-Stokes |
| $RQL$ | Rich burn - Quick quench - Lean Burn |
| $RTDF$ | Radial TDF |
| $RZ$ | Recirculation Zone |
| $SFC$ | Specific Fuel Consumption |
| $SGS$ | Sub-Grid Scale |
| $SS$ | Suction Side |
| $TDF$ | Temperature Distribution Factor |
| $TE$ | Trailing Edge |
| $TET$ | Turbine Entry Temperature |
| $THCPL$ | Unsheathed thermocouple |
| $TS$ | Traverse System |
| $UNIFI$ | University of Florence |

**Operators**

$< \Phi >_\theta$ Circumferentially-averaged

$< \Phi >_r$ Radially-averaged

$\bar{\Phi}$ Time-averaged

**Greek letters**

$\beta$ Azimuthal position in the CS

$\gamma$ Ratio of specific heat

$\mu$ Dynamic viscosity

$\mu_1$ First order moment (mean)

$\mu_2$ Second order moment (variance)

$\mu_3$ Third order moment (skewness)

$\mu_4$ Fourth order moment (kurtosis)

$\nu$ Kinematic viscosity

$\rho$ Density

$\sigma$ Standard deviation

$\tau$ Blowing ratio, time-lag

$\tau_w$ Wall shear stress

$\Theta$ Reduced temperature

$\Upsilon$ Momentum flux ratio

$\Xi$ Non-dimensional temperature coefficient

$u_\tau$ Shear velocity

**Subscripts**

40 Plane 40

40+ Plane 40+

41 Plane 41

$\theta$ Tangential component

$CI$ Inner Cavity (coolant flow)

$CO$ Outer Cavity (coolant flow)

*cool* Coolant flow

$M$ Mainstream (swirlers)

*meas* Measured on the experimental grid

$r$ Radial component

*res* Resolved

$RMS$ Root Mean Square

*sgs* Sub-grid scale

*sw* Swirler

*tot* Total (sgs + res)

$x$ Axial component

**Variables**

$\Delta t$ Duration of the signal

$\dot{m}$ Mass flow rate

$\dot{q}$ Heat flux

$\vec{V}$ Velocity vector

$B(\alpha, \beta)$ Euler beta function

$D$ Diameter

$f$ Frequency

$HTC$ Heat Transfer Coefficient

$k$ Turbulent kinetic energy

$L$ Characteristic length

$M$ Mach number

$N$ Number of samples

$P$ Pressure

$p$ Probability

*pdf* Probability density function

$QI$ Quality index

$R$ Radius

$R_{V_x V_x}$ Autocorrelation coefficient on $V_x$

$Re$ Reynolds number

$S$ Characteristic surface

| | |
|---|---|
| $S_N$ | Swirl Number |
| $St$ | Strouhal |
| $T$ | Temperature |
| $t$ | Time |
| $T_{ad}$ | Adiabatic flame temperature |
| $T_{aw}$ | Adiabatic wall temperature |
| $t_{CS}$ | CS through flow time |
| $T_{mode}$ | Most probable temperature |
| $t_{turb}$ | Turbulent timescale |
| $T_{wall}$ | Wall metal temperature |
| $TU$ | Turbulence intensity |
| $U_{ref}$ | Mean axial velocity at swirler exit |
| $V$ | Instantaneous velocity |
| $V'$ | Velocity fluctuation |
| $y$ | Distance to the wall |
| $y^+$ | Local Reynolds friction number |

# General introduction

## Aeronautical gas turbines

Nowadays, engines powering modern and large commercial or military aircraft essentially rely on gas turbine technologies. Such engines are indeed delivering enough thrust with respect to their own weight making them the only engine technology suitable to operate most aircraft. In the aeronautical industry, gas turbines provide the energy required for the motion of the aircraft either directly by the ejection of a fast moving jet propelling the airframe forward (turbojet, turbofan engines Fig. 1a) or via mechanical power transmission to a propeller (turboprops driving an open rotor or turboshafts for helicopter engines Fig. 1b). Irrespectively of such aspects, all gas turbine engines are composed of successive components dedicated to specific thermodynamic changes of the flow. First, the air enters through the engine intake (labelled as station 4 in Fig. 1) and crosses one or more compressors until station 1 where it mixes with fuel and burns in the combustion chamber. The highly energetic burnt gases are then expanded through a turbine localized between station 2 and 3 to finally be expelled through a rear nozzle. For a turbojet or turbofan, the thrust is obtained by the expansion of the hot gases in the outlet nozzle while torque engines collect shaft power by a free turbine located at the rear of the engine.

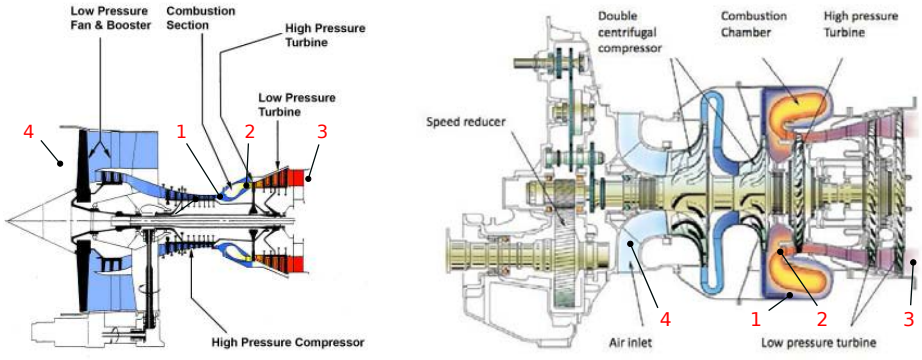


**(a)** Turbofan engine. **(b)** Turboshaft engine.

**Figure 1:** Cross sections of aeronautical gas turbines.[1]

[1] `www.safran-group.com`

The successive thermodynamic changes imparted to the flow throughout the successive engine components ($4 \rightarrow 1 \rightarrow 2 \rightarrow 3$) correspond to a Brayton thermodynamic cycle depicted in Fig. 2 in an entropy ($S$) - temperature ($T$) diagram.

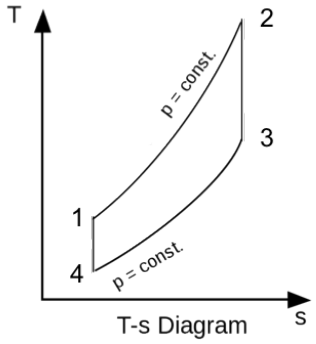


**Figure 2:** Brayon thermodynamic cycle.

Considering an ideal cycle (no-loss), the flow follows a compression ($4 \rightarrow 1$), a heat addition by combustion ($1 \rightarrow 2$) and an expansion ($2 \rightarrow 3$). For combined cycles, heat can be extracted after the expansion phase thanks to a heat exchanger ($3 \rightarrow 4$) but such solution is not technologically applicable for aeronautical propulsion. The thermodynamic representation of an aeronautical engine points to two crucial quantities monitoring the engine operation: *(i)* the Overall Pressure Ratio (OPR) defined as the pressure ratio between station 1 and 4; *(ii)* the Turbine Entry Temperature (TET) corresponding to the temperature at station 2. Both OPR and TET are found to impact the engine performance which is assessed by: *(i)* the specific thrust (output thrust divided by the engine inlet mass flow rate) or similarly the specific power for turboshaft engines; *(ii)* the Specific Fuel Consumption (SFC) defined as the fuel flow rate divided by the output thrust or power. Both quantities are somehow coupled with specific consequences on the engine behaviour. The following observations are usually accepted for existing or currently developed engines. Specific thrust improves significantly with TET (see Fig. 3a), at the expense of an increase of the SFC (Fig. 3b). At the same time fuel consumption being highly undesired, it may be improved by increasing the OPR, an engine capacity essentially relying on the compressor capacity of attaining a desired level of compression in the engine. The final engine performance thus results from compromises between the desired levels of SFC, thrust and the accessible values of OPR and TET which are today limited by the current technological solutions able to satisfy the mechanical integrity of the engine, weight, cost etc. Overall, significant gains in engine performance were obtained in the last 40 years by pushing away the limits for OPR and TET while improving the design of the different engine components. Nowadays, each individual engine module reaches efficiency levels to a point where any gain can only be the result of a significant effort and cost or a major technological breakthrough. As a consequence, researchers and design teams tend to focus more on the interactions between engine components as gains in overall engine performance can be obtained by better apprehending the interfaces. Indeed, all the engine components interact with their neighbours and a

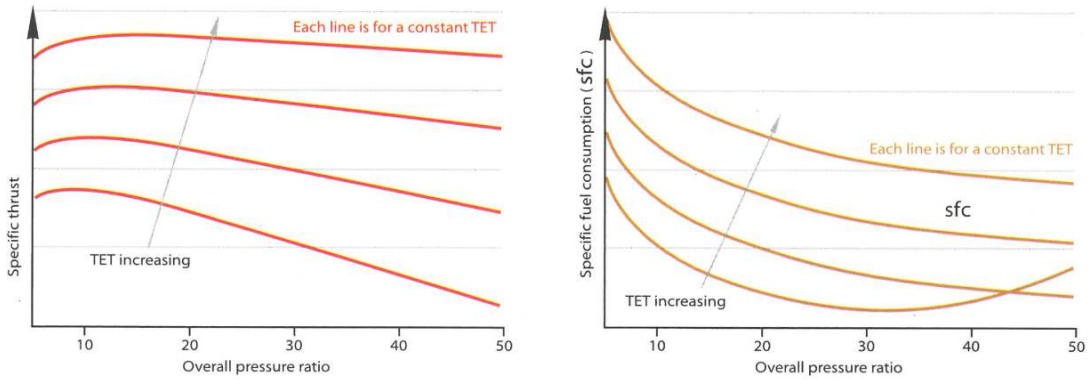


**(a)** Specific thrust versus OPR. **(b)** SFC versus OPR.

**Figure 3:** Performance of an aero-engine gas turbine based on the SFC (a) and specific thrust (b) [1].

gas turbine is a complex 3-D fully unsteady machine which cannot be adequately represented by a succession of independent modules. This new trend for integrated design of multiple components constitutes a major change for industry where each module is usually developed by dedicated teams.

Because of the complex modular structure of a gas turbine, many interfaces exist throughout the main flowpath from the air intake to the exhaust. Amongst all, the most important ones are located around the combustion chamber: compressor-combustor and combustor-turbine. Indeed, in light of the increase of TET and OPR observed in the last decades, these portions of the engine are subject to increasingly strong constraints. For the compressor-combustor interface, it is known that heterogeneities exiting the compressor can significantly alter the flow distribution in the chamber while combustion unsteadiness can affect the performance of the compressor [2–6]. The combustor-turbine interface is even more sensitive since it is located at the most critical part of the engine in terms of temperature, pressure and stress levels. Indeed, the temperature in the combustion chamber (peak above 2200 K) is much larger than the melting point of the combustor and turbine walls which therefore have to be cooled.[2] The implementation of cooling technologies remains in itself a complex issue as it has to be efficient while relying on a minimum amount of fresh air to be injected locally to maximize the amount of air available for emission control and save engine performance.[3] This optimization process is even more complexified by the actual change of technology taking place in the design of the combustion chambers. Indeed, with the generalization of Lean Burn configurations for aero-engine combustors, the amount of fresh air for the cooling of the walls reduces compared to more classical Rich burn - Quick quench - Lean Burn (RQL). For the former (Fig. 4a) cooling is only provided by effusion cooling devices to save air and shield the chamber walls from the hot gases. For

[2]To give an example usual TET are about 1600 K while the turbine blades melt at 1200 K.

[3]In 1976 Cox [7] estimated that each 1% additional cooling air can decrease the take-off thrust by 2.25%.

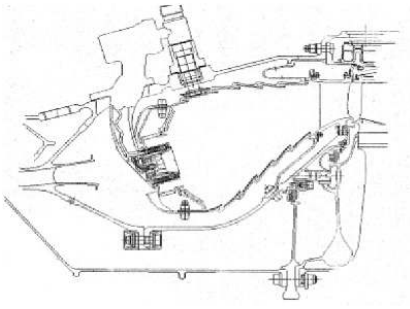

**(a)** Lean Burn: GE TAPSII [8].

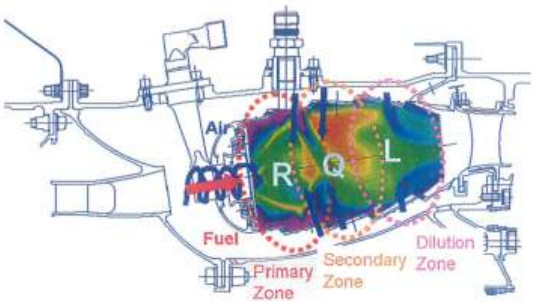


**(b)** RQL [9].

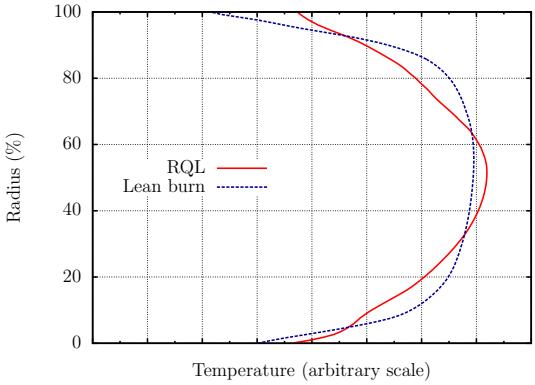


**(c)** Typical temperature profiles at the combustor exit.

**Figure 4:** Configurations of current aero-engine combustors.

RQL architectures (Fig. 4b) dilution holes however cool down the main combustor hot flow stream by feeding the chamber with a lot of fresh air prior to its entry in the turbine stages. A result of such different technological constraints is that the temperature profile at the inlet of the turbine (schematically shown in Fig. 4c) features a strong central peak for the RQL case while it is more uniform in the central region with a rapid and intense cooling in the near wall region for the Lean Burn case. In terms of individual components, the main objective of the new generation of Lean Burn combustors is not necessarily to improve the exit temperature profile but instead to reduce NOx production with an increased durability of the combustor. It nonetheless comes at the expense of a high level of swirl in the chamber as well as advanced cooling systems for which design methodologies are less mature than for RQL combustors and still cause difficulties in the design of turbine stages.

Regardless of the technological layout of the combustion chamber, an increasingly harsh environment at the exit of the combustor is always detrimental to the turbine. It is for the turbine particularly important to control the velocity and temperature distributions at the combustor exit as they directly impact both the work extraction of the stages as well as drive the wall heat transfer on the vanes and rotor surfaces and consequently its life duration. This is the entire problematic of the combustor-turbine interface treatment and the adequate prediction of the combustor exit quantities by means of Computational Fluid Dynamics (CFD), which constitute the core of this thesis.

# Available computational tools

The rapid evolution of computer science and the significant increase of available computational power contributed to a fast and efficient development of CFD not only in the research community but also in the industrial design processes. Such numerical methods drastically changed the design practices for gas turbines in the last 30 years and helped gaining efficiency for every single components of the engine.

Today, many reacting and non-reacting Navier-Stokes (NS) equation solvers are able to simulate the flow inside aeronautical gas turbines. Three main numerical approaches exist [10]: Reynolds-Averaged Navier-Stokes (RANS), Large Eddy Simulation (LES) and Direct Numerical Simulation (DNS) as illustrated in Fig. 5:

- In RANS simulations, the NS equations are ensemble-averaged (or time-averaged) so only the mean motion is resolved and a turbulence model is used to represent the action of the fluctuations [12]. Despite their lack of universality, RANS models are widely used in industry because they are cheap and allow quick simulations providing a satisfactory estimate of the flow field when properly used.

- LES approaches allow a more accurate representation of the energetic content of the flow, at the expense of an increased computing cost. Conceptually, the idea of LES is to compute the time-dependent flow solution by filtering the NS equations so only the biggest scales of the flow (highly energetic) are resolved while a model (usually dissipative) accounts for the small scales (less energetic) [13, 14]. The transition between resolved and modelled scales

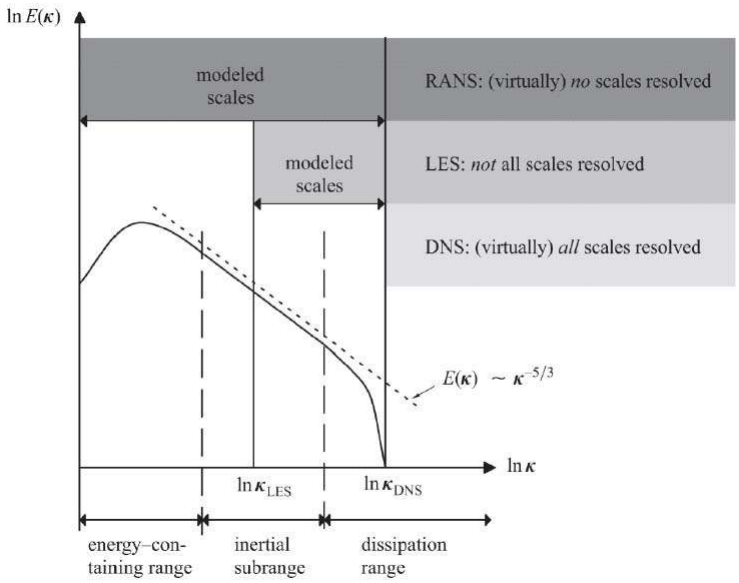


**Figure 5:** Conceptual representation of RANS, LES and DNS approaches [11].

is obtained by the filtering operation which in most cases depends explicitly on the mesh size.

- In DNS all the scales of the problem are resolved in time and space, thus requiring a very fine spatial and temporal discretization which is today only affordable for academic test cases or research programs [15].

As this thesis focuses on the simulation and qualification of the combustor-turbine interface, a proper prediction of the turbulent and highly unsteady flow inside the combustion chamber is required. LES being now the reference approach to simulate such flows [16–20], it has been a natural choice to rely on the AVBP solver[4] developed by CERFACS and IFP-EN for the numerical study of the combustor-turbine interaction.

# Objectives and outcomes of this thesis

This PhD thesis was launched and funded by Turbomeca (SAFRAN group) in partnership with CERFACS within the framework of the European project FACTOR[5] (Full Aerothermal Combustor Turbine interactiOn Research). The main objective is to improve the current characterization of the combustor-turbine interface to impact existing design processes and improve gas turbine efficiency. To do so, a first step is dedicated to the development of a new test rig in close collaboration with the University of Florence in Italy (UNIFI). This includes the definition and integration of measurement techniques and the use of pre-test LES to analyse the flow in the test module. A second step focuses on the qualification of the combustor-turbine interface by means of high fidelity simulations and the use of advanced diagnostics.

The outcomes of this study in light of its initial objectives are summarized in the following points:

- The development within the FACTOR project of a new non-reactive Combustor Simulator (CS) representative of modern Lean Burn engines. In this context, the use of LES for pre-test simulations during the design phase to validate design choices proves that LES can be employed at early stages of the development as confirmed by a posteriori validation of such blind test computations.

- In collaboration with UNIFI, a new test rig installed at Florence now produces a comprehensive and exhaustive experimental database qualifying advanced simulations and exit chamber quantities useful for the design and understanding of the combustor-turbine interface.

- From such exercises, analyses of the methodology result in a best practice for the numerical computation of the CS.

[4] `www.cerfacs.fr/~avbp`
[5] `www.factor-fp7.eu`

- Advanced diagnostics and validation procedures to take advantage of the rich time-resolved fields provided by LES are furthermore proposed in an attempt to improve the design process existing today for the combustor module but also for the turbine. At this occasion it is shown that it is sometimes possible and necessary to go beyond the simple analysis of mean (and RMS) fields to qualify predictions. This is demonstrated by application of the proposed diagnostics to existing gas turbines (not reported here) but also for validations against experimental data on FACTOR CS.

- Finally, integrated simulations of the CS fitted with vanes at its exit highlight the resulting potential effect and the influence of the clocking for the specific case of a Lean Burn architecture.

Some specific elements of the work performed during this thesis were published in various articles and are listed here:

[a] C. Koupper, G. Caciolli, L. Gicquel, F. Duchaine, G. Bonneau, L. Tarchi, and B. Facchini. "Development of an Engine Representative Combustor Simulator Dedicated to Hot Streak Generation". In: *Journal of Turbomachinery* 136.11 (2014)

[b] C. Koupper, T. Poinsot, L. Gicquel, and F. Duchaine. "Compatibility of Characteristic Boundary Conditions with Radial Equilibrium in Turbomachinery Simulations". In: *AIAA Journal* 52.12 (2014), pp. 2829–2839

[c] C. Koupper, L. Gicquel, F. Duchaine, T. Bacci, B. Facchini, A. Picchi, L. Tarchi, and G. Bonneau. "Experimental and Numerical Calculation of Turbulent Timescales at the Exit of an Engine Representative Combustor Simulator". In: *ASME Turbo Expo 2015: Turbine Technical Conference and Exposition*. GT2015-42278. 2015

[d] C. Koupper, L. Gicquel, F. Duchaine, and G. Bonneau. "Advanced Combustor Exit Plane Temperature Diagnostics Based on Large Eddy Simulations". English. In: *Flow, Turbulence and Combustion* (2015), pp. 1–18

[e] T. Bacci, G. Caciolli, B. Facchini, L. Tarchi, C. Koupper, and J.-L. Champion. "Flowfield and temperature profiles measurements on a combustor simulator dedicated to hot streaks generation". In: *ASME Turbo Expo 2015: Turbine Technical Conference and Exposition*. GT2015-42217. 2015

[f] T. Bacci, B. Facchini, A. Picchi, L. Tarchi, C. Koupper, and J.-L. Champion. "Turbulence field measurements at the exit of a combustor simulator dedicated to hot streaks generation". In: *ASME Turbo Expo 2015: Turbine Technical Conference and Exposition*. GT2015-42218. 2015

The paper referred as [a] in the previous list was presented under the reference GT2014-25120 during the ASME Turbo Expo (Turbine Technical Conference and Exposition) held in Dusseldorf, Germany in June 2014. Note that all six papers are reproduced in Appendix D.

# Outline of the manuscript

To address the objectives and results presented previously, the outcome of the work is constructed around four main parts and eight chapters:

**Part I** contains a detailed introduction to combustor turbine interactions.

- Chapter 1 proposes a literature review to introduce the specific issues associated with the combustor-turbine interface along with the main experimental and numerical results from previous studies. The need for a new engine-representative test-rig in Europe within the FACTOR project is justified at this occasion.

**Part II** details the development of a Lean Burn engine-representative CS for FACTOR.

- Chapter 2 focuses on the development of the CS, the proposed methodology and the validation of the design choices by the use of pre-test LES.
- Chapter 3 details the set up of the trisector rig used for validation of the CS design with a special insight given on the instrumentation and definition of the operating points.
- Chapter 4 ultimately summarizes the experimental results obtained on the trisector rig and compares them with the blind-test LES for *a posteriori* validation of the computational methodology.

**Part III** proposes further exploitation of the CS data by use of advanced diagnostics.

- Chapter 5 discusses the methodology for the LES of the aerothermal field of the CS. The influence of numerical parameters is discussed and a best practice is proposed based on the comparison with experimental results.
- Chapter 6 enhances the analysis of the flow at the exit of the CS by characterizing turbulence quantities. Both turbulence intensity and the turbulent integral scale are evaluated from experiments and numerics. Note that the way to properly compare the two approaches is specifically discussed.
- Chapter 7 proposes a new statistical representation of the temperature field at the exit of combustors to account for the intrinsic unsteadiness of the flow at this interface.

**Part IV** finally focuses on the integrated simulations of the CS fitted with vanes at its exit.

- Chapter 8 brings new elements on the analysis of the influence of the turbine on the combustor flow based on advanced and validated LES of FACTOR CS fitted with a pair of vanes.

# Part I

# An introduction to combustor turbine interactions

The first part of this manuscript proposes a literature review of the extensive research performed on the combustor-turbine interactions. Special attention is given to the description of the main facilities dedicated to the subject and the most important findings obtained in the last thirty years.

# Chapter 1

# Literature review

## Contents


1.1 The combustor and turbine modules . . . . . **12**

1.1.1 Technological layout and flow characteristics . . . . . 12

1.1.2 Characterisation of the temperature field distortions . 15

1.2 Influence of the combustor on the turbine . . . . . **18**

1.2.1 Research facilities dedicated to hot streak transport . . 18

1.2.2 Main results of the past studies . . . . . 25

1.3 Influence of the vanes on the combustor . . . . . **34**

1.3.1 Potential effect . . . . . 34

1.3.2 Acoustics . . . . . 37

1.4 Concluding remarks . . . . . **39**


The common practice for the development of gas turbine components is to design each module separately: compressors, chamber, turbines, etc. This design process requires a very precise definition of the interfaces between modules and supposes that there is no interaction between the different parts of the engine. It is acknowledged that this is not true and that further research is required to improve the design techniques. One of the most critical connection in gas turbines is the combustor-turbine interface because of the harsh environnement and the large stresses encountered in the high pressure turbine.

Combustor-turbine interactions have hence been extensively studied since the 80's to improve design practices and gain in efficiency of turbines. However and because of the complex phenomena occurring in the combustion chamber and the difficulty to perform measurements in such extreme conditions, this topic is still open and improvements from both an experimental and numerical side is still needed. Combustor-turbine interaction is a two-way process: *(i)* the combustor exit flow and temperature non-uniformities have a strong influence on the turbine flow while *(ii)* the presence of the turbine modifies the flow in the rear part of the

combustion chamber. After a brief introduction to the combustor-turbine interface in Section 1.1, a summary of the extensive research performed on the influence of combustor exit non-uniformities on the turbine in the last 30 years is proposed in Section 1.2. The influence of the turbine on the combustor flow is comparatively a much more recent field of research. The main results on this topic primarily related to the potential effect induced by the presence of the vanes are presented in Section 1.3. Finally, main conclusions are drawn in Section 1.4 and the need for the new research program FACTOR is introduced and commented.

## 1.1 The combustor and turbine modules

### 1.1.1 Technological layout and flow characteristics

The combustor (see Fig. 1.1) is a key element of any gas turbine as it constitutes the only energy input in the machine which contributes to the rotation of the compressors, the turbines and of course the production of useful work. The main objective of a combustion chamber is to feed the turbine with a continuous flow at high temperature and pressure, composed by a mixture of air and combustion products which is no more flammable (mainly for safety reasons [27]). To do so and for recent combustors, the high velocity air exiting the compressor is slowed down by a diffuser and guided towards the combustor primary zone through swirlers to create low velocity conditions favourable for combustion to proceed. Fuel (either liquid or gas) is injected in this region and burns with the air, producing an increase of the gas temperature up to about 2 500 K. As this mixture is far above the melting temperature of the walls, fresh air is introduced in the rear part of the combustor to cool down the flow and control pollutant emission levels. As mentioned earlier, this

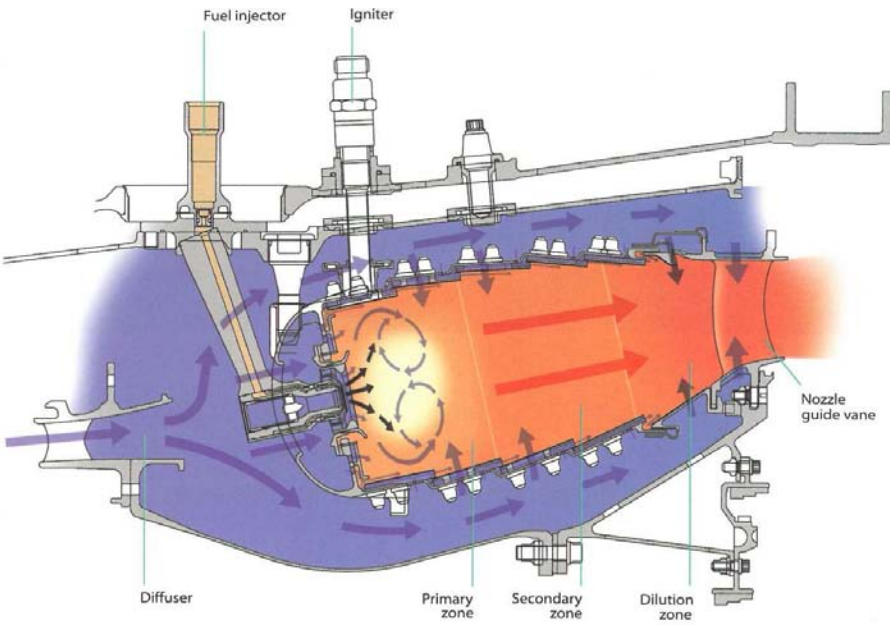


**Figure 1.1:** Typical axial combustor [1].

cooling is usually supplied by dilutions holes for RQL architectures while for Lean Burn technologies only effusion cooling and films through the liners are used [9] (see Fig. 1.2).

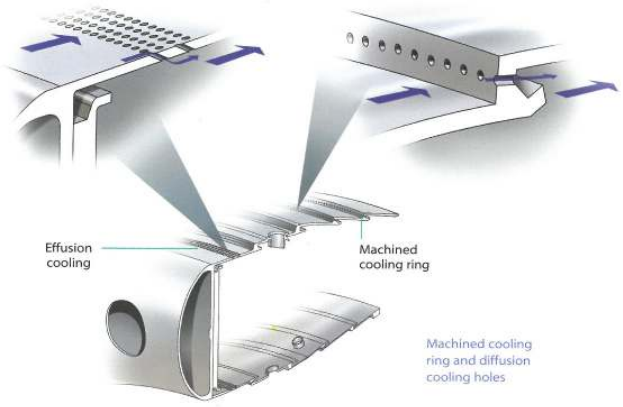


**Figure 1.2:** Effusion cooling systems for combustors [1].

This flow composed of burnt products and cooling air is more or less uniformly mixed and enters the High Pressure (HP) turbine whose first element is the row of Nozzle Guide Vanes (NGVs) visible in Fig. 1.1. The objective of the successive turbine stages is to expand the flow to a lower pressure and temperature level by extracting energy from the fluid which is then used to drive the compressor stages. The HP turbine is composed of a row of NGVs (also called stators) followed by a row of rotating rotor blades: the High Pressure Rotor (HPR). In most of the recent engines the turbine is driven by the impact of the gas flow on the blades (impulse) and its subsequent reaction as it accelerates through the converging blade passage (see Fig. 1.3a). The NGVs are thus shaped to swirl and accelerate the gas flow in the direction of the rotor's rotation to maximize the turbine efficiency. While doing so, a high pressure zone associated with lower velocities forms on the Pressure Side (PS) of the aerofoil whereas the accelerating gas on the Suction Side (SS) strongly reduces the pressure level (see Fig. 1.3b). These pressure differences between SS and PS, added to the axial pressure difference due to the flow expansion impart strong axial and torque loads to the NGVs which have also to withstand the thermal stresses induced by the high temperature level and gradients encountered at the exit of the combustor.

The discrete position of the burners (and possibly dilution holes) all around the combustor circumference leads to the formation of significant temperature gradients which are reinforced in the radial direction by the film cooling devices and core flow mixing. As a result, the flow field at the exit of the combustion chamber usually features a distinct zone of higher temperature: the so-called Hot Streak (HS). The measured combustor exit temperature field of a modern Rolls-Royce engine [29] is shown in Fig. 1.4: in this example, the HS generated by the burner is located in the center, showing both a radial and circumferential distortion of the temperature.

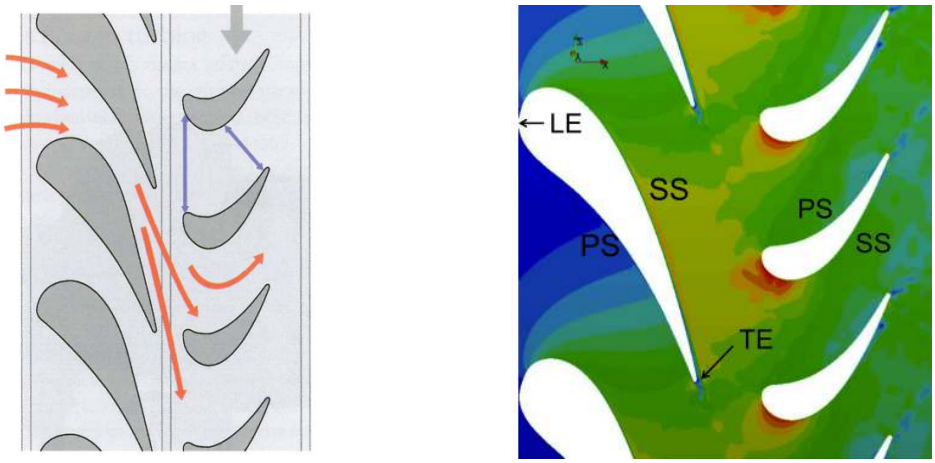


**(a)** Impulse-reaction turbine [1]. **(b)** Mach number in a turbine stage [28].

**Figure 1.3:** Flow characteristics of a HP turbine stage.

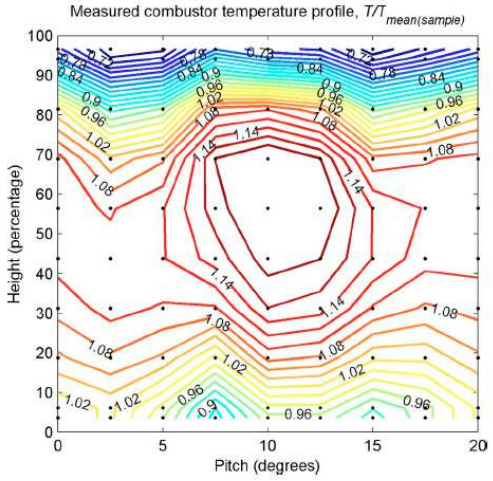


**Figure 1.4:** Temperature field measured over one pitch at the exit of a Rolls-Royce engine combustor [29].

The presence of such temperature non-uniformities at the inlet of the HP turbine is a challenge for the control of heat transfer on the turbine surfaces. This is especially true for the NGVs which are directly fitted at the exit of the combustor and have to face a flow temperature usually hundred of degrees above the melting temperature of the nickel-based alloys used for blades [30]. To allow a high turbine inlet temperature while preserving the vanes life, proper cooling inside the stators is usually required. This cooling air extracted from the compressors is usually discharged through holes located on the vane airfoils (see Fig. 1.5a) from the Leading Edge (LE) to the Trailing Edge (TE). As the amount of cooling air has to be minimized to preserve the engine thermal efficiency, other techniques are also employed [1], for example by reducing the vane thermal conduction (Thermal Barrier Coatings, single crystal casting...). Even if the flow expansion through the NGV row reduces the temperature level, the HPR still has to withstand important

thermal stresses. Cooling is hence also required (not shown in Fig. 1.5b) and its technological implementation is made even more complex due to the rotation of the module [1, 31]. In addition to the thermal stresses, the rotor blades have therefore to cope with the tremendous centrifugal force (typically around 18 tonnes per blade [1]) and they require an efficient fixation mechanism on the disc (usually by use of a fir-tree fitting as shown in Fig. 1.5b). The rotor blades may finally incorporate a shroud at the tip (see Fig. 1.5b) which reduces the overtip leakage (efficiency gain) but increases the weight.

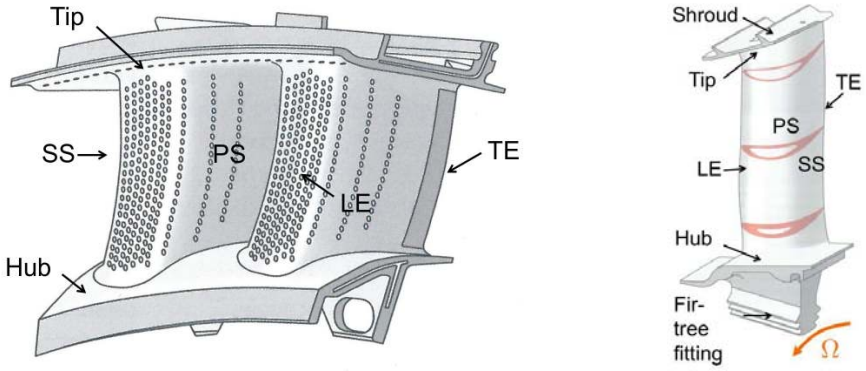


**(a)** Nozzle Guide Vane. **(b)** High Pressure Rotor blade.

**Figure 1.5:** Characteristics of a typical NGV and HPR (adapted from [1]).

In this context of high thermal and mechanical stresses as well as the difficulty of implementing cooling systems, the adequate characterisation of the temperature field at the turbine inlet readily becomes of primary importance. To do so, different mathematical measures of the temperature distortions are today used in the gas turbine community and the main ones are discussed hereafter.

### 1.1.2 Characterisation of the temperature field distortions

The first important information that impacts the turbine operation is the mean temperature at the turbine inlet (so-called *Plane 40*), usually noted $\overline{T}_{40}$ and previously referred as TET. This quantity is critical since identified in the reference thermodynamic cycle and is needed for performance calculations. Note that $\overline{T}_{40}$ can be estimated by considering that all the fuel is burnt in the chamber (without heat losses) and that the mixture exits the chamber at chemical equilibrium yielding the adiabatic flame temperature. Note that for this theoretical estimation of $\overline{T}_{40}$, the temperature of the fresh gas at the inlet of the combustor, often noted $\overline{T}_{30}$, is needed.[1] Having knowledge of these macro parameters, a lot of different measures can be used to quantify the degree of non-uniformity of the temperature field at the turbine inlet (i.e. in plane 40). There is actually no proper consensus on the use of a specific quantity to qualify these distortions. Povey et al. [29]

[1] In the case of multiple inlets or various cooling devices etc. the precise definition of $\overline{T}_{30}$ is subject to caution.

propose the definition of a set of measures commonly used today in industry: the Temperature Distorsion Factors (TDF). Amongst them, the Overall TDF (OTDF) measures the divergence of the hottest point in plane 40 comparatively to the mean temperature in the same plane. It is therefore a single value evaluated at the given axial position $x_0$ (corresponding to the plane 40) and defined by:

$$OTDF(x_0) = \frac{Max_{(r,\theta)}\left(T(x_0, r, \theta)\right) - \overline{T}_{40}}{\overline{T}_{40} - \overline{T}_{30}}, \tag{1.1}$$

where $T$ stands for the temperature. Similarly, the Radial TDF (RTDF) measures the temperature non-uniformity of the flow field averaged in the circumferential direction for a given axial position $x_0$. It is also a single value, defined by:

$$RTDF(x_0) = \frac{Max_{(r)}\left(\langle T(x_0, r, \theta)\rangle_\theta\right) - \overline{T}_{40}}{\overline{T}_{40} - \overline{T}_{30}}, \tag{1.2}$$

where $\langle\rangle_\theta$ is the circumferential averaging.

When a more local definition of the temperature is required at a given axial position $x_0$, one can use the Local OTDF (LOTDF, two-dimensional field) or the Local RTDF (LRTDF, 1-D radial profile), respectively defined by:

$$LOTDF(x_0, r, \theta) = \frac{T(x_0, r, \theta) - \overline{T}_{40}}{\overline{T}_{40} - \overline{T}_{30}}, \tag{1.3}$$

$$LRTDF(x_0, r) = \frac{\langle T(x_0, r, \theta)\rangle_\theta - \overline{T}_{40}}{\overline{T}_{40} - \overline{T}_{30}}. \tag{1.4}$$

In the context of non-reactive test rigs, these definitions are not well defined and alternative definitions derived from Eqs. (1.3) and (1.4) are sometimes used [29]:

$$LOTDF'(x_0, r, \theta) = \frac{T(x_0, r, \theta)}{\overline{T}_{40}}, \tag{1.5}$$

$$LRTDF'(x_0, r) = \frac{\langle T(x_0, r, \theta)\rangle_\theta}{\overline{T}_{40}}. \tag{1.6}$$

Note that other definitions exist as evidenced by the proposition of Barringer and coworkers [32–35] that propose a radial profile of temperature to follow:

$$LRTDF''(x_0, r) = \frac{\langle T(x_0, r, \theta)\rangle_\theta - \overline{T}_{40}}{\overline{T}_{40}}. \tag{1.7}$$

Because of the great diversity in the definition of these non-dimensional temperature coefficients, extra care has to be taken when they are employed especially for comparisons between different cases. Moreover, the use of such indicators to qualify the temperature field is questionable as they provide limited information which may not be representative of the full unsteady and spatial temperature distribution. Indeed, both time and space averaging operations employed in the

construction of the TDF are responsible for a loss of information so very distinct temperature fields may produce the same TDF. As the treatment of data at the combustor turbine interface is being more and more discussed, the exclusive use of such 0-D or 1-D indicators to qualify a combustor design becomes more and more criticised [36, 37]. Some new elements on this specific issue will be presented in Chapter 6.

Although the potential limits of these measures of the temperature distortions have been acknowledged, they still constitute a basis for the design of turbines [29, 38, 39]. Amongst them, the LRTDF defined in Eq. (1.4) is the most common representation of the temperature field at the turbine inlet and it constitutes an important target during the design phases of the combustor. As the first development stages of new combustion chambers currently rely mainly on CFD, the numerical solvers need to be sufficiently predictive and provide a good estimate of the temperature field at the combustor exit. Very few results [40–42] were published on this topic because of the lack of experimental validation (measurements are complex at the combustor-turbine interface) and industrial confidentiality. To give an example, Fig. 1.6 reproduces the comparison between LES, RANS and measurements of the LRTDF at the exit of two combustion chambers: a reverse-flow combustor (Fig. 1.6a) investigated by Boudier et al. [41] and an axial chamber (Fig. 1.6b) studied by James et al. [42]. One can see that accurately predicting the LRTDF is a tough task with clear difficulties for RANS methods and improvements in the numerical prediction quality when LES is used [20, 43]. This study also highlights the difficulty to have exhaustive measurements of temperature at the combustor exit, as the experimental LRTDF profile is here given by very few points. These observations emphasize that even before studying the impact of such temperature profiles on the turbine, the adequate characterization of the flow at the exit of a combustor constitutes in itself a challenging task for both numerical and experimental approaches. Leaving aside this issue (that will be discussed in details in Parts II and III of this thesis), the significant radial non-uniformities observed in Fig. 1.6 justify the extensive research that was performed in the last 35 years on the influence of combustor exit non-uniformities on the turbine flow. An overview of this effort is presented in the following section.

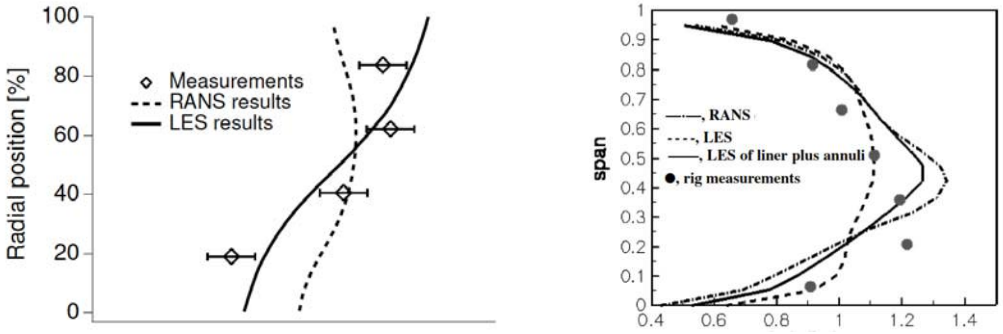


**(a)** Reverse-flow real combustor [41]. **(b)** Developmental axial combustor [42].

**Figure 1.6:** LRTDF profiles obtained by CFD or measurements.

## 1.2 Influence of the combustor on the turbine

The fact that the combustor exit non-uniformities impact the turbine is known since the 70's and most of the early research on such issues was experimental and not numerical. All these experimental investigations led to the discovery of the most important mechanisms driving the transport of HSs in HP turbines. Numerical treatment and simulations were initiated mostly in the 90's to complement these findings. The most important and known facilities dedicated to this issue are presented hereafter.

### 1.2.1 Research facilities dedicated to hot streak transport

Povey et al. [29] and Dorney et al. [44] proposed an exhaustive review of the existing HS simulators for turbine testing. This work, as well as other literature reviews, shows that no less than ten rigs devoted to HS studies have been created since the 80's. The majority of the known and reported facilities are located in the USA. It is only recently that interesting facilities appeared in Europe such as the ILPF [45, 46] in the UK and the ongoing European project FACTOR. The different test rigs can be classified in three main categories: early facilities used to analyse the governing mechanisms; engine representative test rigs (developed afterwards) and specific facilities dedicated to the study of a precise phenomena.

#### First investigations and early facilities

The very first facilities built in the early 80's were designed for proof-of-concept investigations. It is not intended here to present them in details but the three most important ones are introduced:

**The Warm Core Turbine Test Facility (WCTTF)** located at the Nasa Lewis Research Center, Cleveland, Ohio was developed in 1983. It has been described in details by Stabe, Whitney and Moffitt [47, 48]. The experimental results were also recently used as a basis for numerical studies by Dorney et al. [49]. To the authors knowledge, it is the only reactive facility dedicated to the study of HSs. For this test rig, a scaled down HP turbine stage is fed by the burnt mixture of a primary flow annular can combustors with added cooling air coming from four slots, as indicated in Fig. 1.7a.

**The Large Scale Rotating Rig (LSRR)** located at the United Technologies Research Center appeared also in 1983. For this facility, the HS was simulated by a local density change (isothermal flow) through the injection of $CO_2$ upstream of the turbine components (see Fig. 1.7b). The $CO_2$ concentration was then tracked by gas analysers on the surface of a true-scale 1.5 turbine stage. Results were published by Joslyn and Dring [50–52], Butler et al. [53] and Roback and Dring[54, 55].

**The Rotating Blow-Down Facility (RBDF)** located at the Massachusetts Institute of Technology, Cambridge (USA) was developed in 1983. The facility (Fig. 1.7c) was specifically designed by Shang [56] and co-workers to be more engine-representative and adjustable than previous rigs. Four hot streaks were generated by a controllable heat exchanger and then transported through a HP turbine stage while different translating rakes allowed to measure the temperature and pressure profiles at multiple stations of the test rig. Shang and co-workers also reported experimental results [57] and CFD simulations based on this rig configuration [58].

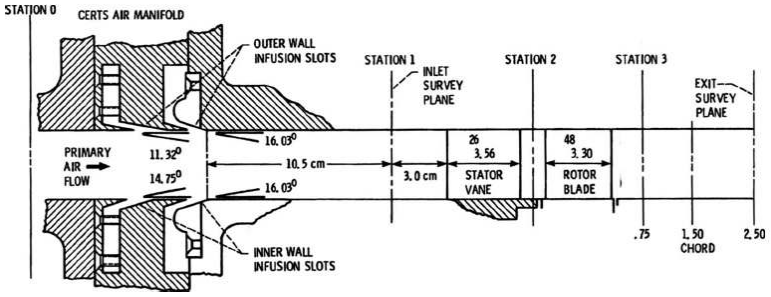


**(a)** Flow path through the Warm Core Turbine Test Facility [47].

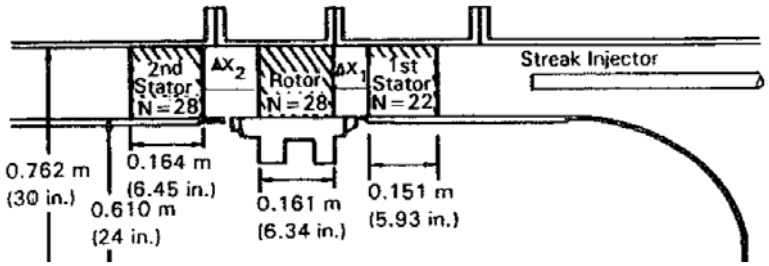


**(b)** Large Scale Rotating Rig HS cascade [54].

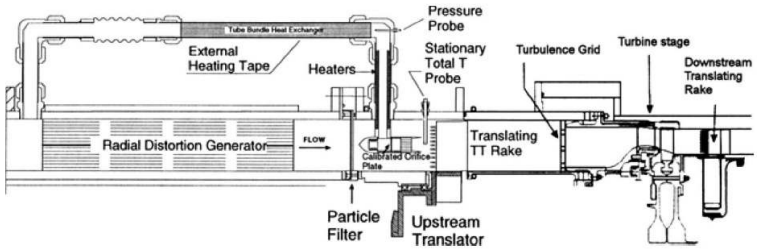


**(c)** MIT HS generator and test rig [57].

**Figure 1.7:** Pioneer facilities for the study of HSs.

The first results obtained with these facilities allowed better understanding of the flow and heat transfer dynamics in HP turbines. However, even if these test rigs usually feature engine hardware turbine stages, they do not reproduce a realistic flow field at its inlet. Therefore, in the late 90's larger facilities were developed with the aim of being more engine representative.

**Engine representative facilities**

More realistic test rigs started to operate ten to fifteen years ago in the USA and UK. They differ from the previous ones by a more realistic layout, a complex and heavy instrumentation and a blow-down operating mode when early facilities operated continuously. These facilities were designed to get a deep insight on HS interaction with turbines and provided a large amount of information. An overview of these test rigs is given here:

**The Isentropic Light Piston Facility (ILPF)** was built at QinetiQ, Hamphsire, UK in 2002 and constitutes the first large test facility on this topic built in Europe. A piston was used to rapidly compress air to feed a HP turbine stage in a blow-down mode, as shown in Fig. 1.8a. The test rig is described by Hilditch et al. [45] and Chana et al. [46]; with test results published by Povey and coworkers [62, 63]. As part of the Brite-Euram Turbine Aerothermal External Flows programme (TATEF II), the facility was upgraded in 2008 [29, 59]. The main targets of these improvements were: getting a strong, well-defined temperature profile (referred as *Enhanced-OTDF* generator), reducing run-to-run variations while using a rolling device to study HS-NGV clocking effect. During this project, a HP turbine called MT1 was installed and instrumented on the rig. It now constitutes a widely used basis for the studies of HS transport [64, 65].

**The Turbine Research Facility (TRF)** located at the Air Force Research Laboratory, Dayton, OH appeared in 2004. A heated and pressurized nitrogen tank was discharged through a combustor emulator (see Fig. 1.8b) feeding the HP turbine with fully controllable profiles of pressure and temperature. It was extensively used and led to the publication of results by Barringer, Thole and Polanka [33–35]. A detailed description of the facility is proposed by Barringer et al. [32] and Anthony et al. [66].

**The Turbine Test Facility (TTF)** was installed at Ohio State University in 2004. This heavily instrumented rig features a combustor emulator that can generate local distortions of pressure and temperature (12 or 19 HSs) feeding a HP turbine with cooling and purge flows (see Fig. 1.8c). The first report by Haldeman, Dunn and Mathison [60, 67–71] investigates time-averaged aerodynamic and heat transfer for a low Reynolds number case using a 1.5 HP turbine stage hardware. The second report campaign covers a wider range of operating conditions for a heavily cooled single stage HP turbine. Time-averaged results have been published by Haldeman and cowerkers [72, 73] while unsteady performance has been reported recently by Nickol et al. [74].

**The Loughborough University test rig** was mounted within the Rolls-Royce University Technology Center in Combustor Aerodynamics. This annular rig shown in Fig. 1.8d features real engine hardware: an axial flow compressor, a RQL combustor (composed of 20 sectors) and removable uncooled NGVs.

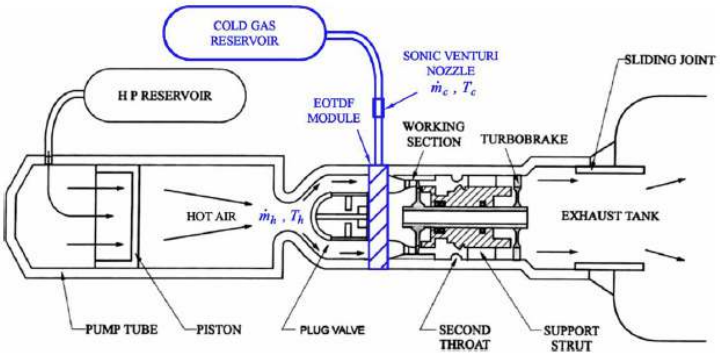


**(a)** QinetiQ Enhanced Isentropic Light Piston Facility rig [59].

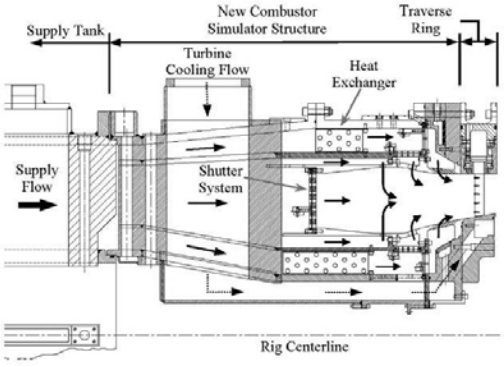


**(b)** Combustor emulator installed at the Turbine Research Facility [32].

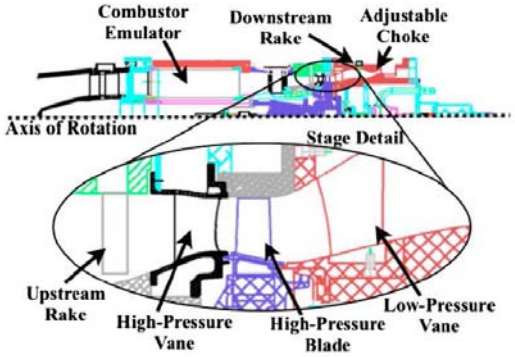


**(c)** General layout and test section of the Turbine Test Facility [60].

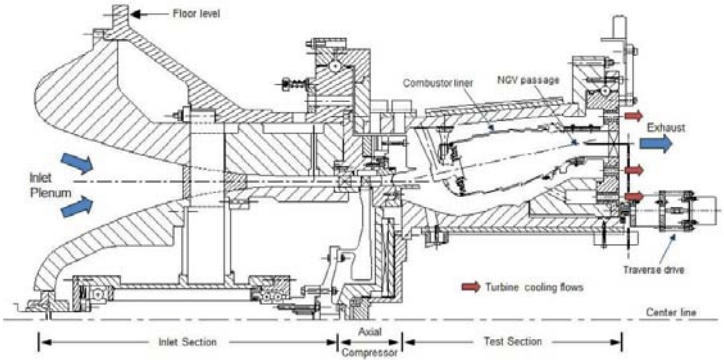


**(d)** Fully Annular Isothermal Test Facility installed at Loughborough University [61].

**Figure 1.8:** Engine representative facilities for the studies of HSs.

The flow is isothermal and the HSs are simulated by the injection of $CO_2$ which is then tracked by gas analysers mounted on moving racks. It is dedicated to the study of compressor-combustor [6] and combustor-turbine interactions [61, 75].

All these large test rigs provided an exhaustive database on the transport of HSs in HP turbines that was often used as a basis for numerical studies. In parallel to these wide-scope investigations, smaller scale facilities were built in the last ten years to address very specific issues.

### Smaller scope rigs

It is worth introducing two test rigs developed to study specific points present in combustor-turbine interactions:

**The University of Texas at Austin** published in 2004 experimental results conducted by Jenkins and Bogard [76, 77] on the interaction between NGVs film cooling and HSs. The rig installed in a low speed wind tunnel features an array of electrical resistances to generate a HS and three scaled-up NGVs film-cooled at cryogenic conditions (see Fig. 1.9a). Their work aimed at reducing the hot spot strength by adequate positioning of HS and use of film cooling.

**The University of Oxford** recently presented a new blow-down experimental facility dedicated to the combustor-turbine interaction for heavy duty gas turbines. As described by Luque et al. [78], special insight is put on the interaction between the wake shed from the combustor lateral wall and the NGVs, which is a can-combustor specific issue. The test section of the facility is a linear cascade featuring four vane passages with adjustable clocking as shown in Fig. 1.9b. Swirl and turbulence are generated upstream the test section and the flow is isothermal (no HS).

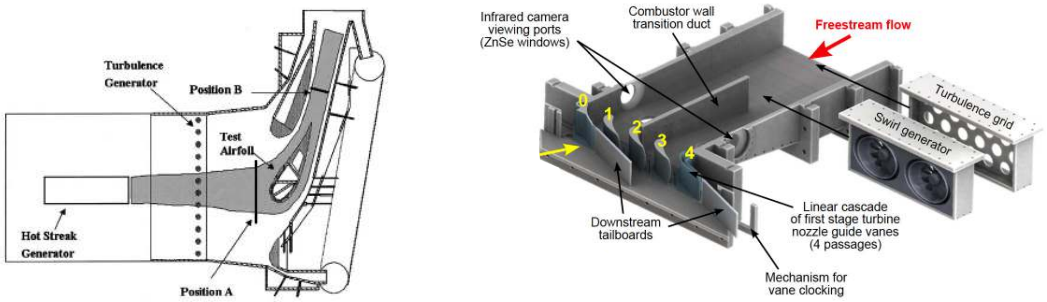


**(a)** HS rig of the University of Texas at Austin [76].

**(b)** Heavy duty gas turbine linear cascade at the Osney Lab [78].

**Figure 1.9:** Small scope facilities for the study of HSs.

### Summary and comparison

An exhaustive overview of the main test facilities is presented in Table 1.1 by summarizing all the rigs main characteristics. The on-going European project FACTOR (to be presented in Section 1.4) is also introduced in the list for comparison. To ease the comparison in terms of temperature range, both maximum and minimum temperature ratios at the vane inlet from the last column of Table 1.1 are plotted in Fig. 1.10 for all the identified facilities. Note that the relative position of the measurement plane with the vane Leading Edge (LE) is not always given and will vary between cases.

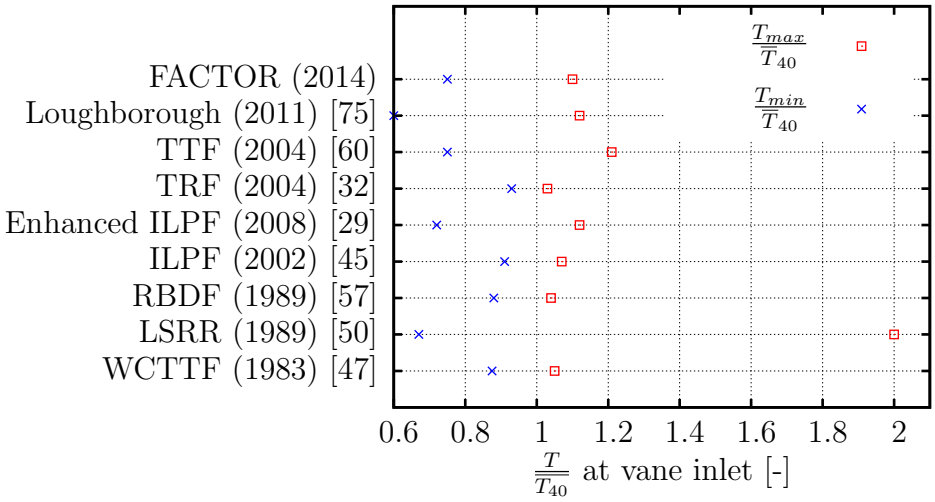


**Figure 1.10:** Maximum and minimum temperature relative to the mean temperature at vane inlet (or upstream when data is unavailable).

When analysing the data of Table 1.1 and Fig. 1.10, the following conclusions can be drawn:

- The vast majority of the test rigs are non-reactive and use air.
- In the last 20 years, only short-duration blow-down facilities were created. They are easier to implement but prevent the use of specific measurement techniques (transient infra-red thermography for example).
- True scale engine hardware is generally used.
- The count between burners or equivalently HS generators, NGVs, High Pressure Rotors (HPRs) and Low Pressure Vanes (LPVs) is generally not CFD-friendly (i.e. the full annulus machines are to be computed because there is no periodicity count).
- The temperature distortion at the vane inlet is usually contained within $-25\%$ and $+10\%$ of the mean temperature. Larger discrepancies between

| **Facility** | **Rig elements**<br>Min. count HS : NGV : HPR : LPV | **Flow conditions** | **Operating time** | **HS generation** | **Temperature range** $\frac{T_{min}}{\overline{T}_{40}}$ | $\frac{T_{max}}{\overline{T}_{40}}$ |
|---|---|---|---|---|---|---|
| **Warm Core Turbine Test Facility** (Nasa Lewis Research Center) - 1983 [47, 48] | Scale ×0.77 HP turbine stage (26 NGVs, 48 rotor blades)<br>1 : 1 : 1.85 : - | Air and Natural gas<br>$P \simeq 3.1bar$<br>$\overline{T}_{40} = 672K$ | Continuous | Annular can combustor and cooling air from 4 infusion slots. Circular or elliptical HS. | 0.875 | 1.05 |
| **Large Scale Rotating Rig** (UTRC) - 1989 [54] | Scale ×1.0 1.5 turbine stage (22 NGVs with TE cooling, 28 rotor blades, 28 LP vanes)<br>1 : 1/22 : 1/28 : 1/28 | Air and $CO_2$ (HS tracking)<br>$P \simeq P_{amb}$<br>$\overline{T}_{40} = T_{amb}$ | Continuous | Single HS simulated by density ratio (isobaric flow).<br>Hot streak or (*cold streak* ⋆). | 1.0<br>*0.67* (⋆) | 2.0<br>*1.0* (⋆) |
| **Rotating Blow-Down Facility** (MIT) - 1989 [56, 57] | Scale ×0.75 HP turbine stage (36 NGVs, 61 rotor blades)<br>1 : 3 : 5.1 : - | Argon-freon-12 | Blow-down (300ms) | Tube-bundle heat-exchanger to generate four HS. | 0.88 | 1.04 |
| **Isentropic Light Piston Facility** (QinetiQ) - 2002 [45, 46] *(△ Enhanced version in 2008* [29, 59]) | Scale ×1.0 1.5 HP turbine stage (32 NGVs, 60 rotor blades, 26 LP vanes)<br>1 : 1 : 1.87 : 0.81 | Air<br>$P \simeq 4.6bar$<br>$\overline{T}_{40} = 444K$ | Blow-down (500ms) | Air compressed and heated by piston for HS; cooling air (ambient $T$) introduced from 32 annular slots. | 0.91<br>*0.72* (△) | 1.07<br>*1.12* (△) |
| **Turbine Research Facility** (Air Force Research Lab) - 2004 [32, 66] | Scale ×1.0 1 or 1.5 HP turbine stage<br>1 : 1 : - : - | Nitrogen<br>$P \simeq 2 - 7bar$<br>$\overline{T}_{40} = 444K$ | Blow-down (2-5s) | Heated and pressurized tank feeding mainstream and cooled stream (dilution holes + film cooling). Various profiles of temperature and total pressure profiles are possible. | 0.93 | 1.03 |
| **Turbine Test Facility** (Ohio State University) - 2004 [60, 71] | Scale ×1.0 1.5 HP turbine stage (38 cooled NGV, 72 uncooled rotor blade with purge flow, 38 LP vanes)<br>1 : 2 : 3.8 : 2 | Air | Blow-down (50-100ms) | Controllable heater rods inserted in Inconel honeycomb cells to generate a uniform inlet *or* a radial profile *or* HSs. | 0.75 | 1.21 |
| **Loughborough University** (Rolls Royce UTC) - 2011 [61, 75] | Scale ×1.0 uncooled NGVs (40)<br>1 : 1 : - : - | Air and $CO_2$ (HS tracking)<br>$P \simeq P_{amb}$<br>$\overline{T}_{40} = T_{amb}$ | Continuous | RQL combustor (engine hardware). No temperature distortion but $CO_2$ seeding in the fuel injector to mimic the HS. | 0.6 | 1.12 |
| **FACTOR** - 2014 | Scale ×1.0 1.5 HP Turbine stage (40 film cooled NGVs, 60 rotor blades with purge flow, 20 LP struts)<br>1 : 2 : 3 : 1 | Air<br>$P \simeq 1.5bar$<br>$\overline{T}_{40} = 450K$ | Continuous | Lean-burn CS with axial swirler for hot air stream and cold air from effusion cooling. | 0.75 | 1.1 |

**Table 1.1:** Summary of the main characteristics of the major HS rigs.

the test facilities are observed for the minimum temperature (coolant) than for the maximum (HS).

- There is no facility representative of a Lean Burn technology, i.e. featuring a HS with a strong swirled flow at the turbine inlet.

All these test rigs provide a large amount of experimental data and were a basis for CFD simulations that led to a better understanding of the transport of HSs in HP turbines for RQL-like combustors. It is now intended to provide a comprehensive overview of the major findings published in the last 30 years on this topic.

### 1.2.2 Main results of the past studies

The study of the transport of HSs through the turbine stages mainly involves three topics which are now discussed in the following order: aerodynamics, heat transfer and turbulence.

#### Aerodynamics of the HP turbine

One of the key issues associated with the transport of HSs through HP turbines is the transport of temperature and pressure profiles from the combustor exit to the turbine exit. Barringer et al. [35] provided a certain amount of experimental results on this issue. They observed that whatever was the stage inlet temperature and pressure distortions, the flow at the NGV exit features almost uniform thermal conditions in the circumferential direction. These observations were confirmed by the experimental results conducted by Mathison et al. [60] on the Turbine Test Facility. In this last specific study, radial profiles of temperature are measured at the NGV inlet, rotor LE (in the rotating frame, i.e. relative temperature) and downstream of the Low Pressure Vane (LPV) as shown in Fig. 1.11. The experiments were conducted for both cooled (film cooling, TE injection, purge) and uncooled NGV as respectively shown by the blue and red curves in Fig. 1.11. For both configurations, the rotor strongly mixes the flow resulting in an almost completely uniform exit temperature. Indeed, the temperature distortion ($T/\overline{T}_{in}$) initially from 0.8 to 1.1 at the inlet is finally reduced to 0.62-0.7 at the LPV exit. The influence of cooling flows on the temperature profile is found to be uniform over most of the span with a zone of enhanced cooling at the blade tip (probably due to vane outer endwall cooling). At the LPV exit, the temperature reduction induced by the coolant flow is nearly uniform.

Barringer et al. [35] explained the intense mixing observed over the pitch by the elevated freestream turbulence and secondary flow mixing. For all the configurations, the flow at the hub is hotter at vane exit than at vane inlet because of secondary flows convecting hot fluid pockets from midspan towards the hub. Contours of temperature along with secondary flow vectors in the vane exit passage are extracted from a low-Reynolds RANS simulation and shown in Fig. 1.12 for inlet profiles $B$ (almost uniform) and $D$ (distorted). The cold fluid migration from tip to hub is easily visible and much more pronounced for profile $D$ which features

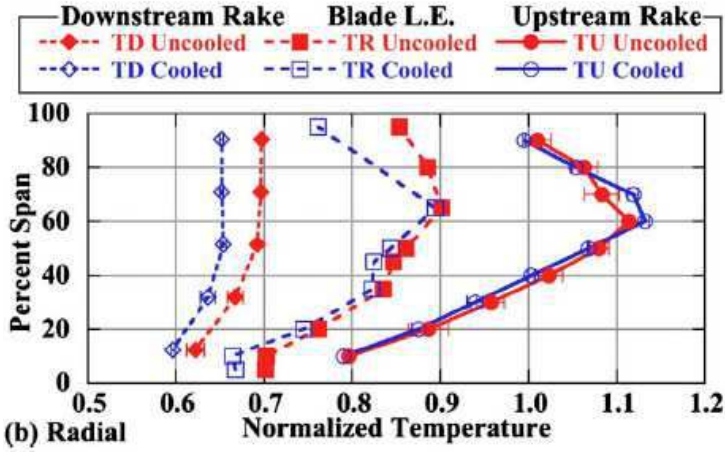


**Figure 1.11:** Migration of the radial temperature profile measured through the turbine. From right to left: NGV inlet, rotor LE, LP Vane exit [60].

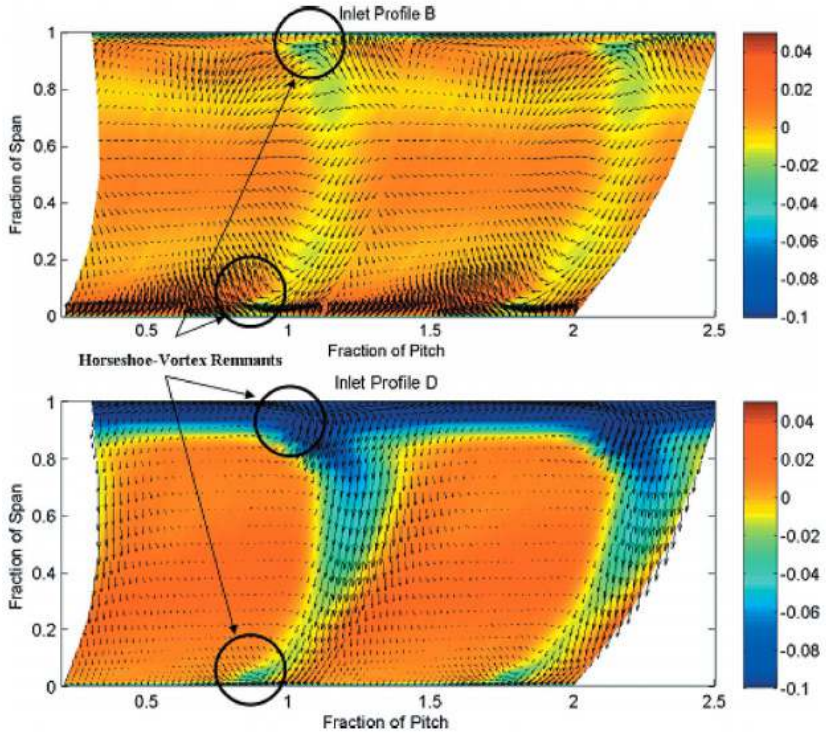


**Figure 1.12:** CFD prediction of the temperature field and secondary flow vectors in the vane exit passage for a uniform (top) and distorted (bottom) inlet profile [35].

much higher pressure at tip and hub than profile *B*.

Recent unsteady RANS simulations of a 180° sector of two HP turbine stages were performed by Dyson et al. [36]. At the inlet of the turbine, the authors imposed either a HS described by 2-D fields of total pressure, temperature and flow angles or the corresponding circumferentially averaged profiles (1-D). Numerical results shown in Fig. 1.13 indicate that the temperature field at the inlet of the

second rotor pictures better mixing with a 2-D inlet than with a 1-D inlet profile. Indeed, for the 2-D inlet case, a pronounced large radial migration of the HS is observed in the first vane passage resulting in enhanced mixing.

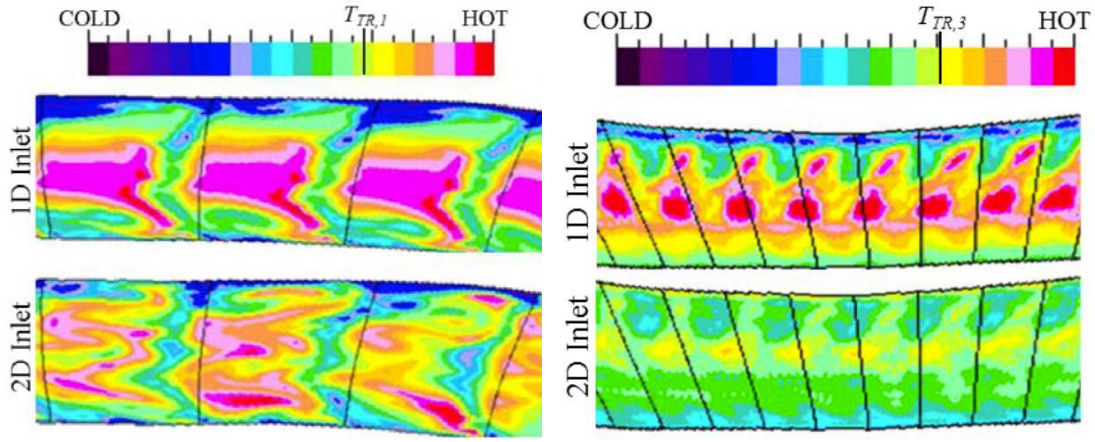


**(a)** First rotor inlet. **(b)** Second rotor inlet.

**Figure 1.13:** Time-averaged temperature predicted by CFD at inlet of the two rotors using either a 1-D or 2-D inlet boundary condition [36].

To understand this complex migration of the temperature profile through the turbine, the path of the HS has to be investigated through local visualisation and probing. This was first performed experimentally in the 90's by Roback et al. [54] who studied cold and hot streak migration through a rotor passage by means of density ratio changes. The HS was simulated with $CO_2$ and injected at the vane mid-pitch. The measurements reproduced in Fig. 1.14 indicate a strong accumulation of the HS on the blade PS, whereas the cold streak (lower temperature than the core flow) migrated on the blade SS compared to the neutral streak. This preferential migration of the HS on the blade PS was first linked by Butler et al. [53] to the Kerrebrock-Mikolajczak effect [79]. Postulating that Mach number and flow angles are roughly uniform at the NGV exit, a higher absolute velocity has to appear for the HS since $V = M\sqrt{\gamma r T}$. Then, in the relative frame of reference of the rotor, the HS has a velocity oriented toward the PS compared to the cooler fluid. This preferential migration of the HS is hence explained by a change in incident angle induced by the temperature difference: this is the so-called segregation effect.

Numerical results by He et al. [80] complement these findings by observing that the HSs preferentially migrate on the rotor PS independently of their relative position with respect to the NGV (clocking). The entropy contours in Fig. 1.15 show a similar migration of the HS for both clocking positions. They also evidence an enhanced heating zone on the blade PS when the HS is aligned with the passage.

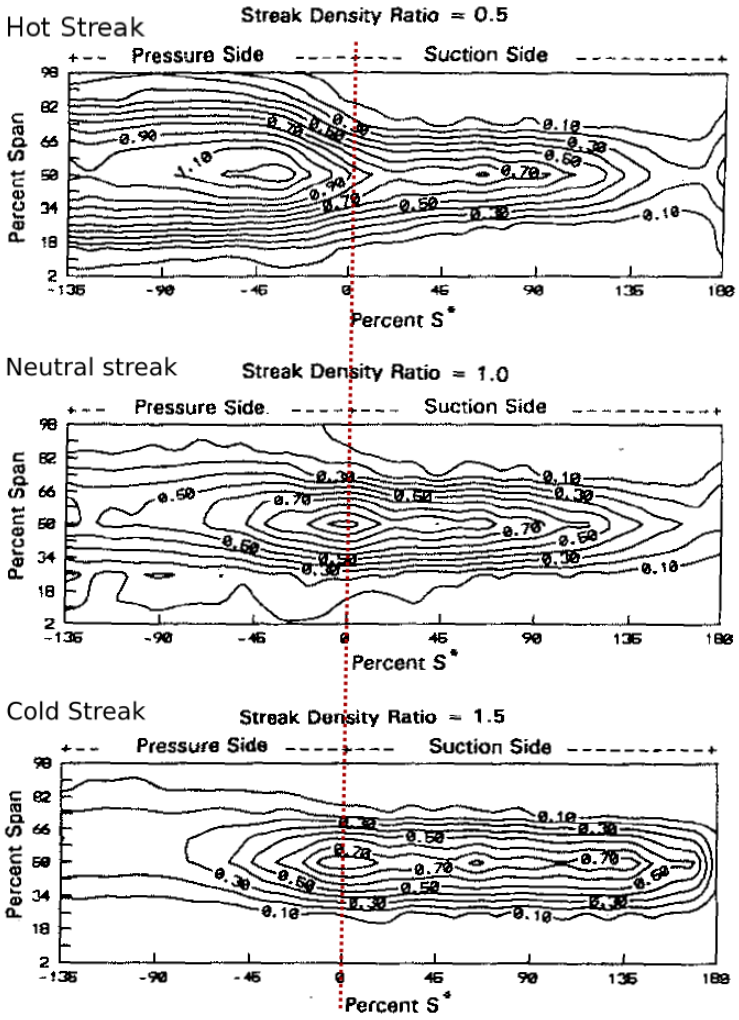


**Figure 1.14:** Measurement of the trace concentration of the hot (top), neutral (center) and cold (bottom) streak on the rotor blade SS and PS [54].

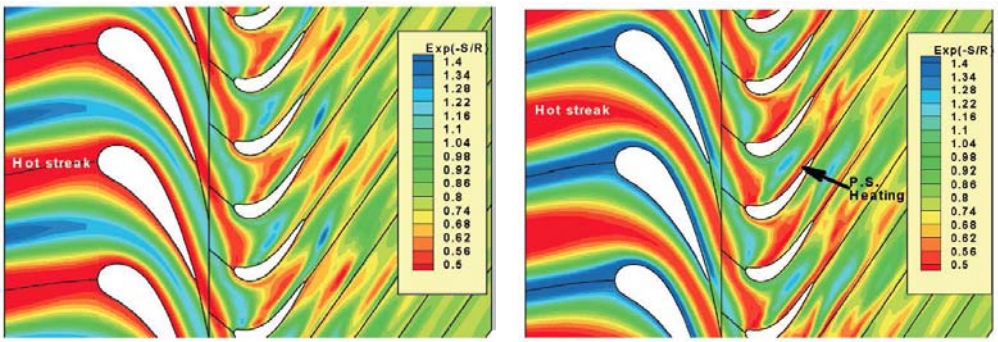


**(a)** HS centered on NGV LE. **(b)** HS centered on NGV passage.

**Figure 1.15:** Instantaneous entropy contours showing the systematic migration of the HS towards the blade PS [80].

The observation of Fig. 1.15 reveals that the clocking of the HS dramatically changes the entropy level in the vicinity of the walls of the NGV. This was confirmed by 3-D RANS simulations conducted by Povey et al. [63] and Qureshi et al. [65] based on the ILPF test rig configuration. The authors show that when the HS is aligned with the NGV passage (left side of Fig. 1.16), cold flow is transported towards the vane SS (hot flow towards PS). A HS aligned with the vane LE would lead to higher heat transfer on the vane SS (right side of Fig. 1.16).

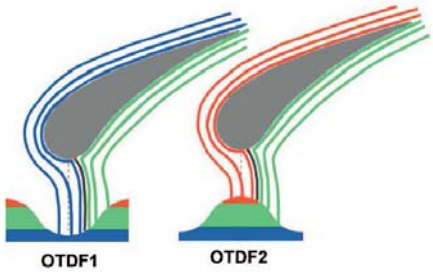


**Figure 1.16:** Streamlines emitted by a HS located at vane mid-passage (left) and aligned with LE (right) [63].

In this context, it is clear that the HS-NGV clocking and the complex transport of HSs trough the HP turbine certainly impact the heat transfer on the vanes as well as on the rotor blades surfaces. This problematic was extensively studied from both an experimental and numerical point of view and is now discussed.

### Heat transfer

The first module experiencing higher temperature levels and heterogeneities is the NGV row. Many studies therefore focus on the heat transfer on the vanes surface and its dependency to non-uniform temperature inlet conditions. Recent 3-D RANS simulations by Salvadori et al. [64] of the MT1 turbine stage show that compared to a uniform inlet temperature profile, the heat transfer is increased up to 50% on the SS and 20% on the PS when using temperature distortion profiles at the inlet. Experiments performed on the same turbine stage by Qureshi et al. [65] show that the vane wall at midspan can be as high as 20% and 5% hotter than the mean inlet temperature when a non-uniform inlet condition is used as shown in Fig. 1.17. This temperature difference is explained by the migration of the HS towards the SS, as schematically illustrated on the right side of Fig. 1.16. Various authors studied the influence of the HS-NGV clocking on the heat transfer on the vanes in order to reduce (or at least control) its level. Povey et al. [63] reports that the HS-NGV clocking changes the vane surface Nusselt number by $\pm 20\%$ on the SS but has a negligible effect on the PS, which confirms the previous findings.

The heat transfer on the rotor blades is another critical point of turbine design as this rotating part faces centrifugal forces in addition to the thermal stresses. The heat load in the rotor directly depends on the way the HS was transported through the vanes and its possible interaction with the cooling flows (purge, wall cooling etc.). As an example, CFD analyses by Salvadori et al. [64] shown in Fig. 1.18

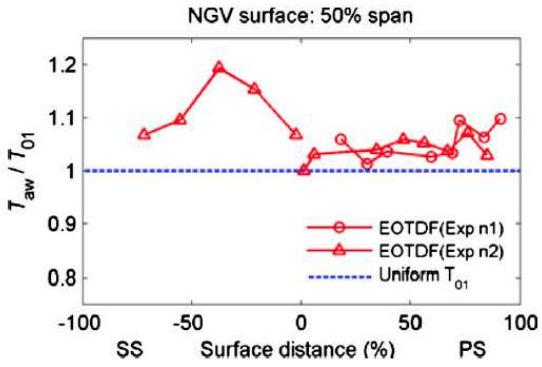


**Figure 1.17:** Measured fluid temperature on the NGV wall for two tests with a temperature distortion (EOTDF) at the turbine inlet [65].

provide Nusselt contours on the MT1 rotor blade PS (relative to uniform inlet). The heat load is increased by 60% at midspan as a result of the HS preferential migration on the PS. At hub and tip, large decreases of heat transfer are directly created by the stage inlet temperature profile (cold air close to walls). Experiments by Shang et al. [58] show that the increase in the wall temperature of the blade depends nonlinearily on the level of the inlet temperature distortion.

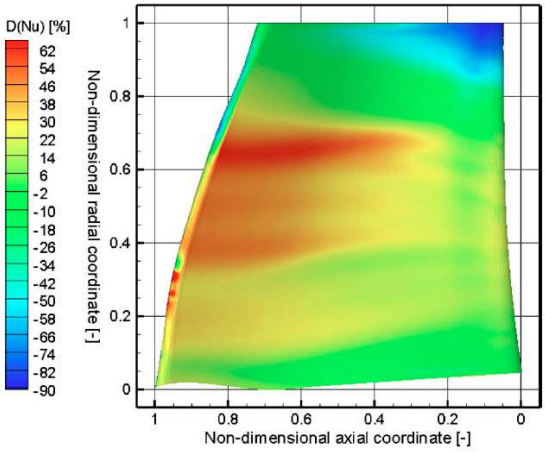


**Figure 1.18:** CFD prediction of the Nusselt number on the HPR PS, relative to uniform inlet temperature [64].

Most of these studies investigating the heat transfer on the rotor blade surface intend to relate the heat flux to the temperature distortion alone. However, the heat flux $\dot{q} = HTC(T_{aw} - T_{wall})$ is driven by the difference between the wall metal temperature $T_{wall}$ and the adiabatic wall temperature[2] $T_{aw}$ as well as the Heat Transfer Coefficient $HTC$. Recently, Rahim et al. [81] performed numerical simulations to discriminate the predominant factor in the heat transfer of the HPR: either $T_{aw}$ or $HTC$. They found that for typical RQL engines (HS without swirl), the heat transfer is driven by $T_{aw}$ (see Fig. 1.19a) while for Lean Burn

[2]i.e. the fluid temperature on the wall.

engines (swirling HS at inlet) it is driven by *HTC* (see Fig. 1.19b). Once swirl is introduced the heat transfer is therefore no longer driven by convective processes only but is subject to aerodynamic interactions. The swirl direction combined with the different NGV shapes can hence lead to ± 40% changes in the rotor heat flux, especially in the tip region, keeping unchanged the integrated performance parameters which indicates some potential need for combined aerodynamic and heat transfer optimizations.

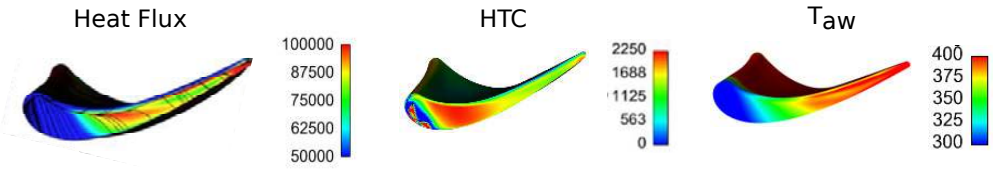


**(a)** Temperature distortion only *(RQL)*.

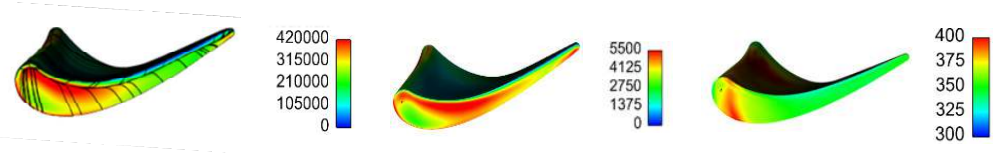


**(b)** Temperature distortion and swirl *(Lean-Burn)*.

**Figure 1.19:** Discrimination of the parameters governing the heat transfer on the rotor tip in the absence (top) and presence (bottom) of swirl at the turbine inlet [81].

Downstream of the HP turbine stage, the LPVs are also affected by the presence of HS but with lower impacts. Experiments conducted by Povey et al. [62] report a heat transfer increase on the PS as high as 10 to 20% when a HS is injected at the turbine inlet. The authors assumed that this specific migration on the PS was mainly due to secondary flows within the vane passage along with an incidence angle segregation as stated previously (Kerrebrock-Mikolajczak effect).

Aside from the vanes and blades both inner and outer endwalls are also affected by the presence of HSs which may migrate radially in the turbine and alter the coolant protection. To quantify the impact of having HSs reaching the endwalls, Roback et al. [54] performed various experiments by injecting a HS at different positions in the spanwise direction. When injected at 75% span (i.e. close to the blade tip), the authors observe an important radial shift, showing a flow deflection towards the tip. When injected at 25% span, the flow field disturbance is less important but the accumulation on the hub endwall is still four times more important compared to a mid-span HS. Note that in other facilities the HS was found to migrate towards the hub (like Shang [56] at MIT) and thus no general rule can be drawn. However, in other cases the HS may not migrate and the colder flow in the near wall region is maintained, thus protecting the wall. Povey et al. [63] reported significant reduction in Nusselt numbers at endwalls when us-

ing a non-uniform vs. uniform temperature profile (30 to 50% at hub and 25 to 35% at casing). The authors estimate that this decrease is mostly temperature induced rather than caused by a change in heat transfer coefficient because the aerodynamic flow field is not altered by the uniform and non-uniform temperature distributions. This trend was confirmed by CFD simulations by Qureshi et al. [65].

**Turbulence**

Among all the data collected on the different test facilities, little attention appears to be paid on the characterization of the turbulence field at the exit of the combustion systems (a very first explanation is that it is complex to measure such fields in realistic conditions). Depending on the way turbulence intensity is defined[3], most authors report values between 20 and 30% at the turbine inlet [32, 75, 82]. In specific contexts, such turbulence levels can significantly affect the flow in the turbine. Indeed, it has been shown that large scale turbulence can enhance the heat transfer on the vane walls and promote earlier boundary layer transition [83–85]. Barringer et al. [35] also report that a turbulence intensity increase at the vane inlet leads to broadened wakes and improves mixing at the vane exit. Very few studies are available on the interaction between turbulence and HS, except the experimental investigations [76, 77] on the rig of the University of Texas at Austin. They observed that the mainstream turbulence levels ($TU = 3.5\%$ or $20\%$) has very little impact on the HS attenuation and that under moderate turbulent conditions the HS remains more compact with higher temperature gradients. This more coherent shape of the HS is illustrated in Fig. 1.20, showing the normalized temperature field $\Theta_R = \frac{T-T_\infty}{T_{HS,peak}-T_\infty}$ obtained from experiments. Finally, the authors report that the proper combination of vane film cooling and high turbulence can help reducing the hot streak peak temperature by 74%. Indeed, in their specific configuration, the film cooling on the SS nearly eliminates the HS on this side of the vane.

A review by Radomsky et al. [86] shows that most of the results published on this topic were obtained in test rigs where turbulence is generated by calibrated grids. Only recently, Cha et al. [75] reported experimental and numerical computations of turbulence at the exit of a RQL combustor fitted on the Loughborough University isothermal test rig. The turbulence intensity[4] measured by means of Hot Wire Anemometry (HWA) was found to increase from 30-35% to 65% throughout the NGV passages. Integral scales of turbulence were also calculated based on the autocorrelation of the HWA signals. Experimental results (Fig. 1.21a) show that the lengthscale also increases through the vanes: from about 25% of the NGV chord length at the inlet to 50% at the exit. Turbulent lengthscales were also estimated from LES results but with a different methodology (approximation based on the mean strain rate and the turbulent kinetic energy). Even if the di-

[3]Many definitions are commonly employed and mainly differ by the number of velocity components and the normalization.

[4]Note that Cha et al. [75] define $TU$ as the RMS of the axial velocity divided by the mean axial velocity in the investigation plane.

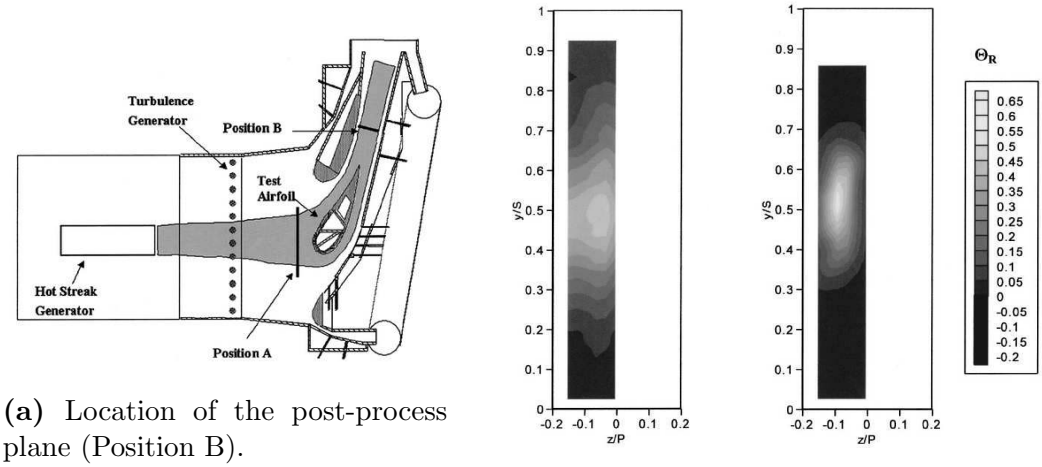


**(a)** Location of the post-process plane (Position B).

**(b)** $TU = 20\%$.

**(c)** $TU = 3.5\%$.

**Figure 1.20:** Measurements of temperature at the exit of the vanes (position B) for two turbulence intensity levels generated at the inlet of the NGVs [76].

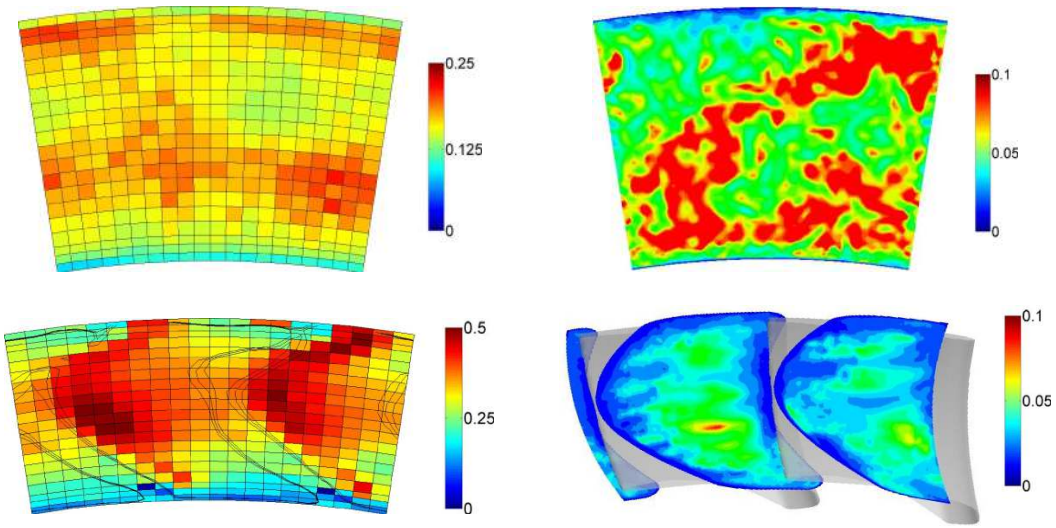


**(a)** Experiments.

**(b)** LES.

**Figure 1.21:** Turbulence lengthscale divided by the NGV chord at the combustor exit (top) and NGV exit (bottom) [75].

rect comparison with the experiments is subject to caution, the LES estimates are shown in Fig. 1.21b. Overall, the numerical prediction is not satisfactory: neither the level (50% difference) nor the distribution of the experiments are reproduced. More surprisingly, LES predicts a decrease of the turbulent lengthscale by a factor of 2 throughout the NGV passages which is the exact opposite of the experimental results. Such results indicate that characterizing turbulence from experiments and numerics at the exit of realistic combustors (and comparing them properly) is a tough task and that there is clear room for improvement.

## 1.3 Influence of the vanes on the combustor

Historically, the combustor and turbine communities present in industry or academia are two distinct entities. While the influence of the combustor exit conditions on the turbine has been extensively investigated since the 80's, the influence of the HP NGV on the combustor flowfield is a very recent field of research. So-far, only numerical investigations were performed on this topic and no experimental validation is available. It is therefore very difficult to assess the actual quality of the simulations. Moreover, performing CFD at this interface is challenging because of the very different nature of the flow field in the combustor (high swirl, combustion processes, low-Mach flow) and in the turbine (highly compressible, near-wall and boundary layer flow). Only few CFD solvers allow to simulate both the combustor and the turbine in a single domain. Some results of such integrated simulations published in the last six years are presented and discussed here.

Because of the scarcity of solvers being able to cope with both combustor and turbine flows, there is an emerging use of coupling approaches. In such methods, a dedicated solver is used for the chamber and another one for the turbine, information being exchanged both ways. However, such coupled approaches are mainly used to feed the turbine with realistic data and the backward influence of the turbine on the combustor is usually not discussed. It is not intended here to comment the methodology into details but information on LES/RANS coupling can be found in Schluter and coworkers [87–91] as well as Collado Morata [92], RANS/RANS approaches are discussed by Salvadori et al. [93] and Insinna et al. [94] for example.

### 1.3.1 Potential effect

One of the only published fully integrated simulation of the NGV action on the combustor flowfield was performed by Roux et al. [95]. In this work, reactive LES simulations were performed on a periodic sector of a real annular gas turbine including (or not) two NGVs. The results indicate significant changes of the flow field especially in the rear part of the combustor, the primary zone remaining mostly unchanged. As shown by Fig. 1.22, the temperature distortion at the turbine inlet is significantly affected with local differences up to 130 K with or without NGV. The unsteady flow field is also affected: the RMS values of velocity in the rear part of the combustor are multiplied mostly by 5 and locally by 10 with the NGV. The temperature RMS field shown in the bottom part of Fig. 1.22 indicates that the presence of vanes tends to create coherent patterns while without vanes the field is almost uniform. These differences in unsteady activity are further analysed by the authors via a Fourier analysis of the pressure signal in the chamber, as shown in Fig. 1.23. Very distinct modes are observed: without NGVs a single mode is found at 790 Hz with an amplitude of $P_{RMS} = 3000$ Pa, when with NGVs the main mode appears at a lower frequency (440 Hz) but with an almost doubled amplitude ($P_{RMS} = 5500$ Pa).

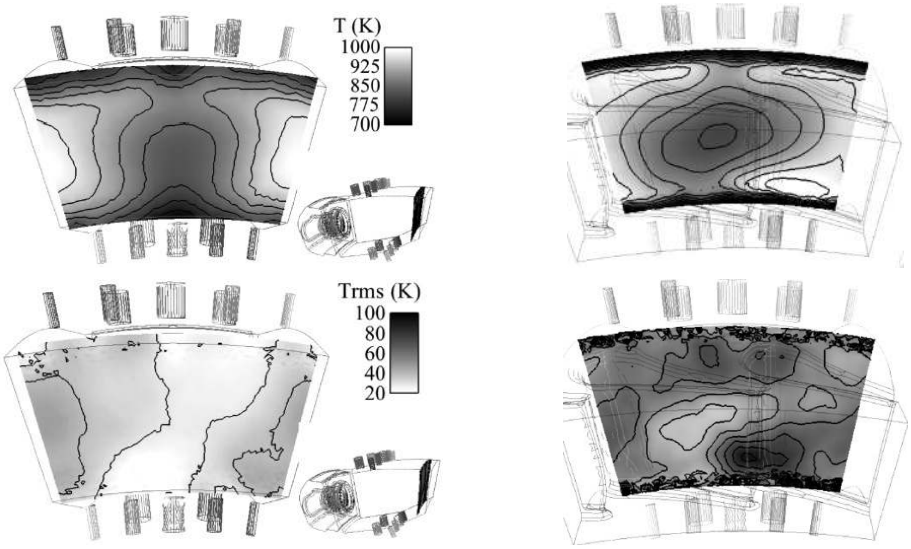


**(a)** Without NGVs. **(b)** With NGVs.

**Figure 1.22:** Mean (top) and RMS (bottom) temperature field predicted at combustor exit, with and without NGVs [95].

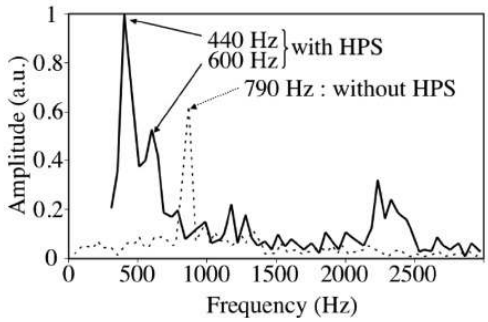


**Figure 1.23:** Fourier spectrum of the numerical signal of pressure in the chamber with and without NGV (referred as HPS) [95].

The same LES solver was used by Collado and co-workers [92, 96] to compute the flow inside a periodic sector of the combustor of a helicopter engine with and without NGV. The computational domain features a reverse flow chamber when Roux et al. [95] studied a purely axial one. Comparisons are performed at the exit of the combustor, located 3 mm upstream the vane LE. Figure 1.24 shows the mean and RMS values of temperature. The influence of the presence of a vane in plane 40 is less important than in the previous study. Nonetheless, the vane seems to induce a preferential migration of the HS towards the PS (Fig. 1.24b). The comparison of radial profiles of temperature shows a limited difference between the two cases because the presence of the vane mainly induces an azimuthal disturbance. The temperature fluctuations are similarly distributed with or without NGV and with the same magnitude.

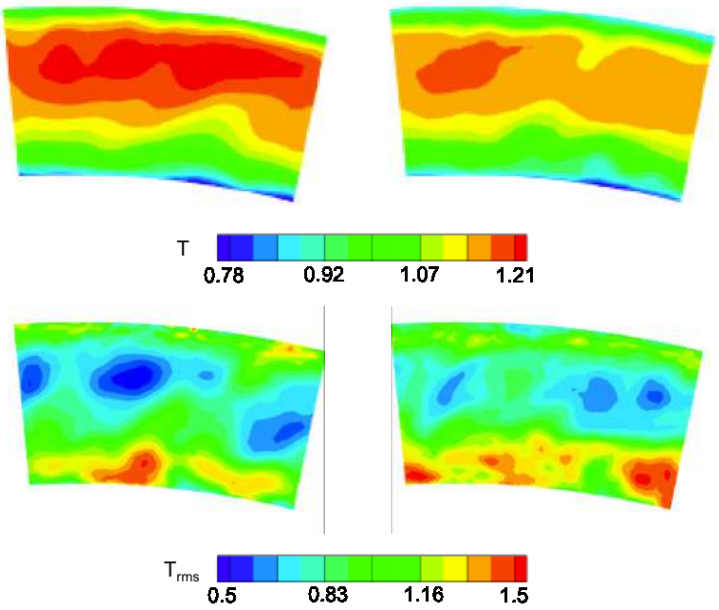


**(a)** Without NGV. **(b)** With NGV.

**Figure 1.24:** Mean (top) and RMS (bottom) temperature field predicted at combustor exit, with and without NGV [92, 96].

Other results of integrated simulation covering the combustor and the turbine were published by Klapdor [27, 97] who extended a RANS incompressible solver well suited for the combustor to the compressible domain for the turbine flow. Steady-state simulations of the Rolls-Royce engine BR710 combustor (with cooling liners and dilution holes), fitted with and without NGV (2 vanes) were finally performed. The temperature field upstream the NGVs was found to be quite insensitive to the presence of vanes as shown in Fig. 1.25. Quantitatively, the OTDF and LRTDF are almost identical for the two cases. This result is in contradiction with the strong differences highlighted by Roux et al. [95]. However, the geometrical configurations and numerical approaches being radically different, it is hard to conclude on a general rule. Regarding the aerodynamic field, Klapdor observed that the mass flow rate in the most downstream cooling liner was increased by 7% with the NGVs highlighting the fact that the potential effect of the

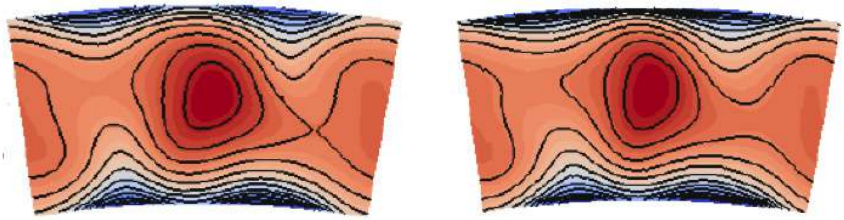

**(a)** Without NGVs. **(b)** With NGVs.

**Figure 1.25:** Temperature predicted by CFD 25% ACL upstream the vanes [27].

vanes can affect the mass flow distribution of the cooling systems in the combustor. The influence of the NGVs was found to affect the flow up to 75% Axial Chord Length (ACL) upstream the vane LE with largest deviations reaching ±30% for the velocity magnitude at 25% ACL as illustrated in Fig. 1.26.

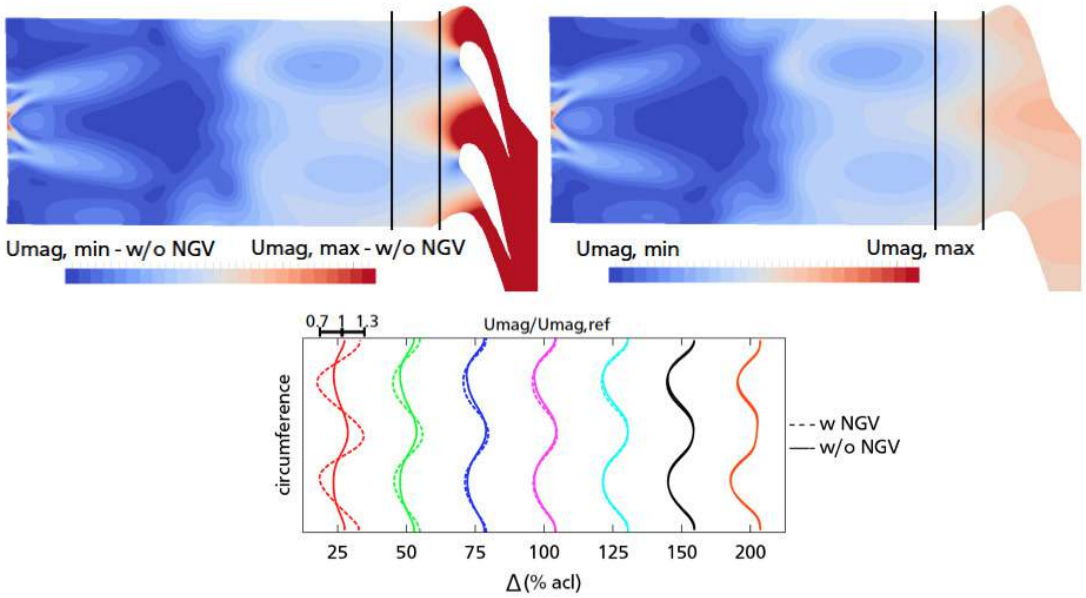


**Figure 1.26:** Velocity magnitude field at midpsan with (top left) and without (top right) NGVs and velocity profiles at different positions (bottom) [27].

### 1.3.2 Acoustics

In addition to the potential effect induced by the presence of the NGVs, the blockage created by the restriction of the flow passage changes the acoustic condition at the exit of the combustor. Indeed, for most of the recent aero-engines the HP turbine stages operate at *chocked condition* and the sonic throat leads to the (partial) reflection of the acoustic waves. The chocking of the NGV rows enhances two acoustic mechanisms:

(i) acoustic waves generated by the flame are reflected at the sonic throat and come back into the chamber;

(ii) entropic waves due to the generation of hotspots by the chamber are partly converted into acoustic waves that can travel back into the chamber [98] or down through the turbine stages [99, 100] (indirect combustion noise).

When acoustics waves go back into the chamber they can couple with the flame creating combustion instabilities [98]. In the worst cases, these instabilities are not damped by the technological systems, they are amplified and ultimately lead to the degradation of the combustion chamber. Recent numerical studies investigating the dynamics and stability of modern combustion systems —mainly through

LES— observe an emerging need for realistic outlet acoustic conditions. This can typically be performed either by introducing the NGVs in the computational domain [101] or an equivalent reduction of the chamber exit cross section [98, 102]. As an example, the thermo-acoustic behaviour of a recent aeroengine combustor was numerically studied by Motheau [98] using a contraction at the exit as shown in Fig. 1.27. The use of Dynamics Mode Analysis (DMD) on the LES data demonstrated that pockets of fluctuating entropy were created inside the chamber and convected to the downstream nozzle where they created acoustics perturbations that excited back the flame. An illustration of the instability is given in Fig. 1.28 by the pressure signal recorded by a probe located inside the chamber for two operating points which differ by the inlet temperature of the cold gases. The dotted line corresponds to a stable regime while for the solid line a combustion instability appears, leading to the apparition of strong harmonic fluctuations at a fundamental low-frequency (unstable mode).

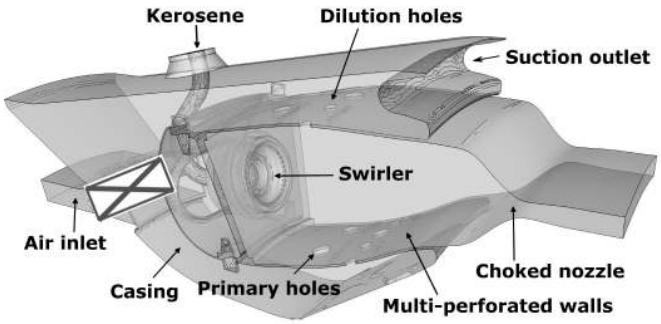


**Figure 1.27:** Numerical domain for the LES of a recent aero-engine with a section reduction at the outlet [98].

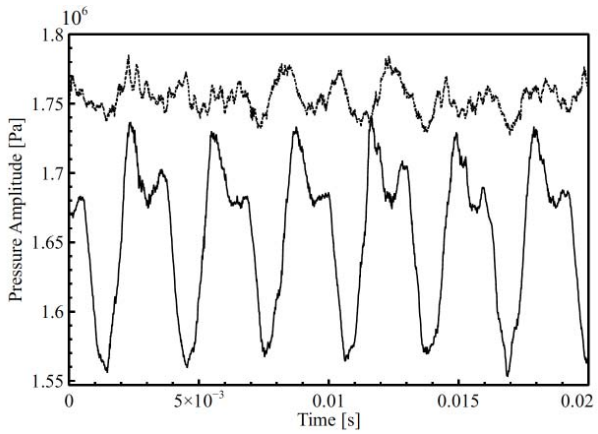


**Figure 1.28:** Pressure signal for a stable (—) and an unstable (- -) operating mode of the combustor depending on the inlet conditions [98].

All these recent studies illustrate that in the context of advanced LES of combustion systems, there is a need to better take into account the acoustic changes induced by the presence of the turbine. This is crucial for the study of combustion instabilities and indirect combustion noise [28, 102]. It further underlines the

two way coupling present in real engine (when only one way coupling was initially targeted: i.e. combustor impact on the turbine).

## 1.4 Concluding remarks

The literature review presented in this chapter proposed an overview of the current knowledge of the physical phenomena occurring at the combustor turbine interface. The following major conclusions and perspectives for future work can be drawn from this analysis:

- The influence of combustor exit non-uniformities on the turbine flow is important and affects different aspects of the turbine design: heat transfer, secondary flows, efficiency, clocking issues... It is now known that using 1-D profiles at the turbine inlet is not sufficient to fully characterize the incoming flow and turbine design practices tend to rely more and more on (time-averaged) 2-D fields.

- The combustor exit flow field is still poorly described in industry or in current facilities in terms of unsteady characterisation: turbulent intensity and lengthscale, characteristic frequencies etc.

- There is currently no HS test rig representative of modern Lean Burn engine, i.e. featuring both swirl and temperature distortion at the turbine inlet. Published studies on such flow configurations are only numerical analyses which lack experimental validations.

- The influence of the turbine flow on the combustor is a much more recent field of study (10 years) and is based only on numerical simulations. The potential effect resulting from the presence of the vanes close to the combustion chamber is known to exist but its extent and implications are not mastered. There is a need for validated high fidelity simulations to investigate this specific issue, especially in light of the more and more compact engine designs that are appearing.

- The presence of a chocked nozzle downstream of the combustor changes the acoustic behaviour of the chamber compared to an unchocked one and may favour critical engine operating conditions with strong thermo-acoustic instabilities. When numerically studying such mechanisms, one needs to account for the sonic throat ideally by inserting a real NGV inside the computational domain or at least a cross section reduction (it is not proven that the two solutions are equivalent).

The European project FACTOR was created in 2010 within the framework of the FP7 European research program to address part of the issues listed here. The core of the FACTOR project is to develop a new test facility in Europe to investigate the transport of HS in Lean Burn configurations and provide a basis

for the validation of CFD codes. FACTOR should benefit from the experience of previous rigs to use the best technologies. To benefit all, the consortium regroups most of the major engine manufacturers and research laboratories linked to this subject in Europe. Among them, DLR (Göttingen site, Germany) was selected to build a new facility hosting a modern aero-engine Combustor Simulator (CS) and a 1.5 high pressure turbine stage (see Fig. 1.29) operating at realistic Reynolds and Mach numbers.

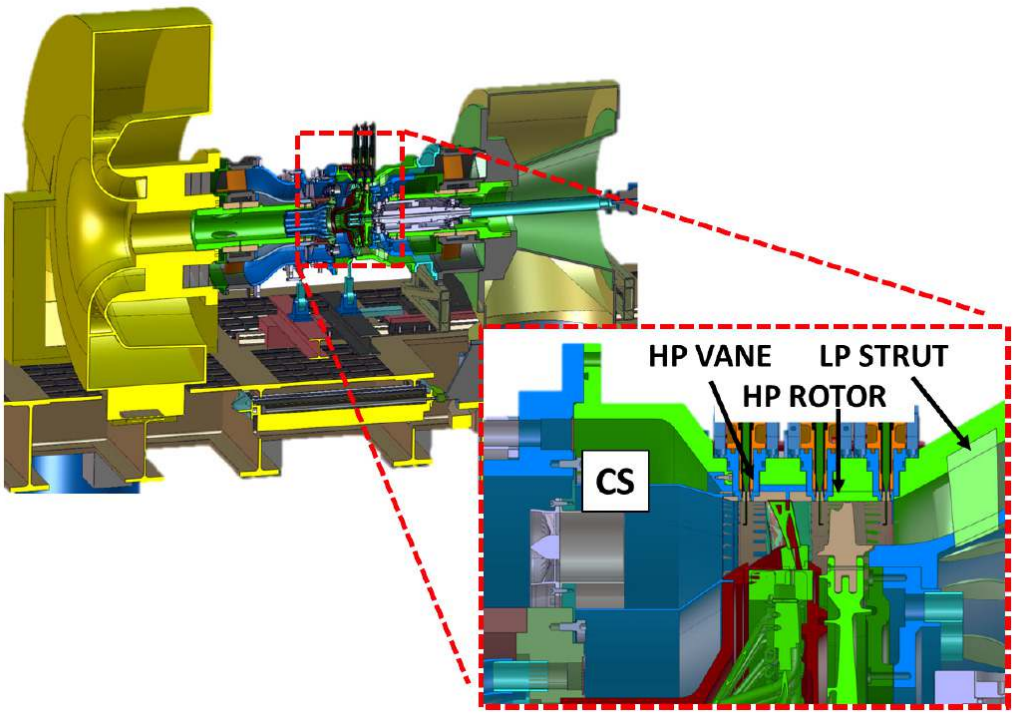


**Figure 1.29:** Sketch of the FACTOR rig to be installed at DLR [103].

The main conclusions of this literature review are used to define the technical requirements retained for FACTOR:

(i) Representative of Lean Burn combustors: realistic HS, swirl and turbulence level at turbine inlet;

(ii) Temperature distortion between $-25\%$ and $+10\%$ of the main temperature in plane 40;

(iii) True scale 1.5 HP turbine stage (360°) with engine representative features (vane film cooling, purge flows, secondary air system, disk front and rear cavities, squealer at blade tip...);

(iv) Possibility to study different clocking positions HS-NGVs;

(v) Operating in continuous mode to allow advanced measurements;

(vi) CFD-friendly count for periodic simulations: one HS for two vanes, three rotor blades and one low pressure strut (1HS:2NGVs:3HPRs:1LPV);

(vii) Non-reactive for simplicity and cost.

Within the FACTOR project, Turbomeca is in charge of the design of a CS representative of Lean Burn configurations. Part of such work was performed during this thesis in collaboration with CERFACS and is now detailed in Part II of this manuscript.

# Part II

# Development of an engine representative combustor simulator dedicated to hot streak generation

This second part of the manuscript focuses on the development of the combustor simulator for the FACTOR project and is organized as follows:

- First, Chapter 2 presents the design process and gives a numerical insight on the flow topology inside the combustor simulator relying on pre-test LES.
- Second, the development of a trisector test rig version of the combustor simulator for experimental validation is introduced in Chapter 3 with a special insight given on the instrumentation and definition of the chosen operating points.
- Finally, Chapter 4 proposes a comparison between simulations and experiments to assess the design of the combustor simulator and validate the numerical methodology.

Some elements of the development of the combustor simulator and the validation of the design choices presented in Chapters 2 and 3 were published in the following article:

> C. Koupper, G. Caciolli, L. Gicquel, F. Duchaine, G. Bonneau, L. Tarchi, and B. Facchini. "Development of an Engine Representative Combustor Simulator Dedicated to Hot Streak Generation". In: *Journal of Turbomachinery* 136.11 (2014)

Experimental results presented in Chapter 4 were published in:

> T. Bacci, G. Caciolli, B. Facchini, L. Tarchi, C. Koupper, and J.-L. Champion. "Flowfield and temperature profiles measurements on a combustor simulator dedicated to hot streaks generation". In: *ASME Turbo Expo 2015: Turbine Technical Conference and Exposition*. GT2015-42217. 2015

# Chapter 2

# Design of the combustor simulator and preliminary assessment by LES

## Contents


2.1 Design process of the combustor simulator for FACTOR . . . . **46**
2.1.1 Requirements and target . . . . . 47
2.1.2 Final design and operating conditions . . . . . 48
2.2 Numerical insight on the flow topologies with and without confinement . . . . . **50**
2.2.1 Set up of the LES . . . . . 50
2.2.2 Flow inside the chamber . . . . . 52
2.2.3 Duct effect on the swirler flow . . . . . 55
2.2.4 Hydrodynamic instability: the PVC . . . . . 58
2.3 Intermediate conclusions on the initial design phase . . . . . **62**


The literature review on the combustor-turbine interface presented in Chapter 1 indicates that there is a need for a new engine-representative test rig in Europe on that topic. The FACTOR project was launched in 2010 to directly address this issue. To meet this purpose a non-reactive CS needs to be designed and is the objective of this chapter.

One presents here the design process of the CS and details on how the use of LES is introduced in this design phase. The development of the CS is presented in Section 2.1 including the initial requirements, the development of the technological solutions as well as the final design. The final configuration of the CS features a confinement duct whose length is voluntarily made variable to allow adjustments if necessary. To better apprehend the impact of this confinement on the flow topology, pre-test LES are performed on three duct sizes for which results are presented in Section 2.2.

## 2.1 Design process of the combustor simulator for FACTOR

The design process followed to develop, validate and test the CS is schematically shown in Fig. 2.1 and detailed below:

Step A Requirements and targets are proposed by the FACTOR consortium as detailed in Section 2.1.1.

Step B Based on these requirements, approximately 40 RANS simulations are performed by Turbomeca and GDTech on successive geometries and flow configurations. The main parameters under study are the geometry of the CS, the multiperforated plates characteristic (number, position, size, permeability, injection angle), the flow split between mainstream and coolant, the swirler velocity profiles and dimensions. These numerical simulations lead to a proposal for the CS geometry and flow conditions presented in Section 2.1.2.

Step C LES are performed on the configuration retained in step B to validate the design choices. At this occasion, the trisector approach for the UNIFI rig and the isothermal operating point (see Chapter 3) are validated by the use of LES.

Step D The conclusions obtained from the pre-test LES of step C allow to propose a final configuration to be tested experimentally. To allow possible adjustments before the DLR test campaign, the geometry is not frozen but a duct whose length can be changed is positioned at the exit of the swirler. More details on the introduced confinement effect will be given in the following.

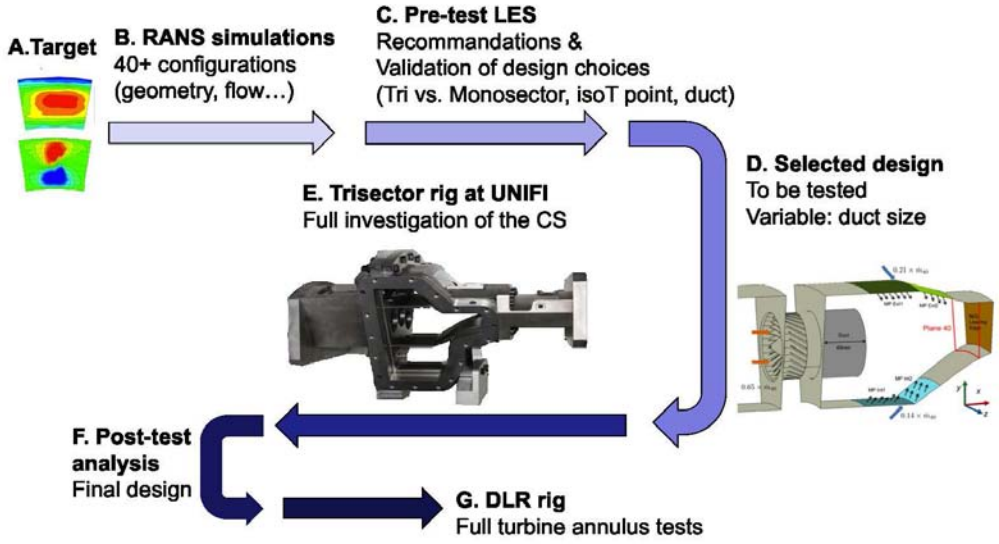


**Figure 2.1:** Schematic view of the CS design process from the beginning until the full turbine tests at DLR.

Step E To increase the degree of confidence in the numerical predictions of the full configuration to be measured at DLR, an experimental validation on a simpler model is necessary. In addition to the FACTOR rig implemented at DLR in Göttingen, a trisector test module is mounted at UNIFI to perform a detailed characterisation of the combustor aerothermal flowfield as presented in Section 3.1.

Step F The test campaign conducted at UNIFI between October 2013 and February 2014 provided a large amount of experimental results that is used for comparison with the LES *a posteriori* validation of the simulations. The final configuration of the CS is then validated for manufacturing and future use on the DLR rig.

Step G The full test campaign on the DLR rig comprising the CS and the HP turbine stage is expected for late 2015.

### 2.1.1 Requirements and target

The requirements for the design of the FACTOR CS derive from the conclusions of the literature review, the technological limitations and the desired measurement techniques. Since the CS should be representative of a Lean Burn combustor from a recent aero-engine, the following specificities are retained:

(i) Fully annular axial chamber featuring 20 sectors of 18°;

(ii) Although non-reactive, the flow should contain temperature peaks and mixing: i.e. use at least two streams with distinct temperature values;

(iii) Flow split: around 2/3 of hot air mass flow going through swirlers (mainstream $\dot{m}_M$) and 1/3 of air mass flow used for cooling ($\dot{m}_{cool}$);

(iv) Cooling is provided by multiperforated liners only, without dilution holes;

(v) The swirler should have a swirl number around 0.7 using the definition by Beér et al. [104] shown later in Eq. (2.1);

(vi) A level of turbulence intensity around $10 - 20\%$ at the combustor exit.

Technological constraints of the DLR test facility impose to respect the following additional limits:

(vii) The targeted temperature profile should be obtained by mixing only a stream of cold air (referred as coolant) whose temperature $T_{cool}$ should be close to the ambient conditions and a hot air flow at the temperature $T_M < 700K$;

(viii) The mean adiabatic total temperature at the exit of the CS should be $\overline{T}_{40} = 450$ K.

The concatenation of all these requirements lead to the velocity and temperature targets at the exit of the CS shown in Fig. 2.2. This plane referenced hereafter as *plane 40* is located 0.5 Axial Chord Length (ACL) upstream the NGV LE (i.e. 20 mm), whose position is referred as *plane 40+*.

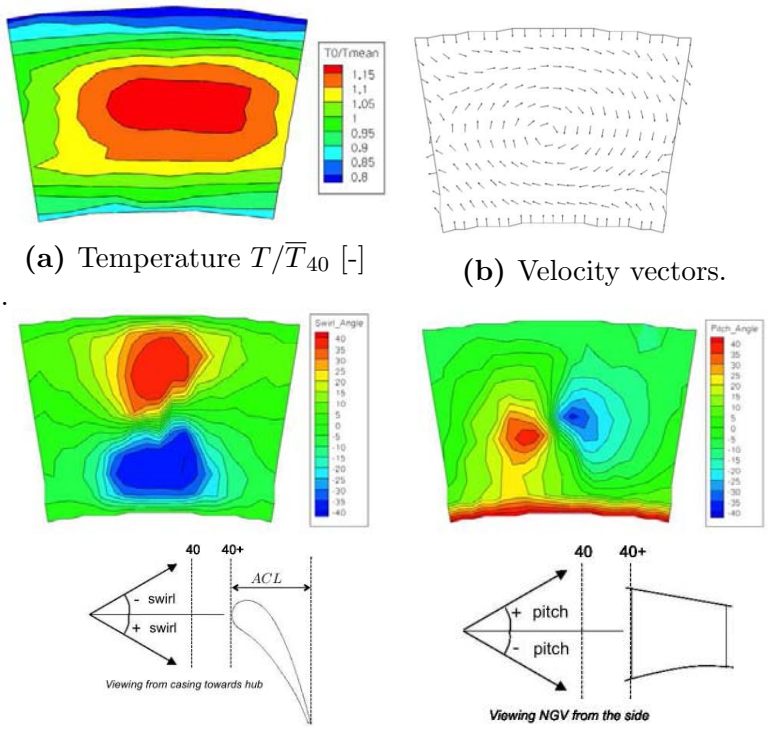


**(a)** Temperature $T/\overline{T}_{40}$ [-]

**(b)** Velocity vectors.

**(c)** Swirl angle [°].

**(d)** Pitch angle [°].

**Figure 2.2:** Target fields to be obtained in plane 40 for the FACTOR CS (looking downstream).

### 2.1.2 Final design and operating conditions

A single sector of the design retained after the use of RANS as well as LES and proposed for experimental investigation at UNIFI is schematically shown in Fig. 2.3a. The total mass flow in plane 40 ($\dot{m}_{40} = 0.240$ kg/s per sector) is the result of a specific split: 65% through the swirlers ($T_M = 531$ K) and 35% injected in the chamber through effusion cooling ($T_{cool} = 300$ K) to obtain the target mean total temperature (450 K) at the turbine inlet. The operating conditions of the turbine impose an absolute total pressure in plane 40 of 149 kPa. An outer and inner large cavity (see Fig. 2.4a) are installed on both sides of the CS to deliver respectively 21% ($\dot{m}_{CO}$) and 14% ($\dot{m}_{CI}$) of the total mass flow to the multiperforated plates (blue and green zones in Fig. 2.3a). In contrast with what is found for a real engine, the mass flow rate feeding the two cavities and the hot stream swirled jet are regulated independently by control valves. Detailed characterization and flow check of the effusion cooling system can be found in appendix A.

The axial swirler has an external diameter $D_{sw} = 63$ mm and contains 30 flat vanes disposed around a central hub of diameter $D_h = 22$ mm, as shown in Fig. 2.3b. Flow checks were performed on the swirlers in an open-loop suction type wind tunnel at UNIFI [103] as well as on the test rig. The swirler (without duct) was found to create a pressure drop around 3.5% at nominal mass flow rates, which is in line with the pressure drop created in the injection system of modern gas turbine combustors.

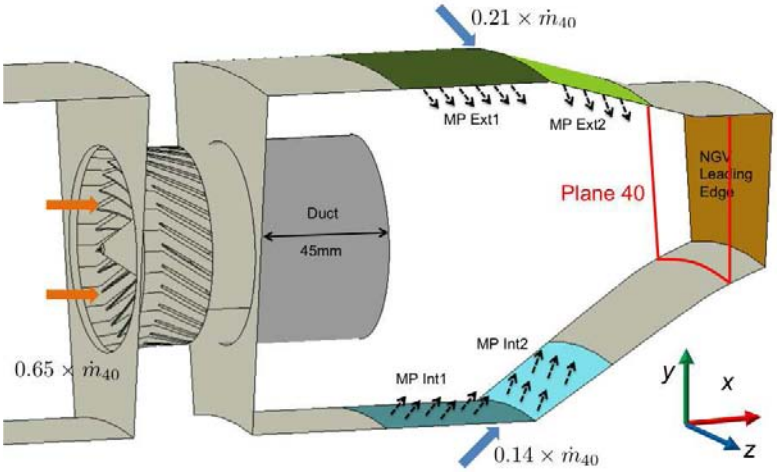


**(a)** Representation of the flowpath in the CS.

**(b)** Detail of the swirler.

**Figure 2.3:** Schematic view of the CS: the multiperforated liner is shown in color and the inner and outer feeding cavities are not shown.

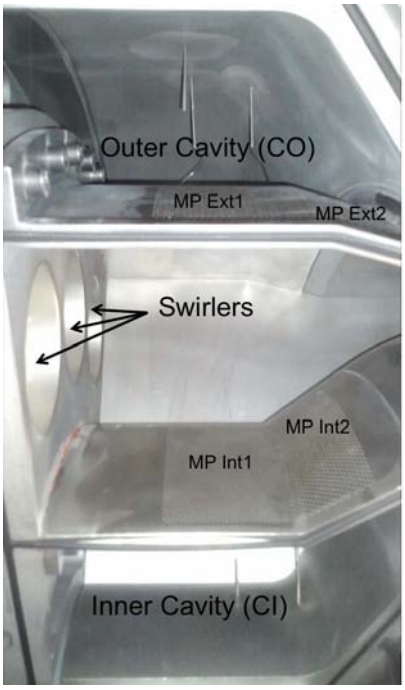


**(a)** Mainstream (without duct) and cavities.

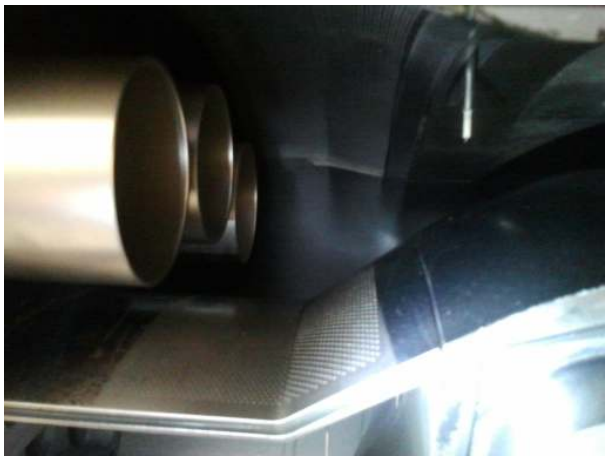

**(b)** CS fitted with the 55 mm duct.

**Figure 2.4:** Real hardware of the CS on the UNIFI trisector rig.

For flexibility and better control of the hot streak characterisation, a duct can be fitted in the CS at the exit of the swirler to confine and preserve the hot spot. The effect of the length of this duct is the only variable that should be tested on the trisector rig. Its length is arbitrarily made variable over a range of 0 mm (hereafter case labelled D00) to 55 mm (D55). A photo of the UNIFI trisector rig with the latter duct is shown in Fig. 2.4b. The positioning of the duct at the exit of the swirler is expected to have a significant impact on the flow field and shall be used for properly achieving the targeted profiles in plane 40. To assess the actual impact of this duct on the flow topology, a priori LES are performed on different configurations and results are now reported.

## 2.2 Numerical insight on the flow topologies with and without confinement

It is proposed here to give an overview of the flow topology inside the CS for three duct lengths (0, 45 and 55 mm), relying on the results provided by the LES. By presenting and comparing the different flow fields, one intends to better understand the flow dynamics inside the entire CS before analysing the experimental results which provide data in limited zones. First, the set-up of the simulations is introduced in Section 2.2.1. Then results are discussed focusing on the mean flow field in the CS (Section 2.2.2), the potential effect of the duct imposed confinement on the swirler flow (Section 2.2.3) and finally the hydrodynamic unsteadiness issued by the swirler (Section 2.2.4).

### 2.2.1 Set up of the LES

Regardless of the duct length, the computational domain used for LES of the CS presents the same features. As shown in Fig. 2.5, only one sector of the geometry ($1/20 = 18°$) is simulated and periodicity is enforced on the two lateral sides. The inlet of the mainstream flow feeds a large plenum with hot air at the nominal

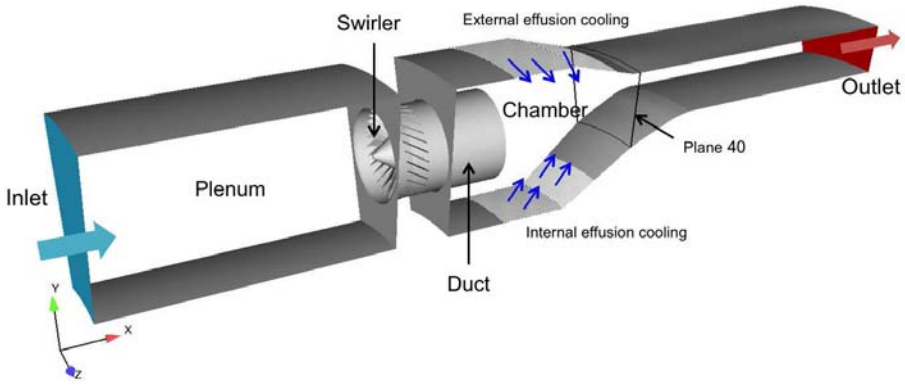


**Figure 2.5:** Schematic view of the numerical domain of the CS.

mass flow rate. The other inlets are linked to the effusion cooling systems whose treatment is of importance for the FACTOR configuration as they cover a large portion of the CS liners and inject 35% of the total mass flow rate. The cost of meshing all the effusion cooling holes ($< 0.5$ mm diameter, 5164 holes/sector) along with the upstream cavities being definitely prohibitive, an adiabatic homogeneous injection model is used to account for the momentum injection at the multiperforated plates [105]. To mimic such cooling devices, cooling air is injected at the desired mass flow rate through the surfaces indicated by arrows in Fig. 2.5. Detailed information on this model and its implications for the FACTOR CS are given in Appendix A. All other walls use a law-of-the-wall approach associated with an adiabatic condition. The outlet of the computational domain is located sufficiently far downstream the region of interest and a 3-D characteristic boundary condition [106, 107] is used to avoid acoustic reflections while maintaining the pressure level close to the target value. In the three cases the mesh is unstructured and contains only tetrahedral cells[1]. A view of the mesh is given in Fig. 2.6 through a cross-section view performed in the central plane of the CS.

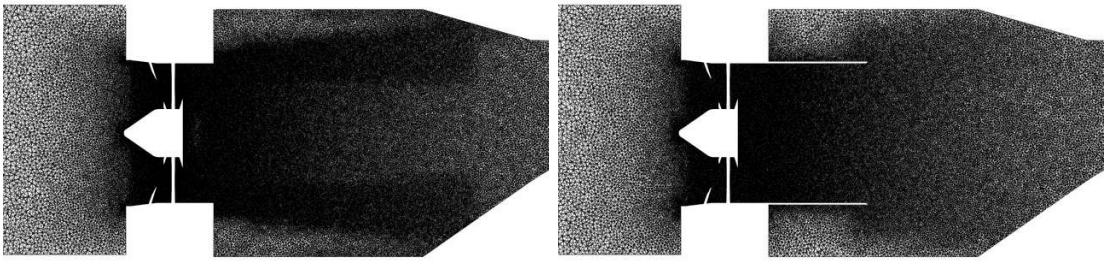

**(a)** D00. **(b)** D45.

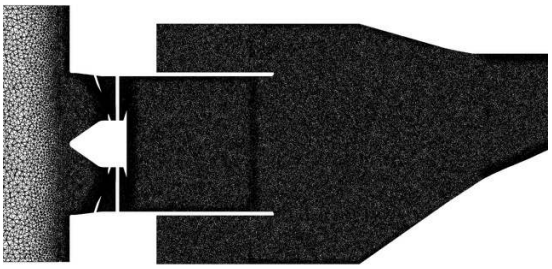

**(c)** D55.

**Figure 2.6:** Mesh in the central plane of the CS for the three duct lengths.

The LES are performed using the AVBP solver [108] which is presented in details in Appendix C and the characteristics of the simulations are recalled in Table 2.1. Based on previous works using the AVBP solver [31, 92, 109], it is decided for these *a priori* LES to use the TTGC scheme [110] for the spatial and temporal discretization (third order in space and time) and the standard

[1]Note that in each case only the simulation performed on the most refined mesh is reported here. The detailed list of the simulations is given in Appendix C.

Smagorinsky SGS model [111] to express the turbulent viscosity. In the following, the LES predictions are analysed based on the mean and RMS fields of the physical quantities. Therefore, once the flow is established and statistically at steady state, the LES are time-averaged over 140 ms. As the through flow time of the CS is about 12 ms from plenum inlet to the domain exit, this translates in more than 10 through flow times, which seems adequate for the convergence of (at least) the lower order statistical quantities.

| Duct | Operating point | Mesh nodes | Mesh cells | Scheme | SGS model | Physical time [ms] | Timestep [s] |
|---|---|---|---|---|---|---|---|
| D00 | DP | 12.2M | 68.5M | TTGC | Smagorinsky | 155 | $3.7 \cdot 10^{-8}$ |
| D45 | DP | 5.2M | 29.1M | TTGC | Smagorinsky | 149 | $5.8 \cdot 10^{-8}$ |
| D55 | DP | 8.9M | 51.0M | TTGC | Smagorinsky | 144 | $4.3 \cdot 10^{-8}$ |

**Table 2.1:** Summary of the LES of the FACTOR CS using different duct lengths.

### 2.2.2 Flow inside the chamber

Some streamlines are computed from the time-averaged solutions of the D00, D45 and D55 cases and shown in Fig. 2.7 for the central plane of the CS (2-D field). The presence of the duct (and its size) has a noticeable impact on the topology of the flow. Without confinement, the flow expands radially into the CS very shortly after the exit of the swirler. This radial motion brings some hot air towards the multiperforated liners of the CS, which then mixes with the coolant before reaching the exit of the CS. With a mid-size duct (D45), the swirling flow reaches more directly the exit of the CS with much less radial deviation, the main jet being more constrained. For the longest duct (D55), this is even more amplified and the main swirled jet does not expand and exits directly the chamber.

These flow behaviours are strongly coupled with the position and dimension of the different reverse flow zones (shown by a blue contour in Fig. 2.7) whose positioning is also known to be critical for combustion as they help anchoring the flame in the chamber. Two main structures usually identified for such burners [112–115] are found here:

**The Central Toroidal Recirculation Zone (CTRZ)** is located in the central region of the CS after the swirler. To help figuring out the 3-D shape of this zone, Fig. 2.8 shows the countour of the CTRZ based on the time-averaged solutions of the three cases (superposed onto the same geometry for clarity).

- For the D00 case, the CTRZ starts right at the exit of the swirler and creates a lot of blockage (about one third of the flow passage at the inlet of the CS) which forces the jet to spread radially. Note that this CTRZ is not axisymmetrical and has a flat shape aligned in the diagonal direction of the CS.

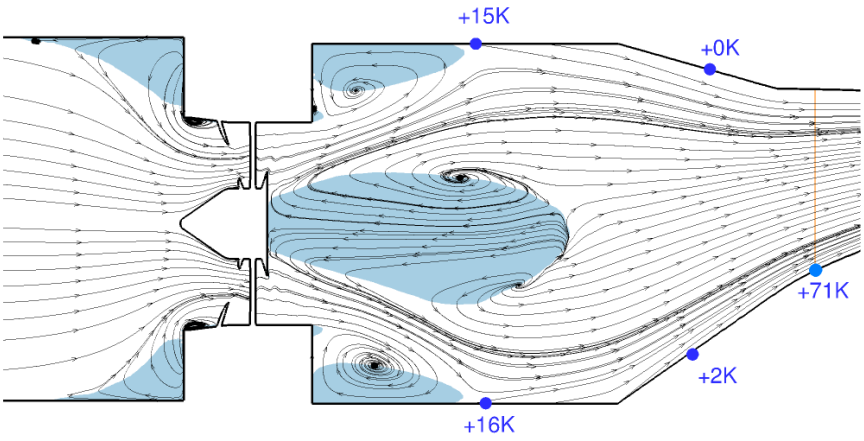


**(a)** D00.

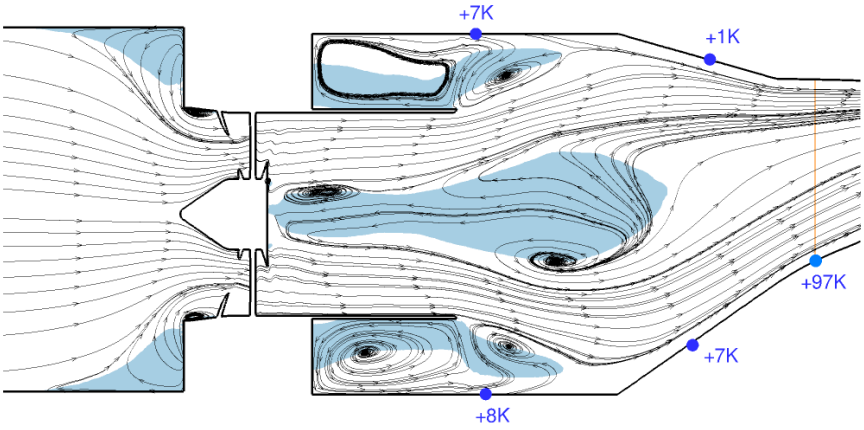


**(b)** D45.

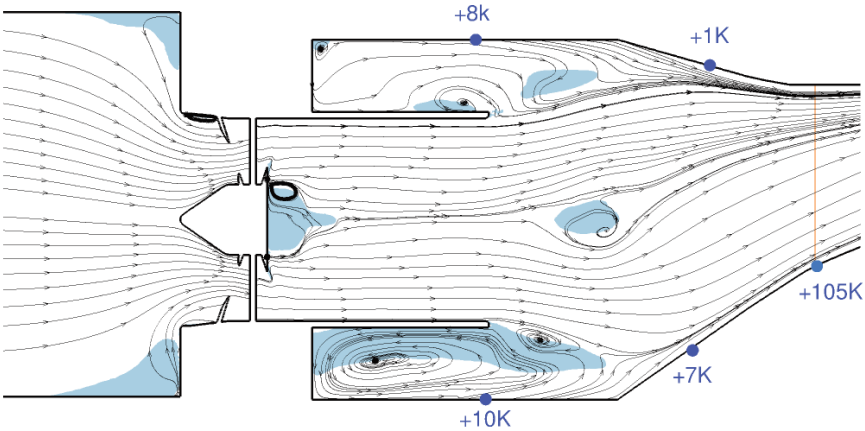


**(c)** D55.

**Figure 2.7:** Some streamlines obtained from a time-averaged velocity field in the central plane of the CS, reverse flow zones (light blue) and experimental measurements of the wall temperature relative to the coolant flow (blue dots).

- For the D45 case, the CTRZ remains cylindrical and locates around the swirler axis until the exit of the duct where it expands radially forming a lightbulb shape. The axial extent of the CTRZ for this case goes beyond the main part of the CS and partly exist in the contraction exit section of the chamber (see Fig. 2.7b) contrarily to the D00 case (Fig. 2.7c).
- For the D55 case, the little recirculation zone formed in the wake of the swirler hub and at the origine of the CTRZ of the two previous cases does not extend inside the duct anymore. Only a little CTRZ is created shortly after the duct exit pointing to two independent recirculation bubbles. The main consequence is a flow reaching very quickly the exit of the CS with little interaction with the coolant flow.

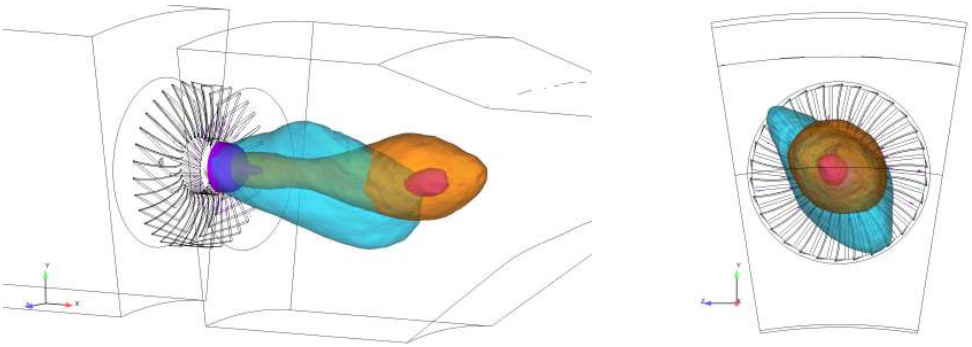

**(a)** View from the side. **(b)** View from downstream.

**Figure 2.8:** CTRZ of the D00 (blue), D45 (orange) and D55 (purple) cases.

**The Corner Recirculation Zones (CRZs)** are located in the corners of the CS and around the duct (as well as in the upstream plenum). All the ducted cases differ from the D00 configuration by the presence of large CRZs above and below the duct which restrain the radial expansion of the jet even after the duct exit. This flow blockage seems to provide a thermal protection of the CS walls as it prevents them from being directly impacted by the hot air stream. This observation is confirmed by experimental measurements of the wall temperature obtained on the UNIFI trisector rig[2] by thermocouples placed inside the liner. These relative wall temperatures measured at steady-state are reported in Fig. 2.7, the reference being the coolant flow temperature. One observes that for the first axial stations the wall heating is about two times smaller for D45 and D55 than D00. If looking at the wall temperature measured in plane 40 (orange line), it is found to strongly increase with the duct size since the longer the duct is the less interaction with coolant flows.

In light of the very different flow behaviour observed in the CS for the three duct sizes, one may wonder if the presence (or absence) of a duct induces strong

[2]See Chapter 3 for details.

changes on the flow field through the swirler. This point is now discussed in the following section.

### 2.2.3 Duct effect on the swirler flow

The flow field is investigated in the plane located at $x/D_{sw} = 0$ referred in the following as the inlet plane of the CS. The positions of all the post-processing planes employed in this work are indicated in Fig. 2.9a for reference. Circumferentially and time-averaged profiles of the velocity components in the swirler frame of reference shown in Fig. 2.10 confirm that the flow topology inside the swirler is indeed affected by the presence of a duct. The unducted case differs from the ducted configurations on three main points:

- First, the profile of the axial velocity component quantitatively confirms the observation that the CTRZ is larger without duct (see Fig. 2.7): about 40% of the swirler radius vs. respectively 20 and 10% for the D45 and D55 cases.

- Second, the absence of duct allows the flow to spread out radially at the inlet of the CS, which results in a significative positive radial velocity value all over the span. In contrast, for the ducted cases the radial velocity is about four times smaller because of the constraint imposed by the duct.

- Finally, this confinement is found to conserve the tangential velocity imparted to the fluid by the swirler as it prevents the jet from spreading out. This results in a larger swirl velocity component all over the span for D45 and D55 than D00.

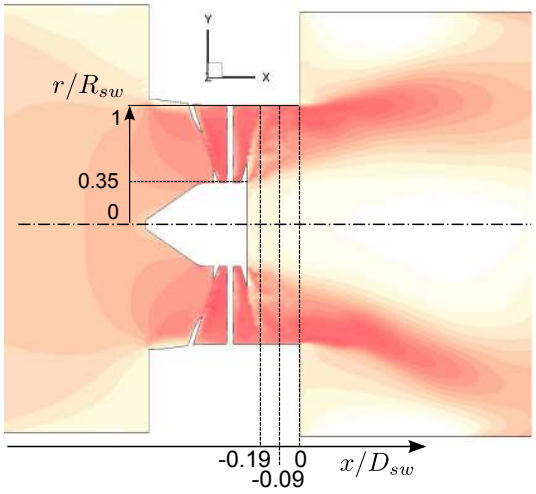


**(a)** Axial and radial cuts inside the swirler, superposed to a field of axial velocity.

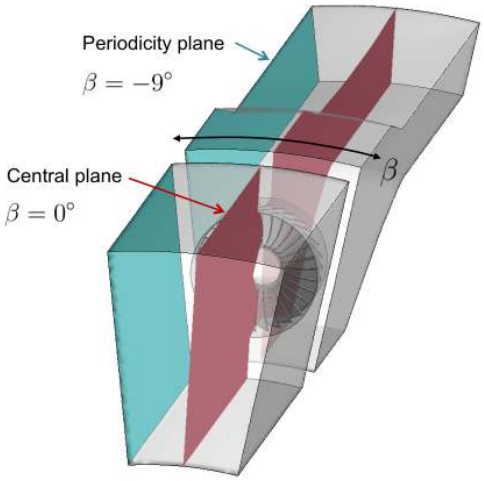


**(b)** Azimuthal cuts inside the CS.

**Figure 2.9:** Position of the CS post-processing planes used in this work.

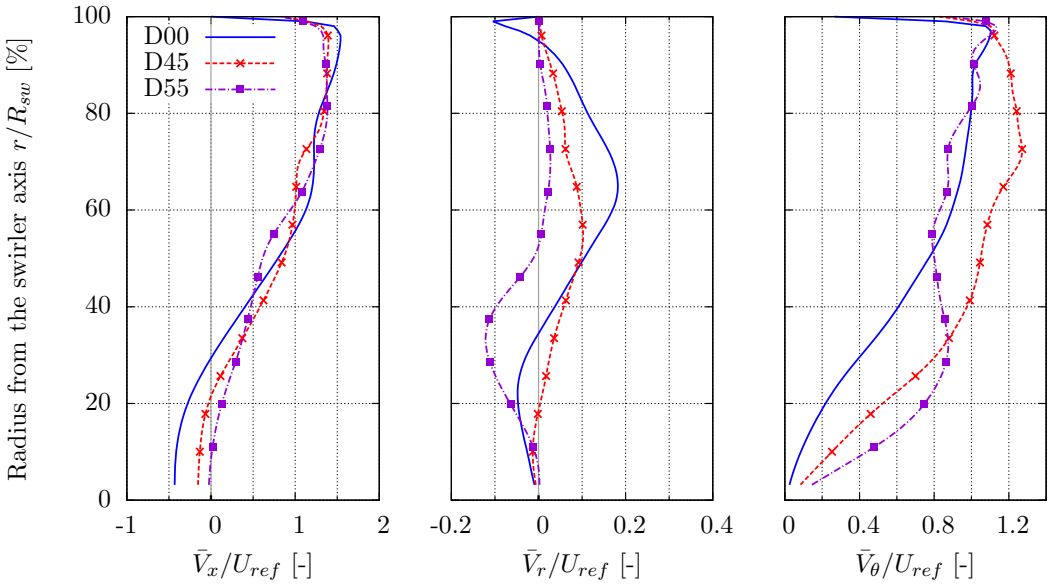


**Figure 2.10:** Circumferentially-averaged velocity profiles in the swirler frame of reference at the inlet of the CS.

As the velocity profiles of Fig. 2.10 are significantly different for the three cases, one may wonder how the corresponding swirl numbers $S_N$ are affected. This global parameter compares the axial flux of tangential momentum $G_\theta$ to the axial thrust $G_x$ and is of importance for the design of the CS as it constitutes one of the targets defined in Section 2.1.1. The most common expression for $S_N$ proposed by Beér et al. [104] is:

$$S_N = \frac{G_\theta}{R_{sw} G_x} = \frac{\int_0^{R_{sw}} \bar{\rho} \bar{V}_x \bar{V}_\theta r^2 dr}{R_{sw} \int_0^{R_{sw}} \bar{\rho} \bar{V}_x^2 r dr}, \tag{2.1}$$

where $\bar{V}_x$ and $\bar{V}_\theta$ are circumferentially-averaged values in our case. A more exhaustive definition [104] accounts for the local pressure in the expression of the axial thrust $G_x$:

$$S_N = \frac{G_\theta}{R_{sw} G_x} = \frac{\int_0^{R_{sw}} \bar{\rho} \bar{V}_x \bar{V}_\theta r^2 dr}{R_{sw} \int_0^{R_{sw}} \left( \bar{\rho} \bar{V}_x^2 + (\bar{P} - P_{40}) \right) r dr}, \tag{2.2}$$

where $P_{40}$ is the mean static pressure in plane 40. The swirl number is computed from Eqs. (2.1) and (2.2) at various axial positions from the vanes exit to the duct exhaust and plotted respectively in Figs. 2.11a and 2.11b. Relying only on the simple expression for $S_N$ (Fig. 2.11a), the swirl number is found to remain superior to 0.6 and converge precisely towards this value[3] just before the flow expansion into the CS (i.e. at the exit of the duct) for all the cases. The use of the full expression (Fig. 2.11b) allows to discriminate the different cases. For the D00 and D45 cases, one observes large values of $S_N$ which indicates that the

[3]Note that it is close to the target value of 0.7 defined in Section 2.1.1.

axial pressure gradient on the denominator of Eq. (2.2) is negative because of the depression zone inside the large CTRZ. For the D55 case, $S_N$ remains below 0.6 because the time-averaged axial pressure gradient is positive (no CTRZ in the duct).

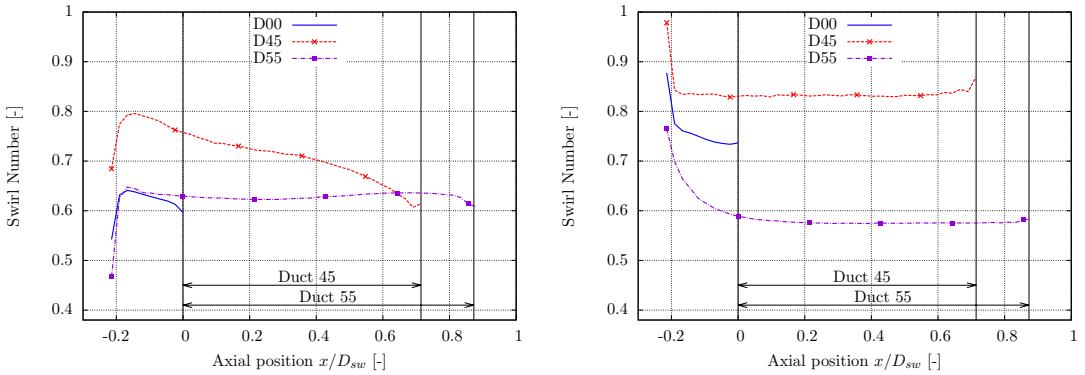


**(a)** Simple expression Eq. (2.1) **(b)** With the pressure term Eq. (2.2)

**Figure 2.11:** Swirl number at various axial stations.

In light of such results, the D55 case seems a little specific because of the absence of large CTRZ in the duct (Fig. 2.8) and the associated lower value of $S_N$ (Fig. 2.11b). However, these observations being made on the basis of time-averaged fields, possible unsteady features of the flow are inaccessible. With this aim, analyses are performed on a set of 1975 successive instantaneous solutions of the LES of the D55 case (sampled ad 20 kHz) to investigate the time-evolution of the position of the reverse flow zones. As shown in Fig. 2.12, large differences are observed between the time-averaged contour of the CTRZ (purple) and the time-envelope of all the positions featuring some reverse flow at any time (blue). Such investigations indicate that: *(i)* reverse flow is locally observed inside the duct at all times; *(ii)* the time-envelope contour of this reverse flow zone is wide and centered on the swirler axis suggesting a rotating motion of the CTRZ; *(iii)* the

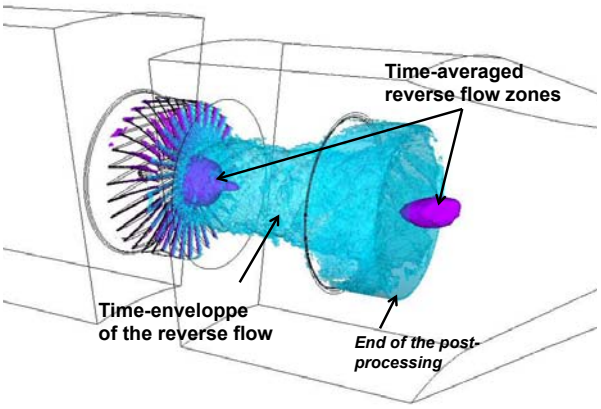


**Figure 2.12:** Time-averaged (purple) and time-envelope (blue) contours of the reverse flow zones for the D55 case.

reverse flow zones imply local instantaneous depressions that do not exist when time-averaging the quantities and thus an under-prediction of $S_N$ in Eq. (2.2). The swirler velocity profiles for the D55 case seem to promote a vortex breakdown with the apparition of an unstable CTRZ inside the duct that cannot be seen on a time-averaged solution.

It is now proven that a CTRZ forms at the swirler exit for the three cases as a direct consequence of the swirler velocity profiles and the associated high values of $S_N$ The presence of a CTRZ at high swirl conditions is known to possibly lead to the apparition of a hydrodynamic instability typical of such combustion chambers [116–118]: the Precessing Vortex Core (PVC). Such instability is the result of the vortex region of the flow becoming unstable and starting to precess about the swirler axis. To assess if this instability is present for FACTOR CS and affects the flowfield, further investigations are now detailed.

### 2.2.4 Hydrodynamic instability: the PVC

The presence of a PVC can be detected by monitoring the pressure or velocity fluctuations in the region where it is supposed to form, i.e. the boundary of the reverse flow [119, 120]. With this aim, Fig. 2.13 shows an isosurface of pressure lower than the mean value in the CS on an arbitrary instantaneous solution for the D00, D45 and D55 cases. Such contours evidence for all cases the presence of a vortical structure similar to a finger turning around the CTRZ, typical of a PVC [116]. The observation of successive snapshots of the flow field qualitatively indicates that this large structures rotates around the swirler axis at about 500 Hz for all three cases. However, for the D45 case the selected isosurface of pressure

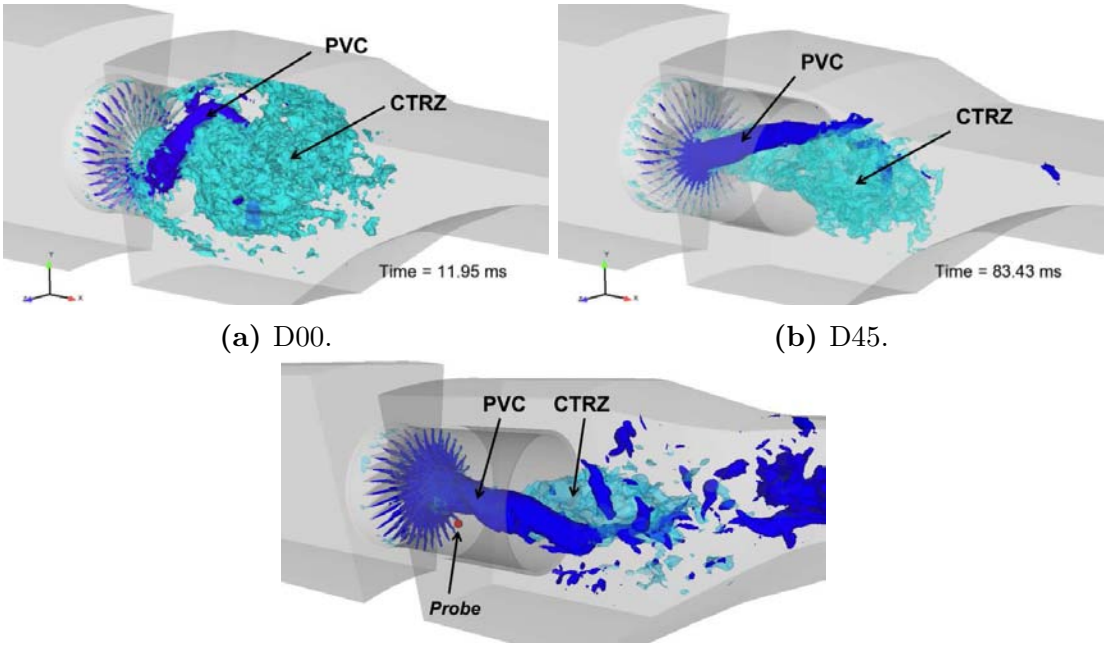


**(a)** D00. **(b)** D45.

**(c)** D55.

**Figure 2.13:** Visualization of the PVC on an instantaneous LES solution.

sometimes disappears or divides into multiple fingers. To address if this is due to a specific behaviour of the PVC or just a visualization issue, it is proposed to perform spectral analysis of the pressure signals by means of spectrograms. Such procedure allows to assess the evolution in time of the Power Spectral Densities (PSD) of a signal, i.e. evaluate if a periodic phenomena is present all over the duration of the signal. PSDs are calculated over a set of windows of half the total duration of the signal, each of them taken at successive initial times with an overlap of 1/16. All the different PSDs are then stacked to form the spectrogram of the signal under investigation. This procedure is applied to the simulations of the D00, D45 and D55 cases using the pressure signal recorded by a probe whose location is indicated by a red dot in Fig. 2.13c. The corresponding spectrograms are shown in Fig. 2.14 after being normalized by the maximum PSD amplitude in each case. To account for the different levels of swirl found at the exit of the swirler, a Strouhal number is used instead of the frequency:

$$St = \frac{f D_{sw}}{\overline{V}_{\theta_{sw}}}, \tag{2.3}$$

where $\overline{V}_{\theta_{sw}}$ is the mean value of the swirl velocity component in the inlet plane of the CS (computed from the profiles shown in Fig. 2.10).

One observes on the spectrograms of Fig. 2.14 the continuous presence of a tonal activity at a Strouhal number between 0.5 and 0.6 for all three cases which constitutes a typical characterization of a PVC [118, 121]. The precise Strouhal numbers and frequencies associated with such peaks are reported in Table 2.2 along with the corresponding confidence margin based on the frequency resolution of each numerical signal. In light of the accuracy of the frequency characterization (around 10 Hz) and the numerical differences between the three cases (mainly the mesh size), the precise characterization of the phenomenology is subject to caution. However, the spectrograms suggest that: *(i)* the confinement by the duct increases the PVC frequency by 50 Hz (i.e. 12%); *(ii)* for the D45 case, other harmonics can be present of lower amplitude (such as another PVC finger) [118] which could explain the observed structures.

| Case | $f_{PVC}$ [Hz] | $St = \frac{f_{PVC} D_{sw}}{\overline{V}_{\theta_{sw}}}$ [-] |
|---|---|---|
| D00 | 398 ±13 | 0.58 ±0.019 |
| D45 | 446 ±14 | 0.50 ±0.015 |
| D55 | 447 ±7 | 0.60 ±0.009 |

**Table 2.2:** Strouhal number and frequency of the PVC obtained by the LES.

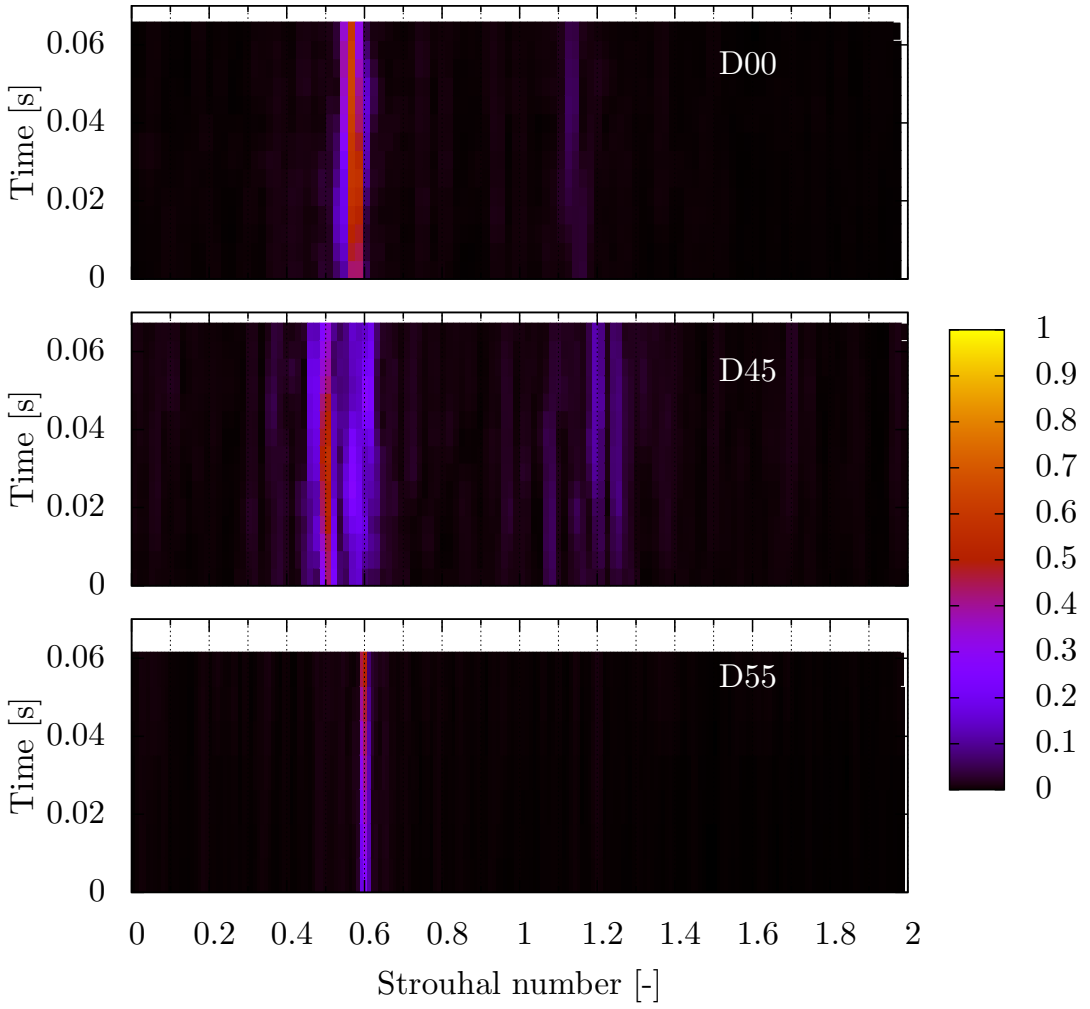


**Figure 2.14:** Spectrograms of the pressure signal recorded by a probe at the inlet of the CS.

A final characterization of the PVC location in the CS is proposed by performing PSDs at each single node of the numerical domain over a set of instantaneous solutions obtained from the LES. This analysis is performed for all the cases using 1100 snapshots sampled at 10 kHz (resulting in a frequency resolution of 9 Hz). Figure 2.15 shows the map of the PSD amplitude corresponding to $f_{PVC}$ (see Table 2.2) normalized by the maximum amplitude in the plane. This figure highlights the location of the PVC by the contours of maximum values of the PSD modulus. In all cases the PVC forms at the exit of the swirler and the pressure perturbation is even noticeable inside the vane passages. This PVC then aligns with the axial direction in the ducted cases while it shows a more pronounced radial opening for the D00 case. Such contours for the D55 case confirm the presence of a classical PVC shape even if no large CTRZ is present except the little recirculation bubble observed in Fig. 2.8. For the ducted cases one can observe the presence of two circular spots of higher PSD amplitude which lie in the shear region downstream

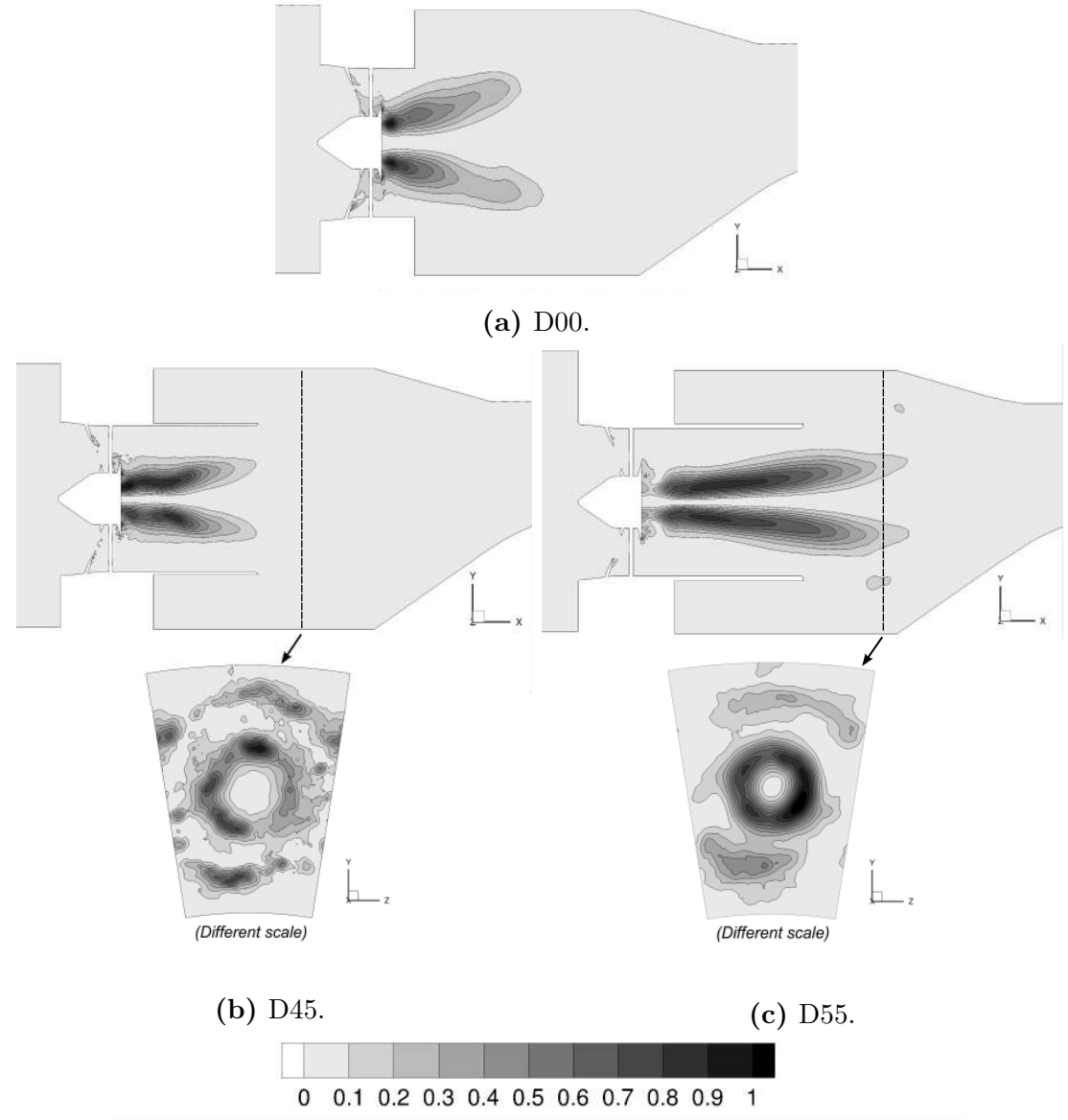


**(a)** D00.

**(b)** D45.

**(c)** D55.

**Figure 2.15:** Non-dimensional PSD coefficient at the PVC frequency computed on the pressure signal.

of the duct edge indicating the potential forcing by the PVC of the duct exit shear layers. This is further evidenced by performing an axial cut a little downstream of the duct exit and normalizing the map by the maximum PSD values in this plane (bottom part of Fig. 2.15b and 2.15c). A circular zone appears above the duct radial extent, exactly in the shear region mentioned previously. Such results do confirm that the effect of the PVC is not localized only in the zone around the CTRZ but may interact with other regions of the flow potentially affecting the mixing. In the D00 and D45 cases, the trace of the PVC is limited to the first half of the CS while for the D55 case it is visible very far downstream the swirler exit (even if it does not go beyond the contraction at the exit of the CS). However, non-reported PSDs performed in plane 40 show that no periodic activity is present

at this specific location. Such numerical results tend hence to indicate that the PVC does not reach plane 40 which reduces the possibility of measuring it during the test campaign.

## 2.3 Intermediate conclusions on the initial design phase

At the end of the numerical development phase of the CS, the following intermediate conclusions can be drawn:

- A frozen design of the CS compatible with the FACTOR requirements is proposed based on RANS and LES results. A duct whose length is made variable is introduced at the exit of the swirler and should be used for adjustments.
- A set of three LESs of the CS using three duct lengths provide us with a fairly wide numerical characterization of the CS flow and highlights the important effect of the confinement.
- The duct size is found to impact the location and dimensions of the reverse flow zones (CTRZ and CRZs), the thermal protection of the liners, the swirler velocity profiles, the Swirl number and the position of the PVC.

Based on such results and other non-reported simulations [21], a good confidence is given in the design of the CS and its ability to reach the FACTOR target. However, before mounting the CS on the full annular machine at DLR, further validation is required through an experimental investigation of the module. This is performed on a trisector configuration of the CS, as now described in Chapter 3.

# Chapter 3

# Trisector test rig experimental validation and investigation

## Contents


3.1 UNIFI trisector rig . . . . . **64**
3.1.1 Presentation of the test facility . . . . . 64
3.1.2 Instrumentation . . . . . 65
3.2 Isothermal operating point . . . . . **70**
3.2.1 Algebraic representation of the test rig . . . . . 70
3.2.2 Selection of the isothermal operating point . . . . . 75
3.2.3 Validation by LES . . . . . 77
3.3 Summary of the available experimental investigations . . . . . **84**


Before the full annulus test campaign on the DLR rig, the CS is chosen to be experimentally investigated at UNIFI (Florence, Italy) in collaboration with Turbomeca. In this context and with the support of LES for validation [21], a trisector configuration of the CS is retained for the UNIFI test campaign (instead of the full annulus) to ease the use of a large number of measurements.

The UNIFI test facility hosting the trisector rig and the detailed instrumentation of the module are presented in Section 3.1. Various measurements are planned to deeply characterize the flow field at different locations. Amongst them, Hot Wire Anemometry (HWA) is selected for turbulence measurements and requires the flow to be isothermal. Therefore, an isothermal operating point representative of the nominal conditions has to be defined. The methodology proposed for its selection and the validation by LES are presented in Section 3.2. A conclusion recalling all the performed measurements is finally proposed in Section 3.3.

# 3.1 UNIFI trisector rig

## 3.1.1 Presentation of the test facility

The intermediate experimental facility hosted by UNIFI is dedicated to the investigation of three sectors of the final CS geometry (see Fig. 3.1a) and constitutes in itself a unique detailed experimental validation of the CS design. In this context, it is decided to use only three sectors of the DLR geometry (see Fig. 3.1b) to allow deep investigations inside the chamber. As measurements are focused on the central sector, the influence of the two lateral walls is supposed to be negligible. This assumption is confirmed by running and comparing LES of a periodic monosector (representative of the full annular machine) and a trisector domain with the lateral walls. The velocity profiles as well as mean and RMS temperature fields in plane 40 are found to be identical. The mean flow in the central sector is marginally affected by the presence of walls which validates the trisector approach. Full results were published [21] and can be found in Appendix D.

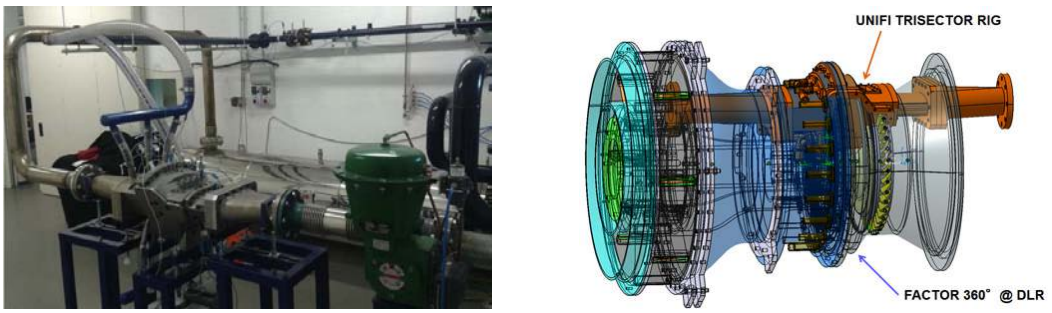


**(a)** Test cell of the trisector rig. **(b)** Full annulus and trisector rigs.

**Figure 3.1:** FACTOR test rigs.

The test rig was manufactured during the summer of 2013 and installed in a new UNIFI facility as illustrated in Fig. 3.2. Air is compressed by two screw compressors, crosses a chiller to cool the mass flow down to ambient temperature and remove the humidity before to feed a 2 $m^3$ vessel used to damp pressure fluctuations. The air flow is then separated into two coolant lines (feeding the inner and outer cavities) while the mainstream goes through a 600 kW electrical heater which rise the fluid temperature up to the desired value. The mass flow rates are set up by throttling several valves. Finally a last vee-valve is used at the rig exit to control the pressure inside the CS. All valves and heater are automatically controlled by means of a Proportional Integral Derivative (PID) system. The behaviour of the main measured quantities during a warm-up sequence is shown in Fig. 3.3. Steady-state is reached when the metal temperatures measured in plane 40 reach an asymptotic value (obtained after a transient of $\pm$ 60 min) at which the experimental investigations start. The operating conditions are very stable during the investigations (1 to 2 hours): the maximum oscillation of mass flow is $\pm 1.5\%$ and $\pm 0.5\%$ for temperature and pressure.

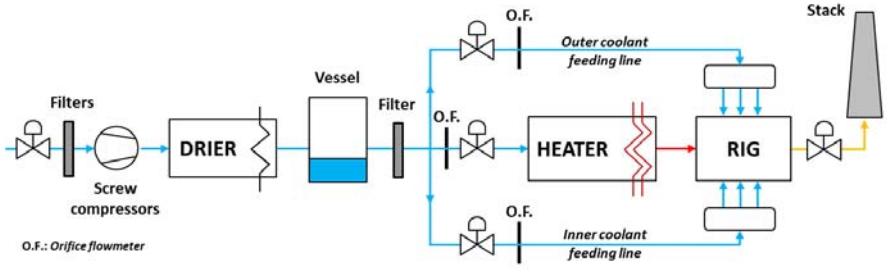


**Figure 3.2:** Sketch of the test facility

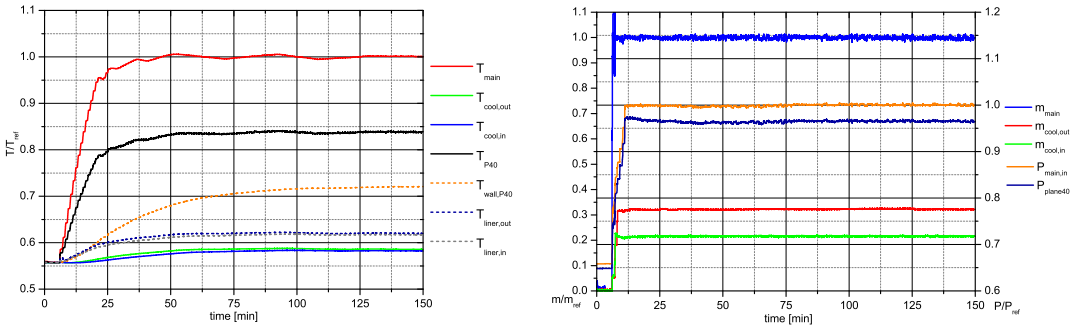


**(a)** Fluid — and metal - - temperatures. **(b)** Mass flow rates and pressures.

**Figure 3.3:** Warm up of the test rig [21].

### 3.1.2 Instrumentation

The development of the trisector test rig is made in close collaboration with UNIFI[1] to be representative of the final DLR rig while allowing advanced measurements inside the CS. As a result the final layout of the test rig is strongly influenced by the constraints imposed by the planned measurement techniques (see Fig. 3.4). Two main investigations are planned: Particle Image Velocimetry (PIV) inside the CS and aerothermal investigations of the flow field in planes 40 and 40+ by means of an automatic Traverse System (TS) provided by Turbomeca. For the former, large optical access to the CS is introduced: the two lateral walls of the CS can be replaced by wide windows. The use of boroscopes is made necessary because of the complex geometry and holes are integrated in the geometry of the rig. A special connecting flange is designed to host the TS on the outer casing for aerothermal measurements at the exit of the CS.

#### Monitoring probes

For monitoring purposes, the test rig is equipped with 16 static pressure taps and 14 T-type thermocouples whose locations[2] are shown in Fig. 3.4. The maximum uncertainty on pressure measurements is ±52 Pa and ±0.5 K for the thermocou-

[1]Without involving other FACTOR partners except PROGESA (the manufacturer).
[2]Non-indicated probes are located in the different feeding lines and in the adjacent two sectors.

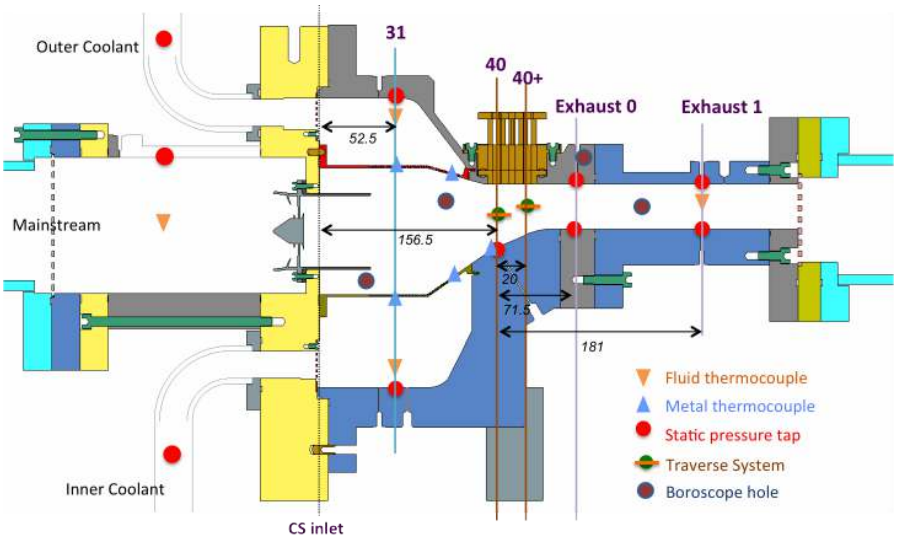


**Figure 3.4:** Location of the instrumentation in the central plane of the trisector rig.

ples. Two thermocouples are welded on the cold surface (plenum sides) of the inner and outer multiperforated liners to measure the temperature of the effusion cooling plates. Three thermocouples are also located in the metal in the inner casing near plane 40. The metal being very thick in this region, its thermal inertia is large and the measured temperature is a good criteria to assess the steady-state condition, as indicated in Fig. 3.3a. Mass flow rates are measured on each line (see Fig. 3.2) by means of calibrated orifices with a $2-3\%$ error. More details on the acquisition and data treatment of the monitoring probes can be found in Caciolli [103].

### Particle Image Velocimetry

PIV measurements on the trisector rig are the only source of information addressing the flow inside the CS for the FACTOR project. A very brief explanation of the basic principle of PIV is given here but extensive details on PIV and its implementation on the trisector rig can be found in Caciolli [103]. PIV is a non-intrusive whole field technique, which provides all at once the two velocity components in the investigation plane. The property actually measured is the distance and direction travelled by particles introduced in the flow (seeding) within a known time interval. To detect the motions of the particles, the investigated area is successively illuminated by two light sheets generated by a laser operating at a fixed time interval. The position of the particles is detected by a CCD-Camera positioned perpendicularly to the light-sheet and synchronized with the laser. The images of the first and second pulse of the laser are then cross-correlated to produce an average particle displacement vector. In this manuscript, only isothermal PIV in the central plane of the CS is reported. As illustrated in Fig. 3.5, a boroscope is used to introduce the laser sheet inside the CS because of the complex access. Such a device is a rigid tube with a set of lenses driving the light from the laser exit until the tube tip where a mirror prism deflects the light to an angle of 90° forming a

light sheet at a specified focal distance. The CCD-camera is located on the side of the rig and records the light going through the lateral window. Seeding (olive oil) is introduced upstream the central swirler via an in-house droplet generator using compressed air. A measurement sequence lasts roughly 30 s out of which 480 image pairs taken at a frequency of 12 Hz, with a time interval between two images of about 15 $\mu$s to correctly capture the high velocities at the swirler exit. Five successive camera frames —each one overlapping the others— are needed to cover the investigated region, which requires accurate positioning and calibration of the camera. An example of such measurements (raw image obtained with the camera) using here only two positions is shown in Fig. 3.5b (without seeding).

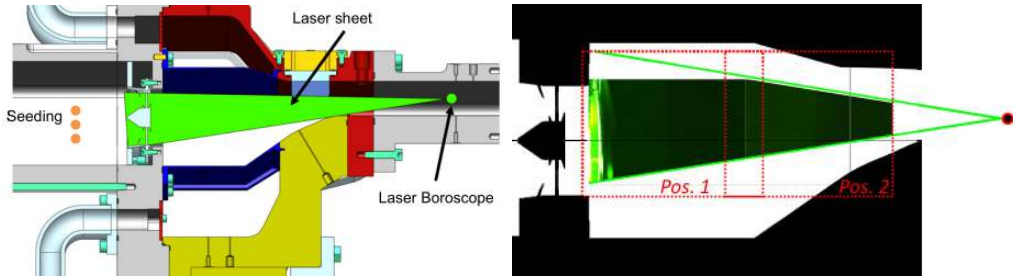


**(a)** PIV set-up [103]. **(b)** Example of direct measurement.

**Figure 3.5:** PIV investigation in the CS central plane.

### Aerothermal measurements in plane 40 and 40+

An exhaustive characterization of the aerothermal field at the CS exit is performed thanks to different probes mounted on the TS fixed on the outer casing of the central sector. Through three stepper motors, the TS is able to produce a radial and azimuthal displacement with a positioning accuracy below 0.1 mm. The TS can be fitted onto three different connecting flanges to perform different measurements either in plane 40 or 40+. It is worth noting that as the center of rotation of the TS differs from the rig center, the investigated area does not cover the full central sector. The density and shape of the experimental investigation mesh depend on the measurement technique and will be detailed in the following. Three kinds of probes can be fitted on the TS: a five Holes pressure Probe, a specific unsheathed thermocouple and split-fiber probes for Hot Wire Anemometry.

**Five holes pressure probe (5HP)** A 5HP is mounted on the TS to provide measurements of velocity (magnitude and directions), pressure and temperature. Such a probe is constructed by surrounding a central pressure port with four equally spaced ports located on a cone angled around the central port. Pressures in the five ports are measured simultaneously and the pressure difference between two diametrically opposed holes are correlated to the flow angles. According to the manufacturer (AEROPROBE), the average error on the measured angles is below 0.1°. Because of the elbow shape of the probe (see Fig. 3.6a), it is inserted downstream plane 40 so that the probe tip is exactly in correspondence with plane

40. As shown by the experimental mesh in Fig. 3.6b, only 76% of plane 40 is investigated because the probe elbow does not allow to reach the inner region. For each point of the mesh, pressure data is acquired for 2 s at 2 kHz. A thermocouple is fitted on the axis of the probe to estimate the density of the flow based on pressure measurements. Note that recorded temperature is partially biased by the presence of the probe itself (7.44 mm from axis to tip), so more accurate temperature measurements are also performed using an unsheathed thermocouple.

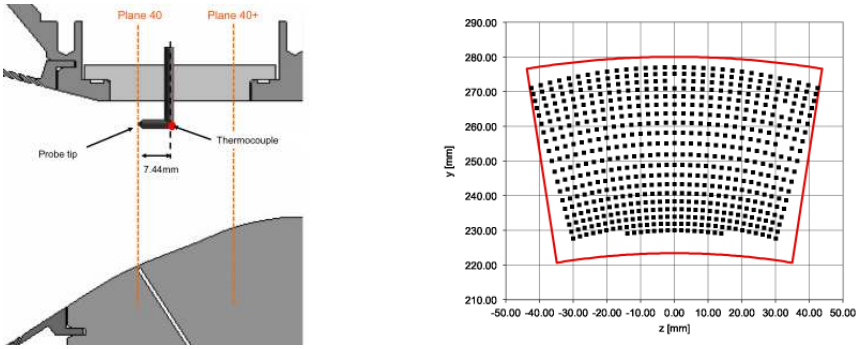


**(a)** Position of the 5-holes probe. **(b)** 600-points mesh in plane 40.

**Figure 3.6:** Set-up of the TS for the 5HP.

**Unsheathed thermocouple (THCPL)** Detailed measurement of temperature exactly in plane 40 and 40+ are performed using a unsheathed K-type thermocouple manufactured by Turbomeca, as shown in Fig. 3.7a. This probe consists of two fine wires (120 $\mu$m diameter) placed inside a ceramic barrel inserted in a metallic tube. The very low thermal inertia of the wires allows to measure temperature fluctuations up to its cut-off frequency (about 2 kHz). The temperature signal is recorded for 4 s at 5 kHz for each point of the mesh, with an uncertainty below 1.5 K. Unfortunately, because of a filtering or acquisition issue encountered during the test campaign, the cut-off frequency of the chain was found to be around 100 Hz so only time-averaged results were obtained. As the thermocouple is straight and inserted directly from above in the measurement plane, the investigation mesh covers about 87% of plane 40 as shown in Fig. 3.7b.

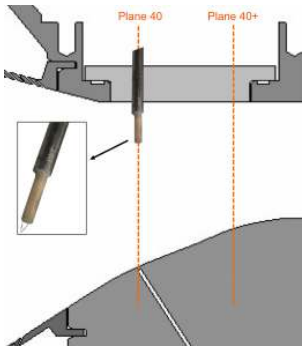


**(a)** Detail of the thermocouple.

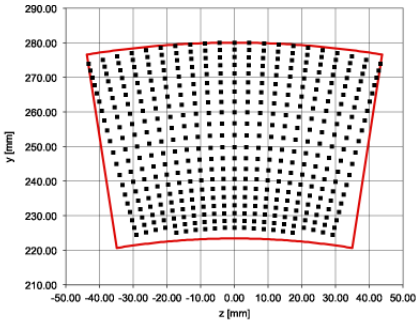


**(b)** 432-points mesh in plane 40.

**Figure 3.7:** Set-up of the TS for the THCPL.

**Hot Wire Anemometry (HWA)** To quantify turbulence levels and distribution, HWA is intended using the constant temperature approach. This technique allows a local measure of the instantaneous velocity by evaluating the quantity of heat convected away from the wire by the fluid. The main advantage of HWA is that very thin wires with low inertia are used so that velocity fluctuations can be measured using high acquisition frequency systems. In this study, two split fiber probes (R56 and R57, manufactured by DANTEC) are successively used on the TS (see Fig. 3.8a), each of them measuring two velocity components. The final velocity field (both mean and fluctuating parts) is then reconstructed based on the two measurements projected from the TS coordinates onto the CS coordinates. Details on the methodlogy can be found in Bacci et al. [26]. Acquisition is performed at 20 kHz during 5 s for each point. Because of the shape of the probes and their great fragility, the investigation mesh covers a limited portion of the central sector (about 65%) as shown in Fig. 3.8b.

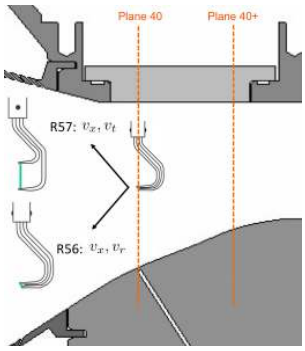


**(a)** The two split-fiber probes.

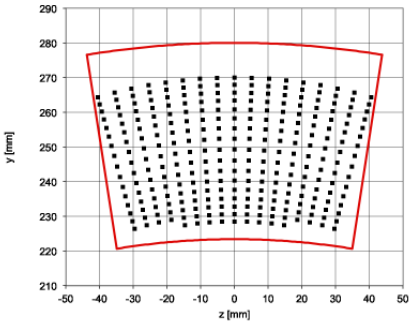


**(b)** 281-points mesh in plane 40.

**Figure 3.8:** Set-up of the TS for HWA.

The main drawback of HWA is that isothermal fluid conditions are required to correlate the heat loss directly to the fluid velocity. The rig therefore has to be operated at isothermal conditions. The selection of an Isothermal Operating Point (IOP) representative of the Design Point (DP) becomes therefore an issue and is discussed in the next section.

## 3.2 Isothermal operating point

Turbulence measurements by means of HWA require the selection and validation of an IOP representative of the DP. A novel approach is proposed herafter in Section 3.2.1, based on the methodology suggested by Champion [122]: a macro-analysis of the governing parameters of the CS can be obtained through an algebraic representation of the test rig. Based on the conclusions of this analysis, the final choice of the IOP is discussed in Section 3.2.2 before showing LES validation of this choice in Section 3.2.3

### 3.2.1 Algebraic representation of the test rig

The main objective of the algebraic representation of the test rig is to isolate the effect of a change in the operating conditions of the rig and attribute the corresponding changes to the flow physics. The former can be described by control parameters regulated by the user (pressure, temperature...) while the latter are typical non-dimensional numbers (Reynolds, Mach numbers...). The objective of this analysis is thus to isolate a set of isothermal control parameters that allows to conserve the same non-dimensional numbers as at DP conditions. If such operating conditions exist, then the flow would be governed by the same physics and present similarities irrespectively of the isothermal or non-isothermal conditions.

#### Control parameters

The first step to build the algebraic representation of the test rig is to list the control parameters which can be regulated and control the test rig operating conditions (see Fig. 3.9):

- Mainstream (swirler) [subscript M for clarity]
  - Temperature $T_M$ (at DP: 531 K)
  - Pressure $P_M$ (at DP: 153 kPa)
  - Mass flow rate $\dot{m}_M$ (at DP: 0.156 kg/s per sector)
- Outer cavity [subscript CO]
  - Temperature $T_{CO}$ (at DP: 300K)
  - Pressure $P_{CO}$ (at DP: 153kPa)
  - Mass flow rate $\dot{m}_{CO}$ (at DP: 0.050 kg/s per sector)
- Inner cavity [subscript CI]
  - Temperature $T_{CI}$ (at DP: 300K)
  - Pressure $P_{CI}$ (at DP: 153kPa)
  - Mass flow rate $\dot{m}_{CI}$ (at DP: 0.034 kg/s per sector)

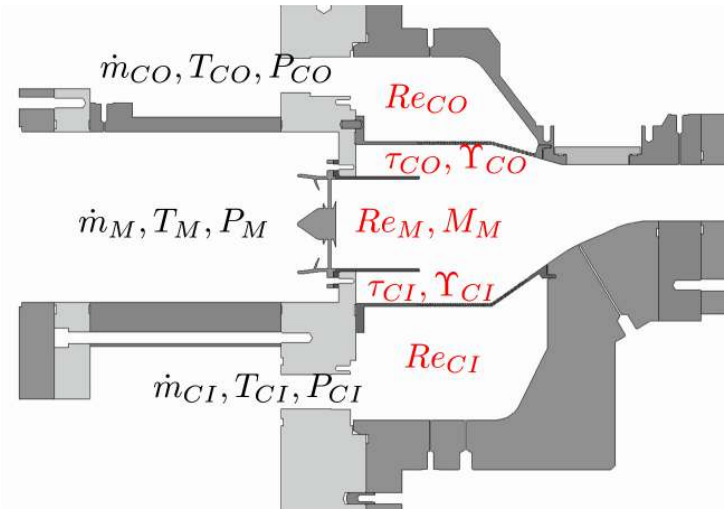


**Figure 3.9:** Sketch of the rig showing the control parameters (black) and non-dimensional numbers (red).

The configuration of the UNIFI trisector reduces the set of degrees of freedom since the two cooling cavities feeding the multiperforated plates share the same pressure and temperature: $P_{CO} = P_{CI}$ and $T_{CO} = T_{CI} = T_{cool}$. Moreover, the pressure drop created by the swirler and the liners are almost identical (around 3%), so one can reasonably assume that $P_M = P_{CO} = P_{CI} = P$. Finally, the test section is governed by six control parameters: $(\dot{m}_M, P, T_M, \dot{m}_{CO}, T_{cool}, \dot{m}_{CI})$. These parameters are bounded by the rig constraints: for example the exit pressure has to be above the atmospheric pressure ($P_M \gtrsim 110$ kPa), the maximum temperature is limited by the heater capacity ($T_M \leq 700$ K) and the total mass flow rate can not exceed the compressor capacity ($\dot{m}_M + \dot{m}_{CO} + \dot{m}_{CI} \leq 1.0$ kg/s).

### Non-dimensional numbers

A great variety of non-dimensional numbers can be found to describe the physics of the flow in the CS. By nature, the FACTOR chamber is engine-representative which makes the task more complicated. As a first approach, the CS can be represented by a central hot flow surrounded by two colder cross-flows. The different streams can be described by the following non-dimensional numbers:

- Mainstream
  - Reynolds number at swirler exit $Re_M$
  - Mach number at swirler exit $M_M$
- External and internal cavities [subscript $i = CI, CO$]
  - Reynolds number of the holes $Re_i$
  - Blowing ratio $\tau_i = \rho_i V_i / \rho_M V_M$

– Momentum flux ratio $\Upsilon_i = \rho_i V_i^2 / \rho_M V_M^2$

Note that in the two cavities, the Mach number is expected to be very low (effect of the plenum) and subject to very minor modifications therefore not meaningful.

We finally have a set of eight non-dimensional numbers describing the flow: $(Re_M, M_M, Re_{CO}, \tau_{CO}, \Upsilon_{CO}, Re_{CI}, \tau_{CI}, \Upsilon_{CI})$, shown in red in Fig. 3.9.

**Link between non-dimensional numbers and control parameters**

The selected non-dimensional numbers have to be expressed as a function of the control parameters of the rig. Mach number dependencies are straight-forward:

$$M = \frac{V}{\sqrt{\gamma r T}} \propto \frac{\dot{m}\sqrt{T}}{P}. \tag{3.1}$$

Here, the ratio of specific heat $\gamma$ is assumed to be constant because of the limited temperature and pressure variations.

The Reynolds number is linked to the mass flow rate and viscosity:

$$Re = \frac{\rho V L}{\mu} = \frac{\dot{m} L}{S\mu}, \tag{3.2}$$

where $L$ is a characteristic length and $S$ a surface used to define the mass flow rate. Under FACTOR moderate temperature and pressure changes, the air viscosity is assumed to be independent of pressure and follow a power-law for temperature:

$$\mu = \mu_{ref} \left( \frac{T}{T_{ref}} \right)^{2/3}, \tag{3.3}$$

with $\mu_{ref}$ and $T_{ref}$ the reference values of viscosity. Finally Eq. (3.2) turns into:

$$Re = \frac{\dot{m} L}{S\mu_{ref} \left( \frac{T}{T_{ref}} \right)^{2/3}} \propto \frac{\dot{m}}{T^{2/3}}. \tag{3.4}$$

The blowing ratio is easily expressed as a function of the mass flow rates:

$$\tau_i = \frac{\rho_i V_i}{\rho_M V_M} = \frac{\dot{m}_i S_M}{S_i \dot{m}_M} \propto \frac{\dot{m}_i}{\dot{m}_M} \qquad i = CI, CO. \tag{3.5}$$

Finally the momentum flux ratio $\Upsilon$ is expressed using $\tau$ and the ideal gas law to yield:

$$\Upsilon_i = \frac{\rho_i V_i^2}{\rho_M V_M^2} = \tau_i^2 \frac{\rho_M}{\rho_i} = \tau_i^2 \frac{P_M T_i}{P_i T_M} \propto \left( \frac{\dot{m}_i}{\dot{m}_M} \right)^2 \frac{T_i}{T_M} \qquad i = CI, CO. \tag{3.6}$$

All non-dimensional numbers can therefore be written as a function of the rig control parameters as listed in Table 3.1. Looking at these parameters and their relationships the following conclusions can be drawn:

(i) The blowing ratios $\tau_i$ are unchanged if the flow split between the different lines is kept constant.

(ii) If the mass flow split is kept constant, the momentum flux ratio $\Upsilon_i$ is a ratio of densities corresponding to the hot and cold streams.

(iii) The temperature ratio between the hot and cold streams (1.77 at DP) is not a pertinent non-dimensional number on its own as it is a combination of $\tau_i$ and $\Upsilon_i$.

| Swirler | Outer cavity | Inner cavity |
|---|---|---|
| $M_M \propto \frac{\dot{m}_M \sqrt{T_M}}{P}$ | $Re_{CO} \propto \frac{\dot{m}_{CO}}{T_{cool}^{2/3}}$ | $Re_{CI} \propto \frac{\dot{m}_{CI}}{T_{cool}^{2/3}}$ |
| $Re_M \propto \frac{\dot{m}_M}{T_M^{2/3}}$ | $\tau_{CO} \propto \frac{\dot{m}_{CO}}{\dot{m}_M}$ | $\tau_{CI} \propto \frac{\dot{m}_{CI}}{\dot{m}_M}$ |
| | $\Upsilon_{CO} \propto \left(\frac{\dot{m}_{CO}}{\dot{m}_M}\right)^2 \frac{T_{cool}}{T_M}$ | $\Upsilon_{CI} \propto \left(\frac{\dot{m}_{CI}}{\dot{m}_M}\right)^2 \frac{T_{cool}}{T_M}$ |

**Table 3.1:** Expression of the non-dimensional numbers of the trisector test rig.

### Algebraic representation

The eight non-dimensional numbers identified in this study are governed by the control parameters of the rig which can be adjusted to the desired values. These equations are not linear and identifying the action of a single control parameter on the non-dimensional ones is not trivial. It is proposed here to linearize the equations using a logarithmic formulation to yield the following algebraic relation:

$$\vec{S} = M.\vec{C}, \tag{3.7}$$

with:

$$M = \begin{pmatrix} 1 & -2/3 & 0 & 0 & 0 & 0 \\ 1 & 1/2 & -1 & 0 & 0 & 0 \\ 0 & 0 & 0 & 1 & -2/3 & 0 \\ 0 & 0 & 0 & 0 & -2/3 & 1 \\ -1 & 0 & 0 & 1 & 0 & 0 \\ -2 & -1 & 0 & 2 & 1 & 0 \\ -1 & 0 & 0 & 0 & 0 & 1 \\ -2 & -1 & 0 & 0 & 1 & 2 \end{pmatrix}, \tag{3.8}$$

$$\vec{C} = log \begin{pmatrix} \dot{m}_M/\dot{m}_{M_{DP}} \\ T_M/T_{M_{DP}} \\ P/P_{DP} \\ \dot{m}_{CO}/\dot{m}_{CO_{DP}} \\ T_{cool}/T_{cool_{DP}} \\ \dot{m}_{CI}/\dot{m}_{CI_{DP}} \end{pmatrix}, \vec{S} = log \begin{pmatrix} Re_M/Re_{M_{DP}} \\ M_M/M_{M_{DP}} \\ Re_{CO}/Re_{CO_{DP}} \\ Re_{CI}/Re_{CI_{DP}} \\ \tau_{CO}/\tau_{CO_{DP}} \\ \tau_{CI}/\tau_{CI_{DP}} \\ \Upsilon_{CO}/\Upsilon_{CO_{DP}} \\ \Upsilon_{CI}/\Upsilon_{CI_{DP}} \end{pmatrix}.$$

$M$ is the matrix of a linear application $f : \mathbb{R}^6 \longrightarrow \mathbb{R}^8$. The vectors $\vec{C}$ and $\vec{S}$ respectively represent a variation of the control parameters and non-dimensional numbers vs. the reference state (design point conditions).

**Kernel of the linear application $f$**

To operate the rig at isothermal conditions, one looks for an operating point with the same non-dimensional numbers but with different control parameters (where $T_M = T_{cool}$). In an algebraic form, this means that one searches a vector of control parameters whose image by $f$ is a vector of unchanged non-dimensional numbers $\vec{S} = log(1) = \vec{0}$ i.e. the kernel of $f$. Any vector $\vec{u}$ of $\mathbb{R}^6$ belongs to the kernel of $f$ if $M.\vec{u} = \vec{0}$. This system can be resolved and the kernel of $f$ is found to be any colinear vector of :

$$\vec{u} = \begin{pmatrix} 1 \\ 3/2 \\ 7/4 \\ 1 \\ 3/2 \\ 1 \end{pmatrix}. \tag{3.9}$$

This means that the non-dimensional numbers $\vec{S}$ are all unchanged if all the control parameters obey the following variation with respect to the DP values:

$$\begin{array}{ll} \dot{m}_M & \times a \\ T_M & \times a^{3/2} \\ P & \times a^{7/4} \\ \dot{m}_{CO} & \times a \\ T_{cool} & \times a^{3/2} \\ \dot{m}_{CI} & \times a \end{array} , \tag{3.10}$$

where $a$ is any scalar whose value is only determined by the rig constraints.

The evolution of the control parameters as a function of $a$ is illustrated in Fig. 3.10 and noting that DP conditions are obtained for $a = 1$. In practice, the green hatched zone shows values of $a$ that are impossible to respect because of a too high mass flow rate while the blue hatched zone shows unachievable values of pressure. In-between these two zones ($0.85 < a < 1.18$), pressure and mass flow conditions are achievable and an operating point can be selected based only on the possible values for the swirler and cooling line temperatures. Figure 3.10 or directly Eq.(3.10) proves however that there is no operating point in the kernel of $f$ that allows to have $T_{cool} = T_M$. Therefore, in the configuration of the UNIFI trisector rig, it is impossible to find an IOP that conserves all the non-dimensional numbers. The IOP has therefore to be selected based on the conservation of a selected number of non-dimensional numbers as presented in the next section.

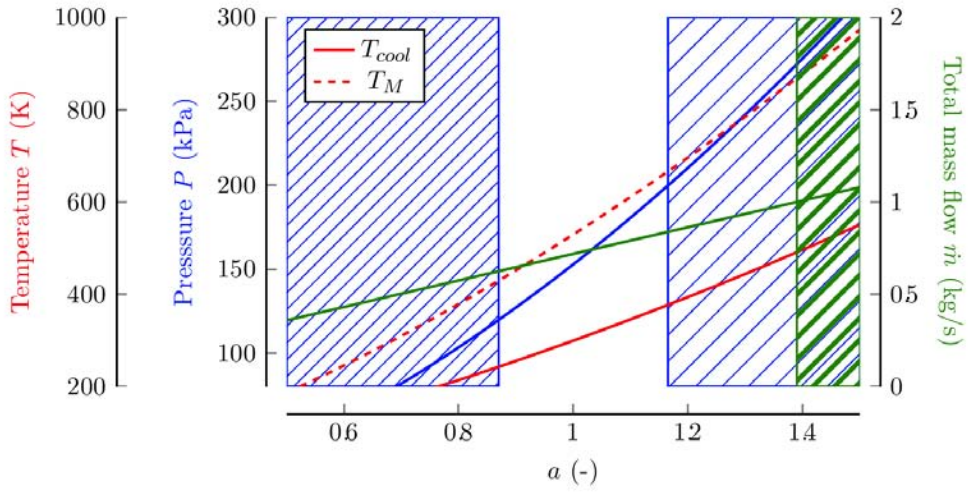


**Figure 3.10:** Evolution of the control parameters if the non-dimensional numbers are conserved (illustration of the kernel of $f$).

### 3.2.2 Selection of the isothermal operating point

As the algebraic method proves that the rig constraints do not allow to conserve all the non-dimensional numbers, a new method has to be used to find an acceptable IOP. It is proposed here to conserve only a limited number of non-dimensional numbers by modifying the mass flow rates ($\dot{m}_M, \dot{m}_{CO}, \dot{m}_{CI}$) and pressure $P$ while

setting all the temperatures to $T_{amb}$. The analysis in Section 3.2.1 demonstrates that the flow split has to be conserved to preserve the blowing ratios $\tau_i$, which is preferable. Therefore, the two adjustable control parameters end up being the total mass flow ($\dot{m} = \dot{m}_M + \dot{m}_{CI} + \dot{m}_{CO}$) and the CS pressure ($P$).

A graphical method is proposed here to define the operating point that allows to conserve the maximum number of non-dimensional numbers. Figure 3.11 shows the lines on which such numbers are conserved (with $\pm 5\%$ error bars) in a $(P, \dot{m})$ chart. Because of the conservation of the flow split, the blowing ratios $\tau_i$ are unchanged and the momentum flow ratios $\Upsilon_i$ are multiplied by $T_M/T_i = 1.77$ at isothermal conditions (see Table 3.1). These parameters are not affected by pressure and mass flow and are thus not shown in Fig. 3.11. The line corresponding to the conservation of the axial Mach number in plane 40 is also shown to have an estimate of the flow regime ($M_{40}$).

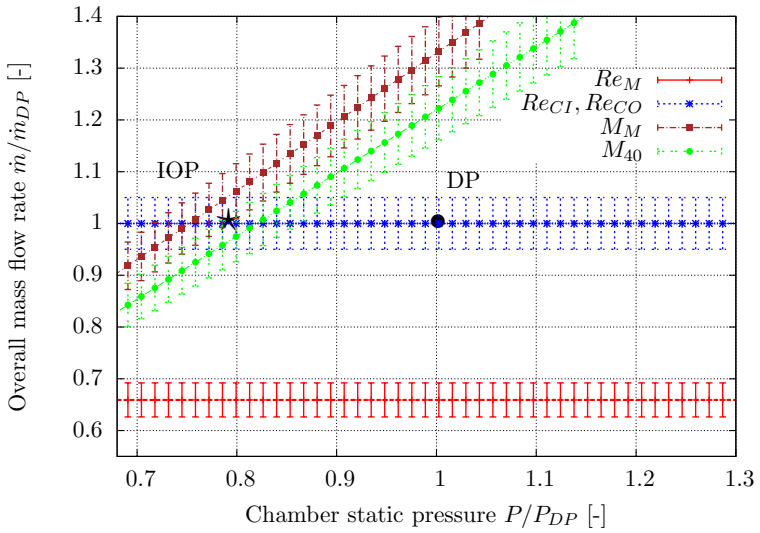


**Figure 3.11:** $(P, \dot{m})$ map with lines conserving the non-dimensional parameters.

The IOP, identified by $\star$ on Fig. 3.11 that conserves most of the non-dimensional numbers is shown along with the DP conditions marked as $\bullet$. At the IOP the overall mass flow rate is conserved and the pressure in the chamber is reduced ($-22\%$). The corresponding changes in non-dimensional parameters are listed in Table 3.2. Note that the four effusion cooling plates are designed to all operate at the same momentum $\rho V$ and therefore exhibit the same $\tau_i$ and $\Upsilon_i$ (in Table 3.2 only the first two plates are reported, see Appendix A). At IOP, the swirler Reynolds number $Re_M = U_{ref} D_{sw}/\nu_M$ is not conserved but both values still correspond to fully developed turbulent regimes without significant differences expected for the turbulence intensity for example. The proposed IOP leads therefore to the conservation of most non-dimensional parameters and moderate changes for $Re_M$ or $\Upsilon_i$ and is therefore assumed to be quite representative of the DP. This assumption needs however further validation which is proposed to be done using numerical simulations of the flow at the two operating conditions as presented in the next section.

| | | | DP | IOP |
|---|---|---|---|---|
| Control parameters | Total mass flow per sector [kg/s] | $\dot{m}_{40}$ | 0.240 | 0.240 |
| | Flow split swirlers [-] | $\dot{m}_M/\dot{m}_{40}$ | 65% | 65% |
| | Flow split outer cavity [-] | $\dot{m}_{CO}/\dot{m}_{40}$ | 21% | 21% |
| | Flow split inner cavity [-] | $\dot{m}_{CI}/\dot{m}_{40}$ | 14% | 14% |
| | Static pressure in plane 40 [kPa] | $P_{40}$ | 147.65 | 115.00 |
| | Swirler inlet temperature [K] | $T_M$ | 531 | 300 |
| | Cooling cavities temperature [K] | $T_{CO} = T_{CI}$ | 300 | 300 |
| | Reference velocity [m/s] | $U_{ref}$ | 51.5 | 37.5 |
| Non-dim. parameters | Swirler Reynolds number | $Re_M$ | 111 000 | 168 500 |
| | Swirler Mach number | $M_M$ | 0.112 | 0.108 |
| | Effusion cooling Reynolds | $Re_{CO}$ | 2344 | 2344 |
| | | $Re_{CI}$ | 2339 | 2339 |
| | Blowing ratio | $\tau_{CO}$ | 1.75 | 1.75 |
| | | $\tau_{CI}$ | 1.75 | 1.75 |
| | Momentum flux ratio | $\Upsilon_{CO}$ | 1.67 | 2.95 |
| | | $\Upsilon_{CI}$ | 1.67 | 2.95 |
| | Plane 40 Mach number | $M_{40}$ | 0.108 | 0.113 |

**Table 3.2:** Operating conditions for the isothermal (IOP) and non-isothermal (DP) points on the trisector test rig.

### 3.2.3 Validation by LES

A numerical validation of the selected IOP is required to confirm the proposition. First, the impact of the operating conditions on the mean flow field need to be evaluated along with the possible change of the swirl number. Second and more importantly, the characteristics of turbulence have to be compared between DP and IOP as the change of the Reynolds number $Re_M$ is known to impact turbulence. As far as turbulence quantification is concerned, the choice of LES is straightforward as it is known to have a good predictability of turbulent flows. For this purpose, two distinct LES are performed on the D00 configuration with the same mesh and numerical settings (see Table 3.3) but only the boundary conditions are changed according to Table 3.2 to account for the change in operating condition: either non-isothermal (DP) or isothermal conditions (IOP).

| Duct | Operating point | Mesh nodes | Mesh cells | Scheme | SGS model | Physical time [ms] | Timestep [s] |
|---|---|---|---|---|---|---|---|
| D00 | DP | 6.0M | 34.2M | TTGC | Smagorinsky | 155 | $4.4 \cdot 10^{-8}$ |
| D00 | IOP | 6.0M | 34.2M | TTGC | Smagorinsky | 145 | $4.4 \cdot 10^{-8}$ |

**Table 3.3:** LES of the FACTOR CS at DP and IOP conditions.

The main results are presented with a first insight on the mean and RMS velocity fields in the CS before comparing turbulence distribution. Note that for proper comparisons, all the velocity fields are normalized by $U_{ref}$ (defined as the mean axial velocity at the swirler exit in Table 3.2), to account for the change in density imposed by the conservation of the total mass flow rate.

### Velocity fields

The time-averaged axial velocity field $\bar{V}_x/U_{ref}$ in the central plane of the CS (see Fig. 2.9b for the position) is shown in Fig. 3.12 for both simulations. An isoline of $\bar{V}_x = 0$ shows the contour of the reverse flow zones located in the center of the CS and in the corners. Overall the topology of the flow is not significantly altered by the change in operating condition: the CTRZ is located at the same position and the radial opening of the jet exiting the swirler is not changed. One can however notice that for the isothermal case (Fig. 3.12b), the upper CRZ is attached immediately to the inlet of the CS ($x/D_{sw} = 0$) and the angle of the jet is smaller than for the non-isothermal case (Fig. 3.12a).

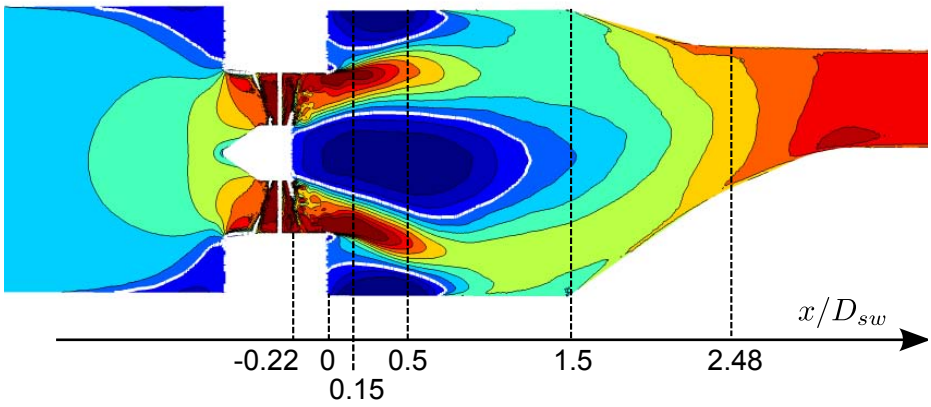


**(a)** Non-isothermal LES (DP).

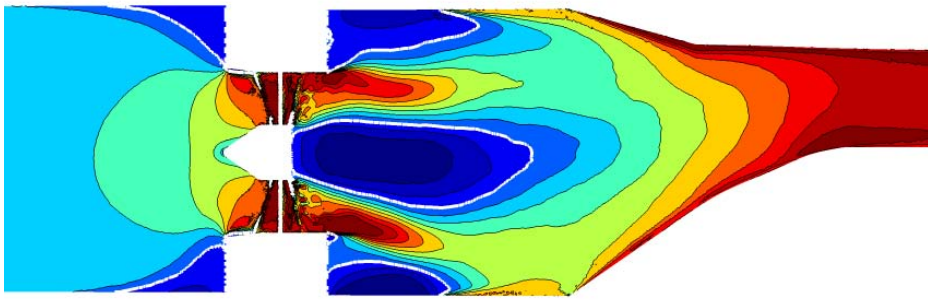

**(b)** Isothermal LES (IOP).

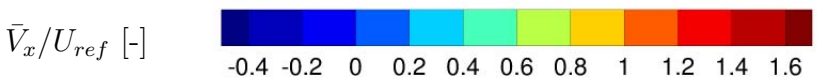


**Figure 3.12:** Time-averaged axial velocity field in the central plane and contours of the reverse flow zones (white line).

More quantitatively, time and circumferentially-averaged profiles of axial momentum $\bar{\rho}\bar{V}_x$ are plotted in Fig. 3.13 at different axial positions (see Fig. 3.12a for reference): immediately after the CS inlet (Fig. 3.13a), at the position of maximum reverse flow on the centerline (Fig. 3.13b), before the geometrical contraction (Fig. 3.13c) and in plane 40 (Fig. 3.13d). Overall, the mass flow is similarly distributed all over the CS radius for the two operating points, both in terms of mean and RMS values (shown by error bars). The plots in Figs. 3.13a and 3.13b confirm the previous finding; i.e. the recirculation zone in the upper corner reduces the radial opening of the jet exiting the swirler at isothermal conditions. This local change however does not impact the flow in plane 40 (Fig. 3.13d) where the mass flow distribution is unaltered. Regarding the flow angles in plane 40, circumferentially and time-averaged profiles of swirl and pitch angles are shown in Fig. 3.14 (for the sake of simplicity the corresponding 2-D fields are not presented here.). The flow angles differ by no more than 2° all over the span, which is not significant.

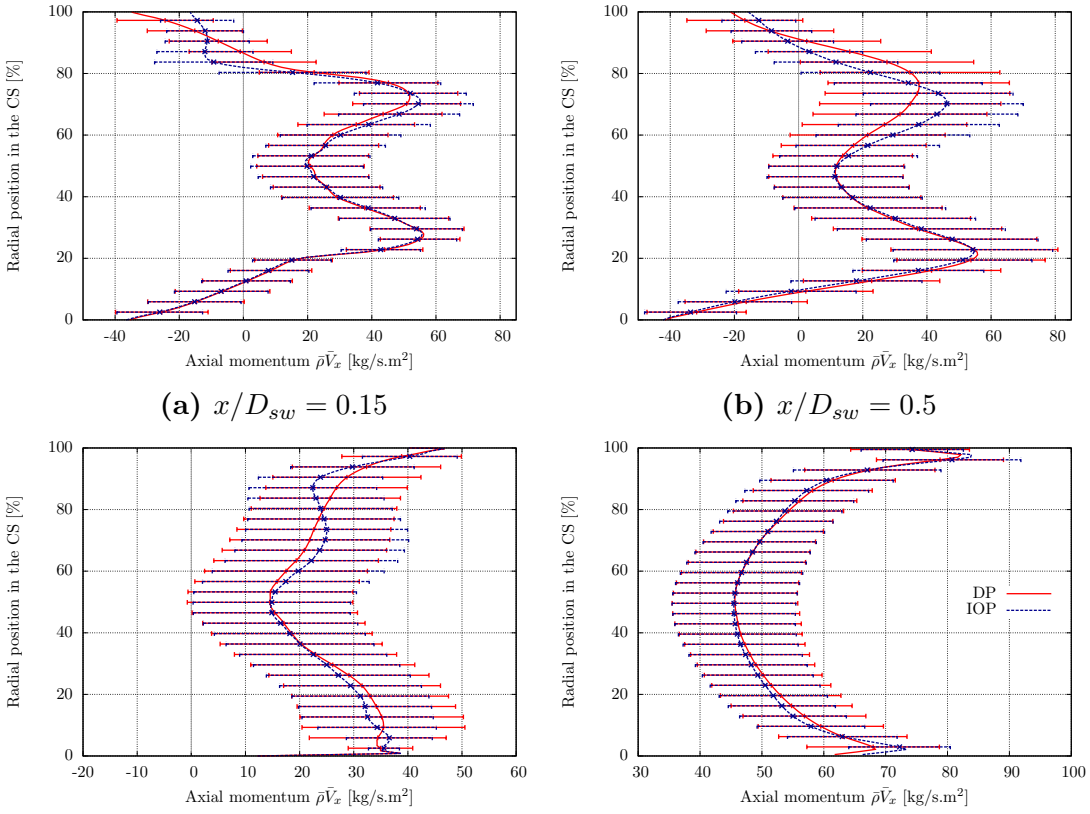


**(a)** $x/D_{sw} = 0.15$ **(b)** $x/D_{sw} = 0.5$

**(c)** $x/D_{sw} = 1.5$ **(d)** $x/D_{sw} = 2.48$ (Plane 40)

**Figure 3.13:** Circumferentially-averaged profiles of mean (line) and RMS (error bars) axial momentum in the CS.

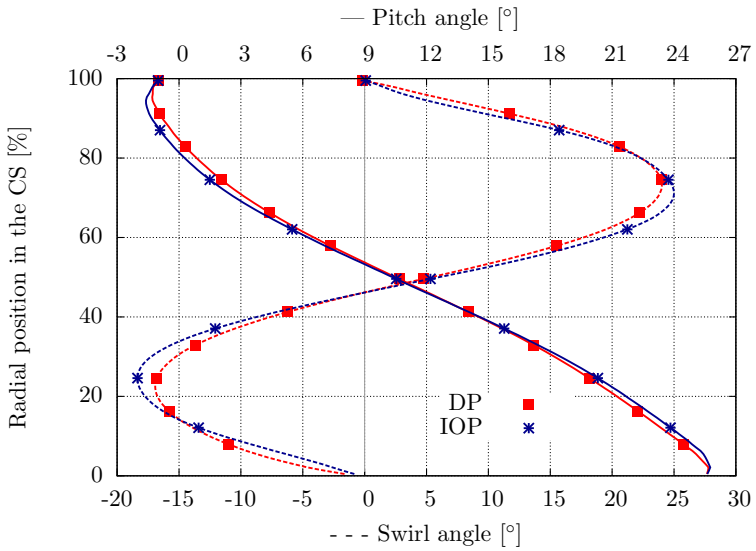


**Figure 3.14:** Circumferentially-averaged profiles of flow angles in plane 40.

The flow at the inlet of the CS ($x/D_{sw} = 0$) is now investigated in Fig. 3.15 by plotting the time and circumferentially-averaged velocity components in the swirler frame of reference. An immediate conclusion derived from this comparison is that under the scaling hypothesis, the velocity field is exactly preserved. This means that there is no change in the flow topology that could be attributed to the different viscosities, pressure level or potential effects from the CS itself. Note that the negative radial velocity located at 95% of the radius is due to the remnants of a centripetal motion created in the wakes of the vanes of the swirler. The swirl numbers computed using Eq. (2.1) from the velocity profiles shown in Fig. 3.15

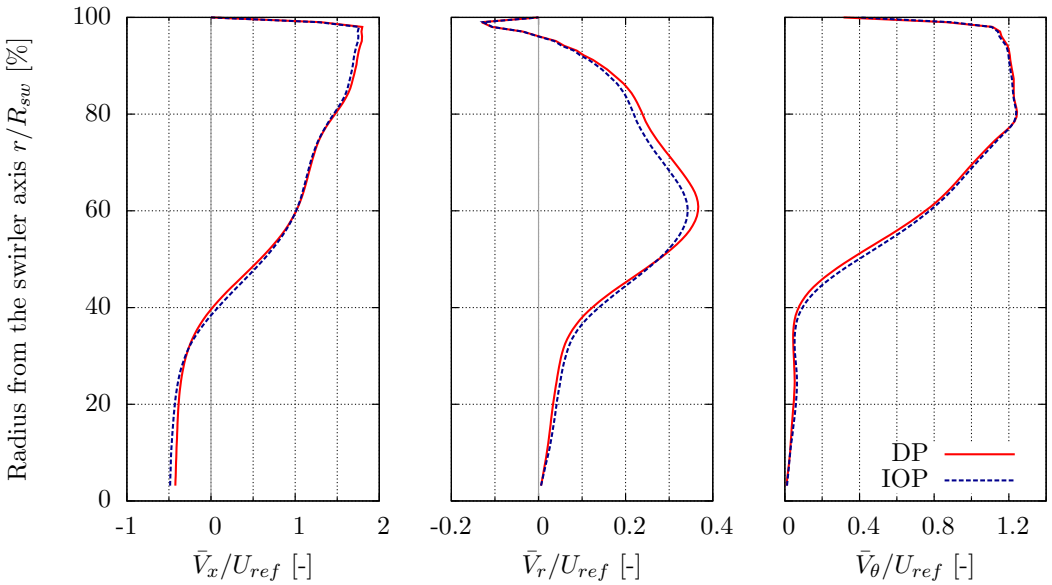


**Figure 3.15:** Circumferentially-averaged velocity profiles at the inlet of the CS in the swirler frame of reference

respectively yield 0.6 and 0.61 for the DP and IOP. As the velocity profiles are very similar, there is no surprise that the corresponding swirl numbers are equivalent.

The comparison of both mean (and some RMS) velocity fields showed that relatively small differences exist between the two operating conditions which overall yield a similar flow topology. As the IOP is used for turbulence measurements by means of HWA, it is now proposed to compare the turbulence levels obtained at both operating conditions.

### Turbulence fields

The turbulence level can be assessed from a LES by computing the resolved turbulent kinetic energy[3] defined as:

$$k_{res} = \frac{1}{2}(V^2_{x,RMS} + V^2_{r,RMS} + V^2_{\theta,RMS}). \tag{3.11}$$

The circumferentially-averaged profile of $k_{res}$ at the inlet of the CS is non-dimensionalized by $U^2_{ref}$ and plotted in Fig. 3.16. The maximum value of $k_{res}$ is similarly found at $r/R_{sw} \simeq 40\%$, i.e. above the limit of the reverse flow zone. The good agreement between the two curves indicates that about the same scaled proportion of turbulent kinetic energy is generated by the swirler at both operating conditions.

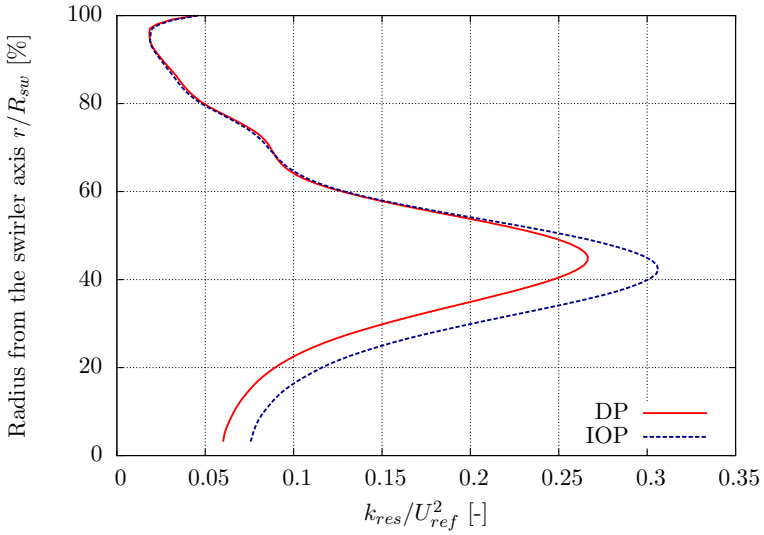


**Figure 3.16:** Circumferentially-averaged profile of turbulent kinetic energy at the inlet of the CS.

[3]Both the resolved and modelled turbulent kinetic energy should be summed but the LES quality being good, the latter contribution is sufficiently small to be neglected (see Section 5.2 for details).

This being said, one can observe in Fig. 3.17 the fields of $k_{res}/U_{ref}^2$ in two azimuthal cuts in the CS: the central and periodicity planes (see Fig. 2.9b for the positions). The comparison of Figs. 3.17a and 3.17b clearly shows that turbulence is generated mostly in the shear zones above and below the high velocity jet exiting the swirler, regardless of the operating point. The peak of $k_{res}$ observed at midspan in Fig. 3.16 can be identified in Fig. 3.17 and corresponds to the shear zone below the main jet of the swirler. The periodicity plane shows an important pocket of large values of $k_{res}$ close to the swirler. In this region the jet exiting the swirler radially meets the jet of the adjacent swirler (periodicity condition), giving rise to a very intense mixing zone. Overall, the relative magnitude of turbulence $k_{res}/U_{ref}^2$ is slightly lower for the isothermal case. This is especially noticeable in the shear region between the swirler jet and the slow moving flow close to the corner recirculation zone: the turbulence level is about 20% lower at isothermal conditions. Such a difference can be explained by the change in swirler Reynolds number and possibly by flow instabilities induced by the temperature differences that can be found at DP conditions and could be reduced at IOP. Further investigations are however necessary to properly conclude on this issue which is also mesh and model-dependent but out of the scope of these two simulations.

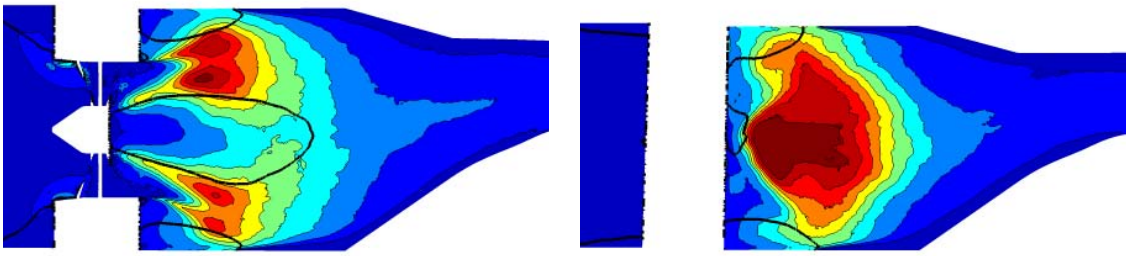

**(a)** Non-isothermal LES (DP).

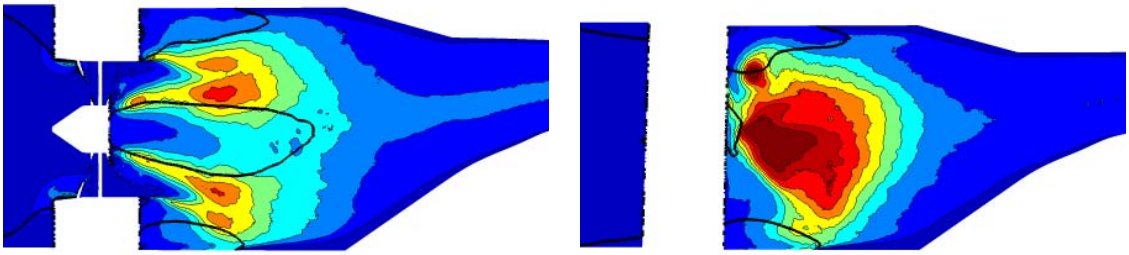

**(b)** Isothermal LES (IOP).

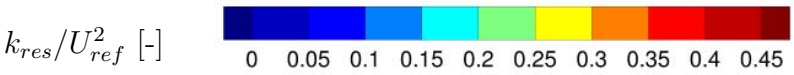


**Figure 3.17:** Turbulent kinetic energy in the central plane (left) and periodicity plane (right) and contours of the reverse flow zones (black line).

Although local differences of turbulence level are found inside the CS, the most important validation point concerns the turbulence in plane 40, which is the precise quantity to be measured by means of HWA. Figure 3.18 shows the contours of the turbulence intensity defined as:

$$TU = \frac{\sqrt{2/3k_{res}}}{||\vec{V}||}. \tag{3.12}$$

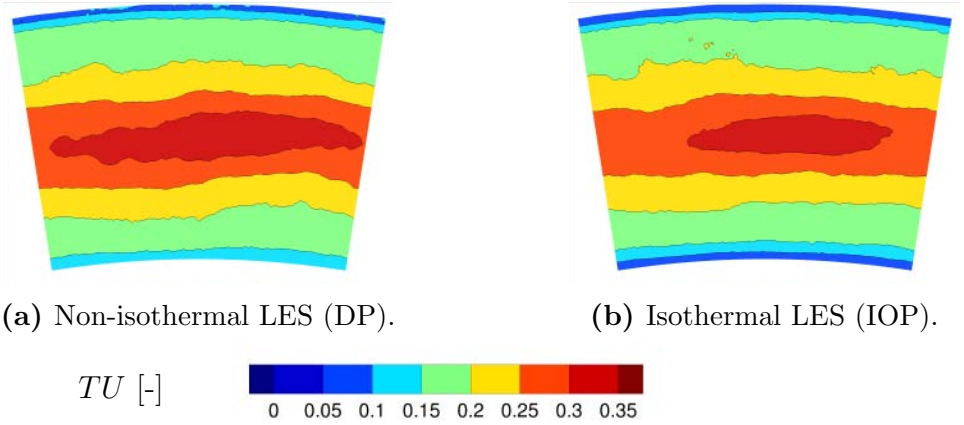


**(a)** Non-isothermal LES (DP). **(b)** Isothermal LES (IOP).

**Figure 3.18:** Turbulence intensity in plane 40.

For this quantity, both operating conditions show an organization following an almost purely radial distribution with very little azimuthal heterogeneities. Both cases show the same distribution and levels of $TU$ with maximum levels (25-35%) at mid-height and much lower values near the walls (0-10%). Overall, turbulence intensity is found to be similar in both cases, even if it is a little higher than the target value (10 to 20%) defined in Section 2.1.1.

All the comparisons presented here show that the change in operating conditions and the associated modification of the swirler Reynolds number do not dramatically alter the flow field. Under the scaling hypothesis, the velocity field, flow angles and turbulence distributions are found to be marginally affected. The main differences concern the turbulence levels in the shear regions around the jet exiting the swirler that may be affected by the absence of density gradients at IOP [123]. Nevertheless, the flow field in plane 40 (which will be experimentally investigated) and especially the turbulence intensity map (Fig. 3.18) are supposed to be unchanged between DP and IOP flow conditions. This observation comforts the choice of the IOP to be used on the trisector rig.

## 3.3 Summary of the available experimental investigations

Based on the work presented in this chapter and the encouraging LES results, the FACTOR consortium agreed for the manufacturing of the trisector rig in early 2013. The trisector rig test campaign was performed from October 2013 to February 2014, including TS measurements in planes 40 and 40+ as well as isothermal PIV. Non-isothermal PIV (at DP) should be performed in spring 2015 during a second part of the test campaign. The measurements matrix on the UNIFI trisector rig is presented in Table 3.4 for the four studied duct lengths and the two operating conditions.

| Case | Position | Measurement | D00 | D35 | D45 | D55 |
|---|---|---|---|---|---|---|
| Non-isothermal (DP) | Plane 40 | 5HP | ✓ | ✓ | ✓ | ✓ |
| | | THCPL | ✓ | ✗ | ✓ | ✓ |
| | | PIV | ➠ | ✗ | ✗ | ➠ |
| | Plane 40+ | 5HP | ✓ | ✗ | ✓ | ✓ |
| | | THCPL | ✓ | ✗ | ✓ | ✓ |
| | Central plane | PIV | ➠ | ✗ | ✗ | ➠ |
| Isothermal (IOP) | Plane 40 | 5HP | ✓ | ✗ | ✗ | ✓ |
| | | HWA | ✓ | ✗ | ✓ | ✓ |
| | | PIV | ➠ | ✗ | ✗ | ➠ |
| | Plane 40+ | HWA | ✓ | ✗ | ✓ | ✓ |
| | Central plane | PIV | ✓ | ✗ | ✗ | ✓ |

**Table 3.4:** Experimental matrix for the UNIFI trisector rig summarizing the performed (✓), pending (➠) and not-planned (✗) measurements.

The measurements provided a large database which was even complemented by additional tests reported by Caciolli [103]. Such experimental results need to be analysed first to assess the design of the CS and second to validate the numerical approach by a direct confrontation with the pre-test LES. This exercise is now proposed in Chapter 4.

# Chapter 4

# Experimental flow characterization and validation of the computational approach

## Contents


4.1 Isothermal PIV inside the chamber . . . . . **86**

4.2 Time-averaged aerothermal field in plane 40 . . . . . **90**

4.2.1 Flow velocity . . . . . 91

4.2.2 Temperature field . . . . . 97

4.3 Conclusions . . . . . **99**


The test campaign performed on the UNIFI trisector rig provided a detailed characterization of the CS flow which is now compared to the corresponding LES results. Such comparisons intend to assess the design of the CS and benchmark the pre-test LES against the measurements based on conventional criteria as well as available data.

Because of the large changes of flow topology induced by the confinement (see Chapter 2), numerics and experiments are compared for an unconfined case (D00) and a ducted case (D55)[1]. First the investigations focus on the flow inside the CS —and mainly at the exit of the swirler— based on the PIV results (Section 4.1). Second LES predictions are confronted to the measurements obtained with the TS fitted at the CS exit in Section 4.2. Finally, conclusions on the design of the CS and the quality of the LES results are ultimately proposed in Section 4.3

[1]The characteristics of the LES can be found in Table 2.1.

## 4.1 Isothermal PIV inside the chamber

PIV is performed at isothermal conditions (IOP) for the D00 and D55 configurations during a preliminary test campaign. Despite the asset of being a non-intrusive technique, PIV measurements and their proper comparison with LES results are subjected to four main sources of uncertainties:

- The postprocessing method was assessed [25] to create an uncertainty on the measured velocity of 4% for the highest velocities and 20% for the lowest ones (recirculation zones).

- Because of the complex access, inaccuracies in the positioning of the laser sheet can exist.

- Only the mainstream flow is seeded with particles (i.e. 2/3 of the total mass flow) creating a blind zone in the near-wall region where data thus needs to be handled with care.

- Both simulations being performed at DP, scaled flow-field are used for comparisons with PIV as detailed and validated previously in Section 3.2.

With the knowledge of such limitations, an overview on the flow topology in the central plane of the CS is given first before producing more quantitative comparisons with the LES results.

Figure 4.1 shows the field of the time-averaged reconstructed velocity magnitude (axial and radial components only) in the central plane of the CS while the contours of the reverse flow zones are shown in Fig. 4.2. Qualitatively, PIV and LES results agree well except for the orientation of the jet exiting the swirler which clearly shows differences. For the D00 case, the upper part of the jet is almost straight in the LES (blockage by the CRZ) while PIV measurements show a more pronounced radial motion of fluid and a wider jet (this is especially visible for the lower part of the jet). LES of the D55 case shows that the jet is almost axial when it exits the duct while it is clearly more radially oriented in the experiments. The differences might be explained by the blockage created by a longer CRZ in the LES than in the measurements (Fig. 4.2b) preventing the radial expansion of the jet. PIV of the D55 case also shows a deviation of the high velocity jet in the vicinity of the inner wall, possibly because of the interaction of the mainstream with the coolant flow. The difference with LES in this region may point out modelling issues associated with the effusion cooling model used for the multiperforated plates. Despite these local differences and recalling the potential uncertainties in the experimental data, it is worth noting that overall the reverse flow zones are very well predicted by the LES as illustrated in Fig. 4.2. For the D00 case the dimensions and position of the inner CRZ agree very well with experimental findings. The axial extent of the CTRZ is also accurately predicted. For the D55 case, the LES precisely locates the small CTRZ forming after the duct in accordance with PIV measurements.

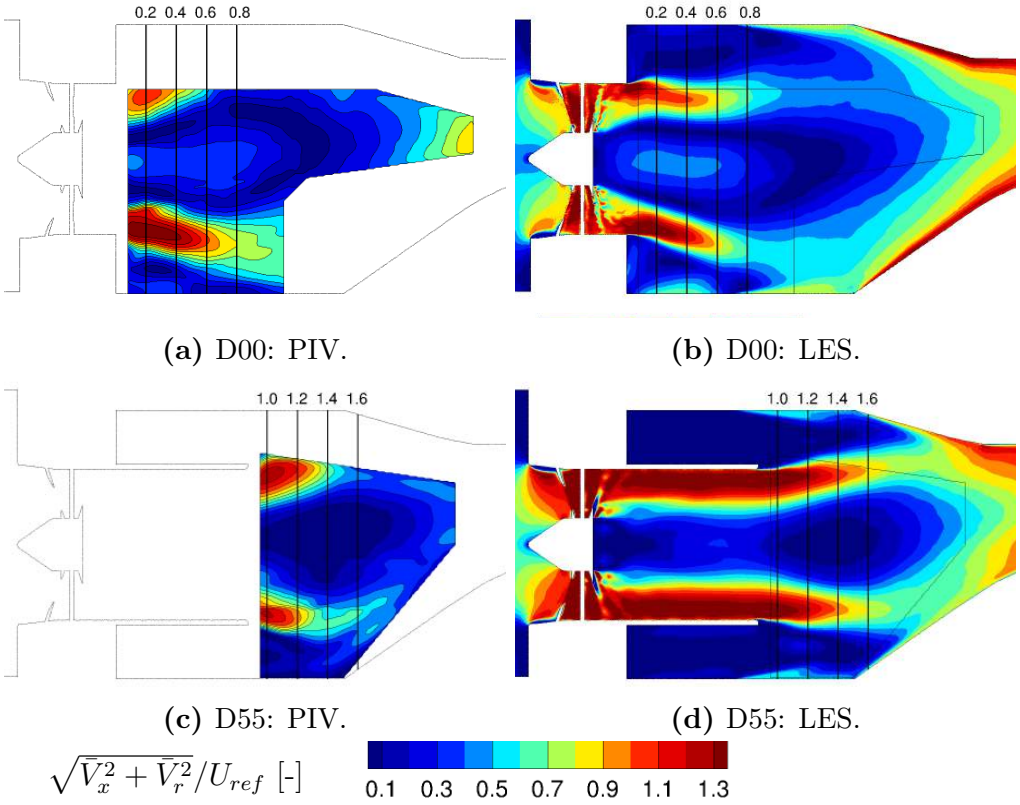


**(a)** D00: PIV. **(b)** D00: LES.

**(c)** D55: PIV. **(d)** D55: LES.

**Figure 4.1:** Contours of time-averaged velocity magnitude in the central plane.

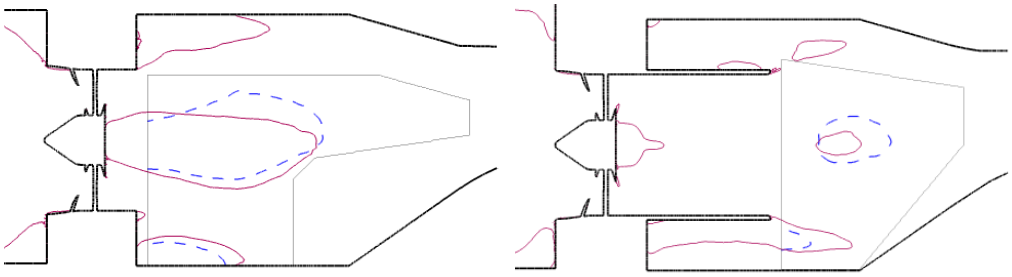

**(a)** D00. **(b)** D55.

**Figure 4.2:** Contours of the reverse flow zones in the central plane obtained by LES (purple line) and PIV (blue dots).

For a more quantitative comparison, the axial and radial velocity component profiles are extracted at various axial positions (see Fig. 4.1 for reference) and shown in Fig. 4.3 for the D00 case and Fig. 4.4 for the D55 case. For this specific diagnostic and because of uncertainties on the exact positioning of the PIV laser sheet, the velocity components of the LES are averaged over $\pm 0.5°$ around the central plane of the CS. For both configurations, the LES provide a very good estimate of the axial velocity at all the studied axial positions, both in terms of magnitude and position confirming the overall capacity of the tool in an a posteriori validation process.

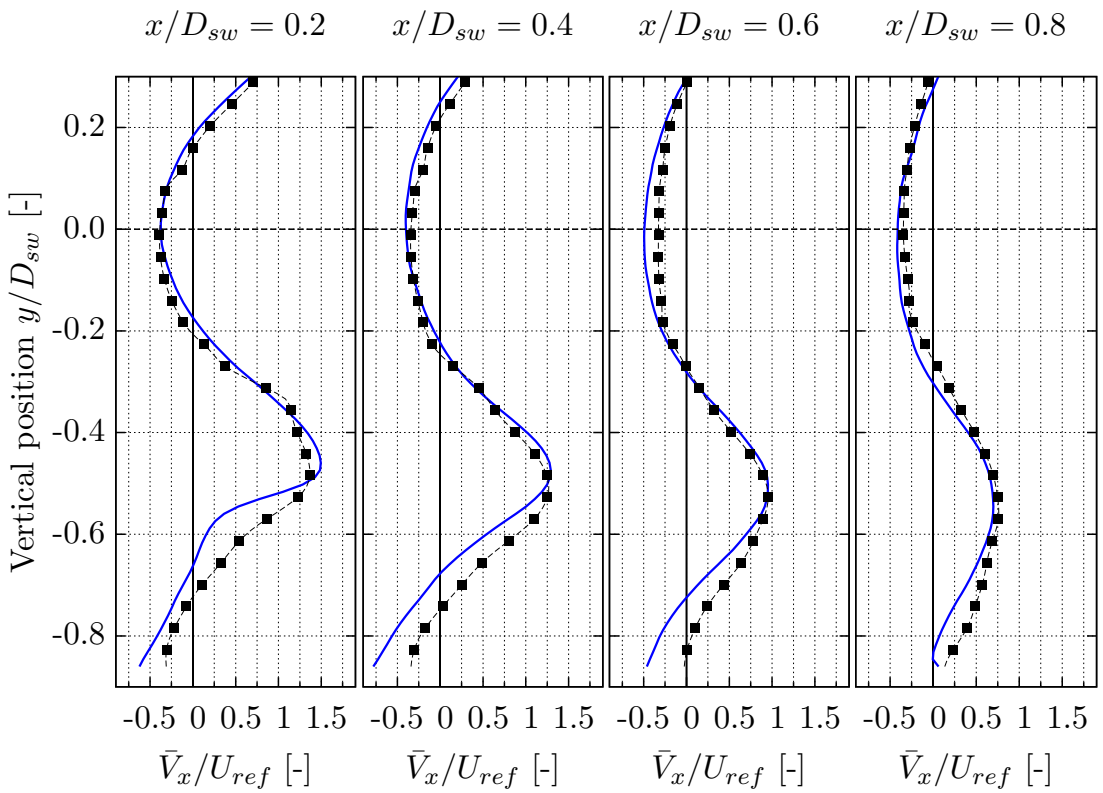


**(a)** Axial velocity.

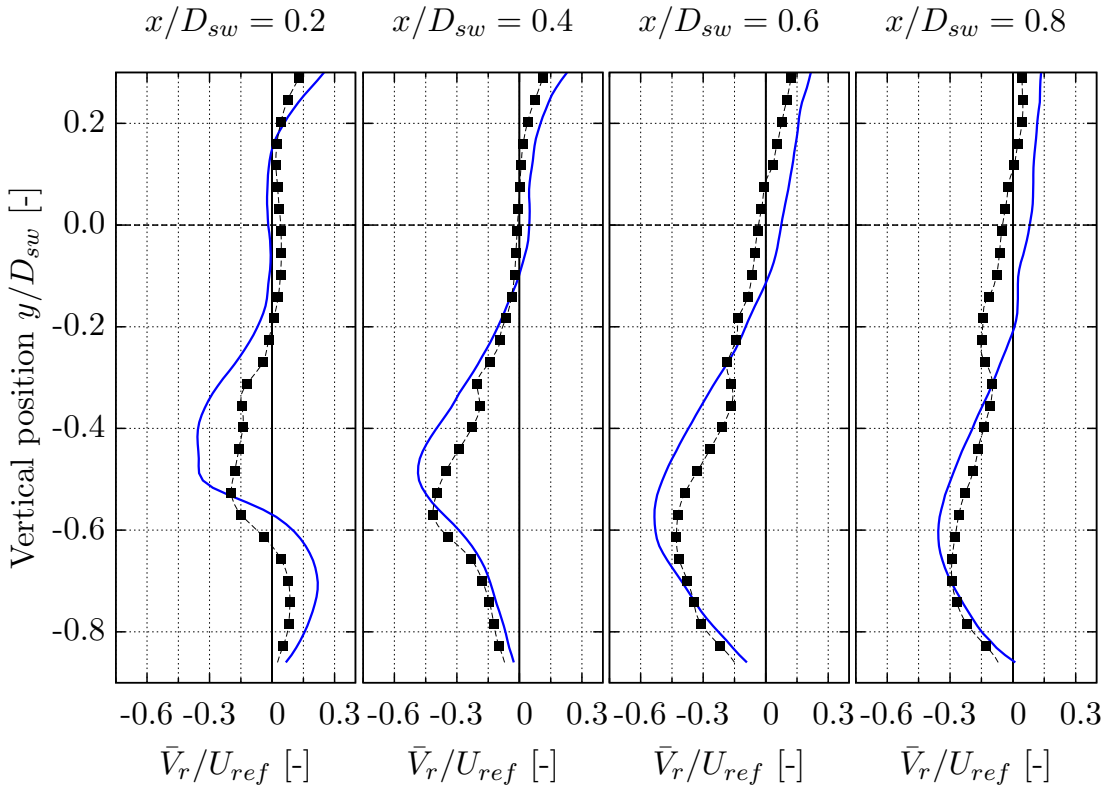


**(b)** Radial velocity.

**Figure 4.3:** Vertical profiles of the time-averaged velocity components for the D00 case (line: LES, squares: PIV).

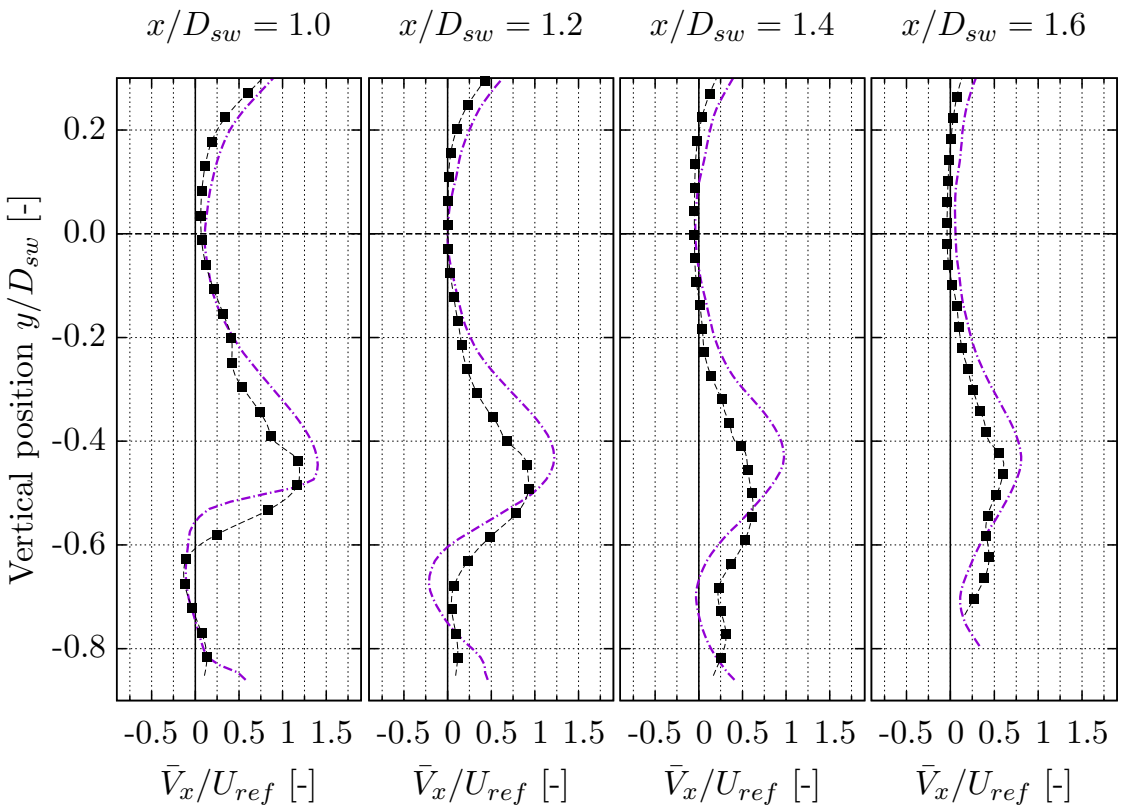


**(a)** Axial velocity.

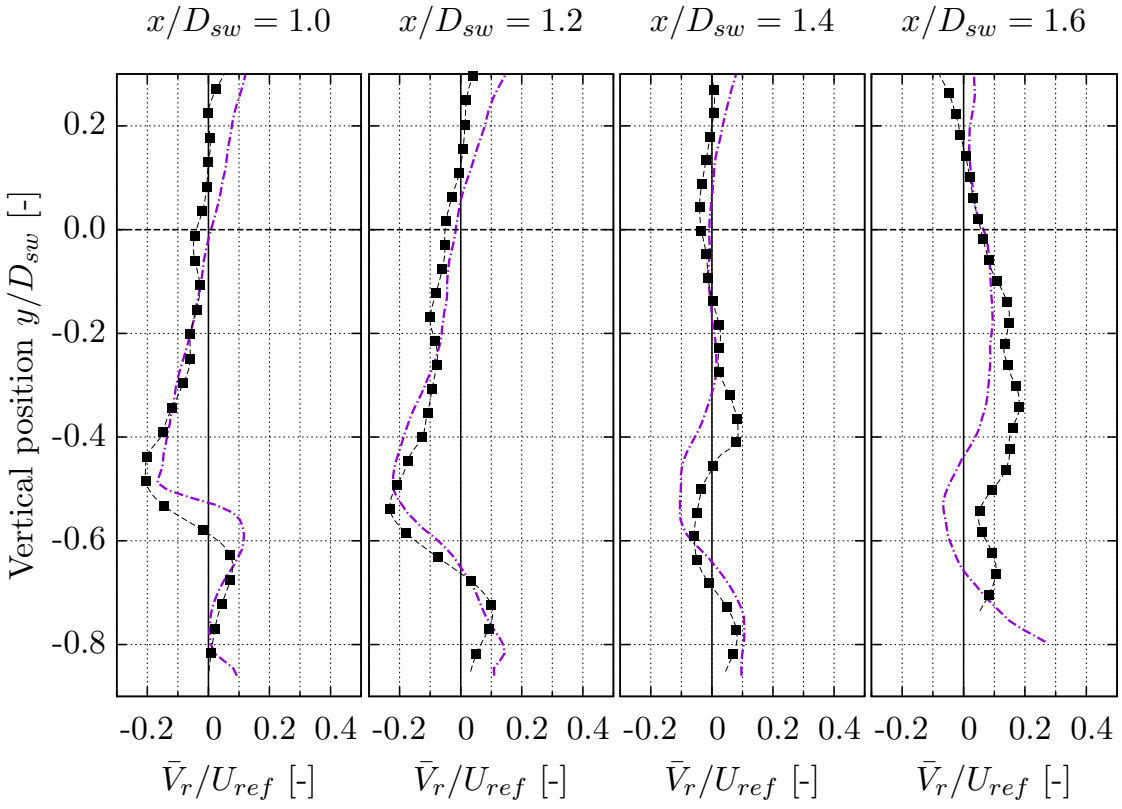


**(b)** Radial velocity.

**Figure 4.4:** Vertical profiles of the time-averaged velocity components for the D55 case (line: LES, squares: PIV).

Having in mind the good LES prediction of the flowfield in the CS, it is now proposed to analyse numerical and experimental results at the exit of the module which constitutes a key point of the CS design.

## 4.2 Time-averaged aerothermal field in plane 40

One of the important objectives of the FACTOR project being to have a well defined flow field at the inlet of the turbine, the assessment of the CS design mostly relies on the flow quantities in plane 40. Amongst them, the velocity and temperature fields are of primary importance as they should be representative of a Lean Burn combustor, i.e. feature a high level of swirl and a well-defined central hot spot. It is proposed here to compare the experimental and numerical results for such quantities, relying on the conventional design criteria i.e. 2-D fields in plane 40 and the corresponding circumferentially-averaged profiles when necessary.

The specificities of the experimental and numerical data available at the combustor exit impose to respect a precise methodology when performing comparisons. First, as the experimental investigation area does not cover all the surface of plane 40 (blue line in Fig. 4.5), the numerical results are projected onto the experimental grid[2] (orange line). This zone is considered as a reference zone on which circumferentially-averaged profiles can be computed following the CS radii (black lines). However, because of the non-concentricity between the CS and the TS, the circumferentially-averaged variables at the extreme positions (A and B in Fig. 4.5) are calculated with very few points and are thus removed from the curves presented hereafter.

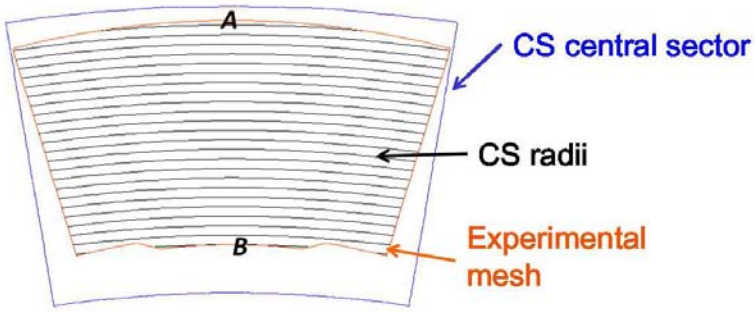


**Figure 4.5:** Layout of the experimental measurements and LES in plane 40.

LES predictions are now compared to the measurements obtained using the TS in plane 40, first in terms of velocity (Section 4.2.1) and then temperature (Section 4.2.2), considering in all cases the time-averaged results.

[2]See Section 3.1.2 for details on the experimental grids.

### 4.2.1 Flow velocity

The aerodynamic flow at the exit of the CS is investigated first in terms of flow angles (swirl and pitch) and second in terms of mass flow distributions. One can refer to Table 3.4 in Chapter 3 for a summary of the available measurements.

#### Swirl angle

The swirl angle measured by the 5HP is shown along with the LES results in Fig. 4.6. For the D55 case, one observes the persistence of the swirling core (preserved by the duct) while the D00 case shows both a lower absolute level of swirl and less azimuthal heterogeneities. In that respect, the D55 case is closer to the requirements for a Lean Burn CS since the swirl angle is found to be important (extrema values as high as $\pm 40°$) and non-uniformly distributed (central HS). The simulations capture well the change of pattern between the D00 and D55 cases and the associated extreme swirl angle values. If the agreement between experiments and numerics is very good for the D55 case, the LES of the D00 case does not perfectly reproduce the measured migration of the HS towards the right side. This difference (or at least part of it) could be attributed to the periodicity conditions used for LES which may not reflect the experimental trisector configuration. Indeed, recent hybrid RANS-LES simulations performed by FACTOR partners [124] on a trisector configuration (without duct) support this hypothesis. This non-

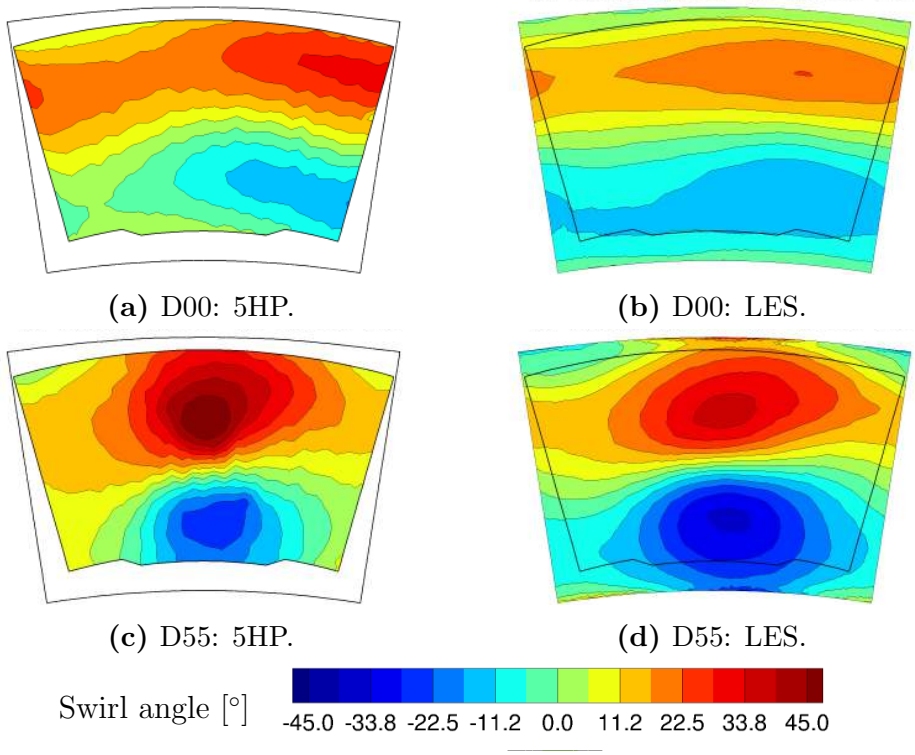


**(a)** D00: 5HP. **(b)** D00: LES.

**(c)** D55: 5HP. **(d)** D55: LES.

**Figure 4.6:** Swirl angle in plane 40 from 5HP measurements and LES (looking downstream).

periodicity is found to be less important for the ducted cases probably because the imposed confinement limits the azimuthal variations as observed for the D45 case [21]. A more quantitative analysis is proposed in Fig. 4.7 by comparing the circumferentially-averaged profiles of swirl in plane 40. Through such profiles, it is clearly noticed that LES and 5HP agree well in the upper part ($R > 50\%$) while in the lower third of plane 40 the simulations overpredict the swirl magnitude by up to 10° (D00) and 12° (D55). A possible explanation might be that the simulations features a too weak interaction between the swirling mainstream and the coolant flow which is supposed to reduce the swirl by mixing the two flows. Indeed, the model used in the LES to account for the mass flow rate through the effusion cooling plates does not guaranty the initial amount of flow momentum normal to the wall, strongly reducing the thickness of the cold film (see Appendix A). As a result, the HS exiting the swirler encounters a too thin coolant flow along the inner

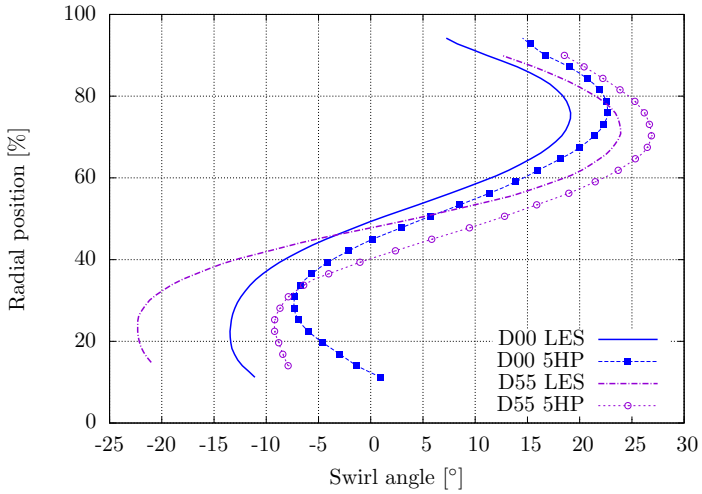


**Figure 4.7:** Circumferentially-averaged profiles of swirl angle in plane 40.

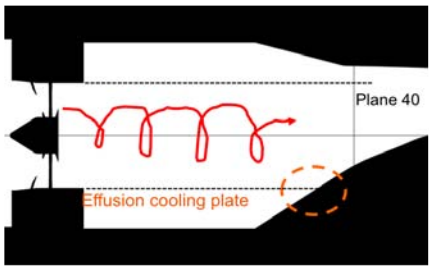


**(a)** Schematic representation of the path of the HS in the CS.

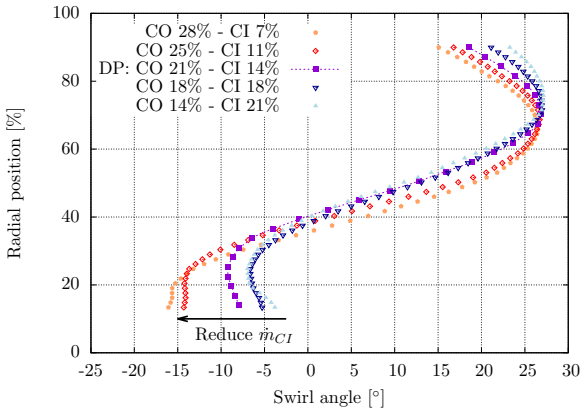


**(b)** Circumferentially-averaged swirl angle.

**Figure 4.8:** Experimental investigation (5HP) of the effect of the coolant flow split on the swirl angle in plane 40 (D55 case).

liner (see Fig. 4.8a), which ends up in less mixing. To support this hypothesis, one can rely on a set of additional experimental operating points performed during the trisector campaign and for which different flow splits between the inner, outer and mainstream flows were tested. By assuming that the thickness of the cooling film directly depends on the mass flow rate in the multiperforated plate, the experimental tests where the inner coolant mass flow rate ($\dot{m}_{CI}$) is reduced should tend to be closer to the LES results. Plots of the swirl angle in plane 40 obtained from these tests, shown in Fig. 4.8b, confirm that: *(i)* reducing the inner coolant mass flow increases the swirl angle in the bottom part of plane 40; *(ii)* reducing the outer coolant mass flow has a much reduced influence on the swirl angle in plane 40. This tends to comfort the hypothesis that the film cooling is too thin in the LES and thus does not interact enough with the mainstream.

### Pitch angle

The contours of pitch angle in plane 40 shown in Fig. 4.9 confirm the large change in flow topology between the ducted and unducted cases which is very well captured by the simulations. For the D00 configuration, the pitch distribution is almost purely radial and reflects the flow deviation by the inner liner while for the D55 case, it reflects the remnants of the swirling mainstream flow which is still coherent and pronounced in this direction. The circumferentially-averaged profiles of the pitch angle are shown in Fig. 4.10. The observation of this plot is very interesting

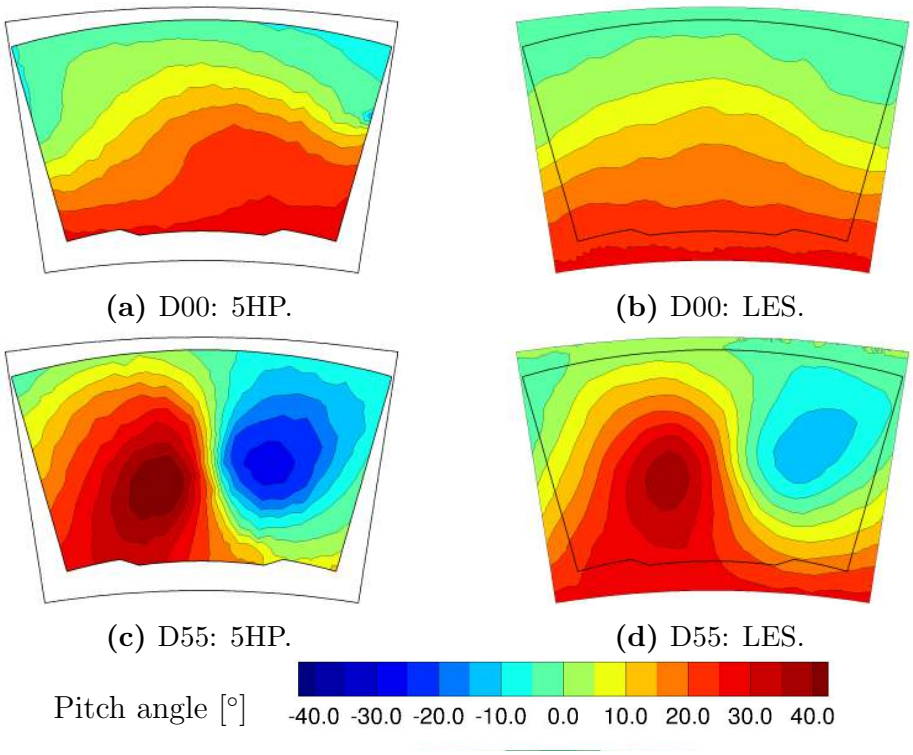


**(a)** D00: 5HP. **(b)** D00: LES.

**(c)** D55: 5HP. **(d)** D55: LES.

**Figure 4.9:** Pitch angle in plane 40 from 5HP measurements and LES (looking downstream).

as it highlights how the circumferential averaging operation transforms completely different flow fields (Figs. 4.9a vs 4.9c) into almost identical 1-D profiles. This demonstration emphasizes the limits of the very common industrial practice that uses only 1-D radial profiles to characterize the velocity profile at the inlet of a turbine.

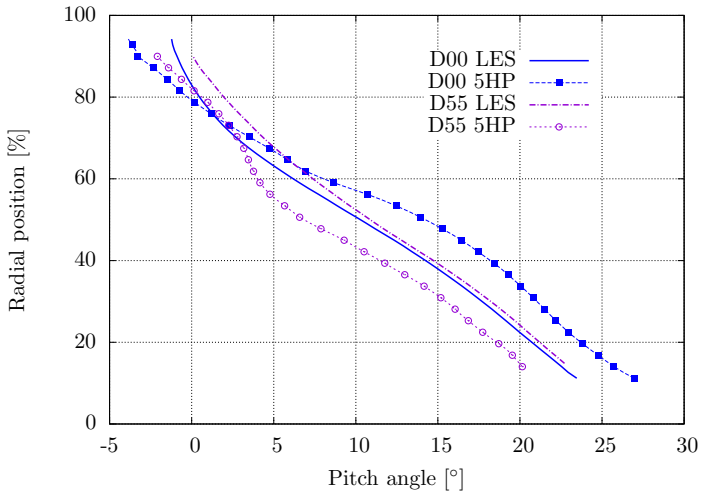


**Figure 4.10:** Circumferentially-averaged profiles of pitch angle in plane 40.

The pitch angle contours and profiles have to be seen in light of the previously described swirl angle since they reflect the rotating motion of the HS. In that respect, the D55 case features a well defined swirling core with large differences in flow angles both in the radial and the azimuthal directions, which is typical of Lean Burn configurations. The ducted configuration therefore constitutes a better candidate for the FACTOR final CS than the unducted case.

### Mass flow distribution

The measurement of the mass flow distribution (namely axial momentum) in plane 40 is obtained both by 5HP and HWA at isothermal conditions. Even if the 5HP constitutes the reference measurement for the aerodynamic field in plane 40, it is proposed to investigate the differences between the two experimental techniques to better illustrate the level of uncertainties present in the data prior to conclude on the numerical predictions quality.

On one hand, the accuracy of the 5HP measurement is bounded to the use of a density that is computed from the ideal gas law considering the static pressure measured at the probe tip and the temperature recorded by a thermocouple located 7.44 mm downstream and therefore subject to flow distortions because of the presence of the probe (see Fig. 3.6a). On the other hand, HWA hardware is much less invasive and the post-processing is direct but measurements are performed at the IOP (see Section 3.2). Having knowledge of the intrinsinc difference of the two approaches, the fields of axial momentum in plane 40 measured at isothermal and non-isothermal conditions are presented in Fig. 4.11 for the D00 case. The central

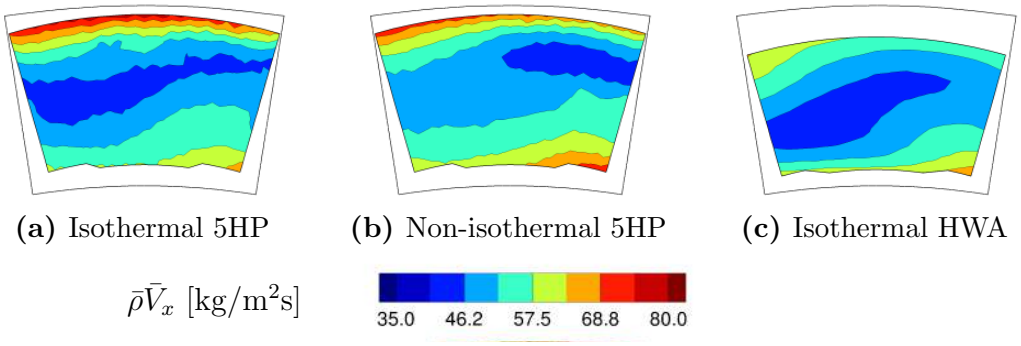


**(a)** Isothermal 5HP **(b)** Non-isothermal 5HP **(c)** Isothermal HWA

**Figure 4.11:** Axial momentum in plane 40 from 5HP and HWA measurements for the D00 case (looking downstream).

region of plane 40 is characterized by slow moving hot air flow resulting in low values of the axial momentum. In the near wall region, the axial momentum is higher because of the larger density and higher velocity of the coolant flow. The 5HP measurements indicate that the mass flow distribution is not dramatically affected by the operating conditions, which gives an experimental confirmation of the findings of Section 3.2. If the results obtained by HWA seem at first sight comparable to the 5HP ones, a more quantitative comparison shows that this is not the case. Indeed, the corresponding circumferentially-averaged profiles plotted in Fig. 4.12 indicate a significant difference between HWA and 5HP both in terms of shape, profile and position of the peak. HWA measurements indicate a more symmetrical profile which is centered on the mid-radius position while the 5HP results locate the peak at 65% of the radius in plane 40. Such differences obtained solely by the use of two distinct measurement techniques performed on the same operating point (IOP) highlight the limits the experimental approach and helps putting things into perspective when it comes to its comparison with LES.

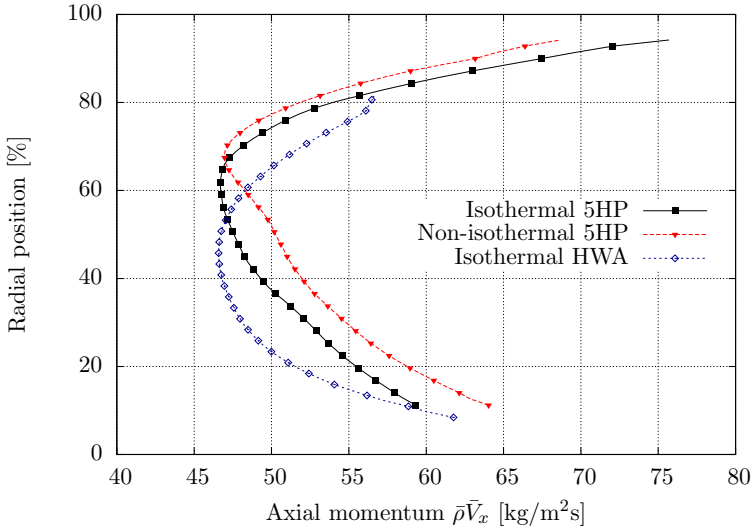


**Figure 4.12:** Circumferentially-averaged profile of axial momentum in plane 40 (D00 case).

It is now proposed to compare the LES results to the HWA measurements for which post-processing errors and flow disturbances are smaller. Figure 4.13 shows the contours of axial momentum obtained from HWA and LES for the D00 and D55 cases. Both approaches highlight the effect of the duct on the mass flow distribution in plane 40. A central circular zone of lower velocity is indeed present for the D55 case while for the unducted case the axial momentum is more uniform in the azimuthal direction. Note also that for the D00 case the flow distortion caused by the non-periodicity of the experiments is visible on the HWA measurements.

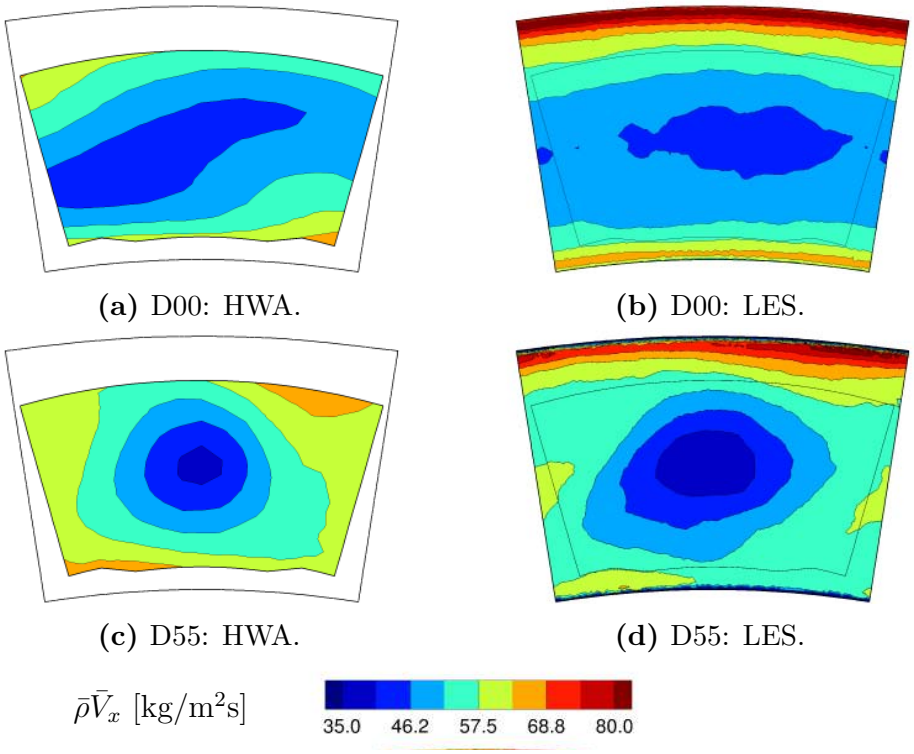


**(a)** D00: HWA. **(b)** D00: LES.

**(c)** D55: HWA. **(d)** D55: LES.

**Figure 4.13:** Axial momentum in plane 40 from HWA measurements and LES (view from upstream).

The radial profile of axial momentum plotted along the centerline of plane 40 (without any azimuthal averaging) is shown in Fig. 4.14. The curves indicate clearly that both the radial position of the peak of minimum mass flow and its value are very well predicted by the LES. The numerical results only differ from measurements when approaching walls where part of the mass flow comes from the coolant.

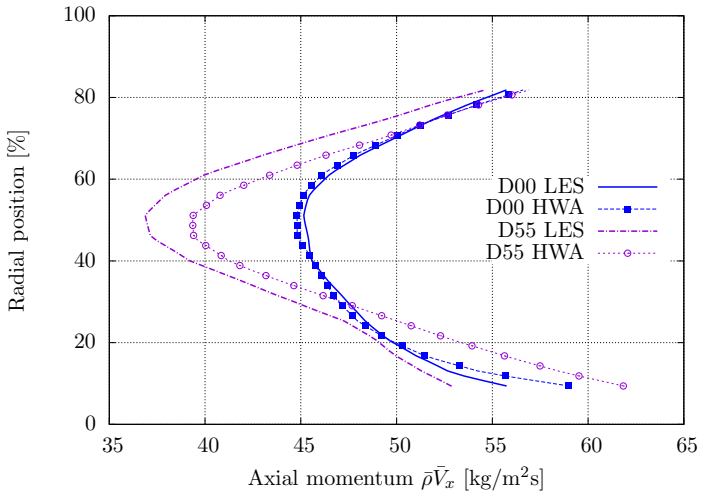


**Figure 4.14:** Profile of axial momentum on the centerline of plane 40.

### 4.2.2 Temperature field

The temperature field measured at the combustor exit by the THCPL is now compared with the LES results. One needs first to introduce a non-dimensional temperature coefficient to account for the intrinsic differences between LES and experiments. These differences are of different kinds:

(i) LES use adiabatic walls while the trisector rig is not insulated and of course subject to heat losses which can cool down the flow in the vicinity of the wall and conduction processes which can heat up the coolant streams.

(ii) The inlet boundary conditions of LES are constant in terms of mass flow rate and temperature while the operating conditions may vary. If the mass flow and pressure variations are small for one single experimental run, the coolant temperature is directly linked to the ambient temperature (see Section 3.1) which was found to evolve significantly for the different tests[3].

(iii) The accurate definition of the cold junction temperature of the THCPL was found to be difficult and some uncertainty remains on the value of the absolute temperature. To reduce possible errors, a relative temperature should be hence used instead (which is the actual quantity measured by the THCPL).

To account for all these remarks, it is proposed to adapt the LOTDF introduced in Eq. (1.3) according to the following definition:

$$\Xi(x_0, r, \theta) = \frac{T(x_0, r, \theta) - \overline{T}_{40,meas}}{\overline{T}_{40,meas} - \overline{T}_{coolant}}, \tag{4.1}$$

where $\overline{T}_{40,meas}$ is the time and space-averaged temperature over the experimental investigation area (LES results are projected on this zone) and $\overline{T}_{coolant}$ is the mean

[3]The first experimental investigations were performed in October (coolant up to 310 K) while the test campaign ended in February (coolant about 285K).

of the inner and outer coolant temperature. This quantity $\Xi$ has the advantage of allowing comparisons between LES and experiments by trying to get rid of the absolute level of temperature imposed by the operating conditions.

| | Case | $\overline{T}_{40,meas}$ [K] | $\overline{T}_{coolant}$ [K] |
|---|---|---|---|
| D00 | THCPL | 472 | 299 |
| | LES | 465 | 300 |
| D55 | THCPL | 450 | 295 |
| | LES | 459 | 300 |

**Table 4.1:** Reference temperatures for the calculation of $\Xi$.

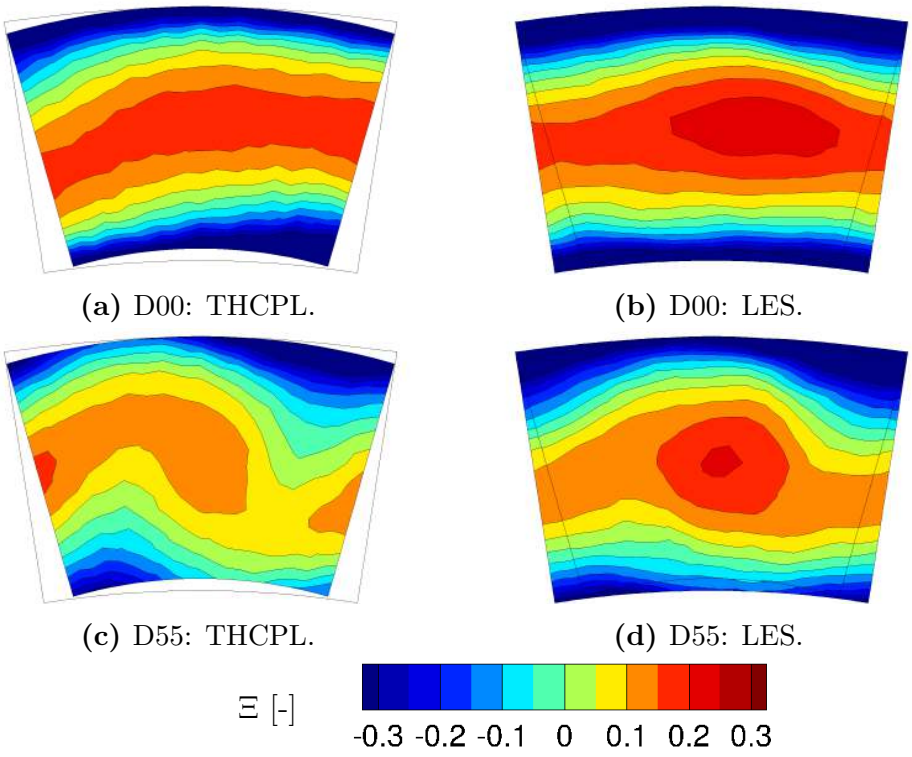


**(a)** D00: THCPL. **(b)** D00: LES.

**(c)** D55: THCPL. **(d)** D55: LES.

**Figure 4.15:** Non-dimensional temperature coefficient in plane 40 from THCPL measurements and LES (looking downstream).

The temperature coefficient $\Xi$ is computed in plane 40 for all the experimental and numerical cases and is shown in Fig. 4.15 (reference temperatures are reported in Table 4.1). The first observation is that the large differences observed previously between the aerodynamic field of the ducted and unducted cases are also visible in the temperature field. Even if the disparities are less pronounced than for the previously discussed flow angles, one still observes an almost purely radial distribution of temperature for the D00 case while the D55 case exhibits more azimuthal heterogeneities and a significant distortion of the hot core. In that respect, the

D55 case features a central hotspot which is well discriminated and thus constitutes a better candidate to match the FACTOR requirements. This being said, the simulations capture very well the change of temperature distribution induced by the presence of a duct. The only differences concern the distortion of the HS for the D00 case which is not perfectly captured by LES because of the periodicity hypothesis discussed earlier.

The circumferentially-averaged profiles of temperature are shown in Fig. 4.16. Note that to complement the profiles, the averaged value of the wall temperature measured by three thermocouples placed inside the inner wall in plane 40 are reported by dots and give a lower limit for the fluid temperature for $R \to 0$. The agreement between LES and experiments is very good for all configurations, especially in light of the results reported in the open literature presented in Chapter 1. The main differences are located in the near wall region and might be attributed to the effusion cooling model or a possible heating effect of the flow by the solid.

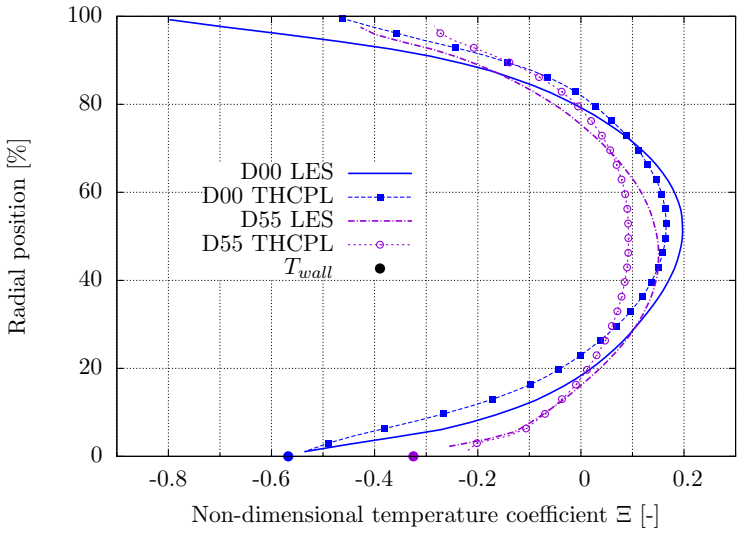


**Figure 4.16:** Circumferentially-averaged profiles of the temperature coefficient Ξ in plane 40.

## 4.3 Conclusions

All the analyses of the LES performed on the ducted and unducted configuration of the CS and their comparison to the available experimental results allow to draw the following conclusions:

- The presence of a duct has a strong impact on the topology of the flow and leads to dramatically different flow fields at the exit of the CS.
- The D55 case is found to be the best candidate to match the FACTOR requirements for a Lean Burn CS as it features high levels of swirl and a well-defined central HS.

- Overall, the blind-test LES are found to provide a very good prediction of the flow field inside the CS for all the investigated geometrical configurations.
- The presence of walls on the UNIFI trisector rig leads to a distortion of the flow in plane 40 that cannot be captured by the periodic LES and do not ease the comparison.
- The possible influence of the homogeneous injection model for effusion cooling and the interaction with the mainstream is pointed out and may explain the bad prediction of swirl angle especially in the lower part of plane 40.
- The use of averaging operations (e.g. azimuthal-averaging for the radial profiles) has to be handled with care as it is observed in many cases that a similar result can correspond to significantly different physical realities.

Based on these conclusions, the final design of the CS using the 55 mm duct was validated by FACTOR consortium and the module shall be installed on the DLR full annulus rig in 2016. In parallel and within the context of this PhD work, further investigations are performed using the trisector rig as a basis. These results are reported in Part III of this manuscript.

# Part III

# Advanced diagnostics for the exploitation of the combustor simulator setup

It is proposed in this third part of the manuscript to take advantage of the experience gained on the combustor simulator setup to improve the numerical and experimental characterization of the flow entering the turbine by use of advanced diagnostics to be identified and constructed. With this aim, this part is organized as follows:

- First, to complement the analysis of LES results, the sensitivity of the simulations to the numerical settings is investigated in Chapter 5.
- Second, Chapter 6 focuses on the characterization of turbulent quantities (intensity and integral scale) exiting the combustor simulator.
- Finally, Chapter 7 details a new proposal to take into account unsteady temperature fields in such flows and typically apply associated diagnostics to plane 40 of any gas turbine combustor.

The turbulence characterization at the exit if the comustor simulator detailed in Chapter 6 was published in two separate papers, the first one dedicated to the HWA methodology and turbulence intensity results:

> T. Bacci, B. Facchini, A. Picchi, L. Tarchi, C. Koupper, and J.-L. Champion. "Turbulence field measurements at the exit of a combustor simulator dedicated to hot streaks generation". In: *ASME Turbo Expo 2015: Turbine Technical Conference and Exposition*. GT2015-42218. 2015

while the second one focuses on the evaluation of an integral scale of turbulence:

> C. Koupper, L. Gicquel, F. Duchaine, T. Bacci, B. Facchini, A. Picchi, L. Tarchi, and G. Bonneau. "Experimental and Numerical Calculation of Turbulent Timescales at the Exit of an Engine Representative Combustor Simulator". In: *ASME Turbo Expo 2015: Turbine Technical Conference and Exposition*. GT2015-42278. 2015

The new proposal for the representation of temperature discussed in Chapter 7 was published in:

> C. Koupper, L. Gicquel, F. Duchaine, and G. Bonneau. "Advanced Combustor Exit Plane Temperature Diagnostics Based on Large Eddy Simulations". English. In: *Flow, Turbulence and Combustion* (2015), pp. 1–18

# Chapter 5

# Sensitivity of the LES to the numerical parameters

## Contents


5.1 Numerical parameters under study . . . . . **104**
5.1.1 Mesh . . . . . 104
5.1.2 Sub-grid scale model . . . . . 104
5.1.3 List of the cases . . . . . 106
5.2 LES quality criteria . . . . . **106**
5.3 Prediction of the mean flow and turbulence . . . . . **109**
5.3.1 Flow field inside the swirler . . . . . 110
5.3.2 Flow field in the chamber . . . . . 114
5.4 Comparison with experimental results . . . . . **117**
5.4.1 PIV results in the central plane . . . . . 117
5.4.2 Swirl and temperature distortion in plane 40 . . . . . 119
5.5 Conclusions . . . . . **121**


The comparison between experimental and numerical results presented for the D00 and D55 cases in Chapter 4 indicated a very good agreement between the two approaches. This being said, there is a need to assess how sensitive the simulations are to the numerical parameters in the optics of finally evaluating the numerical tool and defining best practices.

To do so, a set of four LES are performed on the unducted case using different meshes or turbulent models described in Section 5.1. First, the notion of LES quality is addressed in Section 5.2 by use of different indicators. The investigations then focus in Section 5.3 on the resolution of the mean flow and turbulence level. The LES are ultimately compared to some experimental results in Section 5.4 with the aim of defining best computational practices. The conclusion proposed in Section 5.5 finally recalls the main outcomes of this study.

## 5.1 Numerical parameters under study

In the specific context of the non-reactive mixing of the FACTOR CS, the three major parameters that may affect the LES results are the mesh size, the Sub-Grid-Scale (SGS) model and the modelling of the effusion cooling walls. As today only the homogeneous injection model is available in AVBP, the latter point is not addressed here. The impact of the two former parameters is however evaluated and discussed hereafter before construction of any new analysis on LES predictions.

### 5.1.1 Mesh

One of the most important parameter for LES is the spatial discretization as the extent and number of resolved scales directly depends on the local mesh size. Its impact is evaluated here by use of three fully unstructured meshes (all containing only tetrahedral elements) and respectively labelled: coarse (15.8 Million cells), medium (34.2M) and fine (68.5M). As shown in Fig. 5.1, the mesh is not refined isotropically between cases. The central region of the CS in the medium and coarse cases shows a fairly uniform grid size while in the fine mesh the jet and external shear zone exiting the swirler are more refined. Note indeed that the number of cells at the root of two adjacent vanes of the swirler was found to be a critical point (only 1 mm wide). This region respectively counts a minimum of 4, 6 and 10 cells for the coarse, medium and fine meshes as shown by Fig. 5.1. Note also that the smallest cell size strongly impacts the timestep of the LES (see Table 5.1) as it is limited by the explicit compressible approach through the Courant Friedrichs Lewy condition (CFL).

### 5.1.2 Sub-grid scale model

In the LES formalism, SGS tensors and vectors are introduced to describe the interaction between the non-resolved and resolved motions [12]. Supposing that the effect of the small scales on the larger ones is purely dissipative, this influence can be modeled by the introduction of a turbulent viscosity $\nu_{sgs}$ in the NS equations [125]. Three models for the turbulent viscosity are benchmarked in this work (details on their formalism are given in Appendix C):

**The Smagorinsky model [111]** is the most common SGS model because it is cheap and robust but known to be too dissipative for shear flows and to badly behave in wall bounded flows [12];

**The Dynamic Smagorinsky [126]** constitutes an improvement of the standard Smagorinsky model thanks to a dynamic evaluation in space and time of the closure coefficient present in all model [1];

**The WALE model [127]** was developed to better handle near wall regions by switching off the SGS model when approaching walls.

[1] This model was benchmarked versus the standard Smagorinsky one but differences were found to be negligible and results are not reported here.

**(a)** Coarse.

**(b)** Medium.

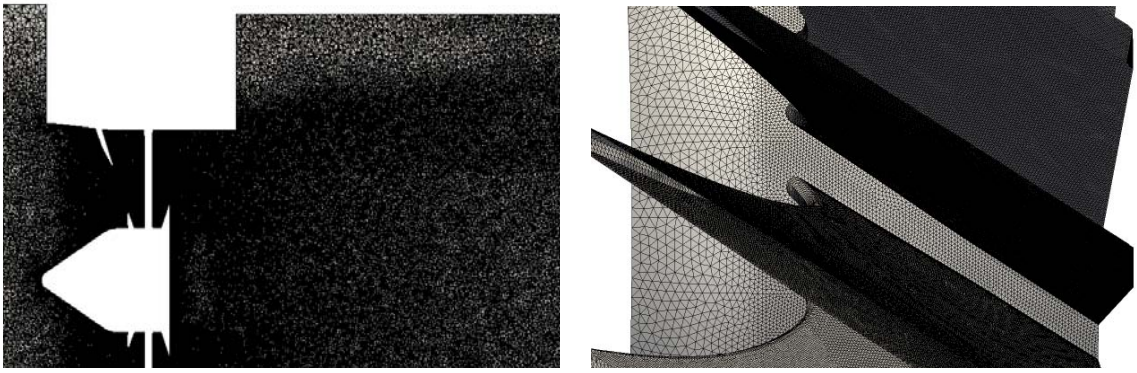

**(c)** Fine.

**Figure 5.1:** Detail of the mesh in the central plane of the CS (left) and view of the surface mesh of the swirler hub from the vanes tip (right).

### 5.1.3 List of the cases

The matrix of test cases to be investigated is given in Table 5.1. The influence of the mesh density can be observed by comparing simulations 1, 2 and 3 all performed with the same Smagorinsky model. The impact of the SGS model can be evaluated by observing cases 2 and 4 both performed on the medium mesh.

| Case | Duct | Operating point | Mesh nodes | Mesh cells | Scheme | SGS model | Physical time [ms] | Timestep [s] |
|---|---|---|---|---|---|---|---|---|
| 1 | D00 | DP | Coarse: 2.7M | 15.8M | TTGC | Smagorinsky | 154 | $6.5 \cdot 10^{-8}$ |
| 2 | D00 | DP | Medium: 6.0M | 34.2M | TTGC | Smagorinsky | 155 | $4.4 \cdot 10^{-8}$ |
| 3 | D00 | DP | Fine: 12.2M | 68.5M | TTGC | Smagorinsky | 155 | $3.7 \cdot 10^{-8}$ |
| 4 | D00 | DP | Medium: 6.0M | 34.2M | TTGC | WALE | 157 | $4.4 \cdot 10^{-8}$ |

**Table 5.1:** Summary of the LES of the FACTOR CS without duct.

Such tests are needed because the association of a mesh size (coarse, medium, fine) and a SGS model (Smagorinsky or WALE) governs the production of turbulent viscosity in the different regions of the flow. The impact of such addition of viscosity in the NS equations has to remain limited not to affect the simulation results. To assess this property, the quality of the LES can be evaluated using different indicators which are now detailed.

## 5.2 LES quality criteria

The quality of a LES may be defined by its ability to properly resolve the flow field without introducing a bias by the creation of uncontrolled turbulent viscosity. To investigate this point, two quality indexes $QI$ are commonly employed for LES.

A first criterion compares the resolved turbulent kinetic energy $k_{res}$ to the total turbulent kinetic energy (i.e. resolved and modelled):

$$QI_k = \frac{k_{res}}{k_{tot}} = \frac{k_{res}}{k_{res} + k_{sgs}}, \tag{5.1}$$

with $k_{sgs}$ the SGS contribution which can be explicitly related to the turbulent viscosity $\nu_{sgs}$ [125]:

$$k_{sgs} = \frac{1}{(C_m \Delta)^2} \nu_{sgs}^2, \tag{5.2}$$

where $\Delta$ is the LES filter length, equal to the cell characteristic length and the constant $C_m$ is equal to 0.09137. It is commonly admitted [128] that no less than 80% of the turbulent kinetic energy has to be resolved.

With the same objective, Celik et al. [129] propose a quality index $QI_\nu$ based on the proportion of turbulent viscosity in the total simulation effective viscosity

(assuming here that the numerical viscosity is negligible):

$$QI_\nu = \frac{1}{1 + \alpha_\nu \left( \frac{\nu_{sgs}}{\nu_{sgs} + \nu} \right)^n}, \tag{5.3}$$

where $\nu$ is the laminar kinematic viscosity estimated with the Sutherland relation from Eq. (C.7) and the constants $\alpha_\nu$=0.05 and $n = 0.53$ are calibrated based on DNS results [129].

The contours of these two quality indices in the central plane of the CS are shown in Fig. 5.2. For more quantitative comparisons, the two indicators are spatially-averaged at successive axial positions from the inlet to the outlet of the domain and the corresponding curves are shown in Fig. 5.3. The patterns of quality criteria highlight the presence of various zones labelled by a letter in Fig. 5.2a:

**Inlet plenum (A)** In this zone, relatively poorly meshed and featuring an almost laminar flow, the velocity gradients and RMS values are low. As a result, $QI_k$ is high (but decreases with the mesh refinement) and $QI_\nu$ remains low. Because $k_{res}$ and $k_{sgs}$ are both small, a little reduction of $k_{sgs}$ strongly impacts $QI_k$ as illustrated by the higher level of $QI_k$ obtained with the WALE model. This makes the use of such quality indices not very relevant in this region.

**Swirler (B)** This critical zone of the domain features a sudden drop of $QI_k$ (Fig. 5.3a) linked to a creation of turbulent viscosity (Fig. 5.3b) for the two less refined meshes. For the fine mesh, the small cells inside the swirler allow to comparatively reduce the level of turbulent viscosity as shown by the higher values of $QI_\nu$ in Fig. 5.2 (observe the absence of the yellow contour around the vanes). The impact of the WALE model is also noticeable here: the SGS model switches off near the walls which increases both $QI_k$ and $QI_\nu$.

**Chamber (C)** In the main volume of the CS, $QI_k$ is above 0.95 in all cases while $QI_\nu$ is more sensitive to the mesh refinement and drops below 0.8 for the coarse mesh only. In all cases, the near wall regions ($C_1$) are less refined and thus feature lower levels of $QI_\nu$, expect for the WALE case since no turbulent viscosity is created near walls. Note finally that the presence of the effusion cooling plates ($C_2$) gives rise to important velocity gradient which are not fully resolved, thus locally increasing $QI_k$.

Overall, the two quality indices indicate that turbulence is well resolved inside the CS. Indeed, more than 95% of the turbulent kinetic energy is resolved in the CS volume except in the swirler for the coarse and medium mesh where the ratio drops to 50%. The fine mesh provides very good results as $QI_k$ is greater than 90% everywhere except in the inlet plenum. It is finally noted that the simulations feature limited levels of turbulent viscosity in the regions of interest as indicated by $QI_\nu$ which remains greater than 0.75 everywhere and for all cases.

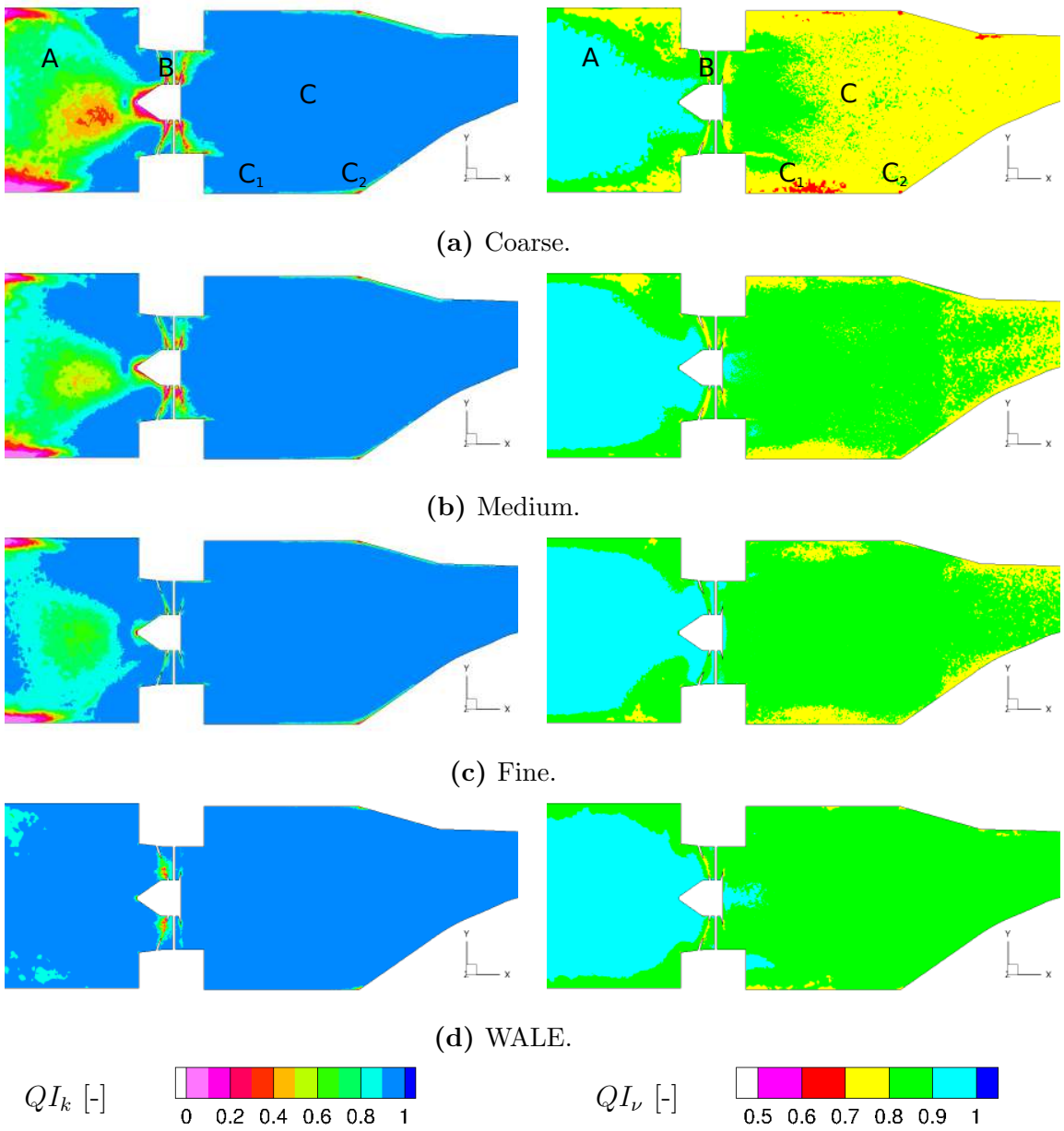


**(a)** Coarse.

**(b)** Medium.

**(c)** Fine.

**(d)** WALE.

**Figure 5.2:** Quality indices of the LES in the central plane of the CS for the four simulations.

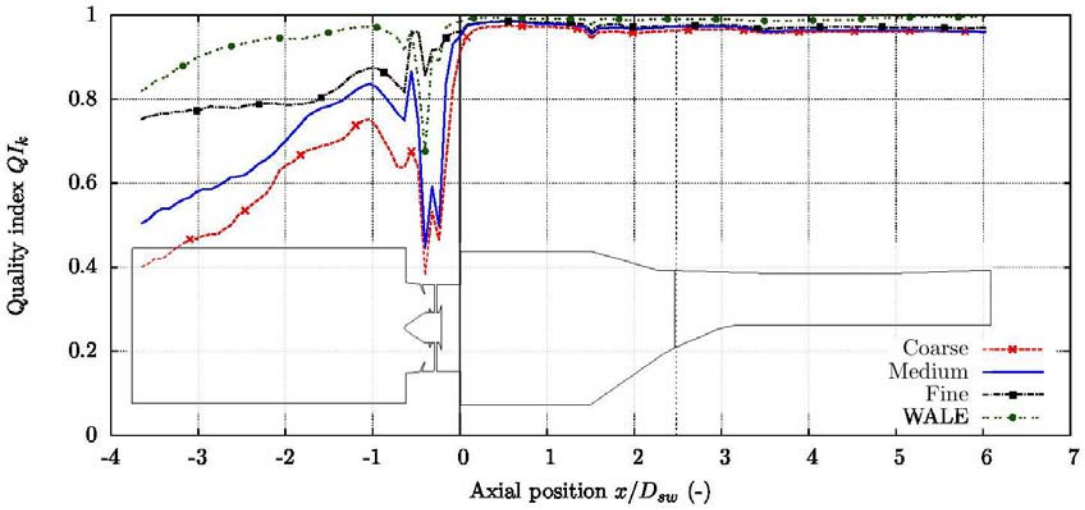


**(a)** Quality index based on the the resolved turbulent kinetic energy $QI_k$.

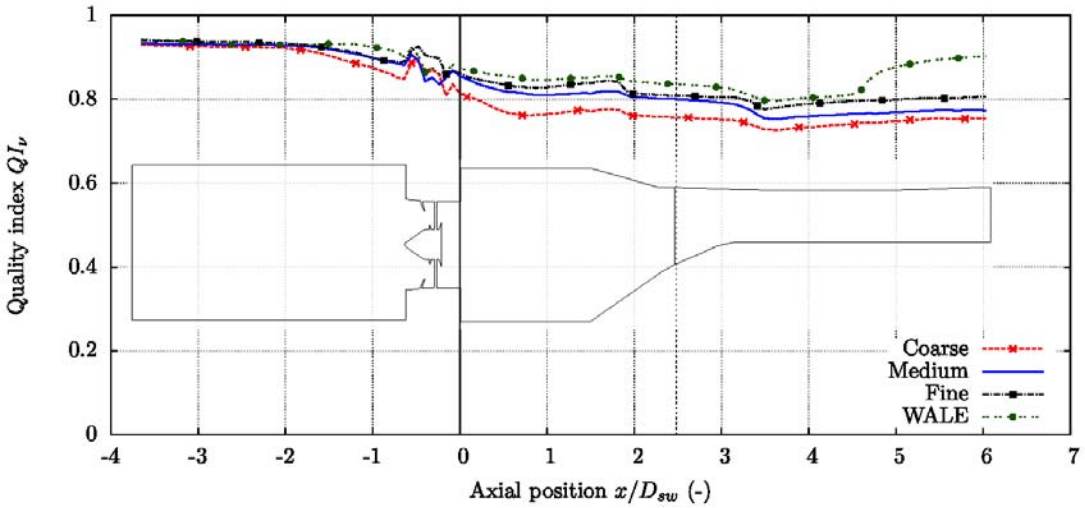


**(b)** Quality index based on the turbulent viscosity $QI_\nu$.

**Figure 5.3:** Spatially-averaged quality indices at successive axial stations from the inlet to the outlet of the numerical domain.

In light of the different levels of quality indices observed in the swirler region, one may however wonder if the prediction of the flow field and the associated generation of turbulence are impacted. This specific question is now addressed in the following section where the swirl is first investigated followed by the flow field prediction in the chamber.

## 5.3 Prediction of the mean flow and turbulence

The results of the different simulations of Table 5.1 are compared first focusing on the resolution of the flow field inside the swirler in Section 5.3.1, general comparisons in the CS being provided in Section 5.3.2.

### 5.3.1 Flow field inside the swirler

To assess if the mesh and SGS model impact the prediction of the distribution of velocity at the inlet of the CS, time and circumferentially-averaged profiles of velocity are compared in Fig. 5.4. If the axial velocity is almost identically predicted by the four simulations, both radial and tangential velocities are found to differ and very differently captured by the fine mesh. First, the position of the maximum radial velocity is similarly located ($r/R_{sw} \simeq 60\%$) but the LES on the fine mesh predicts a much lower magnitude (about 1/3 smaller) with a centripetal motion of fluid behind the swirler hub ($r/R_{sw} < 35\%$). Second, with the fine mesh, the swirl velocity is distributed almost linearly all over the radius while all other cases predict a zone without swirl which extends from the swirler axis up to the height of the swirler hub, followed by a high swirl zone in the jet exiting the vanes.

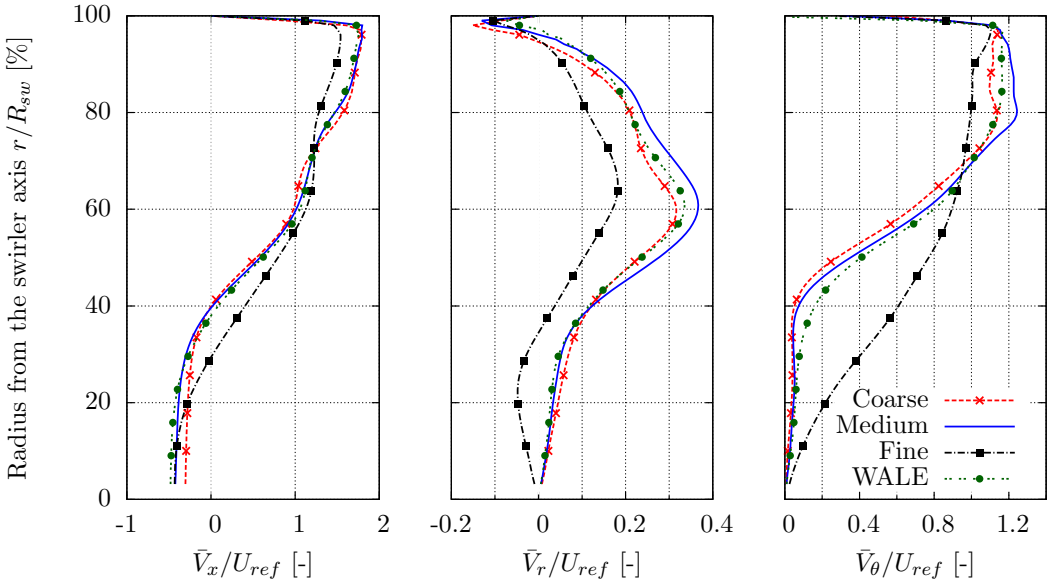


**Figure 5.4:** Circumferentially-averaged velocity profiles at the inlet of the CS in the swirler frame of reference.

With such different profiles of swirl velocity, one could expect a modification of the flow swirl number for the LES performed on the fine mesh. Surprisingly, the swirl numbers computed from these velocity profiles and shown in Table 5.2 are almost identical for the four simulations. This can be explained by the integrated expression of $S_N$ in Eq. (2.1) which gives more weight to the large radius and highlights that this global parameter is not sufficient to fully characterize a swirling flow field.

| Case (D00) | $S_N$ from Eq. (2.1) [-] |
|---|---|
| Coarse | 0.57 |
| Medium | 0.60 |
| Fine | 0.59 |
| WALE | 0.59 |

**Table 5.2:** Swirl number computed at the inlet of the CS.

As the swirling motion is one of the main source of turbulence in the CS, one may wonder if these different predictions of the velocity profiles translate into different levels of turbulence. Comparing the circumferentially-averaged profiles of resolved turbulent kinetic energy in Fig. 5.5 at three axial stations from the vanes exit to the inlet of the CS (see positions in Fig. 2.9a), one immediately notices that for the medium and coarse mesh, $k_{res}$ is almost zero at the swirler exit. Turbulence is then produced and resolved further downstream in the shear zone below the jet. As a result, the peak of $k_{res}$ initially centred on the hub radial position ($r/R_{sw} = 0.35$) progressively drifts radially up to about mid-height. The fine mesh and the WALE cases however provide comparable levels of $k_{res}$ at the swirler exit and are about ten times larger than the two other cases. Further downstream the fine mesh and WALE cases agree well in the upper part ($r/R_{sw} > 0.4$) but in the inner region the fine mesh shows higher levels of turbulence.

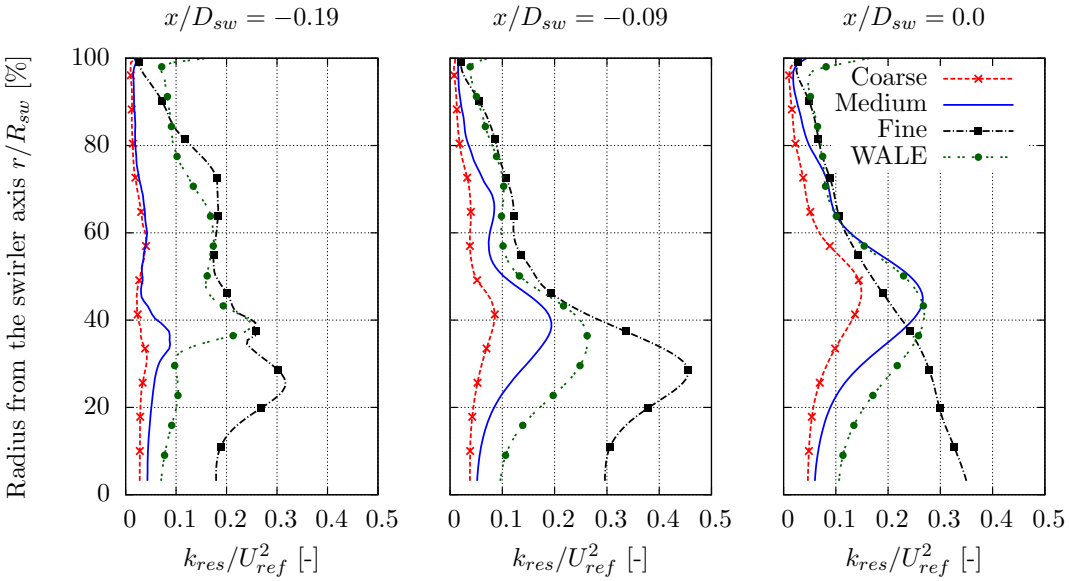


**Figure 5.5:** Circumferentially-averaged profiles of resolved turbulent kinetic energy at successive axial stations after the exit of the swirler vanes.

To understand why the fine mesh case (and more marginally the WALE case) differs from the other simulations both in terms of mean flow and turbulence level, one needs to investigate the flow inside the swirler itself. To do so, Fig. 5.6 shows

the contours of resolved turbulent kinetic energy and time-averaged normal velocity to an orthogonal section between two adjacent vanes of the swirler (a single arbitrary passage is selected here). It immediately appears that the fine mesh results differ from the other ones with significant non-uniformities of velocity and a much higher turbulence level. This indicates that the number of cells between two vanes has a significant impact both on the resolution of the flow structures (e.g. radial heterogeneities in Fig. 5.6c) and on the turbulence level (too coarse meshes do not allow the resolution of turbulence). The turbulence contours of Fig. 5.6 also indicate that higher levels of $k_{res}$ can be obtained if the WALE model is used.

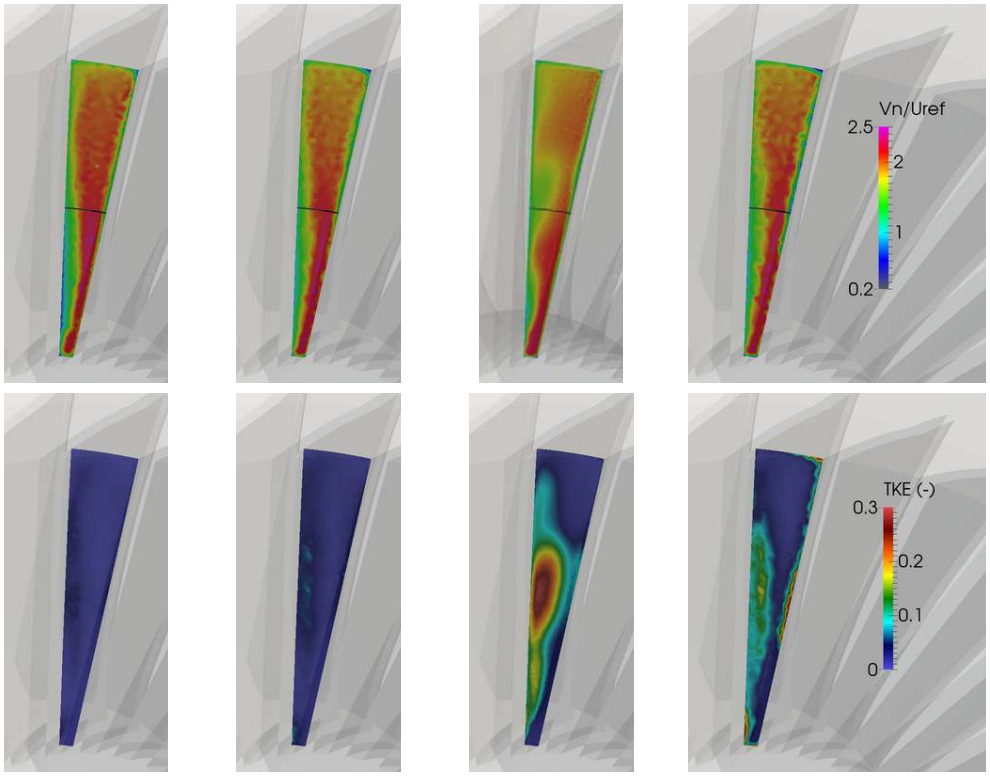


**(a)** Coarse. **(b)** Medium. **(c)** Fine. **(d)** WALE.

**Figure 5.6:** Time-averaged normal velocity $V_n/U_{ref}$ (top) and resolved turbulent kinetic energy $k_{res}/U_{ref}^2$ (bottom) in an arbitrary passage between two vanes of the swirler.

All these observations point towards the resolution of the channel flow between two vanes and the associated computation of the near wall flow. The dramatic difference between the fine mesh and the other cases suppose a significant change of boundary layer resolution. To evaluate this hypothesis, the flow behaviour at walls needs to be further investigated. In this context, the first quantity of interest is the resolved wall shear stress defined as:

$$\tau_w = \mu \left. \frac{\partial u}{\partial y} \right|_{y=0}, \tag{5.4}$$

where $y$ is the normal distance to the wall. The wall shear stress is a known

indicator and relates to the shear velocity $u_\tau = \sqrt{\tau_w/\rho}$ obtained for our simulations by use of a law of the wall. The shear velocity is explicitly related to the edge of the cells located on the wall by the local friction Reynolds number $y^+$ defined as:

$$y^+ = \frac{y u_\tau}{\nu}. \tag{5.5}$$

Therefore, $y^+$ values govern the wall shear stress and ultimately drive the flow in the boundary layer region. Such values are computed for the four simulations and shown on the swirler vanes and hub in Fig. 5.7 (the WALE case is not shown since equivalent to the medium mesh case). One can observe at first sight a sudden drop of the $y^+$ values between the medium and fine meshes. While the contours on the vanes indicate $y^+$ levels around 80 for the medium and coarse meshes, these values do not exceed 30 to 40 for the fine mesh.

A more accurate comparison is given by a scatter plot of all $y^+$ values at midspan of the swirler (i.e. on both sides of the 30 vanes) shown in Fig. 5.8. This plot confirms that while all the simulations feature $y^+$ values ranging from 40 to 100, the fine mesh reduces this range to about 20-40. This drop of the $y^+$ values

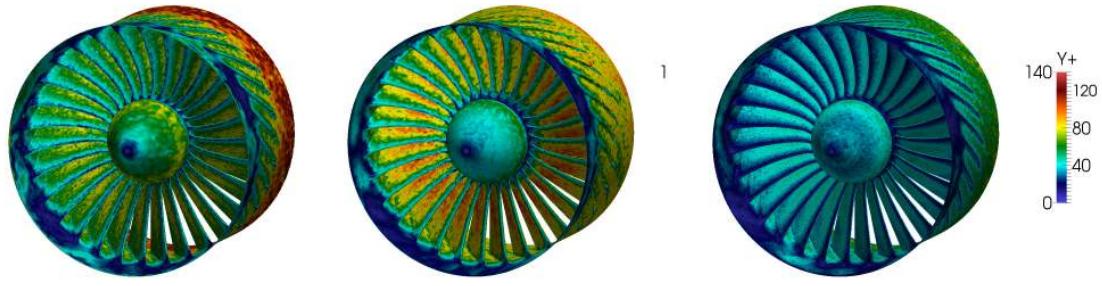


**(a)** Coarse. **(b)** Medium. **(c)** Fine.

**Figure 5.7:** Time-averaged values of $y^+$ in the swirler.

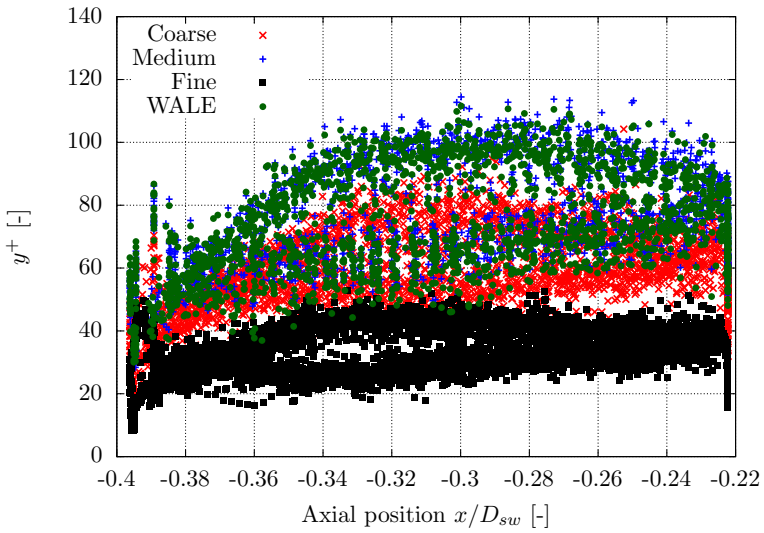


**Figure 5.8:** Scatter plot of $y^+$ at midspan of the swirler vanes.

caused by the better wall resolution is the main explanation to the substantially different flow regimes observed previously. Note that the coarse mesh provides $y^+$ values slightly lower than the ones obtained on the medium mesh because the cells on the vanes surface are a little smaller, even if there are less cells on the hub of the swirler (i.e. in the passage).

Having now the knowledge of the different predictions of the velocity and turbulence inside the swirler, one may wonder how the results of the four simulations differ inside the chamber and in the exit of the combustor.

### 5.3.2 Flow field in the chamber

First, time-averaged contours of the axial velocity component are shown in Fig. 5.9 at two angular positions inside the CS (central plane and periodicity plane). The results indicate that small differences exist between the four cases: *(i)* the jet exiting the swirler has a smaller radial opening for the fine mesh (to be linked to the radial velocity profile in Fig. 5.4); *(ii)* for the WALE case the radial opening of the swirler jet is constrained by a larger CRZ in the upper corner; *(iii)* the CTRZ of the fine mesh simulation is thinner at the inlet of the CS and expands afterwards.

Finally, contours of resolved turbulent kinetic energy are shown in Fig. 5.10 at the same azimuthal positions in the CS. The results indicate that the global patterns of $k_{res}$ are very similar in all cases except the fine mesh which differs on various points. First, one observes the presence of an annular region of higher $k_{res}$ ($\times 4$ compared to the other cases) in the CTRZ just downstream of the swirler hub (see position A in Fig. 5.10c). The coarse and medium meshes are probably not sufficiently refined to properly capture the dynamics of this important shear zone where the flow exiting the swirler vanes ($\bar{V} \simeq 100$ m/s) comes in contact with the reverse flow ($\bar{V} \simeq$ 5-10 m/s). Second, the level of $k_{res}$ in the shear zone around the jet entering the CS (position B) is reduced for the fine mesh. Third, the turbulent kinetic energy in the periodicity plane (C) is also smaller for the fine mesh, possibly because of the lower radial expansion of the jet (see velocity profiles in Fig. 5.4). Overall, the SGS model (WALE or Smagorinsky) more marginally impacts the results as observed by comparing Figs. 5.10b and 5.10d.

The comparison of the four LES simulations highlights local non negligible differences in terms of mean flow field and turbulence levels. It is now proposed to compare these results to the experimental ones to ultimately define a computational best practice.

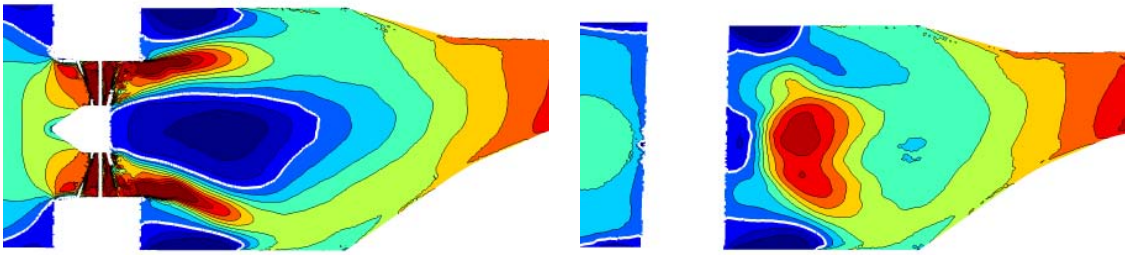

**(a)** Coarse.

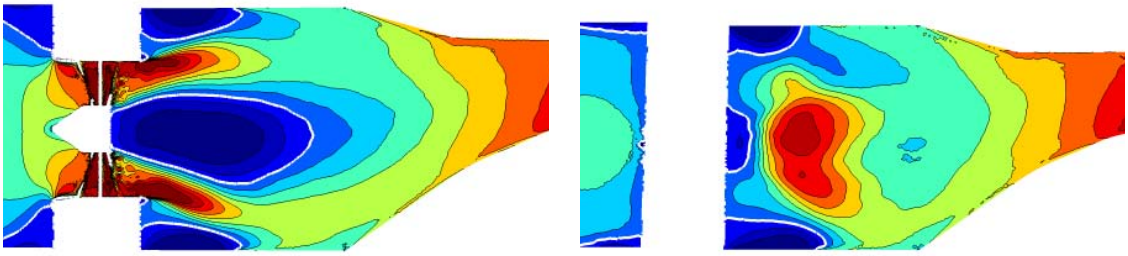

**(b)** Medium.

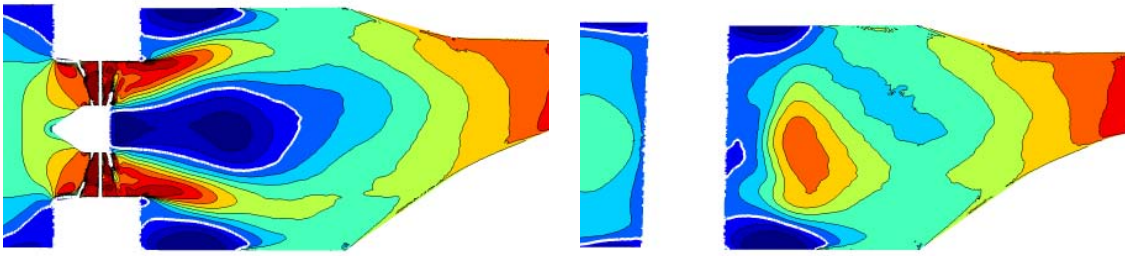

**(c)** Fine.

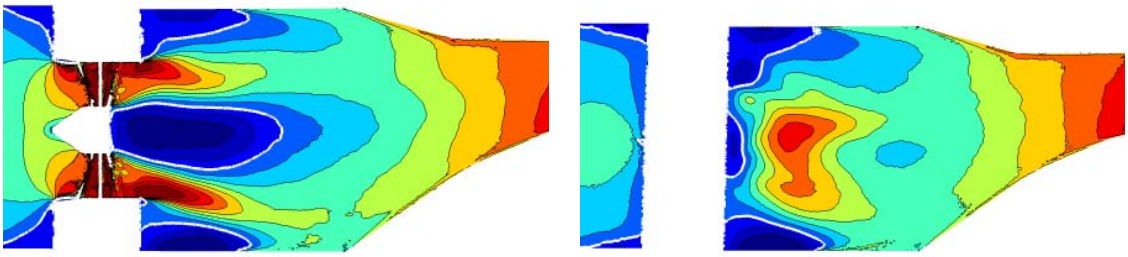

**(d)** WALE.

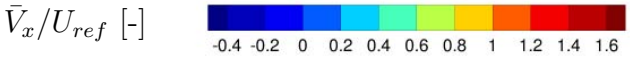


**Figure 5.9:** Time-averaged axial velocity in the central plane (left) and periodicity plane (right) and contours of the reverse flow zones (white line).

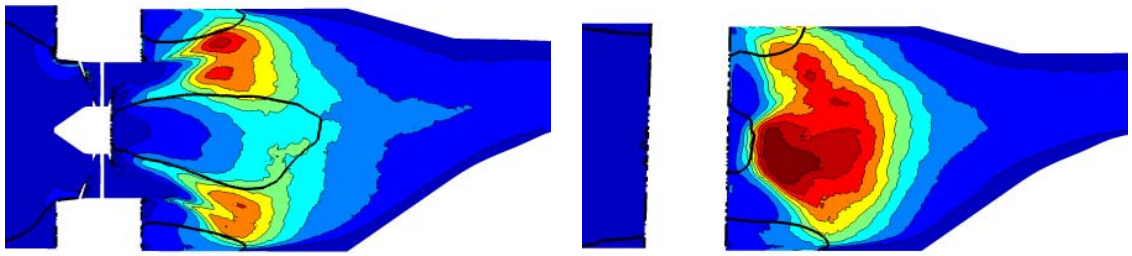

**(a)** Coarse.

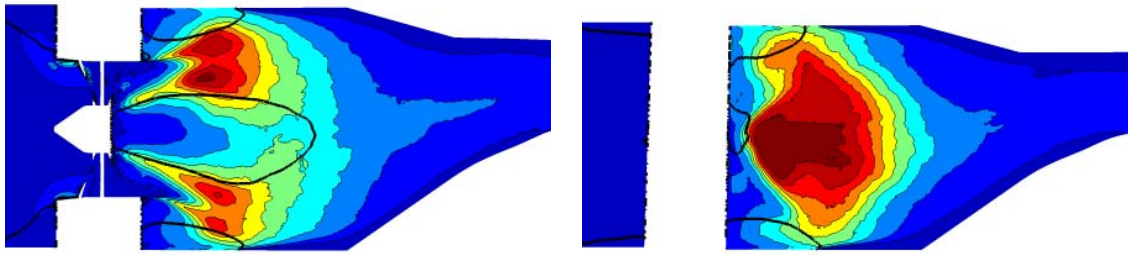

**(b)** Medium.

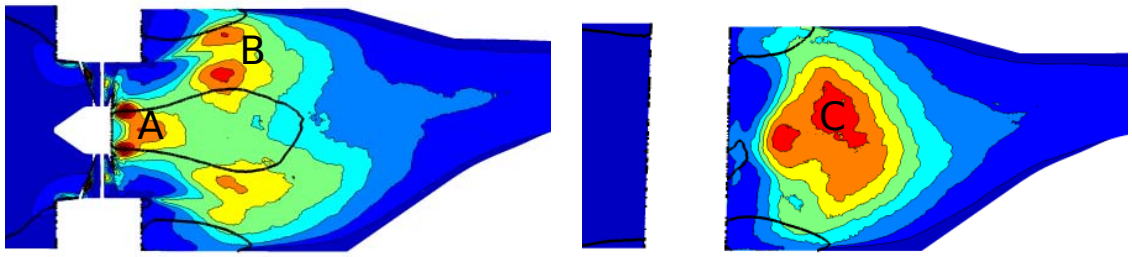


**(c)** Fine.

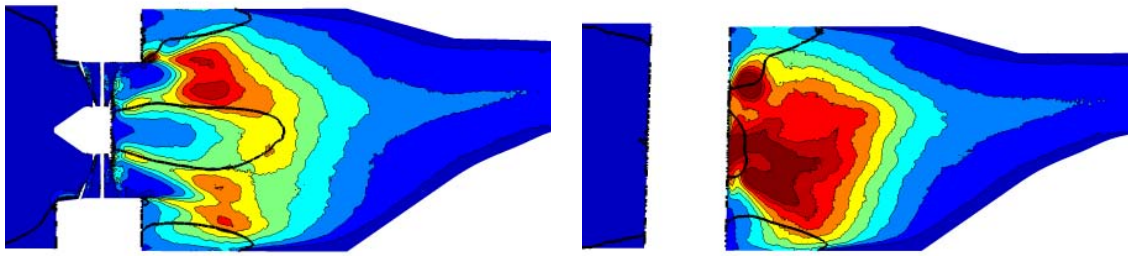

**(d)** WALE.

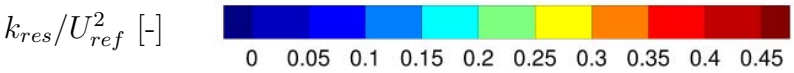


**Figure 5.10:** Resolved turbulent kinetic energy in the central plane (left) and periodicity plane (right) and contours of the reverse flow zones (black line).

## 5.4 Comparison with experimental results

It is not intended here to provide a detailed and exhaustive comparison between numerics and experiments but instead to focus on the most important results[2]. LES predictions are hence first confronted to PIV results in the CS (Section 5.4.1) before focusing on the two major targets of the FACTOR CS: the swirl level and temperature distortion in plane 40 (Section 5.4.2).

These comparisons furthermore complement the previous set of comparisons (Chapter 4) dedicated to the effect of the confinement duct introduced for the design phase of the FACTOR CS. Here, only the D00 (no duct) case is detailed for which an exhaustive set of measurements is obtained (see Table 3.4) at both isothermal and non-isothermal conditions.

### 5.4.1 PIV results in the central plane

Based on the conclusions of Section 4.1, the PIV measurements obtained at the IOP are now compared to the results of the simulations performed at the DP. The axial and radial velocity components in the central plane of the CS are extracted at four axial stations whose positions are given in Fig. 5.11 and plotted in Fig. 5.12. The profiles indicate that at all axial stations the fine mesh provides the best results both in terms of magnitude and position of the peak (corresponding to trace of the jet). Note also that in agreement with previous observations, close to the swirler exit ($x/D_{sw} = 0.2$) all the simulations except the fine case overpredict the maximum axial velocity by about 35%. A consequence is that further downstream ($x/D_{sw} \geq 0.4$), the medium and coarse cases provide a less accurate prediction of the position of the peak. It is worth noting that the WALE case improves the comparison with PIV and clearly distinguishes from the simulation performed on the same mesh (medium) with the Smagorinsky model (this is especially true for the radial velocity).

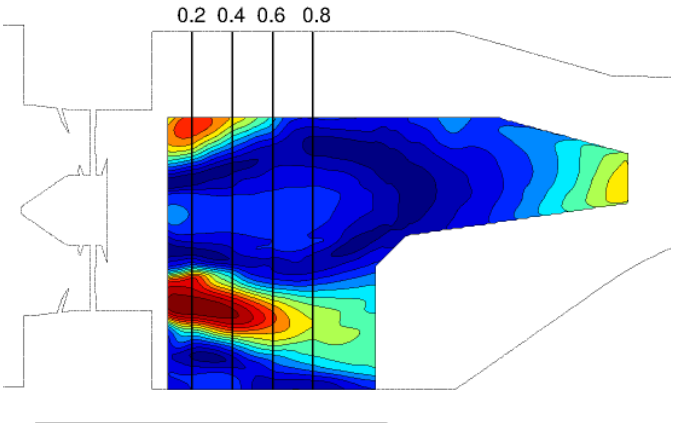


**Figure 5.11:** Position of the axial stations used for postprocessing (PIV result of the D00 case).

[2]If necessary, full results are available in Appendix B.

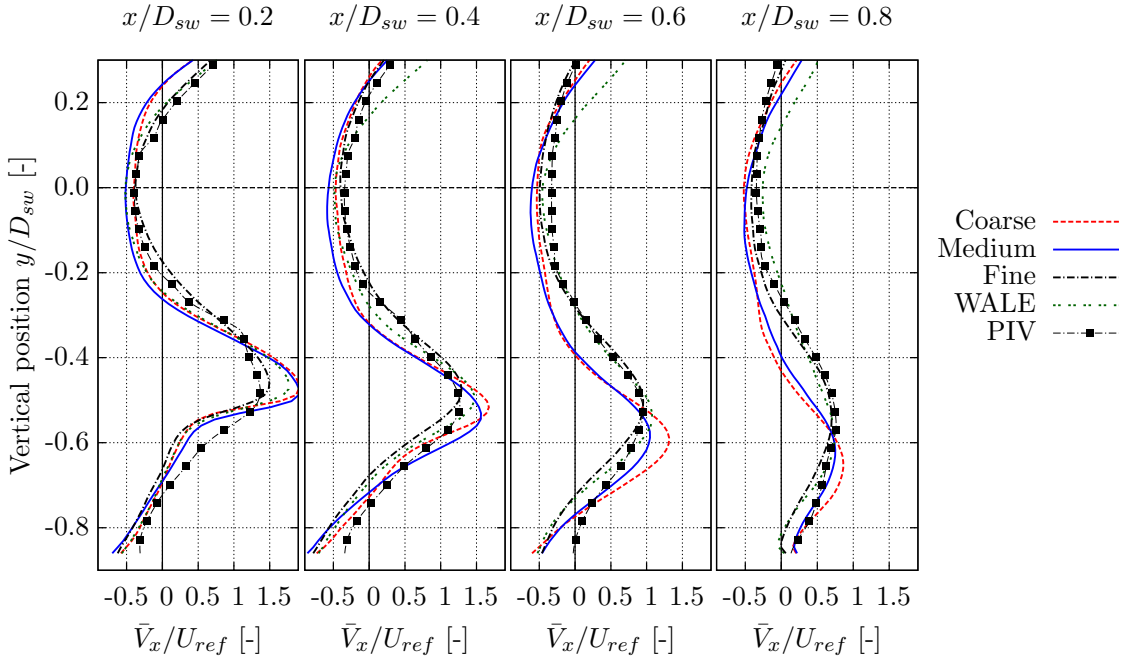


**(a)** Axial velocity.

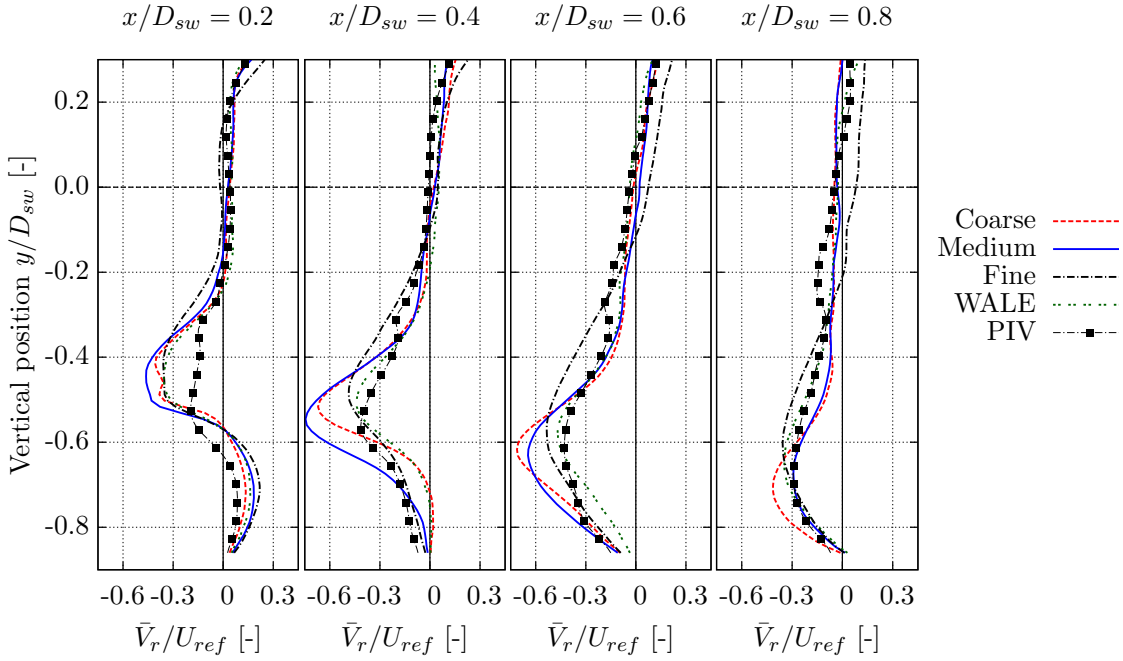


**(b)** Radial velocity.

**Figure 5.12:** Vertical profiles of the time-averaged velocity components for the D00 case.

### 5.4.2 Swirl and temperature distortion in plane 40

The contours of swirl angle obtained by means of 5HP measurements and LES predictions are shown first in Fig. 5.13. It immediately appears that the LES on the fine mesh qualitatively compares better with the 5HP results. Indeed, although most simulations predict a pure shear flow, the fine mesh results show a more nucleic shape and even captures part of the HS migration towards the right side. The circumferentially-averaged profiles of swirl angle shown in Fig. 5.14 indicate that none of the simulations really improves the results in the lower part. This supports the hypothesis formulated in Chapter 4 that such discrepancies are due to the modelling of the effusion cooling. Despite this difference, the simulations are in reasonnably good agreement with the measurements especially in light of the capacity of industrial CFD solutions.

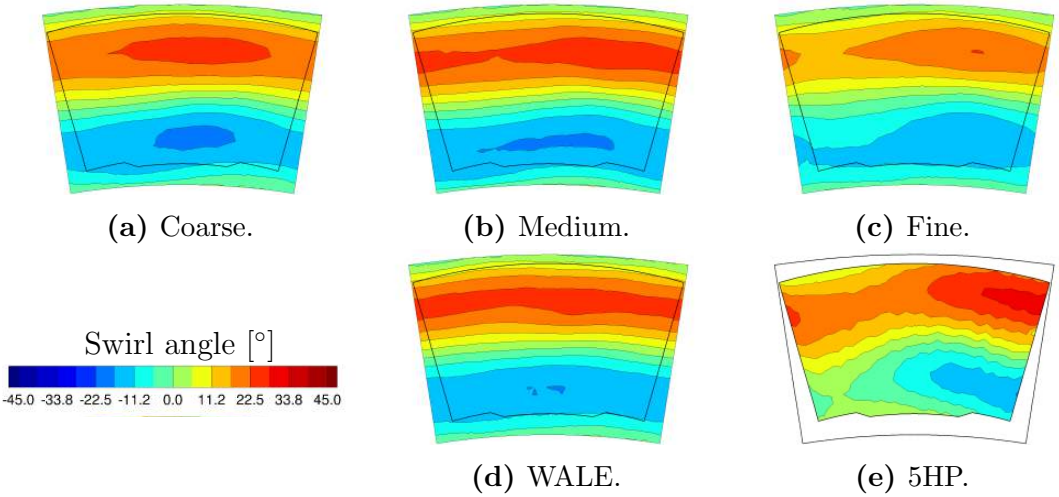


**(a)** Coarse. **(b)** Medium. **(c)** Fine.

**(d)** WALE. **(e)** 5HP.

**Figure 5.13:** Swirl angle in plane 40 from 5HP measurements and LES of the D00 case (looking downstream).

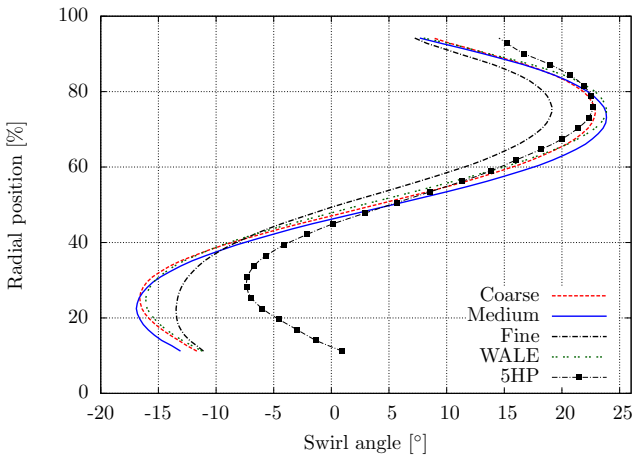


**Figure 5.14:** Circumferentially averaged profile of swirl angle in plane 40 for the D00 case.

The fields of temperature measured by the THCPL and obtained by LES are now compared in Fig. 5.15 by use of the coefficient $\Xi$ previously defined in Eq. (4.1). At first sight, all the simulations seem to provide similar results even if once again the LES on the fine mesh predicts more azimuthal heterogeneities. Note also that even if the comparison with the experiment is partially biased by the non-periodicity of the trisector rig configuration (see Chapter 4), good agreement is observed for all cases. This is confirmed by the corresponding circumferentially-averaged profiles shown in Fig. 5.16. One can also notice that the fine mesh provides a slightly better prediction especially at mid-height (position of the peak).

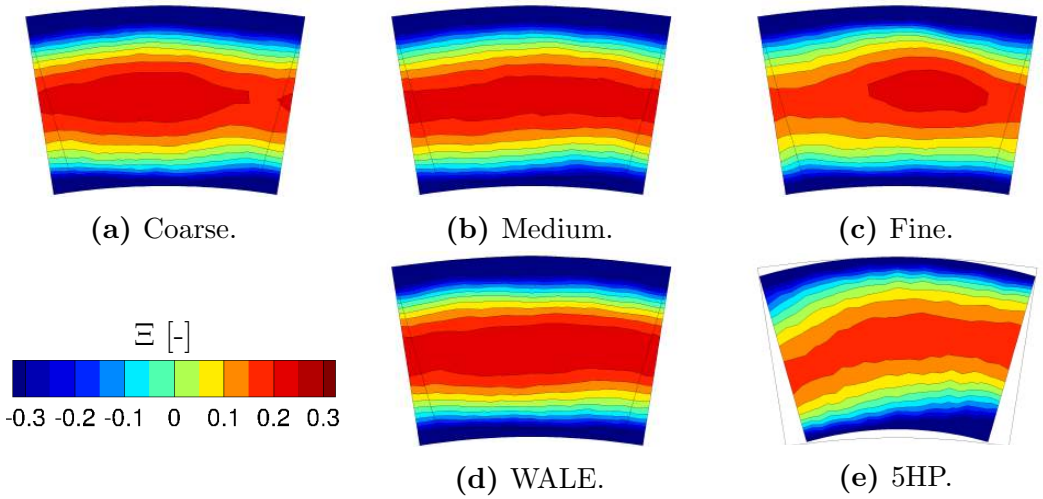


**(a)** Coarse. **(b)** Medium. **(c)** Fine.

**(d)** WALE. **(e)** 5HP.

**Figure 5.15:** Non-dimensional temperature coefficient in plane 40 from THCPL measurements and LES of the D00 case (looking downstream).

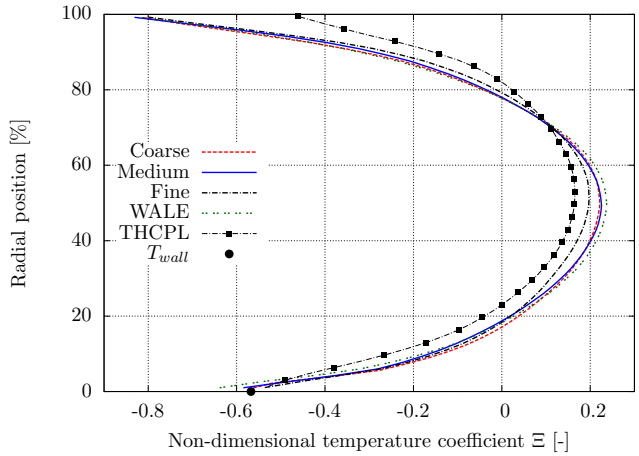


**Figure 5.16:** Circumferentially averaged profile of the temperature coefficient in plane 40 for the D00 case.

## 5.5 Conclusions

The conclusions gathered from the numerical sensitivity analysis complemented by the direct confrontation of predictions with the measurements are reported here:

- The quality indices indicate that overall the turbulence is well resolved in the CS and limited levels of turbulent viscosity are observed in the zones of interest. The fine mesh in particular allows to resolve at least 90% of the turbulent kinetic energy in the domain (except the inlet plenum).
- The analysis of the flow inside the swirler (velocity profiles and turbulence level) indicates that there is a threshold effect between the fine mesh and the two other ones.
  - This threshold effect can be related to the near wall resolution (via the $y^+$ values) which is confirmed by the different levels of quality indices observed in the swirler region.
  - The better resolution of the flow obtained with the fine mesh inside the swirler leads to different distributions of velocity and turbulence in the CS which in turn improve the prediction of the flow field as suggested by the comparison with the experimental results in plane 40.
- Overall the LES are found to be sensitive first to the mesh size and then to the SGS model. This last contribution is however reduced if a sufficiently fine mesh is used.
- In light of unpublished results[3] obtained by common RANS industrial tools, the LES results presented here definitely constitute an improvement of the current methodology. The sensitivity analysis detailed here also highlights that if a certain care is given to any LES set-up, the comparison with experimental results may be significantly improved.

The LES ability to properly resolve the flow in the CS being proven and bounded by the different reported analyses and comparisons, the results may be further exploited to gain a better knowledge of the flow. It is therefore proposed to complement the classical analyses of the experimental and numerical results by proposing advanced diagnostics in Chapters 6 and 7.

[3]Non-disseminated RANS and unsteady RANS simulations performed by different partners of the FACTOR consortium.

# Chapter 6

# Advanced diagnostics for the numerical and experimental turbulence characterization

## Contents


6.1 Configurations under study and available data . . . . . **124**

6.2 Turbulence intensity in plane 40 . . . . . **125**

6.2.1 Assessment of the convergence . . . . . 125

6.2.2 Comparison between experiments and LES . . . . . 126

6.3 Evaluation of an integral scale of turbulence . . . . . **129**

6.3.1 Methodology . . . . . 129

6.3.2 Sensitivity to the measurement parameters . . . . . 132

6.3.3 Comparison between experiments and LES . . . . . 136

6.4 Conclusions . . . . . **139**


It is intended in this chapter to characterize the turbulence in plane 40 based both on experiments and numerics. Such analysis is of primary importance as feeding the turbine with a well known and engine-representative turbulence is one of the ambitious and innovative aspects of the FACTOR project in contrast to the other test rigs.

Section 6.1 proposes a brief summary of the operating conditions and geometries under study for this analysis. In Section 6.2, the turbulence intensity is evaluated at the exit of the CS by means of HWA measurements which are then compared to the LES predictions. Then, it is proposed in Section 6.3 to evaluate an integral scale of this turbulence based on the experimental and numerical signals. Finally, general conclusions are given in Section 6.4.

## 6.1 Configurations under study and available data

Since it was observed in Chapter 2 that the duct confinement leads to large changes in the flow topology, it is proposed here to characterize the turbulence quantities in plane 40 for the D55 and the D00 cases. For the latter case, only the LES performed on the finest mesh is considered as it was found in Chapter 5 to provide the best results. The characteristics of the two simulations under study are recalled in Table 6.1. The experimental counterpart is provided by the HWA measurements performed at isothermal conditions for the two duct lengths as indicated previously in Table 3.4.

| Duct | Operating point | Mesh nodes | Mesh cells | Scheme | SGS model | Physical time [ms] | Timestep [s] |
|---|---|---|---|---|---|---|---|
| D00 | DP | 12.2M | 68.5M | TTGC | Smagorinsky | 155 | $3.7 \cdot 10^{-8}$ |
| D55 | DP | 8.9M | 51.0M | TTGC | Smagorinsky | 144 | $4.3 \cdot 10^{-8}$ |

**Table 6.1:** Summary of the LES of the FACTOR CS used for the characterization of turbulence.

Before performing any comparison between LES and HWA results, one needs to recall the differences between the two approaches which are of two kinds:

**The operating conditions** HWA measurements at isothermal conditions (IOP) are confronted to non-isothermal (DP) simulations. As indicated in Section 3.2, the change of operating conditions impacts the swirler Reynolds number which is known to be a governing factor for turbulence. Even if the simulations performed at both operating conditions (see Section 3.2.3) indicate that no major change is to expect, any comparison is subject to caution.

**The available physical time** One of the key differences between LES and HWA is the total duration of the signal. Indeed, for HWA the instantaneous signal of each velocity component is recorded during 5 s at 20 kHz successively for all the investigated points. For LES, successive instantaneous solutions are stored at a given frequency all over the duration of the simulation which is limited to few hundred milliseconds because of CPU cost. Such differences (summarized in Table 6.2) may introduce a bias that will need to be investigated.

| | Duration $\Delta t$ [s] | Acq. Frequency $f$ [Hz] |
|---|---|---|
| HWA (all ducts) | 5.0 | 20 000 |
| LES D00 | 0.112 | 9 785 |
| LES D55 | 0.140 | 20 000 |

**Table 6.2:** Characteristics of the HWA and LES data.

It is now proposed to evaluate the turbulence intensity in Section 6.2 and an integral scale of turbulence in Section 6.3 based on both experimental and numerical results. Such diagnostics are performed keeping in mind the intrinsic differences between the two approaches whose influences will be discussed in details.

## 6.2 Turbulence intensity in plane 40

For both experimental and numerical results, the turbulence intensity is evaluated from Eq. (3.12) using the mean and RMS values of the three components of velocity. For HWA, such data is provided by recording the instantaneous signal of each velocity component successively for all the 281 measurement points in plane 40 (see Table 6.2 for values). For LES the equivalent is reconstructed from a set of successive instantaneous solutions (respectively 1100 and 2791 solutions for the D00 and D55 case, see Table 6.2). A first possible source of discrepancies between the numerical and experimental approaches is obviously the limited duration of the LES as compared to the HWA signal which is about 35 times longer. This difference may affect the convergence of the calculation of the RMS values and thus impact the turbulence intensity level. This hypothesis is investigated in Section 6.2.1 before comparing HWA and LES results in Section 6.2.2.

### 6.2.1 Assessment of the convergence

The convergence of the calculation of the RMS values (and thus directly $TU$) is assessed by monitoring the RMS value of the axial velocity computed on signals of increasing duration. Such curves are computed for all the points in plane 40 (281 measurements points and 4000+ mesh nodes). For each point, normalization is obtained by the final value for the entire case and evolutions are plotted in Fig. 6.1 illustrating a convergence envelope. First, one observes that the convergence of the RMS values is much longer for the experimental data, possibly because of recorded noise or the flow higher frequency and energetic content. Such a difference if compared to LES seems natural since only the large scale and more correlated information of the flow are targeted by such approaches. Despite such differences in timescales potentially present between the two approaches, this diagnostic confirms that using the total duration of the signals yields RMS values converged within $\pm$ 5% of the final value of both cases. Note nonetheless that the LES case still shows about 3 to 4% variations at the end of the simulation, which directly translates into a known uncertainty on the turbulence intensity.

Having knowledge of the bias introduced by the convergence of the RMS values, it is now proposed to compare the HWA and LES results in terms of the turbulence intensity.

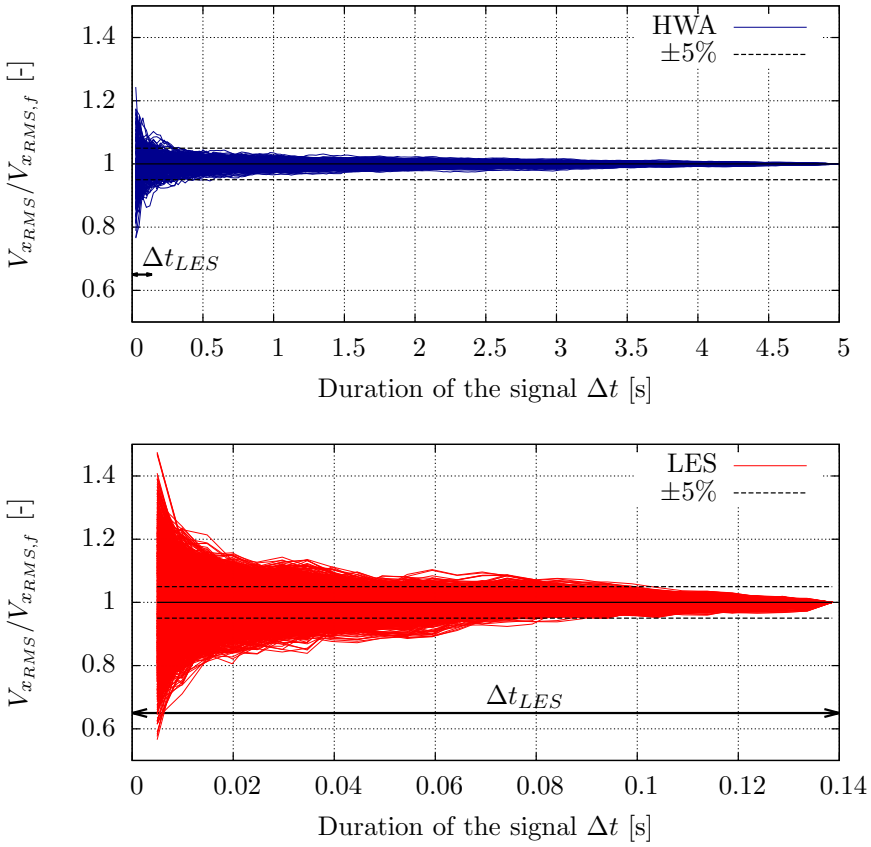


**Figure 6.1:** Convergence of the RMS values of the axial velocity signal in plane 40 (D55 case) for HWA (top) and LES (bottom).

### 6.2.2 Comparison between experiments and LES

The HWA set-up used for this turbulence characterization is known to introduce uncertainties at many levels: sensitive calibration process, bad behaviour of the probes for large flow angles, reconstruction of the three velocity components by projection etc. As a result, it has been estimated [26] that for this specific exercise on the FACTOR CS, $TU$ is estimated with an uncertainty of about 12% with a 95% confidence. To get rid of the impact of such uncertainty on the absolute level of turbulence intensity, it is proposed in the following to compare LES and HWA based on relative fields, i.e. $TU/\overline{TU}_{40}$ where $\overline{TU}_{40}$ is the mean value of $TU$ on the experimental region. Such values are reported in Table 6.3 for all the cases (the LES results are projected onto the experimental region) and the uncertainty interval is reported for HWA measurements. The experimental measurements indicate that overall the level of $TU$ is comparable in both cases with a mean value of $TU$ between 18 and 19%. As compared to the HWA values, the LES prediction is about 27% higher for the D00 case and 51% for the ducted case. Such numerical predictions are of course influenced by the mesh density, the SGS model and possibly the modelling of the effusion cooling as suggested by the analysis of the simulations in Chapter 5. These parameters which are not discussed here,

added to the uncertainty on the experimental measure of $TU$ and the change of operating conditions between LES and HWA allow to put in perspective the analysis of such values.

| | Case | $\overline{TU}_{40}$ [-] | $\frac{\overline{TU}_{40}}{\overline{TU}_{40,HWA}}$ [-] |
|---|---|---|---|
| D00 | HWA | 0.191 ±0.023 | 1 ±0.12 |
| | LES | 0.242 | 1.27 |
| D55 | HWA | 0.184 ±0.022 | 1 ±0.12 |
| | LES | 0.278 | 1.51 |

**Table 6.3:** Spatially-averaged value of turbulence intensity on the investigation region.

Keeping in mind the absolute level of turbulence intensity, the contours of relative $TU$ in plane 40 are shown in Fig. 6.2 while the radial profiles on the centerline (without any averaging operation) are shown in Fig. 6.3. If the overall level of $TU$ is comparable in both cases (recall Table 6.3), turbulence is not similarly distributed. While the ducted case features a high turbulence core, the unducted case shows less azimuthal heterogeneities and a lower maximum value. For the ducted case, the ratio of the minimum to the maximum turbulence intensity in plane 40 is about 2.2 which indicates that in addition to a high level of $TU$, significant turbulence non-uniformities are present at the inlet of the turbine. This observation is in line with the FACTOR requirement for a realistic turbulence intensity at the turbine inlet (i.e. not artificially generated by grids).

Regarding the comparison with LES, the simulations capture very well the change of pattern between the ducted and unducted cases as well as the associated increase of maximum $TU$. The profile of $TU$ on the centerline plotted in Fig. 6.3 shows the excellent agreement between LES and HWA. Furthermore and if compared to previously reported results [75] of similar comparisons relying on LES but for a different geometry, FACTOR results are of particularly good quality.

In light of these encouraging results, it is now proposed to estimate an integral scale of turbulence at the inlet of the turbine. The evaluation of two turbulence quantities is indeed usually required to properly characterize turbulence boundary conditions for turbine flow computations.

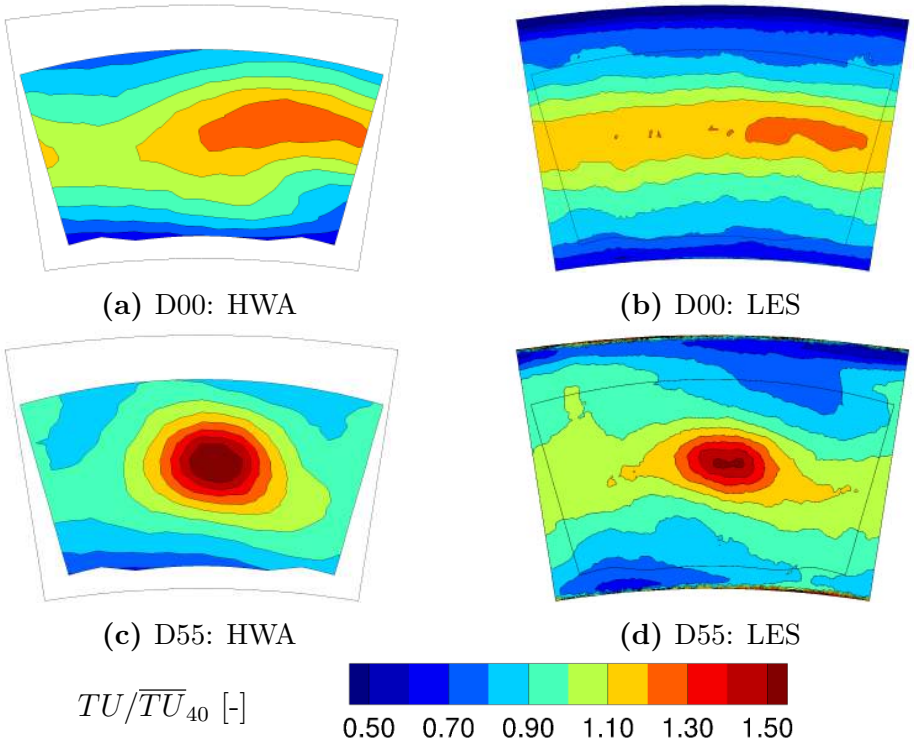


**Figure 6.2:** Relative Turbulence intensity in plane 40 (looking downstream).

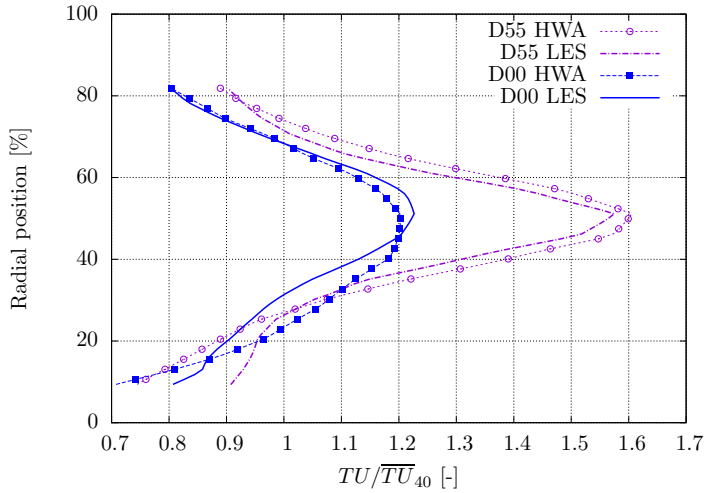


**Figure 6.3:** Profile of relative turbulence intensity on the centerline of plane 40.

## 6.3 Evaluation of an integral scale of turbulence

Evaluating an integral scale of turbulence in a realistic configuration is a challenging task because of the nature of this quantity. Indeed, although critical in terms of fundamental and engineering understanding of turbulent flows, such a quantity is a purely mathematical tool and cannot be measured directly from a flow solution or realization. Manipulation of the data in a statistical context is indeed required. These operations induce the use of advanced postprocessing tools and signal analysis techniques strongly impacting the evaluations. Furthermore and although commonly introduced in the context of turbulence, turbulent integral scales may follow different definitions. It is therefore required first to clearly introduce the notion of turbulent timescale and the computation methodology used here (Section 6.3.1). Then, Section 6.3.2 provides elements on the way to properly compare estimations of turbulent timescales provided by two very different approaches: HWA and LES, each one with its own limitations and signal characteristics. Finally, the ability of LES to predict the turbulent timescales in plane 40 is assessed in Section 6.3.3 by comparison with the HWA results.

### 6.3.1 Methodology

The methodology employed to evaluate the integral scale of turbulence relies on the statistical treatment of the instantaneous signal of velocity for each point under investigation (i.e. all the HWA measurement points and all the CFD nodes for LES). Such exercise is proposed here only for the axial component of velocity but it is applicable to any other component. At each point the instantaneous axial velocity $V_x$ is decomposed into a mean $\bar{V}_x$ and a fluctuating part $V'_x$:

$$V_x = \bar{V}_x + V'_x. \tag{6.1}$$

The root mean square value of $V_x$ is then computed from this discretized velocity data. The autocorrelation coefficient $R_{V_xV_x}$ of the fluctuating part of the axial velocity can also be as a function of a time-lag $\tau$ of the signal. Such a function can then by non-dimensionalized by $V^2_{x,RMS}$ to have $R_{V_xV_x} = 1$ for zero-lag ($\tau = 0$) and to yield:

$$R_{V_xV_x}(\tau) = \frac{\overline{V'_x(t)V'_x(t+\tau)}}{V^2_{x,RMS}} = \frac{\frac{1}{N}\sum_{i=1}^{N}(V'_{x_i} \cdot V'_{x_{i+j}})}{V^2_{x,RMS}} \tag{6.2}$$

where $j = \tau/dt$ gives the discrete possible values of time-lag based on the acquisition timestep $dt = 1/f$. A typical evolution of $R_{V_xV_x}(\tau)$ for the axial velocity signal recorded in a LES is shown in Fig. 6.4.

In the case of fully statistically stationary turbulent flows, the integral turbulent timescale $t_{turb}$ is typically obtained [13, 14] by integrating under the $R_{V_xV_x}$ curve:

$$t_{turb} = \int_{\tau=0}^{\infty} R_{V_xV_x}(\tau)\ d\tau \tag{6.3}$$

Note that mathematically, Eq. (6.3) is well posed if and only if $R_{V_xV_x}$ is well behaved and its integral does exist. This in itself is a strong assumption and precludes from using purely oscillating signals. Likewise and because of the finiteness of any simulation or experimental data notions of convergence, sapling and data processing are required to ensure a relevant estimation of $t_{turb}$. All of these issues really complicate the context and specific care is needed to ensure meaningful comparisons.

In the specific context of FACTOR CS, the direct application of Eq. (6.3) can be problematic as $R_{V_xV_x}$ does not necessarily go to zero as $\tau \to \infty$ because of the strong flow spatial heterogeneities and the turbulent anisotropy. An alternate proposal to evaluate the integral timescale is thus preferred: $t_{turb}$ will be evaluated by integrating under the $R_{V_xV_x}$ curve until an arbitrary value of $R_{V_xV_x}$ above which the signal is not considered correlated anymore [130, 131]. Such methodology is illustrated by the hashed zone in Fig. 6.4 if using $R_{V_xV_x} = 0.5$ as threshold value. This calculation process is then repeated for each investigation point in plane 40 in order to obtain a full 2-D map of the turbulent timescale.

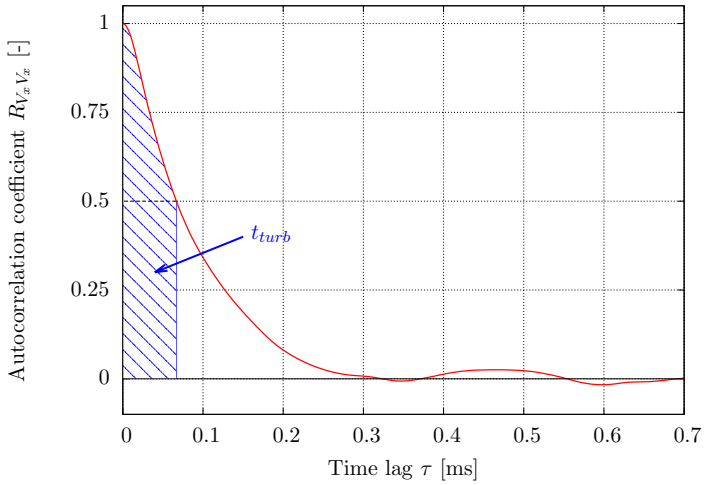


**Figure 6.4:** Typical autocorrelation coefficient of the axial velocity signal (obtained from LES).

To assess the impact of the arbitrary $R_{V_xV_x}$ threshold used for evaluating $t_{turb}$, the turbulent timescale is computed from the HWA signal of the D55 case in plane 40 using clipping values ranging from $R_{V_xV_x} = 0$ (not correlated) to $R_{V_xV_x} = 0.95$. The evolution of the spatially-averaged turbulent timescale is then plotted against the different threshold values in Fig. 6.5. The threshold value has an important impact on the evaluation of $t_{turb}$ as the smallest value (obtained for $R_{V_xV_x} = 0.95$) is twelve times smaller than the largest one (obtained for $R_{V_xV_x} = 0$). If the magnitude of $t_{turb}$ is strongly impacted, its distribution all over plane 40 is not altered. This is evidenced by the corresponding maps of $t_{turb}$ shown in Fig. 6.6 for four clipping values ranging from $R_{V_xV_x} = 0$ to $R_{V_xV_x} = 0.7$. Regardless of the threshold value, a similar pattern is observed with a well-defined core region featuring higher values of $t_{turb}$. The magnitude of the turbulent timescale however

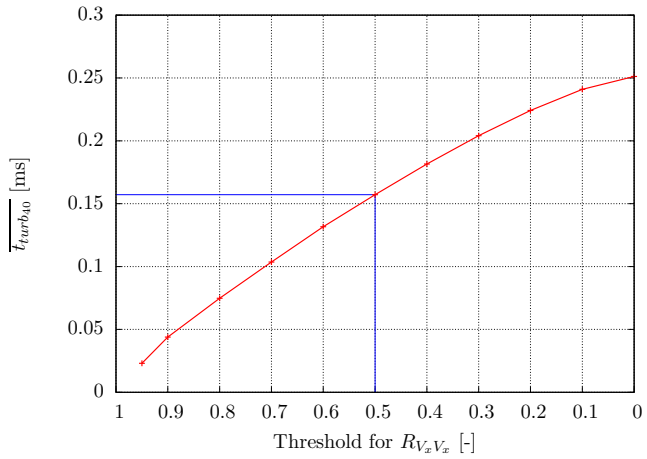


**Figure 6.5:** Influence of the threshold value for $R_{V_xV_x}$ on the evaluation of the spatial-mean turbulent timescale in plane 40 for the HWA signal of the D55 case.

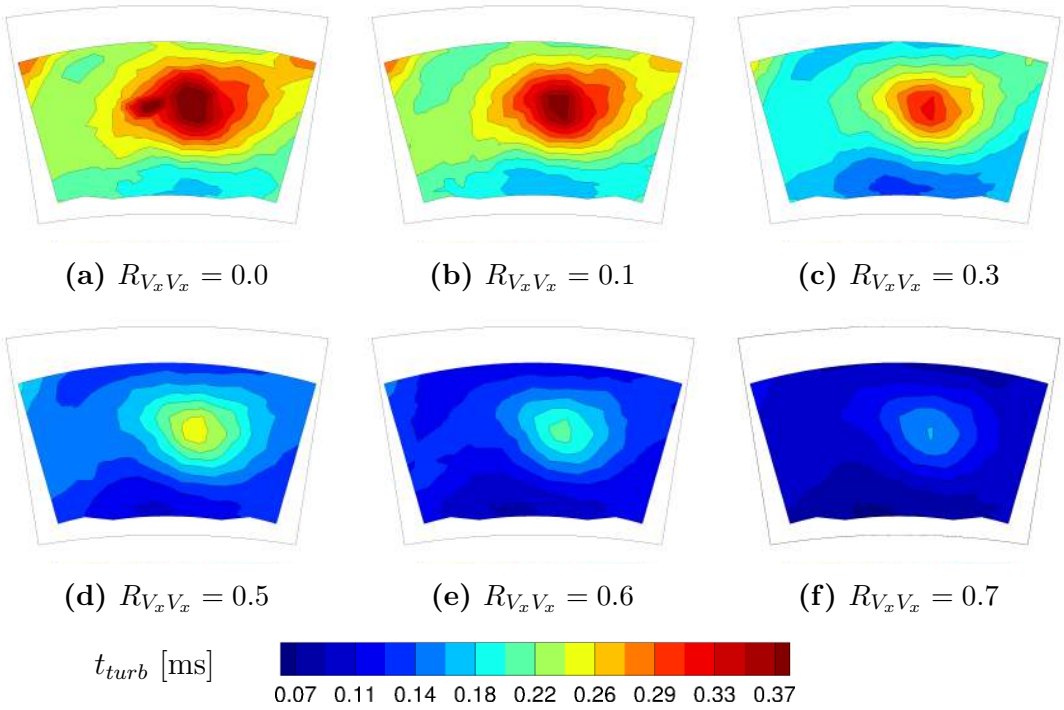


**(a)** $R_{V_xV_x} = 0.0$ **(b)** $R_{V_xV_x} = 0.1$ **(c)** $R_{V_xV_x} = 0.3$

**(d)** $R_{V_xV_x} = 0.5$ **(e)** $R_{V_xV_x} = 0.6$ **(f)** $R_{V_xV_x} = 0.7$

**Figure 6.6:** Influence of the threshold value for $R_{V_xV_x}$ on the evaluation of the turbulent timescale in plane 40 for the HWA signal of the D55 case (looking downstream).

falls very quickly when the threshold increases, especially for $R_{V_xV_x} > 0.3$. The arbitrary choice of a clipping value for $R_{V_xV_x}$ thus significantly impacts the level of the evaluated turbulent timescale and needs to be considered when analysing the results. However, in the optics of comparing numerics and experiments the most important point is to use the same methodology in both cases, regardless of the threshold value which is taken to $R_{V_xV_x} = 0.5$ in the following by analogy with previous studies [31, 132]. Note that when using this clipping value, the turbulent timescale is about 60% smaller than considering the first zero crossing as threshold.

Having defined and assessed a precise methodology for calculating $t_{turb}$, it should now be applied similarly to either HWA or LES data. However, each approach has its own specificities in terms of total duration of the recorded signal $\Delta t$ and associated acquisition frequency $f$ as presented earlier in Table 6.2. If the impact of the total duration on the convergence of the RMS values was found in Section 6.2.1 to be small, there is no guaranty that such result is transposable to the calculation process of $t_{turb}$. Therefore, before performing any comparison, one needs to estimate potential sources of bias introduced in the diagnostics because of these differences.

### 6.3.2 Sensitivity to the measurement parameters

In the following, it is intended to quantify the differences introduced by computing turbulent timescales on signals from different total duration and acquisition frequency. Note that all the analyses presented in this section are performed on the HWA signal because of its long duration (D55 case).

#### Acquisition frequency

The acquisition frequency impacts the evaluation of the turbulent timescale for at least two main reasons: *(i)* the exploitable content of the signal is limited by the Nyquist frequency $f/2$; *(ii)* $f$ limits the possible time-lags $\tau$ to be computed, as $\tau = j \times f$, which finally reduces the resolution of the curve $R_{V_xV_x}(\tau)$ and its accurate integration. To assess the influence of the acquisition frequency, the HWA signal is virtually degraded by taking one point over $N$ to reduce $f$. The turbulent timescale is then computed at each measurement point of plane 40, for four signals: $f = 20$ kHz (all points), $f = 10$ kHz (half the points), $f = 5$ khz (quarter of the points) and $f = 2$ khz (tenth of the points). Note that all four resulting signals have the same total duration $\Delta t = 5$ s but a reduced number of samples. The map of the computed turbulent timescales in plane 40 is shown in Fig. 6.7. The bounds of the central sector are shown in the background to highlight the limits of the investigation zone. The core region of plane 40 features a coherent zone of higher turbulent timescale (0.22-0.24 ms), which corresponds to the remnants of the swirling core. Higher levels of turbulence intensity are measured in this region (see Section 6.2). The timescales are more uniform in the rest of the field (around 0.12-0.16 ms) and seem to decrease in the near wall region (zone of the effusion cooling) which is not fully covered by the investigation window.

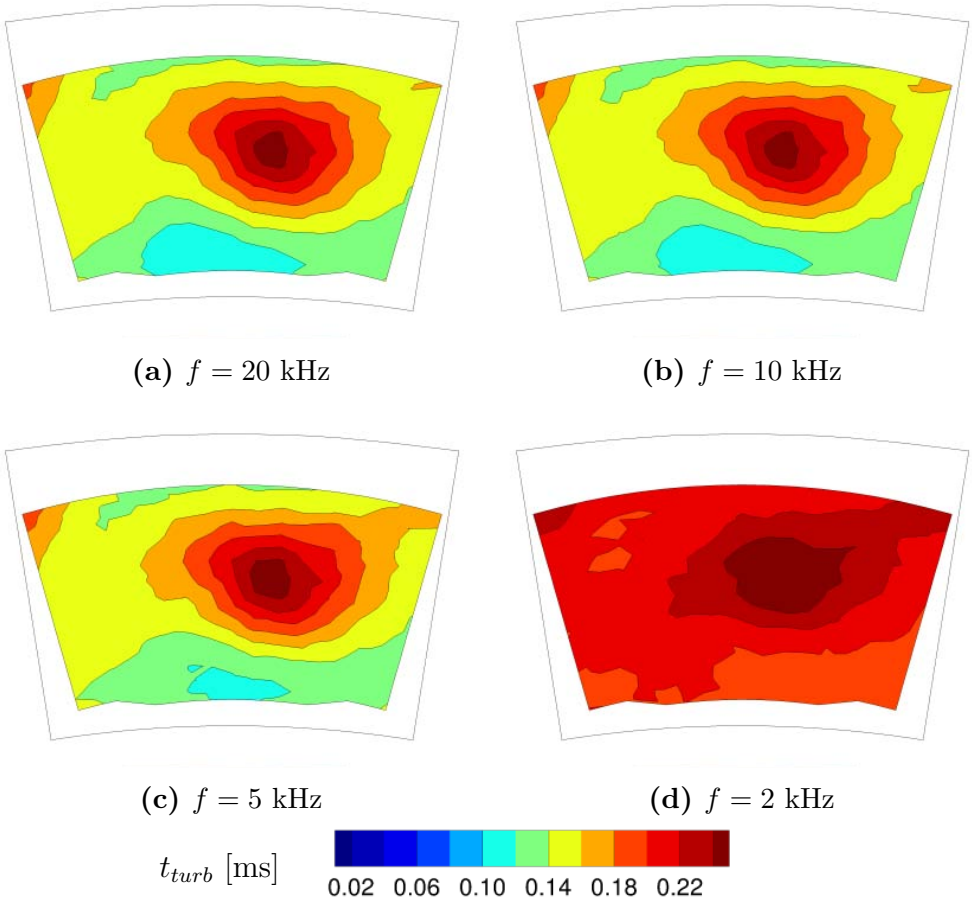


**Figure 6.7:** Impact of the acquisition frequency on the evaluation of the turbulent timescales in plane 40 for the HWA signal of the D55 case (looking downstream).

Regarding the influence of the acquisition frequency, the comparison of the four maps clearly shows that between 20 kHz and 5 kHz, $f$ is sufficiently high to allow a similar estimation of $t_{turb}$. Only moderate differences are found in the inner region for $f = 5$ kHz where the timescale is a little overestimated. This might be explained by an under-resolution of the $R_{V_xV_x}$ curve for low values of $\tau$. However, for $f = 2$ kHz the timescales are clearly overpredicted and this acquisition frequency is definitely too low to properly capture the turbulent activity.

In conclusion, the turbulent timescale estimates can be judged as perfectly converged for $f \geq 10$ kHz, although the analysis at 5 kHz is found to provide a very good estimate of the converged fields. This confirms that LES for the D00 case is sufficiently well sampled ($f = 9.7$ kHz, see Tab. 6.2) to avoid frequency-linked issues if $t_{turb}$ is to evaluated.

### Duration of the signal

**Convergence of the evaluation** The most important difference between the numerical and experimental signals is the total duration $\Delta t$, which is about 35 times longer for HWA than LES. Long signals allow for a better statistical representation of turbulence under the hypothesis of a stationary flow and for short duration signals, the accuracy of any evaluation of $t_{turb}$ can be questionable. To address this issue, $t_{turb}$ is computed over portions of the HWA signal of increasing duration: from $\Delta t = 50$ ms to $\Delta t = 5$ s. This process allows to assess the convergence of $t_{turb}$ with the duration of the signal and define (if possible) a minimum acceptable threshold for convergence. For clarity, the convergence curves of $t_{turb}(\Delta t)$ of all the 281 measurement points are normalized by the final value $t_{turb_f} = t_{turb}(\Delta t = 5$ s) and shown in Fig. 6.8 (for a sampling frequency of 20 kHz). The envelope of the convergence curve of $t_{turb}$ has a symmetrical exponential shape, converging towards $t_{turb_f}$. For short duration signals ($\Delta t < 0.25$ s), differences up to $\pm 35\%$ of the final value are found. To reduce this error below $\pm 2\%$, the curves have to be contained within the identified dashed lines, which occurs for much longer durations of the signal ($2 - 3$ s). This time can be related to the physics of the flow using the through flow time of the CS (noted hereafter $t_{CS}$) computed based on the nominal mass flow and CS length. This new scaling is indicated on the upper horizontal axis of Fig. 6.8 and at least 200 to 300 through flow times seem required for the targeted confidence range. Such long durations of the time signal can not be reached by LES: as an indication the duration of the available LES signal is underlined by an arrow in Fig. 6.8 and is around 12 through flow times. A detailed analysis of all the convergence curves indicates that for ten $t_{CS}$ none of the points has a converged value to $\pm 2\%$. Instead, errors on $t_{turb}$ can reach about $\pm 20\%$ and therefore can be found for LES signals because of such convergence issues.

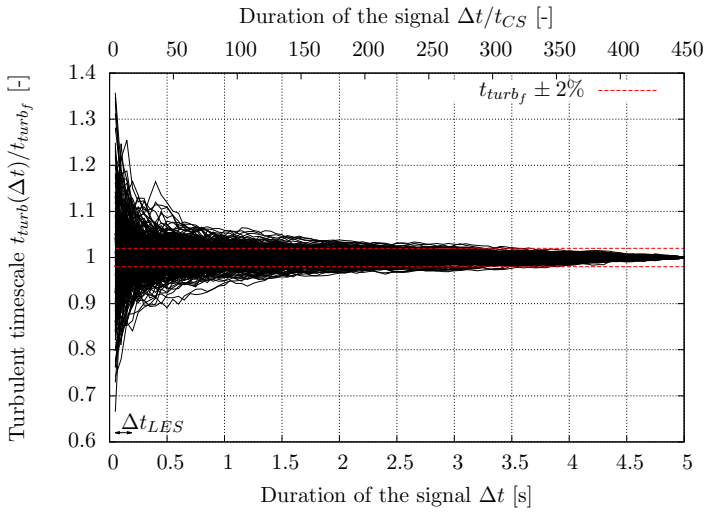


**Figure 6.8:** Convergence of the calculation of $t_{turb}$ in plane 40 with the duration of the signal for the HWA signal of the D55 case.

**Statistical properties of the signal** The problematic of the convergence of $t_{turb}$ for small duration signal is associated with the impossibility to recover all the high order statistical properties of the flow with few temporal samples. In this context —and despite convergence issues— one may ask what is the impact of evaluating turbulence over a single realization of the flow of reduced duration. In other words, quantifying how $t_{turb}$ changes when it is computed over windows of similar duration $\Delta t_{LES}$ taken at different initial times $t_0$.

To address this question, the turbulent timescale is computed over a typical LES window ($\Delta t_{LES}$) and applied as a restriction on the full HWA signal considering 138 different initial times $t_0$ and each corresponding window overlapping the previous one by $\Delta t_{LES}/4$. The evolution of $t_{turb}$ with the initial time of the investigation zone is shown in Fig. 6.9 for an arbitrary single measurement point. The turbulent timescale is normalized by the reference value $t_{turb_f}$ obtained out of the full HWA signal. Here, non-negligible variations around the mean value of $t_{turb_f}$ are visible, which translate here into a standard deviation $\sigma$ of 7.5% of $t_{turb_f}$. Moreover, in this specific case the maximum values reached by the over and under-predictions are respectively found to be +29% and −20% and are definitely significant deviations.

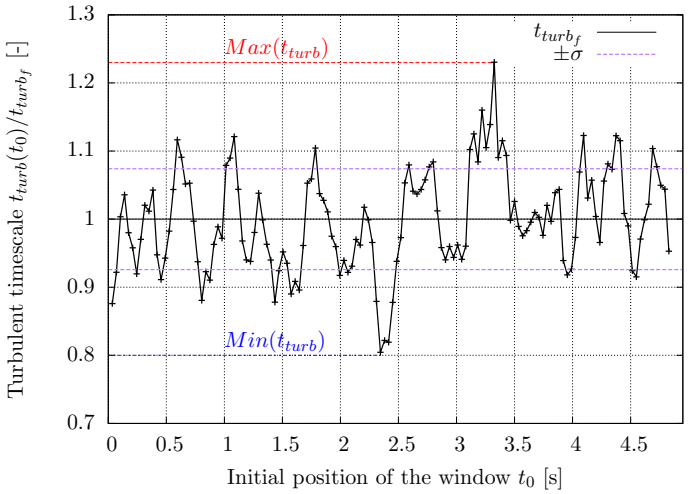


**Figure 6.9:** $t_{turb}$ calculated over the duration $\Delta t_{LES}$ taken at different initial times of the HWA signal for an arbitrary point in plane 40.

To have a more exhaustive understanding, this methodology is now applied to all the measurement points in plane 40. Figure 6.10 shows the maximum and minimum turbulent timescales calculated over the 138 windows, as well as the associated standard deviation $\sigma$. Even if the fields of Figs. 6.10b and 6.10c do not correspond to a single evaluation of $t_{turb}$ but to the concatenation of all the minima (or maxima), they indicate that significant differences can be found. More importantly, the standard deviation associated with the calculation of $t_{turb}$ over all the windows (Fig. 6.10a) is on average $\overline{\sigma}_{40} = 6.4\%$. The standard deviation is higher ($7 - 9\%$) in specific regions which are difficult to associate to distinct flow events or its organization (see Fig. 6.10c).

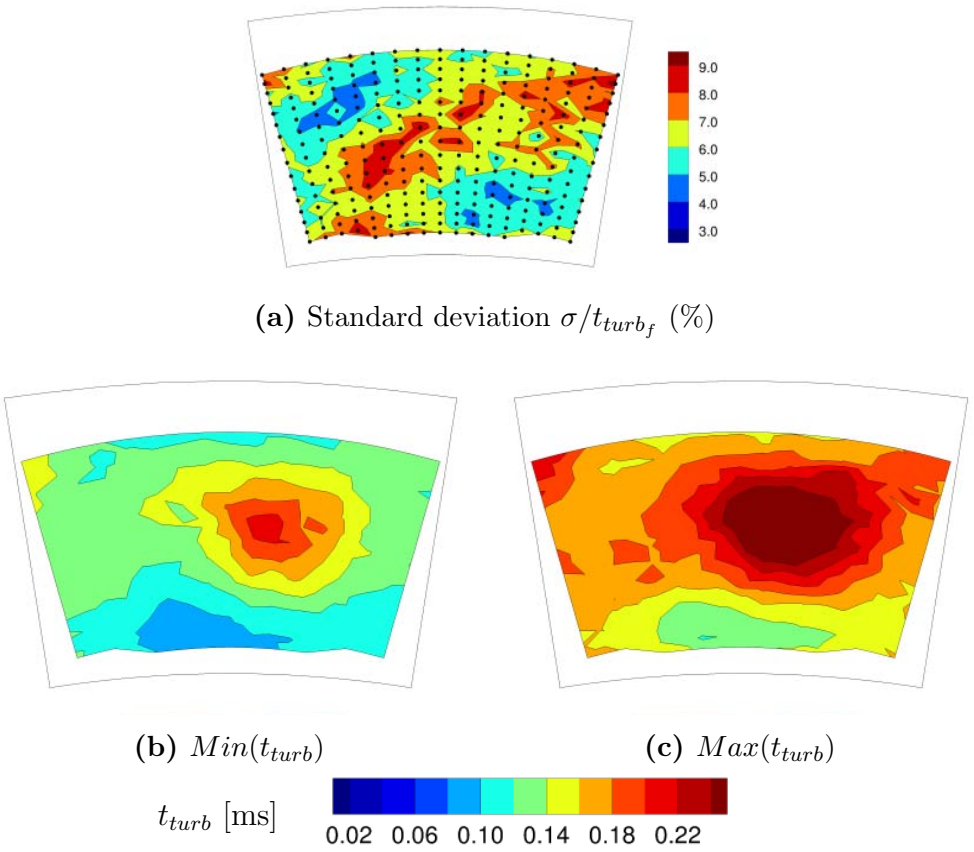


**(a)** Standard deviation $\sigma/t_{turb_f}$ (%)

**(b)** $Min(t_{turb})$ **(c)** $Max(t_{turb})$

**Figure 6.10:** Maximum and minimum difference and standard deviation of the calculation of $t_{turb}$ performed on 138 windows of duration $\Delta t_{LES}$ taken at various initial times $t_0$ of the HWA signal.

The different analyses presented here allow us to understand and estimate the inherent differences between the experimental and numerical signals. First, the acquisition frequency is found to allow good evaluations of $t_{turb}$ for $f > 5$ kHz, which validates the LES acquisition frequency of both D00 and D55 cases. Then, convergence and stationary issues associated with having short duration signals are pointed out. The differences are found to intrinsically imply an average deviation of $\pm 6.4\%$ and possible local errors of about $\pm 25\%$. Having now knowledge of these differences, the estimations of the turbulent timescales issued from the experimental data and LES predictions are now compared.

### 6.3.3 Comparison between experiments and LES

To properly compare the results obtained by HWA and LES at two distinct operating conditions, it is proposed to non-dimensionalize the fields of turbulent timescales by the mean value $\overline{t_{turb_{40}}}$ computed over the HWA investigation area and reported in Table 6.4. Such scaling allows to compare the distribution of $t_{turb}$ as well as the relative magnitudes independently from the operating condi-

tions. Note that this last point is not fully valid as evidenced by the discussions of Chapter 3 and as evidenced by the given references values in Table 6.4.

| | LES | HWA |
|---|---|---|
| D00 isothermal | 0.127 | 0.244 |
| D00 non-isothermal | 0.096 | - |
| D55 isothermal | - | 0.157 |
| D55 non-isothermal | 0.062 | - |

**Table 6.4:** Spatial mean turbulent timescales on the investigation region $\overline{t_{turb_{40}}}$ [ms].

Figure 6.11 shows the non-dimensional turbulent timescales evaluated in plane 40 by HWA[1] and LES for the D00 and D55 cases. The fields of turbulent timescales are very different for D00 and D55, both in terms of magnitude and distribution. The overall magnitude of $t_{turb}$ is larger for D00 than D55 as indicated by the spatial mean values in plane 40 $\overline{t_{turb_{40}}}$ reported in Table 6.4. If comparing experiments with the numerical prediction, it is worth noting that both HWA and LES give very similar estimates of the relative increase of $\overline{t_{turb_{40}}}$ between the D55 and D00 cases: respectively 58% and 54%. Therefore, even if the magnitude of the turbulent timescale is too large in LES, the simulations accurately predict its change of amplitude between the ducted and unducted configurations. In terms of spatial distribution, the pattern of $t_{turb}$ is strongly affected by the presence of the duct: the D55 case shows large timescales only in the swirling core region while $t_{turb}$ is more homogeneously distributed for the D00 case. Large discrepancies of $t_{turb}$ are observed throughout plane 40 depending on the chosen configuration: no less than $\pm 45\%$ of the mean value for the D55 case where variations reach $\pm 20\%$. In both cases, it is further noticed that the pattern of turbulent timescales is well predicted by LES. This is especially true for the D55 case for which a longer signal is available (see Table 6.2) and helps reducing convergence issues.

To provide a more quantitative comparison, turbulent timescale profiles are extracted at midspan and provided in Fig. 6.12a. The graph quantitatively confirms that the difference in distribution and magnitude between D55 and D00 is correctly captured by LES. Moreover, the maximum value of $t_{turb}$ for D55 is similarly found to locate at $\theta \simeq 2°$ and with the same amplitude: about $60 - 65\%$ larger than the mean value. The relative magnitude of the turbulent timescale is furthermore found to be in good accordance between measurements and simulations all over the pitch direction. Finally, the circumferentially-averaged profile of the turbulent timescale provided in Fig. 6.12b confirms the good agreement between LES and HWA. Such plot emphasizes how non-uniform the turbulence at the inlet of the turbine can be, both in terms of magnitude (see Section 6.2) and integral scale.

[1]Note that for experimental results, the non-degraded full duration signal is used (5 s at 20 kHz).

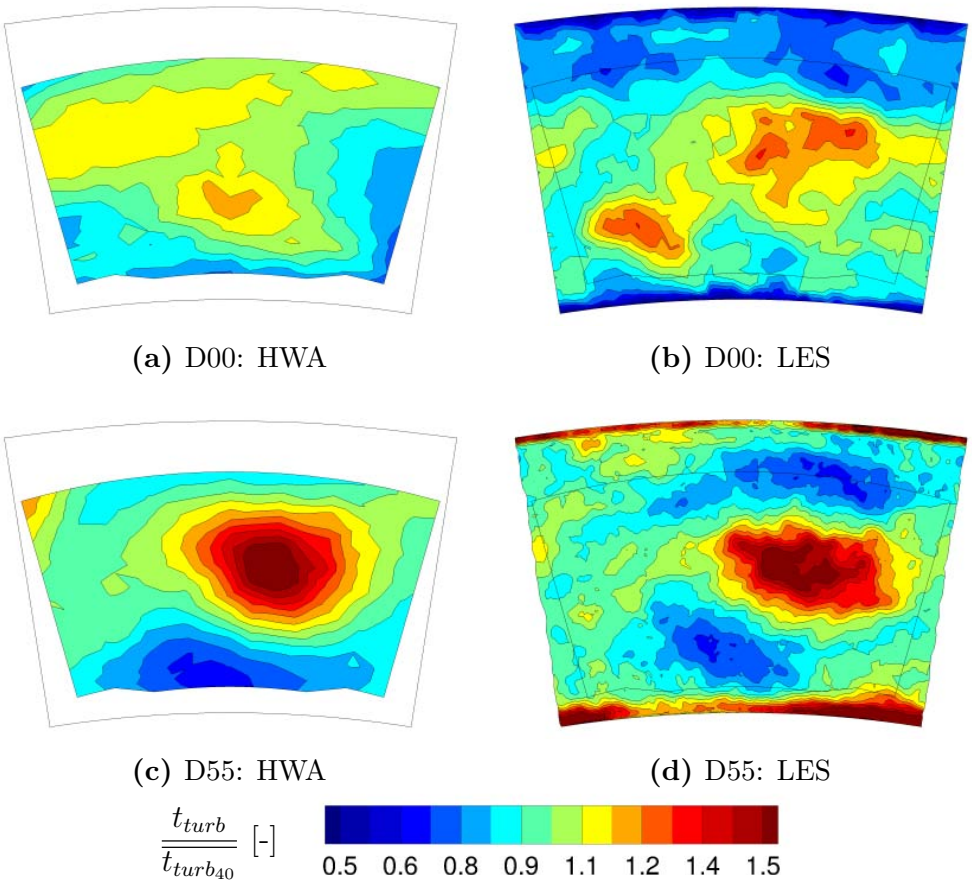


**(a)** D00: HWA **(b)** D00: LES

**(c)** D55: HWA **(d)** D55: LES

**Figure 6.11:** Comparison of the non-dimensional turbulent timescale for HWA and LES with and without duct.

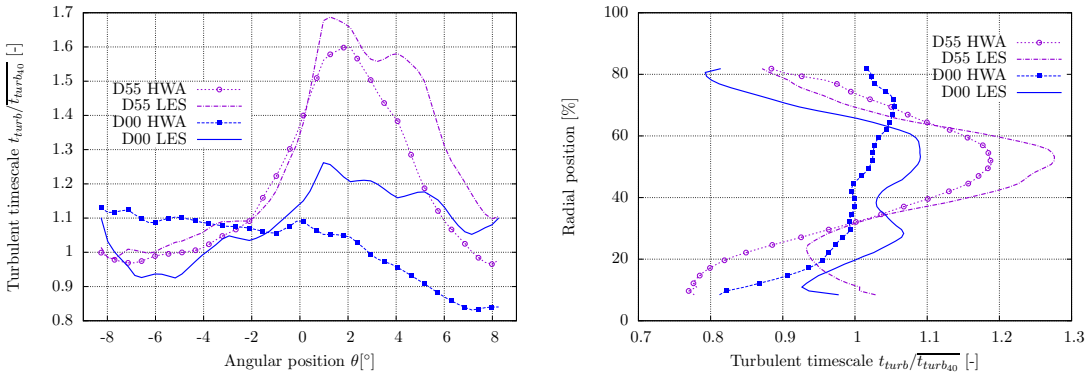


**(a)** Mid-height (R=50%). **(b)** Circumferentially-averaged.

**Figure 6.12:** Non-dimensional turbulent timescale in plane 40: angular profile at midspan (left) and circumferentially-averaged profile (right).

## 6.4 Conclusions

The exercise of experimentally and numerically characterizing the turbulence level and integral scale at the exit of a realistic combustor module provides the following conclusions:

- The specificities of the numerical and experimental signals (acquisition frequency and duration of the signal) impose to clearly indicate the different biases introduced by the two approaches before comparing results.
- Any discussion related to the level of the integral scale of turbulence has to be done in light of the precise definition and methodology employed for its evaluation.
- Having knowledge of the experimental uncertainties and the different operating points (DP and IOP), the distributions of both turbulence intensity and integral timescale predicted by LES are in excellent agreement with the HWA measurements.
- The large change in topology of the flowfield between the unducted and ducted cases is found to impact the turbulence quantities:
  - Regarding the distributions: with the duct, large values of $TU$ and $t_{turb}$ are found only in the remnant parts of the swirling core while without duct both quantities are more smoothly distributed throughout plane 40.
  - Regarding the levels: the spatial-mean $TU$ in plane 40 is almost identical with and without duct while the spatial-mean $t_{turb}$ is 58% (HWA measurement) or 54% (LES prediction) larger without duct than with D55.
- Overall and if compared to the current state of the art on the topic (see Chapter 1), these results are of particularly good quality and clearly indicate the potential of LES for the investigation of high order turbulence quantities of complex flows. With the increasing power of the computational machines, long duration signals will be accessible and allow for improved and more quantitative estimates of such turbulent flow features.

# Chapter 7

# Advanced statistical representation of temperature

## Contents


7.1 Statistical framework . . . . . **142**

7.2 Advanced characterization of the combustor temperature field **146**

7.2.1 Validation of the sampling . . . . . 147

7.2.2 Results and discussion . . . . . 147

7.2.3 Statistical representation of the radial profile of temperature . . . . . 152

7.3 Conclusion . . . . . **154**


From both an experimental and numerical point of view, the treatment and exchange of data at the combustor turbine interface is more and more discussed. It is proposed here to go beyond the common design practices which rely on simple time-averaged temperature profiles as obtained by current tools or used in industry. The main idea is to exploit the time-dependent signal provided by LES of combustion chambers to improve the description of the combustor-turbine interface and eventually provide a more discriminant diagnostic than the traditional Temperature Distortion Factors [29].

First, the treatment of the temperature data is explained in Section 7.1 and a general statistical formulation of the temperature field is proposed to help in a better understanding and qualifying a burner in a design phase. Then, this approach is applied to the FACTOR CS in Section 7.2 considering the LES of the D45 case[1]. Conclusions are finally given in Section 7.3.

[1] Although mainly relying on numerical data, this analysis is of course directly applicable to experimental data if available.

## 7.1 Statistical framework

Before applying any statistical treatment to a set of unsteady data, one has to assume that the simulated flow is a continuous stationary process. If so, any sufficiently long signal obtained from a temporally evolving LES provides a representative statistical description of any flow variable (typically here the temperature). Within this context, each point in the computation or for which a probe is available can be associated with its one point temperature probability density function (pdf), or equivalently an infinite number of moments [133].

Focusing especially on a temperature signal or set of samples, one can expect different types of distributions depending on the mixing process as illustrated in Fig. 7.1:

(a) For a perfectly mixed flow (e.g. the temperature is measured at an infinite distance from the sources), the repeated measurement of temperature at a single position gives the same value. The corresponding pdf features only a Dirac shape centred on the adiabatic temperature $T_{ad}$ if combustion is involved. In the case of a non-reacting flow, $T_{ad}$ is obtained from a simplified energy balance (assuming constant heat capacity):

$$T_{ad} = \frac{\dot{m}_{hot} T_{hot} + \dot{m}_{cold} T_{cold}}{\dot{m}_{hot} + \dot{m}_{cold}}, \tag{7.1}$$

where $\dot{m}_i, T_i$ refer to the mass flow and temperature of the hot and cold streams. In the following, the flow is considered as adiabatic (no heat loss) and thus the adiabatic temperature should equal the mean temperature $\overline{T}$.

(b) In the case of an imperfect mixing of the cold and hot flows, variations around $\overline{T}$ can be introduced. In the hypothetical case where all the measured samples are independent (which is not true for temperature), the distribution of temperature would follow a Gaussian shape centred on $\overline{T}$ (see Fig. 7.1b), as indicated by the Central Limit Theorem [134]. The standard deviation $\sigma$ is typically used to quantify these variations around $\overline{T}$. Note that such distribution is characteristic of the velocity distribution found in Homogeneous Isotropic Turbulence [13, 14].

(c) The case of FACTOR CS is shown in Fig. 7.1c for an arbitrary point at the chamber exit. In this configuration, temperature is distributed following an unimodal non-Gaussian shape. This distribution indicates a specific mixing mode between cold and hot gases within a combustor favouring the passage of hot pockets at the location of interest.

The observation of the pdf in Fig. 7.1c clearly shows that $\overline{T}$ is not sufficient to fully characterize the temperature signal because fluctuations can be large while remaining within bounds related to the operating conditions of the combustor. So additional variables are needed to describe or compare temperature pdfs'. A

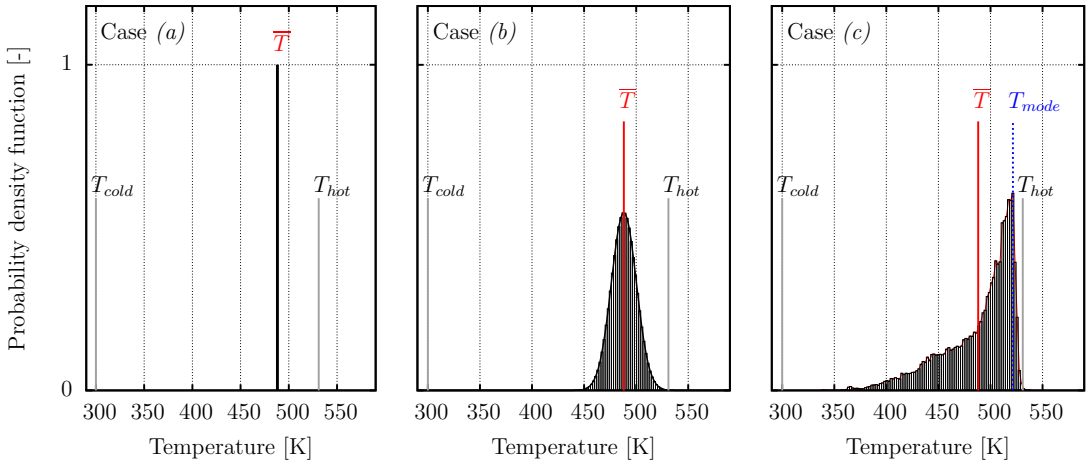


**Figure 7.1:** Typical temperature distributions for different mixing modes.

quantity of interest is the so-called mode temperature $T_{mode}$ or *most probable temperature* at this specific location, i.e. the temperature associated with the peak of the pdf. This mode temperature can be seen as the most probable value measured by a probe at this location for a given period. In Fig. 7.1, the pdfs' of cases *(a)* and *(b)* are centered on $\overline{T} = T_{ad}$ and symmetrical, so $T_{mode} = \overline{T}$. If looking at the exit plane of the CS (case *(c)*) the most probable value is 7% hotter than the mean temperature. Note that in the following the probability associated with the mode temperature is defined as the integral of the pdf over an arbitrary interval defined as $\pm 1/10$ of the standard deviation $\sigma$ around $T_{mode}$:

$$p(T_{mode}) \simeq p\left(T_{mode} - \frac{\sigma}{10} \leq T \leq T_{mode} + \frac{\sigma}{10}\right) = \int_{T_{mode}-\frac{\sigma}{10}}^{T_{mode}+\frac{\sigma}{10}} pdf(T)dT. \tag{7.2}$$

As indicated by the previous discussion, for quantities other than velocity (e.g., scalars or temperature) there is not physical justification that $T_{mode}$ equals $\overline{T}$ or that the pdf is Gaussian, centred around $\overline{T}$ and symmetrical. In fact and in practice, for temperature the only constraint is that it is bounded by $T_{hot}$ and $T_{cold}$, these extremes being fixed and known for a given problem: i.e. the cold gas temperature at the inlet of the combustor and the adiabatic flame temperature at stoichiometry for the most extreme burners [2]. It is also acknowledged in the literature that the temperature distribution could be accurately approached by a $\beta$-distribution [135–137] defined using a reduced temperature over the interval $[0, 1]$:

$$\Theta = \frac{T - T_{cold}}{T_{hot} - T_{cold}}. \tag{7.3}$$

[2]Note that these extrema values apply to the entire flow field in the burner and will differ if a specific location inside the chamber is chosen. Indeed at a given point in the combustor the extreme values of temperature are bounded by $T_{hot}$ and $T_{cold}$ but may not be reached.

The $\beta$-distribution is conveniently parameterized on the basis of the mean $\mu_1 = \overline{\Theta}$ and variance $\mu_2 = \sigma^2$ of the reduced temperature, defined for $N$ samples as:

$$\overline{\Theta} = \mu_1 = \frac{1}{N}\sum_{i=1}^{N}\Theta_i, \tag{7.4}$$

$$\sigma^2 = \mu_2 = \frac{1}{N}\sum_{i=1}^{N}\left(\Theta_i - \overline{\Theta}\right)^2, \tag{7.5}$$

the pdf of the $\beta$-distribution following:

$$pdf_\beta = \frac{1}{B(\alpha,\beta)}\Theta^{\alpha-1}(1-\Theta)^{\beta-1}, \tag{7.6}$$

where $B$ is the Euler beta function which ensures that the total probability integrates to unity and $(\alpha, \beta)$ are two shape parameters algebraically determined by use of $\mu_1$ and $\mu_2$.

Typical $\beta$-pdf's obtained by processing the LES temperature signals recorded at three points (A,B,C) taken at various locations at the exit of FACTOR CS are shown in Fig. 7.2 along with the full exact histograms. For points B and C, the $\beta$-distribution provide an acceptable fit even if the sharp gradients near the limits are not correctly reproduced (especially for the upper bound of point C). This is due to the fact that the minimum and maximum temperatures actually reached at points A, B and C are not equal to the bounds $(T_{hot}, T_{cold})$ used to define $\Theta$ in Eq. (7.3). Indeed, the knowledge of the extreme values implies to have either a full pdf already built or *a priori* knowledge of the local evolution of the limiting temperature values which is usually not accessible in engineering applications. The weakness of modeling approaches postulating any pdf shape type is further complicated by the drawback that it also needs adequate evaluations of the local mean and variance values of the temperature which is far from easy to model.

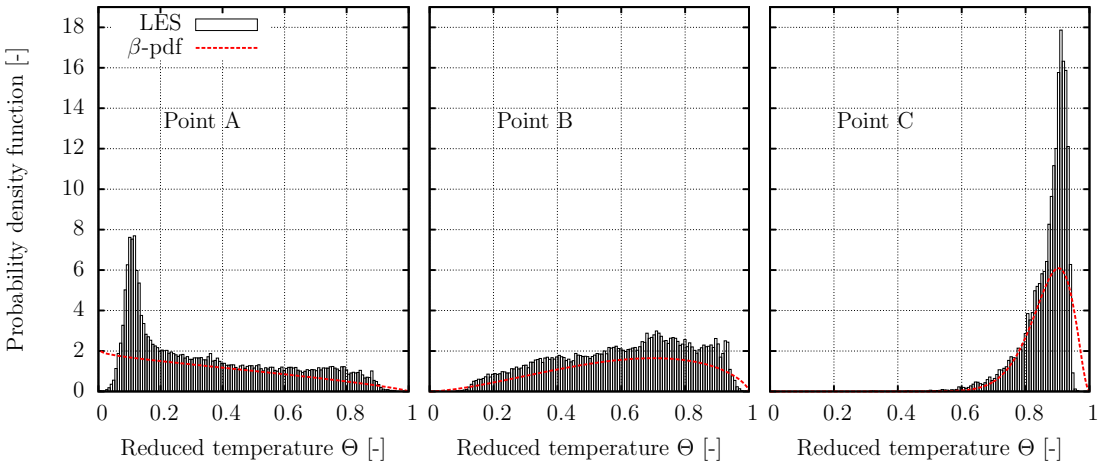


**Figure 7.2:** LES-based histograms of temperature and corresponding reconstructed $\beta$-pdfs'.

Typically and although these last two quantities are provided here and therefore exact for this example, the $\beta$-pdf for point A dramatically fails at reproducing the most probable temperature in the cold region, which is one of the most important outcome of the temperature pdfs'.

Based on theses observations, complete LES-based distributions of temperature are considered. Such pdf's can be qualified in terms of shape by their first and second moments from Eqs. (7.4) and (7.5) as well as high order moments which quantify how much the distribution differs from a Gaussian shape. That is to say that the skewness $\mu_3$ and kurtosis $\mu_4$, defined hereafter should also be investigated:

$$\mu_3 = \frac{1}{N}\sum_{i=1}^{N}\left(\frac{\Theta_i - \overline{\Theta}}{\sigma}\right)^3, \tag{7.7}$$

$$\mu_4 = \frac{1}{N}\sum_{i=1}^{N}\left(\frac{\Theta_i - \overline{\Theta}}{\sigma}\right)^4. \tag{7.8}$$

To illustrate the use of skewnesses and kurtoses in the context of a combustion system, the kurtoses and skewnesses associated with the pdfs' of the points A, B and C are summarized in Table 7.1. The values obtained analytically from the corresponding $\beta$-pdfs' are also indicated for comparison. Overall the $\beta$-distributions correctly capture the trend of the different skewnesses (positive or negative asymmetry) but overpredict the absolute level. The $\beta$-pdf also fails to correctly reproduce the importance of the peak of temperature for point C, as indicated by the under-prediction of the associated kurtosis. It is worth noting that the analysis of the high order moments is subject to caution [138, 139] and a single value of skewness or kurtosis can represent many different shapes of distributions. These parameters therefore have to be used as indicators and commented along with the associated distributions:

(a) **Skewness** A negative value of skewness indicates that the left leg of the distribution is longer or thicker than the right one while a positive value indicates that the right leg is longer or thicker. A value of zero indicates that both legs are identical (like a Gaussian, for which it equals zero), or that the two legs balance out: e.g. one leg is thick and short while the other one is long with small probability values.

(b) **Kurtosis** For unimodal distributions, kurtosis is a measure of the distribution around the mode value [140]: high values are associated with large shoulders and thin long legs while values going to zero represent a more rounded distribution around the mode value, with a small extension away from the mode. Recall for reference that the kurtosis of a Gaussian distribution is $\mu_4 = 3$.

| | | $\mu_3$ | $\mu_4$ |
|---|---|---|---|
| Point A | LES | 0.63 | 2.11 |
| | $\beta$-pdf | 0.86 | 2.27 |
| Point B | LES | -0.33 | 2.10 |
| | $\beta$-pdf | -1.37 | 2.30 |
| Point C | LES | -1.96 | 8.59 |
| | $\beta$-pdf | -50.8 | 3.82 |
| *Gaussian distribution* | | 0.0 | 3.0 |

**Table 7.1:** Skewnesses and kurtoses of the temperature pdfs' at points A, B and C.

An original aspect of the statistical treatment of the unsteady temperature signal is to give access to both $\overline{T}$ and $T_{mode}$ along with an explicit characterization of the pdf shape relative to the ideal Gaussian distribution. It is proposed here to investigate the temperature fields at the exit of the combustor systems based on these specific constants. The non-dimensional temperature coefficient $\Xi$ defined earlier (Chapter 4) in Eq. (4.1) is adapted following:

$$\Xi_{\psi} = \frac{\psi(x,r,\theta) - \overline{T}_{40}}{\overline{T}_{40} - \overline{T}_{30}}, \tag{7.9}$$

where $\psi(x,r,\theta)$ might be either the local mean temperature $\overline{T}$, the mode temperature $T_{mode}$ or a local sample of temperature $T_i$. If $\psi = \overline{T}$, then $\Xi_{\overline{T}}$ is equivalent to the temperature coefficient defined in Eq. (4.1).

Note that whenever qualifying a design for a real reactive combustor several issues may arise and need to be verified prior to the following analyses: *(i)* $\overline{T}_{40}$ may differ from the adiabatic temperature (heat losses); *(ii)* for multiple inlets at different temperatures, how to precisely define $\overline{T}_{30}$ will play a role. All of these issues can explicitly impact the interpretation and exploitation of $< \Xi_{\psi} >_{\theta}$ which is the result of multiple manipulations that can largely smear the actual information present in the pdf, justifying the use of more advanced criteria.

## 7.2 Advanced characterization of the combustor temperature field

The statistical treatment is applied here to the LES of the D45 case (the characteristics of the simulation can be found in Table 2.1). To do so, 1100 instantaneous solutions are saved during the simulation at a constant sampling rate of 9.7 kHz. These snapshots of the flowfield allow to reconstruct a discrete temperature signal at each node of the domain. Because of storage and data treatment issues, the number of solutions is limited and therefore the representativity of the sampling has to be assessed.

### 7.2.1 Validation of the sampling

To validate the representativity of the set of instantaneous solutions against the pseudo continuous numerical solution, the sampled ensemble is compared to a numerical monitoring probe initially introduced in the LES for which sampling follows Table 7.2. Distributions are then obtained for the two sets of data of Table 7.2 through binning. Histograms relying on the same parameters are shown in Fig. 7.3 for the three points (A,B,C) introduced previously and located in plane 40. For distributions showing strong peaks (e.g. points A and C) both ensembles give the same prediction of $\Xi_{T_{mode}}, \Xi_{\overline{T}}, \sigma, \mu_3$ and $\mu_4$. When the standard deviation is larger (e.g. point B), errors of 2 to 5% can be found. Overall the representativity of the set of snapshots is found to be sufficiently satisfactory to perform further analysis on the histograms obtained from the set of snapshots.

| | Set of snapshots | Probe |
|---|---|---|
| Sampling frequency [kHz] | 9.7 | 457.0 |
| Total time [ms] | 143 | 129 |
| Number of samples | 1 100 | 58 882 |

**Table 7.2:** Characteristics of the signal acquired by the probe and the set of snapshots.

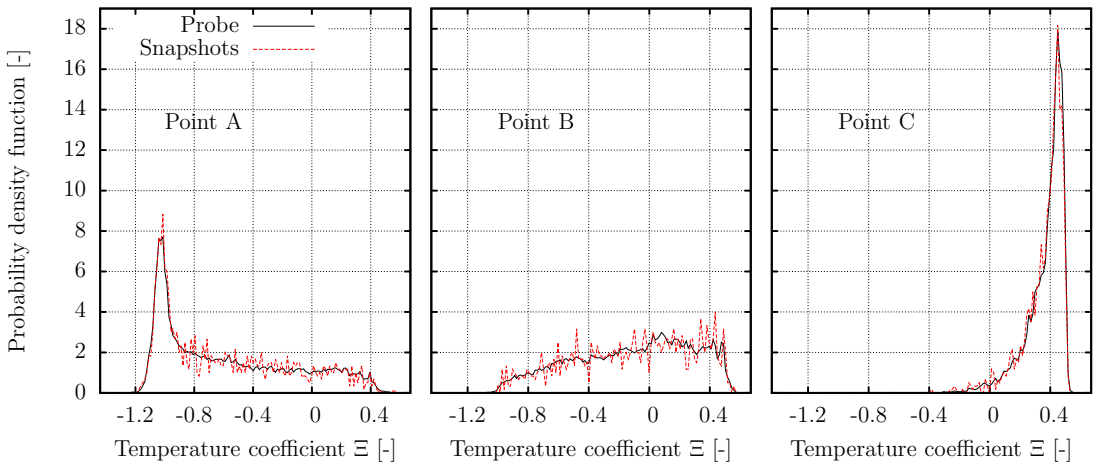


**Figure 7.3:** Histograms obtained by the set of snapshots and the probe signal.

### 7.2.2 Results and discussion

The time distributions of temperature computed based on the 1 100 snapshots of the flow are now presented. Temperature fields in the chamber are discussed first before analyzing local and global distributions in plane 40.

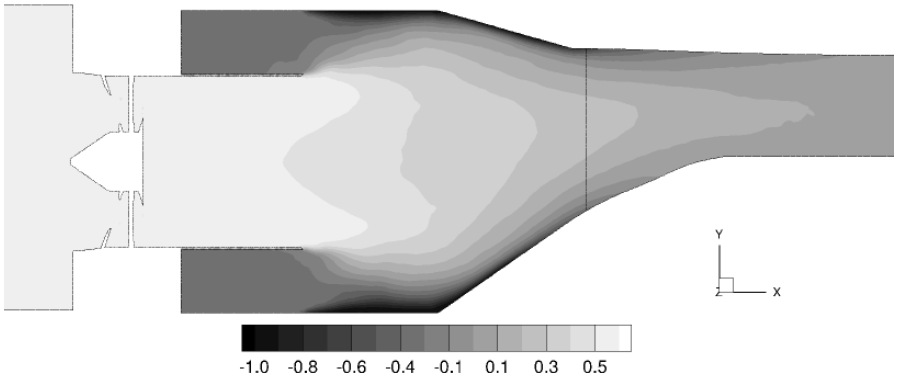


**(a)** Mean temperature coefficient $\Xi_{\overline{T}}$ [-].

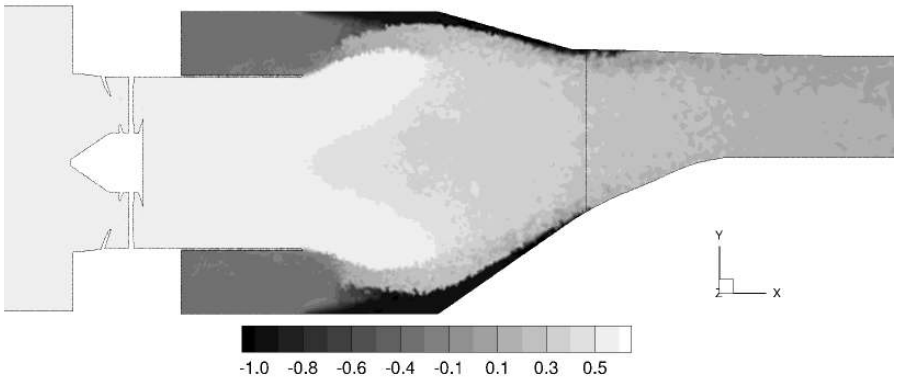


**(b)** Mode temperature coefficient $\Xi_{T_{mode}}$ [-].

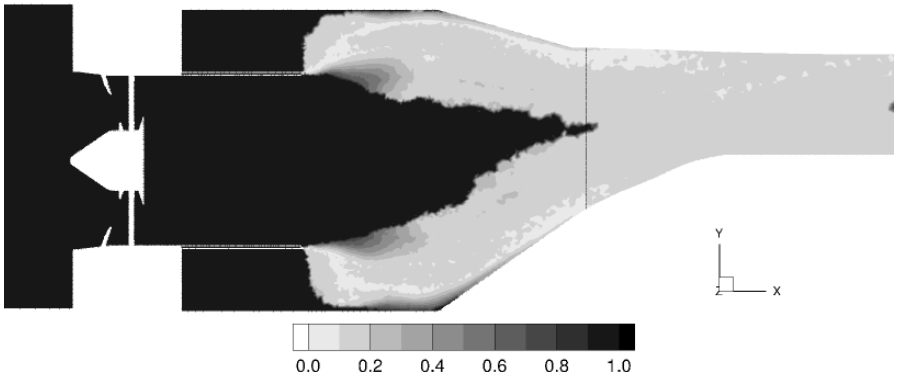


**(c)** Probability of $\Xi_{T_{mode}}$ [-].

**Figure 7.4:** Temperature coefficient and probability of $\Xi_{T_{mode}}$ in the central plane of the CS.

Figure 7.4a and 7.4b respectively show $\Xi_{\overline{T}}$ and $\Xi_{T_{mode}}$ in the longitudinal cross section of the CS. The visualization of $\Xi_{T_{mode}}$ highlights the discrimination in temperature of different zones in the chamber. For extreme conditions where no mixing occurs (i.e. only hot or cold injection) the mean and mode values are equal: this is the Dirac distribution case of Fig. 7.1a. In the trace of the hot jet exiting the duct it is very likely to measure the hot temperature, as there is a little amount of cooling at this position. Nonetheless, the reversing flow induced by

the vortex breakdown does contribute to the mixing and $\Xi_{\overline{T}}$ is below $\Xi_{T_{hot}}$. Near the multiperforated walls the cold fluid injection creates very distinct cold films, which remain coherent and close to the wall. In this region the probability to measure $\Xi_{T_{cool}}$ is high and drops quickly with an increasing distance from the wall because hot fluid is encountered and the flow heats up. Figure 7.4c shows the field of probability associated with the mode temperature, as defined in Eq. (7.2). In the upstream plenum, swirler and duct, $p(\Xi_{T_{mode}}) = 1$, as there is no mixing with the coolant and $\Xi_{\overline{T}} = \Xi_{T_{mode}} = \Xi_{T_{hot}}$ as indicated earlier. The same observation is done in the corner recirculation zones above and below the duct, where there is very little evolution of the fluid temperature once the flow is established. In the hot jet exiting the duct radially, $\Xi_{T_{mode}} = \Xi_{T_{hot}}$ (see Fig. 7.4b) but its probability decreases quickly as the jet penetrates the CS because of the mixing with the colder flow. The central region of the CS shows a stretched triangular shape in which $p(\Xi_{T_{mode}}) \simeq 1$. In this zone, the coolant flow is too far and does not interact directly with the hot stream: the temperature decreases by turbulent diffusion only (no intermittency hot/cold) and there is thus little variation of temperature. Note that $p(\Xi_{T_{mode}}) = 1$ implies $\Xi_{\overline{T}} \simeq \Xi_{T_{mode}}$ with very little mixing locally (i.e. within $\pm\sigma/10$). As we go away from the central axis, $p(\Xi_{T_{mode}})$ reduces significantly until a very low value (around 0.1 in a thin band) because either coolant either mainflow can be measured in these zones. Finally, the probability increases again as we get closer to the multiperforated wall, where it is very likely to measure the coolant temperature, until the wall itself where $p(\Xi_{T_{mode}}) = 1$.

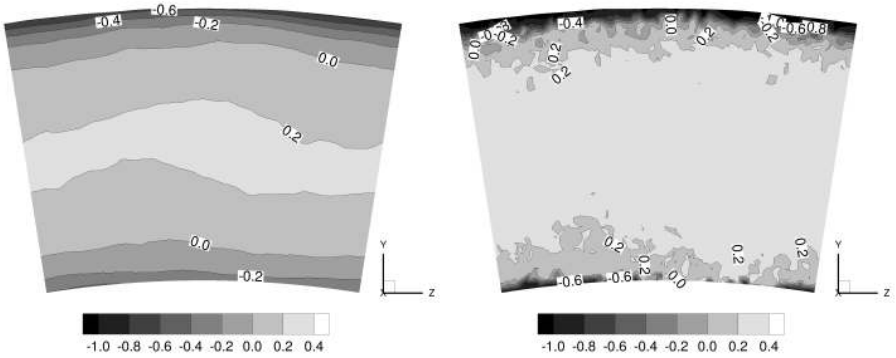


**(a)** $\Xi_{\overline{T}}$ [-]. **(b)** $\Xi_{T_{mode}}$ [-].

**Figure 7.5:** Mean and most probable temperature coefficients in plane 40.

As significant differences between $\Xi_{T_{mode}}$ and $\Xi_{\overline{T}}$ are observed in the central plane, it is likely that the exit of the combustor will show similar differences. Both fields of $\Xi_{T_{mode}}$ and $\Xi_{\overline{T}}$ in plane 40 are shown in Fig. 7.5: there is a large central region of uniform $\Xi_{T_{mode}}$ in the center of plane 40 while $\Xi_{\overline{T}}$ is more smoothly diffused. In the near-wall region, the presence of the upstream film cooling maintains $\Xi_{T_{mode}}$ close to $\Xi_{T_{cold}}$ and a clear transition between coolant flow and mainstream is visible. With stronger radial temperature gradients and higher values in the core, the field of most probable temperature coefficient seems definitely more critical for the turbine.

The corresponding circumferentially-averaged temperature coefficient $< \Xi >_\theta$ is plotted for $\overline{T}$ and $T_{mode}$ in Fig. 7.6, along with the experimental measurement obtained by means of the THCPL. Note that a typical LRTDF (either from simulations or experiments) would be obtained by considering only the $\Xi_{\overline{T}}$ curve in Fig. 7.6. However, the introduction of the mode temperature in this graph indicates very clearly that the temperature is not distributed with a Gaussian shape at the combustor exit. The radial profile of $\Xi_{T_{mode}}$ is hotter than $\Xi_{\overline{T}}$ and shows more pronounced gradients, suggesting that the temperature envelope at the turbine inlet is more critical than depicted by a simple mean temperature analysis. Quantitatively, if spatially averaged over the exit plane, the mode coefficient $< \Xi_{T_{mode}} >_{r,\theta}$ equals 0.11 while $< \Xi_{\overline{T}} >_{r,\theta} = 0$. In dimensional units, this can be translated into a difference of 17 K.

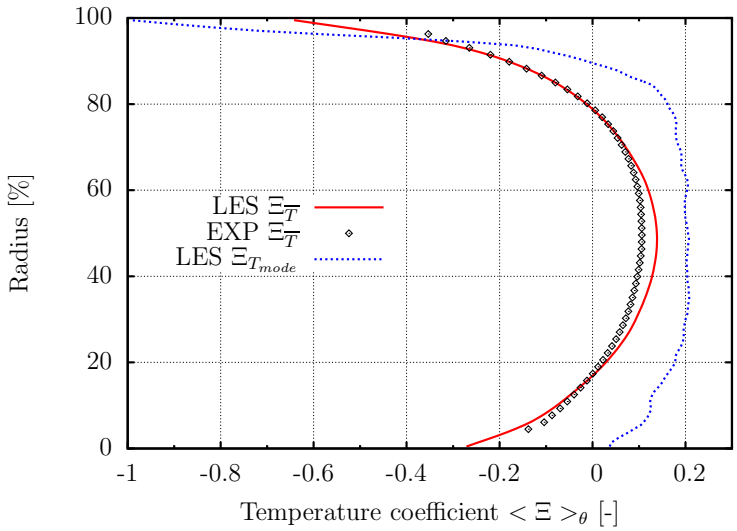


**Figure 7.6:** Circumferentially-averaged profile of the temperature coefficients in plane 40.

To explain such differences, one has to analyze the high order moments of the distribution of temperature in this plane. To do so, skewnesses and kurtoses are calculated at each computational node in plane 40 and shown in Fig. 7.7. Both moments are distributed following a very inhomogeneous pattern over plane 40, which means that the pdfs' of temperature are significantly different for all points at the exit of the combustor. However, the pattern is definitely not random and some zones of similarity can be identified. The central region features highly negative skewness values which means that overall $\Xi_{T_{mode}} > \Xi_{\overline{T}}$ as observed in Fig. 7.5. On the other hand, the near-wall regions exhibit positive values of skewness: the coolant is dominant in this zone ($\Xi_{T_{mode}} \simeq \Xi_{T_{cool}}$) and only punctual incursions of hot fluid occur. The central hot region is associated with larger kurtosis values, highlighting a higher occurrence rate of the most probable temperature with little deviation.

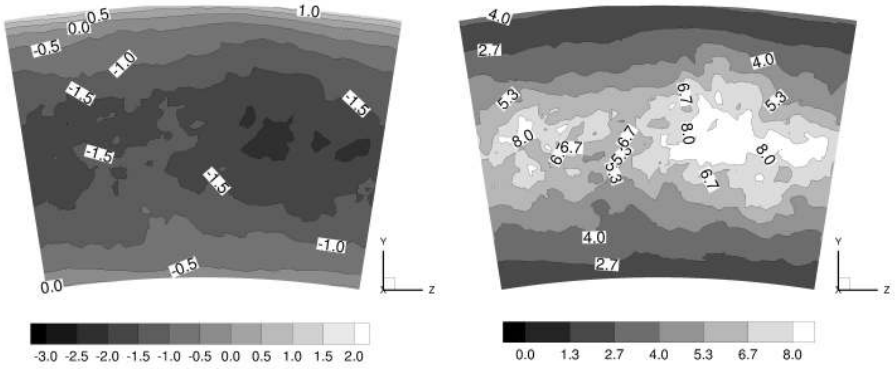


**(a)** Skewness $\mu_3$. **(b)** Kurtosis $\mu_4$.

**Figure 7.7:** Skewness and kurtosis of the pdfs' of temperature in plane 40.

To investigate if such observations are linked to the velocity fields or equivalently the turbulent activity in plane 40, skewnesses and kurtoses of the axial velocity in plane 40 are shown in Fig. 7.8. The contrast with the temperature distribution is strong: $\mu_3$ and $\mu_4$ are very homogeneously distributed. Skewness is very close to zero while kurtosis is equal to 3 almost everywhere, which corresponds to a Gaussian distribution of velocity and a fully established turbulent flow. This specific diagnostic confirms that there is a first order dependency of the temperature distribution in plane 40 on the technological implementation of the cooling systems and its mixing process. Turbulence alone —at least with the associated small scales— is not efficient to properly mix both fluids prior to its entry in the turbine.

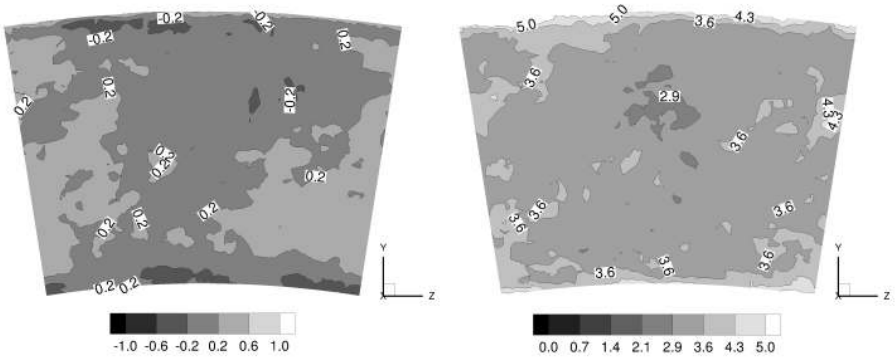


**(a)** Skewness $\mu_3$. **(b)** Kurtosis $\mu_4$.

**Figure 7.8:** Skewness and kurtosis of the pdfs' of axial velocity in plane 40.

Spatially-averaged values of skewness $< \mu_3 >_{r,\theta}$ and kurtosis $< \mu_4 >_{r,\theta}$ of temperature and axial velocity pdfs' are reported in Table 7.3. They represent the mean value in space of the moments of the different distributions, giving an indication of how —on average— all the distributions in plane 40 look like. The values for the axial velocity are close to a Gaussian distribution, which confirms our previous

observation. However, the mean skewness of the temperature distribution is negative, which means that overall the distributions show a mode temperature hotter than the mean value, in agreement with the 17 K difference reported previously.

| | $< \mu_3 >_{r,\theta}$ | $< \mu_4 >_{r,\theta}$ |
|---|---|---|
| Temperature | -1.1 | 4.8 |
| Axial velocity | 0.1 | 3.4 |
| *Gaussian distribution* | 0.0 | 3.0 |

**Table 7.3:** Spatially-averaged skewness and kurtosis of temperature and axial velocity in plane 40.

### 7.2.3 Statistical representation of the radial profile of temperature

The most common way to represent a temperature profile at the exit of the combustor is to draw the radial profile of the circumferentially-averaged mean temperature: the LRTDF [29] shown by the solid line in Fig. 7.6. However, based on our previous observations, it is clear that the mean value is not sufficient to fully describe a temperature distribution because important local changes in the shape of the pdf are usually present but smeared by all averages introduced in the evaluation of the LRTDF. It is proposed here to extend the diagnostic space of the LRTDF (i.e. radius and temperature dimensions) by adding the sampling dimension.

For this purpose, plane 40 is divided into 35 successive radial sections and mean pdfs' of temperature are computed for each radial coordinate as shown in Fig. 7.9. They are the direct illustration of two previous quantitative observations discussed earlier. First, all the pdfs' at given radial locations exhibit very different non-Gaussian shapes, as indicated by the value of skewness and kurtosis calculated

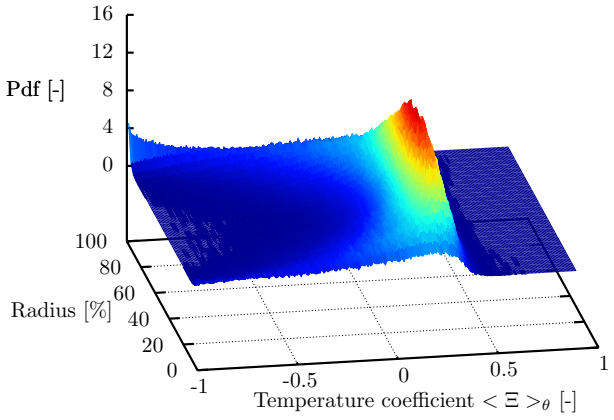


**Figure 7.9:** Circumferentially averaged pdfs' of temperature in plane 40.

previously. Second, the distributions are not centered on the most probable value but skewed towards colder temperatures: this is the translation of the negative mean skewness (see Table 7.3) which results in a larger mode than mean temperature coefficient. Finally, Fig. 7.9 also highlights how temperature is differently distributed within two zones. On one hand, the central region ($30\% < R < 70\%$) features high probability and little dispersion of the pdf (high kurtosis region, see Fig. 7.7b). In this zone, there is a rapid decrease of the probability after $\Xi_{T_{mode}}$, which is close to the maximum value $\Xi_{T_{hot}}$. Indeed, the core temperature is mainly driven by the swirling hot air stream, which is relatively well preserved because of the absence of dilution holes. On the other hand, the near-wall zone shows much wider distributions associated with lower values of the probabilities. The pdf close to the outer wall ($R \rightarrow 100\%$) is very wide and the most probable value is in fact close to the coolant itself $\Xi_{T_{cool}} = -1$. Indeed, this specific region features little interaction between the effusion cooling and the hot stream because the outer wall is above the flowpath exiting the swirler (see Fig. 7.4). This effect is less evident for the inner wall.

An alternative view of Fig. 7.9 is proposed in Fig. 7.10, along with the values of $\Xi_{\overline{T}}, \Xi_{T_{mode}}, \Xi_{T_{min}}$ and $\Xi_{T_{max}}$ extracted from the pdfs'. While usual representations of the combustor exit temperature only feature $\Xi_{\overline{T}}$, Fig. 7.10 completely defines the mixing envelope of the exit plane of the CS. It is worth noting that the radial profile of $\Xi_{T_{mode}}$ represents the most probable temperature at each radial step but is not the most probable temperature profile to be measured at the exit of the combustor. Both mode and mean temperature coefficients are constructed from

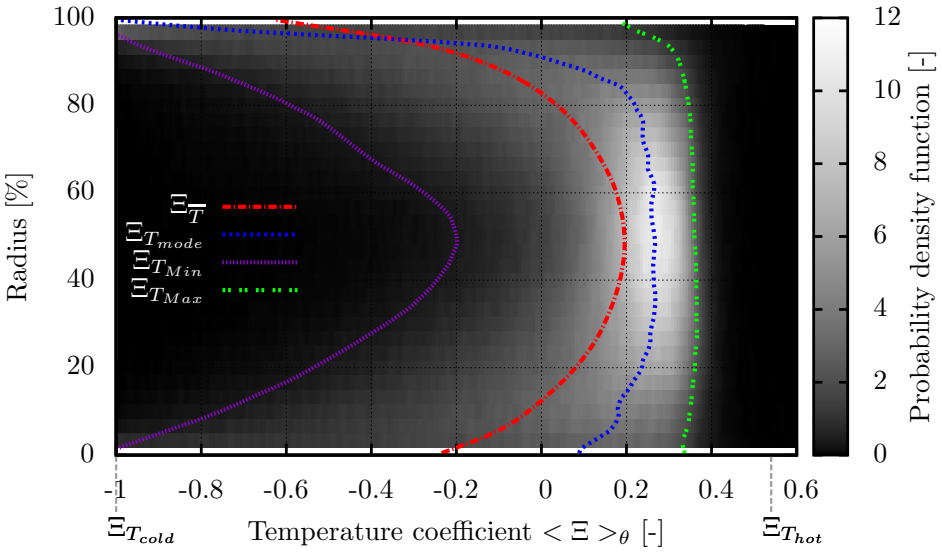


**Figure 7.10:** Temperature coefficient for the mean, mode, minimum and maximum temperatures and associated pdf in plane 40.

these statistics: they cannot be measured on a single realization of the flow. The difference between the profiles of $\Xi_{\overline{T}}$ and $\Xi_{T_{mode}}$ is significative, both in terms of absolute value and distribution. Because of the presence of two zones in the mode temperature (core and near-wall), the radial gradient of $T_{mode}$ is very strong in the transition zone ($R \simeq 10\%$ and $R \simeq 90\%$).

## 7.3 Conclusion

The application of this simple statistical analysis to the unsteady LES data of the CS highlights different points:

- The distributions of temperature in the CS are not Gaussian, with the presence of regions where a most probable temperature largely differs from the mean temperature.
- The analysis of higher order moments (skewness and kurtosis) explains such differences indicating strongly segregated regions of cold or hot fluid in the chamber depending on the technological implementation of the cooling systems.
- A more appropriate characterization of the combustor exit temperature profile is proposed by considering the sampling-dimension in addition to the common (radius, temperature) representation (LRTDF). This new diagnostic allows to fully characterize the temperature envelope of the combustor exit.
- With the generalization of Lean Burn configurations and the progressive disappearance of dilution holes which strongly enhanced mixing, the temperature distribution at the combustor exit will tend to show such discriminated zones. In this context, applying this statistical approach can help assessing the quality of the mixing at the combustor exit.

Even if not reported in this manuscript because of confidentiality considerations, such diagnostic was applied to real combustors of SAFRAN gas turbines. As expected, it was found that combustion chambers based on Lean Burn architectures are more subject to present segregated zones of temperature than RQL configurations. The use of this statistical analysis helped better apprehending the operating temperature envelope to be found at the inlet of the turbine of these real gas turbines.

# Part IV

# Integrated approach of the combustor-turbine interaction in LES

The last part of this manuscript intends to bring new elements on the combustor-turbine interaction in the context of a Lean Burn chamber. At this aim, LES of the combustor simulator equipped with the two vanes of the HP turbine are performed and results are discussed from various perspectives.

In the context of such simulations, a preliminary analysis was performed to assess how the outlet boundary condition complies with the radial equilibrium induced by the presence of the vanes. Results were published in:

> C. Koupper, T. Poinsot, L. Gicquel, and F. Duchaine. "Compatibility of Characteristic Boundary Conditions with Radial Equilibrium in Turbomachinery Simulations". In: *AIAA Journal* 52.12 (2014), pp. 2829–2839

# Chapter 8

# Impact of the presence of vanes at the exit of the combustor simulator

## Contents


8.1 Geometry and mesh . . . . . **158**

8.2 Influence of the clocking position . . . . . **161**

8.2.1 Migration of the hot streak . . . . . 161

8.2.2 Vane surface temperature . . . . . 164

8.3 Potential effect induced by the vanes . . . . . **165**

8.3.1 Mass flow distribution . . . . . 166

8.3.2 Temperature . . . . . 168

8.3.3 Turbulence level . . . . . 171

8.4 Conclusions . . . . . **175**


This chapter reports the results of integrated simulations featuring the FACTOR CS fitted with the two NGVs at its exit. Such numerical analysis intends to complement the existing literature on the two-way interaction between the combustor and the turbine by analysing a Lean Burn configuration (vs. classical RQL configurations).

First, Section 8.1 introduces the geometry and settings of the three LES under investigation. Then, the numerical investigations focus on the influence of the clocking position between the HS and the vanes (Section 8.2), before analysing the potential effect induced in the CS by the presence of the NGVs (Section 8.3). Finally, general conclusions on this analysis are given in Section 8.4

## 8.1 Geometry and mesh

The test section developed within the FACTOR project features one swirler and two NGVs per minimum angular sector of the machine (18°), with the possibility of aligning the vanes at different angular positions with respect to the CS. Note that in the following, the vane located on the left side when looking downstream is referred as NGV1 while the other one is noted NGV2 (see Fig. 8.1). To investigate the possible interactions between the CS and the vanes, simulations are thus performed based on a single sector of the CS (D55 case) equipped with two vanes:

**For the case referred as w/o** the CS is computed alone, without vanes as shown in Fig. 8.1a

**For the case referred as LE** the two vanes are specifically clocked so that the HS exiting the swirler impacts the leading edge of NGV1 as illustrated in Fig. 8.1b by the blue surface which indicates the trajectory of the HS exiting the swirler (supposing it is not deviated). Because of the count ratio between the vanes and the swirler, one NGV over two is impacted by a HS.

**For the case referred as PA** the swirler is aligned with the passage between the two vanes (see Fig. 8.1c). As a result of this specific clocking, one passage over two sees a HS.

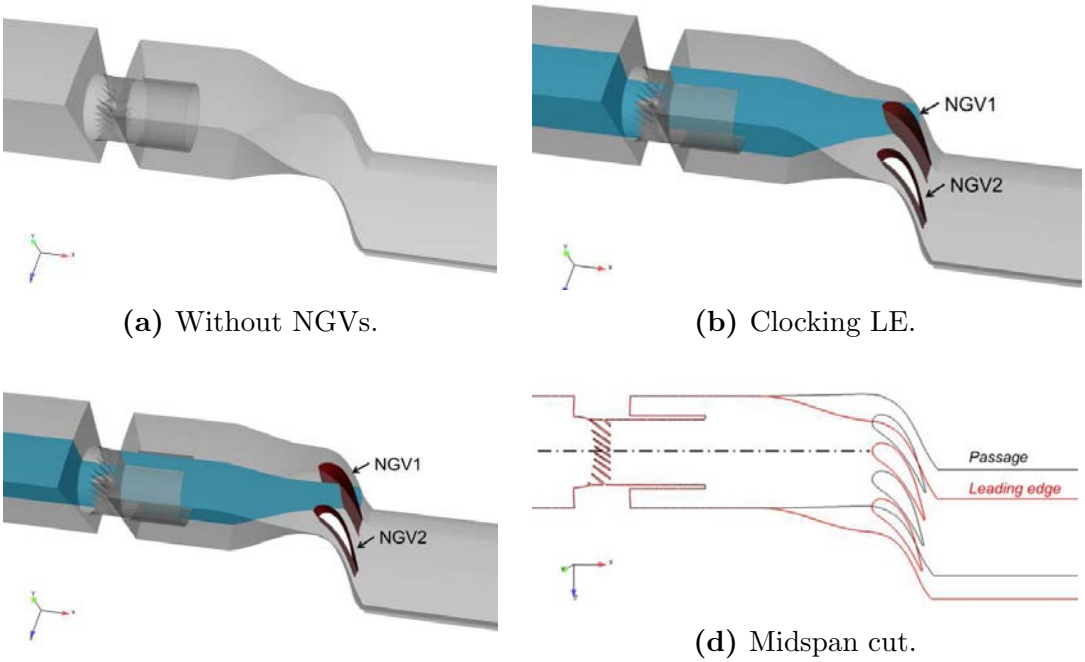


**(a)** Without NGVs.

**(b)** Clocking LE.

**(c)** Clocking PA.

**(d)** Midspan cut.

**Figure 8.1:** Numerical domains of the CS fitted with or without a pair of vanes.

Figure 8.2 shows the reference planes commonly used for data exchange between the combustion and turbine design teams or for comparison with the experiments. Plane 40 (considered as the combustor-turbine interface) was largely investigated in the previous chapters from both an experimental and numerical point of view. Plane 40+ on the other hand typically corresponds to the LE of the vanes and is located here just upstream the LE so that it does not cut the NGVs. As a result, it is placed 17 mm (0.425 ACL) downstream of plane 40 instead of the 20 mm (0.5 ACL) given previously in Section 2.1.1 due to geometrical changes induced by the real NGV shape. Finally, plane 41 is positioned at the interface between the vanes and the rotor (which is not included in these simulations) and is located 1.5 ACL downstream plane 40.

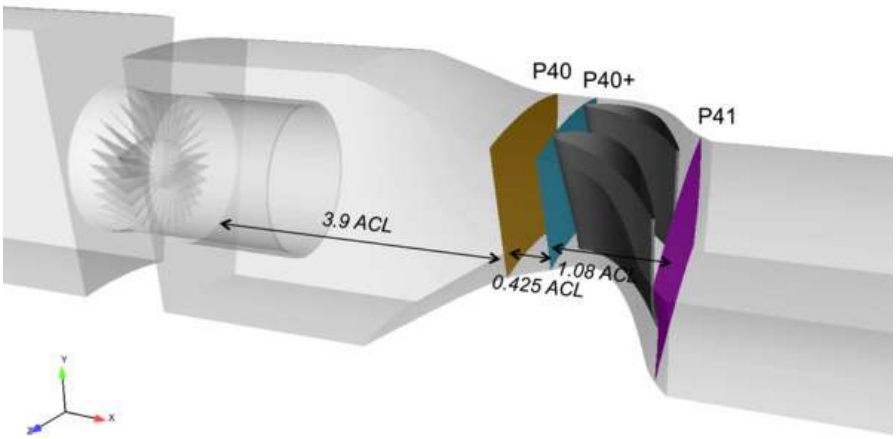


**Figure 8.2:** Planes of interest at the exit of the CS.

The characteristics of all three simulations are recalled in Table 8.1. The two simulations with and without NGVs are performed at the same operating point and only differ by the inclusion of the vanes which reduces the outlet pressure while maintaining the same pressure level in plane 40. Since the vanes impart a strong azimuthal component to the flow, a positive radial pressure gradient (the radial equilibrium) establishes [141, 142]. For the LE case, the radial pressure distortion from the vane hub to tip is found to be as large as 12% of the mean value as indicated by the time and circumferentially-averaged profile of static pressure in plane 41 plotted in Fig. 8.3. It has been shown that such significant pres-

| Case # | Duct | Operating point | Mesh nodes | Mesh cells | Scheme | SGS model | Physical time [ms] | Timestep [s] |
|---|---|---|---|---|---|---|---|---|
| No NGVs | D55 | DP | 8.9M | 51.0M | TTGC | Smagorinsky | 144 | $4.3 \cdot 10^{-8}$ |
| LE | D55 | DP | 13.7M | 71.0M | TTG4A | Smagorinsky | 50.3 | $3.2 \cdot 10^{-8}$ |
| PA | D55 | DP | 13.7M | 71.0M | TTG4A | Smagorinsky | 49.5 | $3.2 \cdot 10^{-8}$ |

**Table 8.1:** Summary of the LES of the FACTOR CS with and without vanes.

sure non-uniformity might be an issue for the outlet boundary condition of RANS calculations and requires to apply a priori treatments (e.g. imposing a computed pressure profile) [143–146]. This issue has been investigated in the particular scope of LES where Navier Stokes Characteristic Boundary Condition (NSCBC) are employed. Different test cases of increasing complexity showed that the 3-D NSCBC formalism [107, 147] used in this work naturally allows the establishment of the radial equilibrium pressure profile while maintaining the mean pressure level to the appropriate target. These results are not detailed here but the analysis was published [22] and is reported in Appendix D.

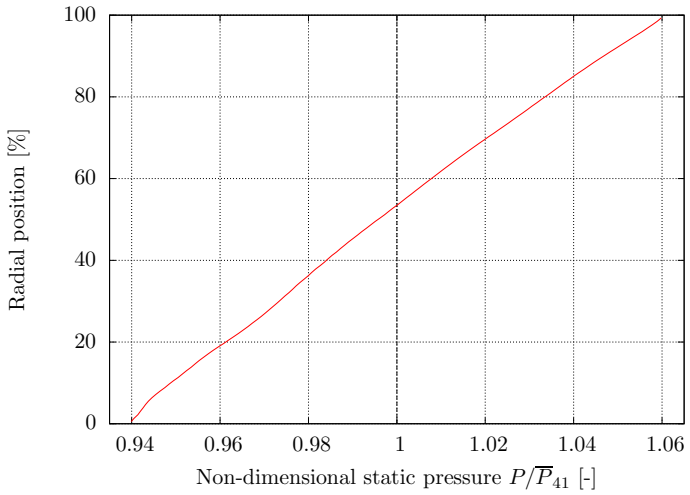


**Figure 8.3:** Radial equilibrium profile of pressure in plane 41 for the LE case.

Regarding the operating point, the NGVs were designed in the FACTOR project to be film-cooled on both PS and SS by an additional injection of 7.5% of the total mass flow in plane 40. This technological feature is however not reproduced in these simulations for the sake of simplicity and the NGV row thus does not operate at the nominal mass flow rate of the FACTOR project. Nonetheless, this difference is not of importance in the context of this work which aims at comparing configurations with and without NGVs and assess the impact of the clocking and potential effect.

As indicated in Table 8.1, the inclusion of the NGVs inside the simulations increases the number of mesh elements by about 20 million cells in both LE and PA cases compared to the w/o case. Around each blade, five layers of prisms are used around the airfoils to better resolve the gradient normal to the wall and tetrahedral cells are used in the rest of the domain. Figure 8.4 shows some views of the surface mesh at different locations around the airfoil. Note that as one is not interested in the flow downstream of the vanes (no rotor etc.), the wakes are not particularly resolved (see Fig. 8.4d).

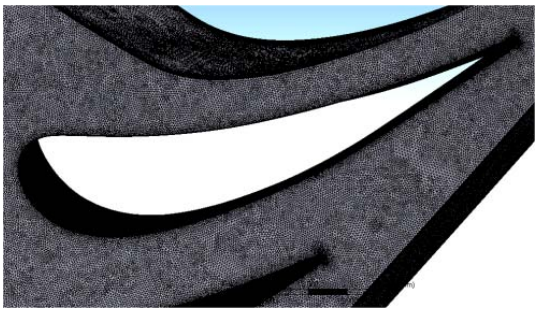

**(a)** Surface mesh at NGV hub.

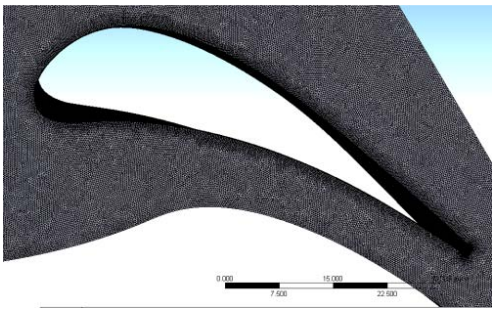

**(b)** Surface mesh at NGV tip.

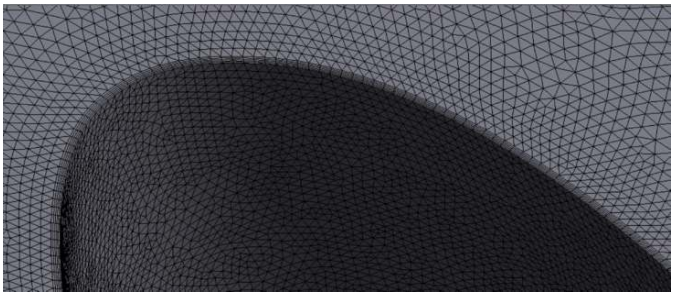

**(c)** Mesh around the LE (at tip).

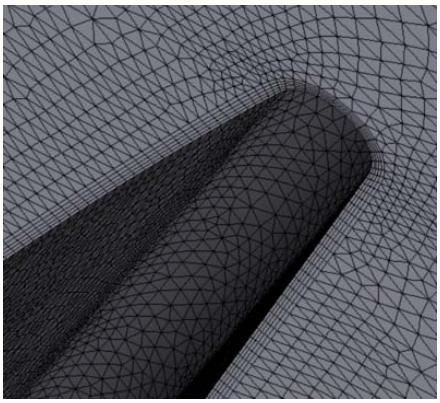

**(d)** Mesh around the TE (at tip).

**Figure 8.4:** Details of the mesh around the NGVs.

It needs also to be underlined that by lack of time and although computations are still on-going, the LES of the CS equipped with vanes could not be simulated for more than 50 ms (see Table 8.1) which restrains a little the possible post-processing analyses in light of the work in Part III for example. The results presented hereafter have therefore to be considered as preliminary analyses and are based only on time-averaged solutions. In terms of organization, Section 8.2 focuses on the differences between the two clocking positions while Section 8.3 evidences the potential effect induced by the presence of the vanes.

## 8.2 Influence of the clocking position

The clocking between the HS generator (i.e. the swirler) and the vanes is known to significantly impact the heat flux on the surfaces of the turbine [63–65] as discussed in Chapter 1. The two clocking positions are therefore compared based on the thermal field with the aim of determining how the HS migrates throughout the vanes and how this affects the wall temperature.

### 8.2.1 Migration of the hot streak

The HS entering the NGVs can be localized by an isocontour of an arbitrary value of the total temperature as shown in Fig. 8.5 for a time-averaged solution. For

the LE case, the HS hits directly the LE, wraps around the vane and remains in contact with the NGV surface. The impact of the HS with the vane seems to promote the mixing as the isocontour of temperature does not reach plane 41 (exit of the NGVs). On the other hand, for the PA case the HS seems to flow smoothly throughout the passage and ultimately reaches plane 40 with a more coherent shape. Even if not clearly visible in Fig. 8.5b, the isocontour of temperature does not touch the SS of NGV2 which may imply a less important heating effect as compared to the LE case (for the NGV1).

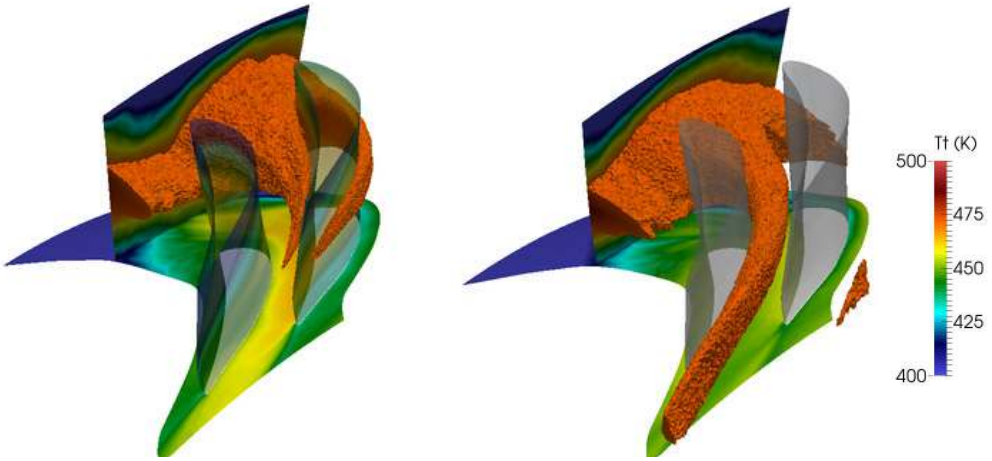


**(a)** Clocking LE. **(b)** Clocking PA.

**Figure 8.5:** HS evidenced by an isosurface of total temperature at 470 K emitted from plane 40.

A more comprehensive illustration of the transport of the HS through the vanes is given in Fig. 8.6 by showing the total temperature fields at successive axial positions. The temperature evolution in the vanes passage confirms that the HS is more preserved for the PA case and is still clearly identifiable at the exit of the NGVs (position A in Fig. 8.6). Interestingly, the evolution of the coolant flow in the passage (especially from the outer cavity) is also affected by the clocking position. Indeed, for the LE case the cold flow initially located near the upper endwall in plane 40 (B) seems to be driven inwards when going through the passage (possibly by secondary flows) and ultimately concentrates into a very segregated zone of cold fluid close to the wake and the SS of NGV2 ($C_1$). On the other hand, for the PA case larger zones of coolant flow are found all over the pitch (D) and a well-defined pocket of cold fluid near the PS of NGV2 ($C_2$) that is not observed for the LE case.

To help apprehending such temperature distributions, Fig. 8.7 shows an isosurface of temperature (380 K) evidencing the flowpath of the coolant flow. While one observes for the LE case a massive migration of coolant flow (from the outer cavity) towards the SS of NGV2 ($C_1$), the cold flow tends to preferentially migrate towards the PS of NGV2 for the PA case, even if a little amount of coolant goes towards the SS ($C_2$). One also observes an accumulation of coolant flow on the SS of

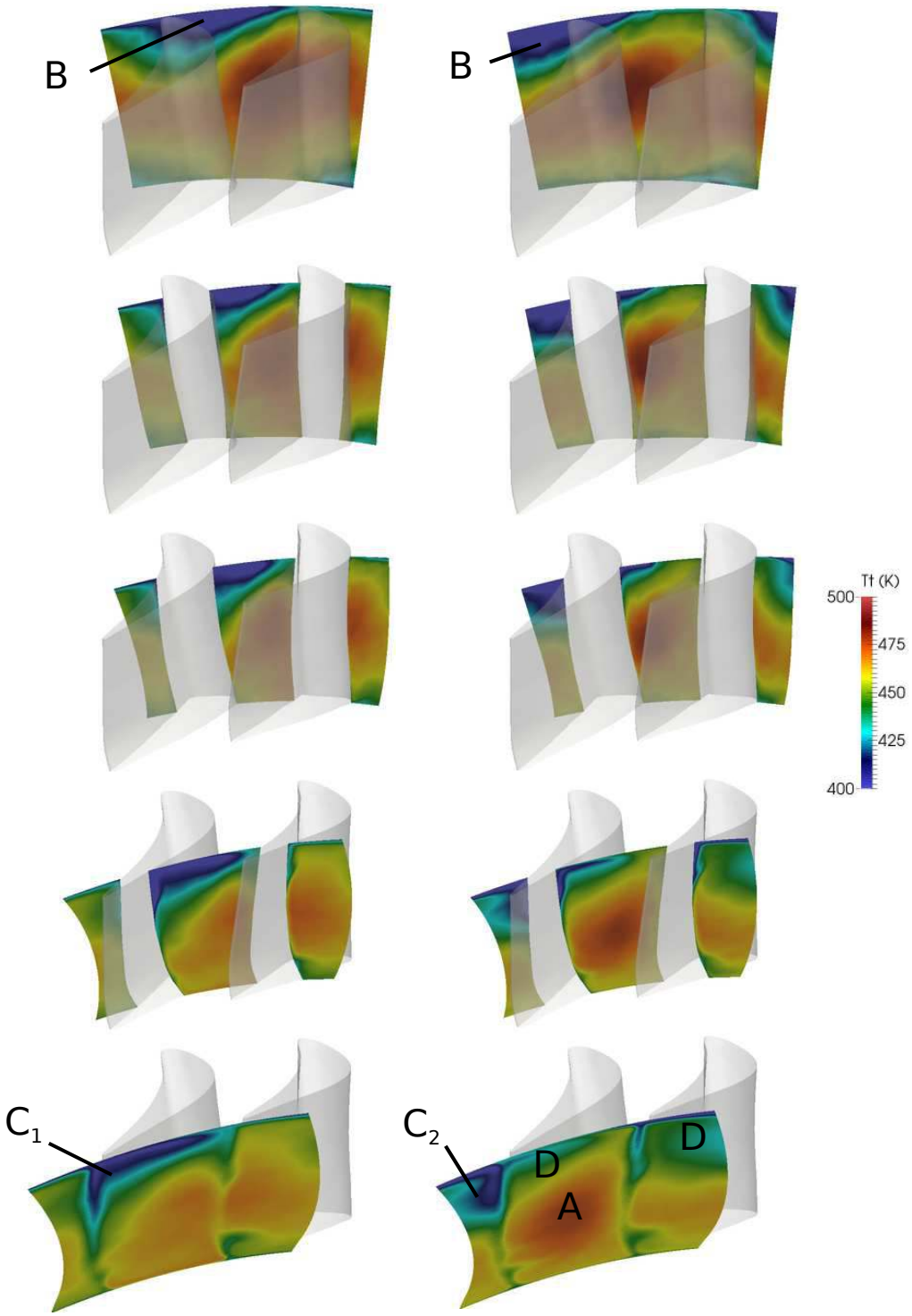


**(a)** Clocking LE. **(b)** Clocking PA.

**Figure 8.6:** Migration of the HS throughout the vanes evidenced by contours of total temperature at different axial positions from plane 40+ to plane 41.

NGV1 ($C_3$) which comes from the adjacent sector. This observation complements previous findings on the importance of the transport of the coolant flow from the combustor to the turbine exit [82, 148] by highlighting the significant impact of the clocking position. This also confirms the importance of using 2-D fields at the inlet of turbine which properly account for such azimuthal heterogeneities.

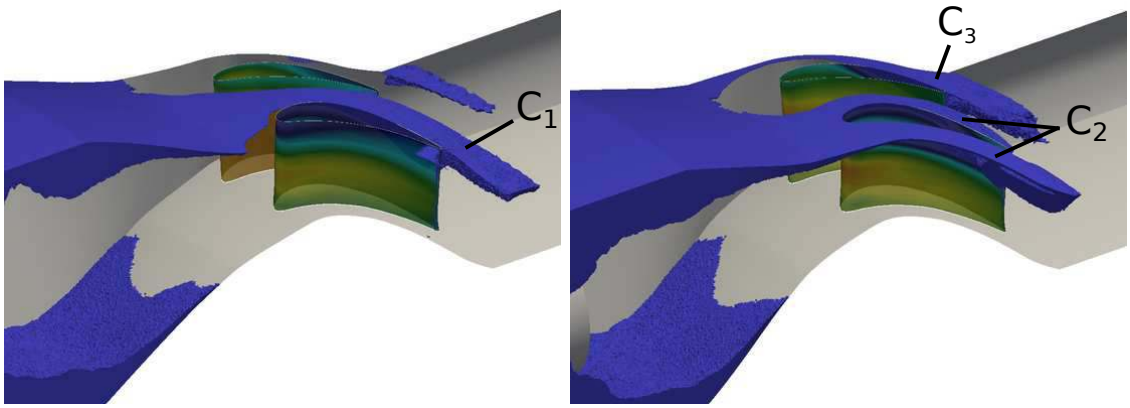


**(a)** Clocking LE. **(b)** Clocking PA.

**Figure 8.7:** Coolant flow evidenced by an isosurface of total temperature at 380 K.

The significantly different temperature distributions observed for the two clocking positions suggest that the heat transfer on the walls is affected. This is for example visible in Fig. 8.5 as the fluid temperature at the inner endwall is much hotter[1] for the LE case. Moreover, passage to passage variations are found as the central passage of the LE case is hotter than the two adjacent ones. If such differences are observed for the endwalls, it is likely to find similar trends on the surfaces of the two vanes. These features are specifically proved in the following section.

### 8.2.2 Vane surface temperature

The adiabatic wall temperature on the skin of the two vanes is shown in Fig. 8.8 for both clocking positions complemented by the corresponding mean surface values. It immediately appears for both cases that: *(i)* the NGV1 is hotter than NGV2 ; *(ii)* most of the hot fluid concentrates on the PS. Despite these similarities, significant differences exist between the two clocking positions. First while NGV2 has about the same mean temperature regardless of the clocking, the NGV1 of the LE is much hotter as it is directly impacted by the HS with a very strong accumulation of hot fluid on the PS. For the PA case, the HS itself has a reduced impact on the adiabatic wall temperature as the hottest flow is located away from the walls (see Fig. 8.5). The different migrations of the coolant flow identified in Fig. 8.7 however significantly impact the wall temperature of the vanes for both clocking positions even if particularly noticeable for the PA case. Indeed, one

[1]With the adiabatic conditions employed for these LES.

observes the local accumulation of coolant on the SS of the vanes ($C_1$,$C_3$) and the massive migration of coolant flow in the tip region all around NGV2 for the PA case ($C_2$). In that respect, the NGV1 for the LE case radically differs from all the other vanes by a very little amount of coolant flow on its surface.

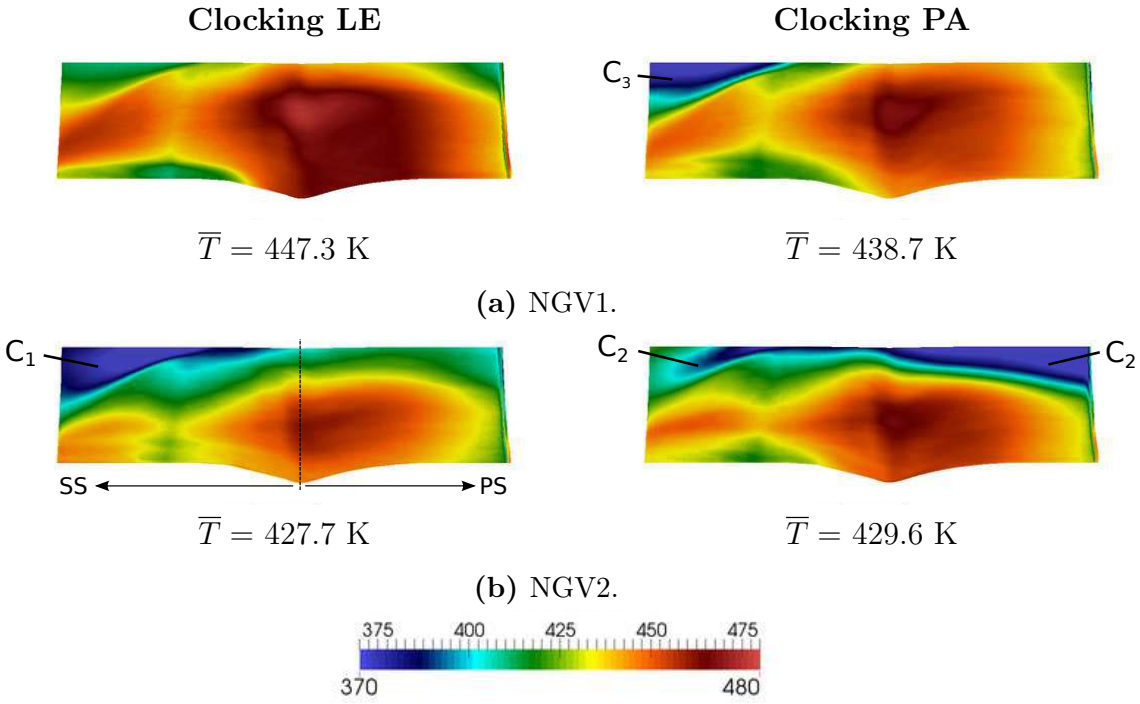


**(a)** NGV1.

**(b)** NGV2.

**Figure 8.8:** Adiabatic wall temperature [K] on the two vanes.

Having knowledge of the large differences observed between the two clocking positions in terms of temperature distributions, it is now proposed to investigate the potential effect created by the presence of the vanes on the flow field inside the CS.

## 8.3 Potential effect induced by the vanes

The existence of a potential effect due to the presence of the vanes at the exit of the chamber has been observed by various authors [27, 92, 95] as described in Chapter 1. The main question —that has not been answered on a universal basis— is:how far upstream the NGVs can the potential effect be observed ? In the specific context of the FACTOR configuration, this also questions its impact on the measurements performed in plane 40 of the trisector rig without vanes when the final DLR rig will be equipped with the HP turbine. To address this issue, it is proposed here to investigate the flow field disturbance upstream of the vanes by comparing the LES without NGVs to the LES with vanes for the two clocking positions. Such comparisons are performed based on the mass flow distributions (Section 8.3.1), temperature fields (Section 8.3.2) and turbulence levels (Section 8.3.3).

### 8.3.1 Mass flow distribution

The influence of the vanes on the mass flow distribution created by the HS is investigated first. To do so, the contours of axial momentum at a constant radius located at midspan of the vanes LE are shown in Fig. 8.9 and indicate that the presence of the vanes impacts the mass flow distribution when approaching the NGVs. Indeed, the blockage created by the NGVs brings the flow towards the passage between the vanes while the flow velocity in front of the vanes LE reduces considerably. As a result of such flow deviation, azimuthal heterogeneities of mass flow distribution are expected upstream of the vanes. This is confirmed by Fig. 8.10

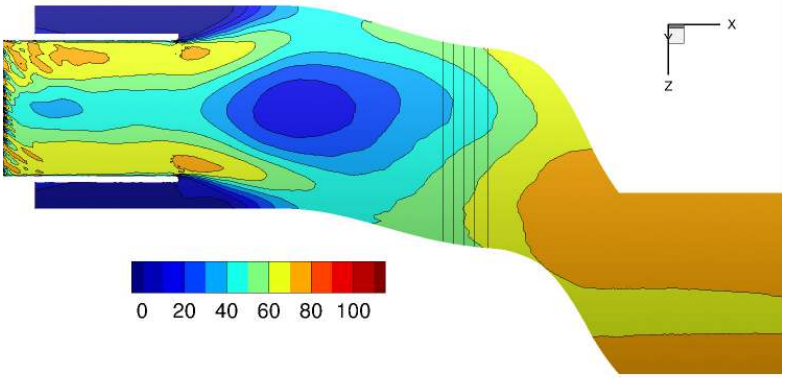


**(a)** Without NGVs.

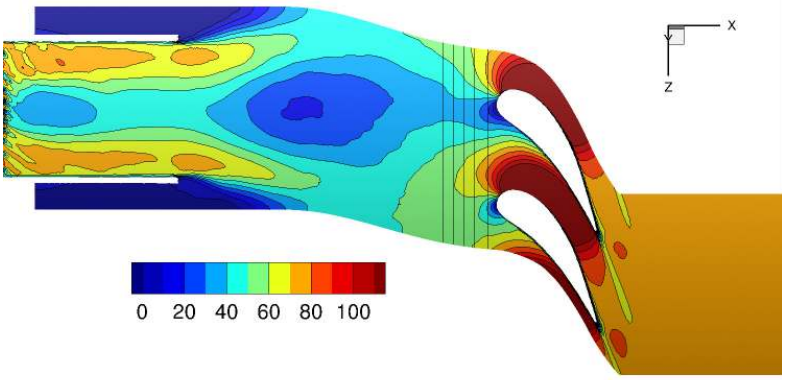


**(b)** Clocking LE.

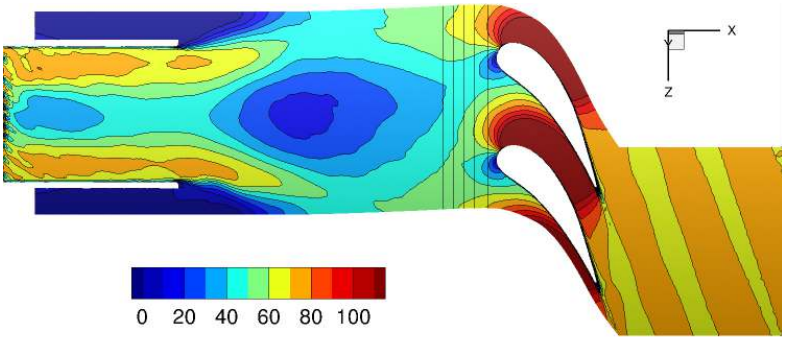


**(c)** Clocking PA.

**Figure 8.9:** Axial momentum $\bar{\rho}\bar{V}_x$ [kg/m$^2$s] at midspan of the vane LE.

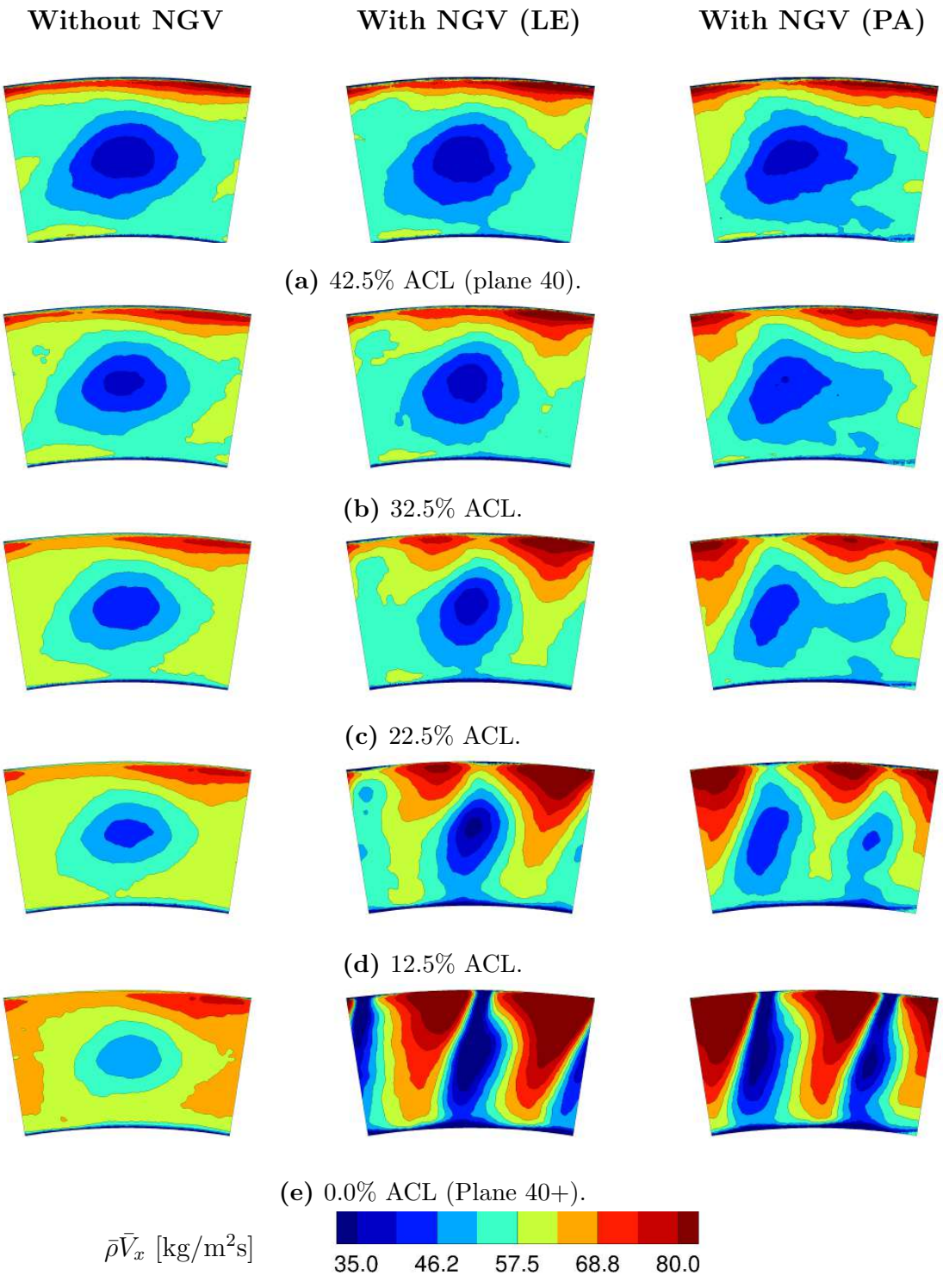


**(a)** 42.5% ACL (plane 40).

**(b)** 32.5% ACL.

**(c)** 22.5% ACL.

**(d)** 12.5% ACL.

**(e)** 0.0% ACL (Plane 40+).

**Figure 8.10:** Axial momentum in the CS at successive axial positions from plane 40 to plane 40+.

which shows the fields of axial momentum at various axial stations from plane 40 to plane 40+, the respective positions being shown by black lines in Fig. 8.9. Note that the axial position is measured in percentage of ACL upstream of plane 40+ which is taken as the reference (plane 40 is thus located at 42.5% ACL). The presence of the vanes indeed impose a noticeable axial momentum redistribution on the azimuthal direction to bring the flow towards the vanes passage when approaching plane 40+. The flow blockage by the vanes thus leads to considerably different fields of axial momentum in plane 40+ (Fig. 8.10e) when comparing the simulations with and without NGVs but also the two clocking positions because of the different position of the passage. Such potential effect is however limited to about 30% ACL upstream the vanes and thus does not affect plane 40.

To complement this analysis, time and circumferentially-averaged profiles of axial momentum produced in Fig. 8.11 indicate that the radial distribution of mass flow is identical for the LE and PA cases which confirms that the clocking position mostly leads to azimuthal non-uniformities non visible on such plot. The inclusion of the NGVs however leads in both cases to a radial redistribution of mass flow compared to the simulation without vanes. In plane 40+, the mass flow rate concentrates in the tip region (+14% vs. w/o) while the hub region is unloaded (-11%). Such increase of axial momentum at the vane tip can possibly be linked to the bended shape of the vanes (see Fig. 8.2) which blocks the flow earlier at tip than hub.

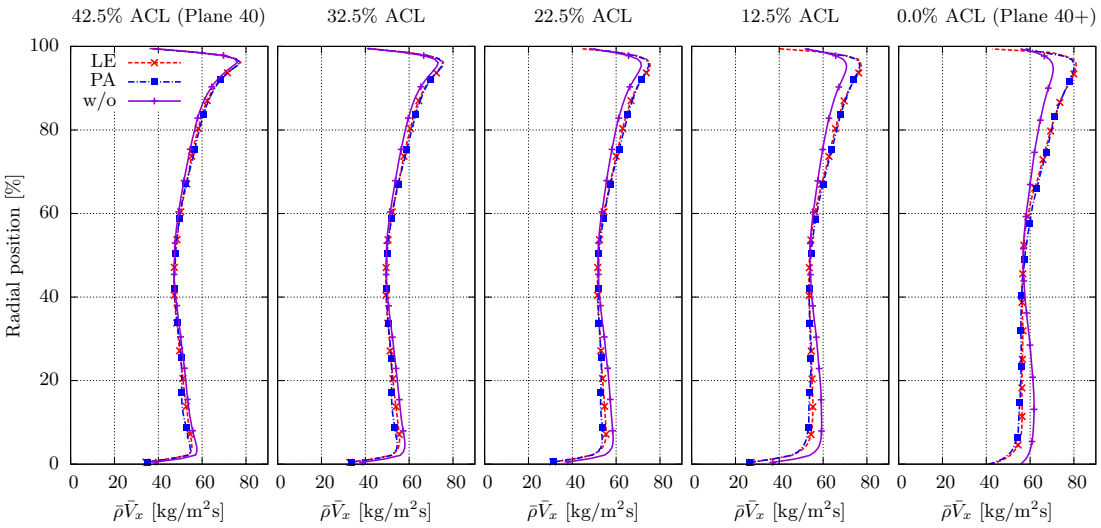


**Figure 8.11:** Circumferentially-averaged profiles of axial momentum at five axial stations from plane 40 to plane 40+.

### 8.3.2 Temperature

The influence of the vanes on the temperature distortion created by the HS is now investigated. Figure 8.12 shows the contours of the temperature coefficient $\Xi$ defined in Eq. (4.1) in a midspan cut. These contours provide an additional illustration of the different HS migrations observed for the two clocking positions. The

comparison between Fig. 8.12b and Fig. 8.12c clearly evidences the better preservation of the HS when it is injected in the passage between two vanes. Upstream of the vanes, the temperature field however seems identical with and without NGVs.

This observation however needs further confirmation which is provided by the contours of temperature coefficient shown in Fig. 8.13 at various axial positions between plane 40 and plane 40+. The comparison of the three simulations indicate that the presence of the vanes does not affect the temperature field upstream plane 40+ as very little differences are observed between maps. In the three cases, the mixing with the cold fluid tends to concentrate the HS in the core region as

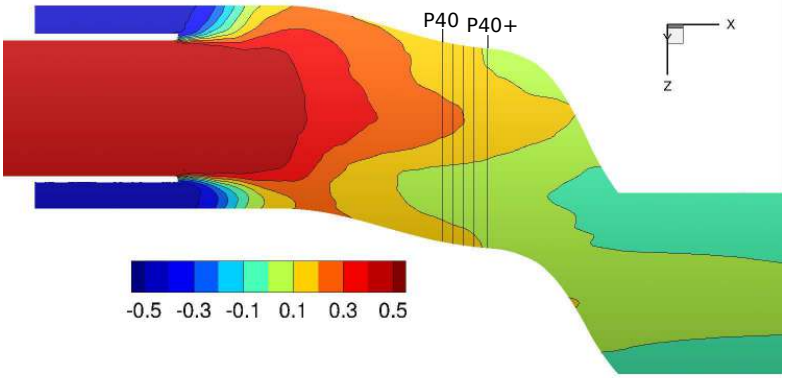


**(a)** Without NGVs.

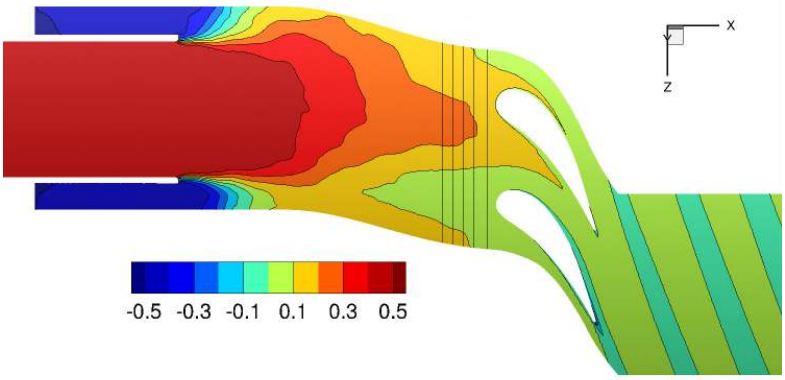


**(b)** Clocking LE.

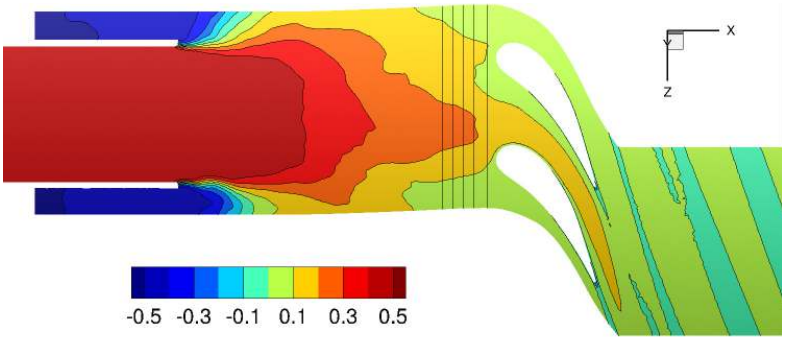


**(c)** Clocking PA.

**Figure 8.12:** Temperature coefficient $\Xi$ [-] at midspan of the vane LE.

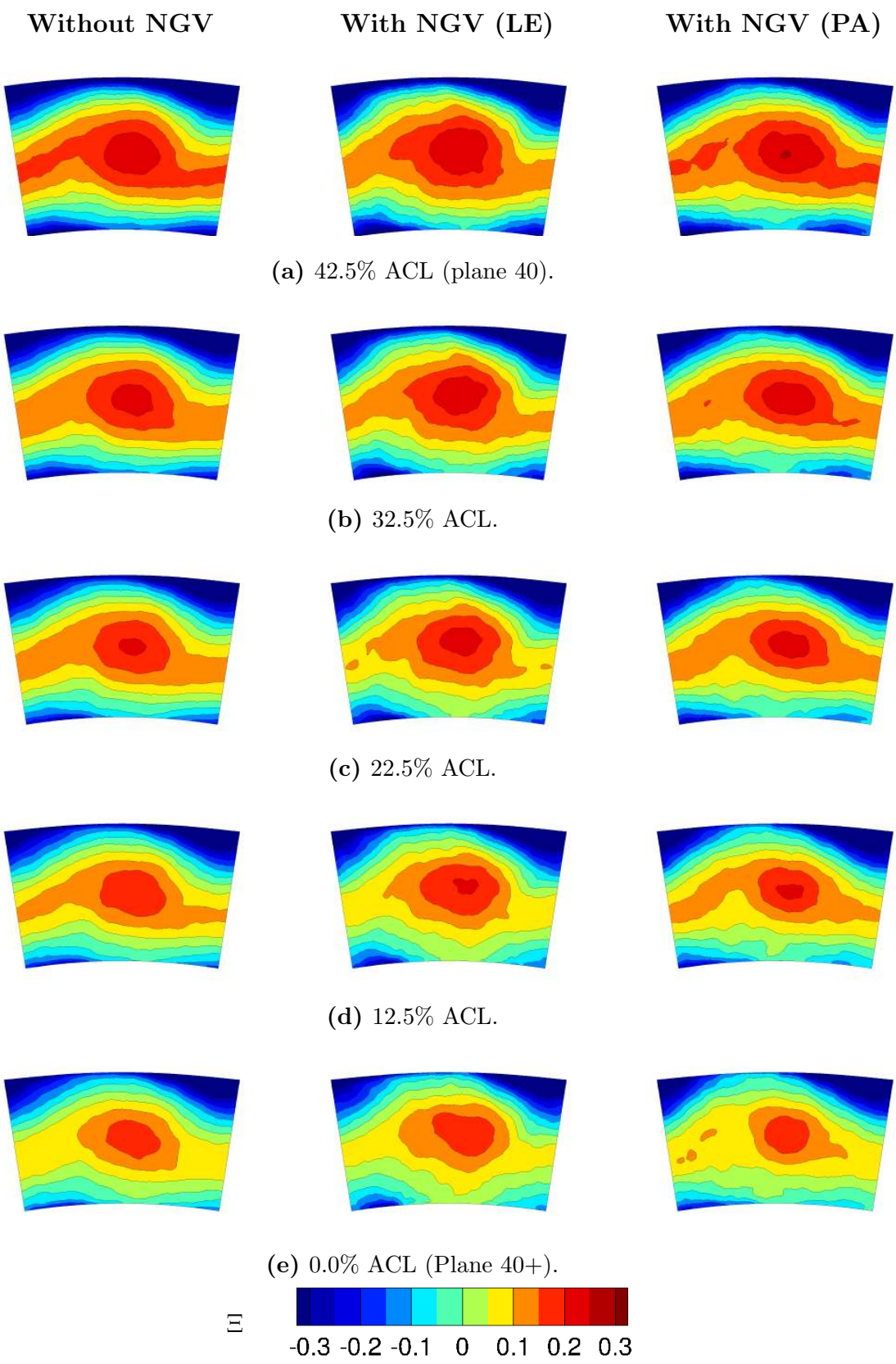


**(a)** 42.5% ACL (plane 40).

**(b)** 32.5% ACL.

**(c)** 22.5% ACL.

**(d)** 12.5% ACL.

**(e)** 0.0% ACL (Plane 40+).

**Figure 8.13:** Temperature coefficient Ξ [-] in the CS at successive axial positions from plane 40 to plane 40+.

the distance to plane 40 increases. At the inlet of the NGVs (Fig. 8.13e), the HS is clearly identifiable in the center the plane and the coolant localizes at the same position for the three cases. Quantitatively, Fig. 8.14 shows the time and circumferentially-averaged profiles of the 2-D fields shown in Fig. 8.13. Such profiles are distinctly not affected by the presence of the vanes which indicates that no radial segregation is introduced by the NGVs. Not-reported plots show similar conclusions can be drawn for the azimuthal direction. One can notice on these graphs that the tip region ($R \rightarrow 100\%$) is much colder than the hub ($R \rightarrow 0\%$), resulting in a strong radial distortion of the temperature profile in plane 40+. This is the direct illustration of the previously mentioned quicker mixing of the inner coolant flow (see the cold flow contours in Fig. 8.7).

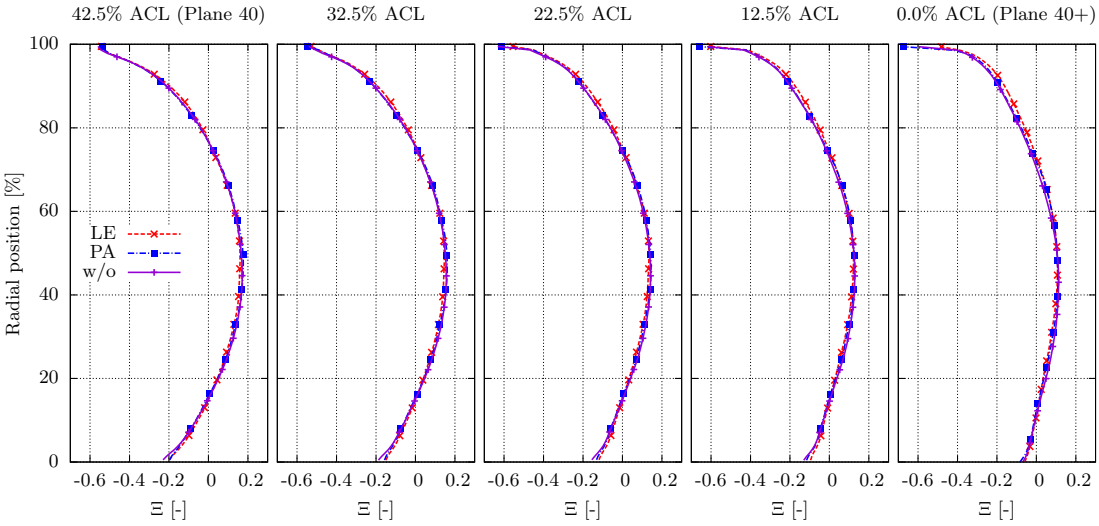


**Figure 8.14:** Circumferentially-averaged profile of temperature at five axial stations from plane 40 to plane 40+.

### 8.3.3 Turbulence level

The impact of the presence of vanes on the turbulence level is now investigated by comparing the different levels of resolved turbulent kinetic energy for the three simulations. Such turbulence results have to be handled with care in light of the analysis performed in Section 6.2 as the total simulated time (50 ms) is a little small to allow a full convergence of the RMS quantities (and thus $k_{res}$). The contours of $k_{res}/U_{ref}^2$ shown in Fig 8.15 indicate that higher levels of turbulence are located in correspondence with the hot gases and transported accordingly throughout the NGVs. The alteration of the turbulence field upstream of the vanes is found to be more important for the PA case than for the LE case. Higher levels of turbulence are indeed observed on the SS of NGV2 and this zone even extends upstream of the vanes.

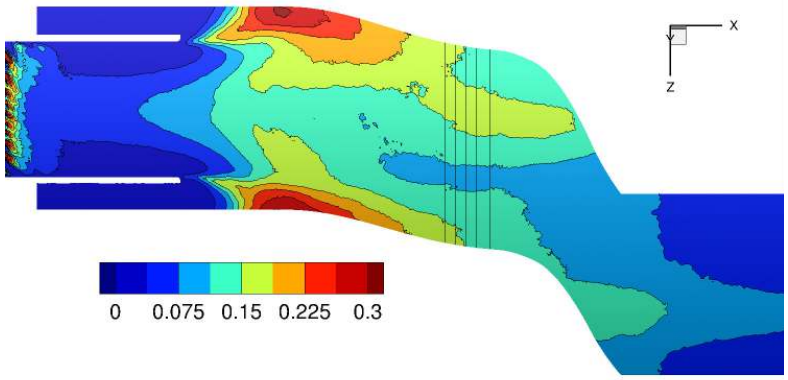


**(a)** Without NGVs.

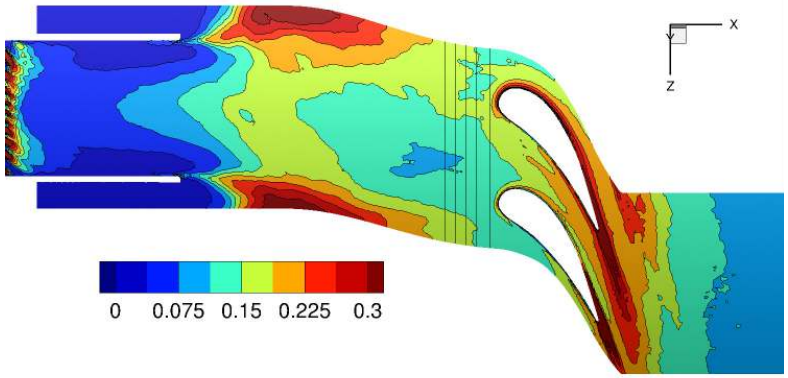


**(b)** Clocking LE.

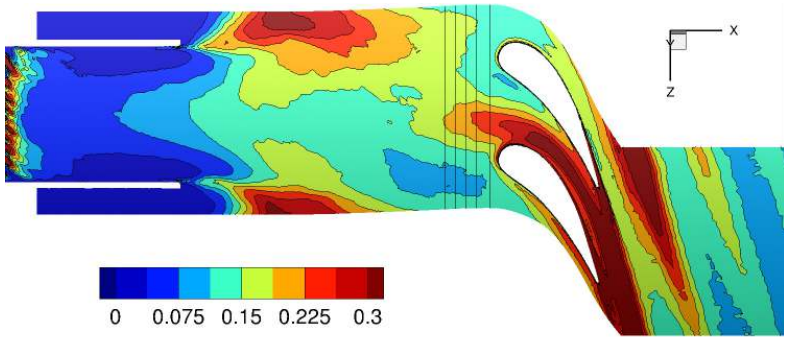


**(c)** Clocking PA.

**Figure 8.15:** Turbulent kinetic energy $k_{res}/U_{ref}^2$ [-] at midspan of the LE.

The fields of $k_{res}/U_{ref}^2$ in the successive axial positions between plane 40 and 40+ are shown in Fig. 8.16 and confirm this observation. In the absence of vanes, the overall turbulence level smoothly decreases downstream of plane 40 and the higher levels in the core are maintained until plane 40+. Comparatively, the presence of vanes slightly increases the turbulence level in plane 40 mainly by reinforcing $k_{res}$ in the center of plane 40+. This is especially true for the PA case and this effect is noticeable upstream of the vanes until plane 40.

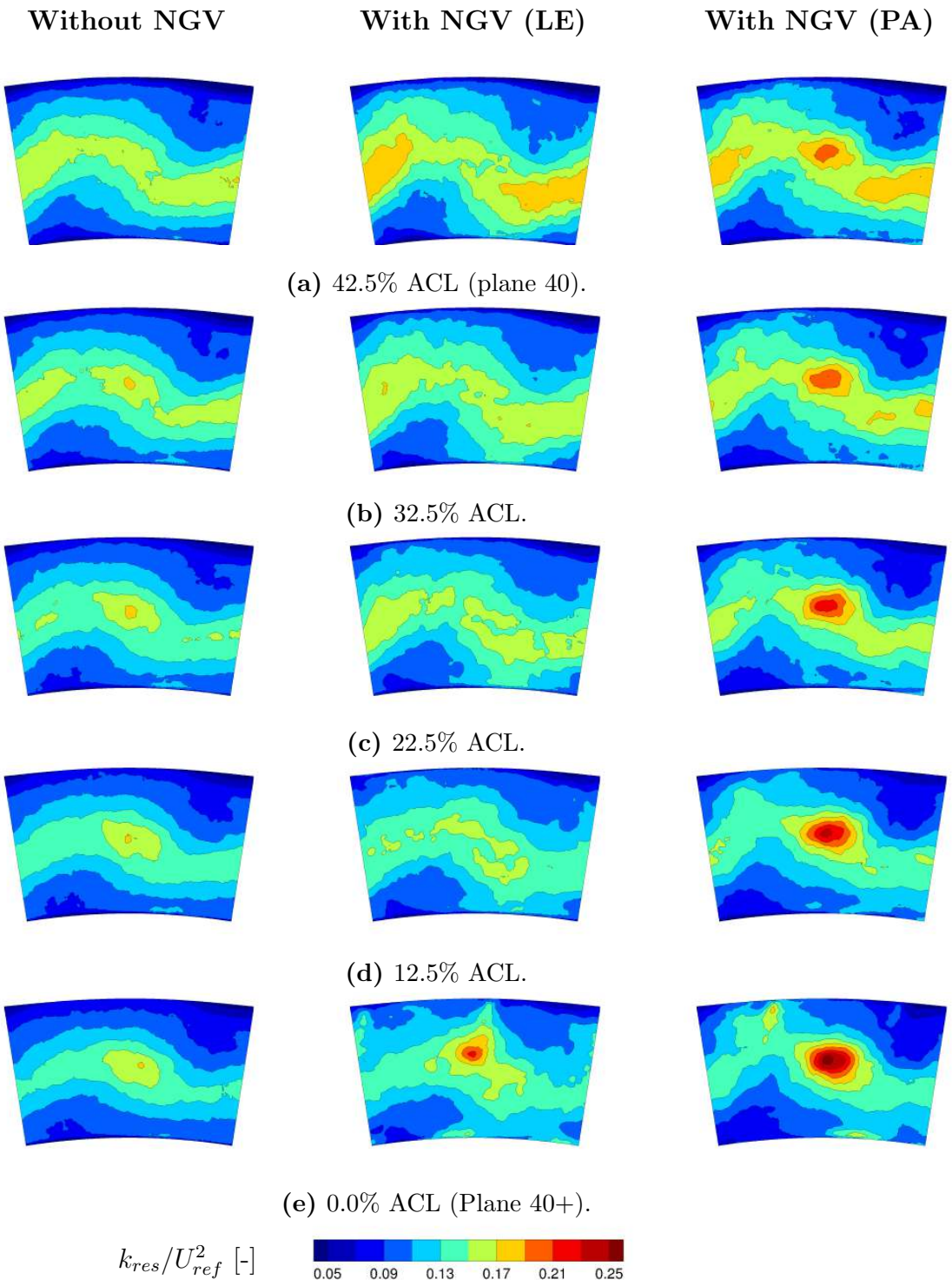


**(a)** 42.5% ACL (plane 40).

**(b)** 32.5% ACL.

**(c)** 22.5% ACL.

**(d)** 12.5% ACL.

**(e)** 0.0% ACL (Plane 40+).

**Figure 8.16:** Turbulent kinetic energy in the CS at successive axial positions from plane 40 to plane 40+.

The circumferentially-averaged profiles corresponding to the 2-D fields shown in Fig. 8.16 are plotted in Fig. 8.17a and indicate that the overall turbulence level is not altered by the presence of vanes. Moreover, based on the azimuthal averaging operation, no difference is observed between the LE and PA cases. A more local comparison is provided in Fig. 8.17b by the profiles of $k_{res}/U^2_{ref}$ along the centerline at the same axial positions. These plots numerically confirm that the maximum turbulence level in the core region is increased for the PA until plane 40. In comparison with the case without NGVs, this local augmentation is limited to 17% in plane 40 but reaches 50% in plane 40+. This is in strong contrast with the LE case for which one observes a local increase of 25% only in plane 40+ (i.e. just in front of NGV1 LE).

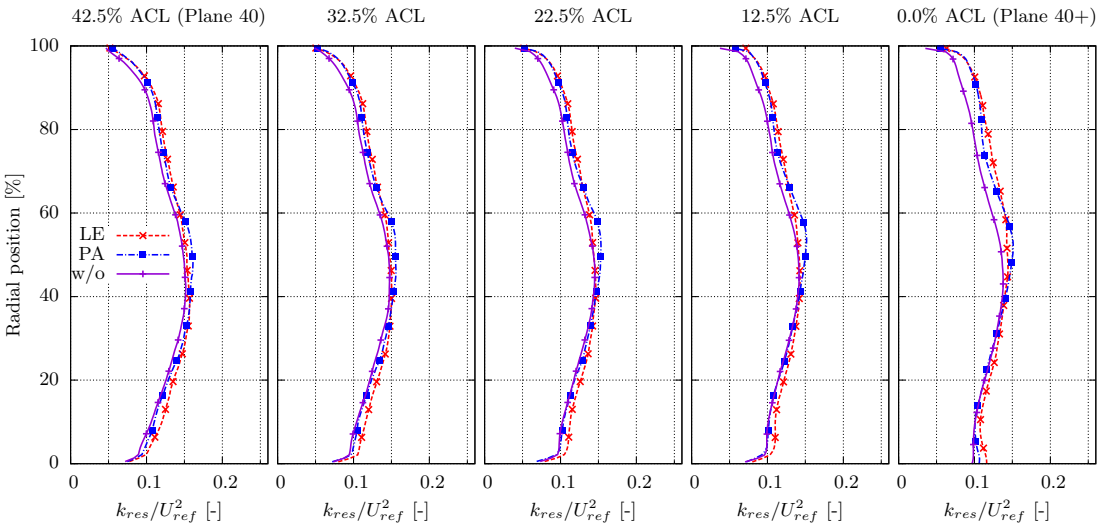


**(a)** Circumferentially-averaged.

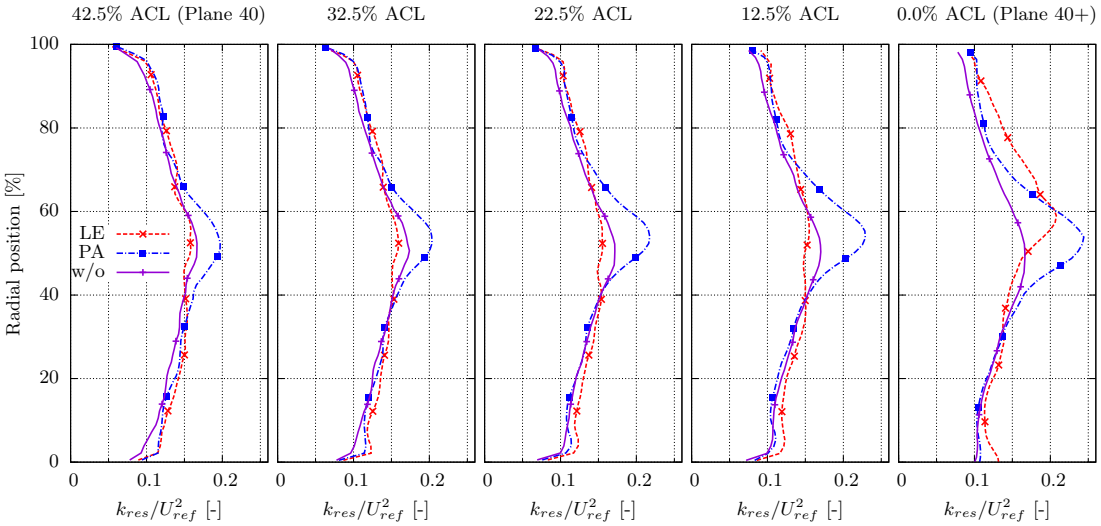


**(b)** On the centerline.

**Figure 8.17:** Radial profiles of turbulent kinetic energy at five axial stations from plane 40 to plane 40+.

## 8.4 Conclusions

Three LES are performed with the aim of investigating the chamber-turbine interactions for a Lean Burn CS featuring high levels of swirl and a temperature distortion. The preliminary results obtained from these simulations with or without vanes indicate that:

- The clocking (HS centered on the LE or the PA) has a noticeable effect on the transport of the HS throughout the vanes. The HS is more preserved for the PA case while temperature non-uniformities are smeared for the LE case after the HS has impacted the LE.
- The path followed by the coolant flow delivered by the CS effusion cooling systems is significantly altered by the presence of vanes and the clocking position.
- The count ratio of 1 HS for 2 NGVs and the different migrations of the coolant flow lead to important discrepancies in the vanes adiabatic wall temperature:
  - For the LE case, the HS impacts the LE of NGV1 and then flows on the vane PS, increasing the adiabatic wall temperature (NGV1 is thus 5% hotter than NGV2).
  - For the PA case, the HS itself has a reduced impact on the wall temperature as the hottest flow is located away from the walls but a strong migration of coolant flow is observed on the PS of NGV2 (as a result NGV2 is 2% colder than NGV1).
- The potential effect induced by the presence of the vanes at the exit of the CS is found to differently affect the flow quantities in the CS. While temperature patterns are not altered, a significant radial and azimuthal mass flow redistribution is observed up to about 25% ACL upstream of the vanes and the turbulence level is affected up to plane 40 for the PA case.
- Overall, the results presented here are in good accordance with the general findings of the literature (see Section 1.3) even if configuration-specific details cannot be properly compared.

The simulations presented here based on time-averaged results shall be further exploited in the future relying on the unsteady data to better apprehend all the flow characteristics. First, extensive characterization of the turbulence (intensity and level) through the vanes can be performed relying on the methodology proposed in Chapter 6 and compared to the existing information [75]. Second, the advanced diagnostics for the analysis of unsteady temperature fields proposed in Chapter 7 can bring new elements on the operating temperature envelope of the NGVs.

# General conclusion and perspectives

The design of a gas turbine does not rely solely on a performance calculation but results from the balance between the maximum engine efficiency and the mechanical integrity of the components. Because gas turbines rapidly imposed themselves as the reference technology to propel most aircraft, tremendous improvements were obtained in the last 40 years in terms of engine consumption and specific thrust or power. Such enhancements were made possible by pushing away the engine cycle limits (pressure, temperature) while improving the design of the different engine components. With this aim, the introduction of reliable and mature CFD techniques in the development processes (almost only RANS approaches) considerably helped optimizing the design of the components. Nowadays, each individual engine module reaches efficiency levels to a point where any gain can only be the result of a significant effort and cost or a major technological breakthrough. As a consequence, researchers and design teams tend to focus more on the interactions between engine components as gains in overall engine performance can be obtained by better apprehending the component interactions.

In this context, many studies were launched since the 90's to better qualify the interface between the combustion chamber and the high pressure turbine as it constitutes the most critical part of the engine in terms of temperature, pressure and stress levels. At this interface, the flow field is by nature highly unsteady because of the combustion and mixing taking place in the burner. Moreover, the discrete position of the fuel injectors and cooling devices inside the chamber enhance the flow non-uniformities. It is known that such flow distortions can cause aero-thermal changes within the high pressure turbine vane and rotor, altering the aerodynamics, secondary flows, blade loading, heat transfer, losses, efficiency and life duration.

These flow features have been extensively studied for RQL combustor architectures for which the main hot flow stream is heavily cooled down by feeding the chamber with a lot of fresh air. Such combustor configuration however tends to be replaced by the so-called Lean Burn architecture for which cooling is only provided by effusion devices to save air for NOx control and shield the chamber walls from

the hot gases. This new generation of combustors features a high level of swirl in the chamber as well as advanced cooling systems for which design methodologies are less mature than for RQL combustors and still cause difficulties in the design of turbine stages.

In this context, the European research project FACTOR was launched in 2010 with the aim of better understanding the transport of HSs from the combustor to the turbine in Lean Burn configurations. To do so, FACTOR partners agreed to build a new test rig hosting a modern aero-engine CS and a 1.5 high pressure turbine stage operating at realistic Reynolds and Mach numbers. Within this framework, this PhD work was funded by Turbomeca in collaboration with CERFACS to improve the current characterization of the combustor-turbine interface. The objectives of this study were determined as follows: (1) Contribute to the design of a non-reactive engine-representative CS; (2) Develop a new test rig in close collaboration with the University of Florence (Italy), including the definition and integration of the measurement techniques and the use of pre-test LES to analyse the flow in the test module; (3) Qualify the combustor-turbine interface by means of high fidelity simulations and the use of advanced diagnostics; (4) Assess the current LES methodology for the calculation of the combustor exit flow quantities relying on the comparison with experiments when available. To address all the objectives of this PhD work, an extensive use of HPC resources was made necessary. A typical simulation of the CS (with a medium size mesh) was obtained after 16 days of non-stop computation over 512 cores (see details in Appendix C). The LES presented in the manuscript were performed on various machines either internal (CERFACS) or external (IDRIS-Genci), for a total CPU cost estimated to about 10.1 Mhrs.

The main outcomes of this PhD work are summarized here within three topics:

**Development and exploitation of the CS**

- Based on a CS design proposed by Turbomeca for which a duct of variable length is introduced at the exit of the swirler, LES were performed to discriminate the best candidate in regard of the FACTOR targets. The configuration with the 55 mm long duct was finally retained based on LES and experimental results as it was found to reasonably well represent the flow at the exit of a Lean Burn chamber: a central hot streak and a high level of swirl and turbulence.

- A test rig featuring three sectors of the CS was developed in collaboration with UNIFI, including the definition of the instrumentation, test matrix and operating points. In addition to the tests performed at nominal conditions, an isothermal operating point required for turbulence measurements by HWA was selected relying on the use of an algebraic model developed specifically for the trisector rig. The choice of this operating point was validated by the use of LES introduced at the early stage of the design.

- The pre-test LES performed in blind conditions were confronted to the rich experimental database obtained on the trisector rig. Overall, a good agreement was observed for all quantities which provided an *a posteriori* validation of the simulations. In light of the current state of the art for the computation of the combustor exit flow quantities, the LES presented here constitute an improvement of the methodology. It was however found that the model used to represent the effusion cooling in the simulations may not accurately reproduce the real 3-D shape of the coolant flow and thus impact the prediction of the flow velocity in the lower part of plane 40.

- The LES methodology was assessed by investigating the sensitivity of the results to the numerical parameters. Three mesh sizes and two SGS models were benchmarked based on four simulations. It was found that the mesh density in the swirler has a strong impact on the prediction of the turbulence level and velocity profiles at the swirler exit which in turn affect the prediction of the flow inside the CS. Overall the mesh size was observed to be more discriminant than the SGS model.

**Advanced diagnostics**

- Even if of importance for the turbine, turbulence quantities are rarely investigated for engine-like configurations because of the difficulty to perform measurements or obtain reliable data from simulations. To address this lack, it was intended to qualify the turbulence at the exit of FACTOR CS, in terms of intensity and integral scale based on experimental (HWA) and numerical (LES) data. Special attention was given to the specificities of the two approaches before performing any comparison. Specifically, the bias introduced by the duration of the signal (35 times smaller for LES than HWA) was quantified and discussed. Having knowledge of all the associated uncertainties and if furthermore compared to the current state of the art on the topic, the agreement between LES and HWA based on relative quantities was found to be excellent. Such results clearly indicate the potential of LES for the investigation of high order turbulence quantities of complex flows.

- An advanced analysis of temperature distributions was proposed relying on the statistical analysis of the time-dependent data provided by LES. This approach highlighted the existence of a most probable temperature different from the mean one, indicating the presence of segregated zones of temperature ascribed to the technological implementation of the cooling systems. A more appropriate characterization of the combustor exit temperature profile was thus proposed by considering the sampling-dimension in addition to the common (radius, temperature) representation (LRTDF). This new diagnostic allows to fully characterize the temperature envelope of the combustor exit. This simple diagnostic can immediately be applied during the design process of a combustor to assess the quality of the mixing at the chamber exit.

**Integrated simulations of the CS with NGVs**

- Three LES were performed to understand the impact of the presence of NGVs at the exit of the CS (for this specific Lean Burn configuration). The clocking position between the HS exiting the swirler and the vanes was found to strongly impact the temperature field in the vanes passage and on the walls:
  - When the HS is injected in front of the LE, it considerably heats up the vane PS compared to the adjacent ones but the temperature field is quite uniform at the vanes exit because of the temperature redistribution.
  - When the HS is injected in the passage, it remains away from the walls preventing them to heat up but crosses the vanes passage without being significantly distorted.
- The potential effect induced by the presence of the vanes was investigated by comparing the flow field inside the CS with and without NGVs. It was found that the potential effect does not alter temperature patterns while a significant radial and azimuthal mass flow redistribution was observed up to about 25% ACL upstream of the vanes. Moreover, the turbulence level was affected by the presence of vanes up to plane 40 when the HS is aligned with the passage.

**Perspectives**

The results obtained on the different topics addressed during this work highlight some possible work perspectives:

(i) The representativity of the effusion cooling model in the LES was found to be questionable. Further work is required to verify such hypothesis and if confirmed, alternate proposals could be produced (meshing the holes, local model etc.).

(ii) The PIV test campaign at DP conditions that will be performed on the trisector rig should bring new elements for the comparison of LES and measurements. Specifically, PIV results that will be obtained in plane 40 at isothermal conditions will complement the already available 5HP and HWA measurements (Chapter 4) and help discriminating the techniques.

(iii) Further analysis could be performed to investigate the LES methodology. First, a wall-resolved simulation would help understanding the impact of the wall law model inside the swirler pointed out in Chapter 5. Second, a LES on the fine mesh and using the WALE SGS model would discriminate the best methodology.

(iv) The calculations of the turbulence timescale by means of two points correlations discussed in Chapter 6 could be applied to LES of any available industrial configurations to compare with this non-reactive CS. Specific tests

(assessment of the convergence of the estimation, verification of the non-periodicity of the signal) have already been implemented in order to safely apply such diagnostics. Finally, the methodology could be benchmarked by testing other approaches (e.g. correlations in space, signal decomposition).

(v) The integrated simulations of the CS with NGVs (Chapter 8) could be further exploited by investigating the unsteady data as soon as enough physical time is available. Specifically, the evolution of the turbulence level and integral scale through the vanes passage could be investigated especially in light of the encouraging results obtained in plane 40. Moreover, the temperature diagnostics proposed in Chapter 7 could be applied to these simulations to assess if the presence of the vanes impacts the time-envelope of temperature.

(vi) An ultimate analysis of the needs for having integrated simulations could be obtained by comparing the LES of the CS alone, the LES of the CS and vanes and a LES of the CS with all the HP turbine stage. In light of the available CPU power, such simulation is now definitely reachable at CERFACS [28].

# Appendix A

# Characterization of the effusion cooling system

## A.1 Description of the multiperforated plates

As detailed in Chapter 2, the FACTOR CS is equipped with two successive effusion cooling systems located on the inner and outer liners. The four multiperforated plates are built on the same principle, with the main dimensions shown in Fig. A.1 and described in Table A.1.

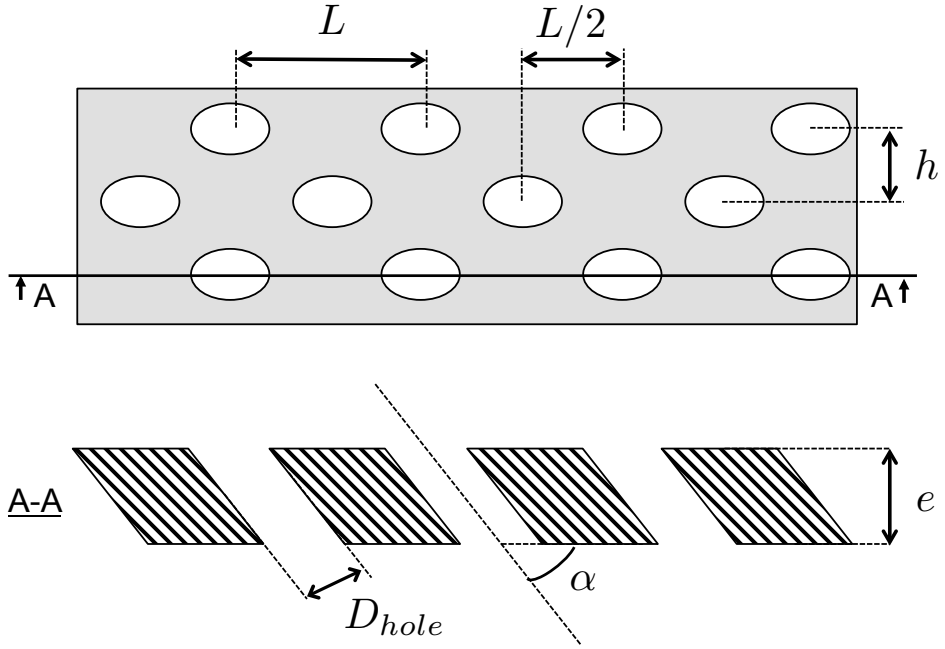


**Figure A.1:** Generic sketch of the multiperforated plates.

The permeability $\sigma$ of each multiperforated plate is defined as the ratio of the surface of the holes on the plate to the total plate surface:

$$\sigma = \frac{S_{holes}}{S_{plate}} \tag{A.1}$$

if the injection is not normal to the walls ($\alpha \neq 90°$), then the print of the hole on the surface is not a circle but an ellipse as shown in Fig. A.1.

| | MP ext 1 | MP ext 2 | MP int 1 | MP int 2 |
|---|---|---|---|---|
| Permeability $\sigma$ [%] | 7.72 | 11.5 | 9.6 | 10.4 |
| Mass flow [% $\dot{m}_{40}$] | 13 | 8 | 10 | 4 |
| $\alpha$ [°] | 60 | 30 | 60 | 30 |
| $L$ [mm] | 2.4 | 1.6 | 1.9 | 2.0 |
| $h$ [mm] | 1.0 | | | |
| $e$ [mm] | 2.0 | | | |
| $D$ [mm] | 0.45 | | | |

**Table A.1:** Geometrical and flow characteristics of the effusion cooling plates of FACTOR CS

## A.2 Experimental flow check on the trisector rig

Errors due to the manufacturing of the multiperforated plates (e.g. nominal diameter of the holes, repartition etc.) may introduce large discrepancies in the effective permeability of such systems. This would translate into an injection of momentum not matching the design conditions. Therefore, a flow check of each multiperforated plate was performed on the UNIFI trisector rig at the beginning of the test campaign.

The flow checks are performed simultaneously for one inner and one outer plate. The test procedure is detailed here:

- The two plates not under studied are blocked with tape (see Fig. A.2a).
- Isothermal ambient conditions are used ($T = T_{amb}$).
- The pressure in plane 40 is set to the DP value (147.65 kPa).
- The mass flow in the main line is set to a very small arbitrary value. Mass flow in one cavity is set to the DP value while the mass flow rate of the other cavity is varied around the DP value (4-6 measurements).
- The pressure drop created by each multiperforated plate is evaluated based on the pressure difference between the static pressure tapings in the cavity and in plane 40 (see Fig. A.2b). Due to the very small velocity of the flow ($M < 0.05$), total pressure is assumed to be equal to the static one.

The measurements of mass flow and pressure allow to calculate the pressure drop $\Delta P/P$ and the Non-Dimensional Mass Flow ($NDMF$) per unit area $NDMF/S$ for each test point:


**(a)** Flow check of MPint1 and MPext2. **(b)** Position of the pressure tapings.

**Figure A.2:** View of the trisector rig CS for the flow checks.

$$NDMF/S = \frac{1}{S}\frac{\dot{m}\sqrt{T}}{P} \tag{A.2}$$

$$\frac{\Delta P}{P} = \frac{P_{up} - P_{down}}{P_{down}} \tag{A.3}$$

The flow function of each multiperforated plate is then plotted as shown in Fig. A.3, with the value corresponding to the DP circled in black. As expected, the pressure drop is around 3.5% for all the plates operating at the DP conditions.

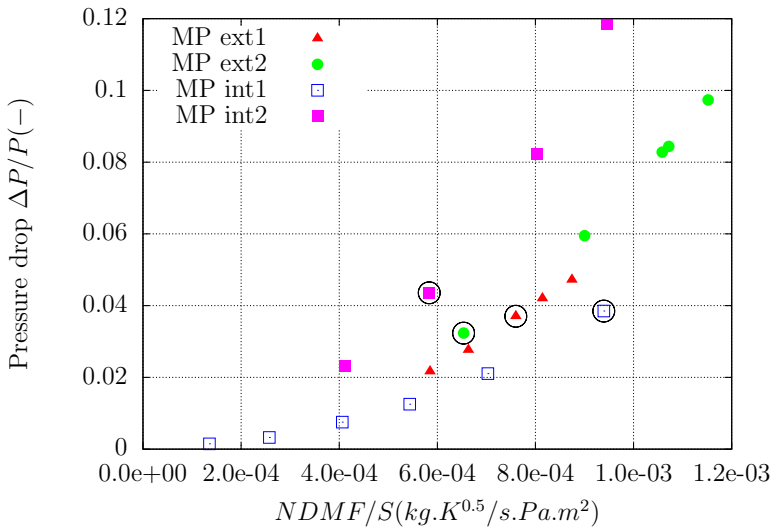


**Figure A.3:** Flow function of the multiperforated plates.

To evaluate the actual permeability of the plates, the effective area of each plate is assessed supposing an isentropic flow. Isentropic Mach number is thus calculated from the pressure difference:

$$M_{is} = \sqrt{\frac{1}{\gamma - 1}\left(\left(\frac{P_{up}}{P_{down}}\right)^{\frac{\gamma-1}{\gamma}} - 1\right)} \tag{A.4}$$

with $\gamma$ the ratio of specific heat of air, equal to 1.4 at ambient conditions. The isentropic velocity is computed from $M_{is}$ and $T_{is} = T$:

$$U_{is} = M_{is}\sqrt{\gamma R T_{is}} \tag{A.5}$$

The effective area $S_{eff}$ of an isentropic flow at a mass flow rate $\dot{m}$, density $\rho_{is} = P_{up}/RT$ and velocity $U_{is}$ is:

$$S_{eff} = \frac{\dot{m}}{\rho_{is} U_{is}} \tag{A.6}$$

The effective area is averaged over all the measurement points for the four plates and provides an estimate of the bulk area of the holes:

$$S_{bulk} = \sum_{1}^{N_{holes}} \pi D^2/4 = \frac{S_{eff}}{C_D} \tag{A.7}$$

with $C_D$ the discharge coefficient which depends on the shape of the holes. For cylindrical holes $C_D$ has a value of the order of 0.7 as used by Turbomeca.

The bulk area gives a direct knowledge of the porosity $\sigma'$ (not to mistaken with the permeability $\sigma$), defined as the ratio of the holes bulk area to the plate area $\sigma' = \dfrac{S_{bulk}}{S_{plate}}$. In the case of a purely streamwise injection (FACTOR CS) the permeability can be computed from the porosity knowing the angle of the holes: $\sigma' = \sigma\cos(\pi/2 - \alpha)$. To avoid any assumption on the real angle of the holes, comparisons between flow checks and design values are made on the porosity $\sigma'$ and shown in Table A.2. The agreement between flow checks for $C_D = 0.7$ and the target value is found to be good, which demonstrates that the trisector multiperforated plates are in agreement with the design values and with the values used for numerical simulations.

| | | Porosity $\sigma'$ [–] | | | |
|---|---|---|---|---|---|
| | | MP ext 1 | MP ext 2 | MP int 1 | MP int 2 |
| **Flow check** | $C_D = 0.65$ | 7.2 | 6.5 | 8.3 | 4.9 |
| | **$C_D = 0.7$** | **6.7** | **6.1** | **7.7** | **4.6** |
| | $C_D = 0.8$ | 5.9 | 5.3 | 6.7 | 4.0 |
| **Target value (design)** | | **6.7** | **5.75** | **8.3** | **5.2** |

**Table A.2:** Geometrical and flow characteristics of the effusion cooling plates of FACTOR CS.

## A.3 Homogeneous model for CFD of effusion cooling systems

The numerical simulation of FACTOR CS (and by extension of any combustor featuring effusion cooling systems) requires to account for the momentum injection through the multiperforated plates.

The most accurate way to include effusion cooling in the numerical simulations would be to insert the cavities and all the holes in the geometry. With this approach, holes must be sufficiently meshed to correctly capture the pressure drop and thus the flow distribution. However, the cost of meshing all the holes (5164 holes/sector in FACTOR CS) is definitely prohibitive. To circumvent such pitfalls, the homogeneous injection model for effusion cooling of Mendez et al. [105] is used to account for the momentum injection at the multiperforated plates. This model has been widely used at CERFACS and Turbomeca and is known to provide satisfactory results for purely streamwise injection, which is the case for the FACTOR CS. It is not intended here to give an extensive review of this method but the basic principles of the model are presented to better understand its implications on the numerical simulations.

Introducing an homogenization, fluxes are averaged over the plate surface ($\Phi_{model}$) without distinction of the wall ($\Phi_w$) or perforation ($\Phi_{jet}$). Though this homogeneous concept yields a good global approximation, it does not reproduce the flow near the wall due to the strong heterogeneity inherited from the suction side and the perforation arrangement relative to the plate size.

The basic principle is to rescale the wall normal velocity $V_n$ to inject the mass flow over the entire plate surface $S_{plate}$ while conserving the streamwise velocity $V_t$ whose momentum is given to the cooling film. In the following, the variables with a superscript ' refer to the model. The model is illustrated in Fig. A.4 for a single hole: the full black arrows are the real velocity components and the dashed red arrows are the vectors of the homogeneous model.

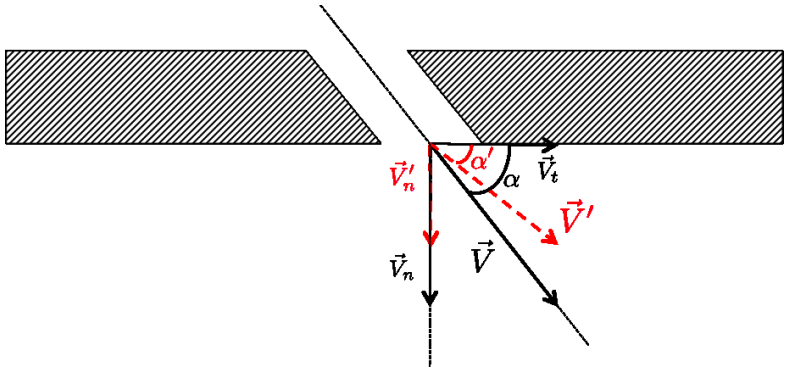


**Figure A.4:** Illustration of the homogeneous injection model for a single hole.

The mass flow conservation over a single hole gives an equation for $V_n$:

$$\dot{m} = \rho V_n' S_{plate} = \rho V_n S_{holes} \tag{A.8}$$

$$\therefore \quad V_n' = \sigma V_n = \sigma \frac{\dot{m} \cos(\pi/2 - \alpha)}{\rho \pi D^2/4} \tag{A.9}$$

while the streamwise velocity is supposed to be conserved:

$$V_t' = V_t = \frac{V_n}{\tan \alpha} \tag{A.10}$$

Therefore, the streamwise injection angle of the model $\alpha'$ is reduced compared to $\alpha$:

$$\tan \alpha' = \sigma \tan \alpha \tag{A.11}$$

A comparison between the real angle $\alpha$ of the geometrical perforations and the angle given by the model $\alpha'$ is shown in Table A.3. The model conserves mass flow and streamwise momentum at the expense of a large reduction of the injection angle on the CS side which leads to less penetration of the cooling film into the flow.

| | MP ext 1 | MP ext 2 | MP int 1 | MP int 2 |
|---|---|---|---|---|
| Geometrical $\alpha$ [°] | 60 | 30 | 60 | 30 |
| Model $\alpha'$ [°] | 7.6 | 3.8 | 9.4 | 3.5 |

**Table A.3:** Streamwise angle of the momentum injection for the perforations and the homogeneous model

# Appendix B

# Full experimental and numerical results in plane 40

All the experimental results obtained in plane 40 for the D00, D45 and D55 configurations are reported in the following along with the corresponding LES results. First the flow velocities are reported by the contours of axial momentum (Fig. B.1), swirl angle (Fig. B.2) and pitch angle (Fig. B.3). Then temperature field (Fig. B.4) and turbulence intensity (Fig. B.5) are reproduced.

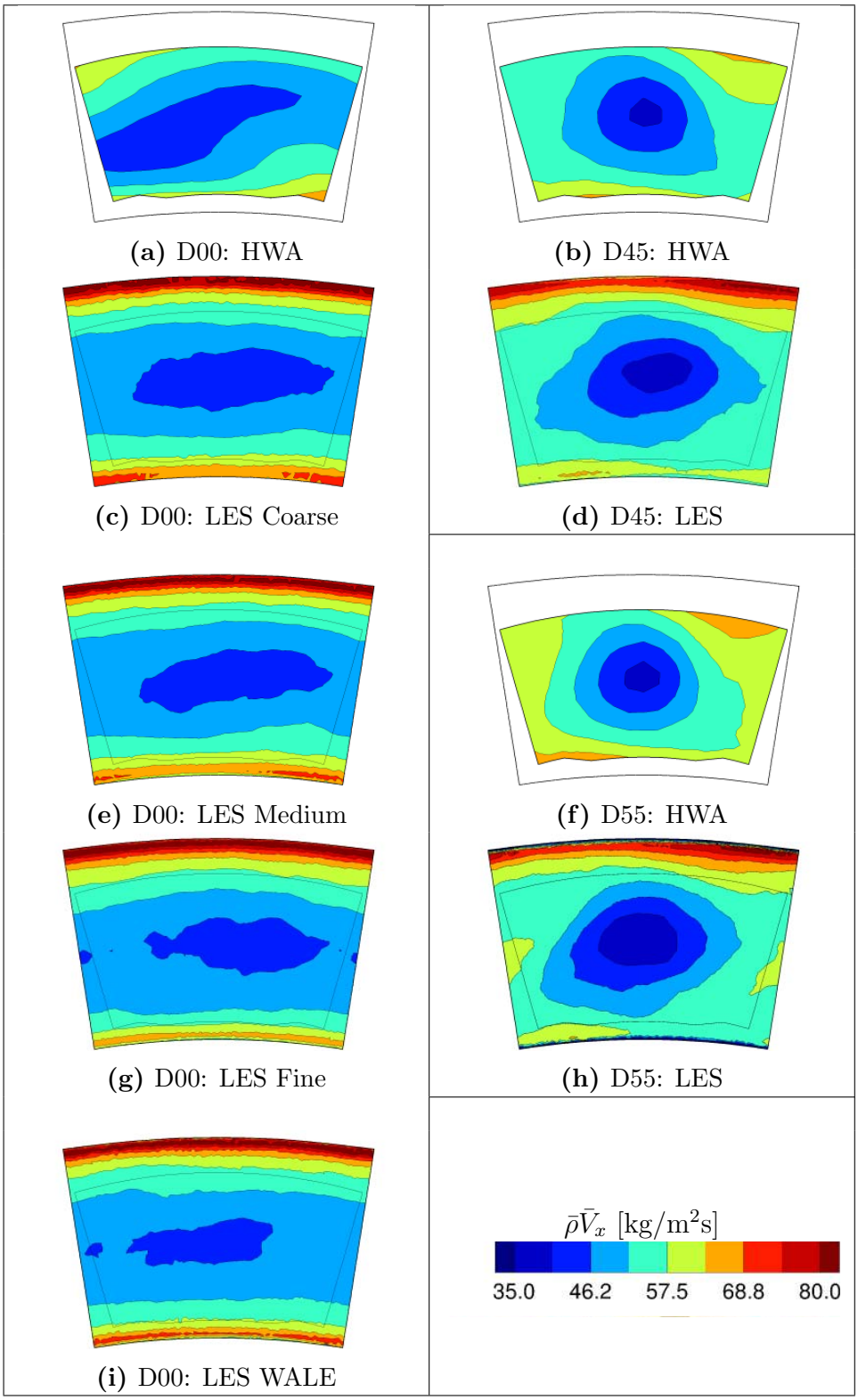


**(a)** D00: HWA **(b)** D45: HWA

**(c)** D00: LES Coarse **(d)** D45: LES

**(e)** D00: LES Medium **(f)** D55: HWA

**(g)** D00: LES Fine **(h)** D55: LES

**(i)** D00: LES WALE

**Figure B.1:** Axial momentum in plane 40 from HWA measurements and LES (looking downstream).

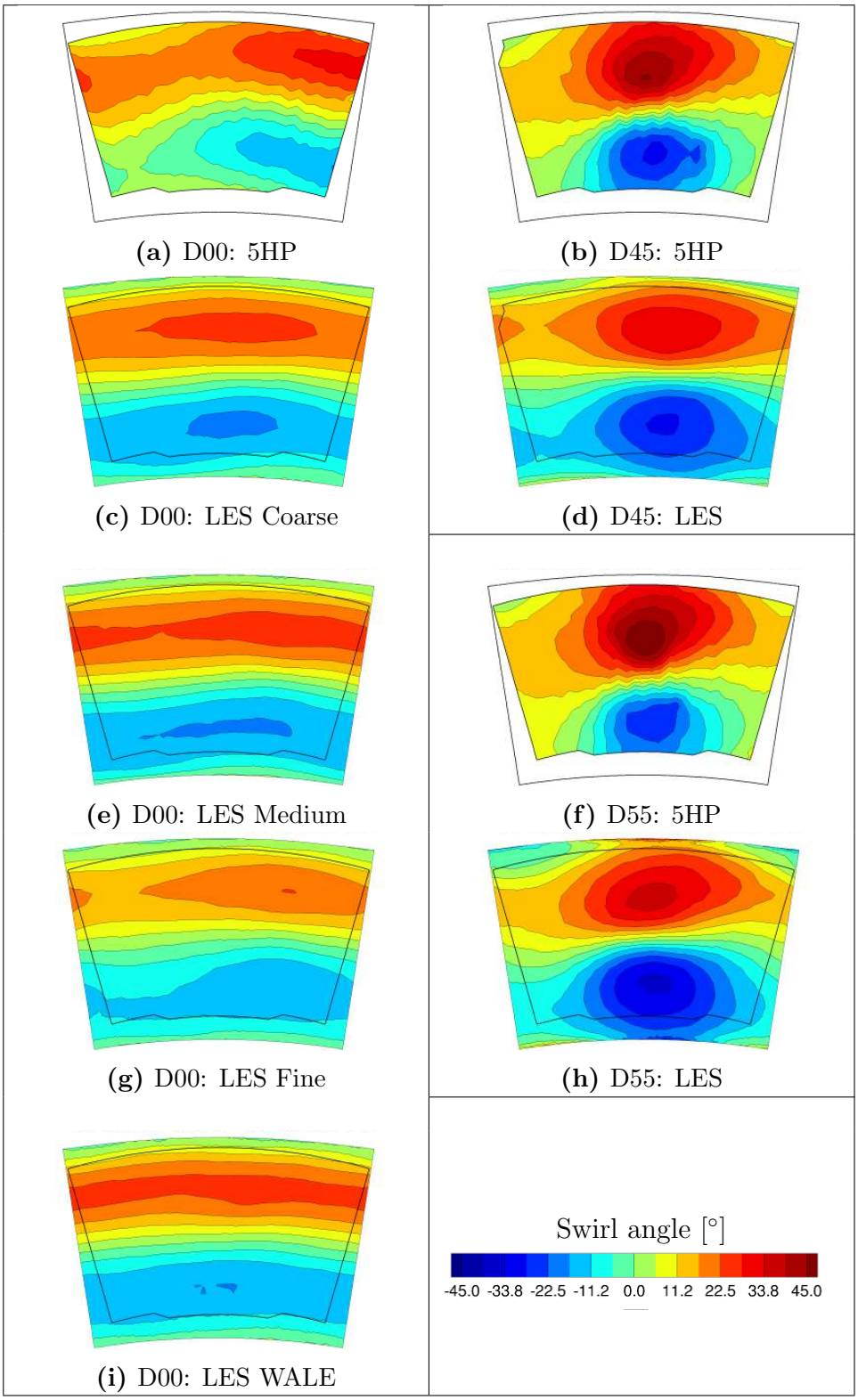


**Figure B.2:** Swirl angle in plane 40 from 5HP measurements and LES (looking downstream).

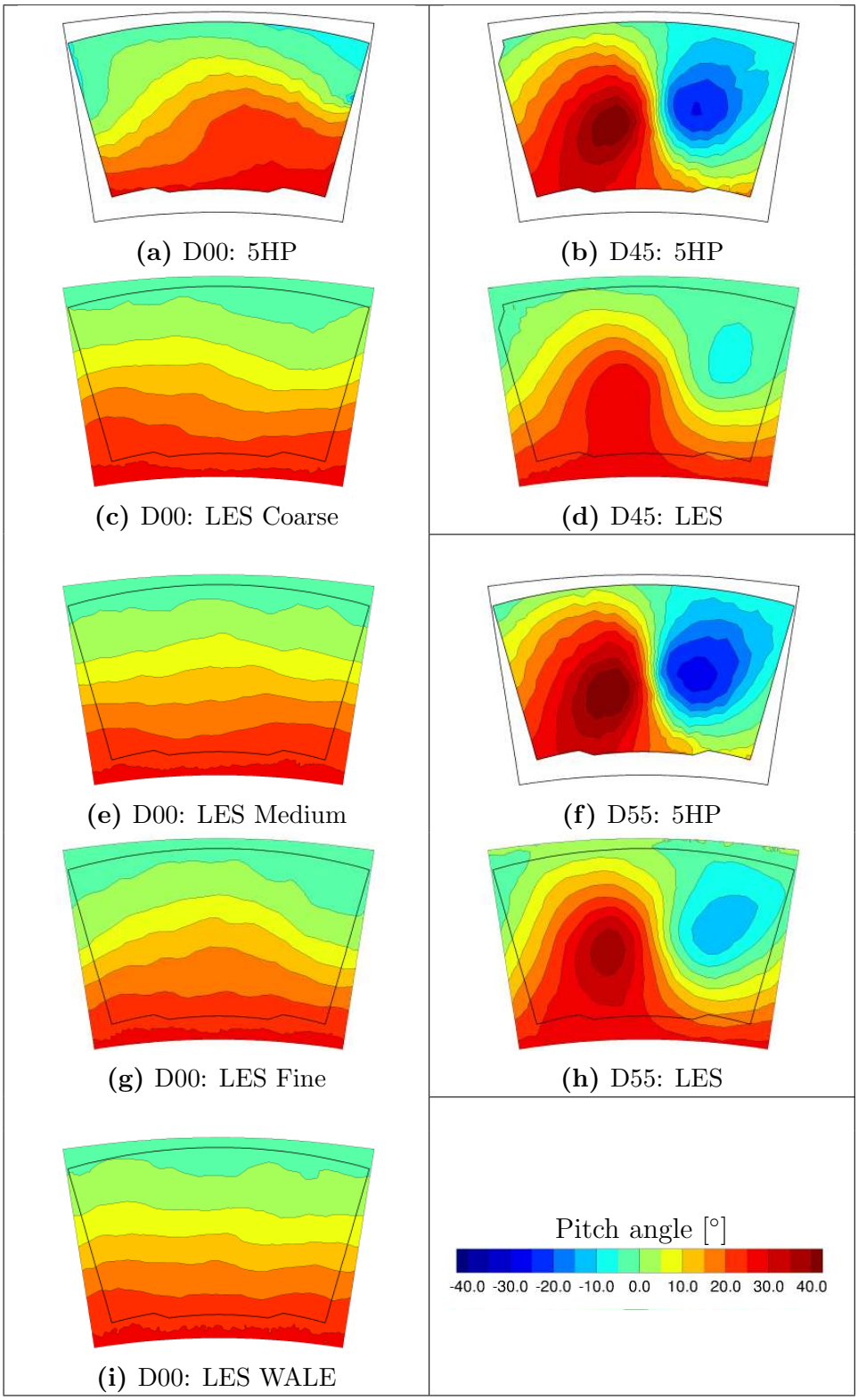


**(a)** D00: 5HP **(b)** D45: 5HP **(c)** D00: LES Coarse **(d)** D45: LES **(e)** D00: LES Medium **(f)** D55: 5HP **(g)** D00: LES Fine **(h)** D55: LES **(i)** D00: LES WALE

**Figure B.3:** Pitch angle in plane 40 from 5HP measurements and LES (looking downstream).

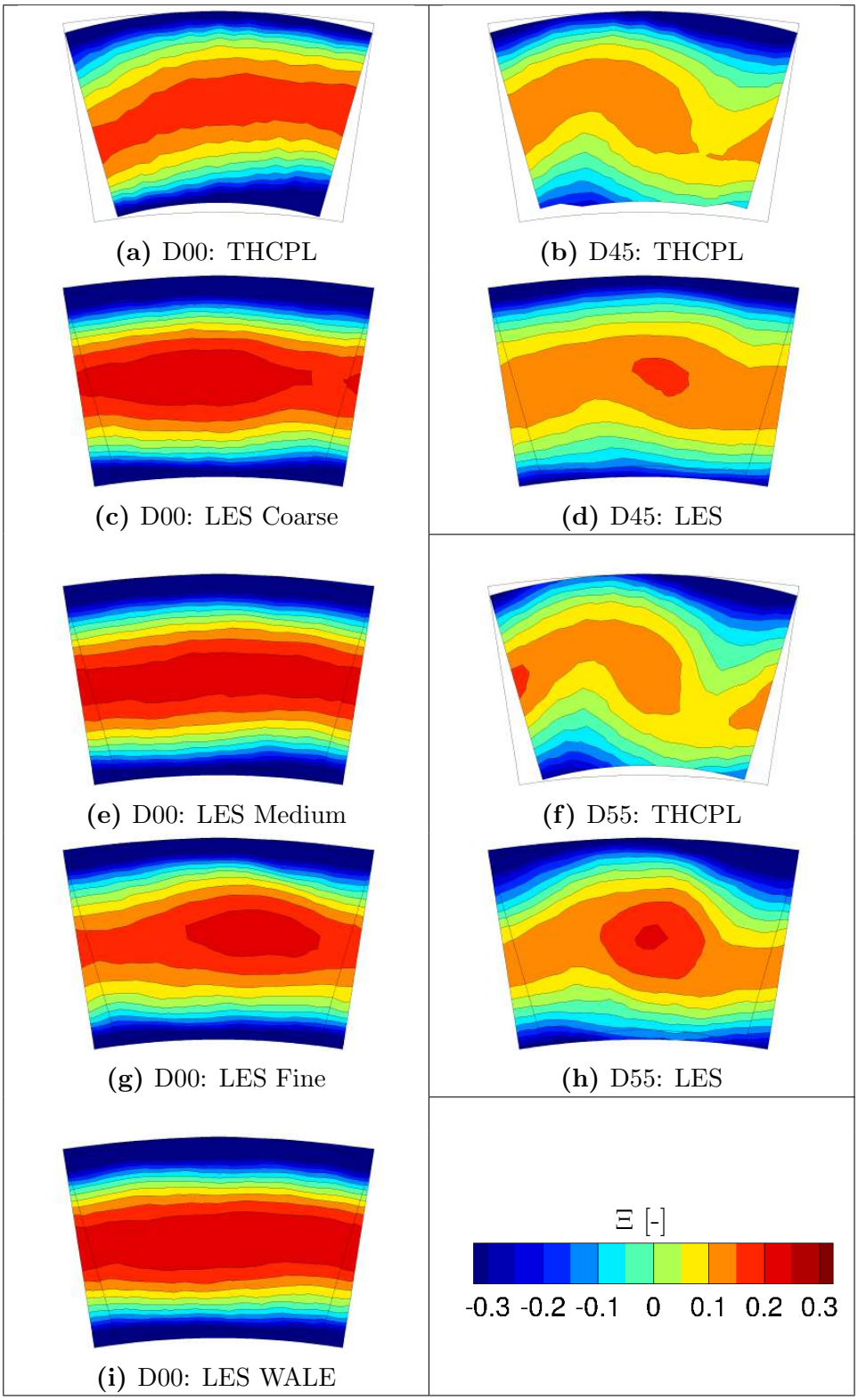


**(a)** D00: THCPL **(b)** D45: THCPL

**(c)** D00: LES Coarse **(d)** D45: LES

**(e)** D00: LES Medium **(f)** D55: THCPL

**(g)** D00: LES Fine **(h)** D55: LES

**(i)** D00: LES WALE

**Figure B.4:** Non-dimensional temperature coefficient in plane 40 from THCPL measurements and LES (looking downstream).

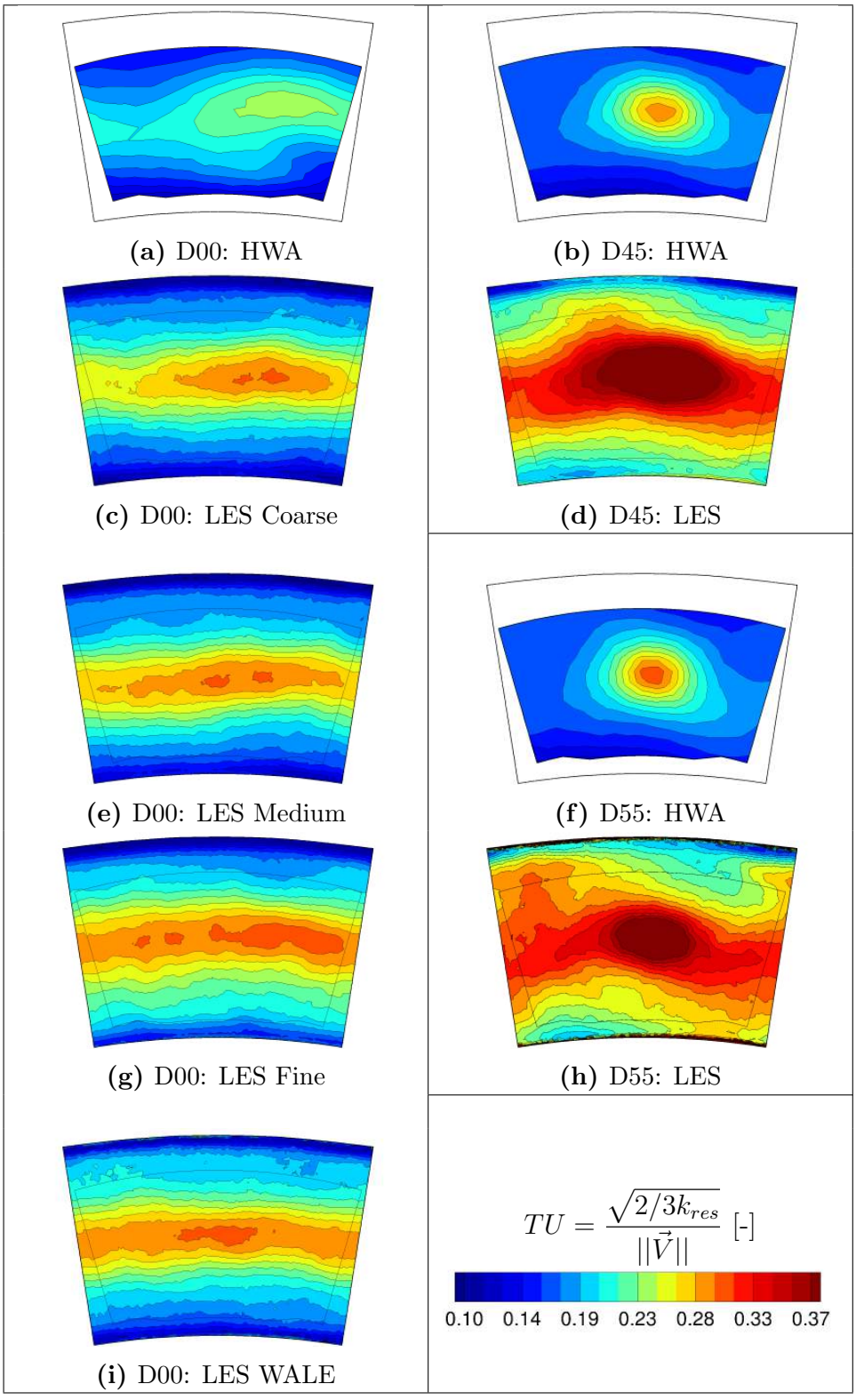


**(a)** D00: HWA **(b)** D45: HWA

**(c)** D00: LES Coarse **(d)** D45: LES

**(e)** D00: LES Medium **(f)** D55: HWA

**(g)** D00: LES Fine **(h)** D55: LES

**(i)** D00: LES WALE

**Figure B.5:** Turbulence intensity from HWA measurements at IOP and LES at DP (looking downstream).

# Appendix C

# Large Eddy Simulations with the AVBP solver

## C.1 LES formalism

### C.1.1 Governing equations

The compressible non-reactive air flow found in FACTOR CS is governed by the NS equations. They constitute a set of three conservation laws which are detailed here using the Einstein's rule of summation for indices, considering no body forces nor radiative heat flux:

$$\frac{\partial \rho}{\partial t} + \frac{\partial}{\partial x_j}(\rho u_j) = 0 \tag{C.1}$$

$$\frac{\partial}{\partial t}(\rho u_i) + \frac{\partial}{\partial x_j}(\rho u_i u_j + P\delta_{ij} - \tau_{ij}) = 0 \tag{C.2}$$

$$\frac{\partial}{\partial t}(\rho E) + \frac{\partial}{\partial x_j}(\rho u_j E + u_i P\delta_{ij} + q_j - u_i\tau_{ij}) = 0 \tag{C.3}$$

In Eqs. (C.1), (C.2) and (C.3) respectively corresponding to the conservation laws for mass, momentum and total energy, the symbols $\tau_{ij}, f_i, E, q_j, Q_r$ denote respectively the viscous stress tensor, the body forces, the total energy, the heat flux vector and the radiative heat flux. The other symbols present in these equations were already introduced in this work and keep their meaning. In these equations, the pressure, temperature and density are linked by the equation of state of a perfect gas:

$$P = \rho r T \tag{C.4}$$

with $r = 287.0$ J/kg.K is the perfect gas constant for pure air. As air is a Newtonian fluid, the viscous stress tensor is linearly dependent on the strain rate which components read:

$$s_{ij} = \frac{1}{2}\left(\frac{\partial u_i}{\partial x_j} + \frac{\partial u_j}{\partial x_i}\right). \tag{C.5}$$

Using fluid particle isotropic considerations and Stokes' hypothesis [149] one obtains the following expression for the viscous stress tensor $\tau_{ij}$:

$$\tau_{ij} = 2\mu \left( s_{ij} - \frac{1}{3} s_{kk} \delta_{ij} \right). \tag{C.6}$$

The dynamic viscosity $\mu$ is assumed to depend only on temperature because of the limited pressure level and variations found in the CS. The Sutherland law (valid from 100 K to 1900 K) [150] is used at this purpose:

$$\mu = \mu_{ref} \left( \frac{T}{T_{ref}} \right)^{2/3} \frac{T_{ref} + 110.4}{T + 110.4}, \tag{C.7}$$

with $\mu_{ref} = 1.71 \times 10^{-5}$ kg/m.s and $T_{ref} = 273.15$ K.

Finally, for the monospecies flow of the CS, the heat flux vector reads:

$$q_i = -\lambda \frac{\partial T}{\partial x_i}, \tag{C.8}$$

where the thermal conductivity is expressed as:

$$\lambda = \frac{\mu C_p}{Pr} \tag{C.9}$$

with the molecular Prandtl number $Pr$ =0.75 for air supposed as constant in time and space.

### C.1.2 LES closure of the NS equations

#### Filtered equations and unclosed terms

LES are based on the hypothesis that the small turbulent structures are more universal in character and isotropic than the large eddies which are the real energy-carrying structures [12]. Based on this separation of scales, the LES principle is to resolve the contribution of the large scales to the flow while modeling the effect of the small scales. The underlying concept of LES is therefore the filtering of the NS equations: any quantity $\phi$ is decomposed as a filtered quantity $\overline{\phi}$ (resolved in the numerical simulation) and the SGS part $\phi''$ due to the unresolved flow motion: $\phi = \overline{\phi} + \phi''$. For a variable density $\rho$, a mass-weighted Favre filtering is introduced such as:

$$\widetilde{\phi} = \frac{\overline{\rho\phi}}{\overline{\rho}}. \tag{C.10}$$

Length-scale separation on any variable $\phi$ is achieved with the spatial Favre filtering operation:

$$\widetilde{\phi(\vec{x},t)} = \frac{1}{\overline{\rho(\vec{x},t)}} \int_{-\infty}^{+\infty} \rho(\vec{x'},t)\phi(\vec{x'},t)G(\vec{x'}-\vec{x})d\vec{x'}, \tag{C.11}$$

where $G$ is the filter function which determines the structure and size of the small scales based on the filter width and shape (tophat, Gaussian etc.) [12]. In most cases, the filter width $\triangle$ is equal to the cubic root of the local cell volume. The balance equations for LES are obtained by filtering the NS equations (C.1), (C.2) and (C.3) yielding:

$$\frac{\partial \overline{\rho}}{\partial t} + \frac{\partial}{\partial x_j}(\overline{\rho}\widetilde{u_j}) = 0 \quad \text{(C.12)}$$

$$\frac{\partial}{\partial t}(\overline{\rho}\widetilde{u_i}) + \frac{\partial}{\partial x_j}(\overline{\rho}\widetilde{u_j}\widetilde{u_i} + \overline{P}\delta_{ij} - \overline{\tau_{ij}} - \overline{\tau_{ij}}^{sgs}) = 0 \quad \text{(C.13)}$$

$$\frac{\partial}{\partial t}(\overline{\rho}\widetilde{E}) + \frac{\partial}{\partial x_j}(\overline{\rho}\widetilde{u_j}\widetilde{E} + \overline{P}\widetilde{u_i}\delta_{ij} + \overline{q_j} + \overline{q_j}^{sgs} - \widetilde{u_i}(\overline{\tau_{ij}} + \overline{\tau_{ij}}^{sgs}) = 0 \quad \text{(C.14)}$$

The laminar filtered stress tensor and the filtered heat flux are respectively approximated by:

$$\overline{\tau_{ij}} = \overline{2\mu\left(s_{ij} - \frac{1}{3}\delta_{ij}s_{kk}\right)} \simeq 2\overline{\mu}\left(\widetilde{s}_{ij} - \frac{1}{3}\delta_{ij}\widetilde{s}_{kk}\right) \quad \text{(C.15)}$$

$$\overline{q_i} = -\overline{\lambda\frac{\partial T}{\partial x_i}} \simeq -\overline{\lambda}\frac{\partial \widetilde{T}}{\partial x_i} \quad \text{(C.16)}$$

Due to non-linearity of the NS equations, Favre averaging introduces two new terms in these equations ($-\overline{\tau_{ij}}^{sgs}, \overline{q_j}^{sgs}$) which require to supply specific closures, i.e. ad-hoc modeling. The first term, also called Reynolds tensor is defined as:

$$\overline{\tau_{ij}}^{sgs} = -\overline{\rho}(\widetilde{u_i u_j} - \widetilde{u}_i\widetilde{u}_j). \quad \text{(C.17)}$$

Various methods of different complexity exist to model $\overline{\tau_{ij}}^{sgs}$ [13, 125]. One focuses here only on the so-called functional approach which supposes that the effect of the small scales on the larger ones is purely dissipative and models this influence by introducing a turbulent (SGS) viscosity $\nu_{sgs}$ in the LES equations. These models are able to represent the global dissipative effects of the small scales but they cannot reproduce the local details of the energy exchange, nor the backscatter process (energy transfer from small to large scales) [12]. Because of its reduced cost, effectiveness and robustness, this is the most common practice. The turbulent viscosity is thus expressed based on the Boussinesq eddy viscosity:

$$\overline{\tau_{ij}}^{sgs} = 2\overline{\rho}\nu_{sgs}\left(\widetilde{s}_{ij} - \frac{1}{3}\delta_{ij}\widetilde{s}_{kk}\right). \quad \text{(C.18)}$$

The second unclosed term is the SGS heat flux vector defined by:

$$\overline{q_i}^{sgs} = \overline{\rho}\left(\widetilde{u_i E} - \widetilde{u}_i\widetilde{E}\right), \quad \text{(C.19)}$$

and is modeled by introducing a SGS heat flux:

$$\overline{q_i}^{sgs} = -\lambda_{sgs}\frac{\partial \widetilde{T}}{\partial x_i}, \quad \text{(C.20)}$$

which is driven by the SGS thermal conductivity $\lambda_{sgs}$:

$$\lambda_{sgs} = \frac{\nu_{sgs}\rho\overline{C_p}}{Pr_{sgs}}. \tag{C.21}$$

where the SGS Prandtl number $Pr_{sgs}$ is usually set to a constant value (about 0.6). When doing do, the SGS thermal conductivity shares the same properties as the turbulent viscosity in all the regions while it has been shown the SGS heat flux should be damped in the near-wall regions [151]. A dynamics model was proposed by Moin et al. [152] to account for local changes in the Prandtl number which may vary strongly especially in boundary layers. Baya Toda [153] implemented such model in a former version of AVBP but found the impact of $Pr_{sgs}$ to be very small which confirmed other findings [92, 154]. In this work, two constant values of turbulent Prandtl number were tested: the nominal value (0.6) and a lower one (0.4). The simulations performed on the D45 geometry without swirler showed that the difference is negligible and results are not reported.

### Models for the turbulent viscosity

In the functional approach, different models exist to evaluate the turbulent viscosity and three models available in AVBP were benchmarked in this work:

**Smagorinsky** The Smagorinsky model [111] developed in the sixties is the most comon SGS model and has been heavily tested for multiple flow configurations. It is based on the equilibrium hypothesis implying that the small scales dissipate entirely and instantaneously all the energy they receive from the larger scales. This model is cheap and robust but known to be too dissipative for shear flows and to badly behave in wall bounded flows [12]. The SGS viscosity is defined as:

$$\nu_{sgs} = (C_s\triangle)^2\sqrt{2\widetilde{s}_{ij}\widetilde{s}_{ij}} \tag{C.22}$$

where $C_s$ is the model constant set to 0.18 in most of the cases. However, it is admitted [12, 153] that this constant should change according to the flow properties.

**Dynamic Smagorinsky** The dynamic Smagorinsky model proposed by Germano et al. [126] differs from the standard one by a dynamic evaluation in space and time of the Smagorinsky coefficient $C_{sd}$. This dynamic procedure applies two filter to the NS equations: the initial one $\widetilde{()}$ of width $\triangle$ and a test filter $\widehat{()}$ of width $\widehat{\triangle}$. The information extracted from the resolved scales (between $\triangle$ and $\widehat{\triangle}$) is used to express $C_{sd}$ by employing the Germano-identity and the Lilly's procedure [155] which are not detailed here. The turbulent viscosity is then computed from Eq. (C.22) as for the standard Smagorinsky model, with the dynamic constant instead of $C_s$. This approach has the great advantage to allow local variations of the constant depending on the flow to be

more representative of the physics than a unique value. However, numerical instabilities can arise because of the local definition of $C_{sd}$, thus smoothing and clipping operations are usually required to avoid having negative $\nu_{sgs}$ or sharp gradients [12, 153].

**WALE** The WALE model [127] was developed for wall bounded flows in an attempt to recover the scaling laws of the wall without any additional procedure. Without a priori knowledge of the geometry, this model automatically identify near wall regions (pure shear) and switches off. The WALE model is expected to better handle near wall regions but it has been shown that it produces viscosity in case of pure rotation which may alter the prediction of vortex motion [153]. The SGS viscosity is defined as:

$$\nu_{sgs} = (C_w \triangle)^2 \frac{(s^d_{ij} s^d_{ij})^{3/2}}{(\widetilde{s}_{ij}\widetilde{s}_{ij})^{5/2} + (s^d_{ij} s^d_{ij})^{5/4}}, \tag{C.23}$$

$$s^d_{ij} = \frac{1}{2}\left(\widetilde{g}^2_{ij} + \widetilde{g}^2_{ji}\right) - \frac{1}{3}\widetilde{g}^2_{kk}\delta_{ij} \tag{C.24}$$

where $\widetilde{g}_{ij}$ is the resolved velocity gradient and $C_w = 0.4929$ is the model constant.

## C.2 AVBP solver

The LES code used in this manuscript to is the AVBP code[1], today property of CERFACS and Institut Français du Petrole Energies Nouvelles (IFPen). The AVBP solver has been extensively used and widely validated on reactive flow numerical simulation, mainly for combustion applications [108, 156–158]. It was designed from the very beginning to be used for massively parallel computations on dedicated architectures, addressing all the issues associated with the High Performance Computing (HPC). The simulations presented in this work (listed in Table C.2) were performed on both internal (CERFACS) and external machines depending on the case and the allocated computational resources. As an example, Table C.1 summarizes the typical CPU effort required for a single simulation of FACTOR CS (case D00 medium mesh) on the different machines used for this work. One observes that even if significant differences exist between the machines, the return time of each simulation is at least half a month. This emphasizes the important computational effort engaged to perform all the simulations presented here.

The code solves the full compressible, multi-species, reactive NS equations, presented previously in the simplified mono-species and non-reactive form suitable for our study. The solver relies on the cell-vertex approach (data stored at mesh nodes) and finite volume method on unstructured or hybrid meshes which gives among other advantages a good robustness against mesh distortion. Temporal integration is performed by an explicit formulation which globally controls the timestep

[1] `www.cerfacs.fr/~avbp`

| **Machine** | **Corail** | **Ada** | **Turing** | **Jade** |
|---|---|---|---|---|
| Owner | CERFACS | IDRIS | IDRIS | CINES |
| Architecture | HP Proliant | IBM x3750 Intel | IBM Blue-Gene/Q | SGI Altix ICE 8200 |
| # of threads [-] | 144 | 512 | 2048 | 1024 |
| CPU time [khrs] | 382 | 202 | 1340 | 332 |
| Return time [days] | 110 | 16 | 27 | 13 |

**Table C.1:** Typical CPU effort for a LES of the CS (140 ms).

to respect the Courant Friedrichs Lewy condition (CFL). LES require numerical schemes providing high order discretizations and especially low-dissipation models (to respect the distribution of energy on the turbulent spectra) which are often offered by central differencing schemes [12]. In AVBP, various numerical schemes are available from low to very high orders and three schemes were used in this work:

**Lax-Wendroff** scheme is a space and time second order centered scheme [159] adapted to the cell-vertex method. It does not have excellent dissipation and dispersion properties and is only used here for transient and initialization of the calculations as it is very cheap.

**TTGC** is a version of the two-step Taylor-Galerkin schemes providing a third order discretization both in space and time [110]. It is known to be a good candidate for LES thanks to its good dissipation and dispersion properties [160]. It is used for all the simulations of the CS without vanes.

**TTG4A** is a fourth order in time, third order is space scheme [161] having better dispersion properties than TTGC but a worse dissipation behaviour [160]. This scheme is employed for the integrated simulations of the CS with NGVs presented in Chapter 8 to avoid any wiggles that may appear when using the TTGC scheme in conjunction with the prismatic elements of the mesh.

In AVBP, the use of centered schemes with low dissipation requires the addition of artificial diffusion operator. Indeed, transport of high gradient may lead to the Gibbs phenomenon [162] with the apparition of non physical node-to-node oscillations called wiggles. To help the diffusion operator in its task, artificial viscosity can be added locally in the field to remove numerical oscillations. A sensor specifically dedicated to unsteady turbulent flow can automatically detect numerical anomalies and increase local viscosity in the limitation of an user defined threshold.

| Geometry | Case | Duct | Operating point | Mesh nodes | Mesh cells | Scheme | SGS model | Physical time [ms] | Timestep [s] | Results in |
|---|---|---|---|---|---|---|---|---|---|---|
|  | 1 | D45 | DP | 2.2M | 12.7M | TTGC | Smagorinsky | 360 | $2.3 \cdot 10^{-7}$ | [21] |
| | 2 | D45 | IOP | 2.2M | 12.7M | TTGC | Smagorinsky | 143 | $2.3 \cdot 10^{-7}$ | [21] |
| | 3 | D45 | DP | 2.2M | 12.7M | TTGC | Smagorinsky Dynamic | 143 | $2.3 \cdot 10^{-7}$ | Unpublished |
|  | 4 | D45 | DP | 6.5M | 38.3M | TTGC | Smagorinsky | 159 | $2.3 \cdot 10^{-8}$ | [21] |
| 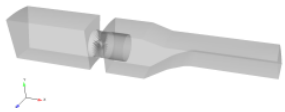 | 5 | D45 | DP | 5.2M | 29.1M | TTGC | Smagorinsky | 149 | $5.8 \cdot 10^{-8}$ | Chap. 2 |
| 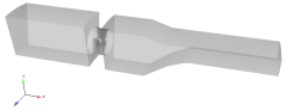 | 6 | D00 | DP | Coarse: 2.7M | 15.8M | TTGC | Smagorinsky | 154 | $6.5 \cdot 10^{-8}$ | Chap. 5 |
| | 7 | D00 | DP | Medium: 6.0M | 34.2M | TTGC | Smagorinsky | 155 | $4.4 \cdot 10^{-8}$ | Chap. 3,5 |
| | 8 | D00 | DP | Fine: 12.2M | 68.5M | TTGC | Smagorinsky | 155 | $3.7 \cdot 10^{-8}$ | Chap. 2,4,5,6 |
| | 9 | D00 | DP | Medium: 6.0M | 34.2M | TTGC | WALE | 157 | $4.4 \cdot 10^{-8}$ | Chap. 5 |
| | 10 | D00 | IOP | Medium: 6.0M | 34.2M | TTGC | Smagorinsky | 145 | $4.4 \cdot 10^{-8}$ | Chap. 3 |
|  | 11 | D55 | DP | 8.9M | 51.0M | TTGC | Smagorinsky | 144 | $4.3 \cdot 10^{-8}$ | Chap. 2,4,5,6 |
| 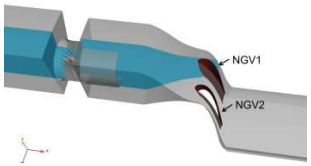 | 12 | D55 LE | DP | 13.7M | 71.0M | TTG4A | Smagorinsky | 50.3 | $3.2 \cdot 10^{-8}$ | Chap. 8 |
| 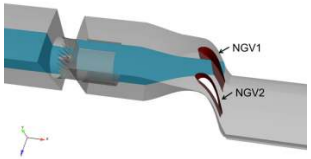 | 13 | D55 PA | DP | 13.7M | 71.0M | TTG4A | Smagorinsky | 49.5 | $3.2 \cdot 10^{-8}$ | Chap. 8 |

**Table C.2:** Summary of the all the LES performed on FACTOR configuration.

# Appendix D

# Publications

Six publications derive from this PhD work and are reproduced herafter for personal and non-commercial use. The published versions can be downloaded directly on the editors' websites.

First, two articles are not specifically discussed in this manuscript but constitute interesting development and validation obtained specifically to meet FACTOR's objectives.

[a] C. Koupper, G. Caciolli, L. Gicquel, F. Duchaine, G. Bonneau, L. Tarchi, and B. Facchini. "Development of an Engine Representative Combustor Simulator Dedicated to Hot Streak Generation". In: *Journal of Turbomachinery* 136.11 (2014). URL: http://dx.doi.org/10.1115/1.4028175

[b] C. Koupper, T. Poinsot, L. Gicquel, and F. Duchaine. "Compatibility of Characteristic Boundary Conditions with Radial Equilibrium in Turbomachinery Simulations". In: *AIAA Journal* 52.12 (2014), pp. 2829–2839. URL: http://dx.doi.org/10.2514/1.J052915

Second, the following two publications present the advanced diagnostics for LES of combustion systems which are detailed in Chapter 6.

[c] C. Koupper, L. Gicquel, F. Duchaine, and G. Bonneau. "Advanced Combustor Exit Plane Temperature Diagnostics Based on Large Eddy Simulations". English. In: *Flow, Turbulence and Combustion* (2015), pp. 1–18. URL: http://dx.doi.org/10.1007/s10494-015-9607-3

[d] C. Koupper, L. Gicquel, F. Duchaine, T. Bacci, B. Facchini, A. Picchi, L. Tarchi, and G. Bonneau. "Experimental and Numerical Calculation of Turbulent Timescales at the Exit of an Engine Representative Combustor Simulator". In: *ASME Turbo Expo 2015: Turbine Technical Conference and Exposition*. GT2015-42278. 2015

Finally, the two following papers, related to paper [c] of the previous list were published in collaboration with UNIFI to report experimental results.

[e] T. Bacci, G. Caciolli, B. Facchini, L. Tarchi, C. Koupper, and J.-L. Champion. "Flowfield and temperature profiles measurements on a combustor simulator dedicated to hot streaks generation". In: *ASME Turbo Expo 2015: Turbine Technical Conference and Exposition*. GT2015-42217. 2015

[f] T. Bacci, B. Facchini, A. Picchi, L. Tarchi, C. Koupper, and J.-L. Champion. "Turbulence field measurements at the exit of a combustor simulator dedicated to hot streaks generation". In: *ASME Turbo Expo 2015: Turbine Technical Conference and Exposition*. GT2015-42218. 2015

**Charlie Koupper**
Turbomeca,
Bordes 64510, France
e-mail: charlie.koupper@turbomeca.fr

**Gianluca Caciolli**
Department of Industrial Engineering,
University of Florence,
Florence 50139, Italy
e-mail: gianluca.caciolli@htc.de.unifi.it

**Laurent Gicquel**
CFD Team, CERFACS,
Toulouse 31057, France

**Florent Duchaine**
CFD Team, CERFACS,
Toulouse 31057, France

**Guillaume Bonneau**
Turbomeca,
Bordes 64510, France

**Lorenzo Tarchi**
Department of Industrial Engineering,
University of Florence,
Florence 50139, Italy

**Bruno Facchini**
Department of Industrial Engineering,
University of Florence,
Florence 50139, Italy

# Development of an Engine Representative Combustor Simulator Dedicated to Hot Streak Generation

*Nowadays, the lack of confidence in the prediction of combustor-turbine interactions and more specifically our ability to predict the migration of hot spots through this interface leads to the application of extra safety margins, which are detrimental to an optimized turbine design and efficiency. To understand the physics and flow at this interface, a full 360 deg nonreactive combustor simulator (CS) representative of a recent lean burn chamber together with a 1.5 turbine stage is instrumented at DLR in Gottingen (Germany) within the European project FACTOR. The chamber operates with axial swirlers especially designed to reproduce engine-realistic velocity and temperature distortion profiles, allowing the investigation of the hot streaks transport through the high pressure (HP) stage. First, a true scale three injector annular sector of the CS without turbine is assembled and tested at the University of Florence. To generate the hot steaks, the swirlers are fed by an air flow at 531 K, while the liners are cooled by an effusion system fed with air at ambient temperature. In addition to static pressure taps and thermocouples, the test rig will be equipped with an automatic traverse system which allows detailed measurements at the combustor exit by means of a 5-hole probe, a thermocouple, and hot wire anemometers. This paper presents the design process and instrumentation of the trisector CS, with a special focus on large Eddy simulations (LES) which were widely used to validate the design choices. It was indeed decided to take advantage of the ability and maturity of LES to properly capture turbulence and mixing within combustion chambers, despite an increased computational cost as compared to usual Reynolds averaged Navier Stokes (RANS) approaches. For preliminary design, simulations of a single periodic sector (representative of the DLR full annular rig) are compared to simulations of the trisector test rig, showing no difference on the central swirler predictions, comforting the choice for the trisector. In parallel, to allow hot wire anemometry (HWA) measurements, the selection of an isothermal operating point, representative of the nominal point, is assessed and validated by use of LES.* [DOI: 10.1115/1.4028175]

## 1 Introduction

The flow field at the exit of a combustor is by nature (i) unsteady, because of the turbulent combustion and mixing processes and (ii) nonuniform, on the circumferential direction because of the discrete position of fuel injectors and dilution holes, as well as on the radial direction because of the liners film cooling devices. Overall at combustor exit, most of the temperature gradient aligns with the radial direction (blade span), with only weak contributions of the circumferential axis (blade pitch). This flow distribution and segregation result in highly three-dimensional unsteady fields at the combustor-turbine interface, both in terms of temperature and pressure.

It is known that such turbine inlet distortion can cause major aerothermal changes within the HP turbine vane and rotor. The aerodynamics, secondary flows, blade loading, heat transfer, losses, and finally efficiency can thus be significantly altered. It has been shown that turbine inlet temperature distortion can result in large changes in heat transfer rate on the HP vanes, as well as on end walls, as shown by Povey et al. [1]. Simulations performed by Simone et al. [2] show an increase in vane heat transfer rate up to +50% on the suction side and +20% on the pressure side when the inlet temperature is not uniform.

In the HP rotor, the hot streak is preferentially convected toward the pressure side (well-known temperature segregation effect [3]), leading to significant changes in the heat transfer coefficient. Early experimental studies by Roback and Dring [4] show that if the hot streak is not positioned at midspan, flow deflections lead to large accumulations of hot fluid at the endwalls. The secondary flow mechanisms are geometry and profiles dependent, and no general rule can be drawn: The hot streak may migrate toward the blade hub [5] or casing [4]. Therefore, if designed for a uniform inlet temperature, the turbine stage efficiency may considerably be altered by the inlet temperature distortion. Finally, the clocking between burners and Nozzle guide Vanes (NGV) is also known to be of primary importance to control the vanes heat transfer: Povey et al. [1] reported changes of ±20% in the vane surface Nusselt number.

All these complex and interdependent phenomena occurring at the combustor-turbine interface are of primary importance for the optimized design of an HP turbine stages. Therefore, various experiments and numerical simulations were performed in the last decades. The complexity of the subject makes this question to be still under study, through both experimental and numerical approaches.

### 1.1 Hot Streak Simulators in Turbine Testing Facilities.

There is a lack in data from real combustor or rotating turbine experiments using nonuniform turbine inlet profile. To address

Contributed by the International Gas Turbine Institute (IGTI) of ASME for publication in the JOURNAL OF TURBOMACHINERY. Manuscript received July 21, 2014; final manuscript received July 24, 2014; published online August 26, 2014. Editor: Ronald Bunker.

  

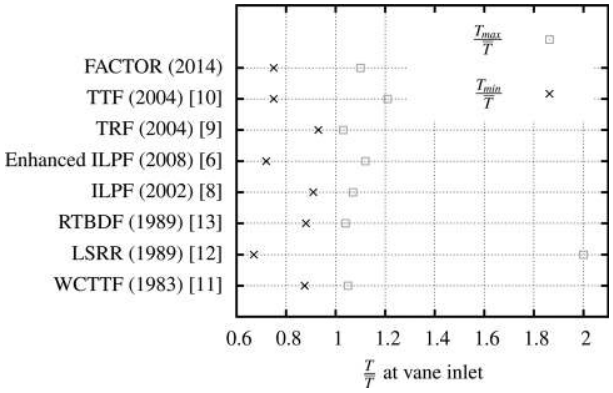


**Fig. 1 Maximum and minimum temperature relative to the mean temperature at vane inlet for hot streak simulators**

this issue, no less than ten rigs devoted to the study of hot streak have been created since the 1980s [6,7]. The majority of the known and reported facilities are located in the USA. It is only recently that interesting facilities were created in Europe such as the ILPF (UK), or the ongoing FACTOR project. In the last decade, complex and heavily instrumented rigs were then designed to get deeper insight on hot streak interaction with turbines:

(1) The Isentropic Light Piston Facility (QinetiQ, Hamphsire, UK, 2002) [8], generates hot spots by the compression of air by a piston. This blow-down facility was recently upgraded (2008) [6] in order to get a strong, well-defined temperature profile, with low run-to-run variation, and using a rotatable device to study hot-streak-vanes clocking effect.
(2) The Turbine Research Facility (Air Force Research Laboratory, Wright-Patterson Air Force Base, Dayton, OH, 2004) [9] is a fully controllable inlet profile generator, both in terms of pressure and temperature, which geometry mimics a typical gas turbine combustor.
(3) The Turbine Test Facility (Ohio State University, 2004) [10] features a heavily instrumented realistic recent turbine stage with cooled vane, rotor blade, and purge flows. Hot streaks are generated by controllable heater rods.

The characteristic temperature ratio between the hot spot and surrounding stream is plotted in Fig. 1 at vane inlet for all the main research facilities on hot streaks since the 1980s [5,6,8–13]. Note that the relative position of the measurement plane with the vane leading edge is not always given and differs between all the cases. Overall, the temperature ratio varies between 0.75 and 1.15, which is representative of a real engine despite the fact that almost all the test rigs are nonreacting for cost and simplicity reasons.

## 2 Development of a CS for FACTOR Project

As indicated in the previous list, there is currently no experimental test infrastructure in Europe dedicated to advanced measurements of a turbine operated together with a realistic CS. To fill in this gap, a new continuous flow facility hosted by DLR is developed within the European project FACTOR. It will host a modern aero-engine CS and a 1.5 HP turbine stage, operating at realistic Reynolds and Mach numbers. Special efforts are made to closely mimic a recent engine configuration to capture all physical scales at the combustor-turbine interface. The target temperature range for the hot streaks generated by the CS is plotted in Fig. 1. The hot spot is expected to be well marked compared to other projects. The desired flowfield at the exit of the CS is specified to mimic as closely as possible real conditions experienced by a modern HP turbine. The target (shown in Fig. 2) is defined within a plane located half an axial chord upstream the NGV (*Plane* 40), while the leading edge of the NGV is referred as *Plane* 40+.

To ease operability and allow the use of different measurement techniques, no combustion is enforced in the chamber and the temperature profile is obtained only by mixing hot and cold air streams. Since FACTOR CS should be representative of a lean burn combustor from a recent aero-engine, the main functional impacts retained are: (i) A full annular axial combustor; (ii) a flow split with around 2/3 of air mass flow going through the swirlers

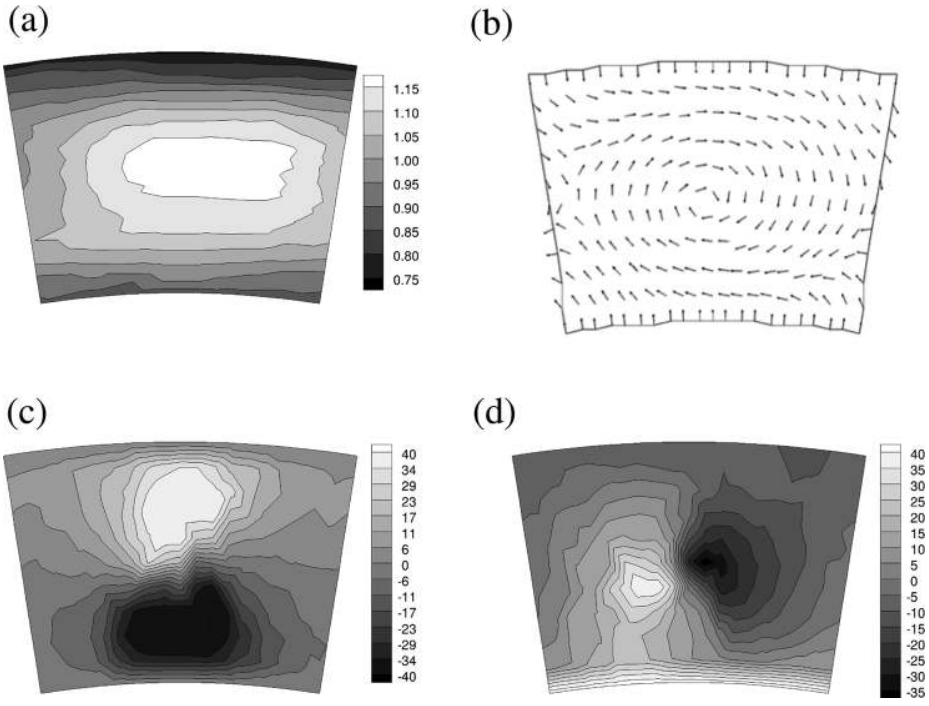


**Fig. 2 Target fields in plane 40 (view from upstream), (*a*) $T/\bar{T}_{40}$, (*b*) velocity vectors, (*c*) swirl angle (deg), and (*d*) pitch angle (deg)**

and 1/3 of air mass flow used for cooling; and (iii) liners are perforated for effusion cooling, and no dilution holes are inserted. It was decided to use 20 swirlers (18 deg sector), while the final facility will host 40 NGVs and 60 rotor blades with various clocking positions. Finally, the CS has to be able to operate in isothermal conditions for HWA measurements.

The generic design of the CS is schematically shown in Fig. 3. The total mass flow in plane 40 is split into 65% through the swirlers (531 K) and 35% for effusion cooling, in order to match the target mean total temperature at turbine inlet (450 K). A duct is used to confine and preserve the hot spot (nominal length $L = 0.7D_{sw}$). The inner and outer liners are multiperforated of 0.45 mm diameter holes aligned in the streamwise direction (no azimuthal injection). The axial swirler has an external diameter $D_{sw} = 63$ mm and contains 30 flat vanes disposed around a central hub.

A wall-resolved steady-state RANS simulation was performed on four vane passages of the swirler, using the commercial code FLUENT. A very fine hybrid mesh was used (total 27 M cells), with 10 $\mu$m prisms on vane walls ($Y^+ < 2$). The realizable $k$-$\varepsilon$ turbulence model [14] was used. Even if full results of this calculation are not reported here, the circumferentially averaged velocity profiles at the exit of the swirler are shown in Fig. 4. The Reynolds number based on the swirler exit mean axial velocity, and outer diameter is estimated at $Re_{sw} = 111{,}000$. The swirl number [15] compares the axial flux of angular momentum $G_\theta$ to the axial thrust $G_x$: $S_N = G_\theta/(R_{sw}G_x)$. In the cylindrical frame of reference $(r,\theta,x)$, the general form for $G_\theta$ and $G_x$ are

$$G_\theta = \int_0^{R_{sw}} \rho u_x u_\theta r^2 dr \tag{1}$$

$$G_x = \int_0^{R_{sw}} \left(\rho u_x^2 + (P - P_{amb})\right) r dr \tag{2}$$

Evaluations of the swirl number calculated without the pressure terms in Eq. (2) and for the profiles shown in Fig. 4 yield $S_N = 0.47$. Considering the pressure terms and the chamber pressure $P_{amb} = P_{40}$, the value reaches 0.52. This is close to the critical value of 0.6 [15], above which strong breakdown occurs.

The entire design process of the CS is based on numerical simulations. Even if advanced techniques and multiple cross-checks were performed, the fidelity of the computational techniques and more specifically the models required for proper predictions of the turbulent mixing of swirled flow is questionable. To increase the degree of confidence in the predicted performance of the full configuration to be measured at a DLR, an experimental validation on a simpler model is necessary. In addition to the FACTOR rig implemented at a DLR in Göttingen, another test module is mounted at the University of Florence (UNIFI) to perform a detailed characterization of the combustor aerothermal flowfield. The CS design and scale are identical for the UNIFI and DLR test rigs. Because of cost constraints, and for easier measurements inside the CS, it is not intended to test the full annular chamber at UNIFI. It is suggested to use only three sectors of the combustor (54 deg) and focus the measurements on the central sector. Indeed, one can reasonably assume that the action of the two lateral swirlers is representative of the full 360 deg configuration. However, this assumption needs to be confirmed by a numerical simulation.

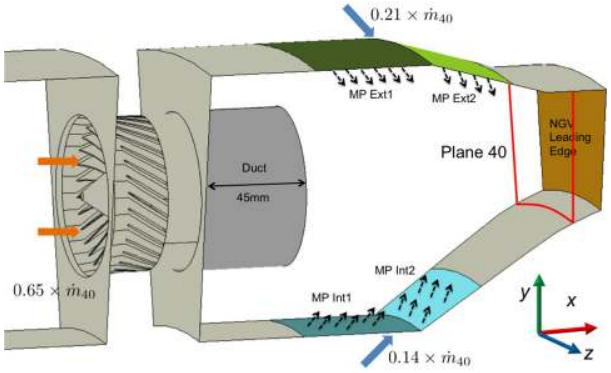


**Fig. 3 Schematic view of the CS: the multiperforated liner is shown in color, and the inner and outer feeding cavities are not shown (see color version online)**

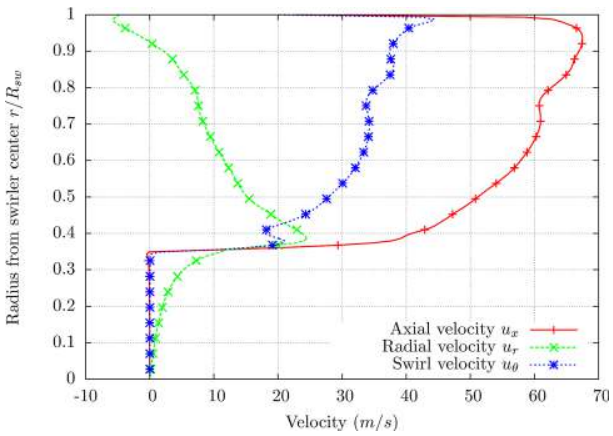


**Fig. 4 Swirler velocity profiles**

## 3 Validation of the Trisector Approach by LES

**3.1 Numerical Setup.** The full annulus configuration installed at a DLR is far too large to be properly numerically simulated, at least during the design phase. However, a single sector with periodicity along the azimuthal direction is fairly representative of a full annulus and can be used as reference to compare with the simulation of the UNIFI trisector rig with lateral walls (see Fig. 5).

It was decided to perform LES of these two configurations, despite an increased computational cost versus more classical RANS approaches. Indeed, LES constitute the state-of-the-art for combustion chambers simulation as they allow a dynamic representation of the large scale motions whose contributions are critical in complex geometries [16,17]. The filtered compressible Navier Stokes are numerically solved by the parallel code AVBP [18]. The solver uses the cell-vertex finite volume approximation and is based on an explicit temporal integration scheme. Therefore, the timestep is limited by the Courant–Friedrichs–Lewy condition (CFL = 0.7). A two-step Taylor–Galerkin numerical scheme [19] provides third-order accuracy in time and space. Such scheme provides low dispersion and diffusion, and is therefore adequate for LES. In this study, the Smagorinsky model [20] is used to account for the subgrid scale viscosity. Such a purely dissipative approach is appropriate for turbulent mixing flow, as

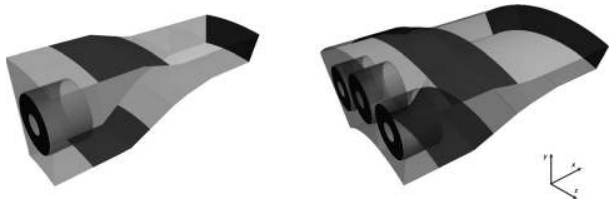

**Fig. 5 Domain of the monosector and trisector simulations**

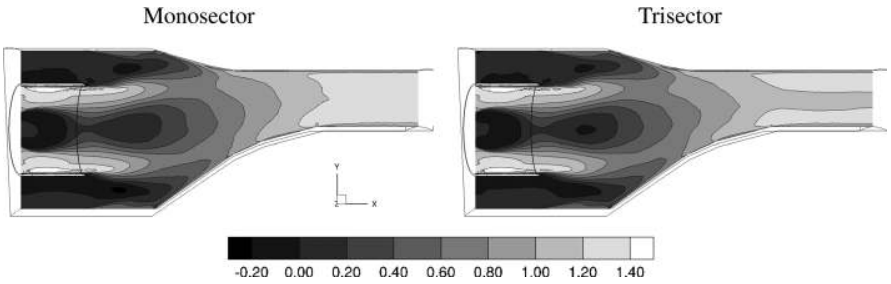


**Fig. 6 Nondimensional axial velocity $U/U_{ref}$ in the central plane**

in combustion chambers the dominant effect of small-scale turbulence is the dissipative effect.

As indicated in Fig. 3, the CS liners are perforated for effusion cooling on four distinct patches. The cost of meshing all the holes (<0.5 mm diameter, 5164 holes/sector) is definitely prohibitive. Therefore, a model is used to account for the momentum injection at the multiperforated plates. Mendez and Nicoud [21] propose an adiabatic homogeneous boundary condition providing satisfactory results for purely streamwise injection, which is the case in FACTOR CS. The fluxes are averaged over the surface of the multiperforated plate without distinction of the wall and the perforation, resulting in a homogeneous boundary condition. Though this homogeneous concept yields a good global approximation, it does not reproduce the flow near the wall due to the strong heterogeneity inherited from the suction side and the perforation. This model is applied on the four effusion cooling liners (dark zones in Fig. 5).

At the inlet, the swirler velocity profiles shown in Fig. 4 are imposed on the annular patches, with a constant temperature $T = 531$ K. All the walls use a law-of-the-wall approach. The outlet is located 110 mm downstream plane 40+, to be sufficiently far from the region of interest. A 3D characteristic boundary condition [22,23] is used to avoid acoustic reflections, while maintaining the pressure level close to the target value.

The geometry and mesh of the trisector is the multiplication of the monosector, and therefore, the central sector has exactly the same mesh in the two configurations. A single sector is meshed with 12.8 M tetrahedral cells, which is voluntarily finer than a standard mesh for such a configuration. In the core of the recirculation zone and near the effusion plates, the cell edge is 0.8 mm. The trisector mesh contains 38.3 M cells. Once the flow is established, the results of both simulations are time-averaged over 150 ms, which are about 10 through flow times. The explicit formalism limits the timestep, which is around $2.4 \times 10^{-7}$s in both simulations (same mesh). The trisector simulation is run over 1024 cores, for a cost of 256.000 computational hours.

**3.2 Numerical Results.** The time-averaged solutions show that the flowfield of the central sector is very similar in both cases. The axial velocity in the central plane is nondimensionalized by the mean axial velocity at the swirler exit ($U_{ref}$) and shown in Fig. 6. A central recirculation zone lays after the swirler hub and extends until the 2/3 of the duct length. Recirculation zones also appear in the region above and below the duct, where there is no mean flow stream and the effusion cooling does not blow out the fluid. Axial velocity is plotted along the centerline (swirler axis) in Fig. 7. One can observe that at the exit of the duct, the axial velocity falls very quickly because of strong diffusion, and even reaches small negative values in the trisector case. However, this second recirculation is too small to affect significantly the flow field. Regarding the combustor exit, the mean solutions are circumferentially averaged in plane 40 and the radial profiles of swirl and pitch angle are shown in Fig. 8. The pitch angles are identical, while the swirl angle is only reduced by 3 deg in the upper part of the channel for the trisector, which is negligible.

The turbulent kinetic energy is calculated as $k = 1/2(u^2_{x,\mathrm{rms}} + u^2_{r,\mathrm{rms}} + u^2_{\theta,\mathrm{rms}})$ and nondimensionalized by $U^2_{\mathrm{ref}}$. Figure 9 shows turbulence fields in the central plane ($\beta = 0$ deg) and at the limit of the central sector (i.e., the periodicity plane for the monosector). Turbulence is mainly created in the shear zone between the hot jet exiting the swirler and the low velocity surrounding air. As velocity profiles are used at the inlet, no turbulence is created at the exit of the swirler, except in the shear zone around the recirculation zone. Overall, the turbulence distribution and levels are identical between the two simulations. Results not reported here show exactly the same trend at the exit of the CS.

The hot spot in plane 40 is shown in Fig. 10. An overall transport of hot fluid is noticeable for the trisector (see Fig. 11): Hot air is blocked in the top left corner (D) and in the bottom right corner (C). Because of the overall swirl (clockwise when looking downstream), a small part of each swirler stream is convected toward

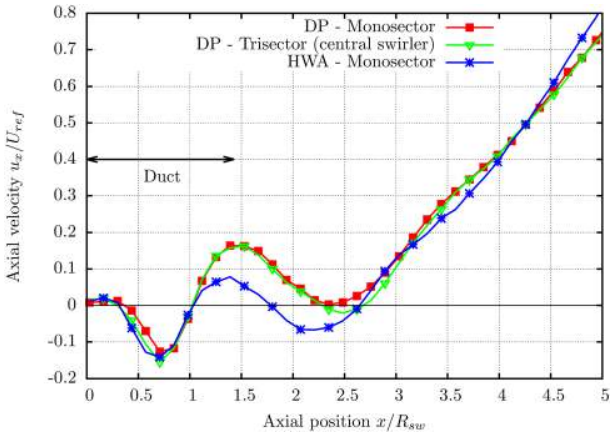


**Fig. 7 Axial velocity $U/U_{ref}$ along the centerline ($x$ axis)**

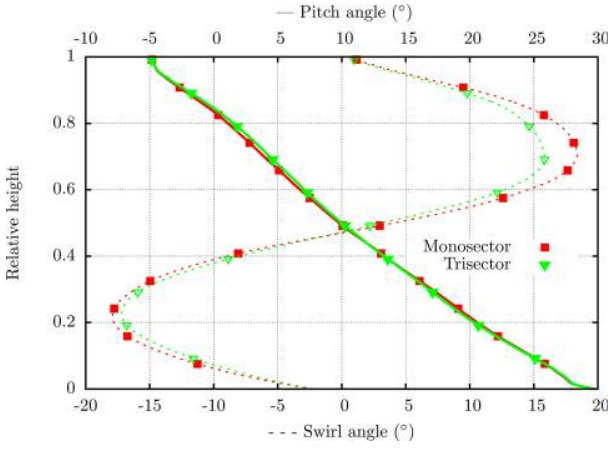


**Fig. 8 Circumferentially averaged profiles of swirl and pitch angle in plane 40**

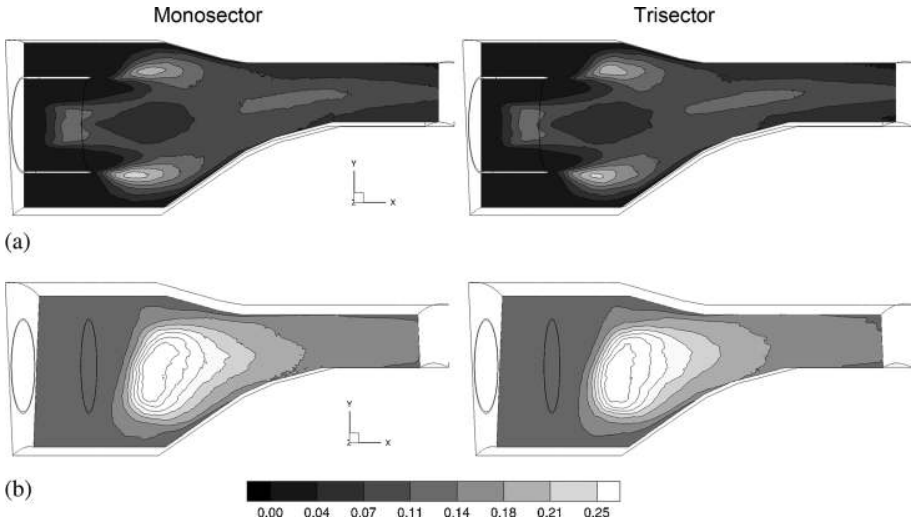


**Fig. 9 Nondimensional turbulent kinetic energy $k/U_{ref}^2$, (*a*) central plane $\beta = 0$ deg and (*b*) periodicity plane $\beta = 9$ deg**

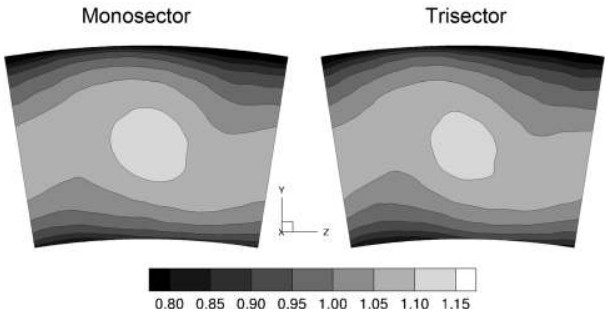


**Fig. 10 Nondimensional temperature field $(T/\bar{T}_{40})$ in plane 40**

the adjacent sector on the right (A → B → C). In the case of a full annulus (periodic simulation), this effect is balanced by the periodicity of the configuration, resulting in a centered hot spot for each sector. For the trisector configuration, the reduced effective confinement effect tends to reduce the strength of the left hot spot while emphasizing the right one. The central sector seems however not affected. This is confirmed by locally calculating the temperature difference $(T_{mono} - T_{tri})/T_{tri}$ which is mostly below 1%, and at maximum is 4%. The solutions are circumferentially averaged and the total temperature is plotted in Fig. 12. Results confirm that the central hot spot is not affected by the presence of lateral walls on the adjacent sectors.

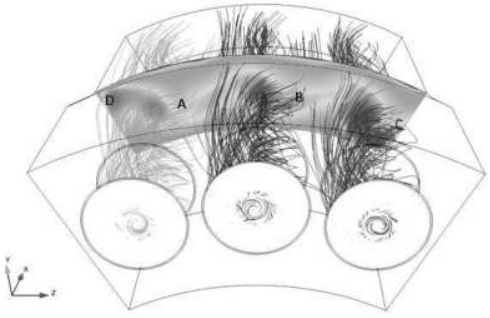


**Fig. 11 Streamlines emitted from each swirler toward plane 40 in the trisector**

Finally, the dynamics and unsteady mixing between the hot swirling core and effusion cooling is similarly predicted in both cases, as indicated by the rms values of temperature shown in Fig. 13. The highest levels of temperature fluctuations (60–70 K) are located in the near wall region, where the effusion cooling mixes with the central hot core. In the central region, fluctuations are lower (20 K) and only attributed to the presence of isolated pockets of colder fluid in the chamber. This indicates that the presence of lateral walls does not alter significantly the intensity of mixing.

## 4 Isothermal Operating Point

**4.1 Selection of the Operating Point.** The test campaign of the trisector rig includes turbulence and velocity measurements at the exit of the CS by means of HWA (see further section). Such measurement technique requires the flow to be isothermal, as the velocity is determined based on the quantity of heat convected away by the fluid. Therefore, an isothermal operating point representative of the nominal conditions has to be selected and validated by a numerical simulation. In order to ensure a similar turbulence level in both isothermal and nonisothermal cases, most nondimensional parameters have to be conserved.

Swirler Reynolds number

$$\mathrm{Re}_{sw} = \frac{\rho_{sw} u_{sw} D_{sw}}{\mu_{sw}}$$

Swirler Mach number

$$\mathrm{M}_{sw} = \frac{u_{sw}}{\sqrt{\gamma R T_{sw}}}$$

Effusion cooling Reynolds number

$$\mathrm{Re}_{cool} = \frac{\rho_{cool} u_{cool} D_{cool}}{\mu_{cool}}$$

Effusion cooling blowing ratio

$$\mathrm{BR} = \frac{(\rho u)_{cool}}{(\rho u)_{sw}}$$

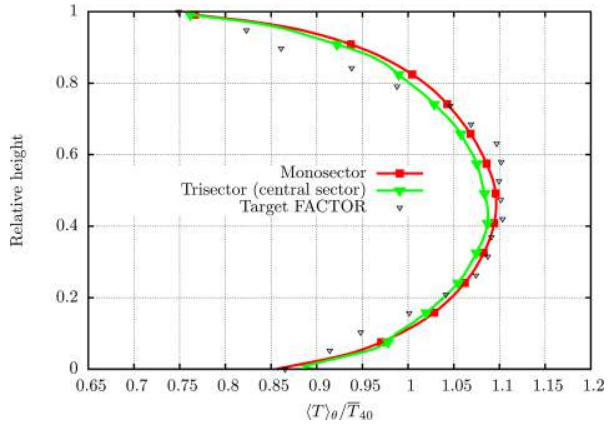


**Fig. 12 Circumferentially averaged profile of total temperature in plane 40**

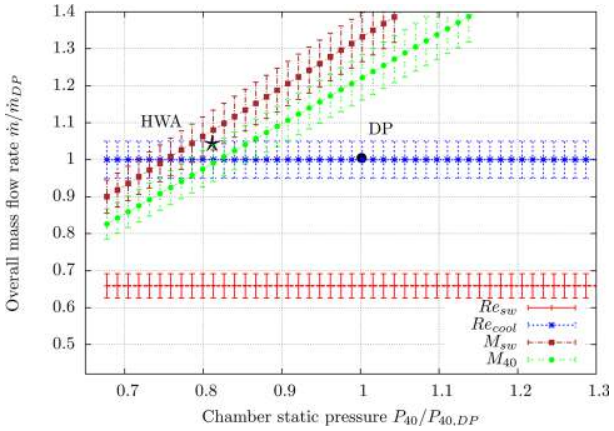


**Fig. 14 Mass flow, pressure map with lines conserving the nondimensional parameters of the test rig**

Effusion cooling momentum flux ratio

$$\text{MFR} = \frac{(\rho u^2)_{\text{cool}}}{(\rho u^2)_{\text{sw}}}$$

The blowing ratio being the ratio of mass flux per unit area, is conserved if the flow split between the hot and cold streams is kept constant, whatever the operating conditions. Momentum flux ratio is similar to $\text{BR} \times u_{\text{cool}}/u_{\text{sw}}$. If the flow split is conserved, the MFR at isothermal conditions increases by a factor $\rho_{\text{cool}}/\rho_{\text{sw}} \simeq 1.77$ versus nominal conditions. It was decided to keep the flow split unchanged to conserve the blowing ratio despite a difference in MFR. The control parameters that govern these nondimensional numbers are limited: Chamber pressure $P$, temperature $T$, and total mass flow $\dot{m}$. However, the rig uses an ambient air chiller to cool down the flow exiting the compressor, and thus the only possible value for the temperature is the same as the cavities temperature at design point (DP): $T = T_{\text{amb}}$. As a consequence, the only possibility is to adjust the total mass flow $\dot{m}$ and pressure $P$ individually. Only a limited number of operating points allow to conserve each nondimensional between isothermal and nonisothermal conditions. Figure 14 shows the lines on which the nondimensional parameters are conserved (with $\pm 5\%$ error bars), in a $(P, \dot{m})$ chart. The DP is shown for reference $(\cdot)$. In the current investigation, where $\dot{m}$ and $P$ are regulated individually,

**Table 1 Operating conditions for the isothermal (HWA) and nonisothermal (DP) points**

| | DP | HWA |
|---|---|---|
| Normalized total mass flow | 1 | 1.04 |
| Flow split swirlers | 65% | 65% |
| Flow split cooling cavities | 35% | 35% |
| Normalized chamber pressure | 1 | 0.81 |
| Swirler inlet temperature | 531 K | 300 K |
| Cooling cavities temperature | 300 K | 300 K |
| Swirler Reynolds number $\text{Re}_{\text{sw}}$ | 111,000 | 175,500 |
| Swirler Mach number $M_{\text{sw}}$ | 0.112 | 0.108 |
| Effusion cooling Reynolds $\text{Re}_{\text{cool}}$ | 2350 | 2440 |
| Plane 40 Mach number $M_{40}$ | 0.104 | 0.109 |

Reynolds numbers are unaffected by pressure, and thus only one value of mass flow allows to conserve the Reynolds numbers. According to this chart, an isothermal operating point is selected $(\star)$ within the rig domain of operability, at a reduced pressure and slightly increased mass flow, as detailed in Table 1. This operating point should now be simulated by LES and compared for validation with the previous simulations.

**4.2 Validation by LES.** As a first approach, it is assumed here that the moderate change of mass flow rate (+4%) and

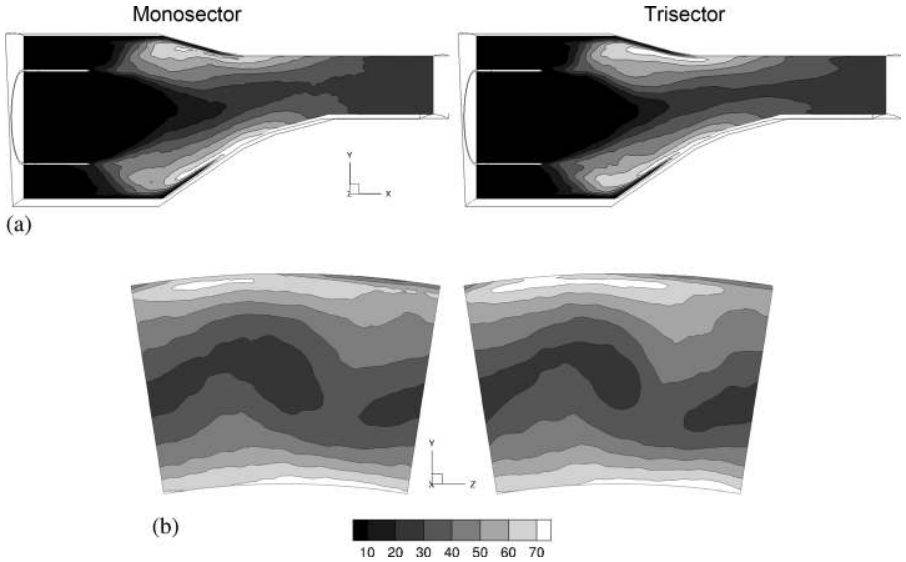


**Fig. 13 Temperature fluctuations $T_{\text{rms}}$ (*K*), (*a*) central plane $\beta = 0$ deg and (*b*) plane 40**

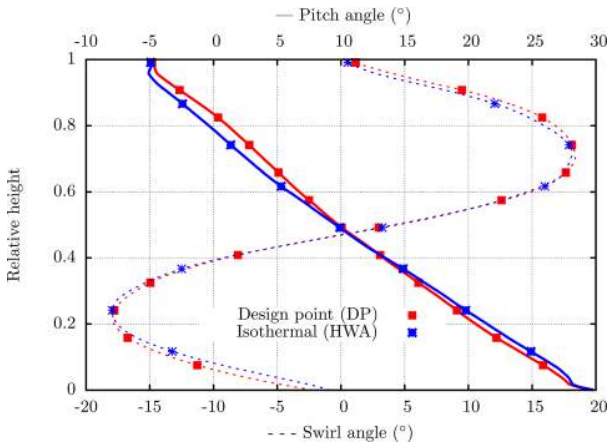


**Fig. 15 Circumferentially averaged profiles of swirl and pitch angle in plane 40**

pressure level (−19%) does not significantly alter the topology of the flow field at the inlet of the swirler. In this case, the inlet velocity profiles can be scaled down to match the isothermal conditions. This is done for each velocity component by

$$\frac{u_{i,\mathrm{HWA}}}{u_{i,\mathrm{DP}}} = \frac{T_{\mathrm{HWA}}\dot{m}_{\mathrm{HWA}}P_{\mathrm{DP}}}{T_{\mathrm{DP}}\dot{m}_{\mathrm{DP}}P_{\mathrm{HWA}}} = 0.725 \tag{3}$$

As this scaling is uniform for $u_x$, $u_r$, $u_\theta$, there is no change in the swirl number, and thus no modification of the flow regime is expected in this region.

The monosector simulation presented previously is now compared to the isothermal simulation which is run and time-averaged for the same physical time. The flowfields are normalized by $U_{\mathrm{ref}}$, which is also scaled down for isothermal simulation (Eq. (3)). The axial velocity along the centerline was plotted in Fig. 7. The extent of the central recirculation zone is identical to the nonisothermal case. The diffusion occurring inside the duct and at its exit seems enhanced by the isothermal conditions, and the reduction of axial velocity finally leads to the formation of a second recirculation bubble. However, this zone length is limited, and velocity finally converges toward the same velocity distribution.

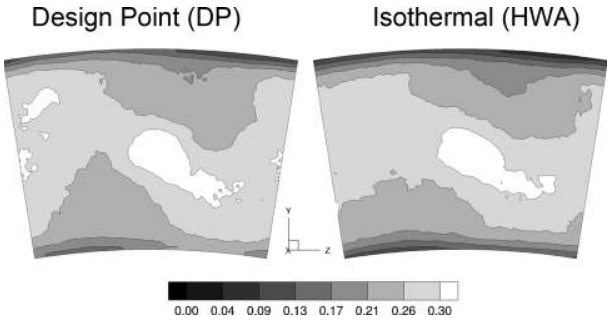


**Fig. 17 Turbulence intensity TU = $\sqrt{(2/3)k}/\|\mathbf{u}\|$ in plane 40**

The circumferentially averaged profiles of swirl and pitch angles in plane 40 are shown in Fig. 15. The modification of operating conditions results in flow angle changes below 2 deg, which is negligible.

As HWA measurements intend to give exhaustive data on turbulence, it is of prime importance that the isothermal operating point is representative of the DP for these quantities. Scaled fields of $k/U_{\mathrm{ref}}^2$ are shown in Fig. 16 for the central plane and the periodicity plane of the CS. Overall the turbulent kinetic energy levels and distribution are very similar. The turbulent kinetic energy absolute values in the shear zone at the duct exit are smaller for an HWA because of the absence of density gradient and a lower velocity gradient than for a DP. Finally, in plane 40, where HWA measurements are performed, the turbulence intensity TU = $\sqrt{(2/3)k}/\|\mathbf{u}\|$ is identical (in the range of 0.2–0.35), as shown in Fig. 17.

**4.3 CS Hydrodynamic Activity.** The hydrodynamic activity created by the swirler is of particular interest for combustion chambers. When the swirl number is sufficiently high, vortex breakdown can occur, and a precessing vortex core (PVC) appears, forming a low pressure rotating finger. In all the simulations reported here, the swirl is strong enough to create a PVC despite the fact that velocity profiles are used instead of resolving the swirler. Such structure can be observed by locally monitoring pressure at the swirler exit.

A virtual probe is located in the duct, 18 mm after the swirler exit at a radius $R = 7$ mm from the axis of the swirler. The pressure signal is recorded during the simulations, with a sampling

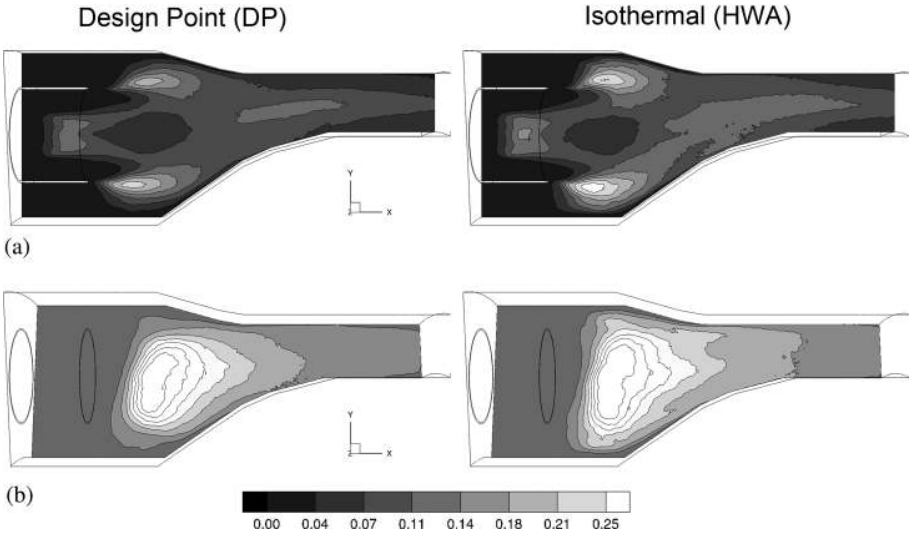


**Fig. 16 Nondimensional turbulent kinetic energy $k/U_{\mathrm{ref}}^2$, (*a*) central plane $\beta = 0$ deg and (*b*) periodicity plane $\beta = 9$ deg**

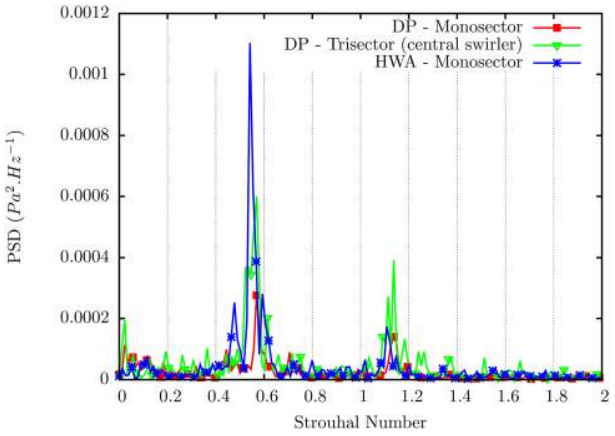


**Fig. 18 PSD of the pressure signal of a probe located inside the duct for the three simulations**

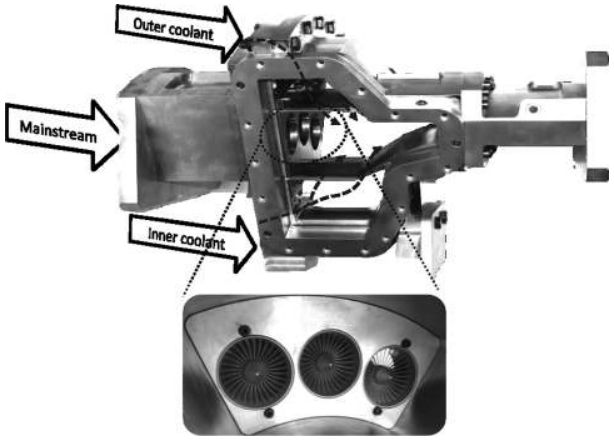


**Fig. 20 Sector test rig and detail of the swirlers (upstream view)**

frequency between 35 and 43 kHz, resulting in a frequency step between 5 and 10 Hz depending on the simulation. The power spectral density (PSD) of the pressure signal from this probe is computed for each case and plotted as a function of the Strouhal number $\mathrm{St} = f D_{sw}/U_{ref}$ in Fig. 18. One can clearly observe that all the simulations exhibit the same tonal activity at $\mathrm{St} \simeq 0.57$ and $\mathrm{St} \simeq 1.14$. The lowest frequency corresponds to the rotation frequency of the PVC, and the highest is its first harmonics, which contains less energy. Therefore, results show that the CS exhibits the same hydrodynamic activity under nonisothermal and isothermal conditions, but the frequency of the PVC is lowered from 530 Hz to 360 Hz.

In sight of these results, it can be concluded that there is no change in the topology of the flow field, neither in the normalized turbulence distribution between isothermal and nonisothermal operating points. Therefore, HWA measurements conducted in isothermal conditions are expected to be representative of the DP.

## 5 Experimental Investigation

**5.1 Test Rig Environment.** The numerical analysis of the CS presented previously confirms the representativity of the trisector layout versus full annulus, and the selection of the isothermal operating point. These results supported the design and operability choices for the trisector rig and allowed to proceed to rig manufacturing, assembly and commissioning at the UNIFI.

The test section is operated in a hot wind tunnel, whose layout is sketched in Fig. 19: Compressed air, discharged by two screw compressors, crosses a chiller, which cools the mass flow down to ambient temperature and removes the humidity. Compressors deliver a mass flow rate of ≈1 kg/s at a maximum pressure of 10 bar; the desired mass flow and pressure level for the tests are adjusted using several valves located along the lines: One modulating valve at the intake of each compressor, one control valve on the mainstream and one on each coolant lines. During the tests, valves are automatically driven through a proportional-integral-derivative (PID) control system to keep constant operating conditions; in particular, the control system, developed with LABVIEW®, can act simultaneously on four valves reaching the desired set point of pressure or mass flow in few seconds.

Along the line a 2 $m^3$ vessel dumps pressure fluctuations. Mass flow is then divided into two different lines: The mainstream and the cooling flows which are independently operated by means of three electronically controlled globe valves. Mainstream mass flow rate is measured by means of a calibrated orifice (standard EN ISO 5167-1) and then sent to a 600 kW electric heater, which rises temperature up to the target value. The heater is automatically controlled by means of a PID system which keeps constant temperature at the inlet of the test rig. Coolant is delivered to the rig through two separated lines: Each line discharges air in a plenum, which is connected with the test article through three pipes. The pipes drive the coolant in a cavity, which works as a feeding plenum for the multiperforated liner. Before reaching the stack, the overall mass flow crosses a final vee-ball valve able to sustain high temperature conditions; this valve is automatically controlled and it is aimed at setting the desired pressure level inside the test section.

Figure 20 shows a picture of the test article: It is possible to observe the two annular multiperforated liners and the housing of the three swirlers, here mounted without ducts.

**5.2 Instrumentation and Test Planning.** The final arrangement of the test rig was strongly influenced by demands of the planned measurement techniques. In particular, measurements will be dedicated to investigate the flow behavior at Plane 40 and Plane 40+, which represent the position of the interface between the combustor and the HP turbine modules. The first measurements aim at investigating the flow and thermal fields resulting from the mixing of the swirled mainstream and the coolant

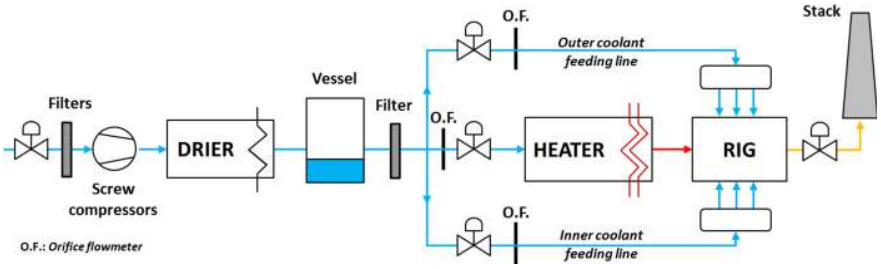


**Fig. 19 Sketch of the test facility**

coming out from the multiperforated liner. Data will be obtained using a 5-hole probe equipped with a special thermocouple; it will give information on the pressure, the velocity and the temperature distributions both in planes 40 and 40+. The probe will be mounted on an automatic traverse system, fixed on the outer casing by means of an adaptive flange that allows the coincidence between the machine axis and the center of rotation of the azimuthal motion. The traverse system, developed in *Turbomeca*, is able of azimuthal and radial displacements, in addition to the probe angulation, through 3 stepper motors; the positioning accuracy is less than 0.1 mm in both directions. Additional information on the unsteady thermal field will be provided by a special high-frequency response thermocouple mounted on the motion system to acquire data up to 2 kHz.

Afterward the traverse system will be employed to analyze the velocity field at the outlet plane of the CS by means of HWA; since this technique is not compatible both with the high temperature of the mainflow and the mixing between hot and cold flows, the numerical analysis described above will provide an "isothermal-room temperature" operating point representative of the nominal conditions. Hot wire tests will add time resolved information on the flow field, especially in terms of turbulence intensity and length scale. This comprehensive experimental database will allow to deepen the knowledge of aerothermal flow field at the combustor exit; moreover, data gathered with high-frequency response probes will allow to assess the reliability and performance of an LES approach.

**5.3 Commissioning of the Test Rig.** In view of the upcoming installation of the automatic traverse system and its related instrumentation, several preliminary tests were carried out to check the operability of the entire test facility and moreover to verify that long-term stable conditions were guaranteed.

The test rig was equipped with several static pressure taps and thermocouples; a custom-tailored LABVIEW-based application provided accurate monitoring and recording of the conventional data from measurement data scanners. A pressure scanner NetScanner™ system 9116 with temperature compensated piezoresistive relative pressure sensors is employed to measure static pressure in 16 different locations inside the rig; the maximum uncertainty is ±52 Pa with a level of confidence of approximately 95%. A HP/Agilent® 34972A data acquisition/switch unit is used to monitor the flow temperature measured by means of several T-type thermocouples (±0.5 K uncertainty, 95% level of confidence). In addition, two thermocouples are welded on each liner and further three of them are located inside the metal, close to the location of Plane 40; metal temperatures are used also to assess the reaching of the thermal steady-state conditions. Mass flow rates were measured by means of calibrated orifices; they are affected by an error of 2–3% according to the standard ANSI/ASME PTC 19.1 [24] based on the Kline and McClintock method [25].

Figure 21 shows the behavior of the main measured quantities in the rig during a warm up sequence: Each quantity is normalized using the nominal value at the inlet of the swirlers. The warm up sequence is concluded when the metal temperatures (dashed lines in Fig. 21(*a*)) reach an asymptotic value, roughly 125 min after the starting of the test. It is possible to appreciate how the PID control systems keep stable the operation of the facility once the steady-state conditions are reached: The maximum oscillation of mass flows is ±1.5%, while for pressures and temperatures is ±0.5%.

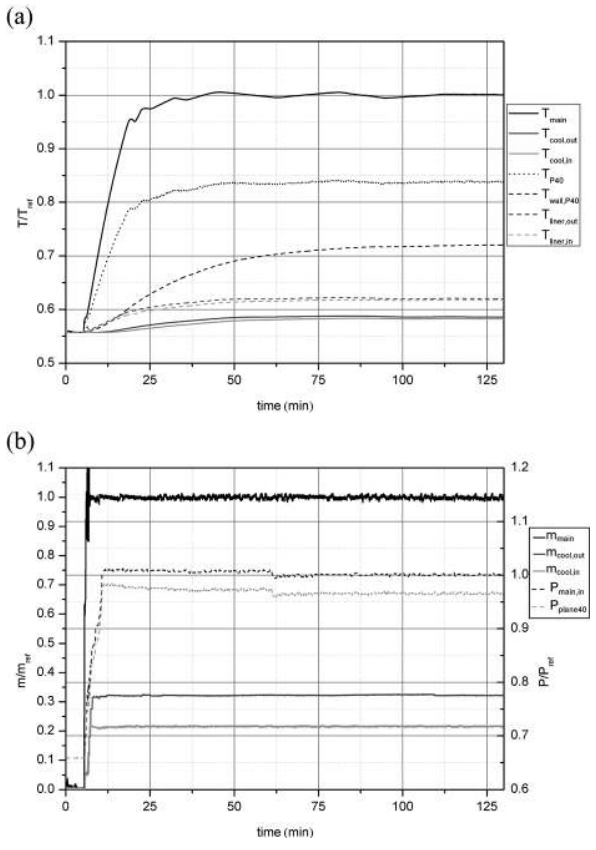


**Fig. 21 Preliminary test: warm up of the test rig, (*a*) fluid and metal temperatures and (*b*) mass flow rates and pressures across the swirlers**

## 6 Conclusion

The design of an engine-representative CS dedicated to hot streak generation was presented. A real scale trisector test rig was developed in order to test the CS before the full annulus turbine testing. State-of-the-art LES were performed on the wall-bounded trisector and a periodic monosector, showing very little difference on the central swirler, which validates this design choice. Especially, the hot spot was found to present a maximum local difference of 4%. An isothermal operating point was selected for an HWA based on the conservation of nondimensional parameters and assessed by LES. Results showed a very similar turbulence distribution between the isothermal and nominal conditions, confirming the choice of this operating point. Finally, a brief description of the trisector rig and its related instrumentation was presented. It was shown that the automatic control system allows the facility to operate at stable conditions for long time runs. In sight of the presented results and the recent successful installation of the test rig, it is expected to finally validate the design of the FACTOR CS in early 2014, before the experimental campaign with the full CS and HP turbine at DLR in 2015.

## Acknowledgment

The research leading to these results (FACTOR project)[1] has received funding from the European Union Seventh Framework Programme (FP7/2007-2013) under Grant Agreement No. 265985. The simulations presented here were performed using HPC resources from GENCI-IDRIS (Grant No. 2013-x20132b5031). Authors wish to express their gratitude to *Avio Aero* and *Progesa* for the manufacturing of the test rig.

## Nomenclature

BR = blowing ratio
$D$ = diameter (m)

[1] www.factor-fp7.eu

$f$ = frequency (Hz)
$k$ = turbulent kinetic energy ($m^2/s^2$)
$M$ = Mach number
$\dot{m}$ = mass flow rate (kg/s)
MFR = mass flow ratio
$P$ = static pressure (Pa)
$R$ = radius (m)
Re = Reynolds number
$S_N$ = Swirl number
St = Strouhal number
$T$ = total temperature (K)
$\bar{T}$ = mean total temperature (K)
TU = turbulence intensity
$u$ = velocity (m/s)
$Y^+$ = nondimensional wall distance
$\beta$ = azimuthal position (deg)
$\gamma$ = ratio of specific heat
$\mu$ = dynamic viscosity (Pa·s)
$\rho$ = density ($kg/m^3$)

## Subscripts

amb = ambient
cool = effusion cooling
$r$ = radial direction
ref = swirler inlet conditions
rms = root mean square
sw = mainstream (swirler)
$x$ = axial direction
40 = plane 40
$\theta$ = circumferential direction

## References


[1] Povey, T., Chana, K. S., Jones, T. V., and Hurrion, J., 2007, "The Effect of Hot-Streaks on HP Vane Surface and Endwall Heat Transfer: An Experimental and Numerical Study," ASME J. Turbomach., **129**(1), pp. 32–43.
[2] Simone, S., Montomoli, F., Martelli, F., Chana, K. S., Qureshi, I., and Povey, T., 2011, "Analysis on the Effect of a Nonuniform Inlet Profile on Heat Transfer and Fluid Flow in Turbine Stages," ASME J. Turbomach., **134**(1), p. 011012.
[3] Butler, T., Sharma, O., Joslyn, H., and Dring, R., 1989, "Redistribution of an Inlet Temperature Distortion in an Axial Flow Turbine Stage," J. Propul. Power, **5**(1), pp. 64–71.
[4] Roback, R. J., and Dring, R. P., 1993, "Hot Streaks and Phantom Cooling in a Turbine Rotor Passage: Part 1—Separate Effects," ASME J. Turbomach., **115**(4), pp. 657–666.
[5] Shang, T., 1995, "Influence of Inlet Temperature Distortion on Turbine Heat Transfer," Ph.D. thesis, Department of Aeronautics and Astronautics Massachusetts Institute of Technology, Cambridge, MA.
[6] Povey, T., and Qureshi, I., 2009, "Developments in Hot-Streak Simulators for Turbine Testing," ASME J. Turbomach., **131**(3), pp. 1–15.
[7] Dorney, D. J., Gundy-Burlet, K. L., and Sondak, D. L., 1999, "A Survey of Hot Streak Experiments and Simulations," Int. J. Turbo Jet Engines, **16**(1), pp. 1–15.
[8] Hilditch, M. A., Fowler, A., Jones, T. V., Chana, K. S., Oldfield, M. L. G., Ainsworth, R. W., Hogg, S. I., Anderson, S. J., and Smith, G. C., 1994, "Installation of a Turbine Stage in the Pyestock Isentropic Light Piston Facility," ASME Paper No. 94- GT-277.
[9] Barringer, M. D., Thole, K. A., and Polanka, M. D., 2007, "Experimental Evaluation of an Inlet Profile Generator for High-Pressure Turbine Tests," ASME J. Turbomach., **129**(2), pp. 382–394.
[10] Mathison, R. M., Haldeman, C. W., and Dunn, M. G., 2012, "Aerodynamics and Heat Transfer for a Cooled One and One-Half Stage High-Pressure Turbine—Part I: Vane Inlet Temperature Profile Generation and Migration," ASME J. Turbomach., **134**(1), p. 011006.
[11] Stabe, R. G., Whitney, W. J., and Moffitt, T. P., 1984, "Performance of a High-Work Low Aspect Ration Turbine Tested With a Realistic Inlet Radial Temperature Profile," AIAA/SAE/ASME 20th Joint Propulsion Conference Cincinnati, OH, June 11-13, AIAA Technical Paper No. 84-1161.
[12] Joslyn, H. D., and Dring, R. P., 1988, "A Trace Gas Technique to Study Mixing in a Turbine Stage," ASME J. Turbomach., **110**(1), pp. 38–43.
[13] Shang, T., Guenette, G., Epstein, A., and Saxer, A., 1995, "The Influence of Inlet Temperature Distortion on Rotor Heat Transfer in a Transonic Turbine," 31st AIAAASME/SAE/ASEE Joint Propulsion Conference and Exhibit, San Diego, CA, July 10–12, AIAA Paper No. 95-3042.
[14] Shih, T.-H., Liou, W. W., Shabbir, A., Yang, Z., and Zhu, J., 1995, "A New k-Eddy Viscosity Model for High Reynolds Number Turbulent Flows," Comput. Fluids, **24**(3), pp. 227–238.
[15] Beér, J., and Chigier, N., 1972, *Combustion Aerodynamics*, Wiley, New York.
[16] Poinsot, T., and Veynante, D., 2011, *Theoretical and Numerical Combustion*, 3rd ed., T. Poinsot & D. Veynante, Toulouse, France.
[17] Sagaut, P., 2006, *Large Eddy Simulation for Incompressible Flows: An Introduction* (Scientific Computation), Springer, Berlin.
[18] Schoenfeld, T., and Rudgyard, M., 1999, "Steady and Unsteady Flows Simulations Using the Hybrid Flow Solver AVBP," AIAA J., **37**(11), pp. 1378–1385.
[19] Colin, O., and Rudgyard, M., 2000, "Development of High-Order Taylor–Galerkin Schemes for LES," J. Comput. Phys., **162**(2), pp. 338–371.
[20] Smagorinsky, J., 1963, "General Circulation Experiments With the Primitive Equations: 1. The Basic Experiment," Mon. Weather Rev., **91**(3), pp. 99–164.
[21] Mendez, S., and Nicoud, F., 2008, "Adiabatic Homogeneous Model for Flow Around a Multiperforated Plate," AIAA J., **46**(10), pp. 2623–2633.
[22] Poinsot, T., and Lele, S., 1992, "Boundary Conditions for Direct Simulations of Compressible Viscous Flows," J. Comput. Phys., **101**(1), pp. 104–129.
[23] Yoo, C. S., and Im, H. G., 2007, "Characteristic Boundary Conditions for Simulations of Compressible Reacting Flows With Multi-Dimensional, Viscous and Reaction Effects," Combust. Theor. Model., **11**(2), pp. 259–286.
[24] Abernethy, R. B., Benedict, R. P., and Dowdell, R. B., 1985, "ASME Measurement Uncertainty," ASME J. Fluids Eng. **107**(2), pp. 161–164.
[25] Kline, S. J., and McClintock, F. A., 1953, "Describing Uncertainties in Single Sample Experiments," ASME J. Mech. Eng., **75**(1), pp. 3–8.

# Compatibility of Characteristic Boundary Conditions with Radial Equilibrium in Turbomachinery Simulations

C. Koupper*
*Turbomeca, 64510 Bordes, France*
T. Poinsot†
*Institut de Mécanique des Fluides de Toulouse, 31400 Toulouse, France*
and
L. Gicquel‡ and F. Duchaine§
*Centre Européen de Recherche et de Formation Avancée en Calcul Scientifique, 31057 Toulouse, France*

DOI: 10.2514/1.J052915

**Setting up outlet boundary conditions in configurations that have a strong rotating motion is a crucial issue for turbomachinery simulations. This is usually done using the so-called radial equilibrium assumption, which is used before the simulation and provides an approximate expression for the pressure profile to impose in the outlet plane. This paper shows that recent methods developed for compressible flows, based on characteristic methods, including the effects of transverse terms, can capture the radial equilibrium naturally without having to impose a precomputed pressure profile. In addition, these methods are also designed to control acoustic reflections on boundaries, and the present work suggests that they could replace classical radial equilibrium assumption approximations when nonreflecting boundary conditions are required at the outlet of a turbomachine simulation, for example, in large eddy simulation. This is demonstrated in two cases: 1) a simple annulus flow with a swirl imposed at the inlet and 2) a transonic turbine vane.**

## Nomenclature

| | | |
|---|---|---|
| $a_0$ | = | speed of sound |
| $C$ | = | true chord length |
| $\mathcal{C}$ | = | constant velocity |
| $\boldsymbol{c}$ | = | velocity vector |
| $c_r$ | = | radial velocity |
| $c_x$ | = | axial velocity |
| $c_\theta$ | = | tangential (swirl) velocity |
| $K$ | = | reflection coefficient |
| $L$ | = | characteristic length |
| $\mathcal{L}$ | = | amplitude of characteristic waves |
| $M$ | = | Mach number |
| $P$ | = | static pressure |
| $\bar{P}_t$ | = | target mean static pressure |
| $T$ | = | static temperature |
| $T_t$ | = | total temperature |
| $R_{\text{air}}$ | = | specific gas constant |
| $R_1$ | = | inner radius |
| $R_2$ | = | outer radius |
| $r$ | = | radius |
| $t$ | = | time |
| $Y^+$ | = | nondimensional wall distance |
| $\alpha_i$ | = | integration constants |
| $\beta$ | = | damping coefficient |
| $\gamma$ | = | ratio of specific heat |
| $\lambda$ | = | wave characteristic velocity |
| $\mu$ | = | dynamic viscosity |
| $\mu_t$ | = | turbulent viscosity |
| $\rho$ | = | density |
| $\sigma$ | = | reflection coefficient |
| $\tau$ | = | characteristic time |

*Subscripts*

| | | |
|---|---|---|
| $t$ | = | transverse terms, or target |
| is | = | isentropic |

## I. Introduction

AMONG all the difficulties encountered in the numerical simulations of fluid dynamics, prescribing an adequate boundary condition (BC) has always been an important point. It is well known in the computational fluid dynamics community that imposing a realistic, nondisturbing outlet boundary condition is complex, if not impossible in most cases. An ideal condition should have a weak influence on the upstream flow, preserve stability, and control acoustic waves reflection and/or dissipation [1–5]. This necessity becomes particularly important for high-fidelity simulations: large eddy simulation (LES) and direct numerical simulation (DNS). Indeed, in such approaches, all (or part) of the turbulence scales are (is) directly resolved in a highly turbulent and unsteady context, and the boundary conditions must not create spurious reflections of acoustic waves inside the domain.

Satisfying all these conditions is difficult, and in practice the most common method is simply to apply a Neumann boundary condition sufficiently far from the region of interest. The convective derivative normal to the boundary is enforced to zero ($\partial/\partial\mathbf{n} = 0$), and the value of the variables at the boundary is extrapolated in the streamwise direction [6]. This simple approach is well suited for almost uniform steady-state flows: exit of a duct, plenum, etc. However, if the flow features important nonuniformities, or a strong gradient (due to a preferential fluid motion, for example), then a uniform Neumann BC is not adequate.

This is especially true for turbomachinery flows as high inhomogeneities are found at the stage exit: wake effect, unsteady flow bubbles, etc. Moreover, the swirling motion of the mean flow created by the deviation in the vane or rotor creates a positive radial pressure gradient: the so-called radial equilibrium. Assuming that pressure is homogeneous in the outlet plane is impossible. The

*Ph.D. Student, 25 Avenue J. Szydlowski; CERFACS CFD Team, 42 Avenue G. Coriolis, 31057 Toulouse, France; charlie.koupper@turbomeca.fr.
†Research Director, 2 Allée du Professeur Camille Soula. Associate Fellow AIAA.
‡Senior Research Fellow, CFD Team, 42 Avenue G. Coriolis.
§Senior Research Fellow, CFD and GlobC Teams, 42 Avenue G. Coriolis.

pressure gradient in the outlet section may be estimated (as it will be demonstrated later) and can be used as a BC at the exit section of a turbine: it is the radial equilibrium assumption (REA).

This approach is common for Reynolds-averaged Navier–Stokes (RANS) simulations of turbine flows. For example, the commercial code Fluent features a radial equilibrium option for the outlet BC: the user specifies the pressure at the hub, and the equations for radial equilibrium are integrated using flow properties obtained inside the domain. A radial profile of pressure is then prescribed as a Neumann BC. Negru et al. [7] use this technique to impose the pressure at the exit of a Francis turbine runner. In the same context of hydraulic turbines, Ferro et al. [8] simulated the inlet guide vanes of a hydraulic bulb turbine using the Fluent radial equilibrium option. Torresi et al. [9] and similarly Kim et al. [10] modelled a high-solidity Wells turbine used for oscillatory water column device (energy conversion), using radial equilibrium in the outlet section. Garg [11,12] studied the heat transfer of a rotating blades of various gas turbines, imposing in a RANS solver a radial equilibrium pressure distribution one true chord after the rotor blade trailing edge. A last example can be found for the RANS computation of the heat transfer of a low-pressure vane by Solano et al. [13], in which the measured pressure at the hub (from experiments) was used to prescribe the radial equilibrium at the outlet section.

For all these studies, imposing an outlet pressure profile is consistent with radial equilibrium but leads to a totally reflecting outlet in terms of acoustic waves. For RANS simulations, which do not capture the acoustic anyway, this is not an issue, but it becomes a problem for LES. Indeed, in the context of compressible LES, Navier–Stokes characteristic boundary conditions (NSCBCs) are commonly employed [1,4,5,14,15]. At an outlet, they allow one to control the influence of the incoming information (through wave amplitude) and thus both the pressure level and reflection coefficient of the BC. To perform a LES of turbomachines, being able to satisfy both the REA and NSCBC condition is of primary importance. This requires one to investigate how NSCBC conditions perform in flows with a strong rotation. It is shown here that the NSCBC formalism can let the physical radial pressure gradient establish naturally so that NSCBC can be used at the outlet of turbines without any additional treatment. This represents a significant improvement over existing techniques because of the following: 1) it allows one to capture the REA naturally, without a priori simplified evaluation of the pressure profile, and 2) it brings the power of non reflecting BCs in a field in which they have been used only for a few cases.

Section II introduces the equation of the simplified radial equilibrium and its physical meaning. Then, the formalism of the Navier–Stokes characteristic boundary condition is presented in Sec. III. Finally, in the last section, the ability of the NSCBCs to deal with the radial equilibrium is assessed in two test cases: a simple annulus (Sec. IV.A) and an industrial high-pressure turbine vane (Sec. IV.B).

## II. Simplified Radial Equilibrium

The radial equilibrium equations were first derived in the 1940s–1950s and published by Smith, Jr., in 1966 [16]. He showed that the whirling motion of a fluid inside a turbomachine creates a centrifugal force that has to be balanced by a centripetal one; a positive radial pressure gradient establishes [17]. By definition, it only applies to axial stations between blade rows where pseudoequilibrium can be achieved. The study was limited to axisymmetric flows, which also implies that the discrete action of the blades is not taken into account.

The usual denomination of radial equilibrium may refer either to the full (American) or simplified (British) definition. In the former case, it is "the complete radial momentum equation arranged in a form [which is] suitable for the determination of the flow field in a turbomachine" [16]. Coupled with a blade aerodynamic computation, it provides the balanced distribution of the flow properties from hub to casing between all vanes. In the simplified version (most common), the full equations are simplified assuming that the radial velocity is zero: $c_r = 0$. To fulfill the latter hypothesis, the axial stations of interest must be far enough from any blade. This condition is met when the outlet section is placed sufficiently far from the vanes. Only the simplified radial equilibrium is studied here.

The simplified radial equilibrium can be obtained by considering a flow with the following properties: no viscous effects; negligible heat conduction; a steady state; no gravity or volumic forces; axisymmetric flow, $\frac{\partial}{\partial\theta} = 0$; no radial velocity, $c_r = 0$.

Under these conditions, the flow is governed by the Euler equations for a compressible flow with the equation of state for the ideal gas. In cylindrical coordinates $(r, \theta, x)$, the momentum equation in the radial direction is

$$\frac{\partial c_r}{\partial t} + c_r \frac{\partial c_r}{\partial r} + \frac{c_\theta}{r}\frac{\partial c_r}{\partial \theta} - \frac{c_\theta^2}{r} + c_x \frac{\partial c_r}{\partial x} = -\frac{1}{\rho}\frac{\partial P}{\partial r} \tag{1}$$

Applying all the assumptions made previously ($c_r = 0$, $\partial/\partial\theta = 0$, and $\partial/\partial t = 0$) to Eq. (1) leads to the simplified radial equilibrium equation,

$$\frac{1}{\rho}\frac{\partial P}{\partial r} = \frac{c_\theta^2}{r} \tag{2}$$

where $P$ is the static pressure, $c_\theta$ is the azimuthal velocity component, and $\rho$ is the density.

## III. Navier–Stokes Characteristic Boundary Conditions

Nonreflecting boundary conditions have been extensively studied in the past decades [1–4,18–20] for LESs or DNSs of compressible flows. In three-dimensional turbulent unsteady flows, wave reflections from the boundaries of the domain have to be carefully controlled. Characteristic boundary conditions have the difficult task to ensure numerical stability and minimal acoustic reflections in regions in which the flow dynamic activity is high.

The characteristic form of the Navier–Stokes equations written for NSCBCs highlights the presence of waves crossing the boundary [3,18]. The outgoing waves leaving the domain can be calculated from the interior points, while the acoustic incoming wave has to be imposed and includes all effects of the domain outside the computational box. Many formulations have been proposed since the 1990s. Thomson [18] applied one-dimensional approximations of the characteristic boundary conditions for Euler equations. Poinsot and Lele [3] extended the formalism for Navier–Stokes equations by introducing the locally one-dimensional inviscid (LODI) assumptions. The LODI formalism is efficient for flows aligned with the direction normal to the boundary. However, when the flow or the acoustic waves do not reach the boundary at a normal angle, the one-dimensional assumptions are too restrictive, and instabilities, reflections, or nonphysical distortions can appear [2,4,20]. Yoo et al. [1] and Yoo and Im [2] proposed to include the transverse terms in the calculation of the incoming wave. This formalism is used here and described in the following.

The three-dimensional compressible Navier–Stokes and total energy conservation equations for a monospecies nonreacting flow can be written into a characteristic form [1] in Cartesian coordinates $(x_1, x_2, x_3)$, without viscous and source terms,

$$\frac{\partial}{\partial t}\begin{bmatrix} c_1 \\ c_2 \\ c_3 \\ \rho \\ P \end{bmatrix} + \begin{bmatrix} (\mathcal{L}_5 - \mathcal{L}_1)/\rho a_0 \\ \mathcal{L}_3 \\ \mathcal{L}_4 \\ \mathcal{L}_2 + (\mathcal{L}_5 + \mathcal{L}_1)/a_0^2 \\ \mathcal{L}_5 + \mathcal{L}_1 \end{bmatrix} + \begin{bmatrix} (\mathcal{T}_5 - \mathcal{T}_1)/\rho a_0 \\ \mathcal{T}_3 \\ \mathcal{T}_4 \\ \mathcal{T}_2 + (\mathcal{T}_5 + \mathcal{T}_1)/a_0^2 \\ \mathcal{T}_5 + \mathcal{T}_1 \end{bmatrix} = \begin{bmatrix} 0 \\ 0 \\ 0 \\ 0 \\ 0 \end{bmatrix} \tag{3}$$

with $a_0 = \sqrt{\gamma RT}$ as the speed of sound, $c$ as the velocity, and $\mathbf{U} = (c_1, c_2, c_3, \rho, P)$ as the primitive variable vector.

The amplitude vector of the characteristic waves $\boldsymbol{\mathcal{L}}$ can be developed as

$$\boldsymbol{\mathcal{L}} = \begin{bmatrix} \mathcal{L}_1 \\ \mathcal{L}_2 \\ \mathcal{L}_3 \\ \mathcal{L}_4 \\ \mathcal{L}_5 \end{bmatrix} = \begin{bmatrix} \frac{1}{2}\lambda_1\left(\frac{\partial P}{\partial x_1} - \rho a_0 \frac{\partial c_1}{\partial x_1}\right) \\ \lambda_2\left(\frac{\partial \rho}{\partial x_1} - \frac{1}{a_0^2}\frac{\partial P}{\partial x_1}\right) \\ \lambda_3 \frac{\partial c_2}{\partial x_1} \\ \lambda_4 \frac{\partial c_3}{\partial x_1} \\ \frac{1}{2}\lambda_5\left(\frac{\partial P}{\partial x_1} + \rho a_0 \frac{\partial c_1}{\partial x_1}\right) \end{bmatrix} \tag{4}$$

The characteristic velocities $\lambda_i$ associated with the waves amplitudes $\mathcal{L}_i$ are

$$\lambda_1 = c_1 - a_0 \tag{5}$$

$$\lambda_2 = \lambda_3 = \lambda_4 = c_1 \tag{6}$$

$$\lambda_5 = c_1 + a_0 \tag{7}$$

where $\lambda_1$ is the velocity of acoustic waves propagating in the negative direction (ingoing wave), while $\lambda_5$ refers to the outgoing acoustic wave. The convection velocity in the positive direction $x_1$ is $\lambda_2 = \lambda_3 = \lambda_4$.

The transverse terms vector $\boldsymbol{\mathcal{T}}$ introduced by Yoo et al. [1] is

$$\boldsymbol{\mathcal{T}} = \begin{bmatrix} \mathcal{T}_1 \\ \mathcal{T}_2 \\ \mathcal{T}_3 \\ \mathcal{T}_4 \\ \mathcal{T}_5 \end{bmatrix} = \begin{bmatrix} (\boldsymbol{c}_t \cdot \nabla_t P + \gamma P \nabla_t \cdot \boldsymbol{c}_t - \rho a_0 \boldsymbol{c}_t \cdot \nabla_t c_1)/2 \\ \nabla_t \cdot (\rho \boldsymbol{c}_t) - (\boldsymbol{c}_t \cdot \nabla_t P + \gamma P \nabla_t \cdot \boldsymbol{c}_t)/a_0^2 \\ \left(\boldsymbol{c}_t \cdot \nabla_t c_2 + \frac{1}{\rho}\frac{\partial P}{\partial x_2}\right) \\ \left(\boldsymbol{c}_t \cdot \nabla_t c_3 + \frac{1}{\rho}\frac{\partial P}{\partial x_3}\right) \\ (\boldsymbol{c}_t \cdot \nabla_t P + \gamma P \nabla_t \cdot \boldsymbol{c}_t + \rho a_0 \boldsymbol{c}_t \cdot \nabla_t c_1)/2 \end{bmatrix} \tag{8}$$

with the subscript $t$ referring to tangential directions $x_2$, $x_3$ with the tangential terms vector $\boldsymbol{c}_t = (c_2, c_3)$.

At a subsonic outflow, all waves exit the domain except the ingoing wave associated with the velocity $\lambda_1 = c_1 - a_0$ corresponding to $\mathcal{L}_1$. The value of the incoming wave $\mathcal{L}_1$ cannot be obtained from interior points and must account for the information propagating into the domain from the exterior. The extension of the LODI method [3] by Yoo et al. [1] leads to the following expression for $\mathcal{L}_1$:

$$\mathcal{L}_1 = K(P - P_t) + (\beta - 1)\mathcal{T}_1 \tag{9}$$

with $K$ a relaxation coefficient. If the outlet pressure $P$ is very different from the target pressure $P_t$, the reflected waves going inward will drive the pressure toward $P_t$. A proposal for the relaxation coefficient was made by Rudy and Strikwerda [21],

$$K = \sigma a_0 (1 - M^2)/L_x \tag{10}$$

where $M$ is the maximum Mach number on the boundary, $\sigma = 0.25$, and $L_x$ is a characteristic dimension in the axial direction. As $K \to \infty$, the outlet boundary condition becomes fully reflecting, while for $K = 0$, the ingoing wave amplitude becomes zero; the boundary condition becomes nonreflecting, but the pressure can drift. Selle et al. [22] suggest using values of $K$ corresponding to $0.1 < \sigma < \pi$ to avoid large reflections and possible errors on the pressure evaluation. Yoo et al. [1] introduce a damping coefficient $\beta \in [0, 1]$, which is applied to the transverse terms in Eq. (9). When $\beta = 1$, the transverse terms are ignored, and the LODI formalism [3] is recovered. Different authors report that $\beta$ should be equal to a reference Mach number [2]. Granet et al. [23] show that using the mean Mach number in the outlet condition gives better results than a local value. This latter option is chosen in the following.

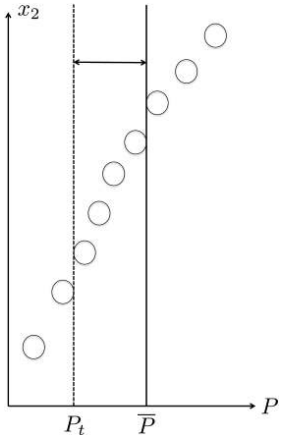


**Fig. 1 Illustration of the patch-averaged formalism for the calculation of the incoming wave.**

The pressure $P$ required to evaluate $\mathcal{L}_1$ in Eq. (9) can be either of the following: 1) the local pressure or 2) the average pressure on the surface. In case 1, the pressure difference $(P - P_t)$ is calculated pointwise; i.e., the relaxation locally applies a different correction at each point of the outlet. This formalism is suitable to impose a pressure profile. In case 2, the wave amplitude is based on the difference between the spatially averaged pressure on the surface and the target pressure $P_t$. The relaxation action is then uniform all over the boundary, whatever is the local offset to the target. This allows local differences of pressure and is thus compatible with the pressure distortion created by a swirling flow. The latter method is illustrated in Fig. 1 for the pressure points located along the $x_2$ axis of a boundary.

A specific property of the NSCBC is that it solves the momentum equation in the outlet section; only the axial acoustic wave $\mathcal{L}_1$ is modified. All other equations including the momentum equation in the radial direction are solved on the outlet surface and therefore can naturally capture the radial equilibrium.

Two test cases presented in the next section aim at assessing this property: a swirling flow in an annulus and a transonic nozzle guide vane. The AVBP solver is used to compute the test cases. It is a three-dimensional code solving the unsteady compressible Navier–Stokes equations using a cell-vertex finite volume approximation. Outlet NSCBCs accounting for the transverse terms [1] have been implemented in AVBP by Granet et al. [23] and are used here. This condition will be referred to as NSCBC 3D [1].

## IV. Test Cases

### A. Annulus

First, the ability of characteristic boundary conditions to recover the REA pressure profile is assessed in a rotating flow in a simple annulus (Fig. 2). The annulus has an aspect ratio of $L/(R_2 - R_1) = 4$ and is meshed with 4,631,800 tetrahedral cells. This geometry is chosen because it allows one to find an analytical solution (Sec. I). This solution is compared to the simulation in Sec. II.

#### *1. Analytical Solution*

The geometry and flow properties are set so that all hypotheses for simplified radial equilibrium are fulfilled: axisymmetry, steady state, no viscosity (Euler), and ideal gas. Two configurations are tested: the free vortex flow ($c_\theta = k/r$ with $k$ a constant) and a constant swirl flow ($c_\theta = C$). The radial pressure profile is obtained by integration of Eq. (2) using the ideal gas relation to link density to pressure:

$$\text{free vortex flow } c_\theta = \frac{k}{r} \qquad P(r) = \alpha_1 \exp\left(-\frac{k^2}{2R_{\text{air}}Tr^2}\right) \tag{11}$$

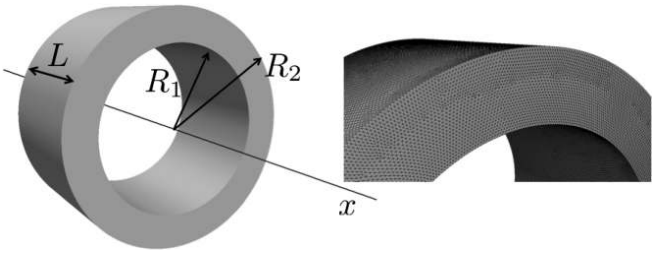


**Fig. 2 Geometry and mesh for the annulus test case.**

$$\text{solid body rotation } c_\theta = \mathcal{C} \qquad P(r) = \alpha_2 r^{(\mathcal{C}^2/R_{\text{air}}T)} \tag{12}$$

where $\alpha_i$ are integration constants that can be determined using a pivot point at which the local pressure is known or via the mean pressure on the outlet plane. The latter strategy is used here for the two cases, targeting the same mean pressure $\bar{P}_t$:

$$\bar{P}_t = \overline{P} = \frac{1}{\pi(R_2^2 - R_1^2)} \iint P(r) r \,\mathrm{d}r \,\mathrm{d}\theta \tag{13}$$

Solving Eq. (13) for the constants $\alpha_i$ gives for Eqs. (11) and (12)

$$\alpha_1 = \frac{\bar{P}_t(R_2^2 - R_1^2)}{\{(k^2/2R_{\text{air}}T)\text{Ei}[-(k^2/2R_{\text{air}}Tr^2)] + r^2 \exp[-(k^2/2R_{\text{air}}Tr^2)]\}_{R_1}^{R_2}} \tag{14}$$

$$\alpha_2 = \frac{\bar{P}_t(R_2^2 - R_1^2)}{2\{[r^{(\mathcal{C}^2/R_{\text{air}}T)} + 2]/[(\mathcal{C}^2/R_{\text{air}}T) + 2]\}_{R_1}^{R_2}} \tag{15}$$

with the common notation $[\Phi(r)]_a^b = \Phi(b) - \Phi(a)$. $\text{Ei}(x)$ is the exponential integral function defined as $\text{Ei}(x) = \int_{-\infty}^{x} e^t/t \,\mathrm{d}t$.

The target pressure $\bar{P}_t = \bar{P} = 100$ kPa appears only in the expressions of $\alpha_1$ and $\alpha_2$ [Eqs. (14) and (15)] and is identical for both cases. It is therefore only a multiplicative constant for the pressure profile as indicated in Eqs. (11) and (12). On the other hand, the shape of the pressure profile, governed by radius-dependent terms, is controlled by gas properties ($R_{\text{air}} = 287$ J · kg$^{-1}$ · K$^{-1}$, $T = 300$ K) and by the swirl profile $c_\theta(r)$. Therefore, the two pressure profiles have the same mean pressure, but the free vortex flow [Eq. (11)] has a stronger pressure gradient than the solid body rotation Eq. (12).

### 2. *Numerical Resolution*

The two swirling flows, Eqs. (11) and (12), are simulated for six values of the reflection coefficient $K$, ranging from 1 to 1000, in order to assess the influence of the level of reflectivity on the radial equilibrium pressure profile. The summary of the test cases can be found in Table 1. The compressible solver AVBP is used here, with the Lax–Wendroff [24] numerical scheme, providing second-order accuracy in time and space. Note finally that to be fully compliant with the REA, only Euler equations are solved here, without the subgrid scale viscosity model. Nonreported results show that for the annulus flow the viscosity effect is very low, and thus solving either Euler or Navier–Stokes equations gives the same results.

The inlet boundary condition imposes the adequate swirl profile $c_\theta(r)$ according to Eq. (11) or (12). The axial velocity is set to $c_x = 5$ m/s for Eq. (11) and $c_x = 30$ m/s for Eq. (12). The corresponding flow through times $\tau = L/c_x$ are 64 ms for Eq. (11) and 11 ms for Eq. (12). The maximum Mach numbers for Eqs. (11) and (12) are 0.29 and 0.17, respectively. The time step is controlled by the Courant–Friedrichs–Lewy (CFL) condition (set to 0.7) and is around $1.5 \cdot 10^{-6}$ s. In each case, the initial velocity field in the annulus is identical to the inlet boundary condition velocity profiles $(c_\theta; c_x)$. At the outlet, NSCBC 3D [1] is used, driving the mean pressure toward the imposed value $\bar{P}_t$. The inner and outer walls use slip conditions for the velocity to avoid any possible near-wall effect on the velocity profile and thus on the pressure distribution. The initial pressure field is uniform $P(r, \theta, x) = \bar{P}_t$, and thus not consistent with the REA, to test the ability of NSCBCs to drive the pressure toward the REA.

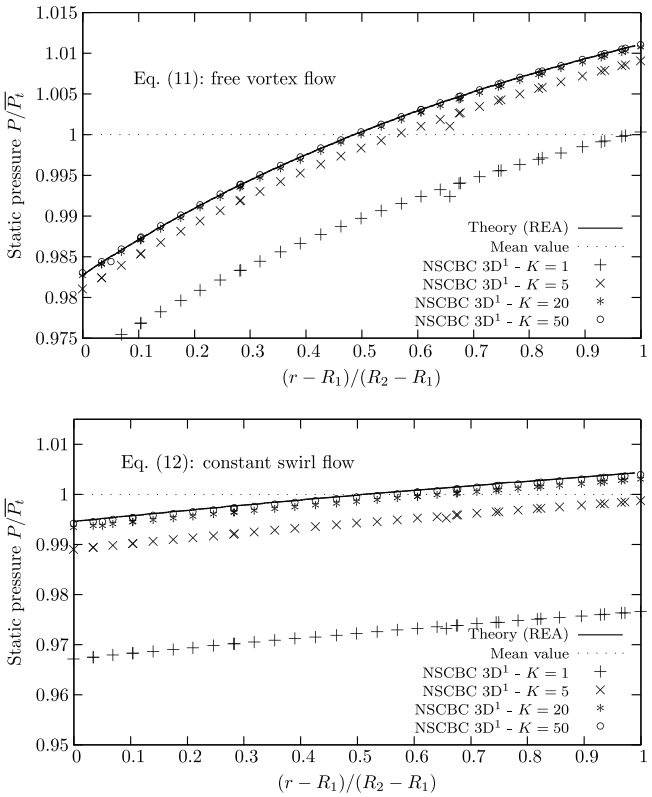


**Fig. 3 Radial profile of static pressure for case Eqs. (11) (top) and (12) (bottom).**

The required time to establish the pressure field is imposed by the domain size, flow properties, and relaxation parameter $K$. Table 1 summarizes the simulation times required to converge the mean pressure at the exit. Convergence is reached when the local pressure is $\pm 0.1\%$ of $P(t \to \infty)$. Increasing the reflectivity of the NSCBC condition (via $K$) allows one to reduce the convergence time down to $0.8\tau$ for Eq. (11) and $2.9\tau$ for Eq. (12), reached for $K \geq 50$. Changing from $K = 1$ to $K = 1000$ allows one to reduce the convergence time by 50 and 140 times for Eqs. (11) and (12), respectively.

As the pressure profile depends only on the radius (purely one-dimensional flow), it can be plotted at the domain exit, as shown in Fig. 3: a radial equilibrium pressure profile establishes at the end of the simulation. The simulations converge toward the theoretical profile as the relaxation parameter at the outlet is increased for both Eqs. (11) and (12). The main action of the relaxation coefficient $K$ is to drive the mean pressure toward the target. For example, in the

**Table 1 Test cases for the annulus test case and required time to converge the pressure field**

| Relaxation coefficient $K$ | | 1 | 5 | 20 | 50 | 500 | 1000 |
|---|---|---|---|---|---|---|---|
| $\sigma = \frac{K}{(1-M^2)(a_0/R_2-R_1)}$ | Eq. (11) | 0.0003 | 0.0013 | 0.0050 | 0.0126 | 0.1257 | 0.2513 |
| | Eq. (12) | 0.0002 | 0.0012 | 0.0047 | 0.0119 | 0.1186 | 0.2371 |
| Physical time to convergence $t/\tau$ | Eq. (11) | 35.6 | 4.7 | 1.0 | 0.8 | 0.8 | 0.8 |
| | Eq. (12) | 252.1 | 36.2 | 5.6 | 2.9 | 2.9 | 2.9 |

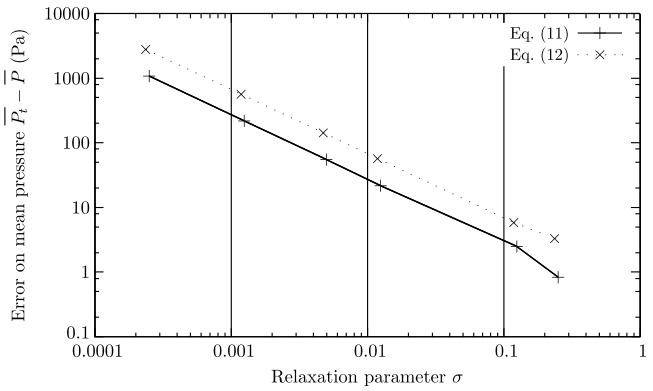


**Fig. 4 Reduction of the error to the target pressure with increasing relaxation parameter $\sigma$.**

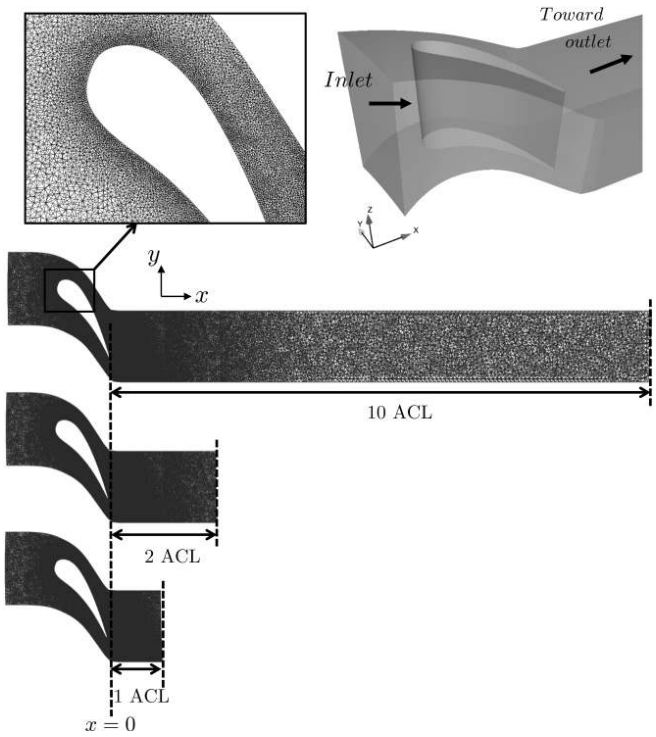


**Fig. 5 Geometry and mesh for the MT1 vane: midspan cut view of the three domains.**

**Table 2 MT1 vane characteristics**

| Parameter | Value |
|---|---|
| Aspect ratio $h/C$ | 0.65 |
| Pitch to chord ratio | 0.85 |
| Inlet angle | 0° |
| Inlet total pressure | 460 kPa |
| Inlet total temperature | 444 K |
| Mean pressure at 1 ACL | 269 kPa |
| Fluid | Pure air |

bottom part of Fig. 3 [Eq. (12)], the pressure obtained for a low relaxation simulation ($K = 1$) has a mean value that is much smaller than the target value $\bar{P}_t$. The reduction of the offset between the mean pressure and the target when increasing the BC reflectivity level is highlighted in Fig. 4. In this log–log plot, one can observe that the error is inversely proportional to the parameter $\sigma$ over the investigated range. The error and the convergence time (see Table 1) are slightly lower for the free vortex flow, Eq. (11), than for the solid body rotation, Eq. (12). This can be explained by the fact that the transverse terms are more important in Eq. (11), $20 \geq c_\theta/c_x \geq 14$, than in Eq. (12), $c_\theta/c_x = 1.7$.

For $\sigma \to \infty$ (fully reflecting BC), the mean pressure would converge to the imposed value, and thus the pressure profile would exactly match the theoretical one. However, this case would also lead to a fully reflecting outlet, a property that may have to be avoided, leading to an intermediate value for $K$ providing both a limited error on pressure and a nonreflecting outlet.

This first test case shows that a characteristic boundary condition can cope on its own with the radial equilibrium, i.e., with a nonuniform outlet pressure dictated by the swirl. Note that this is obtained without having to precompute a pressure profile and impose it at the outlet.

### B. Turbine Vane

The ability of NSCBCs to let the radial equilibrium establish at a swirled flow outlet while controlling wave reflection is now assessed on a real three-dimensional configuration: the uncooled transonic nozzle guide vane (NGV) MT1. This vane was developed and instrumented at Qinetic on the Isentropic Light Piston Facility [25–29] for the European project Turbine Aero-Thermal External Flows 2. A periodic sector (1/32) is considered here. Note that during the test campaign a full turbine stage was experimented, whereas our study focuses only on the NGV.

The MT1 vane was selected as it does not feature technological effects and provides an almost uniform flow deviation. Therefore, the assumption of a constant swirl flow $c_\theta(r) = \mathcal{C}$ is valid, and the analytical determination of the simplified radial equilibrium, which the code should predict, is straightforward.

#### 1. *Geometry*

For the numerical tests, an annulus is attached immediately after the vane trailing edge (Fig. 5). Simulations are performed on three domains of increasing length: for the first one, the annulus is truncated at 1 axial chord length (ACL), the second at 2 ACL, and the longest one at 10 ACL. With short domains, the flow in the outlet section is more swirled and perturbed by the vanes wake, thereby making the task of the outlet condition more difficult. The 10 ACL domain is the baseline configuration: it is assumed that the outlet BC has no influence on the near-vane flowfield for this case. Note that the 1 and 2 ACL domains use the same mesh as the baseline one, simply split at the right location. A full tetrahedral mesh containing 2.69 million nodes (13 million cells) for the 10 ACL domain is created using Gambit, as shown in Fig. 5. The grid is refined in the wake region and around the airfoil (tetrahedral edge length$\simeq$250 $\mu$m at the vane wall). The $Y^+$ values around the vane walls are between 1 and 550, and the flow in the vicinity of the wall is modelled with the adiabatic law of the walls [30,31]. Inner and outer casing walls also use the adiabatic law of the wall. Periodicity along the azimuthal direction is enforced on the two lateral sides. Uniform total temperature and pressure profiles are imposed at the inlet, without

**Table 3 Parameters for the LES and RANS simulations of the MT1 vane**

| Domain | Number of nodes | $\tau$, ms | Solver | Approach | Outlet BC | CPU hours | Number of cores | Wall-clock time (days) |
|---|---|---|---|---|---|---|---|---|
| 10 ACL | 2.69 M | 3.9 | AVBP | LES | NSCBC 3D[1] | 35k | 144 | 13 |
| 2 ACL | 2.62 M | 1.3 | AVBP | LES | NSCBC 3D[1] | 19k | 144 | 6 |
| 1 ACL | 2.59 M | 0.95 | AVBP | LES | NSCBC 3D[1] | 13k | 144 | 4.5 |
| 1 ACL | 2.59 M | 0.95 | Fluent | RANS | Neumann uniform | 0.21k | 8 | 2.2 |
| 1 ACL | 2.59 M | 0.95 | Fluent | RANS | Neumann REA option | 0.26k | 4 | 1.3 |

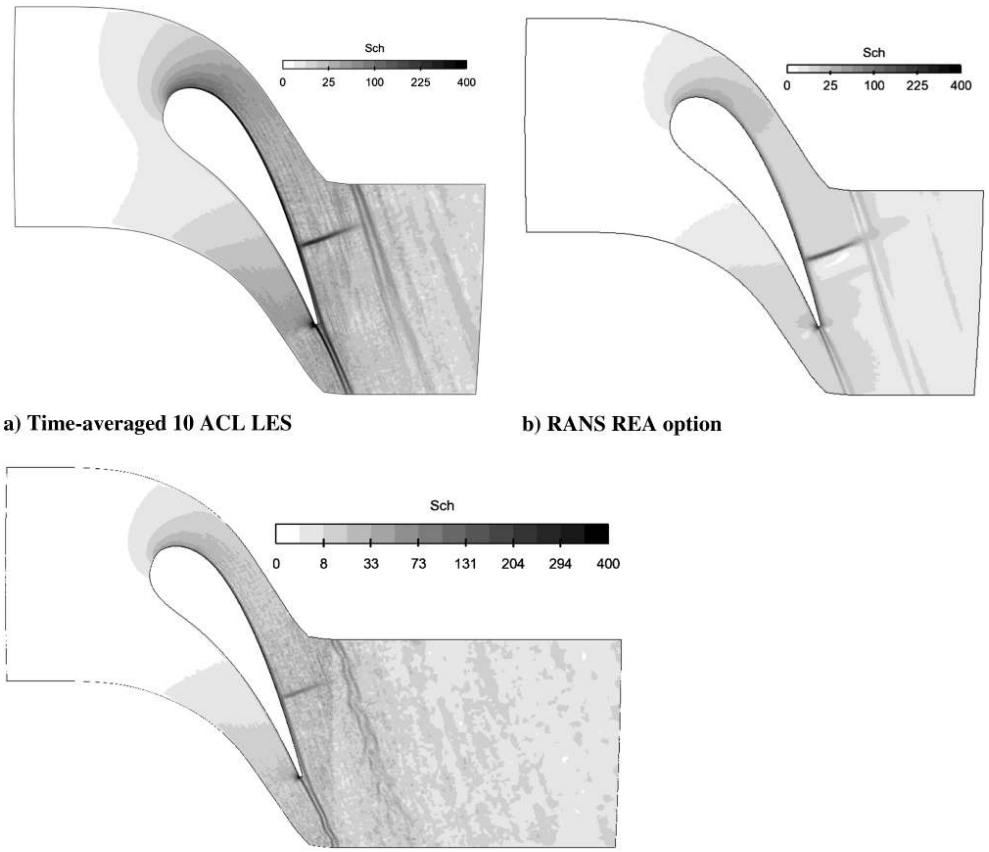


**a) Time-averaged 10 ACL LES** **b) RANS REA option**

**c) Instantaneous 10 ACL LES**

**Fig. 6 Density gradient $|\nabla\rho|/\rho$ in the midspan plane.**

swirl, as shown in Table 2. The Mach number is around 0.12 upstream of the vane leading edge.

*2. Numerical Resolution*

To compare boundary conditions, two Navier–Stokes equation solvers are benchmarked on this test case. Along with the AVBP solver used in Sec. IV.A, the commercial code Fluent Ver. 13 is tested. Following the conclusions of the test case A, AVBP is used with the NSCBC 3D [1]. Fluent uses two distinct outlet BCs: either a typical uniform pressure (Neumann) or a specific radial equilibrium option. For the uniform pressure BC, a Fluent in-house weak enforcement of pressure is used; the face pressure is not directly enforced to the target value but results from a weighted balance [31]. The Fluent radial equilibrium option is based on the Neumann formalism, but the simplified radial equilibrium pressure profile is calculated at each radius using the domain cell data (swirl velocity and density) and then imposed at the exit. The user specifies the pressure at the hub (position of smallest radius) to solve the pressure equation, Eq. (2). Note that knowing the pressure at the hub is not straightforward since the pressure can differ significantly from the mean pressure at the outlet section.

Fluent solves the steady-state compressible Navier–Stokes equations (density-based approach) closed with a RANS model ($k$-$\varepsilon$ realizable [32]). An implicit formalism is used, allowing for CFL numbers up to 10. Turbulence variables are defined at the inlet and outlet with 5% turbulence intensity and a viscosity ratio $\mu_t/\mu = 100$. Convective fluxes are computed with a Roe flux-difference splitting scheme [33], and all equations are discretized with a second-order upwind scheme.

AVBP uses a Smagorinsky subgrid scale model [34] for subgrid turbulence. The numerical scheme (two step Taylor–Galerkin [35]) is third-order accurate in time and space. The global time step is controlled by the CFL number (0.7) and is around $7.5 \cdot 10^{-8}$ s for the LES. The flow through time is estimated as $\tau = \text{length}/c_x$ (Table 3),

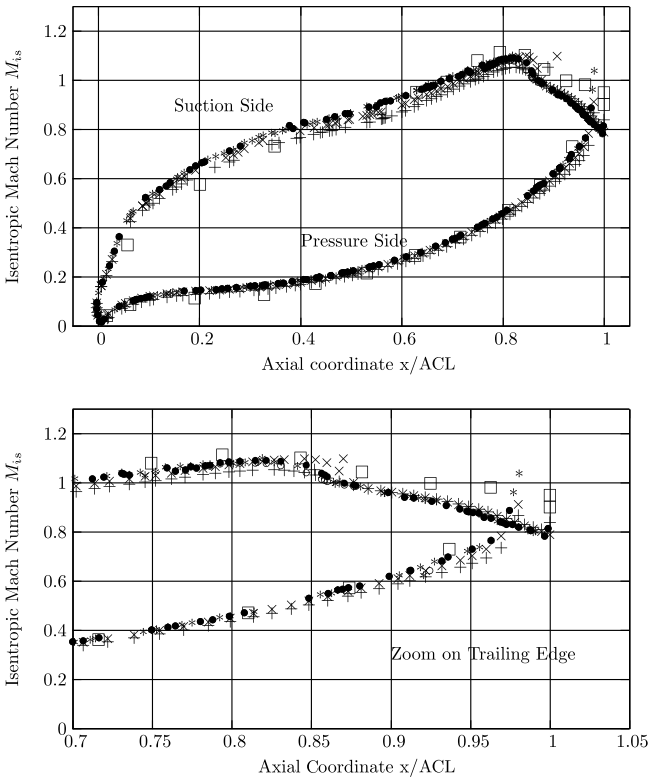


**Fig. 7 Isentropic Mach number on the airfoil surface at vane midspan. AVBP (NSCBC 3D[1]) domain 10 (*), domain 2 (○), domain 1 ACL (•); Fluent domain 1 ACL Neumann uniform (+) and radial equilibrium option (×) and experiments full stage [25] (□).**

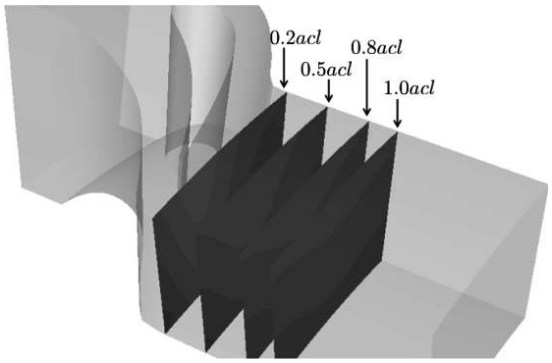


**Fig. 8 Position of the postprocessing planes downstream of the vane.**

where length is the axial extent of each domain and $c_x$ is the mean axial velocity in the annulus. The LESs are time averaged over roughly seven flow through times of the 1 ACL domain.

The LES of the 1 ACL domain is difficult because of the interaction of the wake and the shock with the boundary condition. Strong gradients exist on the boundary. To damp these gradients and related stability issues, viscosity is artificially added [36] in the near-exit region ($x > 0.55$ ACL, where $x = 0$ is the vane trailing edge).

### 3. *Results: Flowfield*

Figure 6 shows a comparison of the time-averaged flowfield of the baseline LES (Fig. 6a) with the RANS simulation using the REA option (Fig. 6b). The vane midspan contours of density gradient $|\nabla\rho|/\rho$ (similar to the Schlieren (Sch) image) highlight the shock on the vane suction side and the boundary layer created on the the suction side. Both solvers seem to predict the same position for the shock, and qualitatively a similar expansion through the turbine. Overall, the density gradients are more pronounced in the entire domain for the LES results. Figure 6c shows the same density gradient contours for an instantaneous solution of the 10 ACL LES, highlighting the dynamic mixing in the wake of the vane. The view is slightly extended compared to Figs. 6a and 6b to show how the wake mixes out with the axial distance. Overall, the density gradient becomes smaller because of the mixing of the wake and the less refined mesh that tends to increase the level of turbulent viscosity in this region.

The isentropic Mach number is used to compare time-averaged pressure profiles along the vane and is defined as

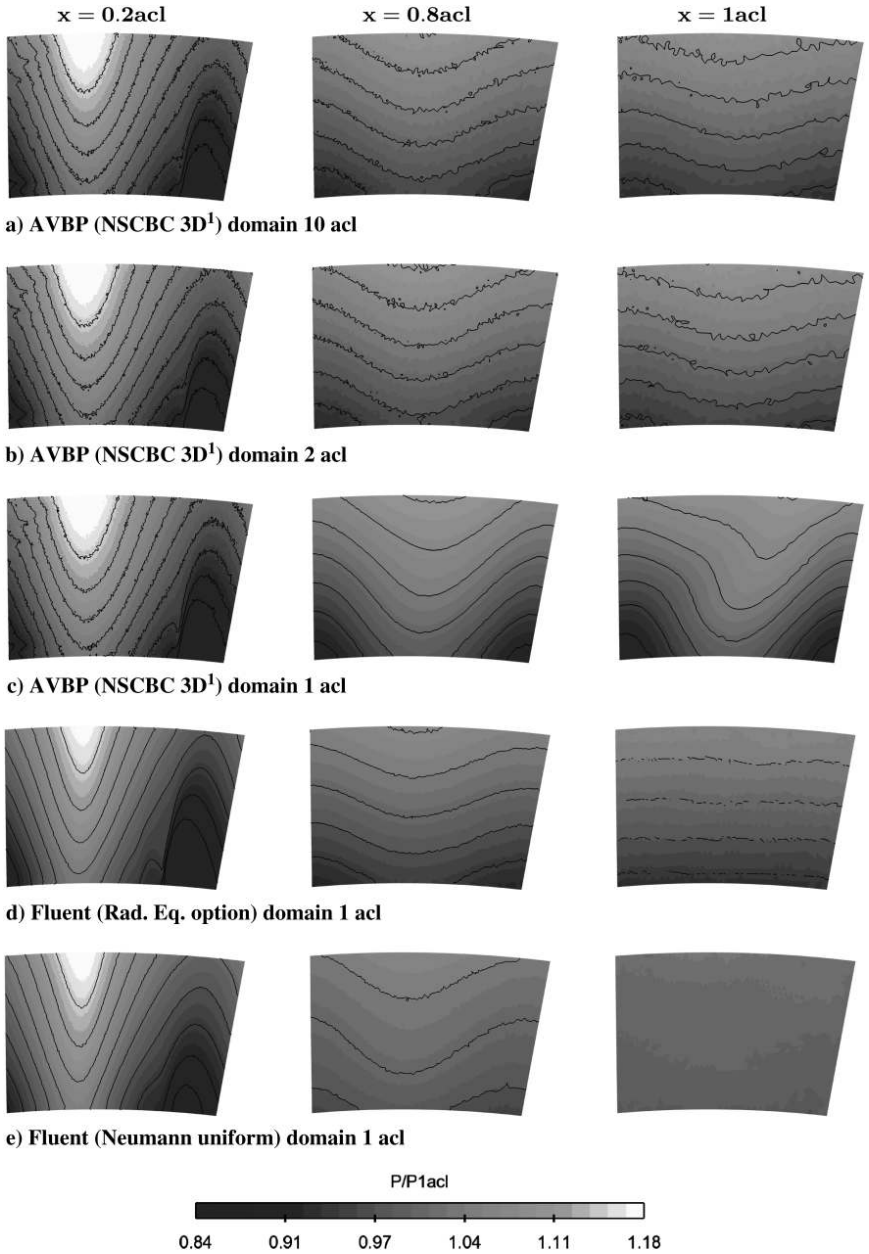


**Fig. 9 Time-averaged non-dimensional static pressure fields (view from downstream).**

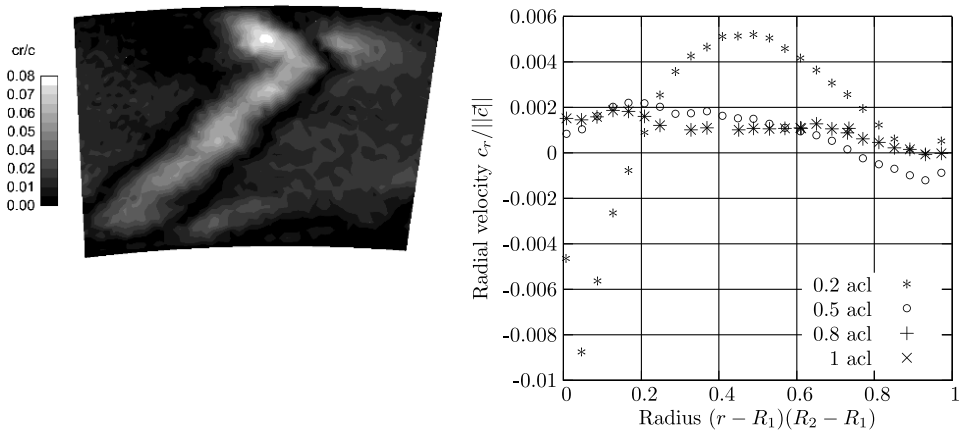


**Fig. 10 Time-averaged field of radial velocity $|\frac{c_r}{\|c\|}|$ in plane $x = 1$ ACL and corresponding circumferentially-averaged profile.**

$$M_{\text{is}} = \sqrt{\frac{2}{\gamma-1}\left[\left(\frac{P_{\text{tot,inlet}}}{P}\right)^{(\gamma-1)/\gamma} - 1\right]} \tag{16}$$

Profiles of $M_{\text{is}}$ are plotted in Fig. 7 at vane midspan, for both RANS simulations and the time-averaged LES. As the MT1 vane was equipped with static pressure tapings at 10%, 50%, and 90% span on both pressure and suction sides, experimental results [25] are also shown for comparison. However, note that they were obtained with the full turbine stage, i.e., including rotor–stator interactions and the rotor potential effect. Therefore, in the rear part of the vane, these simulations of the isolated NGV show a noticeable difference with the experiments. Overall, the agreement is good. This is also confirmed at 10% and 90% span (results not shown here). The position of the BC (1, 2, or 10 ACL) does not influence the flowfield in the vane, as the three LESs predict an identical expansion into the turbine.

The static pressure field is now investigated for different axial locations after the vane trailing edge. The postprocessing planes are shown in Fig. 8. Figure 9 shows the static pressure distribution at three locations: 0.2 ACL, 0.8 ACL, and 1 ACL for the time-averaged solutions. The interval between two pressure isolines (black lines) is 3% of $\bar{P}_{1\ \text{ACL}}$.

For all simulations, mixing increases with axial distance from the trailing edge, and therefore the action of the vanes slowly disappears. At $x \geq 0.8$ ACL, this distribution is mostly one dimensional in the radial direction and slightly distorted by the wake on the pitch. The positive radial pressure gradient created by the swirl motion is visible. At $x = 0.2$ ACL, the pressure field is very similar from one simulation to another, confirming that the position of the BC does not interfere with the flow.

For Figs. 9c–9e, the pressure fields at $x = 1$ ACL are located exactly on the boundary condition. Therefore, the Fluent Neumann uniform BC shows a uniform pressure, while the distribution is clearly radial when the Fluent radial equilibrium option is enabled. The LES of the 1 ACL domain, Fig. 9c, features a smoother pressure field than longer domains, Figs. 9a and 9b, because of the use of artificial viscosity in the final part of the domain. The flowfield at $x = 0.2$ ACL does not seem to be affected by this nonphysical damping.

#### 4. *Comparison with Radial Equilibrium Analytical Profile*

Before comparing the simulations results with the REA, one must check that the hypotheses required for the REA to be valid are fulfilled in this case (see Sec. II):

1) There should be no viscosity. By definition, this assumption cannot be respected. However, one can suppose that for this one-dimensional approach viscous effects are low and that Navier–Stokes equations are properly approached by Euler equations.

2) The flow has to be axisymmetric ($\partial/\partial\theta = 0$), which is essentially true at $x = 1$ ACL, as seen in Fig. 9.

3) The radial displacement should be negligible, $c_r \ll \|\boldsymbol{c}\|$, which is true in the plane 1 ACL as shown by the contours of $c_r/\|\boldsymbol{c}\|$ in Fig. 10 for the 10 ACL LES. As the radial equilibrium is a one-dimensional concept, the radial velocity field has to be averaged in the azimuthal direction, as shown in Fig. 10 for four axial positions after the vane trailing edge. Even if at $x = 0.2$ ACL the streamline curvature imposes a limited radial motion, at $x = 1$ ACL, the radial component is definitely negligible: below 0.2% of $\|\boldsymbol{c}\|$.

4) The flow is supposed to be at a steady state, and therefore LES results have to be time averaged. The level of pressure fluctuations in the plane $x = 1$ ACL is illustrated in Fig. 11 by the pressure signals of two probes located at midspan of the 10 ACL LES. The horizontal solid line shows the time- and circumference-averaged pressure at this radial position. All signals are normalized by the analytical solution given by the REA at this radius. The circumferentially averaged pressure is very close to the pressure predicted by the REA, as it will be detailed later. The time-averaged value of the pressure at probe A is lower than the REA value and a bit higher for probe B. Moreover, $\pm 2\%$ fluctuations to the REA solution are observed. This indicates the following: 1) the local value of pressure is not uniform vs the radius because of the wake effect and similar effects (this would not be possible when imposing a one-dimensional REA profile), and 2) even if relatively small, local fluctuations of pressure are not incompatible with the establishment of the radial equilibrium.

All conditions for the application of the simplified radial equilibrium being essentially fulfilled in plane $x = 1$ ACL, the radial profiles of pressure can be compared with the REA. The theoretical radial equilibrium profile is easily calculated if the flow features a uniform swirl velocity, which is confirmed by the contours $c_\theta/\overline{c_\theta}$ in Fig. 12 for the 10 ACL LES. The two-dimensional field is circumferentially averaged, as shown on the right side of Fig. 12, and does not vary much from $x = 0.2$ to $x = 1$ ACL (maximum deviation to the mean swirl is 5%).

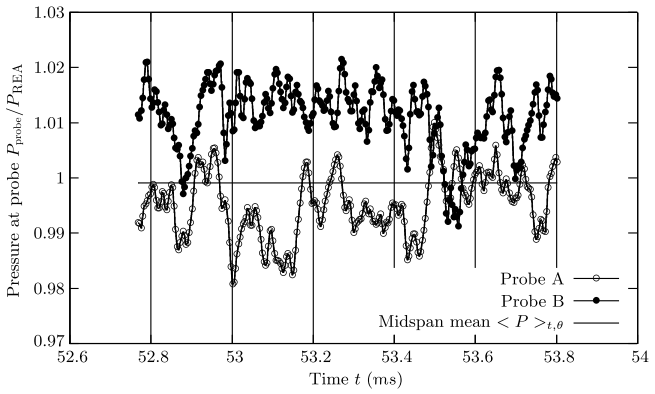


**Fig. 11 Time evolution of pressure for two probes located at midspan in the plane $x = 1$ ACL.**

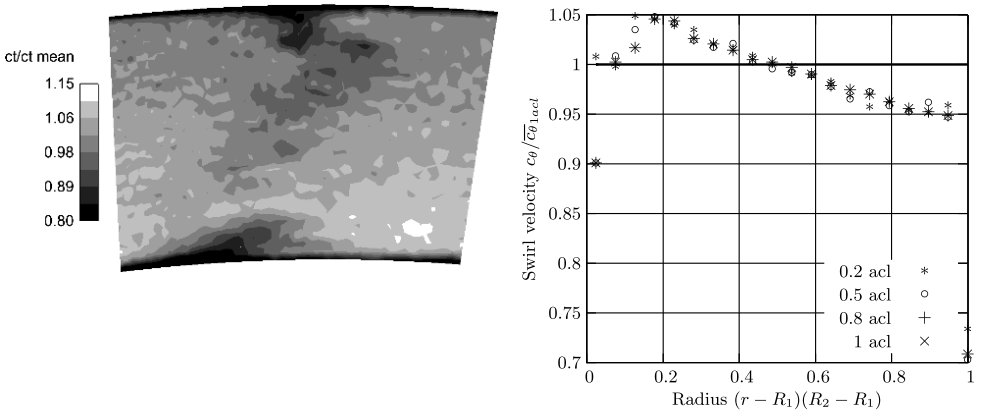


**Fig. 12 Time-averaged field of swirl velocity $\frac{c_\theta}{\overline{c_\theta}}$ in plane $x = 1$ ACL and corresponding circumferentially-averaged profile.**

Pressure profiles are plotted in Fig. 13 between $x = 0.2$ and $x = 1$ ACL downstream of the NGV trailing edge. Simulations and the REA are compared at $x = 1$ ACL only (bottom right in Fig. 13). The difference between analytical radial equilibrium profile and LES results is very low with the NSCBC formalism. The same difference can be found when using a Neumann condition associated with a profile of radial equilibrium (Fluent). However, this procedure is less trivial as the outlet BC pressure has to be specified at the hub, which is usually not known a priori. Finally, in this case, using a classical uniform Neumann BC leads to more pronounced differences on the pressure field and local errors between $-4$ and $+6\%$. In this case, the distortion of the pressure created by the proximity of the BC is visible: at $x = 0.2$ ACL, the pressure profile tends toward a radial equilibrium one (with an offset on the mean pressure), while at $x = 0.8$ and $x = 1$ ACL, it is clearly distorted by the uniform value imposed at $x = 1$ ACL.

## V. Conclusions

Characteristic boundary conditions developed for the LES and DNS of compressible flows in the last ten years have been tested on flows with strong swirl to see whether these methods allowing a control of acoustic waves on boundaries can also cope with the so-called radial equilibrium condition. Results show that characteristic boundary conditions including transverse terms [1,23] naturally allow the establishment of a radial equilibrium pressure profile for

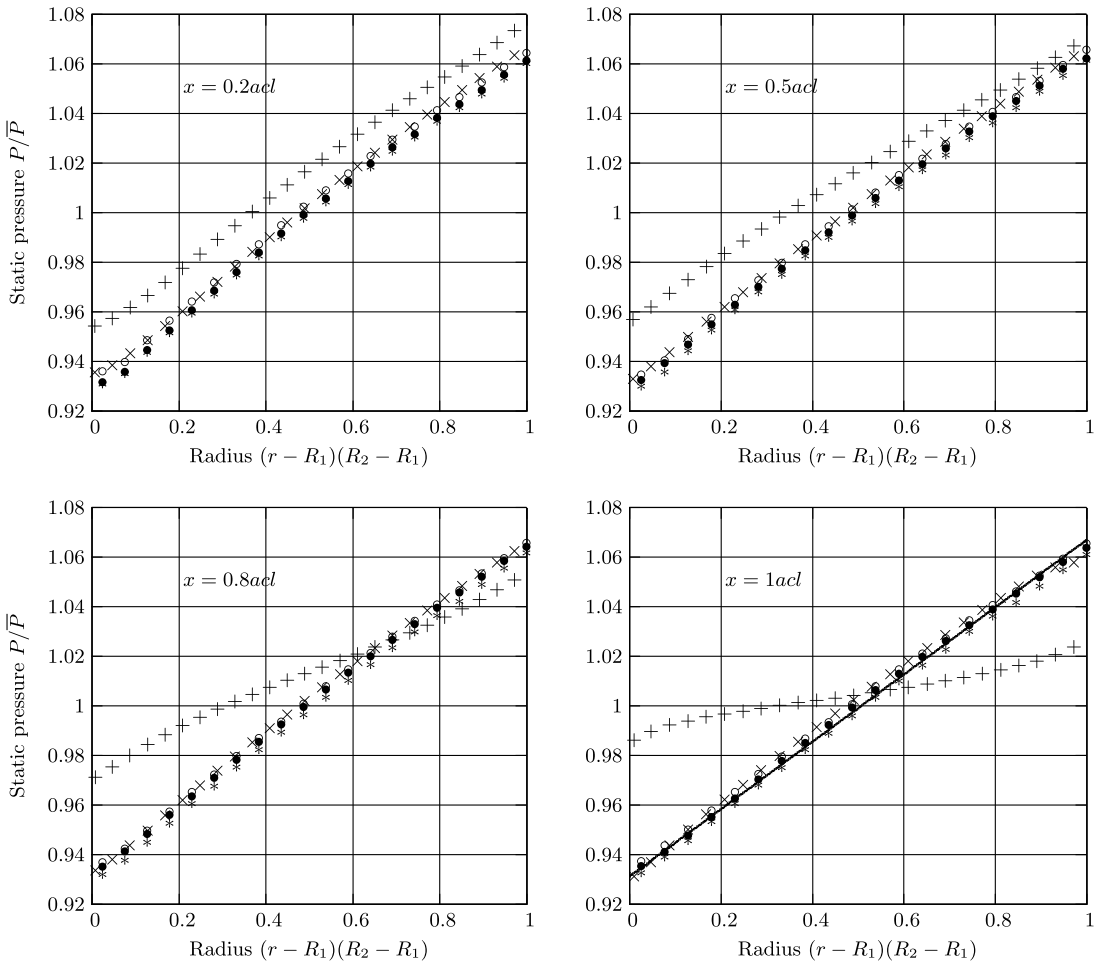


**Fig. 13 Radial profiles of circumferentially averaged static pressure *P*: AVBP (NSCBC 3D[1]3D1) domain 10 (*), domain 2 (○), domain 1 (•), and Fluent domain 1 ACL Neumann uniform (+) and radial equilibrium option (×). The radial equilibrium profile is shown at 1 ACL (solid line).**

swirling flows. The incoming wave amplitude has to be calculated based on the difference between the target and the mean pressures in the outlet section, to allow local differences due to pressure distortion.

On the annulus test case, results show that low values of reflectivity can be used ($\sigma \simeq 10^{-2}$) while avoiding errors on pressure. Simulations of a transonic vane show that the NSCBC formalism lets the radial equilibrium establish despite temporal and local fluctuations due to the vane wake. The circumferentially averaged profile matches the analytical one with $\pm 0.5\%$ accuracy. It is also shown that the position of the boundary condition (10, 2, and 1 ACL) does not influence the flowfield in the vane, which is not the case when using a uniform Neumann BC at the vane outlet.

These results confirm that characteristic methods should be used in turbine computations in which they will have two major advantages:

1) Unlike the usual radial equilibrium method, no assumption is required to precompute a pressure profile to impose in the outlet section. The profile is computed naturally by the code that solves the momentum equation on the outlet surface. This suggests that characteristic methods will provide a correct outlet pressure profile even in cases in which the assumption of the REA does not apply and the REA approximation cannot be used.

2) A second advantage, which has not been discussed here, is that characteristic methods allow one to control wave reflection at the outlet. This property has only limited effects for RANS simulations but is crucial for the LES of compressible swirling flows for which nonreflecting outlet sections are mandatory.

## Acknowledgments

The authors would like to thank the members of the Computational Fluid Dynamics Team at Centre Européen de Recherche et de Formation Avancée en Calcul Scientifique and the methods department at Turbomeca. The MT1 vane data used in this work was obtained from the project Turbine Aero-Thermal External Flows II (TATEF II), funded under the Brite Euram Forth Framework on Turbine Aerothermal External Flows, contract number BRPR-CT97-0519.

## References

[1] Yoo, C. S., Wang, Y., Trouvé, A., and Im, H. G., "Characteristic Boundary Conditions for Direct Simulations of Turbulent Counterflow Flames," *Combustion Theory and Modelling*, Vol. 9, No. 4, 2005, pp. 617–646. doi:10.1080/13647830500307378

[2] Yoo, C. S., and Im, H. G., "Characteristic Boundary Conditions for Simulations of Compressible Reacting Flows with Multi-Dimensional, Viscous and Reaction Effects," *Combustion Theory and Modelling*, Vol. 11, No. 2, 2007, pp. 259–286. doi:10.1080/13647830600898995

[3] Poinsot, T., and Lele, S., "Boundary Conditions for Direct Simulations of Compressible Viscous Flows," *Journal of Computational Physics*, Vol. 101, No. 1, 1992, pp. 104–129. doi:10.1016/0021-9991(92)90046-2

[4] Lodato, G., Domingo, P., and Vervisch, L., "Three-Dimensional Boundary Conditions for Direct and Large-Eddy Simulation of Compressible Viscous Flows," *Journal of Computational Physics*, Vol. 227, No. 10, 2008, pp. 5105–5143. doi:10.1016/j.jcp.2008.01.038

[5] Pirozzoli, S., and Colonius, T., "Generalized Characteristic Relaxation Boundary Conditions for Unsteady Compressible Flow Simulations," *Journal of Computational Physics*, Vol. 248, Sept. 2013, pp. 109–126. doi:10.1016/j.jcp.2013.04.021

[6] Tu, J., Yeoh, G., and Liu, C., *Computational Fluid Dynamics: A Practical Approach*, Elsevier, New York, 2007, pp. 242–250.

[7] Negru, R., Muntean, S., Marsavina, L., Susan-Resiga, R., and Pasca, N., "Computation of Stress Distribution in a Francis Turbine Runner Induced by Fluid Flow," *Computational Materials Science*, Vol. 64, 2012, pp. 253–259. doi:10.1016/j.commatsci.2012.05.073

[8] Ferro, L., Gato, L., and Falcão, A., "Design and Experimental Validation of the Inlet Guide Vane System of a Mini Hydraulic Bulb-Turbine," *Renewable Energy*, Vol. 35, No. 9, 2010, pp. 1920–1928. doi:10.1016/j.renene.2010.01.020

[9] Torresi, M., Camporeale, S., Strippoli, P., and Pascazio, G., "Accurate Numerical Simulation of a High Solidity Wells Turbine," *Renewable Energy*, Vol. 33, No. 4, 2008, pp. 735–747. doi:10.1016/j.renene.2007.04.006

[10] Kim, T., Setoguchi, T., Kaneko, K., and Raghunathan, S., "Numerical Investigation on the Effect of Blade Sweep on the Performance of Wells Turbine," *Renewable Energy*, Vol. 25, No. 2, 2002, pp. 235–248. doi:10.1016/S0960-1481(00)00210-X

[11] Garg, V., "Heat Transfer on a Film-Cooled Rotating Blade Using Different Turbulence Models," *International Journal of Heat and Mass Transfer*, Vol. 42, No. 5, 1999, pp. 789–802. doi:10.1016/S0017-9310(98)00229-4

[12] Garg, V., "Heat Transfer on a Film-Cooled Rotating Blade," *International Journal of Heat and Fluid Flow*, Vol. 21, No. 2, 2000, pp. 134–145. doi:10.1016/S0142-727X(99)00072-7

[13] Solano, J., Pinilla, V., Paniagua, G., Lavagnoli, S., and Yasa, T., "Aero-Thermal Investigation of a Multi-Splitter Axial Turbine," *International Journal of Heat and Fluid Flow*, Vol. 32, No. 5, 2011, pp. 1036–1046. doi:10.1016/j.ijheatfluidflow.2011.05.011

[14] Poinsot, T., and Veynante, D., *Theoretical and Numerical Combustion*, 3rd ed., Centre Européen de Recherche et de Formation Avancée en Calcul Scientifique, Toulouse, France, 2011, pp. 459–498, http://www.cerfacs.fr/elearning.

[15] Baba-Ahmadi, M. H., and Tabor, G. R., "Inlet Conditions for Large Eddy Simulation of Gas-Turbine Swirl Injectors," *AIAA Journal*, Vol. 46, No. 7, 2008, pp. 1782–1790. doi:10.2514/1.35259

[16] Smith, L. H., Jr., "The Radial-Equilibrium Equation of Turbomachinery," *Journal of Engineering for Power*, Vol. 88, No. 1, 1966, pp. 1–12. doi:10.1115/1.3678471

[17] Wu, C.-H., and Wolfenstein, L., "Application of Radial-Equilibrium Condition to Axial-Flow Compressor and Turbine Design," National Advisory Committee for Aeronautics, NACA Annual Rept. NACA-TR-955, Cleveland, OH, 1949, pp. 165–194.

[18] Thompson, K. W., "Time Dependent Boundary Conditions for Hyperbolic Systems," *Journal of Computational Physics*, Vol. 89, No. 2, 1990, pp. 439–461. doi:10.1016/0021-9991(90)90152-Q

[19] Nicoud, F., "Defining Wave Amplitude in Characteristic Boundary Conditions," *Journal of Computational Physics*, Vol. 149, No. 2, 1999, pp. 418–422. doi:10.1006/jcph.1998.6131

[20] Lodato, G., Ham, F., and Pitsch, H., "Optimal Inclusion of Transverse Effects in the Nonreflecting Outflow Boundary Condition," *AIAA Journal*, Vol. 50, No. 6, 2012, pp. 1291–1306. doi:10.2514/1.J051318

[21] Rudy, D. H., and Strikwerda, J. C., "A Nonreflecting Outflow Boundary Condition for Subsonic Navier–Stokes Calculations," *Journal of Computational Physics*, Vol. 36, No. 1, 1980, pp. 55–70. doi:10.1016/0021-9991(80)90174-6

[22] Selle, L., Nicoud, F., and Poinsot, T., "The Actual Impedance of Non-Reflecting Boundary Conditions: Implications for the Computation of Resonators," *AIAA Journal*, Vol. 42, No. 5, 2004, pp. 958–964. doi:10.2514/1.1883

[23] Granet, V., Vermorel, O., Léonard, T., Gicquel, L., and Poinsot, T., "Comparison of Nonreflecting Outlet Boundary Conditions for Compressible Solvers on Unstructured Grids," *AIAA Journal*, Vol. 48, No. 10, 2010, pp. 2348–2364. doi:10.2514/1.J050391

[24] Lax, P., and Wendroff, B., "Systems of Conservation Laws," *Communications on Pure and Applied Mathematics*, Vol. 13, No. 2, 1960, pp. 217–237. doi:10.1002/(ISSN)1097-0312

[25] Povey, T., Chana, K. S., Jones, T. V., and Hurrion, J., "The Effect of Hot-Streaks on HP Vane Surface and Endwall Heat Transfer: An Experimental and Numerical Study," *Journal of Turbomachinery*, Vol. 129, No. 1, 2007, pp. 32–43. doi:10.1115/1.2370748

[26] Povey, T., and Qureshi, I., "A Hot-Streak (Combustor) Simulator Suited to Aerodynamic Performance Measurements," *Journal of Aerospace Engineering*, Vol. 222, No. 6, 2008, pp. 705–720. doi:10.1243/09544100JAERO363

[27] Povey, T., and Qureshi, I., "Developments in Hot-Streak Simulators for Turbine Testing," *Journal of Turbomachinery*, Vol. 131, No. 3, 2009, pp. 1–15. doi:10.1115/1.2987240

[28] Simone, S., Montomoli, F., Martelli, F., Chana, K. S., Qureshi, I., and Povey, T., "Analysis on the Effect of a Nonuniform Inlet Profile on Heat Transfer and Fluid Flow in Turbine Stages," *Journal of Turbomachinery*, Vol. 134, No. 1, 2011, Paper 011012. doi:10.1115/1.4003233

[29] Qureshi, I., Beretta, A., and Povey, T., "Effect of Simulated Combustor Temperature Nonuniformity on HP Vane and End Wall Heat Transfer: An Experimental and Computational Investigation," *Journal of Engineering for Gas Turbines and Power*, Vol. 133, No. 3, 2011, Paper 031901. doi:10.1115/1.4002039

[30] Schmitt, P., "Simulation aux Grandes Échelles de la Combustion Étagée dans les Turbines à Gaz et son Interaction Stabilité-Polluants-Thermique," Ph.D. Thesis, Inst. National Polytechnique de Toulouse, Toulouse, France, 2005.

[31] *ANSYS Fluent User's Guide*, ANSYS, Canonsburg, PA, 2010, pp. 249–339.

[32] Shih, T.-H., Liou, W. W., Shabbir, A., Yang, Z., and Zhu, J., "A New k-$\epsilon$ Eddy Viscosity Model for High Reynolds Number Turbulent Flows," *Computers and Fluids Journal*, Vol. 24, No. 3, 1995, pp. 227–238. doi:10.1016/0045-7930(94)00032-T

[33] Roe, P. L., "Characteristic-Based Schemes for the Euler Equations," *Annual Review of Fluid Mechanics*, Vol. 18, No. 1, 1986, pp. 337–365. doi:10.1146/annurev.fl.18.010186.002005

[34] Smagorinsky, J., "General Circulation Experiments With the Primitive Equations: 1. The Basic Experiment," *Monthly Weather Review*, Vol. 91, No. 3, 1963, pp. 99–164. doi:10.1175/1520-0493(1963)091<0099:GCEWTP>2.3.CO;2

[35] Colin, O., and Rudgyard, M., "Development of High-Order Taylor–Galerkin Schemes for LES," *Journal of Computational Physics*, Vol. 162, No. 2, 2000, pp. 338–371. doi:10.1006/jcph.2000.6538

[36] Colin, O., "Simulation aux Grandes Echelles de la Combustion Turbulente Prémélangée dans les Statoréacteurs," Ph.D. Thesis, Inst. National Polytechnique, Toulouse, France, 2000.

W. K. Anderson
*Associate Editor*

**Flow, Turbulence and Combustion manuscript No.**
(will be inserted by the editor)

# Advanced combustor exit plane temperature diagnostics based on Large Eddy Simulations

## Going further than the radial temperature distribution factor

**C. Koupper · L. Gicquel · F. Duchaine · G. Bonneau**

Received: date / Accepted: date

**Abstract** The accurate description and flow calibration at the exit of a gas turbine combustor is a key point of turbine design. Indeed, the temperature field at the turbine inlet directly impacts both the work extraction by the turbine stages as well as drives the wall heat transfer occurring on the vanes and rotor surfaces. Properly simulating or measuring this critical planar interface has been an extensive topic of research. Despite such efforts, industrial exploitation of the various measures at that interface usually resumes to a quantification of the temperature heterogeneities through the Local Radial Temperature Distortion Factor (LRTDF), thereby loosing major spatial and unsteady information. As lean burn configurations become a standard for aero-engine combustors, the absence of dilution holes reduces the intensity of mixing and the use of more advanced statistical tools should propose an exhaustive representation of the temperature map and mixing quality. Current state-of-the-art numerical design of gas turbine combustor relies on Large Eddy Simulations (LES) giving access to a fully 3-D temporally dependent flow field throughout the combustion chamber. Going beyond LRTDF is therefore possible and advanced analyses of the combustor-turbine interface are accessible to better qualify proposed design changes. In this work, a simple statistical representation of the temperature distribution is introduced and applied for the analysis of a lean burn combustor simulator interface. It is shown that at the exit of this chamber, the temperature samples are distributed following a non-Gaussian shape, highlighting a most probable local temperature largely different from the conventional mean value. The use of high order moments explains such deviations and indicates the presence of strongly segregated zones governed by the technological implementation of effusion cooling systems. Based on this diagnostic,

C. Koupper
CERFACS, 31057 Toulouse, FRANCE and SAFRAN Turbomeca, 64510 Bordes, FRANCE
E-mail: koupper@cerfacs.fr

L. Gicquel · F. Duchaine
CERFACS, 31057 Toulouse, FRANCE

G. Bonneau
SAFRAN Turbomeca, 64510 Bordes, FRANCE

a new and complementary representation of the LRTDF is proposed, accounting for the statistical dimension of the classical (radius, temperature) formulation.

**Keywords** Gas Turbine · Combustor · LES · LRTDF · Temperature

## 1 Introduction

The flow field at the exit of a combustion chamber in a gas turbine is by nature highly unsteady because of the flow large Reynolds number inferring high levels of turbulence, as well as the combustion and mixing taking place in the burner which can result in a wide range of unsteady motions evolving in space and time. It results a highly non-uniform flow distribution at the inlet of the HP turbine. All of these a priori unknown features of new combustor designs are partly explained by the discrete position of the fuel injectors and dilution holes along the azimuthal direction as well as the potential overall radial and azimuthal flow issued by the film cooling and core flow mixing. All of these technological devices result in highly 3-D unsteady fields at the combustor-turbine interface, not only impacting the exit velocity field but also the temperature distribution.

It is known that turbine inlet distortion coming from the combustor flow can cause aero-thermal changes within the high pressure turbine vane and rotor. The aerodynamics, secondary flows, blade loading, heat transfer, losses, efficiency and life duration can be altered by uncontrolled inflow distributions. Numerous authors [1–3] showed that turbine inlet temperature distortion can result in large changes in heat transfer on vanes, rotors and endwalls. Beyond local changes in heat transfer, turbine inlet non-uniformities can lead to very different migration of the hot spot issued by the combustor and entering the high pressure turbine, which can then alter secondary flow and ultimately the turbine efficiency [4,5]. Moreover, large local heterogeneities in the temperature field at the combustor exit impose a reduction of the mean operating turbine inlet temperature (and thus power) by the same amount to preserve the life of the turbine. For example, it is commonly estimated [6] that a local increase of 15 K in the turbine surface temperature reduces its life by a half as far as creep is concerned. Having an accurate and representative characterisation of the temperature field at the exit of the chamber has therefore been a critical issue of turbine design for a long time. Most of the aero-engines combustors developed until recently are based on RQL architectures (Rich burn - Quick quench - Lean Burn) which massively use cooling air for dilution after the primary zone. This usually results in a strongly mixed flow at the inlet of the turbine with very little temperature peaks. The new generation of Lean Burn combustion chambers however employs more air in the primary zone to control the NOx production, at the expense of less fresh air available for cooling. As a result, dilution holes are completely replaced by advanced cooling systems that are usually restrained to the near wall region (slots, films etc.) and the temperature field at the exit of the combustor tends to show radially segregated regions of temperature. Typical temperature profiles observed at the exit of a gas turbine combustor are shown in Fig. 1 for these two architectures: the Lean Burn profile features more pronounced gradients when approaching the inner and outer walls as well as much colder fluid.

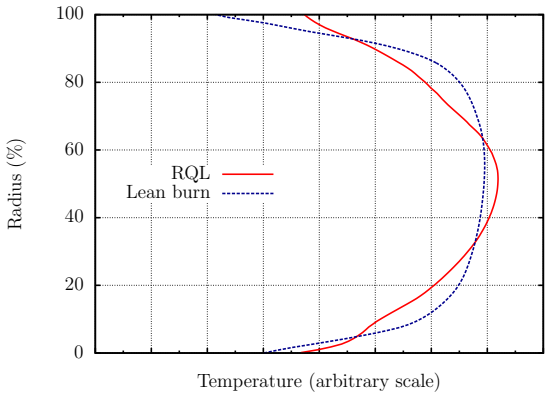


**Fig. 1** Typical circumferentially-averaged temperature profiles at the exit of a gas turbine combustor.

From both an experimental and numerical point of view, the treatment of data at the combustor turbine interface is more and more discussed, and defining proper inlet conditions to the turbine is a key parameter of turbine design. The adequate selection of data to be used at the turbine inlet depends on the final purpose of the study as well as the available information. As far as turbine thermal stress assessment alone is concerned, time-averaged fields of temperature are commonly used. The timescale associated with conduction on the solid part being at least one order of magnitude larger than the fluid timescale, there is a priori no need for considering time-resolved temperature signals. Moreover, mean temperature fields can easily be available through time-averaged measurements of temperature at the combustor exit (test rig), or more commonly via steady-state Computational Fluid Dynamics (CFD) predictions. However, time-averaging temperature intrinsically implies a loss of data: the local operating range and temporal variations of temperature are not known anymore. Quantifying the impact of this loss is a tough task, mainly because of unavailable information or adequate numerical tools. To the authors' knowledge, no experiment using high frequency response hardware is reported in the literature. Despite this lack of experimental data, high fidelity numerical simulations of combustion systems mainly based on Large Eddy Simulations (LES) now represent an emerging source of unsteady data. LES are now mature for the simulation of gas turbine combustors and their ability to predict the mean flowfield and capture turbulence levels is recognized [7–9].

The aim of the current study is to go beyond the common design practices relying on simple time-averaged temperature. The main idea is here to exploit the time-dependent signal provided by LES of combustion chambers to improve the description of the combustor-turbine interface and eventually provide a more discriminant diagnostic than the traditional Local Radial Temperature Distortion Factor (LRTDF) [10]. Although mainly relying on numerical data, this analysis is of course directly applicable to experimental data if available. In section 2, the treatment of the temperature data is explained and a general statistical formulation of the temperature field is proposed to help better understanding and qualifying a burner at a design phase. This approach is finally applied to a non-

reactive lean burn Combustor Simulator (CS) developed for the European research project FACTOR in section 3. This application test case demonstrates that the extended statistical analysis of temperature at a combustor exit can be directly used to assess the mixing quality of combustor systems, which is a key parameter in determining turbine life duration.

## 2 General statistical framework for the characterization of the combustor exit temperature

Before applying any statistical treatment to a set of unsteady data, one has to assume that the simulated flow is a continuous stationary process. If so, any sufficiently long signal obtained from a temporally evolving LES provides a representative statistical description of any flow variable (typically here the temperature). Within this context, each point in the computation or for which a probe is available can be associated with its one point temperature probability density function (pdf), or equivalently an infinite number of moments [11].

Focusing especially on a temperature signal or set of samples, one can expect different types of distributions depending on the mixing process, as illustrated in Fig. 2:

(a) For a perfectly mixed flow (e.g. the temperature is measured at an infinite distance from the sources), the repeated measurement of temperature at a single position gives the same value. The corresponding pdf features only a Dirac centred on the adiabatic temperature $T_{ad}$. In the case of a non-reacting flow, $T_{ad}$ is obtained from a simplified energy balance (assuming constant heat capacity):

$$T_{ad} = \frac{\dot{m}_{hot} T_{hot} + \dot{m}_{cold} T_{cold}}{\dot{m}_{hot} + \dot{m}_{cold}}, \tag{1}$$

where $\dot{m}_i, T_i$ refer to the mass flow and temperature of the hot and cold streams. In the following, the flow is considered as adiabatic (no heat loss), and thus the adiabatic temperature should equal the mean temperature $\overline{T}$.

(b) In the case of an imperfect mixing of the cold and hot flows, variations around $\overline{T}$ can be introduced. In the hypothetical case where all the measured samples are independent (which is not true for temperature), the distribution of temperature would follow a Gaussian shape centred on $\overline{T}$ (see Fig. 2b), as indicated by the Central Limit Theorem [12]. The standard deviation $\sigma$ is typically used to quantify these variations around $\overline{T}$. Note that such distribution is characteristic of the velocity distribution found in Homogeneous Isotropic Turbulence [13, 14].

(c) The case of FACTOR CS is shown in Fig. 2c for an arbitrary point at the chamber exit. In this configuration, temperature is distributed following an unimodal non-Gaussian shape. This distribution indicates a specific mixing mode between cold and hot gases within the combustor favouring the passage of hot pockets at the location of interest.

The observation of the pdf in Fig. 2c clearly shows that $\overline{T}$ is not sufficient to fully characterize the temperature signal because fluctuations can be large while

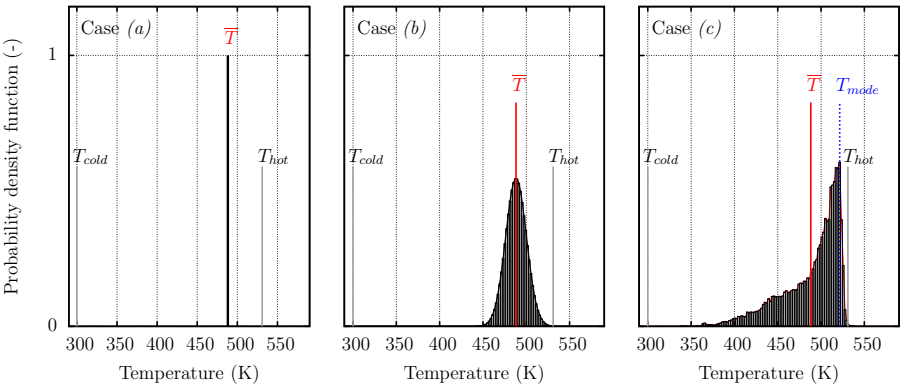


**Fig. 2** Typical temperature distributions for different mixing modes.

remaining within bounds related to the operating conditions of the combustor, and additional variables are needed to describe or compare temperature pdfs'. An additional quantity of interest available through access to the pdf is the so-called mode temperature $T_{mode}$ or *most probable temperature* at this specific location, i.e. the temperature associated with the peak of the pdf. This mode temperature can be seen as the most probable value measured by a probe at this location for a given period. In Fig. 2 the pdfs' of cases *(a)* and *(b)* are centered on $\overline{T} = T_{ad}$ and symmetrical, so $T_{mode} = \overline{T}$. If looking at the exit plane of the CS (case *(c)*) the most probable value is 7% hotter than the mean temperature. The probability associated with the mode temperature is defined as the integral of the pdf over an arbitrary interval defined as $\pm 1/10$ of the standard deviation $\sigma$ around $T_{mode}$:

$$p(T_{mode}) \simeq p\left(T_{mode} - \frac{\sigma}{10} \leq T \leq T_{mode} + \frac{\sigma}{10}\right) = \int_{T_{mode}-\frac{\sigma}{10}}^{T_{mode}+\frac{\sigma}{10}} pdf(T)dT. \quad (2)$$

As indicated by the previous discussion, for quantities other than velocity (e.g., scalars or temperature) there is not physical justification that $T_{mode}$ equals $\overline{T}$ or that the pdf is Gaussian, centred around $\overline{T}$ and symmetrical. In fact and in practice, for temperature the only constraint is that it is bounded by $T_{hot}$ and $T_{cold}$, these extremes being fixed and known for a given problem: i.e. the cold gas temperature at the inlet of the combustor and the adiabatic flame temperature at stoichiometry for the most extreme burners. Its is also acknowledge in the literature that the temperature distribution could be accurately approached by a $\beta$-distribution [15–17] defined using a reduced temperature over the interval $[0, 1]$:

$$\Theta = \frac{T - T_{cold}}{T_{hot} - T_{cold}}. \quad (3)$$

The $\beta$-distribution is conveniently parameterized on the basis of the mean $\mu_1 = \overline{\Theta}$ and variance $\mu_2 = \sigma^2$ of the reduced temperature data, defined for $N$

samples as:

$$\overline{\Theta} = \mu_1 = \frac{1}{N}\sum_{i=1}^{N}\Theta_i, \tag{4}$$

$$\sigma^2 = \mu_2 = \frac{1}{N}\sum_{i=1}^{N}\left(\Theta_i - \overline{\Theta}\right)^2. \tag{5}$$

The pdf of the $\beta$-distribution following:

$$pdf_\beta = \frac{1}{B(\alpha,\beta)}\Theta^{\alpha-1}(1-\Theta)^{\beta-1}, \tag{6}$$

where $B$ is the Euler beta function which ensures that the total probability integrates to unity, and $(\alpha, \beta)$ are two shape parameters algebraically determined by use of $\mu_1$ and $\mu_2$.

Typical $\beta$-pdf's obtained by processing the LES temperature signal recorded at three points (A,B,C) taken at various locations at the exit of FACTOR CS are shown in Fig. 3 along with the full exact histograms. For the points B and C, the $\beta$-distribution provide an acceptable fit even if the sharp gradients near the limits are not correctly reproduced (especially for the upper bound of point C). This is due to the fact that the minimum and maximum temperatures actually reached at points A, B and C are not equal to the bounds $(T_{hot}, T_{cold})$ used to define $\Theta$ (Eq. 3). Indeed, the knowledge of the extrema values implies to have either a full pdf already built or *a priori* knowledge of the local evolution of the limiting temperature values which is usually not accessible in engineering applications. The weakness of such modeling approach postulating any pdf shape type is further complicated by the drawback that it also needs adequate evaluations of the local mean and variance values of the temperature which is far from easy to model. Typically and although these last two quantities are provided here and therefore exact for this example, the $\beta$-pdf for point A dramatically fails at reproducing the most probable temperature in the cold region, which is one of the most important outcome of the temperature pdfs'.

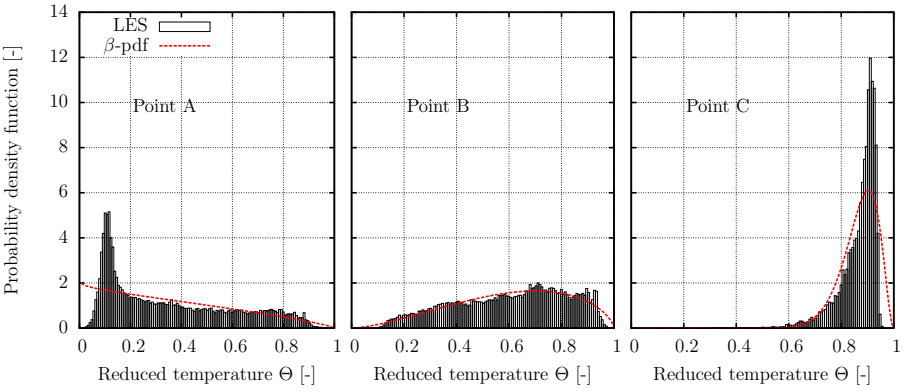


**Fig. 3** LES-based histograms of temperature and corresponding reconstructed $\beta$-pdfs'.

Based on theses observations, complete LES-based distributions of temperature are considered. Such pdf's can be qualified in terms of shape by their first and second moments from Eqs. (5 just like the $\beta$-pdf) as well as high order moments which quantify how much the distribution differs from a Gaussian shape. Specifically the skewness $\mu_3$ and kurtosis $\mu_4$, defined hereafter should be investigated:

$$\mu_3 = \frac{1}{N}\sum_{i=1}^{N}\left(\frac{\Theta_i - \overline{\Theta}}{\sigma}\right)^3, \tag{7}$$

$$\mu_4 = \frac{1}{N}\sum_{i=1}^{N}\left(\frac{\Theta_i - \overline{\Theta}}{\sigma}\right)^4. \tag{8}$$

To illustrate the use of skewnesses and kurtoses in the context of a combustion system, the kurtoses and skewnesses associated with the pdfs' of the points A, B and C are summarized in Table 1. The values obtained analytically from the corresponding $\beta$-pdf are also indicated for comparison. Overall the $\beta$-distributions correctly capture the trend of the different skewnesses (positive or negative asymmetry) but overpredict the absolute level. The $\beta$-pdf also fails to correctly reproduce the importance of the peak of temperature for point C, as indicated by the under-prediction of the associated kurtosis value. It is worth noting that the analysis of the high order moments is subject to caution [18,19], and a single value of skewness or kurtosis can represent many different shapes of distributions. These parameters therefore have to be used as indicators, and commented along with the associated distributions:

(a) **Skewness** A negative value of skewness indicates that the left leg of the distribution is longer or thicker than the right one, while a positive value indicates that the right leg is longer or thicker. A value of zero indicates that both legs are identical (like a Gaussian, for which it equals zero), or that the two legs balance out: e.g. one leg is thick and short while the other one is long with small probability values.

(b) **Kurtosis** For unimodal distributions, kurtosis is a measure of the distribution around the mode value [20]: high values are associated with large shoulders and thin long legs, while values going to zero represent a more rounded distribution around the mode value, with a small extension away from the mode. Recall for reference that the kurtosis of a Gaussian distribution is $\mu_4 = 3$.

| | | $\mu_3$ | $\mu_4$ |
|---|---|---|---|
| Point A | LES | 0.63 | 2.11 |
| | $\beta$-pdf | 0.86 | 2.27 |
| Point B | LES | -0.33 | 2.10 |
| | $\beta$-pdf | -1.37 | 2.30 |
| Point C | LES | -1.96 | 8.59 |
| | $\beta$-pdf | -50.8 | 3.82 |
| *Gaussian distribution* | | 0.0 | 3.0 |

**Table 1** Skewnesses and kurtoses of the temperature pdfs' at points A, B and C.

An original aspect of the statistical treatment of the unsteady temperature signal is to give access to both $\overline{T}$ and $T_{mode}$ along with an explicit characterization of the pdf shape relative to the ideal Gaussian distribution. It is proposed here to investigate the temperature fields at the exit of the combustor systems based on these specific constants. Temperature distortions can be quantified in many different ways [10], depending on the application and habits of the community. One uses here a non-dimensional temperature coefficient $\Xi$ to represent the temperature characteristics at any point in the cylindrical frame of reference $(x, r, \theta)$:

$$\Xi_\psi = \frac{\psi(x,r,\theta) - \overline{T}_{40}}{\overline{T}_{40} - \overline{T}_{30}}, \tag{9}$$

where $\psi(x, r, \theta)$ might be either the local mean temperature $\overline{T}$, the mode temperature $T_{mode}$ or a local sample of temperature $T_i$. $\overline{T}_{40}$ is the spatial and temporal mean temperature at the combustor exit and $\overline{T}_{30}$ is the cold gas temperature at the inlet of the combustor. As most of the design practices use one-dimensional profiles at the inlet of the high pressure turbine (i.e. a fixed location $x_0$), the temperature coefficient $\Xi_\psi$ can be circumferentially averaged to yield:

$$< \Xi_\psi >_\theta = \frac{< \psi(x_0,r,\theta) >_\theta - \overline{T}_{40}}{\overline{T}_{40} - \overline{T}_{30}}, \tag{10}$$

where $<>_\theta$ denotes the circumferential average. If $\psi = \overline{T}$, then $\Xi_{\overline{T}}$ and $< \Xi_{\overline{T}} >_\theta$ are respectively equivalent to the definition of the LOTDF and LRTDF proposed in [10].

Note that whenever qualifying a design several issues may arise and need to be verified prior to the following analyses: *(i)* $\overline{T}_{40}$ may differ from the adiabatic temperature (heat losses); *(ii)* for multiple inlets at different temperatures, how to precisely define $\overline{T}_{30}$ will play a role. All of these issues can explicitly impact the interpretation and exploitation of $< \Xi_\psi >_\theta$ which is the result of multiple manipulations that can largely smear the actual information present in the pdf, justifying the use of more advanced criteria.

## 3 Advanced analysis of a lean burn combustor simulator

### 3.1 Test case description

The methodology proposed in section 2 is applied to the FACTOR CS. The European project FACTOR is dedicated to the study of transport of hot streaks generated in the combustor through the high pressure turbine. A test rig is developped at DLR to host a modern lean-burn aero-engine CS and a 1.5 high pressure turbine stage, operating at realistic Reynolds and Mach numbers. To ease operability and allow the use of different measurement techniques, no combustion is enforced in the chamber and the temperature profile is obtained only by mixing hot and cold air streams. The CS features 20 fully annular sectors, and one of them is schematically shown in Fig. 4. The flow split is representative of a lean-burn chamber, with 65% of air mass flow going through the swirlers and 35% of air mass flow used for cooling (effusion cooling only). The hot air stream goes through an axial swirler of diameter $D_{sw}$ featuring 30 flat vanes, followed by a duct (length $L = 0.7D_{sw}$) used to confine and preserve the hot spot as intense as possible in the chamber until the combustor exit. The Reynolds number associated with the chord of the vanes of the swirler is 170 000. The inner and outer liners are multi-perforated with 0.45 mm diameter holes aligned in the streamwise direction. The exit of the chamber (so-called plane 40) is located $3.5D_{sw}$ downstream the inlet of the CS (see Fig. 4). In this plane, the mean Mach number is about 0.1 while the temperature distortion is contained within +10% and −25% of the mean value $\overline{T}_{40}$, which is representative of typical aero-engines [21, 10].

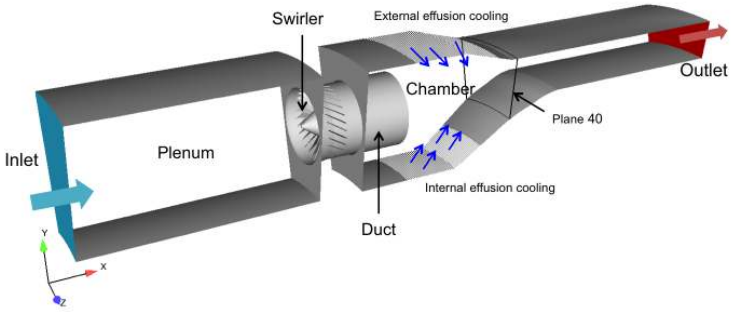


**Fig. 4** Schematic view of the FACTOR CS (cooling cavities are not shown).

### 3.2 Numerical simulations

A single sector version of FACTOR CS is used in this paper, with periodicity enforced on the two lateral faces. A large plenum feeds the swirler with hot air ($\Xi_{T_{hot}} = 0.54$) at the nominal mass flow rate. The cost of meshing all the effusion cooling holes ($<$ 0.5 mm diameter, 5164 holes/sector), liner and plenum being prohibitive, an adiabatic homogeneous injection model is used to account for the

momentum injection at the multiperforated plates [22]. With this approach, cooling air (at a single temperature $\Xi_{T_{cool}} = -1.0$) is injected at the desired mass flow rate through the surfaces indicated in Fig. 4, a scaling correction of the flow axial momentum being introduced by this model and was found to provide reasonably good results for combustors having a purely axial injection of cooling flow [22, 23]. All other wall uses a law-of-the-wall approach. The outlet of the computational domain is located sufficiently far downstream the region of interest, and a 3-D characteristic boundary condition [24, 25] is used to avoid acoustic reflections while maintaining the pressure level close to the target value. A single sector is meshed with 29 M tetrahedral cells. In the core of the recirculation zone and near the effusion plates, the cell edge approaches 0.8 mm. An overview of the mesh in the swirler region is shown in Fig. 5.

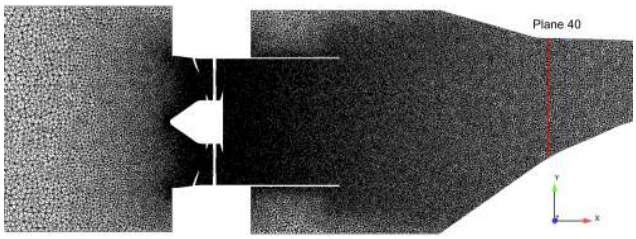


**Fig. 5** Mesh in the longitudinal plane of the CS.

The compressible Navier Stokes are numerically solved by the parallel code AVBP [26] using the LES filtering formalism. The solver uses the cell-vertex finite volume approximation, and is based on an explicit temporal integration scheme. Therefore, the timestep is limited by the Courant Friedrichs Lewy condition ($CFL = 0.7$), and approaches $5 \times 10^{-8}$ s. Numerical explicit integration is obtained using a two-step Taylor Galerkin numerical scheme [27] which provides third-order accuracy in time and space. Such scheme ensures low dispersion and diffusion properties, and is therefore adequate for LES. In this study, the Smagorinsky model [28] is used to account for the sub-grid scale activity. It is a purely diffusive and dissipative model appropriate for turbulent mixing flow.

Once the flow is established and statistically stationary, the simulation is run for 140 ms (i.e. more than 10 through flow times) over which 1100 instantaneous solutions are saved at a constant sampling rate of 9.7 kHz. These snapshots of the flowfield allow to reconstruct a discrete temperature signal at each node of the domain. Because of storage and data treatment issues, the number of solutions is limited, and therefore the representativity of the sampling has to be assessed.

### 3.3 Validation of the sampling

To validate the representativity of the set of solutions against the continuous numerical solution, the sampled ensemble is compared to a numerical monitoring

probe, initially introduced in the LES for which sampling follows Table 2. Distributions are then obtained for the two sets of data of Table 2 through binning. Histograms relying on the same parameters are shown in Fig. 6 for the three points (A,B,C) introduced previously and located in plane 40. For distributions showing strong peaks (e.g. points A and C) both ensembles give the same prediction of $\Xi_{T_{mode}}, \Xi_{\overline{T}}, \sigma, \mu_3$ and $\mu_4$. When the standard deviation is larger (e.g. point B), errors of 2 to 5 % can be found. Overall the representativity of the set of snapshots is found to be sufficiently satisfactory to perform further analysis on the histograms obtained from the set of snapshots.

| | Set of snapshots | Probe |
|---|---|---|
| Sampling frequency (kHz) | 9.7 | 457.0 |
| Total time (ms) | 143 | 129 |
| Number of samples | 1 100 | 58 882 |

**Table 2** Characteristics of the signal acquired by the probe and the set of snapshots.

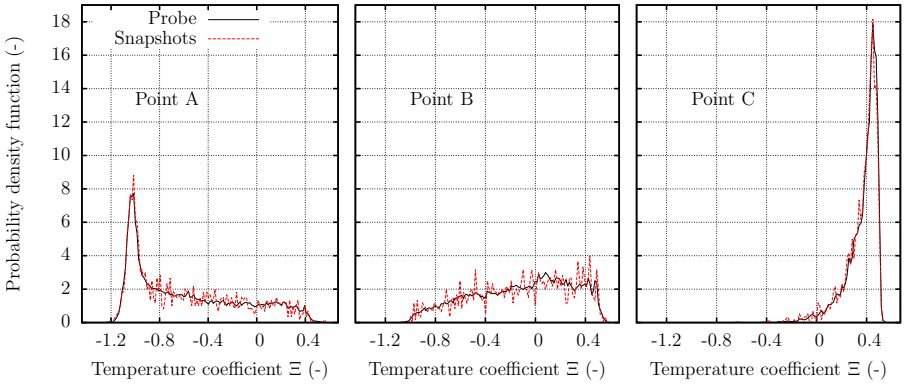


**Fig. 6** Histograms obtained by the set of snapshots and the probe signal.

### 3.4 Results and discussion

First of all, an overview of the flow field in the CS is given in Fig. 7 by the contours of Mach number for the ensemble mean of the instantaneous numerical solutions. In terms of mean flow topology, this flow is consistent with real burner flows [29–31]. The hot air flow reaches high velocity values inside the swirler, which are maintained until the exit of the duct where the jet spreads radially. At the exit of the swirler, the flow has a strong tangential component of velocity, as indicated by the swirl number which is estimated [32] at $S_N = 0.76$. This translates in a vortex breakdown [33] and the formation of a large recirculation zone which is firstly cylindrical and confined by the duct, before to enlarge suddenly at the exit

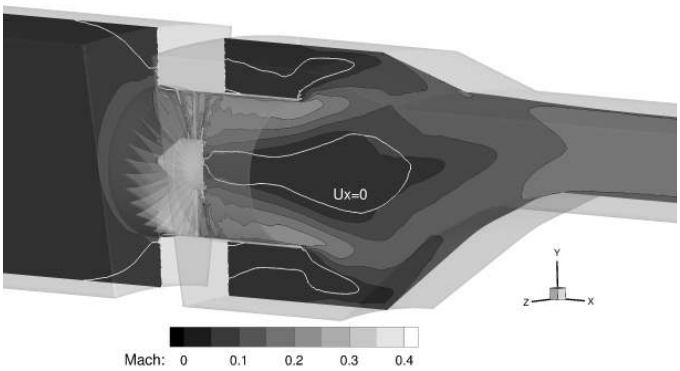


**Fig. 7** Mach number in a longitudinal cross-section of the CS, and isoline of negative axial velocity.

of the duct. Corner recirculation zones are also created below and above the duct, resulting in slow moving fluid in these zones.

It is now proposed to analyse the time distributions of temperature computed based on the 1 100 snapshots of the flow. Temperature fields in the chamber are discussed first, before analyzing local and global distributions in plane 40.

Figure 8(a) and 8(b) respectively show $\Xi_{\overline{T}}$ and $\Xi_{T_{mode}}$ in the longitudinal cross section of the CS. The visualization of $\Xi_{T_{mode}}$ highlights the discrimination in temperature of different zones in the chamber. For extreme conditions where no mixing occurs (i.e. only hot or cold injection) the mean and mode values are equal: this is the Dirac distribution case of Fig. 2a. In the trace of the hot jet exiting the duct it is very likely to measure the hot temperature, as there is a little amount of cooling at this position. Nonetheless, the reversing flow induced by the vortex breakdown does contribute to the mixing and $\Xi_{\overline{T}}$ is below $\Xi_{T_{hot}}$. Near the multiperforated walls the cold fluid injection creates very distinct cold films, which remain coherent and close to the wall. In this region the probability to measure $\Xi_{T_{cool}}$ is high and drops quickly with an increasing distance from the wall because hot fluid is encountered and the flow heats up. Figure 8(c) shows the field of probability associated with the mode temperature, as defined in Eq. (2). In the upstream plenum, swirler and duct, $p(\Xi_{T_{mode}}) = 1$, as there is no mixing with the coolant, and $\Xi_{\overline{T}} = \Xi_{T_{mode}} = \Xi_{T_{hot}}$ as indicated earlier. The same observation is done in the corner recirculation zones above and below the duct, where there is very little evolution of the fluid temperature once the flow is established. In the hot jet exiting the duct radially, $\Xi_{T_{mode}} = \Xi_{T_{hot}}$ (see Fig. 8(b)), but its probability decreases quickly as the jet penetrates the CS because of the mixing with the colder flow. The central region of the CS shows a stretched triangular shape in which $p(\Xi_{T_{mode}}) \simeq 1$. In this zone, the coolant flow is too far and does not interact directly with the hot stream: the temperature decreases by turbulent diffusion only (no intermittency hot/cold), and there is thus little variation of temperature. Note that $p(\Xi_{T_{mode}}) = 1$ implies $\Xi_{\overline{T}} \simeq \Xi_{T_{mode}}$ with very little mixing locally (i.e. within $\pm\sigma/10$). As we go away from the central axis, $p(\Xi_{T_{mode}})$ reduces significantly until a very low value (around 0.1 in a thin band) because either coolant either mainflow

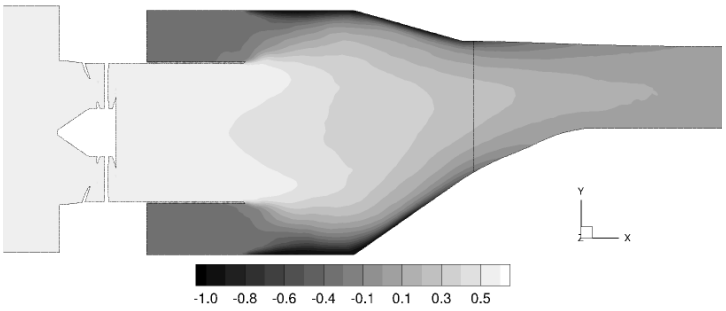


(a) Mean temperature coefficient $\Xi_{\overline{T}}$.

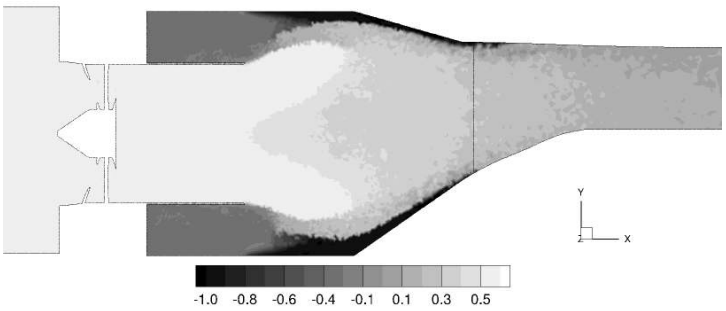


(b) Mode temperature coefficient $\Xi_{T_{mode}}$.

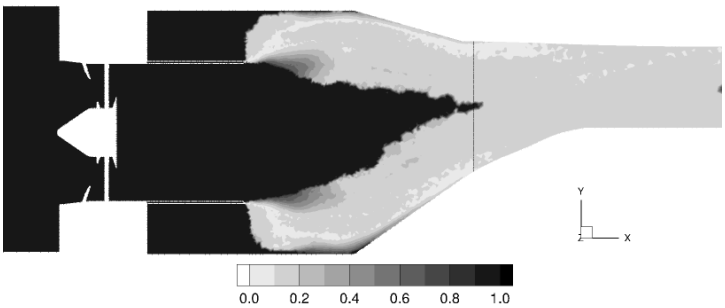


(c) Probability of $\Xi_{T_{mode}}$.

**Fig. 8** Temperature coefficient and probability of $\Xi_{T_{mode}}$ in a longitudinal cross-section of the CS.

can be measured in these zones. Finally, the probability increases again as we get closer to the multiperforated wall, where it is very likely to measure the coolant temperature, until the wall itself where $p(\Xi_{T_{mode}}) = 1$.

As significant differences between $\Xi_{T_{mode}}$ and $\Xi_{\overline{T}}$ are observed in the central plane, it is likely that the exit of the combustor will show similar differences. Both fields of $\Xi_{T_{mode}}$ and $\Xi_{\overline{T}}$ in plane 40 are shown in Fig. 9: there is a large central region of uniform $\Xi_{T_{mode}}$ in the center of plane 40, while $\Xi_{\overline{T}}$ is more smoothly dif-

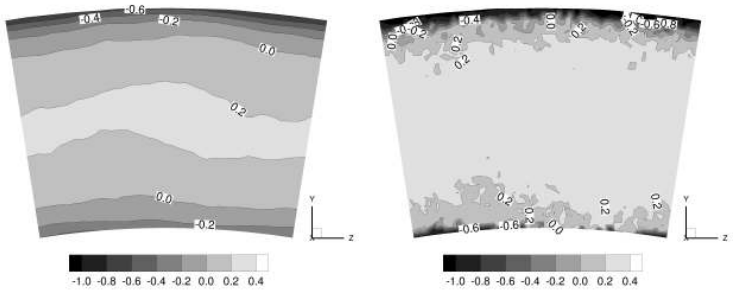


(a) $\Xi_{\overline{T}}$. (b) $\Xi_{T_{mode}}$.

**Fig. 9** Mean and most probable temperature coefficients in plane 40.

fused. In the near-wall region, the presence of the upstream film cooling maintains $\Xi_{T_{mode}}$ close to $\Xi_{T_{cold}}$, and a clear transition between coolant flow and mainstream is visible. With stronger radial temperature gradients and higher values in the core, the field of most probable temperature coefficient seems definitely more critical for the turbine.

The corresponding circumferentially-averaged temperature coefficient $< \Xi >_\theta$ is plotted for $\overline{T}$ and $T_{mode}$ in Fig. 10, along with the experimental measurement obtained by means of an unsheathed thermocouple [34]. Note that to appropriately compare adiabatic LES with non-adiabatic experiments, the mean temperature in plane 40 $\overline{T}_{40}$ used in Eq.(10) is computed on the investigation zone (and is not the adiabatic temperature $T_{ad}$). The mean temperature computed on the LES samples is found to agree well with the time-averaged experimental value, which tends to validate the aerothermal numerical flow predictions. Note that a typical LRTDF (either from simulations or experiments) would be obtained by considering only the $\Xi_{\overline{T}}$ curve in Fig. 10. However, the introduction of the mode temperature

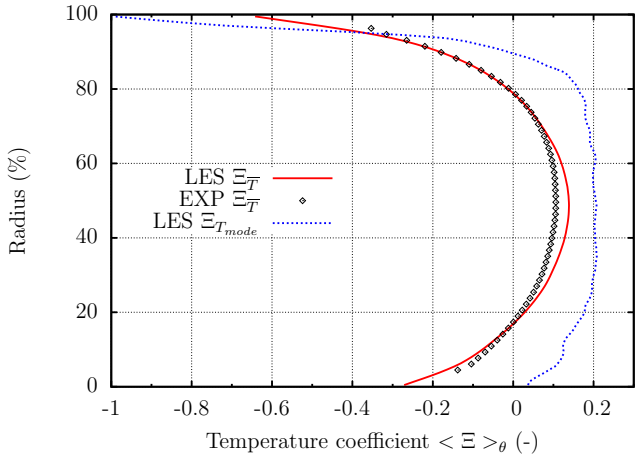


**Fig. 10** Circumferentially-averaged profile of the temperature coefficients in plane 40.

in this graph indicates very clearly that the temperature is not distributed with a Gaussian shape at the combustor exit. The radial profile of $\Xi_{T_{mode}}$ is hotter than $\Xi_{\overline{T}}$ and shows more pronounced gradients, suggesting that the temperature envelope at the turbine inlet is more critical than depicted by a simple mean temperature analysis. Quantitatively, if spatially averaged over the exit plane, the mode coefficient $< \Xi_{T_{mode}} >_{r,\theta}$ equals 0.11 while $< \Xi_{\overline{T}} >_{r,\theta} = 0$. In dimensional units, this can be translated into a difference of 17 K. To explain such differences, one has to analyze the high order moments of the distribution of temperature in this plane. To do so, skewnesses and kurtoses are calculated at each computational node in plane 40 and shown in Fig. 11.

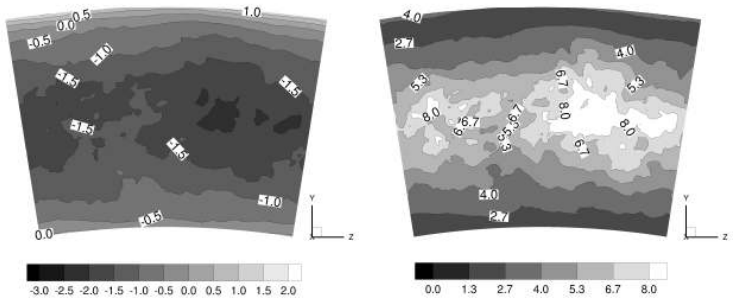


(a) Skewness $\mu_3$. (b) Kurtosis $\mu_4$.

**Fig. 11** Skewness and kurtosis of the pdfs' of temperature in plane 40.

Both moments are distributed following a very inhomogeneous pattern over plane 40, which means that the pdfs' of temperature are significantly different for all points at the exit of the combustor. However, the pattern is definitely not random and some zones of similarity can be identified. The central region features highly negative skewness values, which means that overall $\Xi_{T_{mode}} > \Xi_{\overline{T}}$, as this was observed in Fig. 9. On the other hand, the near-wall regions exhibit positive values of skewness: the coolant is dominant in this zone ($\Xi_{T_{mode}} \simeq \Xi_{T_{cool}}$), and only punctual incursions of hot fluid occur. The central hot region is associated with larger kurtosis values, highlighting a higher occurrence rate of the most probable temperature with little deviation.

To investigate if such observations are linked to the velocity fields or equivalently the turbulent activity in plane 40, skewnesses and kurtoses of the axial velocity in plane 40 are shown in Fig. 12. The contrast with the temperature distribution is strong: $\mu_3$ and $\mu_4$ are very homogeneously distributed. Skewness is very close to zero, while kurtosis is equal to 3 almost everywhere, which corresponds to a Gaussian distribution of velocity and a fully established turbulent flow. This specific diagnostic confirms that there is a first order dependency of the temperature distribution in the exit with the technological implementation of the cooling systems and its mixing process. Turbulence alone —at least with the associated small scales— is not efficient enough to properly mix both fluids prior to its entry in the turbine.

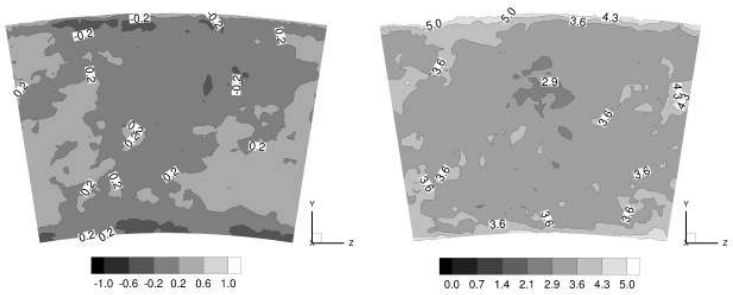


(a) Skewness $\mu_3$. (b) Kurtosis $\mu_4$.

**Fig. 12** Skewness and kurtosis of the pdfs' of axial velocity in plane 40.

| | $< \mu_3 >_{r,\theta}$ | $< \mu_4 >_{r,\theta}$ |
|---|---|---|
| Temperature | -1.1 | 4.8 |
| Axial velocity | 0.1 | 3.4 |
| *Gaussian distribution* | 0.0 | 3.0 |

**Table 3** Spatially-averaged skewness and kurtosis of temperature and axial velocity in plane 40.

Spatially-averaged values of skewness $< \mu_3 >_{r,\theta}$ and kurtosis $< \mu_4 >_{r,\theta}$ of temperature and axial velocity pdfs' are reported in Table 3. They represent the mean value in space of the moments of the different distributions, giving an indication of how —on average— all the distributions in plane 40 look like. The values for the axial velocity are close to a Gaussian distribution, which confirms our previous observation. However, the mean skewness of the temperature distribution is negative, which means that overall the distributions show a mode temperature hotter than the mean value, in agreement with the 17 K difference reported previously.

### 3.5 Statistical representation of the radial profile of temperature

The most common way to represent a temperature profile at the exit of the combustor is to draw the radial profile of the circumferentially-averaged mean temperature: the LRTDF [10] shown by the solid line in Fig. 10. However, based on our previous observations, it is clear that the mean value is not sufficient to fully describe a temperature distribution, because important local changes in the shape of the pdf are usually present and smeared by all averages introduced in the evaluation of the LRTDF. It is proposed here to extend the diagnostic space of the LRTDF (i.e. radius and temperature dimensions) by adding the sampling dimension.

For this purpose, plane 40 is divided into 35 successive radial sections and mean pdfs' of temperature are computed for each radial coordinate, as shown in Fig. 13. They are the direct illustration of two previous quantitative observations discussed earlier. First, all the pdfs' at given radial locations exhibit very different non-Gaussian shapes, as indicated by the value of skewness and kurtosis calculated

previously. Second, the distributions are not centered on the most probable value, but skewed towards colder temperatures: this is the translation of the negative mean skewness (see Table 3) which results in a larger mode than mean temperature coefficient. Finally, Fig. 13 also highlights how temperature is differently distributed within two zones. On one hand, the central region ($30\% < R < 70\%$) features high probability and little dispersion of the pdf (high kurtosis region, see Fig. 11(b)). In this zone, there is a rapid decrease of the probability after $\Xi_{T_{mode}}$, which is close to the maximum value $\Xi_{T_{hot}}$. Indeed, the core temperature is mainly driven by the swirling hot air stream, which is relatively well preserved because of the absence of dilution holes. On the other hand, the near-wall zone shows much wider distributions associated with lower values of the probabilities. The pdf close to the outer wall ($R \rightarrow 100\%$) is very wide, and the most probable value is in fact close to the coolant itself $\Xi_{T_{cool}} = -1$. Indeed, this specific region features little interaction between the effusion cooling and the hot stream because the outer wall is above the flowpath exiting the swirler (see Fig. 8). This effect is less evident for the inner wall.

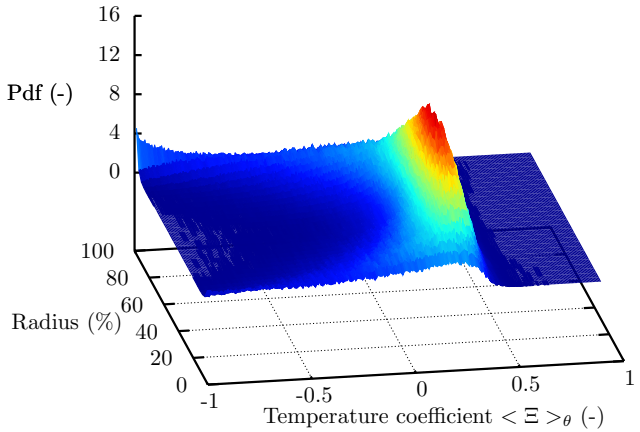


**Fig. 13** Circumferentially averaged pdfs' of temperature in plane 40.

An alternative view of Fig. 13 is proposed in Fig. 14, along with the values of $\Xi_{\overline{T}}$, $\Xi_{T_{mode}}$, $\Xi_{T_{min}}$ and $\Xi_{T_{max}}$ extracted from the pdfs'. While usual representations of the combustor exit temperature only feature $\Xi_{\overline{T}}$, Fig. 14 completely defines the mixing envelope of the exit plane of the CS. It is worth noting that the radial profile of $\Xi_{T_{mode}}$ represents the most probable temperature at each radial step, but is not the most probable temperature profile to be measured at the exit of the combustor. Both mode and mean temperature coefficients are constructed from these statistics: they cannot be measured on a single realization of the flow. The difference between the profiles of $\Xi_{\overline{T}}$ and $\Xi_{T_{mode}}$ is significative, both in terms of absolute value and distribution. Because of the presence of two zones in the mode temperature (core and near-wall), the radial gradient of $T_{mode}$ is very strong in the transition zone ($R \simeq 10\%$ and $R \simeq 90\%$).

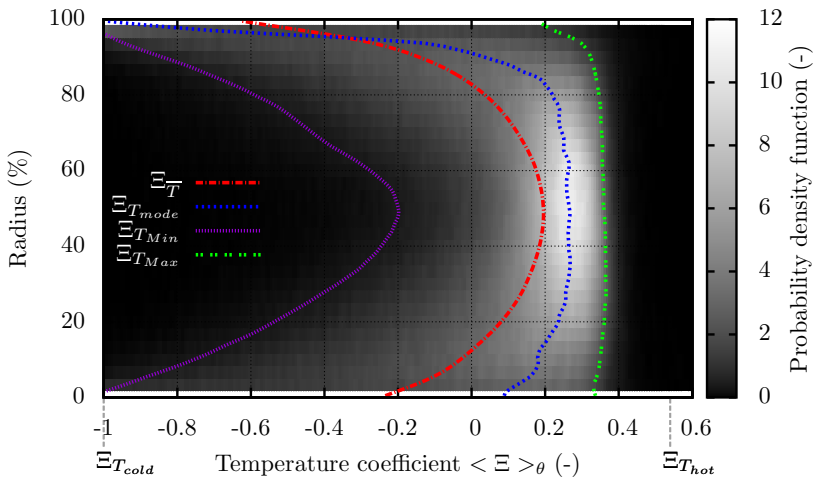


**Fig. 14** Temperature coefficient for the mean, mode, minimum and maximum temperatures, and associated pdf in plane 40.

## 4 Conclusion

While most design processes for high pressure turbines rely on time-averaged fields to describe the exit of the combustor, it is proposed here to take advantage of advanced time-resolved LES to better qualify and understand the physics taking place at this critical interface. Based on samples and with conventional hypothesis introduced in the study of turbulent flow theories, a simple statistical analysis is applied to the unsteady data at the exit of FACTOR CS. It showed that the distributions of temperature of this chamber are not Gaussian, with the presence of regions where a most probable temperature largely differs from the mean temperature. The analysis of higher order moments (skewness and kurtosis) explains such differences indicating strongly segregated regions of cold or hot fluid in the chamber. These observations are also shown to be directly linked to the technological implementation of the cooling systems. With the generalization of lean burn configurations, and the progressive disappearance of dilution holes which strongly enhanced mixing, the temperature distribution at the combustor exit will tend to show such discriminated zones. In this context, applying this statistical approach can help assessing the quality of the mixing at the combustor exit.

Based on this statistical context, a more appropriate characterization of the combustor exit temperature profile is proposed, by considering the sampling-dimension in addition to the common (radius, temperature) representation (LRTDF). This new diagnostic indeed allows to fully characterize the temperature envelope of the combustor exit and shows that the most probable temperature is definitely a more critical parameter for the turbine than the mean value. This conclusion tends to confirm the importance of using time-resolved temperature fields at the turbine inlet to correctly characterize the flow exiting the combustion chamber. What would be the final impact on the turbine wall temperature is already a topic of research in the turbomachinery community.

**Acknowledgements** The test case used for developing this methodology (FACTOR project, *www.factor-fp7.eu*) has received funding from the European Union Seventh Framework Programme (FP7/ 2007-2013) under grant agreement number 265985. The simulations presented here were performed using HPC resources from GENCI-IDRIS (Grant 2013-x20132b5031).

## References

1. T. Povey, K. S. Chana, T. V. Jones, J. Hurrion, The effect of hot-streaks on hp vane surface and endwall heat transfer: An experimental and numerical study, Journal of Turbomachinery 129 (1) (2007) 32–43.
2. S. Salvadori, R. Giovanni, M. Insinna, F. Martelli, Analysis of combustor/vane interaction with decoupled and loosely coupled approaches, in: ASME Turbo Expo 2012: Turbine Technical Conference and Exposition, no. GT2012-69038, ASME, 2012.
3. M. Insinna, D. Griffini, S. Salvadori, F. Martelli, Conjugate heat transfer analysis of a film cooled high-pressure turbine vane under realistic combustor exit flow conditions, in: ASME Turbo Expo 2014: Turbine Technical Conference and Exposition, no. GT2014-25280, 2014.
4. T. Shang, A. Epstein, Analysis of hot streak effects on turbine rotor heat load, Journal of Turbomachinery 119 (3) (1997) 544–553.
5. R. J. Roback, R. P. Dring, Hot streaks and phantom cooling in a turbine rotor passage: Part 1—separate effects, Journal of Turbomachinery 115 (4) (1993) 657–666.
6. P. T. Ireland, G. Dailey, Aerothermal performance of internal cooling systems in turbomachines., in: Internal Cooling in Turbomachinery, VKI Lecture Series, Vol. 2010-05, 2010.
7. P. Sagaut, Large Eddy Simulation for Incompressible Flows: An Introduction, Scientific Computation, Springer, 2006.
8. L. Y. M. Gicquel, N. Gourdain, J.-F. Boussuge, H. Deniau, G. Staffelbach, P. Wolf, T. Poinsot, High performance parallel computing of flows in complex geometries, Comptes Rendus de l'Académie des Sciences - Mathématiques 339 (2011) 104–124.
9. L. Y. M. Gicquel, G. Staffelbach, T. J. Poinsot, Large Eddy Simualtions of gaseous flames in gas turbine combustion chambers, Progress in Energy and Combustion Science 38 (2012) 782–817.
10. T. Povey, I. Qureshi, Developments in hot-streak simulators for turbine testing, Journal of Turbomachinery 131 (3) (2009) 1–15.
11. J. Mendel, Lessons in Estimation Theory for Signal Processing, Communications, and Control, Pearson Education, 1995.
12. F. M. Dekking, A modern introduction to probability and statistics : understanding why and how, Springer, 2005.
13. P. Sagaut, C. C., Homogeneous Turbulence Dynamics, Cambridge University Press, 2008.
14. S. Pope, Turbulent Flows, Cambridge University Press, Cambridge, 2000.
15. S. S. Girimaji, Assumed $\beta$-pdf model for turbulent mixing: Validation and extension to multiple scalar mixing, Combustion Science and Technology 78 (4-6) (1991) 177–196.
16. R. L. Gaffney Jr, J. A. White, S. S. Girimaji, J. P. Drummond, Modeling temperature and species fluctuations in turbulent, reacting flow, Computing Systems in Engineering 5 (2) (1994) 117–133.
17. J. Bakosi, J. R. Ristorcelli, Exploring the beta distribution in variable-density turbulent mixing, Journal of Turbulence 11 (37) (2010) 1–31.
18. D. N. Joanes, C. A. Gill, Comparing measures of sample skewness and kurtosis, Journal of the Royal Statistical Society. Series D (The Statistician) 47 (1) (1998) pp. 183–189.
19. D. Dorić, E. Nikolić-Dorić, V. Jevremović, J. Malisić, On measuring skewness and kurtosis, Quality and Quantity 43 (3) (2009) 481–493.
20. K. P. Balanda, H. L. MacGillivray, Kurtosis: A critical review, The American Statistician 42 (2) (1988) pp. 111–119.
21. C. Koupper, G. Caciolli, L. Gicquel, F. Duchaine, G. Bonneau, L. Tarchi, B. Facchini, Development of an engine representative combustor simulator dedicated to hot streak generation, Journal of Turbomachinery 136 (11) (2014) 1–10.
22. S. Mendez, F. Nicoud, Adiabatic homogeneous model for flow around a multiperforated plate, AIAA Journal 46 (10) (2008) 2623–2633.
23. S. Mendez, F. Nicoud, Large Eddy Simulation of a bi-periodic turbulent flow with effusion, Journal of Fluid Mechanics 598 (2008) 27–65.

24. T. Poinsot, S. Lele, Boundary conditions for direct simulations of compressible viscous flows, Journal of Computational Physics 101 (1) (1992) 104 – 129.
25. C. S. Yoo, H. G. Im, Characteristic boundary conditions for simulations of compressible reacting flows with multi-dimensional, viscous and reaction effects, Combustion Theory and Modelling 11 (2) (2007) 259–286.
26. T. Schoenfeld, M. Rudgyard, Steady and unsteady flows simulations using the hybrid flow solver AVBP, AIAA Journal 37 (11) (1999) 1378–1385.
27. O. Colin, M. Rudgyard, Development of high-order taylor–galerkin schemes for LES, Journal of Computational Physics 162 (2) (2000) 338 – 371.
28. J. Smagorinsky, General circulation experiments with the primitive equations: 1. the basic experiment, Monthly Weather Review 91 (1963) 99–164.
29. M. Boileau, S. Pascaud, E. Riber, B. Cuenot, L. Gicquel, T. J. Poinsot, M. Cazalens, Investigation of two-fluid methods for Large Eddy Simulation of spray combustion in Gas Turbines, Flow, Turbulence and Combustion 80 (3) (2008) 291–321.
30. P. Wolf, R. Balakrishnan, G. Staffelbach, L. Gicquel, T. J. Poinsot, Using LES to study reacting flows and instabilities in annular combustion chambers, Flow, Turbulence and Combustion 88 (1-2) (2012) 191–206.
31. G. Hannebique, P. Sierra, E. Riber, B. Cuenot, Large eddy simulation of reactive two-phase flow in an aeronautical multipoint burner, Flow, Turbulence and Combustion 90 (2) (2013) 449–469.
32. J. Beér, N. Chigier, Combustion aerodynamics, Halsted Press Division, Wiley, 1972.
33. A. K. Gupta, D. G. Lilley, N. Syred, Swirl flows, Abacus Press, 1984.
34. T. Bacci, G. Caciolli, B. Facchini, L. Tarchi, C. Koupper, J.-L. Champion, Flowfield and temperature profiles measurements on a combustor simulator dedicated to hot streaks generation, in: ASME Turbo Expo 2015: Turbine Technical Conference and Exposition, no. GT2015-42217, 2015.

**Proceedings of ASME Turbo Expo 2015: Turbine Technical Conference and Exposition**
**GT2015**
**June 15-19, 2015, Montreal, Canada**

# GT 2015-42278

# EXPERIMENTAL AND NUMERICAL CALCULATION OF TURBULENT TIMESCALES AT THE EXIT OF AN ENGINE REPRESENTATIVE COMBUSTOR SIMULATOR

**Charlie Koupper**
Turbomeca
Bordes, France
CFD Team CERFACS
Toulouse, France
koupper@cerfacs.fr

**Tommaso Bacci**
**Bruno Facchini**
**Alessio Picchi**
**Lorenzo Tarchi**
University of Florence
Florence, Italy
lorenzo.tarchi@htc.de.unifi.it

**Laurent Gicquel**
**Florent Duchaine**
CFD Team CERFACS
Toulouse, France

**Guillaume Bonneau**
Turbomeca
Bordes, France

## ABSTRACT

*To deepen the knowledge of the interaction between modern lean burn combustors and high pressure turbines, a non-reactive real scale annular trisector Combustor Simulator (CS) has been assembled at University of Florence, with the goal of investigating and characterizing the combustor aerothermal field as well as the hot streak transport towards the high pressure vanes. To generate hot streaks and simulate lean burn combustor behaviors, the rig is equipped with axial swirlers fed by a main air flow stream that is heated up to 531 K, while liners with effusion cooling holes are fed by air at ambient temperature. Detailed experimental investigations are then performed with the aim of characterizing the turbulence quantities at the exit of the combustion module, and specifically evaluating an integral scale of turbulence. To do so, an automatic traverse system is mounted at the exit of the CS and equipped to perform Hot Wire Anemometry (HWA) measurements. In this paper, two-point correlations are computed from the time signal of the axial velocity giving access to an evaluation of the turbulence timescales at each measurement point. For assessment of the advanced numerical method that is Large Eddy Simulation (LES), the same methodology is applied to a LES prediction of the CS. Although comparisons seem relevant and easily accessible, both approaches and contexts have fundamental differences: mostly in terms of duration of the signals acquired experimentally and numerically but also with potentially different acquisition frequencies. In the exercise that aims at comparing high-order statistics and diagnostics, the specificity of comparing experimental and numerical results is comprehensively discussed. Attention is given to the importance of the acquisition frequency, intrinsic bias of having a short duration signal and influence of the investigating windows. For an adequate evaluation of the turbulent time scales, it is found that comparing experiments and numerics for high Reynolds number flows inferring small-scale phenomena requires to obey a set of rules, otherwise important errors can be made. If adequately processed, LES and HWA are found to agree well indicating the potential of LES for such problems.*

## NOMENCLATURE

**Acronyms**

| | |
|---|---|
| *CS* | Combustor Simulator |
| *DP* | Design Point |
| *HIT* | Homogeneous Isotropic Turbulence |
| *HP* | High Pressure |
| *HWA* | Hot Wire Anemometry |
| *LES* | Large Eddy Simulation |
| *NGV* | Nose Guide Vane |
| *RMS* | Root Mean Square |
| *RQL* | Rich burn - Quick quench - Lean Burn |

**Symbols**

| | | |
|---|---|---|
| $M$ | Mach number | $[-]$ |
| $R_{uu}$ | Autocorrelation coefficient of $u'$ | $[-]$ |
| $Re$ | Reynolds number | $[-]$ |
| $f$ | Acquisition frequency | $[Hz]$ |
| $t$ | Time | $[s]$ |
| $\Delta t$ | Duration of the signal | $[s]$ |
| $dt$ | Timestep $dt = 1/f$ | $[s]$ |
| $t_{CS}$ | CS through flow time | $[s]$ |
| $t_{turb}$ | Turbulent timescale | $[s]$ |
| $u$ | Instantaneous axial velocity | $[m/s]$ |
| $u'$ | Fluctuating part of axial velocity | $[m/s]$ |
| $\bar{U}$ | Time-averaged axial velocity | $[m/s]$ |
| $U_{ref}$ | Mean axial velocity at swirler exit | $[m/s]$ |
| $u_{RMS}$ | Root mean square value of velocity | $[m/s]$ |

**Greeks**

| | | |
|---|---|---|
| $\rho$ | Density | $[kg/m^3]$ |
| $\sigma$ | Standard deviation | |
| $\theta$ | Tangential coordinate | |

**Subscripts**

| | |
|---|---|
| *C* | Coolant |
| *M* | Mainstream |
| 40 | Plane 40 |
| *MP* | Multiperforated Plate |

## INTRODUCTION

It is known that turbine inlet distortion can cause major aerothermal changes within the High Pressure (HP) turbine vane and rotor. Aerodynamics, secondary flows, blade loading, heat transfer, losses, and finally efficiency can thus be significantly altered. In this context, the physics of the combustor-turbine interface has been studied extensively since the 80's using both experimental and numerical approaches. The harsh environment encountered in this critical region of the engine makes measurements very difficult, and most of the experimental work has been performed on nonreactive and low pressure test rigs [1, 2].

Among all the data collected on the different test facilities, little attention has been paid to the characterization of the turbulence field at the exit of the combustion systems. With the current need for increased gains in turbine efficiency and validation of the turbine design numerical tools, having knowledge of the turbulence entering the turbine becomes a point of interest. Indeed, turbulence levels can significantly affect the flow in the turbine. It has been shown for example that large scale turbulence can enhance the heat transfer on the vane walls, and promote earlier boundary layer transition [3, 4]. Barringer *et al.* [5] also report that a turbulence intensity increase at the vane inlet leads to broadened wakes and more mixing at the vane exit. Regarding heat transfer, Jenkins *et al.* [6, 7] observed that the proper combination of vane film cooling and high turbulence can help reducing the hot streak peak temperature by 74%. However, most of the published results nowadays lack of representativity as measurements were performed on old engine architectures [8, 9], or obtained in test rigs where turbulence is generated by calibrated grids as reported by Radomsky and Thole [10]. Only recently, Cha *et al.* [11] reported experimental and numerical computations of turbulence at the exit of a real engine-hardware RQL (Rich burn-Quick quench-Lean Burn) combustor. They measured turbulence lengthscales of about 25% of the NGV chord length at the inlet of the turbine, and observed an increase through the vanes, which was not captured by the presented Large Eddy Simulations (LES). Overall, the ability of numerical simulations —and especially LES— to predict the turbulence quantities in a combustion system is widely discussed in the literature [12–14], without ad-hoc comparisons with experimental material.

The work presented here exploits the experimental results obtained on a non-reactive Combustor Simulator (CS) representative of a lean burn engine, developed in the framework of the European project FACTOR. The first phase of the test campaign performed at the University of Florence (UNIFI) provided a detailed characterization of the aerothermal field inside the CS. The mean field at the combustor exit was investigated using a five hole probe and an unsheathed thermocouple while Particle Image Velocimetry (PIV) was performed inside the CS [15]. In addition, the turbulence intensity and energetic spectra were measured at isothermal conditions at the exit of the chamber [16] by means of Hot Wire Anemometry (HWA).

In parallel to the experimental activities, LES were performed on different geometrical configurations and operating points based on a periodic single sector of the CS. Non reported results show that experiments and simulations agree well on the mean and RMS quantities. A qualitative example is given in Fig. 1 showing the contour of the reverse flow zones measured by PIV and predicted by LES. The superposition of the two fields confirms that the overall pattern of the flowfield in the CS is correctly captured by LES. A more quantitative comparison is proposed in Fig. 2 showing the axial momentum (mean and RMS values) plotted along the centerline ($\theta = 0°$) at the exit of the CS for the HWA measurements [16] and the LES. Both numerical

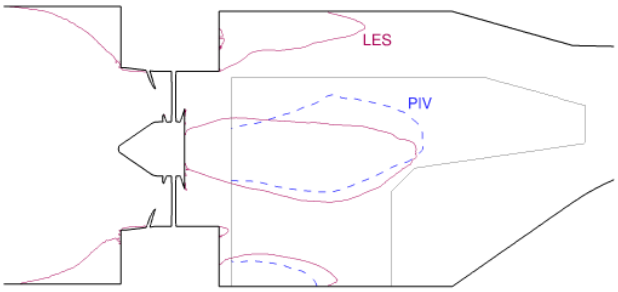


Figure 1: Contour of the reverse flow zones predicted by LES (red line) and PIV (blue dots) in the longitudinal plane of the CS (D00 case).

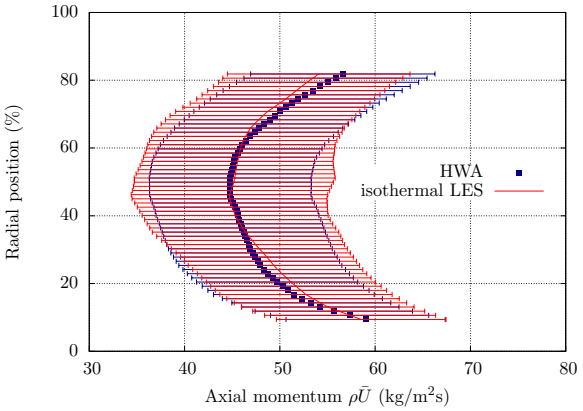


Figure 2: Mean and RMS values of axial momentum $\rho\bar{U}$ in the centerline of the CS exit plane (D00 case).

and experimental approaches agree well on the mean mass flow distribution, as well as on RMS values.

It is intended in this paper to go beyond such first order comparisons between experiments and numerics, and assess the ability of LES to predict high order quantities such as integral scales of turbulence. To do so, two questions need to be addressed: *(i)* How to properly compare the estimations of turbulent timescales provided by two very different approaches: HWA and LES, each one with its own limitations ? *(ii)* Is LES able to predict the distribution and magnitude of turbulent timescales at the exit of an engine representative module ?

After a brief presentation of the experimental facility and the instrumentation, the methodology to compute turbulent timescales is detailed and the associated limitations are discussed. A special insight is given on the specificities introduced by the comparison between experimental and numerical approaches. Finally, HWA and LES results are compared for different geometries of the CS.

## EXPERIMENTAL FACILITY

Within the European project FACTOR, a new continuous flow facility hosted by DLR is developed to receive a CS and a 1.5 high pressure turbine stage operating at realistic Reynolds and Mach numbers. The CS is designed to mimic a recent lean burn combustion chamber, but no combustion is enforced in the chamber to ease operability and allow the use of different measurement techniques. The temperature profile is obtained only by mixing hot ($T_M = 531$ K) and cold ($T_C = 300$ K) air streams. The hot air flow represents 65% of the total mass flow rate in the CS, while the remaining 35% are used for effusion cooling in the CS (no dilutions holes). The generic design of one sector of the CS (over 20) is schematically shown in Fig. 3. A duct is fitted at the exit of the swirler to confine and preserve the hot spot. Two configurations are used in this work: the nominal one with a duct of length 55 mm (referred to as D55), and one without duct (D00). A detailed description of the design of the CS can be found in Koupper *et al.* [17].

In addition to the final FACTOR rig implemented at DLR in Göttingen, three sectors of the CS are mounted at the University of Florence (UNIFI) to perform a detailed characterisation of the combustor aerothermal flowfield and increase the degree of confidence in the predicted performance of the full configuration. Measurements are performed on the central sector of this 1:1 scale trisector configuration, which was found to be representative of the full annulus machine [17]. The UNIFI test facility is presented in details in [15, 17], and an image of the trisector rig is displayed in Fig. 4 (mounted here without ducts). The test rig configuration allows to explore the flow field at the combustor exit (plane 40), located half a NGV axial chord upstream the virtual position of the vanes. An automatic traverse system provided by Turbomeca is fixed on the outer casing and allows to perform measurements in plane 40 by means of a five hole probe

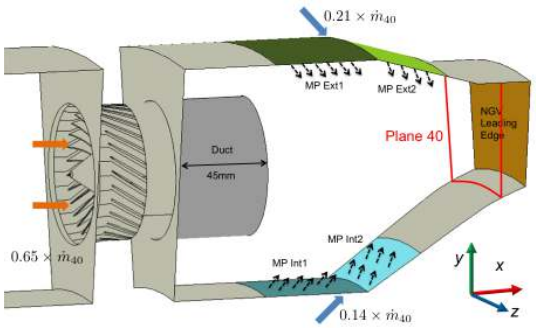


Figure 3: Schematic view of the CS: the multiperforated liner is shown in color, and the inner and outer feeding cavities are not shown.

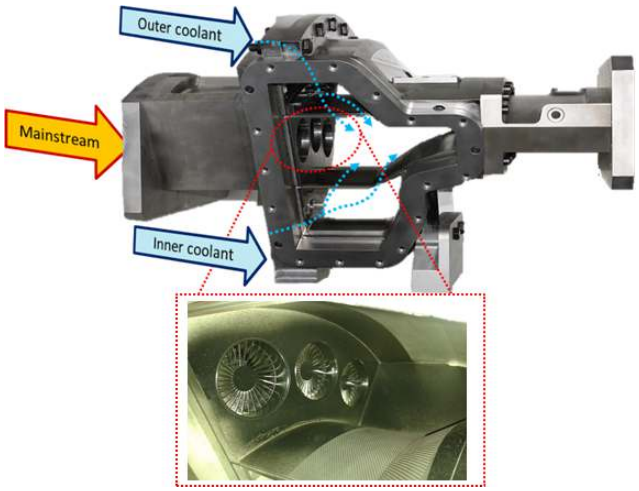


Figure 4: View of the trisector rig and detail of the swirlers and multiperforated liners.

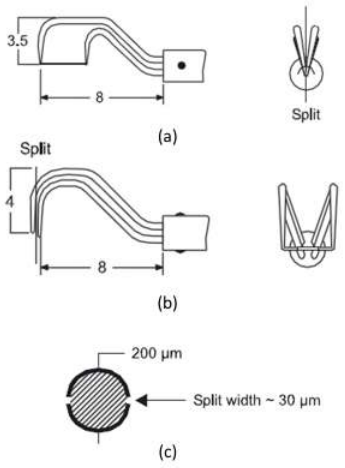


Figure 5: (a) R57 and (b) R56 split-fiber probes and (c) section of the quartz wire.

and a thermocouple (results published by Bacci *et al.* [15]) or a HWA probe as detailed hereafter.

## HOT WIRE ANEMOMETRY MEASUREMENTS

### Experimental set-up

Turbulence quantities are evaluated at the exit of the CS via the measurement of the velocity fluctuations by HWA. Two split-fiber probes are used (see Fig. 5: R56 and R57), each of them featuring a quartz fiber of diameter 200 $\mu$m coated by two sensors (nickel films) fed by certain voltages to keep them at constant temperature. Since the cooling effect on the two sensors changes with both velocity module and direction in the plane orthogonal to the axis of the wire, each probe allows to evaluate two velocity components in the frame of reference of the traverse system. It is therefore necessary to investigate each test point with both probes successively and then combine the results to evaluate the three-dimensional flow field [16]. However, in this study turbulent timescales are computed only on the axial velocity, which is measured independently by the two probes. In the following, only the signal from probe R56 will be used (non reported results show that there are very little differences with R57).

The voltage signal is acquired during 5 s for each measurement point at a frequency of 20 kHz, and converted to velocity components by the calibration process detailed in Bacci *et al.* [16]. 281 points are investigated in plane 40, as shown in Fig. 6. The shape of the split-fiber probes and their fragility prevents from measuring velocity in the inner and outer near-wall region.

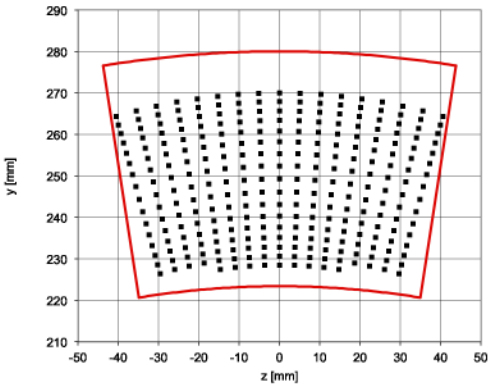


Figure 6: 281-points measurement mesh in plane 40.

### Operating point

As the HWA evaluation of velocity is based on the measure of the heat convected away from the sensor by the fluid, the flow has to be isothermal. An isothermal operating point representative of the Design Point (DP) was selected based on the conservation of the main non-dimensional parameters of the flow, as presented in Koupper *et al.* [17]. Table 1 summarizes the operating conditions of the two points, and the corresponding changes of the non-dimensional parameters. The overall mass flow rate is conserved, while the pressure in the chamber is reduced ($-22\%$). Only the swirler Reynolds number is not conserved, but both values correspond to a fully developed turbulent regime without significant difference of intensity.

| | DP | HWA |
|---|---|---|
| Normalized total mass flow | 1 | 1 |
| Flow split swirlers | 65% | 65% |
| Flow split cooling cavities | 35% | 35% |
| Normalized chamber pressure | 1 | 0.78 |
| Swirler inlet temperature | 531 K | 300 K |
| Cooling cavities temperature | 300 K | 300 K |
| Swirler Reynolds number | 111 000 | 168 500 |
| Swirler Mach number | 0.112 | 0.108 |
| Effusion cooling Reynolds | 2344 | 2344 |
| Plane 40 Mach number | 0.108 | 0.113 |
| $U_{ref}$ (m/s) | 51.5 | 37.5 |

Table 1: Operating conditions for the non-isothermal (DP) and isothermal (HWA) points.

## METHODOLOGY FOR THE CALCULATION OF TURBULENT TIMESCALES

At each measurement point the instantaneous axial velocity $u$ can be decomposed into a mean $\bar{U}$ and a fluctuating part $u'$:

$$u = \bar{U} + u' \tag{1}$$

with the time-averaged value being $\bar{U} = \frac{1}{N}\sum_{i=1}^{N} u_i$ if $N$ is the total number of samples. The root mean square value of the discretized velocity data is computed as:

$$u_{RMS} = \sqrt{\frac{1}{N}\sum_{i=1}^{N}(u_i - \bar{U})^2} \tag{2}$$

The autocorrelation coefficient $R_{uu}$ of the fluctuating part of the axial velocity is then calculated for different time-lags $\tau$ of the signal, and non-dimensionalized by $u^2_{RMS}$ to have $R_{uu} = 1$ for zero-lag ($\tau = 0$):

$$R_{uu}(\tau) = \frac{\overline{u'(t)u'(t+\tau)}}{u^2_{RMS}} = \frac{\frac{1}{N}\sum_{i=1}^{N}(u'_i \cdot u'_{i+j})}{u^2_{RMS}} \tag{3}$$

where $j = \tau/dt$ gives the possible values of time-lag based on the acquisition timestep $dt = 1/f$. A typical evolution of $R_{uu}(\tau)$ for the axial velocity signal recorded in a LES is shown in Fig. 7. In the case of Homogoenous Isotopic Turbulence (HIT), the integral turbulent timescale $t_{turb}$ is typically obtained [18, 19] by integrating under the $R_{uu}$ curve:

$$t_{turb} = \int_{\tau=0}^{\infty} R_{uu}(\tau)d\tau \tag{4}$$

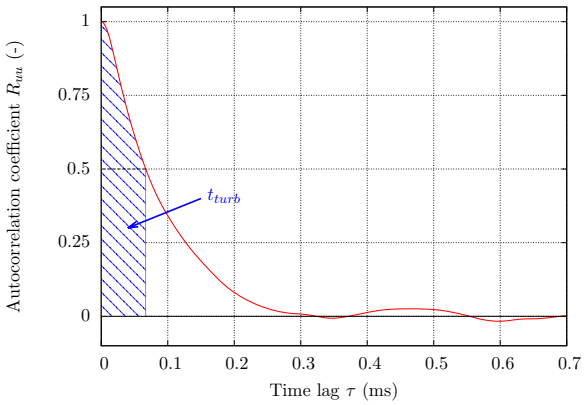


Figure 7: Typical autocorrelation coefficient of the axial velocity signal.

The application of Eq. (4) to complex flow can be problematic as $R_{uu}$ does not necessarily go to zero as $\tau \to \infty$ because of the strong flow spatial heterogeneities and the resulting turbulent anisotropy that can spatially evolve. An alternate proposal to evaluate the integral timescale can be to integrate under the $R_{uu}$ curve until the first zero crossing [20], or to set an arbitrary value of $R_{uu}$ above which the signal is not considered correlated anymore [21–23]. The latter option is chosen here, and the turbulent timescale is obtained by integrating under the curve until $R_{uu} = 0.5$, as shown by the hashed zone in Fig. 7. To assess the impact of this arbitrary threshold, Fig. 8 shows the spatial-mean turbulent timescale in plane 40 $\overline{t_{turb_{40}}}$ computed from HWA measurements, using clipping values ranging from $R_{uu} = 0.95$ (strong correlation) to $R_{uu} = 0$ (not correlated). This curve indicates that for $R_{uu} = 0.5$ the turbulent timescale is 60% smaller than considering the first zero crossing as threshold.

The calculation process (Eqs. 1 to 4) is repeated for each investigation point of the CS exit plane in order to obtain a full 2-D map of the turbulent timescale, similarly for either numerical or experimental signals. However, each approach has its own specificities and limitations on the recorded signal, mostly in terms of total duration $\Delta t$ and acquisition frequency $f$. First of all, because of the computational cost of LES, the total simulated physical time is limited to few hundred milliseconds while the experimental signal is recorded for 5 s. Then, the acquisition frequency of LES might be lower than 20 kHz for storage and file-handling issues. The characteristics of the experimental and numerical signals are recalled in Table 2. Therefore, before performing any comparison, one needs to estimate what might be the bias introduced in such diagnostics because of these differences.

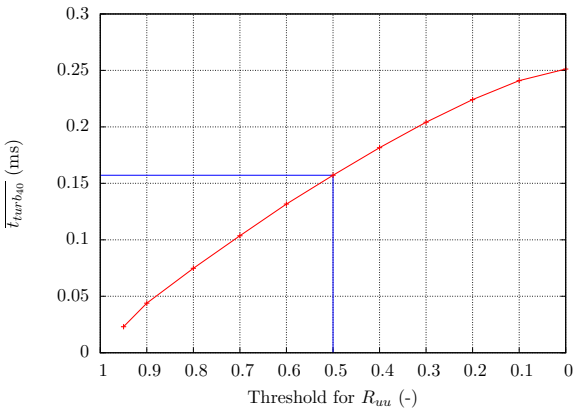


Figure 8: Influence of the clipping value for $R_{uu}$ on the evaluation of the mean turbulent timescale in plane 40.

| | Duration $\Delta t$ (s) | Acq. Frequency $f$ (Hz) |
|---|---|---|
| HWA (all ducts) | 5.0 | 20 000 |
| LES D00 | 0.113 | 9 785 |
| LES D55 | 0.140 | 20 000 |

Table 2: Characteristics of the experimental and numerical signals.

## SENSITIVITY TO THE MEASUREMENT PARAMETERS

In the following, it is intended to quantify the differences introduced by computing turbulent timescales on signals of different total duration and acquisition frequency. All the analyses presented in this section are performed on the HWA signal because of its long duration (D55 case). LES and HWA results are ultimately presented in the last section.

### Acquisition frequency

The acquisition frequency impacts the calculation of the turbulent timescale for at least two main points: *(i)* the exploitable content of the signal is limited by the Nyquist frequency $f/2$; *(ii)* $f$ limits the possible time-lags $\tau$ to be computed, as $\tau = j \times f$, which finally reduces the resolution of the curve $R_{uu}(\tau)$ and its accurate integration. To assess the influence of the acquisition frequency, the HWA signal is virtually degraded by taking one point over $N$ to reduce $f$. The turbulent timescale is then computed at each measurement point of plane 40, for four signals: $f = 20$ kHz (all points), $f = 10$ kHz (half the points), $f = 5$ khz (quarter of the points) and $f = 2$ khz (tenth of the points). Note that all four resulting signals have the same total duration $\Delta t = 5$ s but a reduced number of samples.

A map of the computed turbulent timescales in plane 40 is shown in Fig. 9. The bounds of the central sector are shown in the background to highlight the limits of the investigation zone. The core region of plane 40 features a coherent zone of higher turbulent timescale (0.22-0.24 ms), which corresponds to the remnants of the swirling core. Higher levels of turbulence intensity (20-22%) were measured in this region [16]. The timescales are more uniform in the rest of the field (around 0.12-0.16 ms), and seem to decrease in the near wall region (zone of the effusion cooling), which is not fully covered by the investigations.

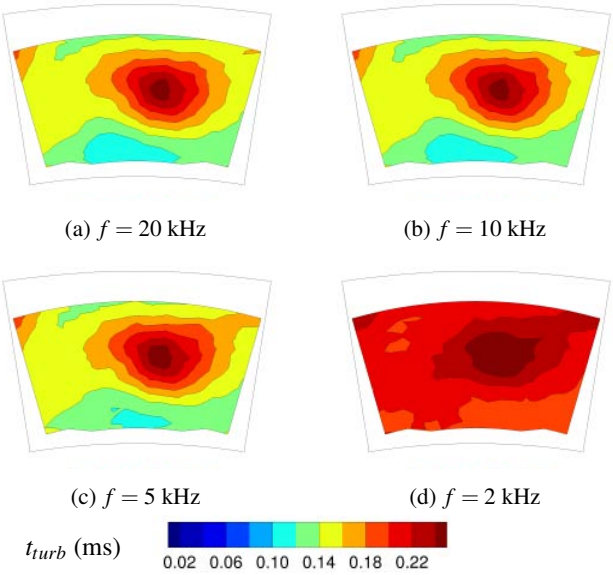


Figure 9: Turbulent timescales in plane 40 for D55 (looking downstream).

Regarding the influence of the acquisition frequency, the comparison of the four maps clearly shows that between 20 kHz and 5 kHz, $f$ is sufficiently high to allow a similar estimation of $t_{turb}$. Only moderate differences are found in the inner region for $f = 5$ kHz where the timescale is a little overestimated. This might be explained by an under-resolution of the $R_{uu}$ curve in the range of low $\tau$. However, for $f = 2$ kHz the timescales are clearly overpredicted, and this acquisition frequency is definitely too low to properly capture the turbulent activity.

In conclusion, the turbulent timescale estimates can be judged as perfectly converged for $f \geq 10$ kHz, although the analysis at 5 kHz was found to provide a very good estimate of the converged fields. This confirms that LES for D00 is sufficiently well sampled ($f = 9.7$ kHz, see Tab. 2) to avoid frequency-linked issues on the calculation of $t_{turb}$.

### Duration of the signal

**Convergence of the calculation** The most important difference between the numerical and experimental signals is the total duration $\Delta t$, which is about 35 times longer for HWA than LES. Long signals allow for a better statistical representation of turbulence under the ergodicity hypothesis of the flow. For short duration signals, the accuracy of the evaluation of $t_{turb}$ can be questionable. To address this issue, $t_{turb}$ is computed over portions of the HWA signal of increasing duration: from $\Delta t = 50$ ms to $\Delta t = 5$ s. This process allows to assess the convergence of $t_{turb}$ with the duration of the signal, and define (if possible) a minimum threshold for convergence.

For clarity, the convergence curves of $t_{turb}(\Delta t)$ of all the 281 measurement points are normalized by the final value $t_{turb_f} = t_{turb}(\Delta t = 5 \text{ s})$ and shown in Fig. 10 (for a sampling frequency of 20 kHz). The envelope of the convergence curve of $t_{turb}$ has a symmetrical exponential shape, converging towards $t_{turb_f}$. For short duration signals ($\Delta t < 0.25$ s), differences up to $\pm 35\%$ of the final value are found. To reduce this error below $\pm 2\%$, the curves have to be contained within the dashed lines, which occurs for much longer durations of the signal ($2-3$ s). This time can be related to the physics of the flow using the through flow time of the CS (noted hereafter $t_{CS}$) computed based on the nominal mass flow and CS length. This new scaling is indicated on the upper horizontal axis of Fig. 10, and at least 200 to 300 through flow times are required to converge such calculation.

Such long durations of the time signal can not be reached by LES which is restrained by the computational effort. For comparison, the duration of the available LES signal is indicated by an arrow in Fig. 10, and is around 12 through flow times. A detailed analysis of all the convergence curves clearly indicates that for around ten $t_{CS}$ none of the points has a converged value to $\pm 2\%$. According to Fig. 10, errors on the calculation of $t_{turb}$ about $\pm 20\%$ can be found for the LES signals because of convergence issues.

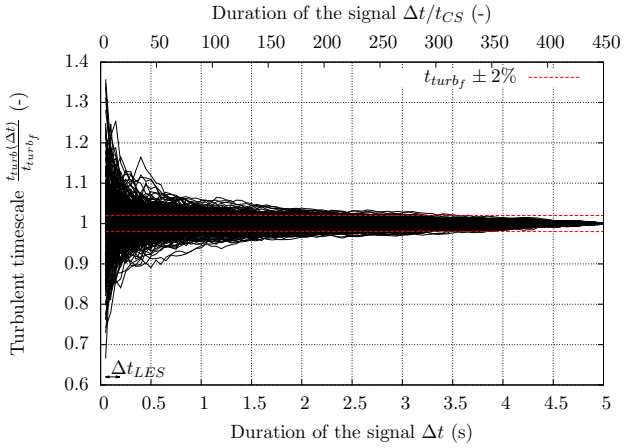


Figure 10: Convergence of the calculation of $t_{turb}$ for all the HWA experimental signals in plane 40.

**Ergodicity of the signal for high order moments** The problematic of the convergence of $t_{turb}$ for small duration signal is associated with the impossibility to recover all the high order statistical properties of the flow with few samples. In this context —and despite convergence issues— one may ask what is the impact of evaluating turbulence over a single realization of the flow of reduced duration. In other words, quantifying how $t_{turb}$ changes when it is computed over windows of similar duration $\Delta t_{LES}$ taken at different initial times $t_0$.

To address this question, the turbulent timescale is computed over a typical LES window ($\Delta t_{LES}$) taken on the full HWA signal at 138 different initial times $t_0$, each window overlapping the previous one by $\Delta t_{LES}/4$. The evolution of $t_{turb}$ with the initial time of the investigation zone is shown in Fig. 11 for an arbitrary single measurement point. The turbulent timescale is normalized by the reference value $t_{turb_f}$ obtained for the full HWA signal. Non-negligible variations around the mean value are visible, which translate here into a standard deviation $\sigma$ of 7.5% of $t_{turb_f}$. Moreover, in this specific case the maximum over and under-predictions are respectively found to be $+29\%$ and $-20\%$, which is definitely significant.

To have a more exhaustive understanding of the question, this methodology is now applied to all the measurement points in plane 40. Figure 12 shows the maximum and minimum turbulent timescales calculated over the 138 windows, as well as the associated standard deviation $\sigma$. Even if the fields of Fig. 12b and 12c do not correspond to a single evaluation of $t_{turb}$, but to the concatenation of all the minima (or maxima), they indicate that significant differences can be found. More importantly, the

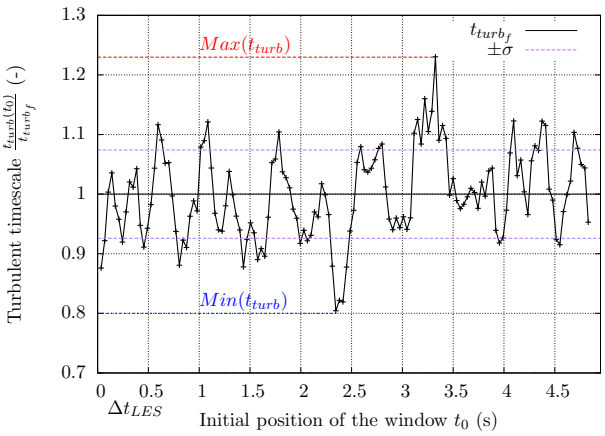


Figure 11: $t_{turb}$ calculated over $\Delta t_{LES}$ taken at different initial times of the HWA signal for an arbitrary point in plane 40.

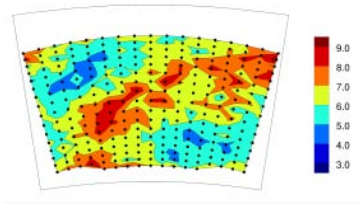


(a) Standard deviation $\sigma/t_{turb_f}$ (%)

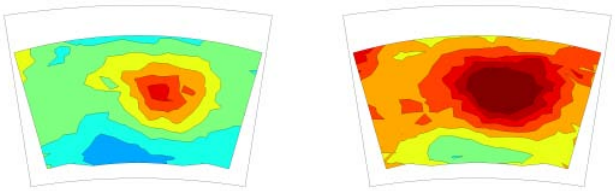

(b) $Min(t_{turb})$ (c) $Max(t_{turb})$

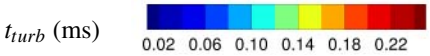


Figure 12: Maximum and minimum difference and standard deviation of the calculation of $t_{turb}$ performed on 138 windows of duration $\Delta t_{LES}$.

standard deviation associated with the calculation of $t_{turb}$ over all the windows (Fig. 12a) is on average $\overline{\sigma_{40}} = 6.4\%$. The standard deviation is higher $(7-9\%)$ in the diagonal region, where it may be driven by the larger values of the maximum turbulent timescale (Fig. 12c).

The different analyses presented here allowed us to understand and estimate the inherent differences between the experimental and numerical signals. First, the acquisition frequency was found to allow good calculations of $t_{turb}$ for $f > 5$ kHz, which validated the acquisition frequency of both D00 and D55 LES. Then, convergence and periodicity issues associated with having a short duration signals were pointed out. This difference was found to intrinsically imply an average deviation of $\pm 6.4\%$, and possible local errors of about $\pm 25\%$. Having knowledge of these differences, the estimations of the turbulent timescales by the two approaches are now compared.

## COMPARISON WITH LARGE EDDY SIMULATIONS

### Numerical setup

As indicated previously, two configurations are numerically investigated and reported here: D00 and D55. The typical numerical domain is shown for the D55 case in Fig. 13. The desired mass flow rate is imposed at the inlet of the plenum by prescribing velocity and temperature, while the operating pressure is controlled by the outlet 3-D characteristic boundary condition [24, 25]. Such condition is required to avoid acoustic reflections, while maintaining the pressure level close to the target value. All the walls use a law-of-the-wall approach. An adiabatic homogeneous boundary condition [26] is used to account for the momentum injection at the multiperforated plates.

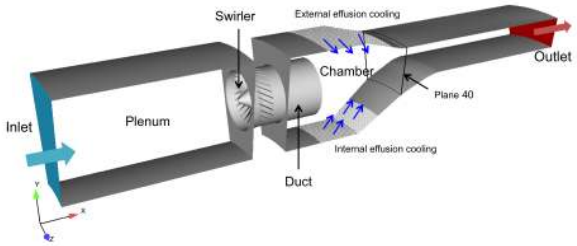


Figure 13: Numerical domain of the LES of D55 configuration.

The D00 configuration was computed prior to the test campaign, and the mesh contains 6.0 M nodes (only tetrahedral elements). The case D55 was meshed based on the conclusions of the experimental and numerical comparison performed on the mean quantities only, and was refined mostly in the swirler region, to reach 11.0 M nodes. The typical tetrahedral edge length in the swirler region is 0.4 mm and 0.8 mm in the chamber.

The LES-filtered compressible Navier Stokes are numerically solved by the AVBP code [27]. The solver uses the cell-vertex finite volume approximation, and is based on an explicit temporal integration scheme. Therefore, the timestep is limited by the Courant Friedrichs Lewy condition ($CFL = 0.7$), to about $4.3 \times 10^{-8} s$. A two-step Taylor Galerkin numerical scheme [28] provides third-order accuracy in time and space. Such scheme provides low dispersion and diffusion, and is therefore adequate for LES. In this study, the Smagorinsky model [29] is used to account for the sub-grid scale viscosity. Such a purely dissipative approach is appropriate for turbulent mixing flows found in combustion chambers.

### Isothermal and non-isothermal simulations

Both D00 and D55 simulations are performed at non-isothermal conditions (DP). To validate the choice of the isothermal operating point presented previously, an isothermal LES was also computed for the D00 configuration and compared to the DP simulation. Both LES were performed on the same mesh, with the same numerical parameters, the only differences are the boundary conditions which correspond to the characteristics of the HWA and DP operating points (see Table 1). Non-reported results show that the two operating points exhibit the same mean flow field, turbulence intensity distribution and levels if correctly scaled by a reference velocity to account for the density change imposed by the conservation of mass flow rate between the two cases. Similar results on previous simulations were reported in [17]. It is proposed here to non-dimensionalize the fields of

| | LES | HWA |
|---|---|---|
| D00 isothermal | 0.127 | 0.244 |
| D00 non-isothermal | 0.096 | - |
| D55 isothermal | - | 0.157 |
| D55 non-isothermal | 0.062 | - |

Table 3: Spatial mean turbulent timescales on the investigation region $\overline{t_{turb_{40}}}$ (ms).

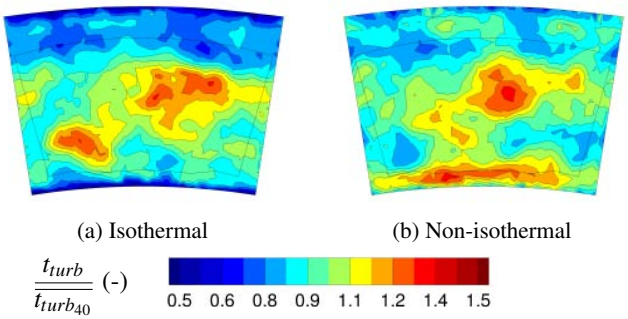


Figure 14: Non-dimensional turbulent timescale for the isothermal and non-isothermal LES of the D00 case.

turbulent timescales by the mean value $\overline{t_{turb_{40}}}$ computed in the HWA investigation area (for LES the results are projected on the experimental mesh). Such scaling allows to compare the distribution of $t_{turb}$ while getting rid of the magnitude which is altered by the operating point. The values of $\overline{t_{turb_{40}}}$ for all cases are reported in Table 3. The comparison of the isothermal and non-isothermal maps (Fig. 14) shows that turbulence is similarly organized in the central region (under the scaling hypothesis). In the near-wall region the DP simulation shows higher values of $t_{turb}$ because of the mixing between coolant and hot air stream being at two different densities. However, as this scaling shall be used to compare isothermal experiments and non-isothermal simulations, only the measured zone will be investigated (black contour in Fig. 14), which does not cover the near-wall region. This scaling technique is now used to compare HWA and LES for the D55 and D00 test cases.

## Comparisons

Figure 15 shows the non-dimensional turbulent timescales calculated on the HWA and LES signals for D55 and D00 in plane 40. Note that for experimental results, the non-degraded full duration signal is used (5 s at 20 kHz). The fields of turbulent timescales are very different for D00 and D55, both in terms of magnitude and distribution.

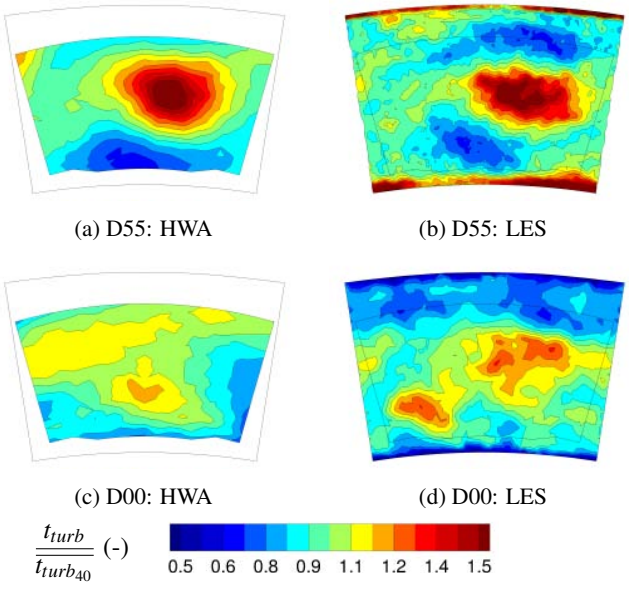


Figure 15: Comparison of the non-dimensional turbulent timescale for HWA and LES with and without duct.

First, the overall magnitude of $t_{turb}$ is larger for D00 than D55 as indicated by the spatial mean values in plane 40 $\overline{t_{turb_{40}}}$ reported in Table 3. It is woth noting that both HWA and LES (at non-isothermal conditions) give a very similar estimate of the relative increase of $\overline{t_{turb_{40}}}$: respectively 58% and 54%. Therefore, even if the magnitude of the turbulent timescale is not correctly captured by LES, the simulation accurately predict the change in amplitude between the ducted and un-ducted configurations. The difference in terms of absolute level of $t_{turb}$ between LES and HWA is nonetheless in the expected range of accuracy as evidenced by the analysis presented previously.

Second, the distribution of $t_{turb}$ is strongly affected by the presence of the duct: the D55 case shows large timescales only in the swirling core region, while $t_{turb}$ is more homogeneously distributed for the D00 case. In both cases, the pattern of turbulent timescales is well predicted by LES. This is especially true for the LES of D55 as the longer signal (see Table 2) helps reducing convergence issues, as discussed previously.

The turbulent timescales are extracted at midspan from Fig. 15 and plotted in Fig. 16. The graph quantitatively confirms that the difference in distribution and magnitude between D55 and D00 is correctly captured by LES. Moreover, the maximum value of $t_{turb}$ for D55 is similarly found at $\theta \simeq 2^{\circ}$ by both approaches, and at the same amplitude: about $60-65\%$ larger than the mean value. The relative magnitude of the turbulent timescales is also in good accordance between measurements and simulations all over the pitch direction.

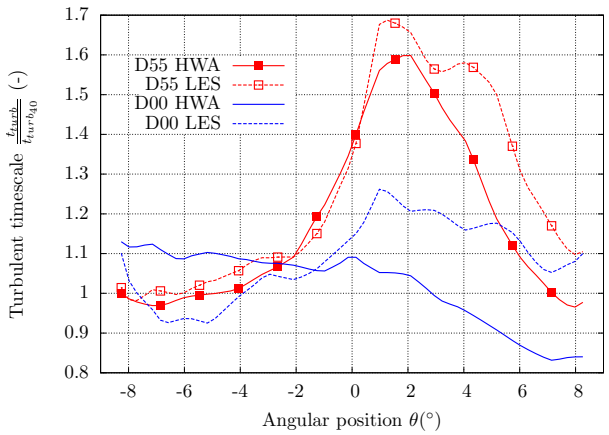


Figure 16: Non-dimensional turbulent timescale at midspan in plane 40.

The turbulent timescale was computed in the entire domain of the LES simulations for the D00 and D55 cases, as shown in Fig. 17 in a longitudinal cross section of the CS from the swirler exit down to the domain exit. For adequate comparison between D00 and D55, dimensional values of $t_{turb}$ are used and scaled by the reference velocity $U_{ref}$ (see Table 1) to account for the change in operating conditions. The central and corner recirculation zones are indicated by a black line corresponding to a zero mean axial velocity $\bar{U} = 0$. The flow topology is significantly altered by the presence of the duct which turns into different distributions of the turbulence timescales. In both cases, reverse flow zones are associated with higher $t_{turb}$, either in the central region, or in corners around the duct. In the case of D55, the little recirculation bubble downstream of the swirler hub also gives rise to larger turbulent scales. In both cases, the jet exiting the swirler is associated with turbulent timescales three times lower than in the reverse flow zones. For the D00 case, the large extent of the central recirculation zone and the quick radial opening of the jet seem to promote the persistence of large eddies generated in the core of the CS, which finally reach plane 40. On the other hand, for the D55 case the high velocity air exiting the duct flows directly towards the exit of the CS because it is constrained by the large corner recirculation zones and the central one. As this jet is associated with lower turbulent timescales, plane 40 shows large scales only in the remnants of the central region as observed in Fig. 15a.

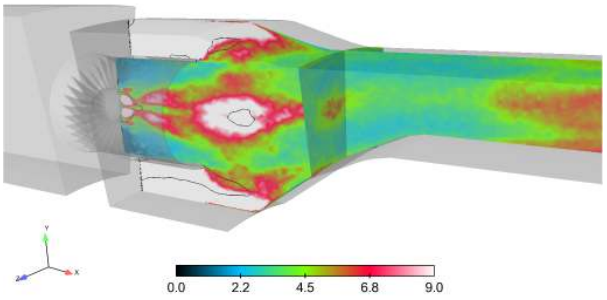


(a) D55: non-isothermal LES

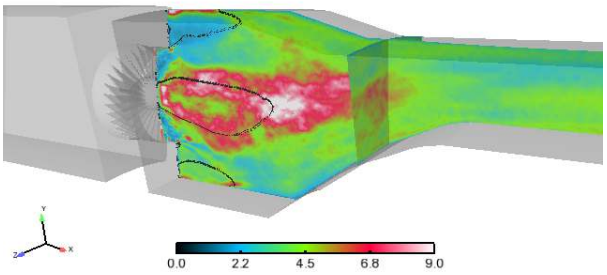


(b) D00: isothermal LES

Figure 17: LES prediction of the turbulent timescale $t_{turb} \times U_{ref}$ in the longitudinal plane of the CS (mm).

## CONCLUSIONS

This paper reports experimental and numerical results obtained on the CS trisector rig of the FACTOR project. Hot Wire Anemometry measurements were performed using split-fiber probes mounted on a traverse system located at the exit of the CS (plane 40). LES and experiments were found to agree well when comparing mean and RMS quantities of the aerothermal field in plane 40. Therefore, it was intended to assess the predictability of LES for higher order statistics in an engine-like configuration, by the evaluation of turbulence integral timescales at the exit of the combustor. The instantaneous axial velocity signal was used to analyse turbulence by means of two points correlations in time. The methodology for calculating turbulent timescales was presented and discussed in the optics of performing comparisons between experiments and advanced numerical simulations relying on LES. The specificities of both approaches, mainly in terms of acquisition frequency and duration of the signal, make that extra care has to be taken before comparing results. It is found that the computation of turbulent timescales on a long duration signal is converged for an acquisition frequency $f \geq 10$ kHz, even if $f = 5$ khz also provides a very good estimate, confirming the sampling rate of 9.7 kHz used for one of

the numerical simulations. The duration of the signal is found to have a very important impact on the estimation of the turbulent timescales, which requires at least 200 through flow times before reaching convergence. This constraint is not compatible with the current durations of LES simulations, limited to about 10 through flow times (vs. 400 for HWA). In this context, the use of short duration signals intrinsically implies possible local errors of $\pm 25\%$, and a standard deviation of 6.4%. This being quantified, fields of turbulence timescales are compared using a non-dimensional formalism to account for the change in density between the isothermal measurements and non-isothermal simulations. Results show that the large change in topology of the flowfield between the un-ducted and ducted cases leads to very different patterns of turbulent timescales. With the duct, large values are found only in the remnant parts of the swirling core while without duct turbulent timescale levels are higher throughout plane 40. This translates into an increase of the spatial-mean turbulent timescale in plane 40 measured to 58% and predicted to 54% by the simulations. Overall, the LES is found to correctly capture the change in pattern and magnitudes between the two configurations. For the configuration with duct, LES and HWA agree very well on the distribution of turbulent timscales throughout the investigation zone. The magnitudes of the timescales are however found to be underestimated in accordance with the quantified limitations issued by to the short duration of the signal. These results nonetheless clearly indicate the potential of LES for the investigation of high order turbulence quantities of complex flows. With the increasing power of the computational machines, long duration signals will be accessible and allow for improved and more quantitative estimates of such turbulent flow features. In the meantime relative comparisons are possible to qualify designs although they need to be handled with care. Issues on the actual impact of these flow characteristics on turbine stages and heat transfer loads also need to be better understood but seems possible in the context of such advanced numerical simulations.

## ACKNOWLEDGMENT

The authors wish to gratefully acknowledge FACTOR (Full Aerothermal Combustor-Turbine interactiOns Research) Consortium for the kind permission of publishing the results herein. FACTOR is a Collaborative Project co-funded by the European Commission within the Seventh Framework Programme (2010-2016) under the Grant Agreement n° 265985. The simulations presented here were performed using HPC resources from GENCI-IDRIS (Grant 2013-x20132b5031).

## REFERENCES

[1] Povey, T., and Qureshi, I., 2009. "Developments in hot-streak simulators for turbine testing". *Journal of Turbomachinery,* ***131***(3), pp. 1–15.

[2] Dorney, D. J., Gundy-Burlet, K. L., and Sondak, D. L., 1999. "A survey of hot streak experiments and simulations". *International Journal of Turbo and Jet Engines,* ***16***(1), pp. 1–15.

[3] Nasir, S., Carullo, J., Karen, W., Thole, A., Luzeng, H., Zhang, J., and Moon, H., 2009. "Effects of large scale high freestream turbulence and exit reynolds number on turbine vane heat transfer in a transonic cascade". *Journal of Turbomachinery,* ***131***.

[4] Ames, F., 1997. "The influence of large-scale high intensity turbulence on vane heat transfer". *Journal of Turbomachinery,* ***119***.

[5] Barringer, M. D., Thole, K. A., Polanka, M. D., Clark, J. P., and Koch, P. J., 2009. "Migration of combustor exit profiles through high pressure turbine vanes". *Journal of Turbomachinery,* ***131***(2), pp. 1–10.

[6] Jenkins, S., Varadarajan, K., and Bogard, D. G., 2004. "The effects of high mainstream turbulence and turbine vane film cooling on the dispersion of a simulated hot streak". *Journal of Turbomachinery,* ***126***(1), pp. 203–211.

[7] Jenkins, S., and Bogard, D. G., 2005. "The effects of the vane and mainstream turbulence level on hot streak attenuation". *Journal of Turbomachinery,* ***127***(1), pp. 215–221.

[8] Goldstein, R., Lau, K., and Leung, C., 1983. "Velocity and turbulence measurements in combustion systems". *Experiments in Fluids,* ***1***(2), pp. 93–99.

[9] Goebel, S. G., Abuat, N., Lovett, J. A., and Lee, C. P., 1993. "Measurements of combustor velocity and turbulence profiles". In American Society of Mechanical Engineers, no. 93-GT-228.

[10] Radomsky, R. W., and Thole, K. A., 1999. "Flowfield measurements for a highly turbulent flow in a stator vane passage". *Journal of Turbomachinery,* ***122***(2), pp. 255–262.

[11] Cha, C. M., Hong, S., Ireland, P. T., Denman, P., and Savarianandam, V., 2012. "Turbulence levels are high at the combustor-turbine interface". In ASME Turbo Expo 2012: Turbine Technical Conference and Exposition, no. GT2012-69130.

[12] Pitsch, H., 2005. "Large-eddy simulation of turbulent combustion". *Annual Review of Fluid Mechanics,* ***38***(1), pp. 453–482.

[13] Klapdor, E., 2010. "Simulation of combustor - turbine interaction in a jet engine". PhD thesis, Technischen Universität Darmstadt.

[14] Cant, S., 2011. "RANS and LES modelling of premixed turbulent combustion". In *Turbulent Combustion Modeling*, T. Echekki and E. Mastorakos, eds., Vol. 95 of *Fluid Mechanics and Its Applications*. Springer Netherlands, pp. 63–90.

[15] Bacci, T., Caciolli, G., Facchini, B., Tarchi, L., Koupper, C., and Champion, J.-L., 2015. "Flowfield and tem-

perature profiles measurements on a combustor simulator dedicated to hot streaks generation". In ASME Turbo Expo 2015: Turbine Technical Conference and Exposition, no. GT2015-42217.

[16] Bacci, T., Facchini, B., Picchi, A., Tarchi, L., Koupper, C., and Champion, J.-L., 2015. "Turbulence field measurements at the exit of a combustor simulator dedicated to hot streaks generation". In ASME Turbo Expo 2015: Turbine Technical Conference and Exposition, no. GT2015-42218.

[17] Koupper, C., Caciolli, G., Gicquel, L., Duchaine, F., Bonneau, G., Tarchi, L., and Facchini, B., 2014. "Development of an engine representative combustor simulator dedicated to hot streak generation". *Journal of Turbomachinery,* ***136***(11), pp. 1–10.

[18] Pope, S., 2000. *Turbulent Flows*. Cambridge University Press, Cambridge.

[19] Sagaut, P., and C., C., 2008. *Homogeneous Turbulence Dynamics*. Cambridge University Press.

[20] Nix, A., Smith, A., Diller, T., Ng, W., and Thole, K., 2002. "High intensity, large length-scale freestream turbulence generation in a transonic turbine cascade". In ASME Turbo Expo 2002: Turbine Technical Conference and Exposition, no. GT2002-30523.

[21] Volino, R. J., Schultz, M. P., and Flack, K. A., 2007. "Turbulence structure in rough- and smooth-wall boundary layers". *Journal of Fluid Mechanics,* ***592***, 12, pp. 263–293.

[22] Coletti, F., Cresci, I., and Arts, T., 2012. "Time-resolved PIV measurements of turbulent flow in rotating rib-roughened channel with coriolis and buoyancy forces". In ASME Turbo Expo 2012: Turbine Technical Conference and Exposition, no. GT2012-69406.

[23] Fransen, R., 2013. "LES based aerothermal modeling of turbine blade cooling systems". PhD thesis, Université de Toulouse - MeGeP - Dynamique des Fluides.

[24] Poinsot, T., and Lele, S., 1992. "Boundary conditions for direct simulations of compressible viscous flows". *Journal of Computational Physics,* ***101***(1), pp. 104 – 129.

[25] Yoo, C. S., and Im, H. G., 2007. "Characteristic boundary conditions for simulations of compressible reacting flows with multi-dimensional, viscous and reaction effects". *Combustion Theory and Modelling,* ***11***(2), pp. 259–286.

[26] Mendez, S., and Nicoud, F., 2008. "Adiabatic homogeneous model for flow around a multiperforated plate". *AIAA Journal,* ***46***(10), pp. 2623–2633.

[27] Schoenfeld, T., and Rudgyard, M., 1999. "Steady and unsteady flows simulations using the hybrid flow solver AVBP". *AIAA Journal,* ***37***(11), pp. 1378–1385.

[28] Colin, O., and Rudgyard, M., 2000. "Development of high-order taylor–galerkin schemes for LES". *Journal of Computational Physics,* ***162***(2), pp. 338 – 371.

[29] Smagorinsky, J., 1963. "General circulation experiments with the primitive equations: 1. the basic experiment". *Monthly Weather Review,* ***91***, pp. 99–164.

**Proceedings of ASME Turbo Expo 2015: Turbine Technical Conference and Exposition**
**GT2015**
**June 15-19, 2015, Montreal, Canada**

# GT2015-42217

# FLOWFIELD AND TEMPERATURE PROFILES MEASUREMENTS ON A COMBUSTOR SIMULATOR DEDICATED TO HOT STREAKS GENERATION

**Tommaso Bacci**
**Gianluca Caciolli**
**Bruno Facchini**
**Lorenzo Tarchi**
Department of Industrial Engineering
University of Florence
via S.Marta 3, 50139, Firenze, Italy
Tel: (+39) 055 4796575, Fax: (+39) 055 4796342
Email: bruno.facchini@unifi.it

**Charlie Koupper**
**Jean-Louis Champion**
Turbomeca
Bordes, France
Email: charlie.koupper@turbomeca.fr

## ABSTRACT

*In order to deepen the knowledge of the interaction between modern lean burn combustors and high pressure turbines, a real scale annular three sector combustor simulator has been assembled at University of Florence, with the goal of investigating and characterizing the generated aerothermal field and the hot streaks transport between combustor exit and the high pressure vanes location. To generate hot streaks and simulate lean burn combustors behavior, the rig is equipped with axial swirlers, fed by main air flow that is heated up to 531 K, and liners with effusion cooling holes that are fed by air at ambient temperature. The three sector configuration is used to reproduce the periodicity on the central sector and to allow to perform measurements inside the chamber, through the lateral walls.*

*Ducts of different length have been mounted on the swirlers, allowing to preserve the hot mainflow from the interaction with coolant. Such configurations, together with the one without ducts, have been tested, using different measurement techniques, in order to highlight the differences in the resulting flow fields.*

*First of all, isothermal PIV measurements have been performed on the combustion chamber symmetry plane, to highlight the mixing phenomena between the mainflow and cooling flows. Then a detailed investigation of the mean aerothermal field at combustor exit has been carried out, for nominal operating conditions, by means of a five hole pressure probe provided with a thermocouple, installed on an automatic traverse system. With the aim of analyzing the hot streaks transport and the flow field modification towards the vanes location, such measurements have been performed on two different planes: one located in correspondence of the combustor exit and the further one placed downstream, in the virtual location of the vanes leading edges.*

*Therefore, an experimental database, describing the evolution of the flow field in a combustor simulator with typical traits of modern lean burn chambers, for different injector geometries, has been set up.*

## NOMENCLATURE

**Symbols**

| | | |
|---|---|---|
| $BR$ | Blowing Ratio | $[-]$ |
| $I$ | Momentum flux ratio | $[-]$ |
| $M$ | Mach number | $[-]$ |
| $Re$ | Reynolds number | $[-]$ |
| $r$ | Radial coordinate | $[-]$ |
| $T_{nd}$ | Non-dimensional temperature | $[-]$ |
| $U$ | Axial velocity | $[m/s]$ |
| $V$ | Tangential velocity | $[m/s]$ |
| $V_{abs}$ | Absolute velocity | $[m/s]$ |
| $V_{sp}$ | Velocity on chamber symmetry plane | $[m/s]$ |
| $W$ | Radial velocity | $[m/s]$ |
| $x$ | Axial coordinate | $[m]$ |

**Greeks**

| | | |
|---|---|---|
| $\rho$ | Density | $[kg/m^3]$ |
| $\theta$ | Tangential coordinate | $[deg]$ |

**Subscripts**

| | |
|---|---|
| *CI* | Coolant Inner |
| *CO* | Coolant Outer |
| *cool* | Coolant |
| *in* | Inner |
| *M* | Mainstream |
| *out* | Outer |

**Acronyms**

| | |
|---|---|
| *CRZ* | Central Recirculation Zone |
| *DLR* | Deutsches Zentrum fur Luft- und Raumfahrt |
| *DP* | Design Point |
| *HP* | High Pressure |
| *LES* | Large Eddy Simulation |
| *NGV* | Nozzle Guide Vane |
| *PID* | Proportional-Integral-Derivative |
| *PIV* | Particle Image Velocimetry |
| *RQL* | Rich-Quench-Lean |

## INTRODUCTION

Annular combustors exits are characterized by circumferential temperature distortions, due to the discrete fuel injection, and radial ones, promoted by the liners cooling systems [1]. Such distortions define hot spots which create hot streaks as the flow migrates downstream. At the same time the aerodynamic field is highly non-uniform with high swirl angles promoted by the swirlers. The combustor exit profiles simulation and the combustor-turbine interaction has been an important and studied issue for years as summarized by Povey and Qureshi [2].

Despite the tight link between the combustor and the turbine due to these non-uniformities, historically the design of the two modules relied on separated approaches and the gap of knowledge on the mutual interaction was bridged by the industrial experience. The introduction of new injectors and new cooling systems for lean combustors changes completely the development of the flow field inside the chamber with respect to Rich-Quench-Lean (RQL) combustors. In particular, the absence of dilution holes reduces the mixing process between the burning gases and the cooling flows, enhancing the temperature distortions and the degree of swirl of the mainflow at the turbine inlet. These effect has a strong impact on the resulting hot streak distribution which, in turn, directly affects the aerodynamics, heat transfer, loading, life, secondary loss, and, therefore, the overall efficiency of the high pressure turbine [2]. For these reasons the characterization of combustor-turbine interaction is assuming primary importance, in order to provide validation data and physical understanding to support a fully integrated design philosophy [3].

Barringer et al. [4] showed that temperature profiles have an important influence on the heat transfer on the first stage vanes and that the pressure field influences both the aerodynamic and the thermal behaviour, since they alter the thermal loads on the vanes. Mathison et al. [5] and Jenkins and Bogard [6] highlighted the importance of investigating such effects for various clocking positions between the swirlers and the vane leading edges and the necessity to analyse the combined effect of hot streaks and first stage vanes cooling system on the rotor. An important amount of work has been carried out at Oxford University, where the effects of less ([7]) and more ([1, 8]) enhanced temperature distortions and aggressive inlet swirl [9, 10] have been separately investigated. Then a new combustor simulator, capable of simulating combined enhanced inlet temperature distortions and aggressive swirl field, has been designed and installed in a short-duration wind tunnel, in order to fill the void in the open literature around experiments that take into account these aspects together [3].

In this work an experimental campaign on a non-reactive three-sector combustor simulator, assembled at the University of Florence within the European project FACTOR (Full Aerothermal Combustor-Turbine interactiOns Research), is described. The simulator presents the main features of recent lean burn chambers, in terms of liner cooling systems and mass flow split between main and cooling flows, and is capable of generating both temperature distortions and a strong swirl field. The rig is used for steady-conditions tests that allow to reach an accurate and detailed description of the flow field inside it. In particular the study is aimed at visualizing the flow field inside simulator, thanks to a PIV campaign, and at evaluating the mean aerothermal field at its exit, in two axial positions, in order to deepen the knowledge on the interaction between the flow structures evolution inside this type of chambers and the generated hot streaks, as well as on their migration to the virtual NGV location. Both the possibility to visualize the flow field inside the chamber and to analyse to hot streaks transport from combustor exit and NGV location represent novel features for this kind of rigs.

Additional works performed on this test rig can be found in Bacci et al. [11], where the turbulence field is characterized, in Koupper et al. [12], where a comparison between experimental and LES results is shown, with particular attention to turbulence timescales, and in Andreini et al. [13], where the results of a hybrid RANS-LES calculation are described.

Since the test rig is not equipped with cascades, no information has been drawn about hot streaks alteration through the high pressure vanes and their influence on the first rotor cascade. Further in the project, a full annular combustor simulator with the same geometry of the three sector rig together with a 1.5 turbine stage is going to be installed in the facility at DLR in Gottingen

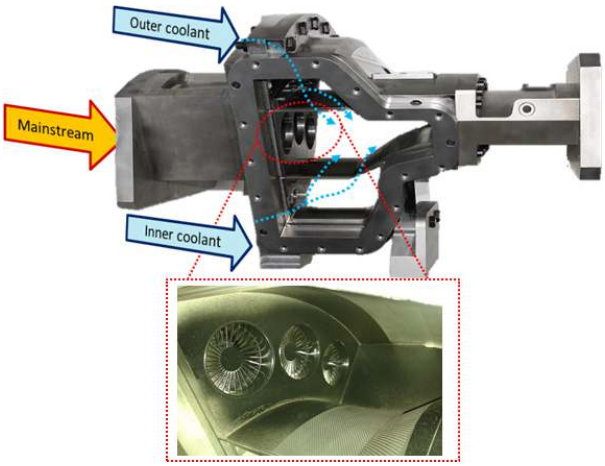


Figure 1: View of the test rig and detail of swirlers and multiperforated liners

(Germany), to investigate the impact of the hot streaks on the HP turbine.

## EXPERIMENTAL FACILITY

### Combustor simulator

The combustor simulator, called Trisector rig, reproduces, in 1:1 scale, 54° of the full annular non-reactive combustor simulator that will be installed at DLR. The three-sector configuration has been adopted in order to recreate periodicity conditions in the central sector, on which tests have been performed; such configuration has been used in many studies like the ones of Andreini et al. [14] and Wurm et al. [15]. A detailed description of the test rig design, with particular attention to some preliminary simulations performed in order to verify that the lateral walls do not affect the central sector flow field, can be found in [16]. A brief account of the DLR rig configuration can be found as well.

The Trisector rig includes many typical features of lean burn combustors: the mainflow enters in the combustion chamber through three axial swirlers (designed and manifactured by Avio Aero, in order to create a flow field typical of lean burn combustors even without the combustion process), while the cooling flows reach inner and outer cavities that feed the multiperforated liners effusion cooling systems; no dilution holes are present. Such features allow to simulate radial and tangential temperature distortions and a highly swirling flowfield as in modern lean burn combustors. Fig. 1 shows a picture of the combustor simulator in which the axial swirlers and the inner multiperforated liner are highlighted.

As mentioned above, vanes and blades are not included and, thus, the potential effects on the flow field due to the presence of the HP stage will not be reproduced; CFD calculations ([17, 18]) have shown that differences both in terms of velocity and temperature fields can be induced by the presence of the NGV, but these effects are confined in an area very close to the NGV leading edges.

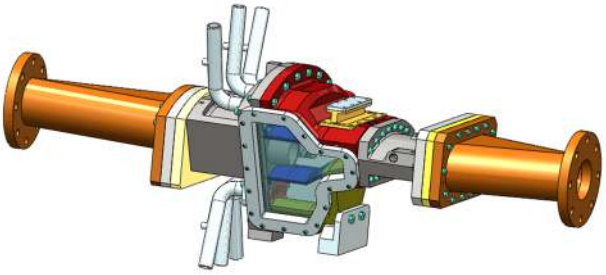

Figure 2: Sketch of the Trisector rig

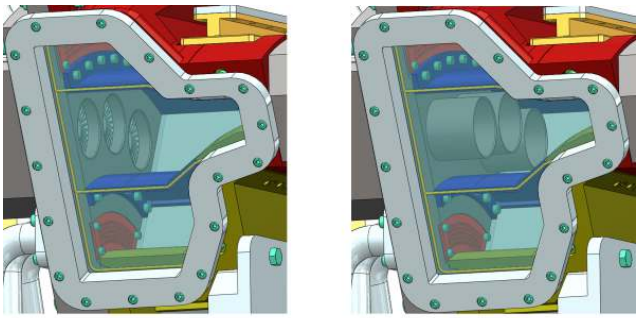


Figure 3: Differences between configurations D00 and D55

A sketch of the rig is displayed in figure 2: different colours indicate the different components that are assembled in the rig, like the outer (red) and inner (yellow) casings, provided with the coolant feeding pipes (light grey), the inner and outer shaped liners, provided with laser-drilled effusion holes (blue), and the inlet and outlet ducts (orange) that connect the annular sector to the cylindrical pipes coming from the compressors and going towards the stack. Special graphite gaskets able to bear up to 300°C were employed to avoid leakages.

In order to test different configurations and understand their influences on the resulting flow field, ducts of different length can be mounted on the swirlers, allowing to preserve the hot mainflow from the interaction with coolant. Three total configurations have been tested: one without ducts, that will be referred to as D00 in the following, and two with ducts of 45 and 55 mm, called respectively D45 and D55. In fig. 2 the rig is equipped with the 55 mm ducts, while the sketches in figures 3 focus on the area of the swirlers in order to highlights the differences between configurations D00 and D55.

The test rig allows the exploration of two different axial positions downstream the combustion chamber: the first plane, called Plane 40, is placed at combustor exit, half an axial chord upstream the NGV virtual position in the DLR rig; the second, called Plane 40+, is located on the virtual NGV leading edges position, 20 mm downstream the first. As it will be explained later, data will be obtained using probes mounted on an automatic traverse system provided by Turbomeca; the system can be fixed on the outer casing by means of an adaptive flange (yellow part on the outer casing in figure 2).

Special attention was dedicated during the design phase to optical accesses: in order to perform optical measurements three large windows were included in the rig. Two wide lateral windows, manufactured with the same shape of the lateral walls to be fully integrated with the geometry of the Trisector rig, are located at sides of the combustor simulator, and a further window, not visible in the picture, is placed in the outer casing in the area of Plane 40 and can be substituted to the adaptive flange. They were designed to guarantee the suitable accesses for a deep investigation of the flow field both in the combustor chamber, not feasible in a full annular configuration, and at its outlet section.

### Test rig environment

The test section is operated in a hot wind tunnel, dedicated to long-duration, steady-state tests, whose layout is sketched in figure 4: compressed air, discharged by two screw compressors, crosses a chiller, which cools the flow down to room temperature and removes the humidity. Compressors deliver a mass flow rate of $\approx 1kg/s$ at a maximum pressure of $10bar$; the desired mass and pressure conditions for the tests are set up throttling several valves located along the lines: one modulating valve at the intake of each compressor, one globe valve for the control of the mainstream, one globe valve on each coolant lines and one final vee-valve at the rig exit. Such configuration allows to set the three mass flow rates and the combustion chamber pressure independently to each other. During the tests, valves are automatically driven through a PID control system to keep constant operating conditions; in particular, the control system, developed in-house with LabVIEW® , can act simultaneously on all the valves to reach the desired set point of pressure or mass flow in few seconds. Along the line a $2m^3$ vessel damps pressure fluctuations. Mainstream mass flow is sent to a 600kW electric heater, which rises temperature up to the target value, that is automatically controlled by means of a PID system which keeps constant temperature at the inlet of the test rig. A grid and a sufficient distance between the rig and the closest curve on the mainflow line are used to ensure a temperatue profile at rig inlet as constant as possible. Coolant is delivered to the rig through two separated lines, as mentioned above: each line discharges air in a plenum, which is connected with the test article through three pipes.

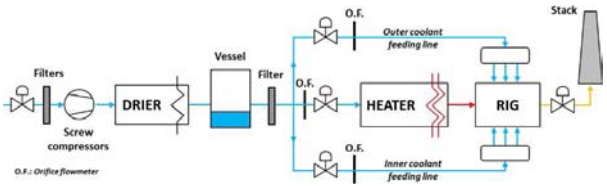


Figure 4: Sketch of the experimental facility

## INSTRUMENTATION AND MEASUREMENT TECHNIQUES

The instrumentations used for this study can be divided in two types according to the goal of their measurements. The first ones are used to monitor the operating conditions of the rig, in terms of mass flow rates, temperatures and pressures in many locations. Further instruments are used for the evaluation of the aerothermal field at combustor simulator exit and for PIV measurements in combustion chamber, the real goals of such study. In the following sections both types of instrumentations are described.

### Monitoring instrumentation

The test rig is equipped with several static pressure taps and thermocouples; a custom-tailored LabVIEW-based application provided accurate monitoring and recording of the conventional data from measurement data scanners. A pressure scanner NetScannerTM System 9116 with temperature compensated piezoresistive relative pressure sensors is employed to measure static pressure in 16 different locations inside the rig; the maximum uncertainty is $\pm 52Pa$ with a level of confidence of approximately 95%. A $HP/Agilent$® 34972$A$ data acquisition/switch unit is used to monitor the flow temperature measured by means of several T-type thermocouples ($\pm 0.5K$ uncertainty, 95% level of confidence). In addition, two thermocouples are welded on each liner and further three of them are located inside the metal, close to the location of Plane 40; metal temperatures are used also to assess the reaching of the thermal steady state conditions. Mass flow rates were measured by means of calibrated orifices (standard EN ISO 5167-1); they are affected by an error of 1% according to the standard ANSI/ASME PTC 19.1 [19] based on the Kline and McClintock method [20].

### PIV set-up

PIV measurements in the combustion chamber have been performed using a Dantec Dynamics PIV system. The system consists of a 120mJ New Wave Solo Nd:YAG pulsed laser, operating with a wavelenght of 532nm, and a FlowSense 2Mpixel camera operating at a data rate of 12Hz. All devices are controlled via the commercial software Dantec FlowManager®, which allows the synchronization of the system and moreover

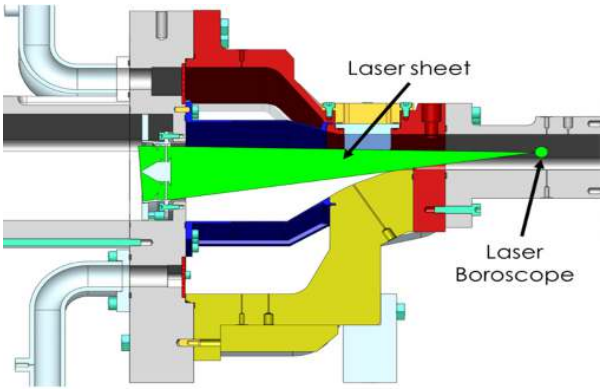


Figure 5: Experimental set-up for combustion chamber PIV measurements

the collecting and the processing of the data. Due to the complex geometry of the Trisector rig, despite the large lateral windows, it has been necessary to perform endoscopic PIV by means of a laser boroscope, which has been inserted in the rig through dedicated holes.

As shown in figure 5, the laser sheet created by the boroscope enlightens the rig in the symmetry plane while the camera focuses the investigation area through one of the wide lateral windows. To have a complete analysis of the combustor simulator, one of the lateral glass windows can be replaced with a metal one provided with several holes for the boroscope: these holes allow to overcome some geometrical constrains of the rig (e.g., laser sheet in figure 5 cannot illuminates the area close to the inner liner due to its shape near the exit of the chamber) and therefore to deepen the investigation inside the chamber. To map a sufficient part of the combustion chamber, thus, tests have been repeated for different camera and laser sheet positions; to avoid loss of information, each framing is slightly overlapped with the neighbouring ones. For each position, 480 image pairs have been taken; the time delay between two laser pulses was adjusted depending on the local expected averaged velocity, between 15 and 20 $\mu s$. The laser sheet thickness was set to about 1 mm to keep the number of loss of pair due to out of plane motions as low as possible. The distance between camera and measurement plane has been set in order to achieve a *scale factor* [21] close to 8, resulting in images dimensions of about 90 x 65 mm. Each set of image pairs have been post processed using an adaptive cross-correlation iterative method with interrogation area shift between two image of the same pair, in order to rise the signal strength due to the capture of the in-plane dropout [22]. The obtained movement vector, calculated trough standard cross correlation algorithm, is used as a new estimate for the window shift in the second iteration; interrogation area refinement from a 256x256 pixel initial windows size to 64x64 final size have been used, through the iterations, in order to achieve the maximum resolution and decrease the number of erroneous vector [21, 23]. The obtained raw vector maps have been validated and filtered and, then, an average vector map for each framing has been computed; finally all the post processed maps have been composed in a single vector map of the whole investigated area.

For what concerns the seeding, oil particles have been used: the seeding necessary for the PIV measurements has been introduced upstream the swirler by means of a Laskin nozzle; a description of such kind of instrument has been given by Kahler et al. [24]. Particles, with a mean diameter of about $\pm 1 \mu m$, have been injected in the mainstream through a pipe as long as the height of the inlet section; the pipe was drilled with several holes of 1 mm in diameter to allow a sufficient mixing between air and seeding before entering the test section. Coolant was not seeded.

The uncertainty evaluation has been carried out using the approach developed by Charonko and Vlachos [25], consisting in correlating the uncertainty bounds to the cross-correlation peak ratio, the ratio of primary to secondary peak height. Despite in PIV measurements several systematic and random sources of error could arise from many aspects like velocity gradients, out-of-plane motion, image shape and illumination, choice of the interrogation area and particle density and diameter, all of these have an influence on the value of the peak ratio; in the referenced work it has been, therefore, decided to evaluate PIV measurements uncertainty bounds basing on such value, without investigating the effect of every single source of error, whose influences and interactions are unpredictable, since they depends on the instantaneous particle image pattern [25].
Since the images postprocess adopted in this work includes a validation method that deletes all the vectors resulting from cross-correlation processes that give peak ratios lower than 1.1, this threshold value has been used for the evaluation of worst-case uncertainty bounds. The calculated uncertainties are as low as about 4 % in the areas with the highest measured velocities, while they rise up to 20 % in low-velocity and recirculation zones (see below).

### Five hole probe set-up

In order to characterize the flow field at combustor exit a five hole probe has been used. It allows to evaluate static and total pressure and both flow angles. In particular they are defined as the pitch angle, the angle between velocity vector and axial direction on plane $r-x$, and the swirl angle, between velocity vector and axial direction on plane $x-\theta$. A J-type thermocouple was mounted on the five hole probe; knowing the flow temperature in the measurement point it is possible to evaluate its density and, thus, the three velocity components [26]. Temperature measurement has been performed both for this goal

and to characterize the thermal field at combustor exit. Since the thermocouple is mounted adjacent to the five hole probe's elbow, the temperature field is measured slightly downstream (7.44 mm) of the above defined measured planes, where the probe pressure taps are located. The measured temperature is partially biased by the presence of the 5-hole probe itself, but it can be considered a good estimate of the real flow temperature. As anticipated above, in order to explore the whole section of the annulus, the five hole probe has been installed on the traverse system, that has been fixed to the outer casing of the rig thanks to an adaptive flange that allows to place the pressure measurement points exactly on Plane 40 or Plane 40+. Such configuration is depicted in fig. 6. Through three stepper motors the traverse system is able of azimuthal and radial displacements, in addition to the probe angulation; the positioning accuracy is less than 0.1mm in both directions.

The five hole probe used in this survey (*Aeroprobe 13049-1*) was calibrated by the manufacturer, between $\pm 60^\circ$ for both angles, at two different Mach number ($M = 0.1,0.2$), to cover the whole velocity range expected in the rig. During the tests, data are acquired by means of a piezoresistive pressure transducer, synchronized with the motion system of the traverse system. According to the manufacturer, with the used pressure transducers, the measurements uncertainty is $< 0.4^\circ$, for flow angles, and $< 0.8\%$ for Mach number. For each point of the mesh, pressure data were acquired for 2s at 2kHz; averaged values were then post processed using the probe calibration files. Thermocouple data acquisition is synchronized to the five hole probe's one;

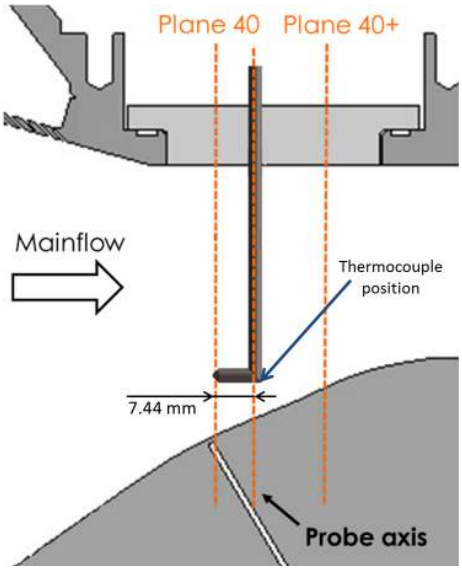


Figure 6: Five hole probe and thermocouple measurement positions

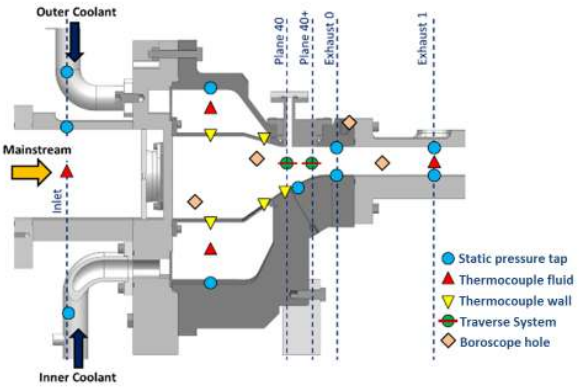


Figure 7: Scheme of Trisector rig instrumentation set-up

an Aeroprobe module is used for signal correction, according to cold joint temperature, and amplification. It is worth noting that the thermocouple measurements stay in the middle between static and total temperature, due to the deceleration induced in the flow; the recovery factor has not been evaluated, but for the Mach number and temperature levels of this application (described in the following sections) the difference between static and total temperature is very low. Combining this source of error to the thermocouple uncertainty ($\pm 1K$, 95% level of confidence, according to the manufacturers), the global measurement uncertainty stays under 1% of the measured temperatures.

Fig. 7 shows the positions of all the probes and instrumentations, used for monitoring and for flow field characterization both at combustor exit and in combustion chamber.

## Operating conditions

The test rig operating point, in nominal conditions, has been established in order to match the most important non-dimensional parameters, that control the behaviour of the flow, at engine representative values. As described in [16] the parameters chosen to describe the physics of the flow in the combustor simulator are mainstream and cooling flows Reynolds numbers ($Re_M$, $Re_1$ and $Re_2$) and mainstream Mach number at swirler exit ($M_M$); moreover, the multiperforated plates can be characterized by the blowing ratios $BR_i = (\rho_i V_i)/(\rho_M V_M)$ and by momentum flux ratios $I_i = (\rho_i V_i^2)/(\rho_M V_M^2)$. Beside the design point, in order to perform early PIV measurements, an isothermal operating point (i.e. both mainflow and coolant at room temperature) has been defined. Such process has been accurately described in [16]. Table 1 summarize the operating conditions, in terms of control parameters, to be set during the test, and of non-dimensional deriving parameters.

| | DP | PIV |
|---|---|---|
| Normalized total mass flow | 1 | 1 |
| Flow split swirlers | 65% | 65% |
| Flow split cooling cavities | 35% | 35% |
| Normalized chamber pressure | 1 | 0.78 |
| Swirler inlet temperature | 531 K | 300 K |
| Cooling cavities temperature | 300 K | 300 K |
| Swirler Reynolds number | 111 000 | 175 500 |
| Swirler Mach number | 0.112 | 0.108 |
| Effusion cooling Reynolds number | 2344 | 2344 |

Table 1: Operating conditions for design point (DP) and isothermal point (PIV)

## EXPERIMENTAL RESULTS AND DISCUSSION

### Preliminary PIV results

PIV measurements were performed inside the combustor chamber to point out the characteristic flow structures generated by the swirlers and by the interaction between mainflow and coolant. At this early stage of the survey, measurements were performed only in isothermal condition: in fact, this condition simplified the operability of the rig and the absence of high temperature allowed to easily use the boroscopes. Such preliminary PIV measurements have been performed only on D00 and D55 configurations.

Figure 8 illustrates the characteristics of the flow field generated by the central injector; the image reports the magnitude of the 2D velocity on the symmetry plane ($V_{sp}$), normalized with respect to the maximum ($V_{ref}$ ). A full investigation of the chamber was not feasible because of the difficult optical access; therefore, to clarify the position of the measuring area in the chamber, the vector map was included within cross section of the combustor simulator.

Measurements highlight some typical flow structures of a modern swirl-stabilized combustor, which are the corner vortex (under the inner jet) and the central recirculation zone (CRZ) generated by the vortex breakdown [27]. Both structures are visible thanks to the plotted vectors. For D00, the two high momentum jets exiting the swirler seems to be quite imbalanced: in fact, the velocity magnitude of the core of the inner jet is roughly 20% greater than the outer jet. Such imbalance between the two jets is probably related to the shape of the CRZ (see below). With respect to radial swirlers (for instance, see the work of Sedalor et al. [28] or Andreini et al. [14]), the axial swirler impresses a small radial momentum to the jets, which exit the injector with a low angle with respect to the axial direction; consequently, the impingement phenomenon of the jet on the liners, typical of the radial swilers, is not present. Furthermore, focusing on the inner jet, a rapid deceleration of the mainflow can be observed, which starts around the first row of effusion holes, 45 mm downstream the swirler plate. An acceleration of the flow is visible at the outlet of the chamber, caused by both the presence of the outer and inner cooling flows, and the vena contraction due to the shape of the inner liner.

Moving the focus on D55 some similar features can be noted; the two jets coming from the duct are still imbalanced, but, differently from the D00 configuration, the outer one is the more intense. On the other hand, the inner jet is smaller and, due to the presence of the liner, seems more pressed to the duct; moreover, it is early deviated towards the acceleration zone, visible roughly in the center of the vena on the right side of the measuring area.

In order to have a better understanding of the phenomena related to vortex breakdown and recirculation zone, fig. 9 shows the axial velocity component ($U$) normalized with the local value of symmetry plane velocity magnitude.

This picture highlights the extension of the central and the corner recirculation zones. For D00, the central recirculation zone is well defined and its closure is very close to the swirler, inside the small room between it and the "actual" inlet of the combustor chamber. It is also slightly lifted off by the presence of the inner coolant injections and the convergent inner liner: this phenomenon is probably the reason that explain the slight imbalance of the two jets from the swirler. The image indicates also that the flow is mainly axial, except for a small area between the two recirculation zones and for the region close to the inner wall, in correspondence of the convergent section at the combustor exit. For D55, the CRZ is completely de-attached from the duct and it is quite small with respect to the no-duct configuration, due to the higher axial momentum at duct exit. In addition, the last portion of a further recirculation zone, assimilable to a corner vortex, is confined between the duct and the inner liner. Finally, the image shows the mainstream lift off close to the inner liner due to the coolant injection and the shape of the wall.

### Five hole probe results

Measurements carried out with the five hole probe at combustor exit have been useful to understand how the flow structures highlighted in the previous paragraph influence the aerothermal field approaching the NGV. Such measurements have been performed for all the three configurations in order to assess the effect of both ducts presence and length. As mentioned earlier in the paper, two measurements planes have been explored in order to evaluate the hot streaks transport and

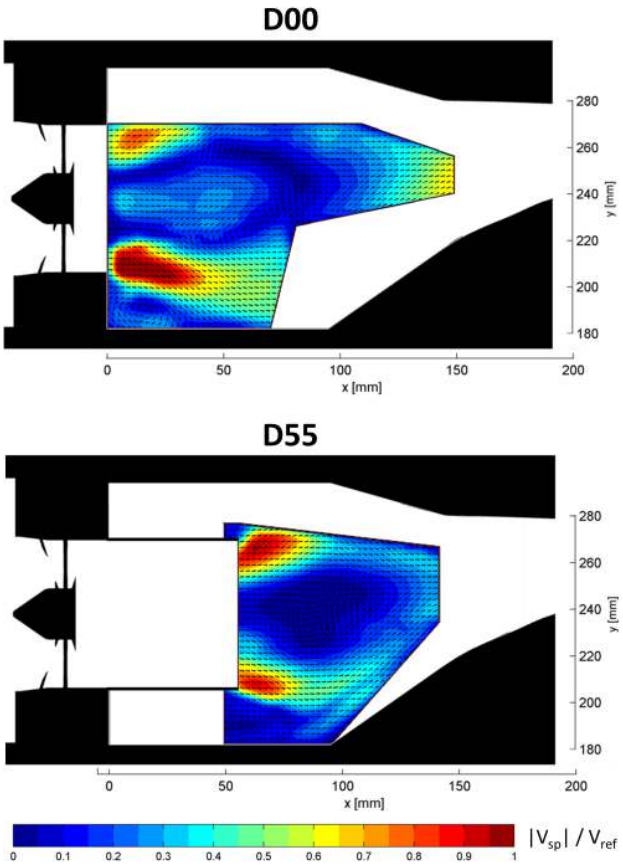


Figure 8: Normalized velocity magnitude in the combustion chamber

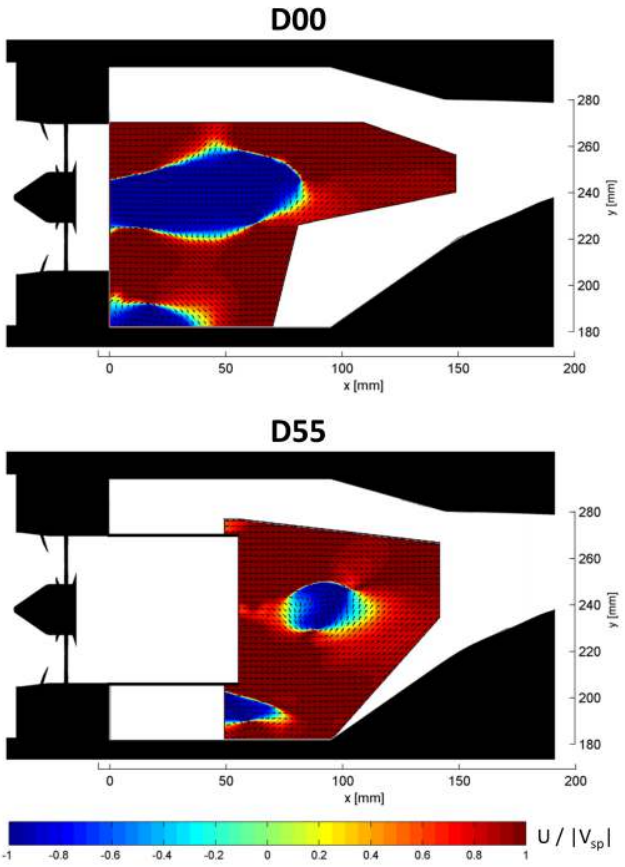


Figure 9: Normalized axial velocity in the combustion chamber

the flow field modifications between combustion chamber exit and NGV virtual position.

First of all the thermal field, measured by the thermocouple, 7.44 mm downstream the defined measurement planes (fig. 6), has been evaluated. Fig. 10 depicts the 2D maps of the annulus section. The investigated area is depicted inside the bounds of the central sector of the rig, in order to have a clear view of the investigation limits. Since the center of rotation of the azimuthal motion of the traverse system is different from the center of the annular outlet duct of the Sector rig, an investigation of the whole central sector is not feasible.

In order to scale the coolant temperature, that cannot be regulated and can change for some degrees among difference tests following ambient temperature, a non-dimensional parameter has been introduced:

$$T_{nd} = \frac{T - T_{cool}}{T_M - T_{cool}} \tag{1}$$

The thermal field resulting from the D00 configuration is characterized by a thin strip of hot flow, located around the middle radius, that crosses the entire tangential extension of the central sector area and it is not bounded on the lateral sides. This is a consequence of the development of the flow field in the combustor chamber, whose main characteristics were highlighted by the PIV measurements: the jet opening at the swirler exit generates a large hot zone which covers, in the proximity of the swirler plate, almost the whole chamber heigh. In correspondence of the first rows of effusion cooling, located roughly at one third of the chamber length, the hot flow rapidly becomes confined in the central area of the chamber due to the coolant injection. Actually, in the first part of the chamber, the swirling flow dissipates a great part of its tangential momentum: therefore, the closure of the hot recirculation zone is quite far from Plane 40, and the strong mix-

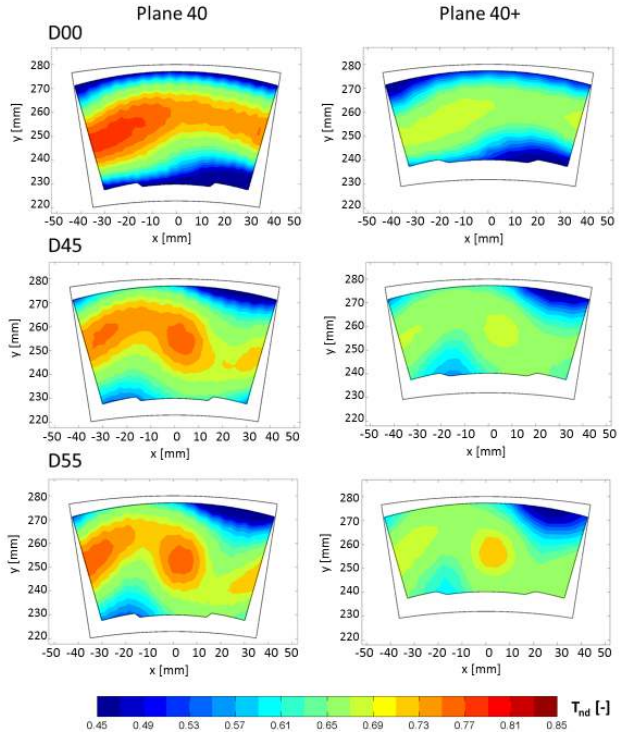


Figure 10: Non-dimensional temperature 2D maps

ing with the coolant, which starts downstream the CRZ closure, quickly reduces the hot streak to a thin film. This phenomenon is sketched in figure 11.

In addition, experimental data point out that the impact of the coolant on the temperature distribution is pretty marked, especially in the inner side: considering that the 5-hole probe, due to its shape, does not allow to measure too close to the wall, the extension of the cooling layer is quite large, as indicated by the dark blue area appearing on right corner in fig. 10. This is a typical feature of lean burn combustors with effusion cooling systems that generate a coolant layer whose thickness increase

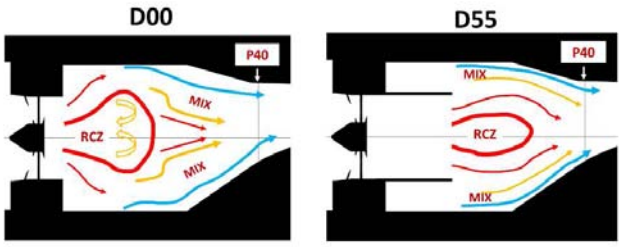


Figure 11: Sketch of the evolution of the mainflow in the combustor

row by row towards the combustor exit with limited mixing with the mainstream.
Finally, the wavy shape of the hot streak is due to the interaction between the high-momentum coolant layer and the swirling mainflow, which is rotating clockwise with respect to the pictures.

The thermal fields resulting from the ducted configurations show a hot spot which is more marked with respect to the D00. This is due to a different development of the flow field in the chamber, sketched in fig. 11: due to the presence of the duct, the CRZ is narrower in comparison with the one obtained without duct, but its closure is nearer to the combustor exit. Consequently, the hot swirling flow is conserved up to the measurement plane, while the region of mixing with the coolant is more bounded, and the coolant layer in Plane 40 is more confined as well. The temperature fields generated by all the tested ducts have the same main features, which are a central "circular" spot within a wavy hot region around the middle radius: even if the differences between the two configurations are not that marked, results confirms that the effects of a longer duct are: the hot spot is more marked and the temperature level in the central area is higher; the tangential momentum of the mainflow is more conserved, resulting in a more cambered hot flow; the mixing with the effusion flow is more intense and more bounded in the regions close to the liners.

Focusing on Plane 40+, it is possible to see that the morphology of the thermal field is unchanged and all the above described features are still present. It is, though, possible to note a hot spot temperature reduction due to the interaction between mainflow and coolant, that leads to a less distorted temperature profile. This reduction can be estimated as about the 2% of the measured dimensional values on Plane 40 for the ducted configurations and even higher than 4% for D00, since the mixing is less bounded and it influences more the hot streak zone.

To have a concise representation of the level of non-uniformity induced in the thermal field approaching the virtual turbine location by the different configurations, fig. 13 summarizes the maximum-to-mean and minimum-to-mean measured temperature ratios and compares it to the ones achieved in the most recent test rigs used for similar goals. D00 shows the maximum distortion, even if the differences between the configurations in the same measurement plane are quite limited; despite this fact the ducted configurations look more adapt to represent annular combustors behaviour due to the more defined hot spot shape. As expected the distortion is lower on Plane 40+, due to the mixing phenomena. In terms of comparison with the other test rigs, it is possible to note that the non-uniformity obtained on Sector rig is a little lower (about 10 %) than in some others. It is worth nothing, though, that such comparison is affected by two issues: the relative position of the measurement plane with the vane leading edge is not always given and differs

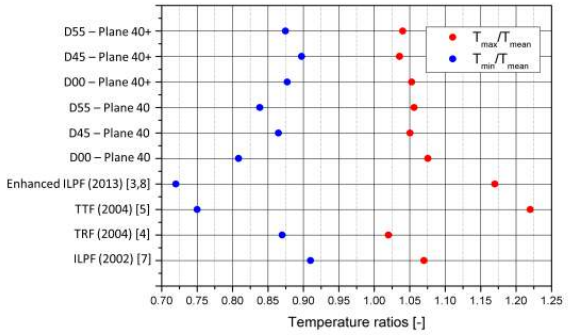


Figure 13: Maximum-to-mean and minimum-to-mean temperature ratios at recent simulators exit

between all the rigs; Sector rig measurements, as seen earlier, do not cover the areas of the section close to the walls, where the flow temperature is the coldest, so the non-uniformity level is a little bit underestimated.

It is also interesting to plot the radial non-dimensional profiles, depicted in fig. 12 in order to get some additional information. Such profiles have been calculated on the centerline of the section, thus for azimut angle $\theta = 0°$ and for $\theta = -4.5$ and $4.5°$; other profiles have been obtained by making a tangential mean of the results for varying radial position. Results show that the thick layer of inner coolant push the peak temperature towards the 60% height of the outlet section rather than at the height that corresponds to the axis of the swirler (around 39%). Circumferentially averaged profiles show that the D00 configuration presents the highest peak value: looking at the 2D maps, it is clear that this is a consequence of a nonbounded hot spot that covers the whole tangential extension of the investigation plane. Near the walls D00 presents the lowest temperatures due to the thicker coolant layer. Averaged temperature profiles of the ducted configurations are quite similar due to the little difference

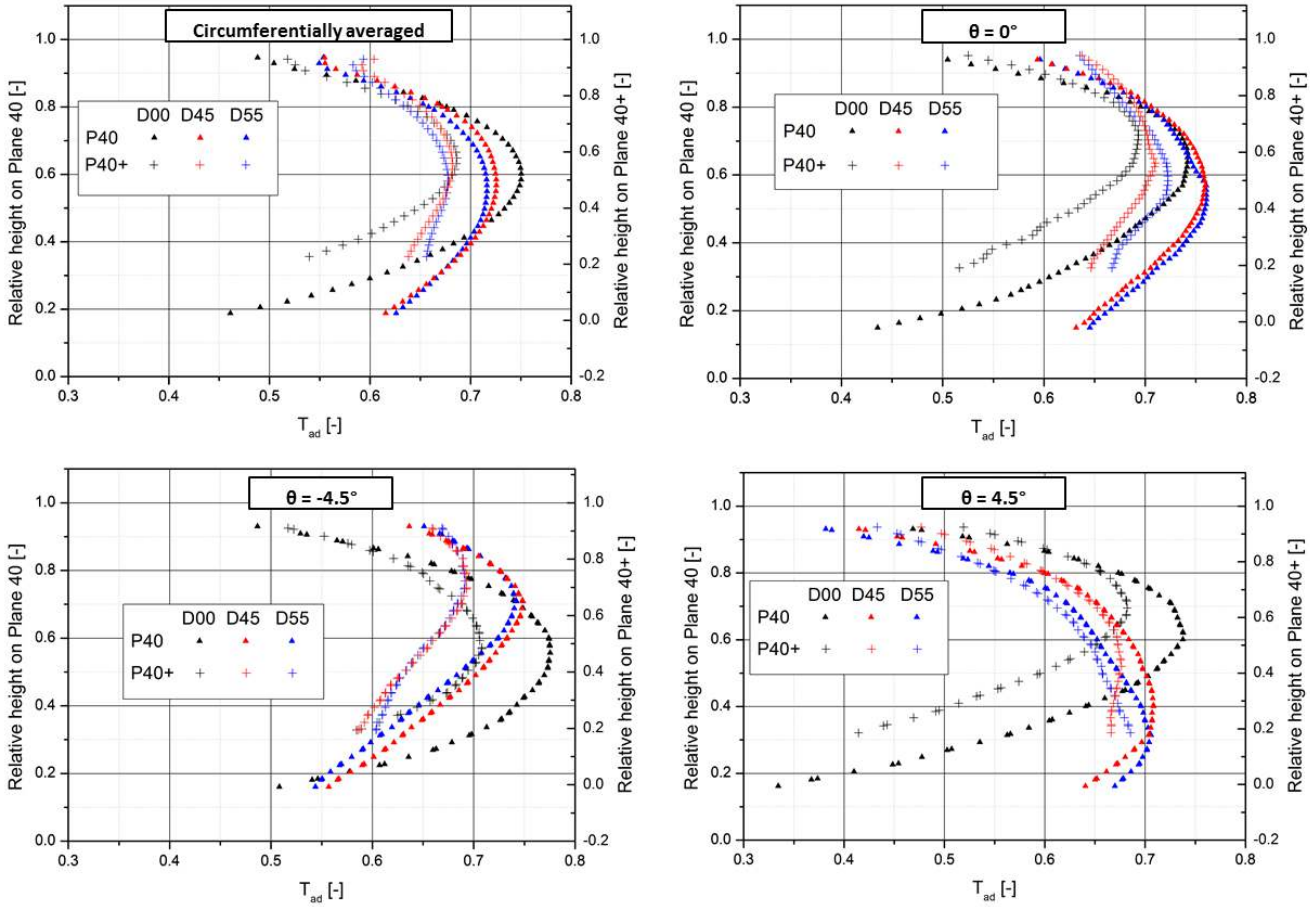


Figure 12: Non-dimensional temperature radial profiles

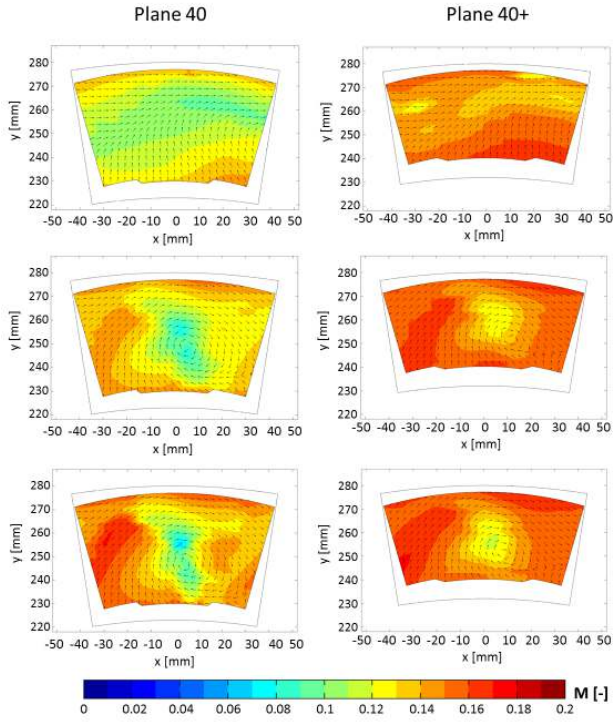


Figure 14: Mach number 2D maps

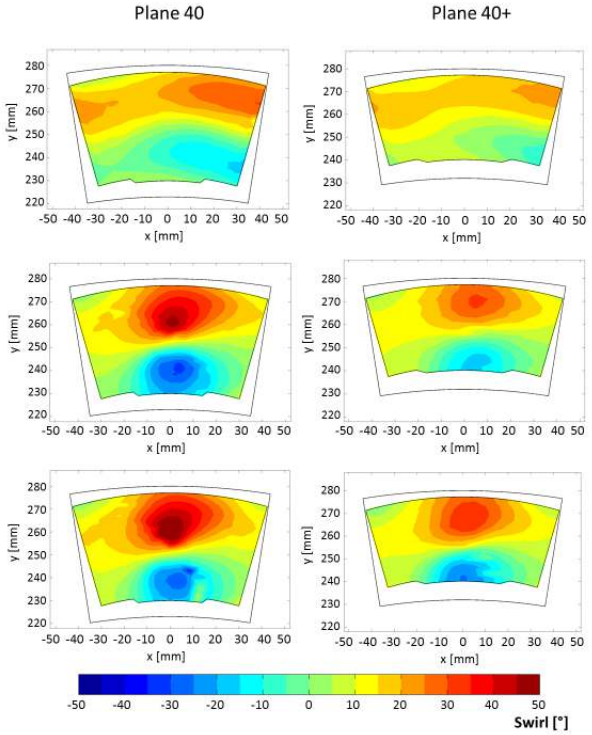


Figure 15: Swirl angle 2D maps

in duct lengths.

The other profiles show that the ducted configurations reach the maximum temperature near the centerline, while D00 does for negative angles, as it was possible to see also from the maps. All this considerations are in agreement with what stated above about the effect of the increasing duct length.
On Plane 40+ the profiles show the same trends but important differences can be noted in terms of maximum temperature in the hot spot, as mentioned earlier. It is also interesting to note that, close to the walls, the temperature differences between Plane 40 and Plane 40+ profiles is far less marked due to the mixing phenomena between mainflow and coolant that occur between the two measurement planes; in some cases Plane 40+ temperature can even be higher, like it especially happens at the upper radii.
Since the thermal field directly affects the heath transfer, the measured profiles at different angular positions are useful to assess its impact on NGV leading edges cooling systems, for different clocking positions between swirlers and vanes.

Afterwards, the focus was moved on the investigation of the aerodynamic field. It has been chosen to characterize it by evaluating the results in terms of Mach number and flow angles, in order to obtain a full description and to analyse parameters that directly affect the performances of the high pressure turbine.
Fig. 14 shows the Mach number 2D maps; vectors indicating the flow direction have also been plotted, useful to have a better visualization of the flow field.

Maps indicate that Mach is quite low in the entire investigation area. Velocity vectors point out that the ducts preserve the rotating core of the mainstream up to the combustor exit. For this reason, for the ducted configuration, velocity and, thus, Mach number are lower in the center of the section, while near the walls they are higher both because of the tangential momentum and because of the acceleration of the nearest flow due to the area reduction at combustor outlet and to the blockage made by the bulk flow coming from the swirler. An important contribution to the Mach number field comes also from the temperature field, since in the center of the section temperature is higher and this brings to an even lower Mach number. The maximum Mach number is reached for D55 configuration and its value is about 0.18. For D00, on the other hand, the mainstream dissipates most of its tangential momentum in the combustor chamber and it conserves only a residual overall rotation towards the right side; therefore Mach number differences between the center of the section and the near walls regions are lower, as well as the maximum value of Mach number itself.

Concerning Plane 40+, the flow structure remains quite

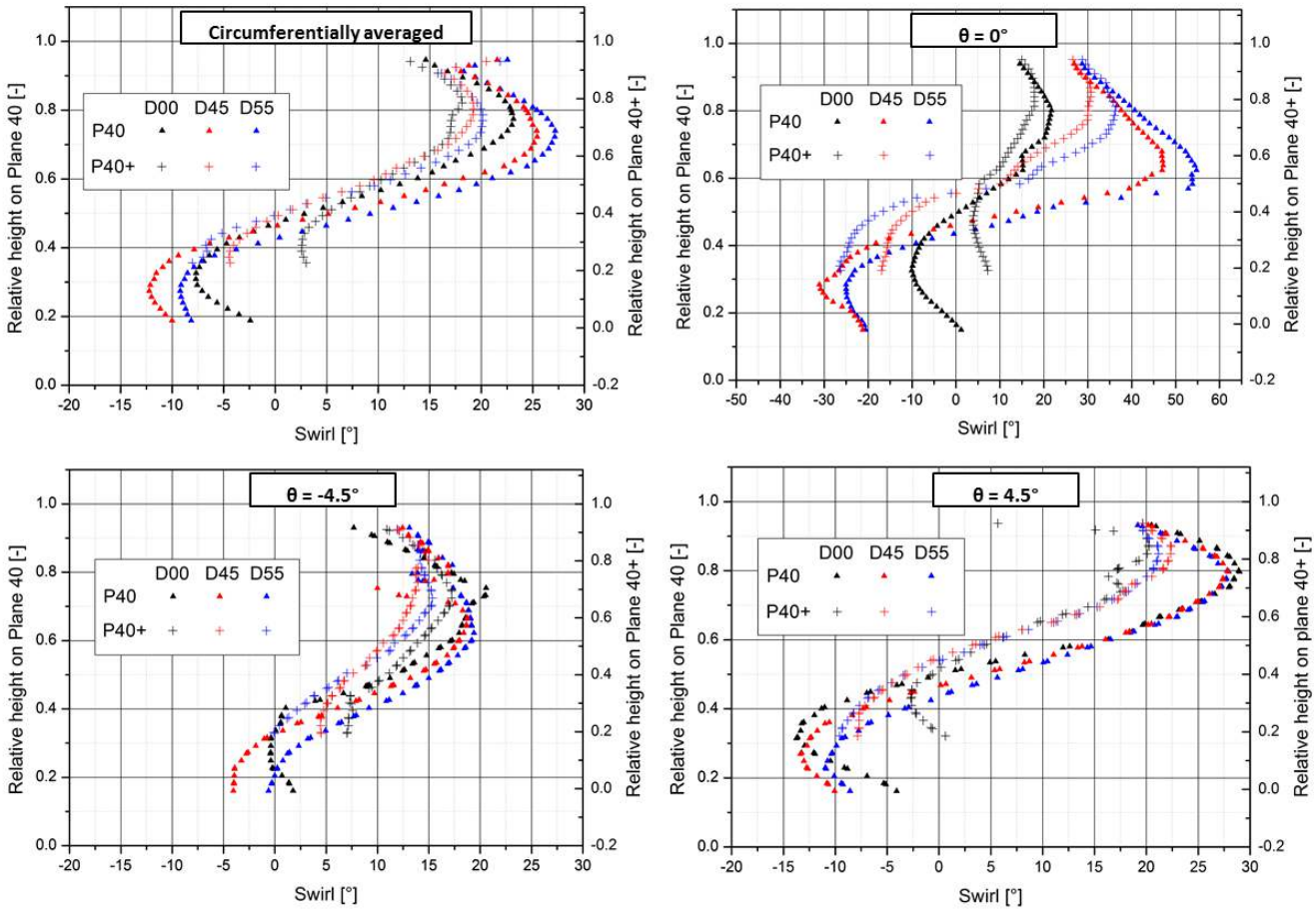


Figure 16: Swirl angle radial profiles

similar both for the ducted configurations and the unducted one; due to the annulus section reduction, however, the Mach numbers result higher of about 12-15% of the measured values on Plane 40.

Moving the focus on the flow angles, it is important to remind that one of the aims of the project, which this study has been carried out within, is to test the HP stage subjected to an aggressive swirled flow coming from the combustor, in order to simulate realistic operating conditions at the turbine inlet. Consequently, the highest attention has to be paid to the swirl angle, since it directly affects the incidence angles on the NGV.

Maps confirm the outcomes from the investigation of the thermal field and of Mach number: without the duct, the interaction with the coolant from the multiperforated plate dissipates the momentum of the rotating mainflow from the swirlers and it impedes the development of a marked central region of hot rotating flow. On the other hand, the introduction of the duct reduces this effect, and the longer the duct, the more the tangential momentum of the mainflow is conserved at the chamber exit. Thus, the resulting flow angles are high for what concerns the ducted configurations, while they are quite small for D00. For D55 the maximum swirl angle exceeds 50°, similarly to other results found in literature (e.g. Qureshi and Povey [9]), while for D00 it hardly reaches 30°, since the shape of the vortex is completely lost. While results from D00 are not satisfying in terms of flow angles magnitude, since it is too low, the ducted configurations show a swirl field strong enough to represent lean burn combustors behaviour. On Plane 40+ a flow angles magnitude reduction can be noted; it reaches 30% in D55 configuration, in the zones of the section in which the tangential momentum is maximum.

Finally fig. 16 shows the swirl angle radial profiles evaluated with the same methodology and in the same angular positions as explained above for the thermal field.

The picture shows that, beyond the considerations taken

above, the absolute value of such angles in the upper part of the annulus is quite bigger than in the lower part, both for all the evaluated tangential positions and for the averaged profiles. This phenomenon is due to the convergence of the inner wall that brings to an axial acceleration of the fluid close to it and to a more intense influence of the inner coolant layer on the rotating core; since the inner angles are lower the rotating vortex presents a shift towards right with respect to the centerline of the section as it was possible to see from the velocity vectors plotted in fig. 14. As stated above, such profiles, the last three ones in particular, are really useful to evaluate the behaviour of the NGV leading edges cooling system, since the swirl profile directly affects the position and the inclination of the stagnation line, and hence the pressure distribution, on the first vanes row.

## CONCLUSIONS

In this work an experimental campaign on a non-reactive three-sector combustor simulator, provided with many features typical of modern lean burn chambers and capable of generating both temperature distortions and a highly swirling flow, has been conducted. Three configurations have been tested: one without ducts mounted on the swirlers and two with ducts of 45 and 55 mm.

The flow field inside the chamber has been evaluated, by means of a PIV campaign, as well as the aerothermal field at the simulator exit, on two axial positions (Plane 40 and Plane 40+), in order to analyse how the flow structures and the mixing phenomena, between mainflow and coolant, influence the resulting flow field at combustor exit; it has been also possible to draw conclusions regarding the hot streaks transport from combustor exit to NGV virtual location.

2D PIV measurements have been carried out on combustion chamber symmetry plane in isothermal conditions. Typical features of aeroengines combustors have been found like the presence of recirculation zones and corner vortexes. In general, for the no-duct configuration, the swirler jet opening, even if limited, creates a large rotating core whose tangential momentum is largely dissipated by the interaction with the liners cooling flows, while it moves downstream. For the ducted configurations, on the other hand, the rotating core is narrower, due to the presence of the ducts, and it is slightly influenced by the interaction with coolant.

This preliminary investigation will be completed in later stages of the experimental campaign: further measurements will be carried out imposing the design working conditions, and a comparison with the isothermal results presented here will highlight the impact of coolant-to-mainstream density ratio on the mixing of the two flows and on the evolution of flow field.

The aerothermal field at combustor exit has been, then, evaluated, for design point (hot) conditions, by means of a five hole probe, equipped with a thermocouple, mounted on a traverse system. Results obtained by the thermocouple showed, in agreement with what seen form PIV, that for the ducted configurations the hot streak is well bounded and the coolant layers close to the walls have limited thicknesses, since the hot mainflow is preserved downstream and the mixing with coolant starts quite near to Plane 40. On the other hand for the no-duct configuration the strong mixing with coolant, that starts quite far form Plane 40, brings to thicker coolant layers and to the hot streak to be a thin strip of hot flow covering the whole tangential span of the section. The achieved level of temperature non-uniformity at combustor exit is similar for all the configurations and comparable, even if a little lower, to the one obtained in other recent rigs used for similar measurements.

For what concerns the aero-field, results from five hole probe measurements showed that, for the same reasons stated above, for the no-duct configuration the mainstream dissipates almost completely its tangential momentum and low flow angles and flow field non-uniformities can be found. For the ducted configurations the swirling vortex, created by the swirlers, is conserved up to Plane 40, instead, and, thus, high flow angles, that can be considered representative of modern lean burn combustors, are measured.

Focusing on the transport of hot streaks and on flow field modification between the two explored planes at combustor exit, it has been concluded that, while the morphology of thermal and aero-fields is conserved, on Plane 40+ both temperature level and flow angles magnitude results damped mainly due to the interaction between the flows. The hot spot temperature reduction, in dimensional terms, can be assessed between 2 and 4%, depending on the configuration, while for swirl angles it rises up to 30% for the ducted configurations.

These results are useful to deepen the knowledge of the flow field evolution and of hot streaks generation and transport inside a modern lean burn combustor; the obtained experimental database can be used, in particular, on behalf of the investigation of the interactions between combustor and high pressure turbine in modern aeroengines.

## ACKNOWLEDGMENT

The authors wish to gratefully acknowledge FACTOR (Full Aerothermal Combustor-Turbine interactiOns Research) Consortium for the kind permission of publishing the results herein. FACTOR is a Collaborative Project co-funded by the European Commission within the Seventh Framework Programme (2010-2016) under the Grant Agreement n° 265985.

## REFERENCES


[1] Qureshi, I., Beretta, A., and Povey, T. Effect of simulated combustor temperature nonuniformity on hp vane and end wall heat transfer: An experimental and computational investigation. *ASME J Eng Gas Turb Power*, 133(3):031901–031901, 2010. ISSN 0742-4795.

[2] Povey, T. and Qureshi, I. Developments in hot-streak simulators for turbine testing. *ASME J. Turbomach.*, 131(3):031009–031009, 2009. ISSN 0889-504X.

[3] Hall, B. F., Chana, K. S., and Povey, T. Design of a non reacting combustor simulator with swirl and temperature distortion with experimental validation. *Proc. ASME Turbo Expo*, (GT2013-95499), 2013.

[4] Barringer, M. D., Thole, K. A., and Polanka, M. D. Effects of combustor exit profiles on vane aerodynamic loading and heat transfer in a high pressure turbine. *ASME J. Turbomach.*, 131(2):021008–021008, 2009. ISSN 0889-504X.

[5] Mathison, R. M., Haldeman, C. W., and Dunn, M. G. Aerodynamics and heat transfer for a cooled one and one-half stage high-pressure turbine - part iii: Impact of hot-streak characteristics on blade row heat flux. *ASME J. Turbomach.*, 134(1):011008–011008, 2011. ISSN 0889-504X.

[6] Jenkins, S. C. and Bogard, D. G. Superposition predictions of the reduction of hot streaks by coolant from a film-cooled guide vane. *ASME J. Turbomach.*, 131(4):041002–041002, 2009. ISSN 0889-504X.

[7] Povey, T., Chana, K. S., Jones, T. V., and Hurrion, J. The effect of hot-streaks on hp vane surface and endwall heat transfer: An experimental and numerical study. *ASME J. Turbomach.*, 129(1): 32–43, 2005. ISSN 0889-504X.

[8] Povey, T. and Qureshi, I. A hot-streak (combustor) simulator suited to aerodynamic performance measurements. *Proceedings of the Institution of Mechanical Engineers, Part G: Journal of Aerospace Engineering*, 2008.

[9] Qureshi, I. and Povey, T. A combustor-representative swirl simulator for a transonic turbine research facility. *Proceedings of the Institution of Mechanical Engineers: Journal of Aerospace Engineering*, 2011.

[10] Qureshi, I., Smith, A., and Povey, T. Hp vane aerodynamics and heat transfer in the presence of aggressive inlet swirl. *ASME J. Turbomach.*, 135(2):021040–021040, 2012. ISSN 0889-504X.

[11] Bacci, T., Facchini, B., Picchi, A., Tarchi, L., Koupper, C., and Champion, J.L. Turbulence field measurements at the exit of a combustor simulator dedicated to hot streaks generation. *Proc. ASME Turbo Expo*, (GT2015-42218), 2015.

[12] Koupper, C., Bonneau, G, Bacci, T., Facchini, B., Tarchi, L., Gicquel, L., and Duchaine, F. Experimental and numerical calculation of turbulent timescales at the exit of an engine representative combustor simulator. *Proc. ASME Turbo Expo*, (GT2015-42278), 2015.

[13] Andreini, A., Insinna, M., Mazzei, L., and Salvadori, S. Hybrid rans-les modeling of a hot streak generator oriented to the study of combustor-turbine interaction. *Proc. ASME Turbo Expo*, (GT2015-42402), 2015.

[14] Andreini, A., Caciolli, G., Facchini, B., Picchi, A., and Turrini, F. Experimental investigation of the flow field and the heat transfer on a scaled cooled combustor liner with realistic swirling flow generated by a lean-burn injection system. *ASME J. Turbomach.*, 137 (3):031012–031012, 2014.

[15] Wurm, B., Schulz, A., Bauer, H.J., and Gerendas, M. Impact of swirl flow on the cooling performance of an effusion cooled combustor liner. *ASME J Eng Gas Turb Power*, 134(12):121503–121503, 2012. ISSN 0742-4795.

[16] Koupper, C., Caciolli, G.a, Gicquel, L., Duchaine, F., Bonneau, G., Tarchi, L., and Facchini, B. Development of an engine representative combustor simulator dedicated to hot streak generation. *ASME J. Turbomach.*, 136(11):111007–111007, 2014. ISSN 0889-504X.

[17] Roux, S., Cazalens, M., and Poinsot, T. Outlet-boundary-condition influence for large eddy simulation of combustion instabilities in gas turbines. *Journal of Propulsion and Power*, 24(3), 2008.

[18] Klapdor, E.V., Pyliouras, S., Eggels, R.L.G.M., and Janicka, J. Towards investigation of combustor turbine interaction in an integrated simulation. *Proc. ASME Turbo Expo*, (GT2010-22933), 2010.

[19] ASME. Measurement uncertainty. *Instrument and Apparatus, Vol. ANSI/ASME PTC 19.1-1985 of Performance Test Code*, 1985.

[20] Kline, S. J. and McClintock, F. A. Describing uncertainties in single sample experiments. *Mechanical Engineering*, 1953.

[21] Dynamics, Dantec. *FlowManager software and Introduction to PIV Instrumentation*. 2000.

[22] Gnirss, M. and Tropea, C. Simultaneous piv and concentration measurements in a gas-turbine combustor model. 45(4):643–656, 2008. ISSN 0723-4864.

[23] Raffel, M., Willert, C. E., and Kompenhans, J. *Particle Image Velocimetry - A pratical guide*. Springer, 1997.

[24] Kahler, C.J., Sammler, B., and Kompenhas, J. Generation and control of tracer particles for optical flow investigations in air. *Experiments in fluids*, 33, 2002.

[25] Charonko, J.J. and Vlachos, P.P. Estimation of uncertainty bounds for individual particle image velocimetry measurements from cross-correlation peak ratio. *Meas. Sci. Technol.*, 2013.

[26] Treaster, A. L. and Yocum, A. M. *The Calibration and Application of Five-Hole Probes*. The Pennsylvania State University Institute for Science and Engineering, 1978.

[27] Beer, J.M. and N.A.Chigier. *Combustion aerodynamics*. Applied Science Publishers, London, 1974.

[28] Sedalor, T., Patil, S., S.Ekkad, Tafti, D., Kim, Y., Moon, H.K., and Srinivasan, R. Study of flow and convective heat transfer in a simulated scaled up low emission annular combustor. *Proc. ASME Turbo Expo*, (GT2010-22986), 2010.

**Proceedings of ASME Turbo Expo 2015: Turbine Technical Conference and Exposition**
**GT2015**
**June 15-19, 2015, Montreal, Canada**

# GT2015-42218

# TURBULENCE FIELD MEASUREMENTS AT THE EXIT OF A COMBUSTOR SIMULATOR DEDICATED TO HOT STREAKS GENERATION

**Tommaso Bacci**
**Bruno Facchini**
**Alessio Picchi**
**Lorenzo Tarchi**
Department of Industrial Engineering
University of Florence
via S.Marta 3, 50139, Firenze, Italy
Tel: (+39) 055 4796575, Fax: (+39) 055 4796342
Email: bruno.facchini@unifi.it

**Charlie Koupper**
**Jean-Louis Champion**
Turbomeca
Bordes, France
Email: charlie.koupper@turbomeca.fr

## ABSTRACT

*In order to deepen the knowledge of the interaction between modern lean burn combustors and high pressure turbines, a real scale annular three sector combustor simulator has been assembled at University of Florence, with the goal of investigating and characterizing the generated flow field. To generate hot streaks and simulate lean burn combustors behavior, the rig is equipped with axial swirlers, fed by main air flow that is heated up to 531 K, and liners with effusion cooling holes that are fed by air at ambient temperature. The three sector configuration is used to reproduce the periodicity on the central sector.*

*Ducts of different lengths have been mounted on the swirlers to reduce the interaction of the mainstream with the coolant. Such configurations have been tested, using different measurement techniques, in order to highlight the differences in the resulting flow fields.*

*The work presented in this paper shows the experimental campaign carried out to investigate the flow turbulence at combustor exit, in isothermal conditions, by means of hot wire anemometry. The goal has been achieved by investigating each test point twice, using an automatic traverse system equipped, in turn, with two split-fiber probes, that allow to measure the velocity components on two planes orthogonal to each other. A method for the time correlation of the signals obtained by the two different tests has been used.*

*In order to analyse the turbulence decay towards the vanes location, such measurements have been performed on two different planes: one located in correspondence of the combustor exit and the further one placed downstream, in the virtual location of the vanes leading edges.*

## NOMENCLATURE

**Symbols**

| | | |
|---|---|---|
| $BR$ | Blowing Ratio | $[-]$ |
| $D_{sw}$ | Swirler diameter | $[m]$ |
| $E1$ | Split-fiber probes first outlet voltage | $[V]$ |
| $E2$ | Split-fiber probes second outlet voltage | $[V]$ |
| $f$ | Frequency | $[Hz]$ |
| $I$ | Momentum flux ratio | $[-]$ |
| $K$ | Turbulent kinetic energy | $[m^2/s^2]$ |
| $k$ | Wave number | $[m^{-1}]$ |
| $M$ | Mach number | $[-]$ |
| $Re$ | Reynolds number | $[-]$ |
| $r$ | Radial coordinate | $[-]$ |
| $St$ | Strouhal number | $[-]$ |
| $Tu$ | Turbulence intensity level | $[-]$ |
| $t$ | Time | $[s]$ |
| $U$ | Axial velocity | $[m/s]$ |
| $U_{ref}$ | Mean axial velocity at swirler exit | $[m/s]$ |
| $\bar{U}$ | Time-averaged axial velocity | $[m/s]$ |

| | | |
|---|---|---|
| $V$ | Tangential velocity | $[m/s]$ |
| $V_{abs}$ | Absolute velocity | $[m/s]$ |
| $\bar{V_{abs}}$ | Time-averaged absolute velocity | $[m/s]$ |
| $V_{cool}$ | Effective cooling velocity | $[m/s]$ |
| $W$ | Radial velocity | $[m/s]$ |
| $x$ | Axial coordinate | $[m]$ |

**Greeks**

| | | |
|---|---|---|
| $\alpha$ | Flow angle | $[deg]$ |
| $\rho$ | Density | $[kg/m^3]$ |
| $\theta$ | Tangential coordinate | $[deg]$ |

**Subscripts**

| | |
|---|---|
| $5HP$ | Five Hole Probe |
| $M$ | Mainstream |
| $R56$ | R56 split-fiber probe |
| $R57$ | R57 split-fiber probe |
| $TR$ | Trisector rig |
| $TS$ | Traverse system |

**Acronyms**

| | |
|---|---|
| DLR | Deutsches Zentrum fur Luft- und Raumfahrt |
| DP | Design Point |
| fft | fast Fourier transform |
| HP | High Pressure |
| HWA | Hot Wire Anemometry |
| ifft | inverse fast Fourier transform |
| LES | Large Eddy Simulation |
| NGV | Nozzle Guide Vane |
| PID | Proportional-Integral-Derivative |
| PID | Particle Image Velocimetry |
| PVC | Precessing Vortex Core |
| RMS | Root-Mean-Square |

## INTRODUCTION

In general it is quite hard to characterize gas turbine combustors flow fields, due to their high unsteadiness and extreme pressure and temperature conditions, that prevent from performing measurements. Therefore it is common to develop scaled (low pressure and temperature) facilities, that allow to carry out accurate measurements and to perform detailed characterizations of aerothermal field and heat transfer phenomena. A detailed description of the most important tests rig of such typology that have been used in past years is given by Povey and Qureshi [1].

Despite measuring turbulence in a real gas turbine is extremely difficult, for the reasons stated above, some old studies, like the one of Zimmermann [2], have been performed on reactive rigs based on real combustors. Additional studies have been carried out on real combustor hardware operated in isothermal conditions [3] or with turbulence generators that resembled combustor liners [4, 5]. These studies showed turbulence intensities at combustor exit between 7 and 30 % [6].

Many following studies focused on the effects of these turbulence levels, mostly generated by dedicated grids [7] instead of representative hardware, on the turbine behaviour. Nasir et al. [6] showed that the large scale freestream turbulence promotes a slightly earlier boundary layer transition on the suction surface; an enhancement in heat transfer, on both suction and pressure sides, has been found as well [6, 8]. Jenkins et al. [9] [10] investigated the combined effects of freestream turbulence with film cooling and vanes clocking position.

An important study, aimed at characterizing combustor-turbine interaction in aeroengines, has been carried out by Cha et al. [11]. Turbulence intensities and lengthscales have been measured at the exit of a complete engine hardware of a modern RQL (Rich-Quench-Lean) combustor, operated in isothermal conditions. Results showed turbulence intensities up to 35 %.

The introduction of new injectors and new cooling systems for lean combustors changes completely the development of the flow field inside the chamber with respect to Rich-Quench-Lean (RQL) combustors. In particular, the absence of dilution holes reduces the mixing process between the burning gases and the cooling flows, enhancing the temperature distortions and the degree of swirl of the mainflow at the turbine inlet. In order to realize scaled non-reactive lean burn combustor simulator, it must be kept in mind that, in real combustors, the heat release plays an important role in the stabilization of the flow generated by the swirlers. For example in non-reacting, highly swirling and diffusing flows, vortex instability in the form of a precessing vortex core or vortex breakdown is unlikely to be well matched to the reacting case [12] and this influences the evolution of the flow inside the simulator. Therefore, in order to achieve combustor representative conditions, in terms of aerothermal and turbulence field, it is not sufficient to adopt real combustor hardware and particular attention must be paid to the simulator design.

In this work an experimental campaign on a non-reactive three-sector combustor simulator, assembled at the University of Florence within the European project FACTOR (Full Aerothermal Combustor-Turbine interactiOns Research), is described. The simulator presents the main features of recent lean burn chambers, in terms of liner cooling systems and mass flow split between main and cooling flows, and is capable of generating both temperature distortions and a strong swirl field. In particular the study is aimed at characterizing the turbulence field at the simulator exit, on two different planes, in order to deepen the knowledge of the turbulence achieved at the exit of this type of combustor simulators and to evaluate its decay, moving towards the NGV location.

Other studies related to this test rig can be found in Bacci et al. [13], Koupper et al. [14] and Andreini et al. [15]. In the first work the mean aerothermal field inside the simulator and at its exit has been investigated, by mean of a five hole probe and a PIV campaign. Some results from the five hole probe have been quite useful for the present study, both for data postprocessing and for results interpretation. In the second work the attention has been moved to turbulent timescales and numerical and experimental results have been compared. In the latter one the results of a hybrid RANS-LES calculation are described.

Since the test rig is not equipped with cascades, no information has been drawn about hot streaks alteration through the high pressure vanes and their influence on the first rotor cascade. Further in the project, a full annular combustor simulator with the same geometry of the three sector rig together with a 1.5 turbine stage is going to be installed in the facility at DLR in Gottingen (Germany), to investigate the impact of the hot streaks on the HP turbine.

## EXPERIMENTAL FACILITY

The combustor simulator, called Trisector rig, reproduces, in 1:1 scale, 54° of the full annular combustor simulator that will be installed at DLR in Gottingen. Temperature and swirl profiles are obtained by mixing hot air (531 K), coming form the swirlers, to cold air streams (300 K) that feed effusion cooled liners. A full description of the Trisector rig and of its environment has been given in [13]. The three-sector configuration has been adopted in order to recreate periodicity conditions in the central sector, on which tests have been performed; such configuration has been used in many studies like the ones of Andreini et al. [16] and Wurm et al. [17]. A detailed description of the test rig design, with particular attention to some preliminary simulations performed in order to verify that the lateral walls do not affect the central sector flow field, can be found in [18]. A 3D model of the rig is displayed in figure 1.

The design phase, carried out by some FACTOR project partners, was aimed at obtaining a combustor representative flow field, in terms of temperature, velocity and turbulence fields, without the effect of combustion. A comprehensive set of RANS CFD calculation was performed to meet the target exit profiles while varying the combustor dimensions, the feeding conditions and the swirler geometry.

In order to test different configurations and understand their influences on the resulting flow field, ducts of different length can be mounted on the swirlers, as shown in fig. 1, allowing to reduce the interaction of the main stream with the coolant. Three total configuration have been tested: one without ducts, that will be referred to as D00 in the following, and two with ducts of 45 and 55 mm (corresponding about to 25 and 30% of the distance between swirlers and combustor exit), called respectively D45 and D55.

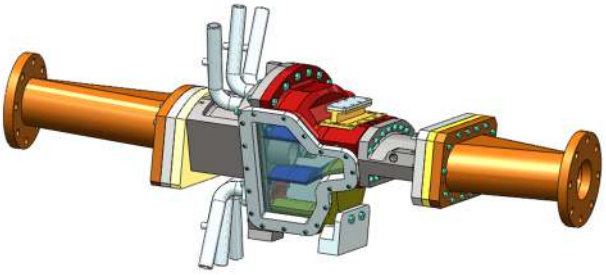

Figure 1: 3D model of the Trisector rig

The test rig configuration allows to perform measurements in two different axial positions in the combustion chamber exit annulus: the first measurement plane, called Plane 40, is placed at combustor exit, half an axial chord upstream the NGV virtual position in the DLR rig; the second is located on the virtual NGV leading edges position, 20 mm downstream the first. As it will be explained later, data will be obtained using probes mounted on an automatic traverse system provided by Turbomeca; the system can be fixed on the outer casing by means of an adaptive flange (yellow part on the outer casing in figure 1).

## INSTRUMENTATION AND MEASUREMENT TECHNIQUES

The instrumentations used for this study can be divided in two types, according to the goal of their measurements. The first ones are used to monitor the operating conditions of the rig, in terms of mass flow rates, temperatures and pressures in many locations. Further instruments are used for the evaluation of the unsteady flow field at combustor simulator exit, the real goal of such study. In the following only the second type of instrumentations is described; a brief account of the first one can be found in [13].

### Turbulence measurements at combustor exit

The turbulence field has been measured by means of hot wire anemometry. Two split-fiber probes have been used. Each probe is provided with two sensors, made by nickel films deposited on a quartz fiber with diameter of 200$\mu m$, as shown in fig. 2, that are fed by certain voltages to keep them at constant temperature. Since the cooling effect on the two sensors change with both velocity magnitude and direction, in the plane orthogonal to the axis of the wire, these probes allow to evaluate two velocity components on such plane and thus a flow angle. The probes have been installed on a traverse system, in order to explore the whole section of the annulus, and inserted through the outer casing of the rig. Through three stepper motors the traverse system

is able of azimuthal and radial displacements, in addition to the probe rotation around its axis; the positioning accuracy is less than 0.1mm in both directions and less than 0.2 ° for the rotation.

Probe R56 is used to evaluate the pitch angle (i.e. the angle between velocity vector and axial direction on plane $r-x$) and so axial and radial components of velocity can be calculated. Probe R57, on the other hand, allows to measure the swirl angle (i.e. the angle between velocity vector and axial direction on plane $x-\theta$) and so axial and tangential velocity components. In order to evaluate the three-dimensional flow field is, therefore, necessary to repeat each test point twice, to investigate it with both the probes and then combine the results.

Fig. 3 shows the positions of all the probes and instrumentations, used for monitoring and for flow field characterization at combustor exit in both measurement planes.

For what concerns the acquisition parameters, it has been decided to acquire data for 5 seconds, in order to obtain a good frequency resolution, at 20 kHz, the maximum achievable by the acquisition system.

## Operating conditions

The test rig operating point, in nominal conditions, has been established in order to match the most important non-dimensional parameters, that control the behaviour of the flow, at engine representative values. As by Koupper et al. [18] the parameters chosen to describe the physics of the flow in the

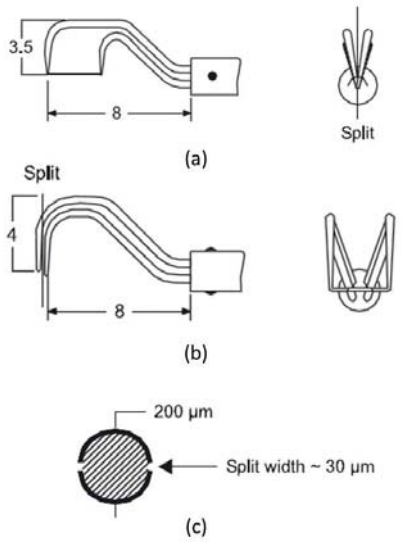


Figure 2: (a) R57 and (b) R56 split-fiber probes and (c) section of their quartz wire

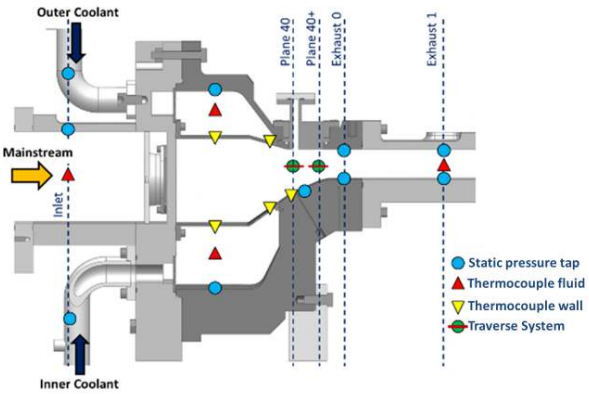


Figure 3: Scheme of Trisector rig instrumentation set-up

| | **DP** | **HWA** |
|---|---|---|
| Normalized total mass flow | 1 | 1 |
| Flow split swirlers | 65% | 65% |
| Flow split cooling cavities | 35% | 35% |
| Normalized chamber pressure | 1 | 0.78 |
| Swirler inlet temperature | 531 K | 300 K |
| Cooling cavities temperature | 300 K | 300 K |
| Swirler Reynolds number | 111 000 | 175 500 |
| Swirler Mach number | 0.112 | 0.108 |
| Effusion cooling Reynolds number | 2344 | 2344 |

Table 1: Operating conditions for design point (DP) and isothermal point (HWA)

combustor simulator are mainstream and cooling flows Reynolds numbers ($Re_M$, $Re_1$ and $Re_2$) and mainstream Mach number at swirler exit ($M_M$); moreover, the multiperforated plates can be characterized by the blowing ratio $BR_i = (\rho_i V_i)/(\rho_M V_M)$ and the momentum flux ratio $I_i = (\rho_i V_i^2)/(\rho_M V_M^2)$. Beside the design point, in order to perform hot wire anemometry measurements, an isothermal operating point (i.e. both mainflow and coolant at room temperature) has been defined. Such process has been accurately described in [18]. Table 1 summarize the operating conditions, in terms of control parameters, to be set during the test, and of some non-dimensional deriving parameters.

## DATA POSTPROCESSING AND CORRELATION

### Data postprocessing

Since split-fiber probes have been used, each test gives as output two voltages, one for each sensor of the probe; this for each measurements point and for each acquisition time. From these two values, it is possible to evaluate two velocity components in the 3D flow field, or a velocity component and a flow angle.

In order to do so, a calibration has been performed, using a plenum with an orifice; measuring temperature and pressure inside the plenum and ambient pressure it is possible to calculate the isentropic velocity exiting from the plenum, that, thanks to the proper shape and roughness of the orifice, can be considered as the actual exit velocity. Above the orifice each probe has been placed and rotated around its axis in order to investigate different angular positions. In this way the probes have been calibrated relatively to the flow angle that they are supposed to measure (i.e. swirl angle for probe R57 and pitch angle for probe R56), so the calibration velocity is always orthogonal to the wire (with the second flow angle equal to zero).

The performed calibration mesh is made of velocity varying from 10 to 80 m/s, with steps of 5 m/s, and flow angle from -64 to 64° with step of 4°. Voltages have been acquired for 5 seconds, then a mean value has been calculated for each calibration point. The uncertainty related to the calibration velocity is about 3 % (due to the uncertainties of the used temperature and pressure sensors), while, since the traverse system has been used to rotate the probe, the angular positioning has an uncertainty that is lower than 0.2 °.

In general, for all kind of hot wire anemometers, many data processing techniques have been developed. Most of them make use of the concept of an *effective cooling velocity*, defined by Maciel and Gleyzes [19] as the velocity which, if it was normal to the wire, would produce exactly the same wire voltage (same cooling effect) as the actual velocity being measured.

Since the calibration has been performed only for the velocity component orthogonal to the wire, it is necessary to consider such component as the effective cooling velocity, assuming no tangential cooling of the wire. It is, thus, not possible to evaluate a calibration coefficient in order to assess its influence as it is suggested by Persico et al. [20]. According to Maciel and Gleyzes [19] such approximation gives satisfactory results for wire length-to-diameter ratios exceeding 600. Since, with split-fiber probes dimensions, this ratio's value is significantly lower, an error source must be expected. According to datasheets such error, in terms of velocity components, can rise up to 10% for second flow angles above 15°.

Thanks to the calibration process it has been possible to associate each couple of output voltages to a value of flow angle $\alpha$ and to a value of effective cooling velocity $V_{cool}$. Since the heat transfer phenomena are governed by the factor between flow velocity and density, it has been decided to reduce the output voltages referring to $\alpha$ and $\rho V_{cool}$. Fig. 4 shows some calibration curves obtained for probe R57 for fixed $\rho V_{cool}$ values (i.e. for fixed cooling velocity at ambient pressure and temperature) and varying angle $\alpha$.

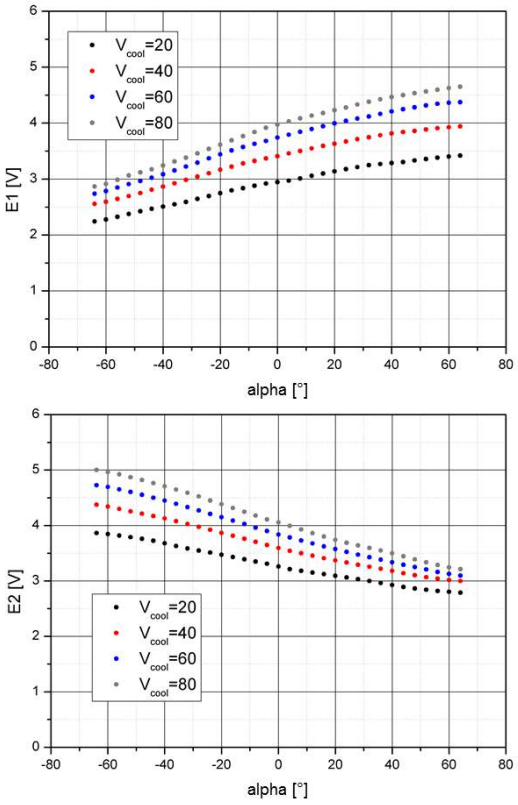


Figure 4: Calibration curves for fixed $\rho V_{cool}$ values for probe R57

For extreme flow angles such curves become flatter; moreover for high negative angles E1 curves for different cooling velocities tend to get closer to each other and the same can be noted for E2 curves for high positive angles. These phenomena indicate a lower sensitivity of the instrument for high flow angles. The amount of scattered data obtained from the calibration has been used to create two interpolating surfaces using a method of neighbour interpolation that is C1 continuous (i.e. continuous first order derivative) except at the scattered data locations.

Fig. 5 depicts the calibration surfaces obtained for probe R57.

It is possible to see that, for a given couple of values $E1$ and $E2$, each surface determines only one value of $\alpha$ or $\rho V_{cool}$. The cooling velocity has been then calculated from $\rho V_{cool}$ using the density values measured by previous tests performed with a five hole probe in isothermal conditions (carried out within the study

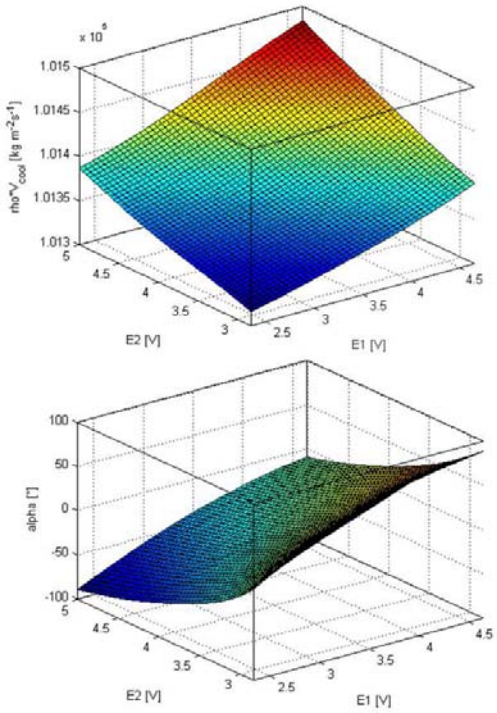


Figure 5: Calibration surfaces obtained for probe R57

presented in [13] even if not shown there).

Once such variables have been found it is possible to calculate the two components of velocity in the plane orthogonal to the probe wire. In particular the relationships are:

$$U_{R56} = V_{cool,R56} cos(\alpha_{R56}) \quad (1a)$$
$$W_{R56} = V_{cool,R56} sin(\alpha_{R56}) \quad (1b)$$
$$U_{R57} = V_{cool,R57} cos(\alpha_{R57}) \quad (1c)$$
$$V_{R57} = V_{cool,R57} sin(\alpha_{R57}) \quad (1d)$$

with $\alpha_{R56}$ corresponding to the pitch angle and $\alpha_{R57}$ to the swirl angle.

In order to verify the data postprocessing method, it has been compared with other methods found in literature, like the one proposed by Ishihara et al. [21], and datasheets that consist in considering the sum $E1+E2$ as a function of only cooling velocity (hypothesis that has been verified within an error of 2%) and the difference $E1-E2$ as a function of both the cooling velocity and the flow angle. Negligible differences have been found between the results obtained using such methods and the adopted one.

## Signals correlation

Once the previous operations have been carried out, two velocity components are available for each probe: in particular, probe R57 gives axial and tangential components, while R56 gives axial and radial ones, in the traverse system reference system. It must be considered, though, that the center of rotation of the azimuthal motion of the traverse system is different from the center of the annular outlet duct of the Sector rig; therefore the radial and tangential directions, in which the velocity components have been evaluated, do not correspond to the rig ones, in which is useful to get the results. In general for given velocity components, in order to obtain such rotation is sufficient to use the following equations:

$$V_{TR} = V_{TS} cos(\theta_{TS} - \theta_{TR}) + W_{TS} sin(\theta_{TS} - \theta_{TR}) \quad (2a)$$
$$W_{TR} = W_{TS} cos(\theta_{TS} - \theta_{TR}) - V_{TS} sin(\theta_{TS} - \theta_{TR}) \quad (2b)$$

The 3D velocity field could be, therefore, calculated combining the results from both the probes. To be noted that, due to the low values of $\theta_{TS} - \theta_{TR}$ (from 0 to 7° going from the sector centerline to the external bounds), the effect of this correction is very limited.

It must be also considered, though, that, such combination must be performed for each measured value in the 5 seconds acquisition span; moreover, it is necessary to find a method to understand how the results obtained from two corresponding tests with the two probes are related in the time domain. For this purpose, it has been decided to use the axial velocity signal, that is measured by both the probes and does not necessitate any correction, since the axial direction remains the same for Trisector and traverse system reference, to "synchronize" the radial and tangential velocity signals.

It is important to note that the two probes do not measure exactly the same axial velocity; figure 6 shows the differences between the measured mean axial velocity expressed in terms of $\frac{\bar{U}_{R56} - \bar{U}_{R57}}{\bar{U}_{R56}}$.

The results from five hole probe measurements, reported in [13], in terms of mean flow field, despite having been found for design point (hot) operating conditions, instead of isothermal ones, are useful, from a qualitative point of view, to understand that the third velocity component effect is at least an important cause of such differences: first of all, for D00, that presents lower flow angles, such relative difference is not so big, since it hardly reaches 5%, while for D55, that has pretty higher flow angles, up to 50°, the difference is bigger than 10%; such values are coherent with the 10% error found in datasheet for high off-axis velocity components. Moreover the maximum differences stay in the spots of the annulus in which the flow angles are expected to be higher.

The adopted method considers the axial velocity signals in

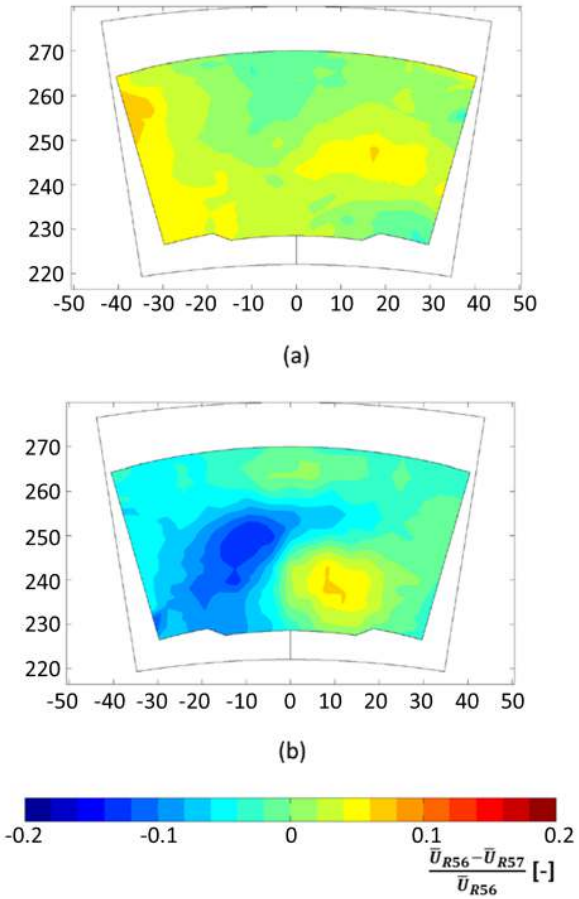


Figure 6: Differences in mean axial velocity measurements between the two probes for (a) D00 and (b) D55

frequency domain and works only on the signals phases; not considering the axial velocity magnitudes allows at least to reduce the just mentioned problem of different measurements.

First of all fast Fourier transform is applied to the time varying axial velocity signals, made of 100000 values in a time span of 5 seconds, of both probes and the respective phases are calculated; it has been thus possible to calculate the difference between such phases as follows:

$$p(f) = phase(U_{R56}(f)) - phase(U_{R57}(f)) \tag{3}$$

which gives an indication on how the signals from the two different probes are related in time.

Then the fast Fourier transform has been applied to tangential and radial velocity signals; magnitudes have been left unaltered, while phases have been combined with $p(f)$ in order to adapt the velocity signals obtained from one probe to the time domain of the other probe. For the adaptation of the radial velocity signal, obtained from probe R56, to the tangential velocity signal obtained from probe R57, the following equations have been used:

$$W_{R56}(f) = fft(W_{R56}(t)) \tag{4a}$$
$$W_{R57}(f) = W_{R56}(f) * (cos(-p(f)) + i * sin(-p(f))) \tag{4b}$$
$$W_{R57}(t) = ifft(W_{R57}(f)) \tag{4c}$$

while the following equations have been used to adapt the tangential velocity signals to the ones obtained from probe R56:

$$V_{R57}(f) = fft(V_{R57}(t)) \tag{5a}$$
$$V_{R56}(f) = V_{R57}(f) * (cos(p(f)) + i * sin(p(f))) \tag{5b}$$
$$V_{R56}(t) = ifft(V_{R56}(f)) \tag{5c}$$

Turbulent velocity signals, like the one considered here, are, in general, characterized by random components; therefore corresponding tests could not be completely repeatable, in terms of frequency spectra, and this phenomenon could affect the utilized timing method. In order to reduce this effect, it has been decided to "smooth" the spectra by averaging the values, both in terms of phases and magnitudes, with steps of 10 Hz. These smoothed signals have been used to calculate the phase shift through eq. 3.

It is worth noting that this method is not exact and brings an uncertainty that cannot be precisely estimated by additional checks, but some useful indications can be drawn by the following analyses. First of all, fig. 7 reports the smoothed frequency spectra, in terms of axial velocity magnitude, for two corresponding tests, in the same measurement point, together with a focus on the low frequencies (i.e. high magnitudes); many measurement positions have been analysed and all of them gave analogous results: it can be noted that, beyond magnitude differences, the two signals present similar treds (i.e. similar spectral content) and therefore these results are encouraging in terms of test repeatability.

Then, in order to evaluate the global effect of the method, it has been applied to axial velocity, measured by both probes. The black and the blue lines in fig. 8 shows the axial velocities measured by the probes in a 0.01 seconds time span in one point of the section, both for D00 and D55. It is possible to see that the two signals are not phased to each other. Then the method has been applied in order to modify the signals from probe R57 and put it in phase with the other, using equivalent relationships to eq. 5. The red lines show the new trends, from which it can be seen that, beyond some differences related to the amplitudes, the timing between the signals is now satisfactory.

Using both eq. 4 and 5, at the end of the process, two sets of three components of velocity are available; such components

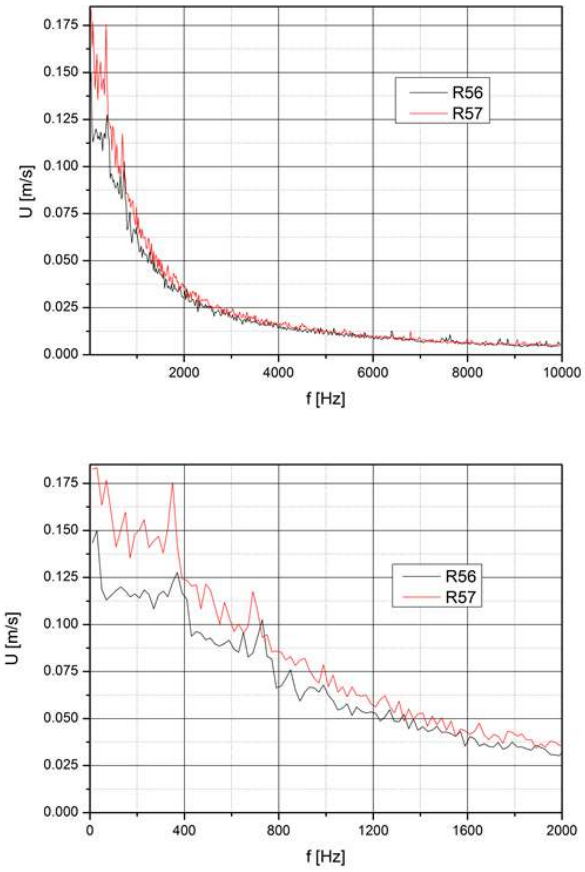


Figure 7: Axial velocity smoothed spectra: full scale and focus on low frequencies

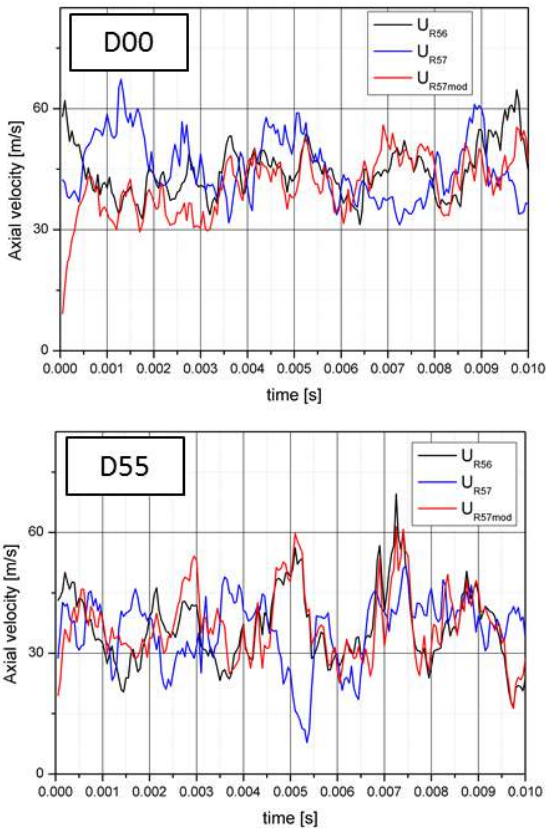


Figure 8: Axial velocity signals before and after timing method application

can now be combined point by point using eq. 2 in order to obtain the desired radial and tangential components, in Trisector rig reference system. These sets differ, in general, because of the differences in the calculated axial velocities; results, in terms of flow angles or turbulence parameters, have been calculated for both sets and then a mean has been made. In order to take into account the problem of the third velocity component, that alter probes' measurements, such mean has been weighted using the flow angles measured in traverse system reference coordinates. If one flow angle is bigger, the biggest weight has been given to the probes that measure that angle; so in the points of the section in which swirl is bigger than pitch, results obtained from probe R57 have a bigger weight than the others and vice versa. The used equations, for a generic measured variable $A$ are reported below:

$$Weight_1 = \frac{swirl_{TS}}{swirl_{TS} + pitch_{TS}} \tag{6a}$$

$$Weight_2 = \frac{pitch_{TS}}{swirl_{TS} + pitch_{TS}} = 1 - Weight_1 \tag{6b}$$

$$A_{final} = A_{R57} * Weight_1 + A_{R56} * Weight_2 \tag{6c}$$

## EXPERIMENTAL RESULTS AND DISCUSSION

Before analysing the obtained results, it is useful to remind the most important problems related to the use of hot wire anemometry in a complex 3D flow like the measured one:

1. Third velocity component sensitivity
2. Flat calibration curve for high flow angles

Despite the second issues is quite marginal due to the high accuracy in angular positioning achieved during the calibration process, it must be kept in mind that the five hole probe, used in [13] to evaluate the mean flow field, is a more reliable instrument,

more adapt to the investigation of three-dimensional flow fields. On the other hand, though, the use of HWA is compulsory in order to characterize the flow unsteady aspect, due to the not sufficient frequency response of the five hole probe.

### Turbulence intensity

Calling $U_{RMS}$, $V_{RMS}$ and $W_{RMS}$ the root mean square deviations calculated for the three components of velocity over the 100000 acquired points and $V_{abs}$ the absolute velocity, calculated by the three components ($V_{abs_i} = \sqrt{U_i^2 + V_i^2 + W_i^2}$ with i, going from 1 to 100000, indicating the time-marching signal), the turbulence intensity has been evaluated, for each point of the measurement mesh, using the following equation:

$$Tu = \frac{\sqrt{\frac{1}{3}(U_{RMS}^2 + V_{RMS}^2 + W_{RMS}^2)}}{\bar{V_{abs}}} \tag{7}$$

with the root-mean-square values calculated as follows:

$$U_{RMS} = \sqrt{\frac{\sum_{i=1}^{100000}(U_i - \bar{U})^2}{100000}} \tag{8}$$

In order to verify that the acquisition frequency is high enough and that the energy content of the cut frequencies does not influence the calculation of Tu, results have been evaluated both for $f_{acq} = 20kHz$ and $f_{acq} = 10kHz$ (simply considering one acquired point over two). Since the results do not differ it has been concluded that the frequency acquisition of 20 kHz is sufficient for this dissertation. Only the results calculated at 20 kHz are shown here, while a full analysis of the effect of the acquisition frequency, regarding turbulence timescales, is reported in [14].

Figure 9 shows the 2D maps for the three configurations both on Plane 40 and Plane 40+.

The ducted configurations show a similar behaviour: the maximum turbulence intensity is reached in the center of the vortex core, that, as shown in [13], is slightly moved towards right, and can be assessed between 25 and 28% on Plane 40; these levels are comparable with what found in past studies on different combustor architectures. The distribution of Tu on the annulus section is not much different from what found by Cha et al. [11] for RQL combustors but the peak values are about 25 % lower. This difference can be ascribed to the different flow field evolution inside the two types of combustors: while in RQL combustors the maximum intensity level is reached near midspan due to the unstable collisions of the opposed, highly penetrating dilution jet flows [11], in Lean Burn chambers this effect is not present, due to the much lower penetration of the effusion cooling jets that form cold layers bounded near the wall; the measured profile is characteristic of strong swirling flow instead, in that turbulence intensity is greatest towards the core [12]. In D55 configuration, for which the distance between the measurement plane and the axial position at which the mainflow exits from the ducts and the vortex dissipation begins, due to the interaction with coolant, is a little bit lower than in D45, the turbulence intensity is slightly higher.

On the other hand, for D00 configuration, the maximum Tu is reached in thin strip zone covering almost the whole midspan, but, since the vortex is almost completely dissipated, its value hardly reaches 18%. The vortex dissipation makes this configuration not satisfying to represents Lean Burn combustors behaviour.

The shape of the probe does not allow to explore the spots of the section close to the inner and the outer walls. Therefore it is not possible to evaluate if, in such positions, the turbulence intensity is partially increased by the interaction between mainflow and coolant, or the distance between the measurement plane and the last rows of effusion holes is sufficient to significantly damp this effect.

Moving the focus on Plane 40+, it is possible to see that the turbulence field morphology remains the same but its values are smaller, due to the effect of the shear stresses between the measurement planes. Such reduction, in the vortex core, can be

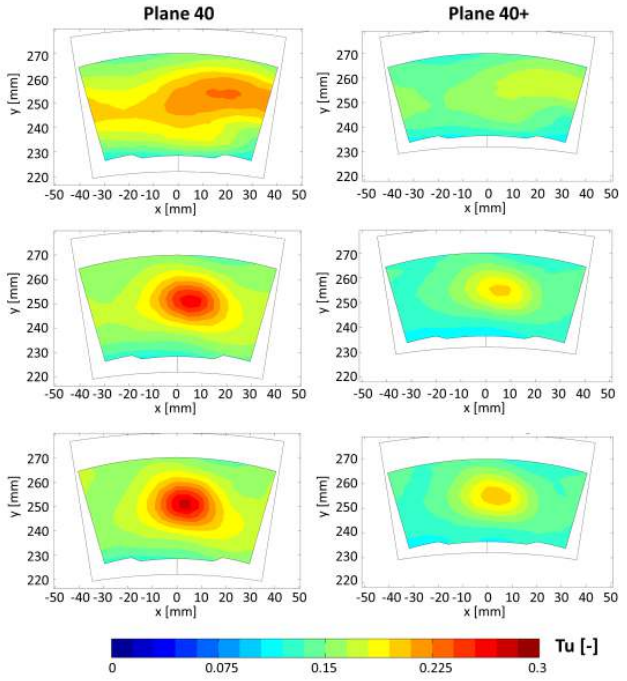


Figure 9: Turbulence intensity 2D maps

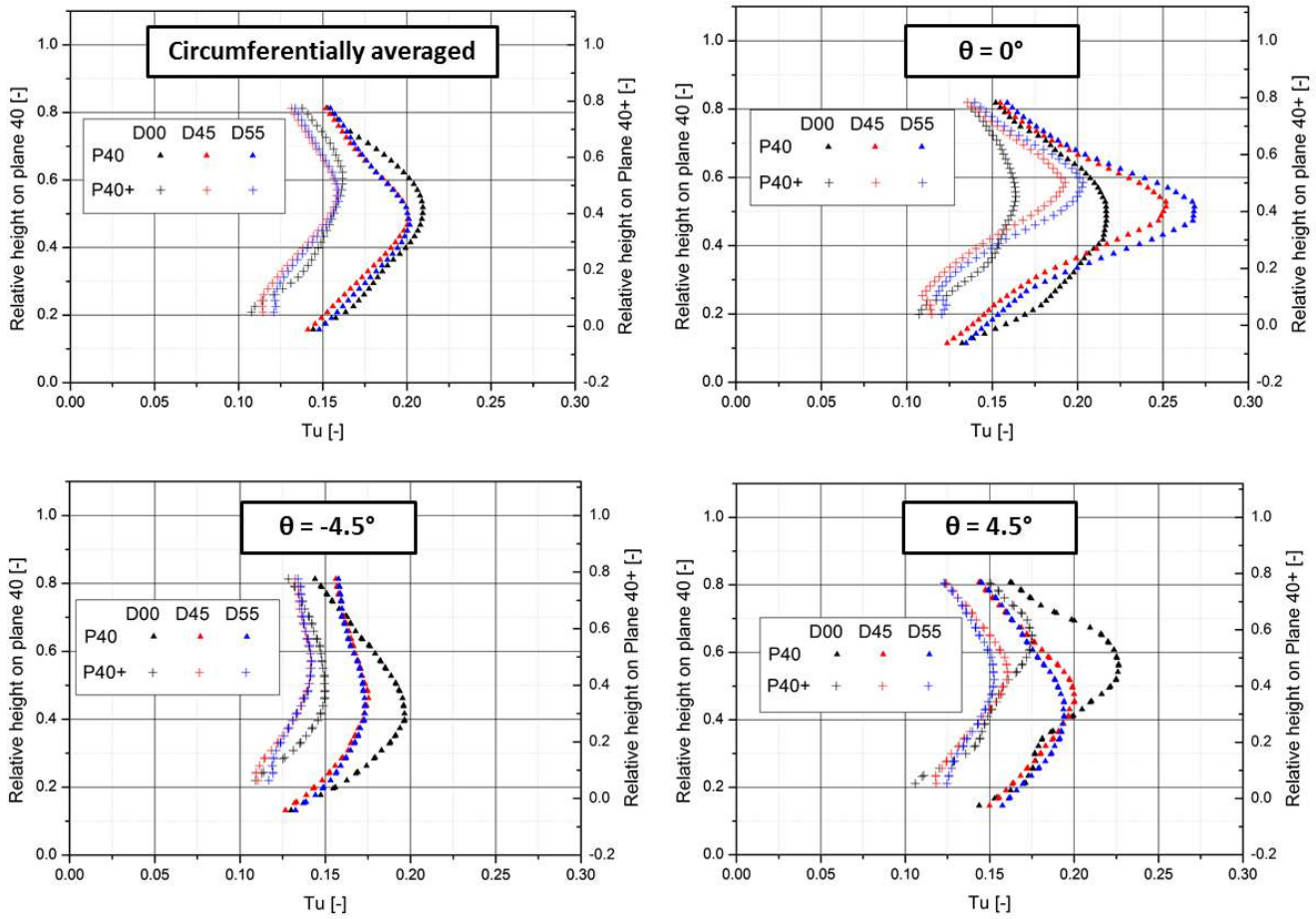


Figure 10: Turbulence intensity radial profiles

evaluated between 25 and 30% of Plane 40 values for all the configurations.

It must be reminded that, while turbulence intensity is highly influenced by the flow field evolution and, in this case, by the vortex structure, it should not be significantly affected by the presence of combustion [2, 22]; therefore this results can be considered a good estimation of the values achieved at the exit of this typology of combustors.

In order to have a more precise description, the radial profiles of such parameter have been evaluated and shown in fig. 10. Such profiles have been calculated on the centerline of the section, thus for azimut angle $\theta = 0°$ and for $\theta = -4.5$ and $4.5°$, possible virtual positions of the NGV leading edges; other profiles have been obtained by making a tangential mean of the results for varying radial position.

The profiles confirm the conclusions taken from the observation of the 2D maps. It is interesting to see that the entity of turbulence intensity reduction between Plane 40 and Plane 40+, in relative terms, is variable in radial direction since at the lowest and highest investigated radii such reduction is smaller (10-15%) than in the vortex core. It is also possible to see that for D00 the turbulence profile, calculated on the centerline on Plane 40+, is quite flat, while for the ducted configurations it is still possible to note a clear point of maximum, that is moved towards higher radii, since the shape of the annulus (as shown in fig. 3) tends to push the vortex in this direction.

## Uncertainty evaluation

In this section the propagation of measurement uncertainty up to the final results is described. It must be kept in mind, however, that it is not possible to reach an exact formulation due to two main reason:

1. it is not possible, due to calibration constrains, to experimentally evaluate the errors introduced by the off-axis velocity. The only available information (from datasheet) has been

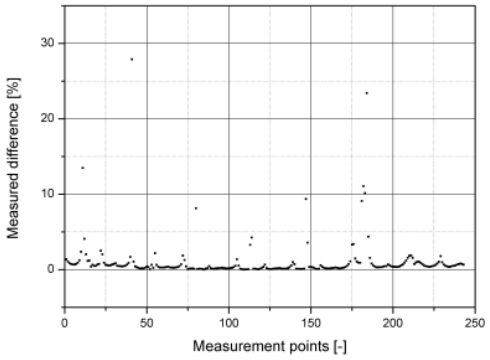


Figure 11: Differences between mean tangential velocity measured by 5HP and HWA (R57)

used, even it is not very accurate

2. the uncertainty introduced by the timing method cannot be estimated; since its effect is quite limited, due to the low values of $\theta_{TS} - \theta_{TR}$ (see eq. 2), it has been neglected in this dissertation

A partial verification of the magnitude order of the first error has been conducted by comparing the mean tangential velocity components measured by the R57 probe ($\bar{V_{R57}}$) over a whole measurement mesh, to the ones evaluated with the five hole probe, converted in TS coordinate system to make the comparison. Fig. 11 shows that the difference, expressed in terms of $\frac{|\bar{V_{R57}} - \bar{V_{5HP}}|}{\bar{V_{5HP}}}$, stays well under 10%, as suggested by datasheet, except for a few points. A similar procedure has been conducted for probe R56, with analogous results.

Table 2 shows the uncertainties progressively found in the following stages of the calculation of *Tu*; contributions related to systematic errors (*bias*), due to the off-axis velocity, and from casual ones have been reported separately. Kline and McClintock method [23] has been used.

The initial sources of uncertainty, beside the off-axis velocity, are caused by calibration (due to the uncertainty of the sensors used to measure the velocity of the calibration jet) and by the correction made using the density values measured by the five hole probe (due to not perfect pressure an temperature repeatability between different tests).

Concerning RMS values, the effect of systematic errors on them has been neglected. This assumption has been verified, for all the measurement points and for every test, by considering a linear trend for these errors, on the instantaneous velocity, with the off-axis flow angle (in TS coordinates). The linear trend does not corresponds to the physical behaviour but it is conservative since it assigns a bigger weigh to the highest flow angles. Errors of 0% and 10% for flow angles of 0 and 15 ° have been assigned. The differences in terms of RMS values, compared to the case with no errors considered, stay within 0.2 % in 95 % of the evaluated points.

At the end of the process an uncertainty of about 12 % has been found. As anticipated in a previous section, the highlighted problems related to the use of HWA do not allow to reach high accuracies, but the instrument is very useful to provide at least a good estimation of the turbulence field.

### Turbulence spectra

After the evaluation of turbulence intensity, that gives an idea of the root-mean-square deviation of instantaneous velocity from its mean value and, thus, of the mean kinetic energy per unit mass associated with the turbulent flow eddies, it is interesting to analyse how such energy is distributed among all the frequencies.

To do so the fast Fourier transform has been applied to the three velocity components, finding their frequency spectra on a discrete number of frequencies from 0 to 10000 Hz. Then the turbulence kinetic energy, for every frequency, has been calculated:

$$K(f_j) = \frac{1}{2}(U(f_j)^2 + V(f_j)^2 + W(f_j)^2) \tag{9}$$

where $f_j$ is a frequency value between 0 and 10000 with a resolution of 0.2Hz.

The frequency spectra, depicted in figure 12 for one point of the section for D00 and D55, have been averaged on steps of 10Hz in order to have a clear view of their trend. The variable

| Sources | Equations | Results | Casual [%] | Bias [%] | Total Uncertainty [%] | Confidence [%] |
|---|---|---|---|---|---|---|
| Off axis velocity (10%), Calibration (3%), Density correction (3%) | Calibration + eq. 1 | Instantaneous velocity (TS coordinates) | 4.2 | 10 | 10.9 | 95 |
| Instantaneous velocity (TS coordinates) | Eq. 2 | Instantaneous velocity (TR coordinates) | 4.2 | 10 | 10.9 | 95 |
| Instantaneous velocity (TR coordinates) | Simple averaging equation | Mean Velocity | 4.2 | 10 | 10.9 | 95 |
| Instantaneous velocity (TR coordinates) | Eq. 8 | RMS value | 4.2 | 0 | 4.2 | 95 |
| **Mean velocity + RMS value** | **Eq. 7** | **Tu** | **6** | **10** | **11.8** | **95** |

Table 2: Uncertainty propagation for Tu calculation

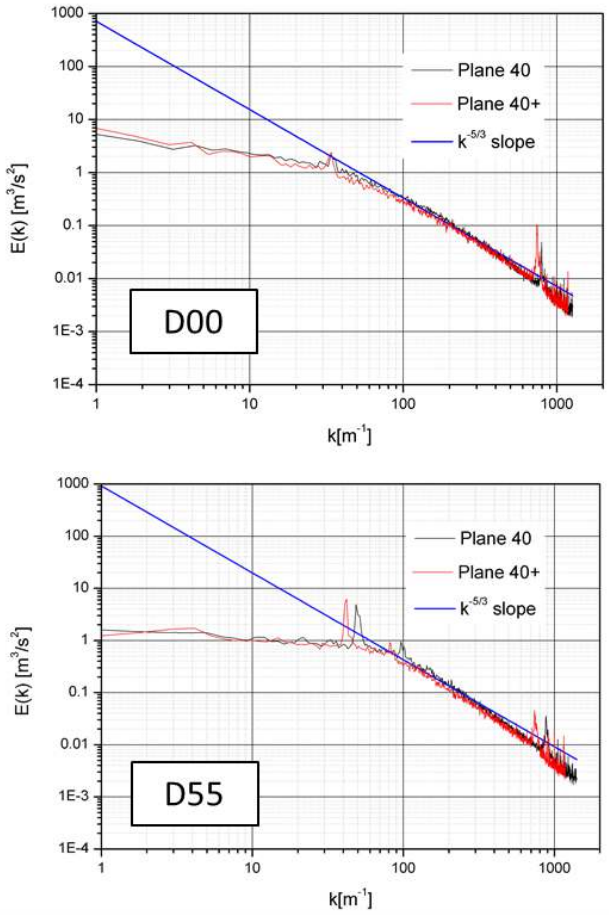


Figure 12: Turbulent kinetic energy spectra

on the x-axis is the wave number, calculated as $k_j = \frac{2\pi f_j}{\bar{V}_{abs}}$, while on the y-axis there is $E(k_j) = \frac{K(k_j)}{dk}$, where $dk$ is the resolution step on the wave number axis. With such visualization the area under the curve between two wave numbers $k_1$ and $k_2$ represents the turbulent kinetic energy $K$ content of the flow within such wave numbers, that are inversely proportional to the size of the turbulent eddies in the flow.

The spectra depicted in the figure are evaluated for only one point of the measurement mesh on Plane 40 and for the correspondent one (i.e. same tangential position and same relative height) on Plane 40+. It is possible to see the typical trend of the turbulence spectra, with amplitude decreasing for increasing frequency [7, 11]. A curve with slope $k^{-5/3}$ has been also plotted in order to compare the measured trend with the one obtained using Kolmogorov hypothesis [24]. The matching is quite good for the central range of frequencies that can, thus, be assessed as the inertial sub-range. For wave numbers of $6-700\ m^{-1}$ the measured spectra start to significantly separate from the Kolmogorov

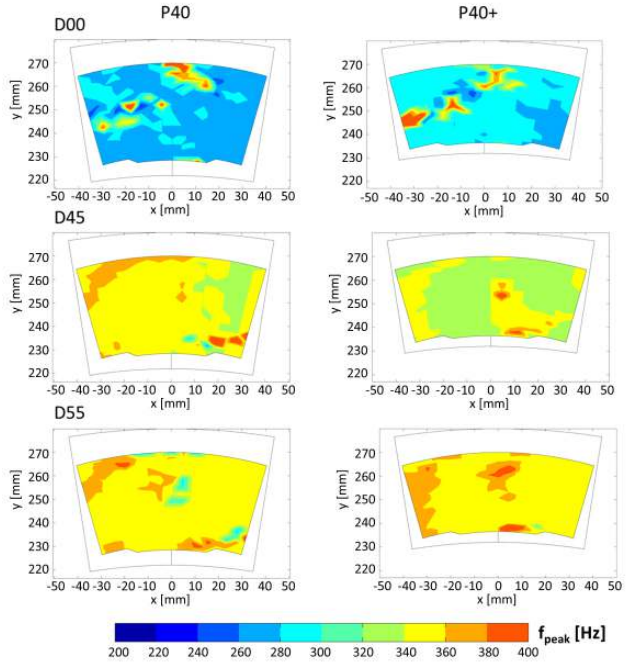


Figure 13: Peak frequencies 2D maps

trend, indicating the beginning of the effect of viscosity.

It can be noted that the spectra measured on Plane 40 and on Plane 40+ show a similar trend. For D55 configuration, both trends present a peak with similar amplitude and for similar wave numbers (between 30 and 50 $m^{-1}$). It is also possible to note a second and less marked peak, relative to a second harmonic, at wave numbers of about 100 $m^{-1}$ for both planes. For D00 a similar behaviour can be recognized even if the peaks are much less evident and no second harmonics are visible. Such study has been repeated for several points of the measurement mesh for all the three configurations and all the measured trends result quite similar in qualitative terms. In order to have a brief description of such trends on the whole section it has been decided to evaluate the peak frequency for every point of the mesh. The following procedure has been applied:

1. Evaluation of a third order polynomial that best approximates the spectrum curve by the method of least squares, in the frequencies interval in which the peak is expected
2. Subtraction of such polynomial to the spectrum curve
3. Evaluation of the point of maximum of the calculated curve

The procedure has been monitored for various measurement points and seemed to give good results. Fig. 13 depicts the peak frequencies 2D maps calculated in this way.

For all the configurations and measurement plane the peak frequency is quite homogeneous on the whole section, beyond

some spots that indicate peak frequencies that are quite different from the ”diffused” value. Such points have been investigated deeply and it has been found that this value are only caused by the fact that the method does not work well since the peak is not well marked. To confirm this conclusion it is worth noting that such deviating spots are more evident for D00, where the peaks are smoothed, as described above.

Figure 13 shows a similar behaviour for the ducted configurations, with peak frequencies of about 350 Hz on Plane 40. For D00 these values are lower and can be assessed around 280 Hz. On Plane 40+ everything is very similar with differences that are more important for D00 configuration but do not overcome 3% of the values measured on Plane 40.

Numerical results from Large Eddy Simulations presented in Koupper et al. [14] have been used to make comparisons and to reach a physical understanding of the measured spectra. The results just presented have been compared to the ones obtained by a LES performed on D55 for design point conditions. Details of such simulation characteristics can be found in [14]. In particular the numerical signal from LES is taken from a virtual probe inside the duct. Fig. 14 depicts this signal compared to the one obtained from D55 test with HWA in the point of the measurement mesh on Plane 40 previously used in fig. 12. LES signals has a frequency resolution of 13.6 Hz, due to the limited acquisition time, so HWA signal has been averaged with analogous frequency step. Since an isothermal test and a design point simulation are compared it is necessary to use Strouhal number, defined as:

$$St = \frac{fD_{sw}}{U_{ref}}$$

where $U_{ref}$ is the mean axial velocity at swirler exit, obtained by LES. Koupper et al. [18] found that Strouhal scaling in order to compare such different operating conditions gave good results.

It is possible to see that, despite the different position of the probes, the signals present similar characteristics. In particular both first and second harmonics are found for very similar Strouhal numbers with values of 0.55 and 1.1 respectively.

Thanks to this comparison it has been concluded that is quite likely that the peak frequency measured on Plane 40 is the PVC frequency, since it corresponds to the one evaluated in the duct by LES simulation. Regarding the PVC, as described above, it must be kept in mind that significant differences can be found if comparing this behaviour to the real combustors one. In particular the effect of the combustion process is to significantly damp the phenomenon [12], that has, therefore, a less important influence on the evolution of the flow field.

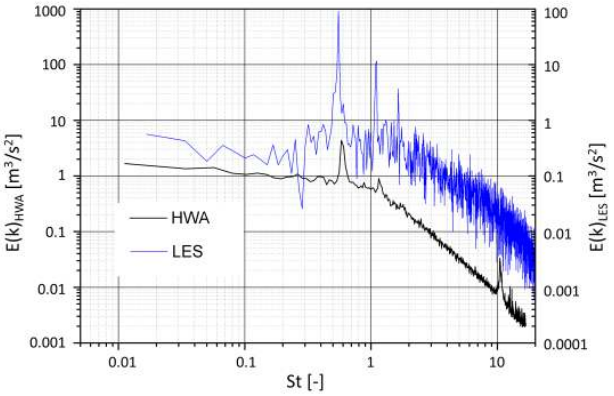


Figure 14: LES-HWA spectra comparison

## CONCLUSIONS

In this paper an experimental campaign conducted on a non reactive lean burn combustor simulator by means of hot wire anemometry has been presented. Two split-fiber probes have been used to evaluate the three-dimensional flow field, in isothermal conditions, at combustor exit on two measurement planes, called Plane 40 and Plane 40+, for three different configurations: one without ducts mounted on the swirlers and two with ducts of 45 and 55 mm. In order to reconstruct the 3D flow field varying in time it has been necessary to combine the results obtained by both the probes for corresponding operating points; a method to correlate the results from different tests in time domain, based on axial velocity signal, that is measured by both the probes, has been used.

Turbulence intensity has been evaluated, showing that, for the ducted configurations, the highest values, up to 28 %, are reached in the rotating core generated by the swirlers that is conserved up to the measurement planes; this is a typical behaviour of the swirl-dominated flow fields, like the ones encountered in Lean Burn chambers. For the unducted configuration, such values are slightly lower since the vortex is almost completely dissipated, due to the enhanced interaction between mainflow and coolant caused by the absence of the duct; much lower fidelity to Lean Burn combustors behaviour must be recognized for this configuration. Reduction of 25-30% of these values can be observed for all the configurations moving from Plane 40 to Plane 40+.

Due to some problems, mainly related to calibration constrains, it has not been possible to reach high accuracies, but the obtained data forms an experimental database providing a good estimation of the turbulence intensities reached at the exit of this kind of combustors.

Turbulence spectra have, then, been evaluated, for some

points of the measurement section, showing the typical behaviour of turbulent flows. For the ducted configurations two well-marked peak frequencies can be recognized; for the unducted configuration only the first, far less marked, can be individuated. The first peak frequency have been evaluated on the whole section: on Plane 40 values of about 350 and 280 Hz have been calculated respectively for both ducted configurations and for the unducted one. Moving on Plane 40+, differences within 3% have been found. A comparison with a numerical signal from LES simulations taken from a probe inside one duct has shown that such peak frequency is likely to correspond to the PVC frequency.

## ACKNOWLEDGMENT

The authors wish to gratefully acknowledge FACTOR (Full Aerothermal Combustor-Turbine interactiOns Research) Consortium for the kind permission of publishing the results herein. FACTOR is a Collaborative Project co-funded by the European Commission within the Seventh Framework Programme (2010-2016) under the Grant Agreement n° 265985.

## REFERENCES

[1] Povey, T. and Qureshi, I. Developments in hot-streak simulators for turbine testing. *ASME J. Turbomach.*, 131(3):031009–031009, 2009. ISSN 0889-504X.

[2] Zimmermann, D.R. Laser anemometer measurements at the exit of a t63-c20 combustor. *NASA Report No. CR-159623*, 1979.

[3] Fossen, G.J. Van and Bunker, R.S. Augmentation of stagnation heat transfer due to turbulence from a dln can combustor. *ASME J. Turbomach.*, 123:140–146, 2001.

[4] Ames, F.E. Experimental study of vane heat transfer and aerodynamics at elevated levels of turbulence. *NASA Contractor's Report 4633*, 1994.

[5] Ames, F. E. The influence of large-scale high-intensity turbulence on vane heat transfer. *ASME J. Turbomach.*, 119(1):23–30, 1997. ISSN 0889-504X.

[6] Nasir, S., Carullo, J. S., Ng, W.-F., Thole, K. A., Wu, H., Zhang, L. J., and Moon, H. K. Effects of large scale high freestream turbulence and exit reynolds number on turbine vane heat transfer in a transonic cascade. *ASME J. Turbomach.*, 131(2): 021021–021021, 2009. ISSN 0889-504X.

[7] Nix, A.C., Smith, A.C., Diller, T.E., Ng, W.F., and Thole, K.A. High intensity, large length-scale freestream turbulence generation in a transonic turbine cascade. *Proc. ASME Turbo Expo*, (GT-2002-30523), 2002.

[8] Radomsky, R. W. and Thole, K. A. Flowfield measurements for a highly turbulent flow in a stator vane passage. *ASME J. Turbomach.*, 122(2):255–262, 1999. ISSN 0889-504X.

[9] Jenkins, S., Varadarajan, K., and Bogard, D. G. The effects of high mainstream turbulence and turbine vane film cooling on the dispersion of a simulated hot streak. *ASME J. Turbomach.*, 126 (1):203–211, 2004. ISSN 0889-504X.

[10] Jenkins, S. C. and Bogard, D. G. The effects of the vane and mainstream turbulence level on hot streak attenuation. *ASME J. Turbomach.*, 127(1):215–221, 2005. ISSN 0889-504X.

[11] Cha, C.M., Ireland, P.T., Denman, P.A., and Savarianandam, V. Turbulence levels are high at the combustor-turbine interface. *Proc. ASME Turbo Expo*, (GT2012-69130), 2012.

[12] Hall, B. F., Chana, K. S., and Povey, T. Design of a non reacting combustor simulator with swirl and temperature distortion with experimental validation. *Proc. ASME Turbo Expo: Turbine Technical Conference and Exposition*, (GT2013-95499), 2013.

[13] Bacci, T., Caciolli, G., Facchini, B., Tarchi, L., Koupper, C., and Champion, J.L. Flowfield and temperature profiles of a combustor simulator dedicated to hot streaks generation. *Proc. ASME Turbo Expo*, (GT2015-42217), 2015.

[14] Koupper, C., Bonneau, G., Bacci, T., Facchini, B., Tarchi, L., Gicquel, L., and Duchaine, F. Experimental and numerical calculation of turbulent timescales at the exit of an engine representative combustor simulator. *Proc. ASME Turbo Expo*, (GT2015-42278), 2015.

[15] Andreini, A., Facchini, B., Insinna, M., Mazzei, L., and Salvadori, S. Numerical investigation of combustor-turbine interaction with hybrid rans-les models. *Proc. ASME Turbo Expo*, (GT2015-42402), 2015.

[16] Andreini, A., Caciolli, G., Facchini, B., Picchi, A., and Turrini, F. Experimental investigation of the flow field and the heat transfer on a scaled cooled combustor liner with realistic swirling flow generated by a lean-burn injection system. *ASME J. Turbomach.*, 137 (3):031012–031012, 2014.

[17] Wurm, B., Schulz, A., Bauer, H.-J., and Gerendas, M. Impact of swirl flow on the cooling performance of an effusion cooled combustor liner. *Proc. ASME Turbo Expo*, (GT2012-68972), 2012.

[18] Koupper, C., Caciolli, G., Gicquel, L., Duchaine, F., Bonneau, G., Tarchi, L., and Facchini, B. Development of an engine representative combustor simulator dedicated to hot streak generation. *ASME J. Turbomach.*, 136(11):111007–111007, 2014. ISSN 0889-504X.

[19] Maciel, Y. and Gleyzes, C. Survey of multi-wire probe data processing techniques and efficient processing of four-wire probe velocity measurements in turbulent flows. *Experiments in fluid*, (66-78), 2000.

[20] Persico, G., Dossena, V., and Gaetani, P. On the capability of fast response total pressure probes to measure turbulence kinetic energy. *XX Biannual Symposium on Measuring Techniques in Turbomachinery Transonic and Supersonic Flow in Cascades and Turbomachines*, 2010.

[21] Ishihara, T., Hibi, K., and Oikawa, S. A wind tunnel study of turbulent flow over a three-dimensional steep hill. *Journal of Wind Engineering and Industrial Aerodynamics*, (95-107), 1999.

[22] Moss, R.W. and Oldfield, M.L.G. Measurements of hot combustor turbulence spectra. *Proc. ASME Turbo Expo*, (91-GT-351), 1991.

[23] Kline, S. J. and McClintock, F. A. Describing uncertainties in single sample experiments. *Mechanical Engineering*, 1953.

[24] Pope, S.B. *Turbulent Flows*. Cambridge Univeristy Press, 2000.

# Bibliography


[1] *The Jet Engine*. 5th edition. Rolls Royce Technical Publications, 2005.

[2] A. G. Barker and J. F. Carrotte. "Influence of Compressor Exit Conditions on Combustor Annular Diffusers, Part 1: Diffuser Performance". In: *Journal of Propulsion and Power* 17.3 (2001), pp. 678–686.

[3] A. G. Barker and J. F. Carrotte. "Influence of Compressor Exit Conditions on Combustor Annular Diffusers Part II: Flow Redistribution". In: *Journal of Propulsion and Power* 17.3 (2001), pp. 687–694.

[4] A. Duncan Walker, Jon F. Carrotte, and James J. McGuirk. "Compressor/Diffuser/Combustor Aerodynamic Interactions in Lean Module Combustors". In: *Journal of Engineering for Gas Turbines and Power* 130.1 (Jan. 2008), pp. 011504–011504.

[5] C. L. Ford, J. F. Carrotte, and A. D. Walker. "The Impact of Compressor Exit Conditions on Fuel Injector Flows". In: *Journal of Engineering for Gas Turbines and Power* 134.11 (Sept. 2012), pp. 111504–111504.

[6] A. Walker, Peacock L. Graham, Jon F. Carrotte, Adrian Spencer, and James J. McGuirk. "Experimental Study of the Unsteady Aerodynamics the Compressor-Combustor Interface of a Lean Burn Combustion System". In: *49th AIAA/ASME/SAE/ASEE Joint Propulsion Conference*. American Institute of Aeronautics and Astronautics, 2013.

[7] G. L. Cox. "Predicting Exit Temperature Profile from Gas Turbine Combustors". In: *Journal of Aircraft* 13.8 (1976), pp. 630–636.

[8] *General Electric TAPS 2 Combustor Final Report*. Tech. rep. U.S. Department of Transportation - Federal Aviation Administration, 2014.

[9] M. Cazalens and J.P.A.J. van Beeck. *Combustion in aero-engines*. Tech. rep. von Karman Institute for Fluid Dynamics, 2012.

[10] J. Tu, G.H. Yeoh, and C. Liu. *Computational Fluid Dynamics: A Practical Approach*. Elsevier Science, 2007.

[11] V. Gravemeier. "The variational multiscale method for laminar and turbulent incompressible flow". PhD thesis. Institute of Structural Mechanics, University of Stuttgart, 2003.

[12] J. Blazek. *Computational Fluid Dynamics: Principles and Applications: Principles and Applications*. Elsevier Science, 2001.

[13] S.B. Pope. *Turbulent Flows*. Cambridge: Cambridge University Press, 2000.

[14] P. Sagaut and Cambon C. *Homogeneous Turbulence Dynamics*. Cambridge University Press, 2008.

[15] P. Moin and K. Mahesh. "Direct Numerical Simulation: A Tool in Turbulence Research". In: *Annual Review of Fluid Mechanics* 30.1 (1998), pp. 539–578.

[16] K. Mahesh, G. Constantinescu, S. Apte, G. Iaccarino, and P. Moin. "Large-eddy simulation of gas turbine combustors". In: *Annual Research Briefs*. Center for Turbulence Research, NASA Ames/Stanford Univ., 2001, pp. 3–17.

[17] K. Mahesh, G. Constantinescu, S. Apte, G. Iaccarino, F. Ham, and P. Moin. "Large eddy simulation of reacting turbulent flows in complex geometries". In: *ASME Journal of Applied Mechanics* 73 (2006), pp. 374–381.

[18] P. G. Tucker and S. Lardeau. "Applied large eddy simulation." In: *Philosophical Transactions of the Royal Society A: Mathematical, Physical and Engineering Sciences* 367.1899 (2009), pp. 2809–2818.

[19] L. Y. M. Gicquel, N. Gourdain, J.-F. Boussuge, H. Deniau, G. Staffelbach, P. Wolf, and T. Poinsot. "High performance parallel computing of flows in complex geometries". In: *Comptes Rendus de l'Académie des Sciences - Mathématiques* 339 (2011), pp. 104–124.

[20] L. Y. M. Gicquel, G. Staffelbach, and T. J. Poinsot. "Large Eddy Simualtions of gaseous flames in gas turbine combustion chambers". In: *Progress in Energy and Combustion Science* 38 (2012), pp. 782–817.

[21] C. Koupper, G. Caciolli, L. Gicquel, F. Duchaine, G. Bonneau, L. Tarchi, and B. Facchini. "Development of an Engine Representative Combustor Simulator Dedicated to Hot Streak Generation". In: *Journal of Turbomachinery* 136.11 (2014).

[22] C. Koupper, T. Poinsot, L. Gicquel, and F. Duchaine. "Compatibility of Characteristic Boundary Conditions with Radial Equilibrium in Turbomachinery Simulations". In: *AIAA Journal* 52.12 (2014), pp. 2829–2839.

[23] C. Koupper, L. Gicquel, F. Duchaine, T. Bacci, B. Facchini, A. Picchi, L. Tarchi, and G. Bonneau. "Experimental and Numerical Calculation of Turbulent Timescales at the Exit of an Engine Representative Combustor Simulator". In: *ASME Turbo Expo 2015: Turbine Technical Conference and Exposition*. GT2015-42278. 2015.

[24] C. Koupper, L. Gicquel, F. Duchaine, and G. Bonneau. "Advanced Combustor Exit Plane Temperature Diagnostics Based on Large Eddy Simulations". English. In: *Flow, Turbulence and Combustion* (2015), pp. 1–18.

[25] T. Bacci, G. Caciolli, B. Facchini, L. Tarchi, C. Koupper, and J.-L. Champion. "Flowfield and temperature profiles measurements on a combustor simulator dedicated to hot streaks generation". In: *ASME Turbo Expo 2015: Turbine Technical Conference and Exposition*. GT2015-42217. 2015.

[26] T. Bacci, B. Facchini, A. Picchi, L. Tarchi, C. Koupper, and J.-L. Champion. "Turbulence field measurements at the exit of a combustor simulator dedicated to hot streaks generation". In: *ASME Turbo Expo 2015: Turbine Technical Conference and Exposition*. GT2015-42218. 2015.

[27] E.V. Klapdor. "Simulation of combustor - turbine interaction in a jet engine". PhD thesis. Technischen Universität Darmstadt, 2010.

[28] D. Papadogiannis. "Integrated simulations of a coupled combustor - high pressure turbine system." PhD thesis. Université de Toulouse - MeGeP - Dynamique des Fluides, 2015.

[29] T. Povey and I. Qureshi. "Developments in hot-streak simulators for turbine testing". In: *Journal of Turbomachinery* 131.3 (2009), pp. 1–15.

[30] P. T. Ireland and G. Dailey. "Aerothermal performance of internal cooling systems in turbomachines." In: *Internal Cooling in Turbomachinery, VKI Lecture Series*. Vol. 2010-05. 2010.

[31] R. Fransen. "LES based aerothermal modeling of turbine blade cooling systems". PhD thesis. Université de Toulouse - MeGeP - Dynamique des Fluides, 2013.

[32] M. D. Barringer, K. A. Thole, and M. D. Polanka. "Experimental evaluation of an inlet profile generator for high-pressure turbine tests". In: *Journal of Turbomachinery* 129.2 (2007), pp. 382–394.

[33] M. D. Barringer, K. A. Thole, and M. D. Polanka. "Effects of combustor exit profiles on vane aerodynamic loading and heat transfer in a high pressure turbine". In: *Journal of Turbomachinery* 131.2 (2009), pp. 1–10.

[34] M. D. Barringer, K. A. Thole, and M. D. Polanka. "An experimental study of combustor exit profile shapes on endwall heat transfer in high pressure turbine vanes". In: *Journal of Turbomachinery* 131.2 (2009), pp. 1–10.

[35] M. D. Barringer, K. A. Thole, M. D. Polanka, J. P. Clark, and P. J. Koch. "Migration of combustor exit profiles through high pressure turbine vanes". In: *Journal of Turbomachinery* 131.2 (2009), pp. 1–10.

[36] T. E. Dyson, D. B. Helmer, and J. A. Tallman. "Large-Scale Simulation of the Clocking Impact of 2D Combustor Profile on a Two Stage High Pressure Turbine". In: *ASME Turbo Expo 2014: Turbine Technical Conference and Exposition*. GT2014-25883. 2014.

[37] K. Mollahosseini, F. Borns, P. Couey, J.-C. Bonaccorsi, and A. Demeulenaere. "3D unsteady multi-stage cfd analysis of combustor-turbine hot streak migration". In: *ASME Turbo Expo 2014: Turbine Technical Conference and Exposition*. Ed. by ASME. GT2014-25963. ASME, 2014.

[38] S. G. Goebel, N. Abuat, J. A. Lovett, and C. P Lee. "Measurements of combustor velocity and turbulence profiles". In: *American Society of Mechanical Engineers*. 93-GT-228. 1993.

[39] Boudier G., Gicquel L.Y.M., Poinsot T. J., Bissières D., and Bérat C. "LES predictions and validations of the exit temperature profiles in an industrial combustion chamber". In: *1st Workshop INCA*. SNECMA, Villaroche, France, 2005, pp. 113–120.

[40] A.F. Bicen, D.G.N. Tse, and J.H. Whitelaw. "Combustion characteristics of a model can-type combustor". In: *Combustion and Flame* 80.2 (1990), pp. 111 –125.

[41] G. Boudier, L.Y.M. Gicquel, T. J. Poinsot, D. Bissières, and C. Bérat. "Comparison of LES, RANS and Experiments in an Aeronautical Gas Turbine Combustion Chamber". In: *Proc. of the Combustion Institute* 31.2 (2007), pp. 3075–3082.

[42] S. James, J. Zhu, and M. S. Anand. "Large-Eddy Simulations as a Design Tool for Gas Turbine Combustion Systems". In: *AIAA Journal* 44.4 (2006), pp. 674–686.

[43] Parviz Moin and Sourabh V. Apte. "Large-Eddy Simulation of Realistic Gas Turbine Combustors". In: *AIAA Journal* 44.4 (2006), pp. 698–708.

[44] D. J. Dorney, K. L. Gundy-Burlet, and D. L. Sondak. "A survey of hot streak experiments and simulations". In: *International Journal of Turbo and Jet Engines* 16.1 (1999), pp. 1–15.

[45] M. A. Hilditch, A. Fowler, T. V. Jones, K. S. Chana, M. L. G. Oldfield, R. W. Ainsworth, S. I. Hogg, S. J. Anderson, and G. C. Smith. "Installation of a turbine stage in the Pyestock isentropic light piston facility". In: *American Society of Mechanical Engineers*. 1994, pp. 1–9.

[46] K. S. Chana, J. Hurrion, and T. Jones. "The Design, Development and Testing of a Non-Uniform Inlet Temperature Generator for the QinetiQ Transient Turbine Research Facility". In: *ASME Conference Proceedings* 2003.36894 (2003), pp. 273–280.

[47] R. G. Stabe, W. J. Whitney, and T. P. Moffitt. *Performance of a high-work low aspect ration turbine tested with a realistic inlet radial temperature profile*. Tech. rep. NASA-TM-83655, AIAA PAPER 84-1161. NASA Glenn Research Center, 1984.

[48] W. J. Whitney, R. G. Stabe, and T. P. Moffitt. *Description of the warm core turbine facility and the warm annular cascade facility recently installed at NASA Lewis Research Center*. Tech. rep. 81A34158. NASA Glenn Research Center, 1980.

[49] D.J. Dorney and K.L. Gundy-Burlet. "Effects of hot streak shape on rotor heating in a high-subsonic single-stage turbine". In: *International Journal of Turbo and Jet Engines* 18.1 (2001), pp. 15–29.

[50] H. D. Joslyn and R. P. Dring. "A Trace Gas Technique to Study Mixing in a Turbine Stage". In: *Journal of Turbomachinery* 110.1 (1988), pp. 38–43.

[51] D. Joslyn and R. Dring. "Three-Dimensional Flow in an Axial Turbine: Part 1—Aerodynamic Mechanisms". In: *Journal of Turbomachinery* 114.1 (1992), pp. 61–70.

[52] D. Joslyn and R. Dring. "Three-Dimensional Flow in an Axial Turbine: Part 2—Profile Attenuation". In: *Journal of Turbomachinery* 114.1 (1992), pp. 71–78.

[53] T. Butler, O. Sharma, H. Joslyn, and R. Dring. "Redistribution of an inlet temperature distortion in an axial flow turbine stage". In: *Journal of Propulsion and Power* 5.1 (1989), pages 64–71.

[54] R. J. Roback and R. P. Dring. "Hot Streaks and Phantom Cooling in a Turbine Rotor Passage: Part 1—Separate Effects". In: *Journal of Turbomachinery* 115.4 (1993), pp. 657–666.

[55] R. J. Roback and R. P. Dring. "Hot Streaks and Phantom Cooling in a Turbine Rotor Passage: Part 2—Combined Effects and Analytical Modeling". In: *Journal of Turbomachinery* 115.4 (1993), pp. 667–674.

[56] T. Shang. "Influence of inlet temperature distortion on turbine heat transfer". PhD thesis. Massachusetts Institute of Technology, Department of Aeronautics and Astronautics, 1995.

[57] T. Shang, Guenette G.R., A.H. Epstein, and A.P. Saxer. "The influence of inlet temperature distortion on rotor heat transfer in a transonic turbine". In: *AIAA Paper No. 95-3042* (1995).

[58] T. Shang and A.H. Epstein. "Analysis of hot streak effects on turbine rotor heat load". In: *Journal of Turbomachinery* 119.3 (1997), pp. 544–553.

[59] T. Povey and I. Qureshi. "A hot-streak (combustor) simulator suited to aerodynamic performance measurements". In: *Proceedings of the Institution of Mechanical Engineers, Part G: Journal of Aerospace Engineering* 222.6 (2008), pp. 705–720.

[60] R. M. Mathison, C. W. Haldeman, and M. G. Dunn. "Aerodynamics and heat transfer for a cooled one and one-half stage high-pressure turbine-part I: Vane inlet temperature profile generation and migration". In: *Journal of Turbomachinery* 134.1 (2012).

[61] C. M. Cha, S. Hong, P. T. Ireland, P. Denman, and V. Savarianandam. "Experimental and Numerical Investigation of Combustor-Turbine Interaction Using an Isothermal, Nonreacting Tracer". In: *Journal of Engineering for Gas Turbines and Power* 134.8 (2012), pp. 081501–081501.

[62] T. Povey, K. S. Chana, and T. V. Jones. "Heat transfer measurements on an intermediate-pressure nozzle guide vane tested in a rotating annular turbine facility, and the modifying effect of a non-uniform inlet temperature profile". In: *Proceedings of the Institution of Mechanical Engineers, Part A: Journal of Power and Energy* 217.4 (2003), pp. 421–432.

[63] T. Povey, K. S. Chana, T. V. Jones, and J. Hurrion. "The effect of hot-streaks on HP vane surface and endwall heat transfer: An experimental and numerical study". In: *Journal of Turbomachinery* 129.1 (2007), pp. 32–43.

[64] S. Salvadori, F. Montomoli, F. Martelli, Kam S. Chana, I. Qureshi, and T. Povey. "Analysis on the effect of a nonuniform inlet profile on heat transfer and fluid flow in turbine stages". In: *Journal of Turbomachinery* 134.1 (2011).

[65] I. Qureshi, A. Beretta, and T. Povey. "Effect of simulated combustor temperature nonuniformity on HP vane and end wall heat transfer: An experimental and computational investigation". In: *Journal of Engineering for Gas Turbines and Power* 133.3 (2011).

[66] R. J. Anthony and J. P. Clark. "A review of the AFRL turbine research facility". In: *ASME Turbo Expo 2013: Turbine Technical Conference and Exposition*. GT2013-94741. 2013.

[67] R. M. Mathison, C. W. Haldeman, and M. G. Dunn. "Heat transfer for the blade of a cooled stage and one-half high-pressure turbine-Part I: Influence of cooling variation". In: *Journal of Turbomachinery* 134.3 (2011).

[68] R. M. Mathison, C. W. Haldeman, and M. G. Dunn. "Heat Transfer for the Blade of a Cooled Stage and One-Half High-Pressure Turbine—Part II: Independent Influences of Vane Trailing Edge and Purge Cooling". In: *Journal of Turbomachinery* 134.3 (2012), p. 031015.

[69] R. M. Mathison, C. W. Haldeman, and M. G. Dunn. "Aerodynamics and heat transfer for a cooled one and one-half stage high-pressure turbine-Part II: Influence of inlet temperature profile on blade row and shroud". In: *Journal of Turbomachinery* 134.1 (2012).

[70] R. M. Mathison, C. W. Haldeman, and M. G. Dunn. "Aerodynamics and heat transfer for a cooled one and one-half stage high-pressure turbine-part III: Impact of hot streak characteristics on blade row heat flux". In: *Journal of Turbomachinery* 134.1 (2012).

[71] C.W. Haldeman, R.M. Mathison, and Dunn M.G. "Design, Construction, and Operation of a Combustor Emulator for Short-Duration High-Pressure Turbine Experiments". In: *AIAA Paper No. 2004-3829* (2004).

[72] C.W. Haldeman, M.G. Dunn, and R.M. Mathison. "Fully cooled single stage HP transonic turbine-part I: Influence of cooling mass flow variations and inlet temperature profiles on blade internal and external aerodynamics". In: *Journal of Turbomachinery* 134.3 (2011).

[73] C.W. Haldeman, M.G. Dunn, and R.M. Mathison. "Fully Cooled Single Stage HP Transonic Turbine—Part II: Influence of Cooling Mass Flow Changes and Inlet Temperature Profiles on Blade and Shroud Heat-Transfer". In: *Journal of Turbomachinery* 134.3 (2012), p. 031011.

[74] J. Nickol, R. M. Mathison, M. Malak, R. Rana, and J. S. Liu. "Time-resolved heat transfer and surface pressure measurements for a fully-cooled transonic turbine stage". In: *ASME Turbo Expo 2014: Turbine Technical Conference and Exposition*. Ed. by ASME. GT2014-26407. ASME, 2014.

[75] C. M. Cha, S. Hong, P. T. Ireland, P. Denman, and V. Savarianandam. "Turbulence levels are high at the combustor-turbine interface". In: *ASME Turbo Expo 2012: Turbine Technical Conference and Exposition*. GT2012-69130. 2012.

[76] S. Jenkins, K. Varadarajan, and D. G. Bogard. "The effects of high mainstream turbulence and turbine vane film cooling on the dispersion of a simulated hot streak". In: *Journal of Turbomachinery* 126.1 (2004), pp. 203–211.

[77] S. Jenkins and D. G. Bogard. "The effects of the vane and mainstream turbulence level on hot streak attenuation". In: *Journal of Turbomachinery* 127.1 (2005), pp. 215–221.

[78] S. Luque, V. Kanjirakkad, I. Aslanidou, R. Lubbock, and B. Rosic. "A new experimental facility to investigate combustor-turbine interactions in gas turbines with multiple can combustors". In: *ASME Turbo Expo 2014: Turbine Technical Conference and Exposition*. GT2014-26987. 2014.

[79] J.L. Kerrebrocke and A.A. Mikolajczak. "Intra Stator Transport of Rotor Wakes and Its Effect on Compressor Performance". In: *Journal of Engineering for Power* 92 (1970).

[80] L. He, V. Menshikova, and B. R. Haller. "Effect of hot-streak counts on turbine blade heat load and forcing". In: *Journal of Propulsion and Power* 23.6 (2007), pp. 1235–1241.

[81] A. Rahim, L. He, and E. Romero. "Rotor blade heat transfer characteristics for high pressure turbine stage under inlet temperature and velocity traverses". In: *ASME Turbo Expo 2014: Turbine Technical Conference and Exposition*. GT2014-26832. 2014.

[82] W. F. Colban, A. T. Lethander, and K. A. Thole. "Combustor turbine interface studies - part 2: flow and thermal field measurements". In: *Journal of Turbomachinery* (2003).

[83] S. Nasir, J.S. Carullo, W.N. Karen, A. Thole, H.W. Luzeng, J. Zhang, and H.K. Moon. "Effects of Large Scale High Freestream Turbulence and Exit Reynolds Number on Turbine Vane Heat Transfer in a Transonic Cascade". In: *Journal of Turbomachinery* 131 (2009).

[84] F.E. Ames. "The Influence of Large-Scale High Intensity Turbulence on Vane Heat Transfer". In: *Journal of Turbomachinery* 119 (1997).

[85] Q. Zhang, L. He, and A. Rawlinson. "Effects of Inlet Turbulence and End-Wall Boundary Layer on Aerothermal Performance of a Transonic Turbine Blade Tip". In: *Journal of Engineering for Gas Turbines and Power* 136.5 (Jan. 2014), pp. 052603–052603.

[86] R. W. Radomsky and K. A. Thole. "Flowfield Measurements for a Highly Turbulent Flow in a Stator Vane Passage". In: *Journal of Turbomachinery* 122.2 (1999), pp. 255–262.

[87] J. U. Schluter, H. Pitsch, and P. Moin. "Consistent Boundary Conditions for Integrated LES/RANS Simulations: LES Outflow Conditions". In: *32nd AIAA Fluid Dynamics Conference and Exhibit*. AIAA 2002-3121. 2002.

[88] J. U. Schluter, H. Pitsch, and P. Moinz. "Boundary conditions for LES in coupled simulations". In: *41st Aerospace Sciences Meeting and Exhibit*. AIAA 2003-69. 2003.

[89] JU Schluter, H. Pitsch, S. Shankaran, S. Kim, JJ Alonso, and P. Moin. "Integration of RANS and LES Flow Solvers for Simultaneous Flow Computations". In: *41st Aerospace Sciences Meeting and Exhibit*. AIAA 2003-85. 2003.

[90] J. U. Schluter, X. Wu, S. Kim, J. J. Alonso, and H. Pitsch. "Integrated RANS-LES Computations in Gas Turbines: Compressor-Diffusor Coupling". In: *42nd Aerospace Sciences Meeting and Exhibit Conference*. AIAA 2004-0369. 2004.

[91] J. U. Schluter, X. Wuy, E. Weidez, S. Hahnx, J. J. Alonso, and H. Pitschk. "Multi-Code Simulations: A Generalized Coupling Approach". In: *17th AIAA Computational Fluid Dynamics Conference*. AIAA 2005-4997. 2005.

[92] E. Collado Morata. "Impact of the unsteady aerothermal environment on the turbine blades temperature". PhD thesis. Université de Toulouse - MeGeP - Dynamique des Fluides, 2012.

[93] S. Salvadori, R. Giovanni, M. Insinna, and F. Martelli. "Analysis of Combustor/Vane Interaction With Decoupled and Loosely Coupled Approaches". In: *ASME Turbo Expo 2012: Turbine Technical Conference and Exposition*. GT2012-69038. ASME, 2012.

[94] M. Insinna, S. Salvadori, and F. Martelli. "Simulation of combustor/NGV interaction using coupled RANS solvers: validation and application to a realistic test case". In: *ASME Turbo Expo 2014: Turbine Technical Conference and Exposition*. GT2014-25433. 2014.

[95] S. Roux, M. Cazalens, and T. Poinsot. "Outlet-Boundary-Condition Influence for Large Eddy Simulation of Combustion Instabilities in Gas Turbines". In: *Journal of Propulsion and Power* 24.3 (2008).

[96] Service Méthodes et Outils Turbomeca. *Transport de FRT dans un distributeur de turbine HP (MACAO lot 310)*. Unpublished Internal Report AA052304. Turbomeca (SAFRAN group), 2009.

[97] E.V. Klapdor. "Towards investigation of combustor turbine interaction in an integrated simulation". In: GT2010-22933. ASME Turbo expo 2010. ASME, 2010.

[98] E. Motheau. "Accounting for mean flow effects in a zero-Mach number thermo-acoustic solver: Application to entropy induced combustion instabilities". PhD thesis. Université de Toulouse - MeGeP - Dynamique des Fluides, 2013.

[99] F. E. Marble and S. Candel. "Acoustic disturbances from gas nonuniformities convected through a nozzle". In: *Journal of Sound and Vibration* 55 (1977), pp. 225–243.

[100] N. A. Cumpsty and F. E. Marble. "The interaction of entropy fluctuations with turbine blade rows; a mechanism of turbojet engine noise". In: *Proceedings of the Royal Society A* 357 (1977), pp. 323–344.

[101] M. Leyko. "Mise en oeuvre et analyse de calculs aéroacoustiques de type SGE pour la prévision du bruit de chambres de combustion aéronautiques". PhD thesis. Institut de Mathématiques et de Modélisation de Montpellier - UM2, 2010.

[102] T. Livebardon, S. Moreau, Laurent Gicquel, T. J. Poinsot, and E. Bouty. "Combustion noise in a helicopter engine: Numerical investigations and experimental validations". In: *Combustion and Flame* (submitted).

[103] G. Caciolli. "A close investigation on the aerothermal behaviour of modern aeroengine combustors". PhD thesis. Università degli Studi di Firenze - School of Engineering - Department of Industrial Engineering of Florence, 2014.

[104] J.M. Beér and N.A. Chigier. *Combustion aerodynamics*. Halsted Press Division, Wiley, 1972.

[105] S. Mendez and F. Nicoud. "Adiabatic homogeneous model for flow around a multiperforated plate". In: *AIAA Journal* 46.10 (2008), pp. 2623–2633.

[106] T.J Poinsot and S.K Lele. "Boundary conditions for direct simulations of compressible viscous flows". In: *Journal of Computational Physics* 101.1 (1992), pp. 104 –129.

[107] C. S. Yoo and H. G. Im. "Characteristic boundary conditions for simulations of compressible reacting flows with multi-dimensional, viscous and reaction effects". In: *Combustion Theory and Modelling* 11.2 (2007), pp. 259–286.

[108] T. Schoenfeld and M. Rudgyard. "Steady and Unsteady Flows Simulations Using the Hybrid Flow Solver AVBP". In: *AIAA Journal* 37.11 (1999), pp. 1378–1385.

[109] P. Quillatre. "Simulation aux grandes échelles d'explosions en domaine semi-confiné". PhD thesis. Université de Toulouse - MeGeP - Dynamique des Fluides, 2014.

[110] O. Colin and M. Rudgyard. "Development of High-Order Taylor–Galerkin Schemes for LES". In: *Journal of Computational Physics* 162.2 (2000), pp. 338 –371.

[111] J. Smagorinsky. "General circulation experiments with the primitive equations: 1. The basic experiment". In: *Monthly Weather Review* 91 (1963), pp. 99–164.

[112] N Syred and JM Beer. "Combustion in swirling flows: a review". In: *Combustion and Flame* 23.2 (1974), pp. 143–201.

[113] J.L. Xia, G. Yadigaroglu, Y.S. Liu, J. Schmidli, and B.L. Smith. "Numerical and experimental study of swirling flow in a model combustor". In: *International Journal of Heat and Mass Transfer* 41.11 (1998), pp. 1485 –1497.

[114] Aldo Coghe, Giulio Solero, and Gianfranco Scribano. "Recirculation phenomena in a natural gas swirl combustor". In: *Experimental thermal and fluid science* 28.7 (2004), pp. 709–714.

[115] Ying Huang and Vigor Yang. "Effect of swirl on combustion dynamics in a lean-premixed swirl-stabilized combustor". In: *Proceedings of the Combustion Institute* 30.2 (2005), pp. 1775–1782.

[116] O Lucca-Negro and T O'Doherty. "Vortex breakdown: a review". In: *Progress in Energy and Combustion Science* 27.4 (2001), pp. 431 –481.

[117] N Syred and JM Beer. "Vortex core precession in high swirl flows". In: *Fluid machinery and fluidics* (1972), pp. 111–120.

[118] Nicholas Syred. "A review of oscillation mechanisms and the role of the precessing vortex core (PVC) in swirl combustion systems". In: *Progress in Energy and Combustion Science* 32.2 (2006), pp. 93 –161.

[119] N. Syred and J.M. Beér. "The damping of precessing vortex cores by combustion in swirl generators". In: *Astronautica Acta* 17 (1972), pp. 783–801.

[120] N. Syred and J.M. Beér. "Vortex core precession in high swirl flows". In: *The Second International JSME Symposium on Fluid Machinery and Fluidics*. Vol. 2. 1972.

[121] Dombard J., Poinsot T. J., Moureau V., Savary N., Staffelbach G., and Bodoc V. "Experimental and numerical study of the influence of small geometrical modifications on the dynamics of swirling flows". In: *Proceedings of the 2012 Summer Program*. Center for Turbulence Research, NASA AMES, Stanford University, USA, 2012, pp. 469 –482.

[122] J.-L. Champion. "Etude expérimentale des films pariétaux de refroidissement produits par une paroi multiperforée - cas des conditions de fonctionnement des chambres de combustion de moteurs aéronautiques". PhD thesis. Poitiers, 1997.

[123] K. Oberleithner, S. Terhaar, L. Rukes, and O. Paschereit. "Why Nonuniform Density Suppresses the Precessing Vortex Core". In: *Journal of Engineering for Gas Turbines and Power* 135.12 (Sept. 2013).

[124] A. Andreini, B. Facchini, M. Insinna, L. Mazzei, and S. Salvadori. "Hybrid RANS-LES modeling of a hot streak generator oriented to the study of combustor-turbine interaction". In: *ASME Turbo Expo 2015: Turbine Technical Conference and Exposition*. GT2015-42402. 2015.

[125] P. Sagaut. *Large Eddy Simulation for Incompressible Flows: An Introduction*. Scientific Computation. Springer, 2006.

[126] M. Germano, U. Piomelli, P. Moin, and W. Cabot. "A dynamic subgrid-scale eddy viscosity model". In: *Physics of Fluids A: Fluid Dynamics (1989-1993)* 3.7 (1991), pp. 1760–1765.

[127] F. Ducros, F. Nicoud, and T. J. Poinsot. "Wall-Adapting Local Eddy-Viscosity models for simulations in complex geometries". In: *ICFD*. Ed. by Baines M. J. Oxford University Computing Lab., UK, 1998, pp. 293–300.

[128] S.B. Pope. "Ten questions concerning the large-eddy simulation of turbulent flows". In: *New Journal of Physics* 6.1 (2004), p. 35.

[129] I. B. Celik, Z. N. Cehreli, and I. Yavuz. "Index of Resolution Quality for Large Eddy Simulations". In: *Journal of Fluids Engineering* 127.5 (Sept. 2005), pp. 949–958.

[130] A.C. Nix, A.C. Smith, T.E. Diller, W.F. Ng, and K.A. Thole. "High intensity, large length-scale freestream turbulence generation in a transonic turbine cascade". In: *ASME Turbo Expo 2002: Turbine Technical Conference and Exposition*. GT2002-30523. 2002.

[131] R. J. Volino, M. P. Schultz, and K. A. Flack. "Turbulence structure in rough- and smooth-wall boundary layers". In: *Journal of Fluid Mechanics* 592 (Dec. 2007), pp. 263–293.

[132] F. Coletti, I. Cresci, and T. Arts. "Time-Resolved PIV Measurements of Turbulent Flow in Rotating Rib-Roughened Channel With Coriolis and Buoyancy Forces". In: *ASME Turbo Expo 2012: Turbine Technical Conference and Exposition*. GT2012-69406. 2012.

[133] J.M. Mendel. *Lessons in Estimation Theory for Signal Processing, Communications, and Control*. Pearson Education, 1995.

[134] F. M. Dekking. *A modern introduction to probability and statistics : understanding why and how*. Springer, 2005.

[135] S. S. Girimaji. "Assumed $\beta$-PDF Model for Turbulent Mixing: Validation and Extension to Multiple Scalar Mixing". In: *Combustion Science and Technology* 78.4-6 (1991), pp. 177–196.

[136] R. L. Gaffney Jr, J. A. White, S. S. Girimaji, and J. P. Drummond. "Modeling temperature and species fluctuations in turbulent, reacting flow". In: *Computing Systems in Engineering* 5.2 (Apr. 1994), pp. 117–133.

[137] J. Bakosi and J. R. Ristorcelli. "Exploring the beta distribution in variable-density turbulent mixing". In: *Journal of Turbulence* 11.37 (2010), pp. 1–31.

[138] D. N. Joanes and C. A. Gill. "Comparing Measures of Sample Skewness and Kurtosis". English. In: *Journal of the Royal Statistical Society. Series D (The Statistician)* 47.1 (1998), pp. 183–189.

[139] Dragan Dorić, Emilija Nikolić-Dorić, Vesna Jevremović, and Jovan Malisić. "On measuring skewness and kurtosis". English. In: *Quality and Quantity* 43.3 (2009), pp. 481–493.

[140] Kevin P. Balanda and H. L. MacGillivray. "Kurtosis: A Critical Review". English. In: *The American Statistician* 42.2 (1988), pp. 111–119.

[141] Jr. L. H. Smith. "The Radial-Equilibrium Equation of Turbomachinery". In: *Journal of Engineering for Power* 88.1 (1966), pp. 1–12.

[142] Chung-Hua Wu and Lincoln Wolfenstein. "Application of radial-equilibrium condition to axial-flow compressor and turbine design". eng. In: (1949), p. 101.

[143] R. Negru, S. Muntean, L. Marsavina, R. Susan-Resiga, and N. Pasca. "Computation of stress distribution in a Francis turbine runner induced by fluid flow". In: *Computational Materials Science* 64.0 (2012), pp. 253 –259.

[144] V.K. Garg. "Heat transfer on a film-cooled rotating blade using different turbulence models". In: *International Journal of Heat and Mass Transfer* 42.5 (1999), pp. 789 –802.

[145] V.K. Garg. "Heat transfer on a film-cooled rotating blade". In: *International Journal of Heat and Fluid Flow* 21.2 (2000), pp. 134 –145.

[146] J.P. Solano, V. Pinilla, G. Paniagua, S. Lavagnoli, and T. Yasa. "Aerothermal investigation of a multi-splitter axial turbine". In: *International Journal of Heat and Fluid Flow* 32.5 (2011), pp. 1036 –1046.

[147] C. S. Yoo, Y. Wang, A. Trouvé, and H. G. Im. "Characteristic boundary conditions for direct simulations of turbulent counterflow flames". In: *Combustion Theory and Modelling* 9.4 (2005), pp. 617–646.

[148] W. F. Colban, K. A. Thole, and G. Zess. "Combustor turbine interface studies - part 1: endwall effectiveness measurements". In: *Journal of Turbomachinery* (2003).

[149] M. Gad-el Hak. "Questions in Fluid Mechanics: Stokes' Hypothesis for a Newtonian, Isotropic Fluid". In: *Journal of Fluids Engineering* 117.1 (Mar. 1995), pp. 3–5.

[150] W. Sutherland. "LII. The viscosity of gases and molecular force". In: *Philosophical Magazine Series 5* 36.223 (1893), pp. 507–531.

[151] W. M. Kays. "Turbulent Prandtl Number—Where Are We?" In: *Journal of Heat Transfer* 116.2 (1994), pp. 284–295.

[152] P. Moin, K. Squires, W. Cabot, and S. Lee. "A dynamic subgrid-scale model for compressible turbulence and scalar transport". In: *Physics of Fluids* 3 (Nov. 1991), pp. 2746–2757.

[153] H. Baya Toda. “Modélisation LES et étude expérimentale des écoulements pariétaux en géométries complexes”. PhD thesis. Université de Montpellier 2 - Institut de Mathématiques et de Modélisation, 2011.

[154] R. Bhaskaran. “Large eddy simulation of a high pressure turbine cascade.” PhD thesis. Stanford University, 2010.

[155] D. K. Lilly. “A proposed modification of the Germano subgrid,Äêscale closure method”. In: *Physics of Fluids A: Fluid Dynamics (1989-1993)* 4.3 (1992), pp. 633–635.

[156] Moureau V., Lartigue G., Sommerer Y., Angelberger C., Colin O., and Poinsot T. J. “Numerical methods for unsteady compressible multi-component reacting flows on fixed and moving grids”. In: *Journal of Computational Physics* 202.2 (2005). jx, pp. 710–736.

[157] K. Truffin. “Simulation aux grandes échelles et identification acoustique des turbines à gaz en régime partiellement premélangé.” PhD thesis. Université de Toulouse - MeGeP - Dynamique des Fluides, 2005.

[158] Gicquel L.Y.M., Cuenot B., Staffelbach G., Vermorel O., Riber E., Dauptain A., and Poinsot T. J. “Panel Session 4-34 - LES Modeling of Combustors: CERFACS Perspective - Invited conference”. In: *ASME Turbo-Expo*. conf. Vancouver, Canada, 2011.

[159] P. Lax and B. Wendroff. “Systems of conservation laws”. In: *Communications on Pure and Applied Mathematics* 13.2 (1960), pp. 217–237.

[160] N. Lamarque. “Schémas numériques et conditions limites pour la simulation aux grandes échelles de la combustion diphasique dans les foyers d’hélicoptère”. PhD thesis. Université de Toulouse - MeGeP - Dynamique des Fluides, 2007.

[161] J. Donea, L. Quartapelle, and V. Selmin. “An analysis of time discretization in the finite element solution of hyperbolic problems”. In: *Journal of Computational Physics* 70.2 (1987), pp. 463 –499.

[162] T. K. Sengupta, G. Ganerwal, and A. Dipankar. “High Accuracy Compact Schemes and Gibbs’ Phenomenon”. English. In: *Journal of Scientific Computing* 21.3 (2004), pp. 253–268.